

**APPENDIX A**  
**DRIFT DEGRADATION ANALYSIS COMPUTER FILES**



## DRIFT DEGRADATION ANALYSIS COMPUTER FILES

The computer files developed for this model report can be accessed through the Technical Data Management System (TDMS) (DTN: MO0408MWDDDMIO.002), and include the inputs and outputs for the following computer rendered simulations:

- 3DEC Inputs & Outputs
- DRKBA Inputs & Outputs
- EarthVision Inputs & Outputs
- FLAC 3D Inputs & Outputs
- FLAC Inputs & Outputs
- FracMan Inputs & Outputs
- NUFT Inputs & Outputs
- PFC Inputs & Outputs
- UDEC Inputs & Outputs.

Archive file descriptions are provided in DTN: MO0408MWDDDMIO.002 for each software item to explain the format of the input and output sub-directories within the DTN.

Calculation files were developed in this model report to perform support calculation activities as described in Section 6.2, Section 6.3, Section 6.4, and associated appendices. These calculations use the standard functions of commercial off-the-shelf software, including both Microsoft Excel 97 SR-2 and Mathcad 2001i Professional. Additionally, DIPS Version 4.03 (see Section 3.2) was used for graphical presentation of fracture data. Table A-1 provides a listing of the calculation files, including the location in this report where specific details of the calculation can be found. The calculation files listed in Table A-1 can be accessed through the TDMS (DTN: MO0408MWDDDMIO.002).

Microsoft Excel 97 SR-2 and Mathcad 2001i Professional were used to perform support calculations to process the nonlithophysal rockfall output from 3DEC for preclosure ground motion ( $1 \times 10^{-4}$  annual probability of exceedance). Excel was used to tabulate the rockfall results, including rock block velocity and impact location. Mathcad was used to calculate the impact bounding velocity for preclosure rockfall. The results from nonlithophysal rockfall analyses with  $1 \times 10^{-4}$  ground motion can be accessed through the TDMS (DTN: MO0408MWDRNLRA.002). Excel was also used to perform support calculations to process the nonlithophysal rockfall output from 3DEC for postclosure ground motions, including  $1 \times 10^{-5}$ ,  $1 \times 10^{-6}$ , and  $1 \times 10^{-7}$  annual probabilities of exceedance. Excel was used to tabulate the rockfall results, calculate the rockfall mass, velocity, impact angle, impact momentum, and impact energy associated with each rock block. These files can be accessed through the TDMS (DTN: MO0408MWDDDMIO.002).

Output files for drift profile prediction and degraded rock mass characteristics in lithophysal units can be accessed through the TDMS (DTN: MO0306MWDDPPDR.000). Input and output files for 3DEC rockfall analyses using  $1 \times 10^{-4}$  ground motion are provided in DTN: MO0404MWD3DRFA.000. Drip shield load results are provided in DTN: MO0407MWDDSLCR.000. The profile of thermal stresses at different times after waste emplacement (extracted from FLAC 3D) is provided in DTN: MO0407SPAMTSHR.000. Intact rock properties used in parts of the drift degradation analyses are summarized in DTN: MO0403MWDRPNLR.000.

Table A-1. List of Drift Degradation Calculation Files

File Name	File Type	Brief Description	References
<i>3DEC lith analysis results.xls</i>	Microsoft Excel 97 SR-2	Calculation file to tabulate the rockfall results for the 3DEC lithophysical rockfall analysis (Section 6.4.3)	N/A
<i>impact velocity bounding cal for preclosure rockfall rev1.mcd</i>	Mathcad 2001i Professional	Calculation file to determine the bounding impact velocity for preclosure rockfall (Section 6.3.1.2.6)	BSC 2004 [DIRS 168489], BSC 2004 [DIRS 169503], BSC 2004 [DIRS 169472], Dowding 1979 [DIRS 101977]
<i>nonlith 1e-4 motion sufficiency study.xls</i>	Microsoft Excel 97 SR-2	Calculation file to determine the number of simulation sufficient for rockfall analyses (Appendix K)	N/A
<i>nonlith 1e-5 motion sufficiency study.xls</i>	Microsoft Excel 97 SR-2	Calculation file to determine the number of simulation sufficient for rockfall analyses (Appendix K)	N/A
<i>nonlith 1e-6 motion sufficiency study.xls</i>	Microsoft Excel 97 SR-2	Calculation file to determine the number of simulation sufficient for rockfall analyses (Appendix K)	N/A
<i>nonlith 1e-7 motion sufficiency study.xls</i>	Microsoft Excel 97 SR-2	Calculation file to determine the number of simulation sufficient for rockfall analyses (Appendix K)	N/A
<i>nonlith rockfall characteristics in emplacement drifts with 1e-4 gm.xls</i>	Microsoft Excel 97 SR-2	Calculation file to tabulate the rockfall results, calculate the rockfall mass, velocity, impact angle, impact momentum, and impact energy associated with each rock block. These data are for preclosure ground motion with an annual probability of exceedance of $1 \times 10^{-4}$ (Section 6.3.1.2.6)	N/A

Table A-1. List of Drift Degradation Calculation Files (Continued)

File Name	File Type	Brief Description	References
<i>nonlith rockfall characteristics in emplacement drifts with 1e-5 gm.xls</i>	Microsoft Excel 97 SR-2	Calculation file to tabulate the rockfall results, calculate the rockfall mass, velocity, impact angle, impact momentum, and impact energy associated with each rock block. These data are for preclosure ground motion with an annual probability of exceedance of $1 \times 10^{-5}$ (Section 6.3.1.2.3)	N/A
<i>nonlith rockfall characteristics in emplacement drifts with 1e-6 gm.xls</i>	Microsoft Excel 97 SR-2	Calculation file to tabulate the rockfall results, calculate the rockfall mass, velocity, impact angle, impact momentum, and impact energy associated with each rock block. These data are for preclosure ground motion with an annual probability of exceedance of $1 \times 10^{-6}$ (Section 6.3.1.2.4)	N/A
<i>nonlith rockfall characteristics in emplacement drifts with 1e-7 gm.xls</i>	Microsoft Excel 97 SR-2	Calculation file to tabulate the rockfall results, calculate the rockfall mass, velocity, impact angle, impact momentum, and impact energy associated with each rock block. These data are for preclosure ground motion with an annual probability of exceedance of $1 \times 10^{-7}$ (Section 6.3.1.2.5)	N/A
<i>Cavingnew.mcd</i>	Mathcad 2001i Professional	Calculation file for analytical solution for lithophysical rock mass degradation (Section 6.4.2.5).	N/A
<i>drift degradation-V1.xls</i>	Microsoft Excel 97 SR-2	Calculation file for summarizing drip shield pressure including both analytical and numerical solutions (Section 6.4.2).	N/A

Table A-1. List of Drift Degradation Calculation Files (Continued)

File Name	File Type	Brief Description	References
<i>FLAC drip shield pressures.xls</i>	Microsoft Excel 97 SR-2	Summary drip shield pressures calculated using FLAC (Section 6.4.2.5)	N/A
<i>UDEC drip shield pressures.xls</i>	Microsoft Excel 97 SR-2	Summary drip shield pressures calculated using UDEC (Section 6.4.2.5)	N/A
<i>Cohesion Degradation V1.xls</i>	Microsoft Excel 97 SR-2	Calculation file for cohesion degradation due to time and thermal effects. Application: DRKBA analyses of nonlithophysal rock. Calculation details provided in Appendix D (Section D5).	N/A
<i>exca vectors V2.xls</i>	Microsoft Excel 97 SR-2	Calculation file for plane equations to describe the 5.5-m-diameter excavation opening. Application: DRKBA analyses of nonlithophysal rock. Calculation details provided in Appendix D (Section D10).	N/A
<i>mcs sensitivity study Tptpmn V1.xls</i>	Microsoft Excel 97 SR-2	Calculation file for rock blocks cumulative frequency of occurrence, Monte Carlo simulations varied. Application: DRKBA analyses of nonlithophysal rock. Calculation details provided in Appendix D (Section D8).	N/A
<i>New_Beta_Tptpmn V1.xls</i>	Microsoft Excel 97 SR-2	Calculation file for beta distribution parameters (a, b, p, q) for joint spacing, trace length, and location. Application: DRKBA analyses of nonlithophysal rock. Calculation details provided in Appendix D (Section D7).	Derman, et al. 1973 [DIRS 108444]

Table A-1. List of Drift Degradation Calculation Files (Continued)

File Name	File Type	Brief Description	References
<i>New-K-Tptpmn V2.mcd</i>	Mathcad 2001i Professional	Calculation file for K factor of joint orientation. Application: DRKBA analyses of nonlithophysal rock. Calculation details provided in Appendix D (Section D7).	N/A
<i>Orient-Tptpmn .xls</i>	Microsoft Excel 97 SR-2	Calculation file for components for the orientation matrix. Application: DRKBA analyses of nonlithophysal rock. Calculation details provided in Appendix D (Section D7).	N/A
<i>Thermal curve V1.xls</i>	Microsoft Excel 97 SR-2	Calculation file for ratio of effective shear stress for thermal effect. Application: DRKBA analyses of nonlithophysal rock. Calculation details provided in Appendix D (Section D5).	N/A
<i>Time thermal cohesion degradation V1.mcd</i>	Mathcad 2001i Professional	Calculation file for cohesion degradation due to time and thermal effects. Application: DRKBA analyses of nonlithophysal rock. Calculation details provided in Appendix D (Section D5).	N/A
<i>tpmn seismic 75 res v2.xls</i>	Microsoft Excel 97 SR-2	Calculation file for rock blocks cumulative percentage of occurrence. Application: DRKBA analyses of nonlithophysal rock. Calculation details provided in Appendix D (Section D6).	N/A
<i>Tptpl/- FracMan Generated Fracture Data.xls</i>	Microsoft Excel 97 SR-2	Calculation file for converting FracMan fracture output to 3DEC input. Application: rockfall models. Calculation details provided in Appendix L.	N/A



Table A-1. List of Drift Degradation Calculation Files (Continued)

File Name	File Type	Brief Description	References
3DEC-S1shtA_TPO.xls	Microsoft Excel 97 SR-2	Calculation file for converting FracMan fracture output to 3DEC input. Application: rockfall models. Calculation details provided in Appendix L.	N/A
3DEC-S1shtB_TPO.xls	Microsoft Excel 97 SR-2	Calculation file for converting FracMan fracture output to 3DEC input. Application: rockfall models. Calculation details provided in Appendix L.	N/A
3DEC-s2sht_TPO.xls	Microsoft Excel 97 SR-2	Calculation file for converting FracMan fracture output to 3DEC input. Application: rockfall models. Calculation details provided in Appendix L.	N/A
3DEC-s3_sht_TPO.xls	Microsoft Excel 97 SR-2	Calculation file for converting FracMan fracture output to 3DEC input. Application: rockfall models. Calculation details provided in Appendix L.	N/A
3DEC-VPPLONG_TPO.xls	Microsoft Excel 97 SR-2	Calculation file for converting FracMan fracture output to 3DEC input. Application: rockfall models. Calculation details provided in Appendix L.	N/A
Drift Deg AMR AA PMap.xls	Microsoft Excel 97 SR-2	Calculation file for descriptive statistics for lithophysical abundance and lithophysical characteristics in the ECRB (Enhanced Characterization of the Repository Block) Cross-Drift. Application: lithophysical rockfall model. Calculation details provided in Appendix O (Section O6).	N/A

Table A-1. List of Drift Degradation Calculation Files (Continued)

File Name	File Type	Brief Description	References
<i>Drift Deg AMR AB A-Trav.xls</i>	Microsoft Excel 97 SR-2	Calculation file for descriptive statistics for lithophysal abundance and lithophysal characteristics in the ECRB Cross-Drift. Application: lithophysal rockfall model. Calculation details provided in Appendix O (Section O6).	GS021008314224.002 [DIRS 161910]
<i>Drift Deg AMR AC T-Trav.xls</i>	Microsoft Excel 97 SR-2	Calculation file for descriptive statistics for lithophysal abundance and lithophysal characteristics in the ECRB Cross-Drift. Application: lithophysal rockfall model. Calculation details provided in Appendix O (Section O6).	GS021008314224.002 [DIRS 161910]
<i>Drift Deg AMR AD L-Litho V1.xls</i>	Microsoft Excel 97 SR-2	Calculation file for descriptive statistics for lithophysal abundance and lithophysal characteristics in the ECRB Cross-Drift. Application: lithophysal rockfall model. Calculation details provided in Appendix O (Section O6).	GS021008314224.002 [DIRS 161910]
<i>Drift Deg AMR AE Mongano.xls</i>	Microsoft Excel 97 SR-2	Calculation file for descriptive statistics for lithophysal abundance and lithophysal characteristics in the ECRB Cross-Drift. Application: lithophysal rockfall model. Calculation details provided in Appendix O (Section O6).	Mongano et al 1999 [DIRS 149850]

Table A-1. List of Drift Degradation Calculation Files (Continued)

File Name	File Type	Brief Description	References
<i>Drift Deg AMR AF T-A-P Fit V1.xls</i>	Microsoft Excel 97 SR-2	Calculation file for descriptive statistics for lithophysical abundance and lithophysical characteristics in the ECRB Cross-Drift. Application: lithophysical rockfall model. Calculation details provided in Appendix O (Section O6).	GS021008314224.002 [DIRS 161910] GS040608314224.001 [DIRS 171367]
<i>lith porosity 3D.xls</i>	Microsoft Excel 97 SR-2	Calculation file for projecting lithophysical porosity in three dimensions. Application: lithophysical rockfall model. Calculation details provided in Appendix T.	N/A
<i>Lithophysical projection to vertical plane.xls</i>	Microsoft Excel 97 SR-2	Calculation file for projecting lithophysical porosity in three dimensions. Application: lithophysical rockfall model. Calculation details provided in Appendix T.	Buesch and Spengler 1998 [DIRS 101433], Buesch et al. 1996 [DIRS 100106], Mongano et al. 1999 [DIRS 149850]
<i>intact strength nonlith v2.xls</i>	Microsoft Excel 97 SR-2	Calculation file for intact rock strength parameters. Application: nonlithophysical rockfall model. Calculation details provided in Appendix E (Section E3).	MO031RCKPRPCS.003 [DIRS 166073], MO0401DQIRIRPTS.003 [DIRS 168905], MO0402DQIRIPPR.003 [DIRS 168901], SN0108SD821723.001 [DIRS 159959], SN0306L0207502.008 [DIRS 165015], SNL02030193001.004 [DIRS 108415], SNL02030193001.009 [DIRS 109614], SNL02030193001.012 [DIRS 108416], SNL02030193001.019 [DIRS 108431], SNL02030193001.020 [DIRS 108432], SNL02030193001.021 [DIRS 108433], SNL02030193001.023 [DIRS 108435], SNL02030193001.026 [DIRS 108436], SNSAND83164600.000 [DIRS 160009], SNSAND84110100.000 [DIRS 160016], SNSAND85070300.000 [DIRS 160020], SNSAND85070900.000 [DIRS 160022], SNSAND85076200.000 [DIRS 160024], SNSAND86113100.000 [DIRS 159594]
<i>joint strength v2.xls</i>	Microsoft Excel 97 SR-2	Calculation file for joint strength parameters. Application: nonlithophysical rockfall model. Calculation details provided in Appendix E (Section E2).	SNL02112293001.003 [DIRS 108412], Olsson and Brown 1997 [DIRS 106453], SNL02112293001.005 [DIRS 108413], SNL 1996 [DIRS 165408], SNL02112293001.007 [DIRS 108414], SNL 1996 [DIRS 165410], GS030283114222.001 [DIRS 161913], BSC 2003 [DIRS 166660], Sections 8.6.4 and 8.6.5)

Table A-1. List of Drift Degradation Calculation Files (Continued)

File Name	File Type	Brief Description	References
<i>rock mass strength v2.xls</i>	Microsoft Excel 97 SR-2	Calculation file for rock mass strength properties. Application: thermal-mechanical calculation and rockfall models. Calculation details provided in Appendix E (Section E4).	GS000608314224.005 [DIRS 166002], USGS 1996 [DIRS 169024]; GS000608314224.006 [DIRS 152572], USGS 1996 [DIRS 169029]; GS950508314224.003 [DIRS 107488], Singleton 1995 [DIRS 107044]; GS960408314224.001 [DIRS 168135], USGS 1996 [DIRS 169025]; GS960408314224.003 [DIRS 168136], USGS 1996 [DIRS 169026]; GS960708314224.009 [DIRS 168137], USGS 1996 [DIRS 169027]; GS960908314224.015 [DIRS 108372], USGS 1996 [DIRS 169030] and USGS 1996 [DIRS 169031]; GS960908314224.016 [DIRS 108373], USGS 1996 [DIRS 169032] and USGS 1996 [DIRS 169033]; GS960908314224.017 [DIRS 108376], USGS 1996 [DIRS 169034]; GS970108314224.002 [DIRS 107490], USGS 1996 [DIRS 169035]; GS970208314224.004 [DIRS 107492], USGS 1997 [DIRS 169036]; GS970608314224.007 [DIRS 158430], USGS 1997 [DIRS 169040]; GS970808314224.009 [DIRS 107494], USGS 1997 [DIRS 169037]; GS970808314224.011 [DIRS 107495], USGS 1997 [DIRS 169038]; GS970808314224.013 [DIRS 107497], USGS 1997 [DIRS 169039]; GS990408314224.003 [DIRS 108404], USGS 1999 [DIRS 169018]; GS990408314224.004 [DIRS 108405], USGS 1999 [DIRS 169019]; GS990408314224.005 [DIRS 108408], USGS 1999 [DIRS 169020]; GS990408314224.006 [DIRS 108409], USGS 1999 [DIRS 169021]; MO0004QGFMPIK.000 [DIRS 152554], MO0311RCKPRPCS.003 [DIRS 166073], Price et al. 1985 [DIRS 106602], SN0108SD821723.001 [DIRS 159959], SN0208F4102102.002 [DIRS 161874], SN0208L0207502.001 [DIRS 161871], SN0211L0207502.002 [DIRS 161872], SN0212F4102102.004 [DIRS 161875], SN0301F4102102.006 [DIRS 161876], SN0305L0207502.005 [DIRS 163373], SN0306L0207502.008 [DIRS 165015], SNL02030193001.001 [DIRS 120572], SNL02030193001.002 [DIRS 120575], SNL02030193001.003 [DIRS 120578], SNL02030193001.004 [DIRS 108415], SNL02030193001.005 [DIRS 122545], SNL02030193001.006 [DIRS 120579], SNL02030193001.007 [DIRS 120582], SNL02030193001.008 [DIRS 120597], SNL02030193001.012 [DIRS 108416], SNL02030193001.013 [DIRS 120614], SNL02030193001.014 [DIRS 109609], SNL02030193001.015 [DIRS 120617], SNL02030193001.016 [DIRS 120619], SNL02030193001.018 [DIRS 109611], SNL02030193001.019 [DIRS 108431], SNL02030193001.020 [DIRS 108432], SNL02030193001.021 [DIRS 108433], SNL02030193001.022 [DIRS 109613], SNL02030193001.023 [DIRS 108435], SNL02030193001.026 [DIRS 108436], SNSAND83164600.000 [DIRS 160009], SNSAND84110100.000 [DIRS 160016], SNSAND85070300.000 [DIRS 160020], SNSAND85070900.000 [DIRS 160022], SNSAND85076200.000 [DIRS 160024], SNSAND86113100.000 [DIRS 159594].
<i>thermal properties</i>	Microsoft Excel 97 SR-2	Calculation file for thermal	SN0307T0510902.003 [DIRS 164196], SN0303T0503102.008 [DIRS

Table A-1. List of Drift Degradation Calculation Files (Continued)

File Name	File Type	Brief Description	References
<i>TM units v2.xls</i>		properties. Application: thermal-mechanical calculation and rockfall models. Calculation details provided in Appendix D (Sections D1 and D5).	162401], SN0404T0503102.11 [DIRS 169129], SNL01B05059301.006, Brodsky et al. 1997. ([DIRS 100653], Table 4-4).
<i>lith-summary-062104.xls</i>	Microsoft Excel 97 SR-2	Summary of lithophysical rock properties. Application: lithophysical rockfall model. Calculation details provided in Appendix S.	Price et al. 1985 [DIRS 106602], SN0208L0207502.001 [DIRS 161871], SN0211L0207502.002 [DIRS 161872]
<i>modified lith-current.xls</i>	Microsoft Excel 97 SR-2	Summary of lithophysical rock properties. Application: lithophysical rockfall model. Calculation details provided in Appendix S.	Price et al. 1985 [DIRS 106602], SN0208L0207502.001 [DIRS 161871], SN0211L0207502.002 [DIRS 161872]
<i>Beta-small scale.xls</i>	Microsoft Excel 97.SR-2	Calculation file for beta distribution parameters (a, b, p, q) for joint spacing, trace length, and location. Application: DRKBA analysis of nonlithophysical rock. Calculation details provided in Appendix D (Section D7)	Derman, et al. 1973 [DIRS 108444]
<i>K-small scale.mcd</i>	Mathcad 2001i Professional	Calculation file for K factor of joint orientation. Application: DRKBA analyses of nonlithophysical rock. Calculation details provided in Appendix D (Section D7).	N/A
<i>small scale fractures results rev1.xls</i>	Microsoft Excel 97 SR-2	Calculation file for rock blocks cumulative percentage of occurrence. Application: DRKBA analyses of nonlithophysical rock. Calculation details provided in Appendix D.	N/A

Table A-1. List of Drift Degradation Calculation Files (Continued)

File Name	File Type	Brief Description	References
<i>small trace filtering.xls</i>	Microsoft Excel 97 SR-2	Calculation file for small-scale joint orientation data. Application: DRKBA analyses of nonlithophysal rock. Calculation details provided in Appendix D (Section D7).	N/A
<i>small.dip</i>	DIPS Version 4.03	Calculation file for the graphical presentation of fracture data. Application: DRKBA analyses of small trace length fracture data. Calculation details provided in Section 6.3.3 and Appendix D.	N/A
<i>Heat_Decay_Cal_L A1450.xls</i>	Microsoft Excel 97 SR-2	Calculation file for heat decay curves. Application: thermal-mechanical calculation. Calculation details provided in Section 6.2.	N/A
<i>LA1450_NUFT_Temp_crss-sctn3.xls</i>	Microsoft Excel 97 SR-2	Calculation file for temperature histories at the drift crown. Application: thermal-mechanical calculation. Calculation details provided in Section 6.2.	N/A
<i>LA1450_R5C10_NUFT_Temp_crss-sctn.xls</i>	Microsoft Excel 97 SR-2	Calculation file for temperature histories at the drift crown. Application: impact analyses on LDTH sub-model. Calculation details provided in Appendix Q (Section Q1).	N/A
<i>ground motion parameters.xls</i>	Microsoft Excel 97 SR-2	Summary of ground motion parameters (Sections 6.3.1.2.1, 6.4.2.2, and Appendix X)	MO0407TMHIS104.003 [DIRS 170599]; MO0306SDSAVDTH.000 [DIRS 164033]; MO0402AVDTM105.001 [DIRS 168890]; MO0403AVDSC106.001 [DIRS 168891]; MO0403AVTMH107.003 [DIRS 168892]; MO0301TMHIS106.001 [DIRS 161868]
<i>* power cal.mcd</i> (* represents multiple files with the ground motion set indicated)	Mathcad 2001i Professional	Calculation file for power spectral density using the fast Fourier transform function in Mathcad. Application: ground motion sensitivity (Section 6.4.2.2).	N/A

**APPENDIX B**  
**DEVELOPMENT OF JOINT DATA FOR THE TPTPLL ZONE**

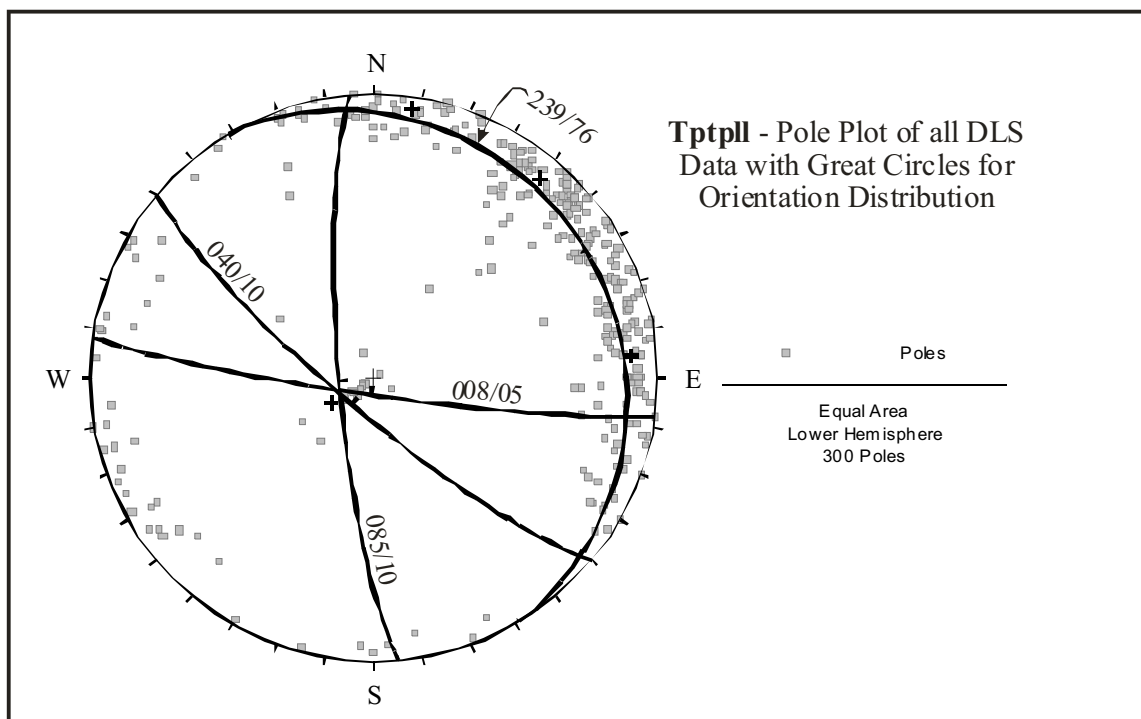




## DEVELOPMENT OF JOINT DATA FOR THE Tptpll ZONE

A description of the generation of representative rock volume using FracMan is presented in Section 6.1.6. This appendix provides details for the development of FracMan rock volume for the Tptpll (lithophysal rock) zone. The FracMan output data for this zone is provided in the file *Tptpll-Fracman Generated Fracture Data.xls* (Table A-1).

To begin the analysis of the Tptpll, the observed vapor-phase partings are identified in the detailed line survey data. This is done by sorting the observed data with respect to dip and identifying those fractures that have a dip of less than 45 degrees. For the Tptpll there are 20 vapor-phase partings. The mean pole orientation is 239/76. Figure B-1 shows the Great Circle for the mean orientation of the vapor-phase partings. The poles for the other sets are also plotted.

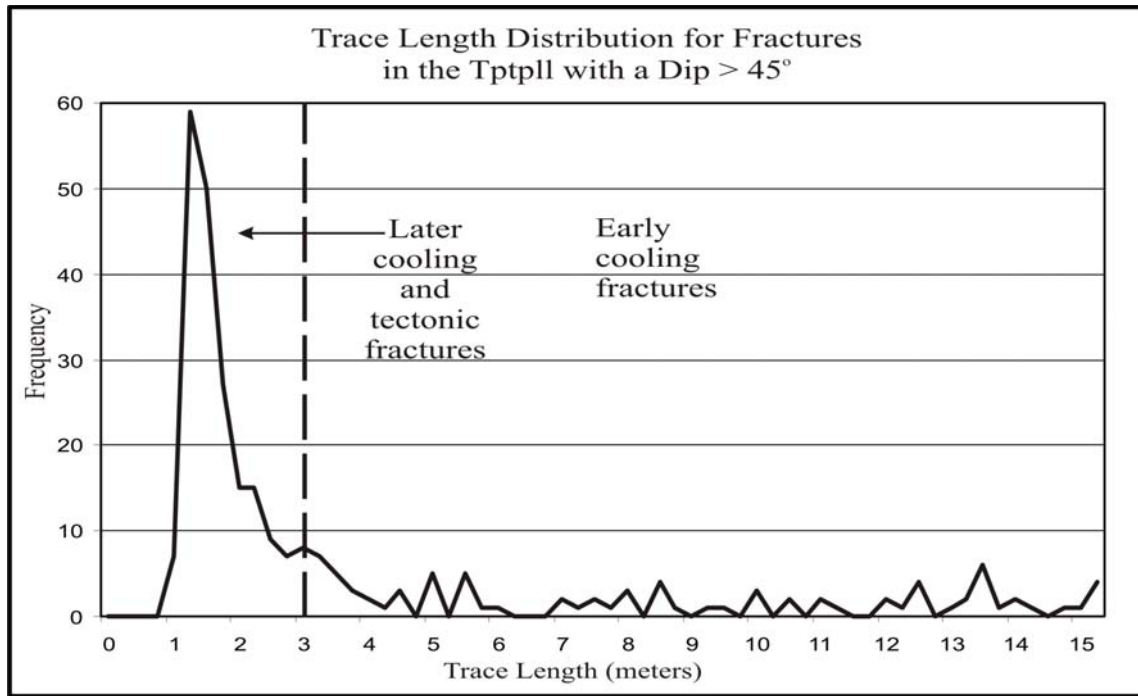


Source: DTN: GS990408314224.001 [DIRS 108396]; GS990408314224.002 [DIRS 105625].

Figure B-1. Tptpll Pole Plot Showing Great Circles for the Tptpll Fractures

The remaining fracture trace lengths are plotted on a histogram and the trace length distribution is evaluated. The distribution is polymodal. A break is defined to separate the long fractures from the short fractures. For the Tptpll, this break occurs at approximately 3 m (Figure B-2). The distribution of poles for both the cooling and later cooling/tectonic fractures is shown in Figure B-1. The set attributes developed from the detailed line survey are provided in Table B-1.

In Figure B-3, the values used as input to the FracMan simulation are shown. Table B-2 is a direct comparison of the observed detailed line survey data with the FracMan output with respect to the number of fractures in each set as well as the proportions of the total in each set. The proportions of fracture types are very important to establish a representative FracMan network. The actual number of fractures is not relevant because the sampling areas are not comparable.



Source: DTN: GS990408314224.001 [DIRS 108396]; GS990408314224.002 [DIRS 105625].

Figure B-2. Trace Length Distribution of the Tptpll Fractures (>45°)

Table B-1. Summary Statistics of the Tptpll Detailed Line Survey Data

Set	Strike & Dip (Trend & Plunge)	Trace Length (mean)	Number of Fractures
Vapor-Phase Partings	329/14 (239/76)	7.2m	20
1 <sup>st</sup> Generation Cooling Joints	130/80 & 175/80 (040/10 & 085/10)	9.5m	71
2 <sup>nd</sup> Generation Cooling and Tectonic Joints	130/80, 175/80, 278/85 (040/10, 085/10, 008/05)	1.6m	209

Source: DTNs: GS990408314224.001 [DIRS 108396]; GS990408314224.002 [DIRS 105625].

NOTE: Strike and dip values were determined graphically using the stereonet shown in Figure B-1.

The most critical comparison is presented in Figure B-4. This is the direct comparison between actual full periphery geologic maps from the ECRB Cross-Drift to synthetic full periphery geologic maps from FracMan. The synthetic full periphery geologic maps are not a replicate, but based on professional expertise and judgment, the FracMan full periphery geologic maps are adequately similar to the observed full periphery geologic maps both for intensity and lengths.

Project Tptpl Task Drift Degradation Date 01-24-03 Modeler Lung-Fahy  
 Seed #: 0725 Fracmeter Unit: 50 Truncation mode Region View Center 0,0,0  
 Direction Scale 100 % displayed Orientation = Pole or Dip Pole 6 # frac sides 6

Frac Set	Model Type	Generation Region & Dimension	Orientation TR,PJ	Dist. Type	k dispersion	Size eqv. Radius	Dist. type	Mean SD	Max. Min.	Elongation	Aspect Ratio	Termin %	Intensity
1	Baecher	100x100x100	239/76	Fisher	70	1.30	Power (3.1)			NA	NA	5	0.02
2	Baecher	100x100x100	040/10	Fisher	70	1.80	Power (3.1)			NA	NA	10	0.05
3	Baecher	100x100x100	085/10	Fisher	70	1.53	Power (3.1)			NA	NA	10	0.02
4	Baecher	100x100x100	040/10	Fisher	100	0.60	Power (3.1)			NA	NA	70	0.035
5	Baecher	100x100x100	085/10	Fisher	100	0.60	Power (3.1)			NA	NA	70	0.007
6	Baecher	100x100x100	008/05	Fisher	100	0.60	Power (3.1)			NA	NA	70	0.002

NN factor      NN export:      WZ inten:      WZ parall:      WZ large:      WZ close      Frac Dim (LL,FB)(5-5)       
 Zone Thick      Fracs      # iterations      Frac Dim (POCS)      Ampl Shaper Fac (POCS)      Box Frac Dim      Spherical/Exp       
 Variogram      Semivariogram Sill      Corr Length     

    .FDT (binary, cant port to non DOS computers, cannot be edited in std word processing )  
    .BAB (babylonian ASCII version of FDT, only frac. data stored. Can be ported to non DOC computers. No std word processing.)  
    .DCM (Std ASCII version of FDT. Only frac data stored. Can be ported to most computers. Can be edited by std. Word processing. Large files)  
    .SAM (ASCII)     .ORS (ASCII)     .PCS (ASCII, for conditioned data)  
    .F2D (ASCII, frac trace data)

Source: DTN: GS990408314224.001 [DIRS 108396]; GS990408314224.002 [DIRS 105625].

NOTE: The parameter, "k dispersion" is determined visually by comparing simulated stereonets to observed stereonets. The parameter, "size eqv. radius" is the mean radius (m). The power law distribution is used for the parameter, "dist. type." The power law is selected because the fracture process generally follows power law physics, such that the number of fractures greater than a given length (x) is proportional to 1/x raised to the power law exponent. The parameter, "intensity" is selected to maintain the proportion of fractures in each set.

Figure B-3. FracMan Input Sheet for the Tptpl

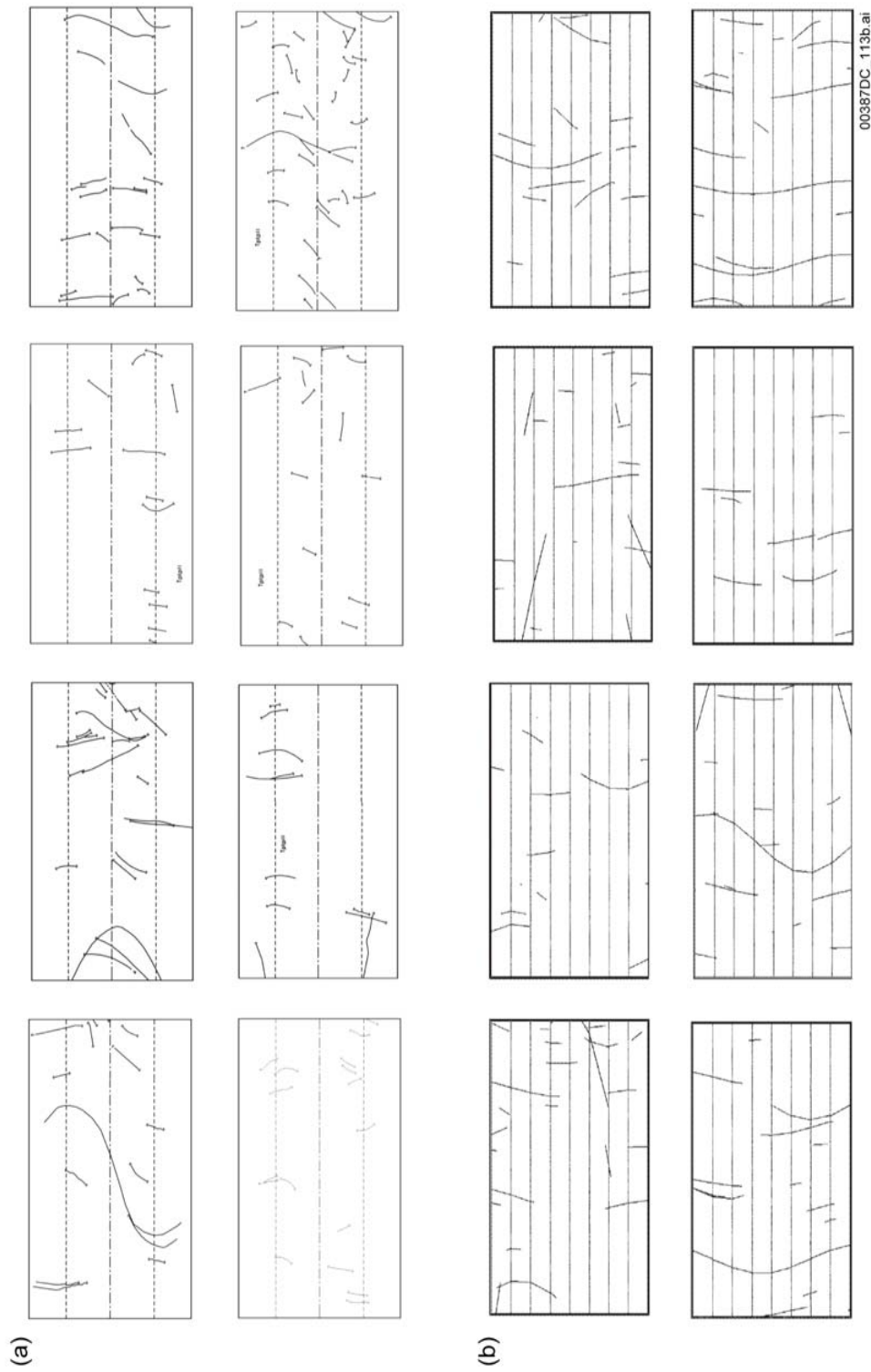
Table B-2. Relative Proportions of Fractures from the Detailed Line Survey Versus FracMan Output for the Tptpl

Detailed Line Survey			FracMan		
Feature	Number of fractures	Proportion	Feature	Number of Fractures	Proportion
Vapor-Phase Partings	20	6%	Vapor-Phase Partings	647	7%
1 <sup>st</sup> Generation Cooling Joints	71	24%	1 <sup>st</sup> Generation Cooling Joints	2494	25%
2 <sup>nd</sup> Generation Cooling and Tectonic Joints	209	70%	2 <sup>nd</sup> Generation Cooling and Tectonic Joints	6738	68%
Total	300	100%	Total	9879	100%

Source: DTNs: GS990408314224.001 [DIRS 108396]; GS990408314224.002 [DIRS 105625].

The orientation comparison is presented in Figure B-5. Pole plots for the detailed line survey data and the FracMan output are compared to ensure that the clusters from the detailed line survey are correctly simulated in FracMan. For the Tptpl this comparison demonstrates that the FracMan output is adequately similar to the observed data. The means are similar and the spread of the data about the mean is similar. Not all observed fractures are simulated because the FracMan output has less scatter and is not a replicate.

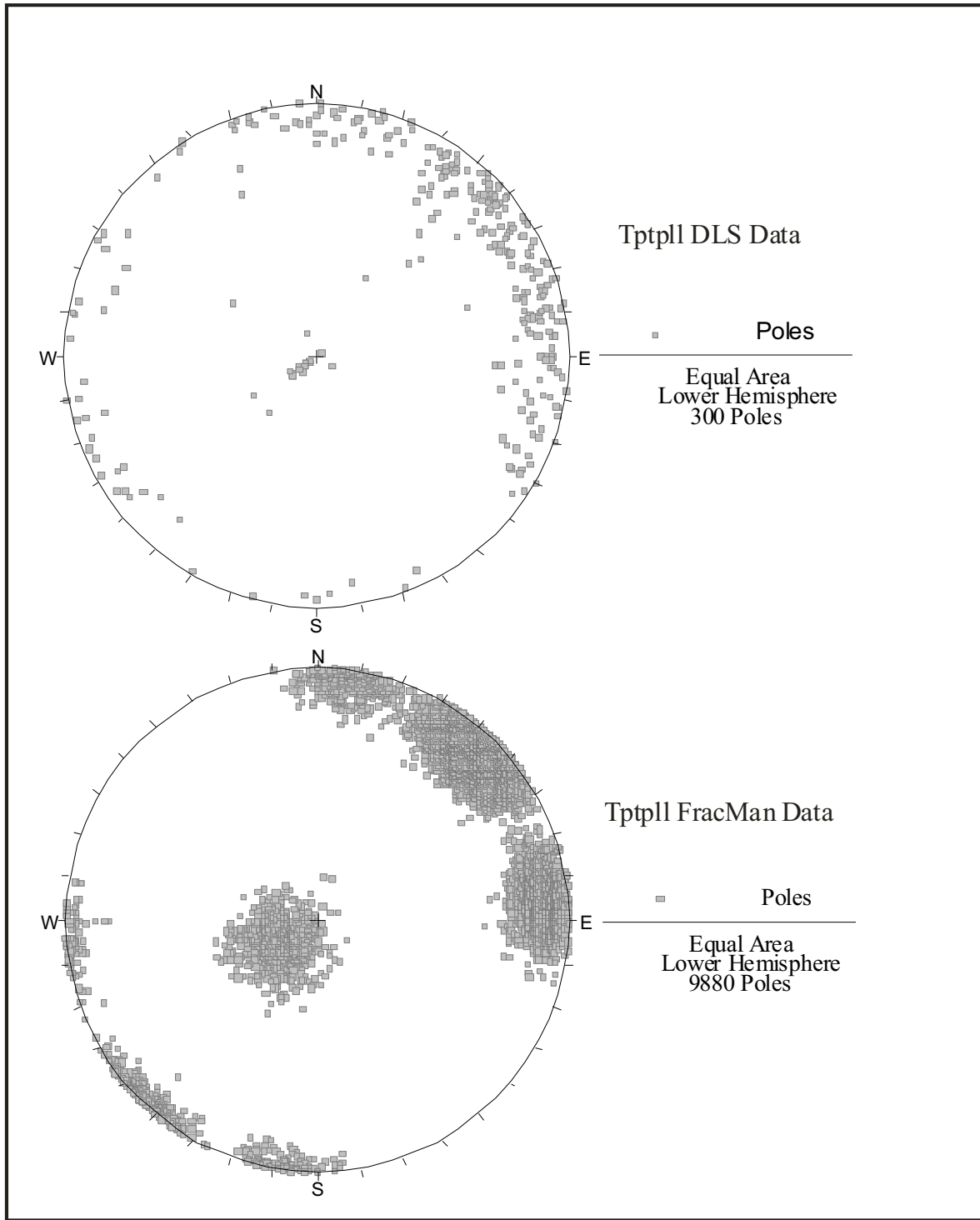
Figure B-6 provides confirmation that the radius distribution of fractures from FracMan matches reasonably well with the observed trace lengths. Figure B-7 shows that fracture intensity, that is the slope, is nearly constant until approximately Station 21+50. At this point a sequence of small offset faults occurs causing the intensity to increase.



Source: DTN: GS990408314224.004 [DIRS 108405]; GS990408314224.005 [DIRS 108408]; GS990408314224.006 [DIRS 108409].

NOTE: The purpose of this figure is to illustrate the geologic structure contained on a full periphery geologic map. The annotated information on this figure is not intended to be legible. (a) from the Tptpl in the ECRB Cross-Drift; (b) with Simulated Full Periphery Geologic Maps from the FracMan Cube.

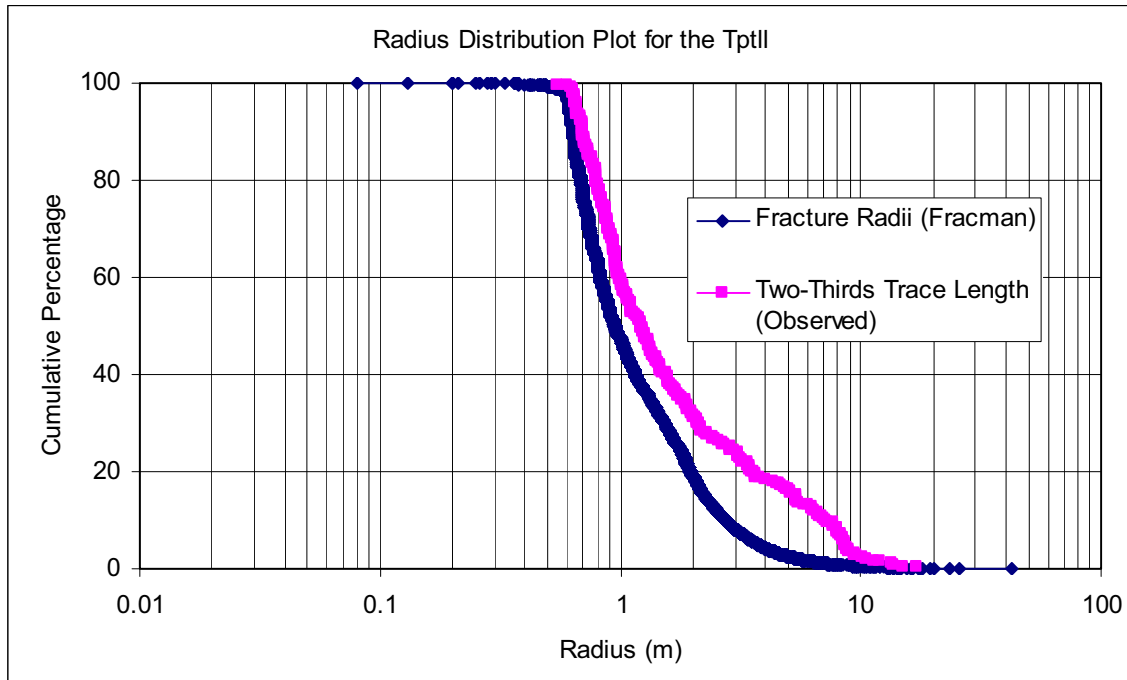
Figure B-4. Comparison of Full Periphery Geologic Maps



Source: DTN: GS990408314224.001 [DIRS 108396]; GS990408314224.002 [DIRS 105625].

NOTE: The FracMan data is representative of the entire rock mass, and is not a replicate of the detailed line survey data. Therefore, the number of poles in FracMan is expected to be much greater than the detailed line survey data. The location of the poles should agree, which is shown by this figure.

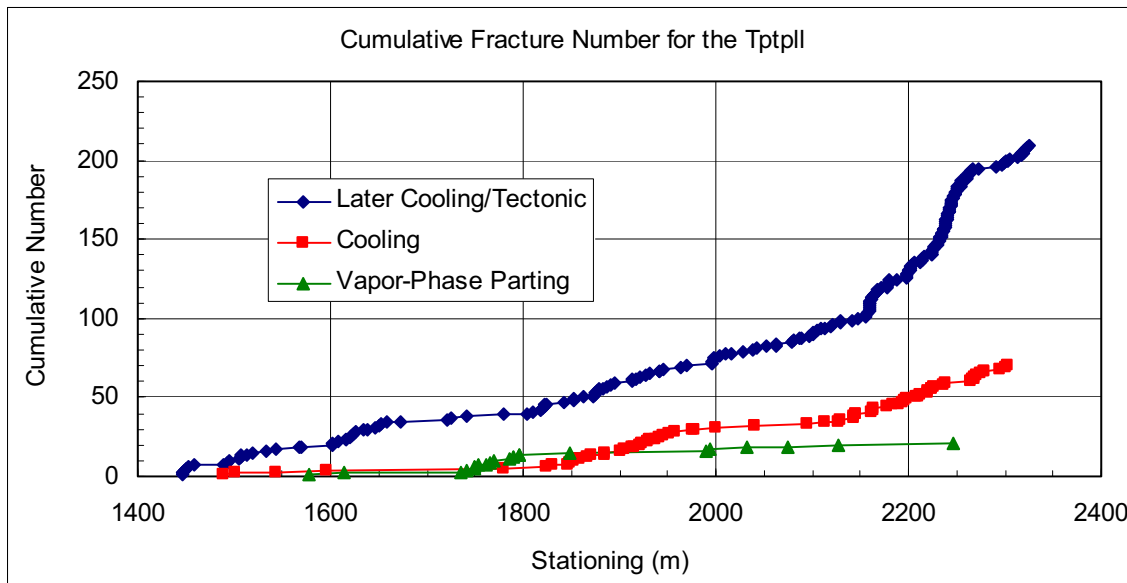
Figure B-5. Comparison of the Observed Tptpl Fracture Poles to the FracMan Fracture Poles



Source: DTN: GS990408314224.001 [DIRS 108396]; GS990408314224.002 [DIRS 105652].

NOTE: This figure compares fracture radii from FracMan to observed trace length data scaled by two-thirds. This is based on the relationship between fracture trace length and radius (see Figure D-11 and Equation 6-3). The mean fracture radius should be about two thirds of the mean trace length observed.

Figure B-6. Comparison of the Observed Trace Length Distribution (Scaled by Two Thirds) to the FracMan Radii Distribution for Tptll



Source: DTN: GS990408314224.001 [DIRS 108396]; GS990408314224.002 [DIRS 105625].

NOTE: Constant slope indicates constant intensity.

Figure B-7. Evaluation of Constant Intensity for Tptll

INTENTIONALLY LEFT BLANK



**APPENDIX C**

**REGIONAL AND LOCAL SCALE THERMAL-MECHANICAL ANALYSIS OF THE  
ROCK MASS SURROUNDING WASTE EMPLACEMENT DRIFTS  
AT YUCCA MOUNTAIN**



# **REGIONAL AND LOCAL SCALE THERMAL-MECHANICAL ANALYSIS OF THE ROCK MASS SURROUNDING WASTE EMPLACEMENT DRIFTS AT YUCCA MOUNTAIN**

## **C1. INTRODUCTION**

This appendix summarizes the results of a three-dimensional thermal-mechanical analysis of the repository site at Yucca Mountain using the finite difference code FLAC3D.

The analysis supports the NUFT drift-scale thermal calculation and to evaluate the edge effect described in Section 6.2 by defining the distribution of stresses around drifts due to progressive heating of the repository area. Unlike the NUFT calculation that simulated complex heat transfer physics (Section 6.2), only the thermal conduction into the rock mass was considered in the analysis in order to compute the thermal stresses around the drifts. Simulation of the rock mass behavior due to excavation and heating of the drifts has been carried out in two steps.

First, a regional scale (small-scale, for instance 1/10,000) calculation of the Yucca Mountain site was constructed. This calculation includes details of topography, stratigraphy and two structural faults. Figure C-1a shows an aerial view of Yucca Mountain, together with a digital elevation calculation generated for the purposes of this calculation. Figure C-1b shows the FLAC3D mesh constructed from the digital elevation calculation and available geological information. In the regional calculation, the heat sources act uniformly distributed over the area delimited by the repository boundaries (see Figure C-1).

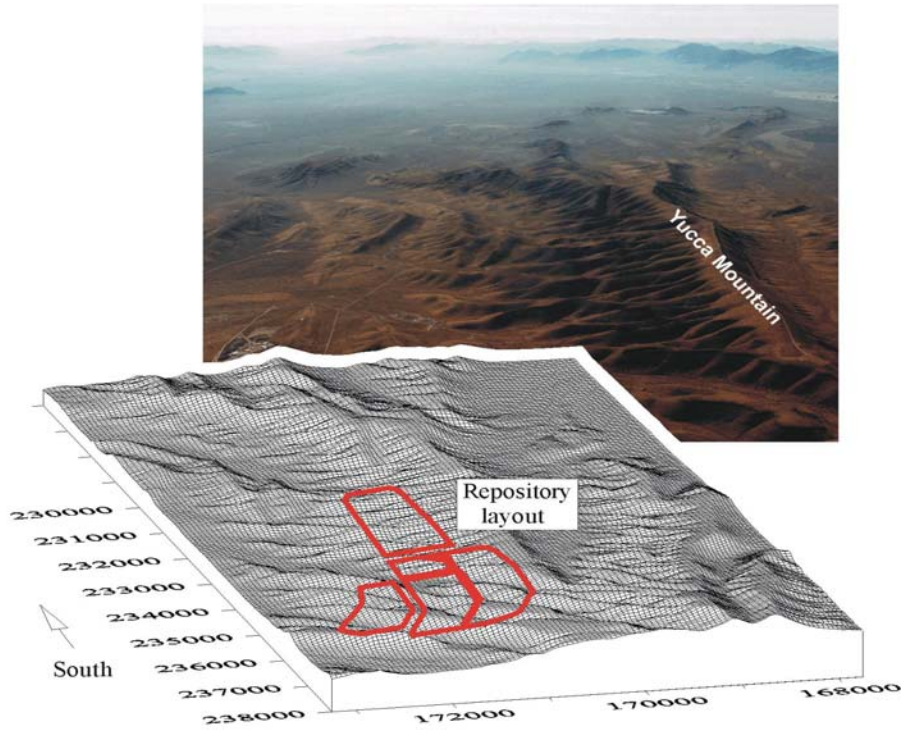
Second, a detailed local scale (large-scale, for instance 1/100) calculation has been constructed at the specified locations at the center (considered to be the hottest) and edge within the proposed repository area (see Figure C-2). This local scale calculation allows the study of induced stresses and displacements on the rock mass surrounding a central drift due to simultaneous application of heat sources in this drift and in neighboring ones.

## **C2. DESCRIPTION OF THE REGIONAL (SMALL) SCALE CALCULATION**

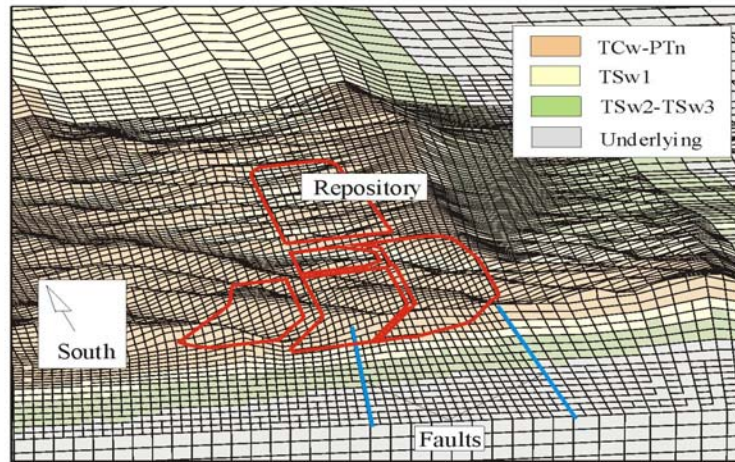
A topographical plan shown of the Yucca Mountain site (the coordinates in the plan view correspond to N-S and W-E geographical system in meters) is seen in Figure C-3. The figure indicates the location of the proposed repository area (red lines), access tunnels (blue lines) and location of available geological cross-sections (black lines). The location of boreholes from where thickness of the strata and in situ stresses have been measured is also shown on this figure.

In the regional scale calculation, the repository area is considered to lie on a horizontal plane at an elevation of 1073 meters (averaged from BSC 2003 [DIRS 164519]). From the available geological information, the two faults, the Solitario Canyon fault in the west and the Ghost Dance fault in the east, have been outlined (the green lines in Figure C-3 represent the traces of the faults on the horizontal plane containing the repository at the 1,073 meter elevation). The spatial location of the faults, as measured and interpreted from the available geological maps (BSC 2004 [DIRS 170029]) and cross-sections extracted from DTN: MO0012MWDGFM02.002 [DIRS 153777] (i.e., Figures M-1, M-2 and M-3), is defined in Table C-1 and depicted in Figure C-4. The details of the cross-section extraction are provided in Appendix M.

a)



b)



NOTE: a) Aerial View of the Yucca Mountain Site and Digital Elevation Calculation Created from Topographic Information.

b) View of the Regional Scale FLAC3D Calculation Constructed from the Digital Elevation Calculation and Available Geological Information.

Figure C-1. Yucca Mountain Repository Site

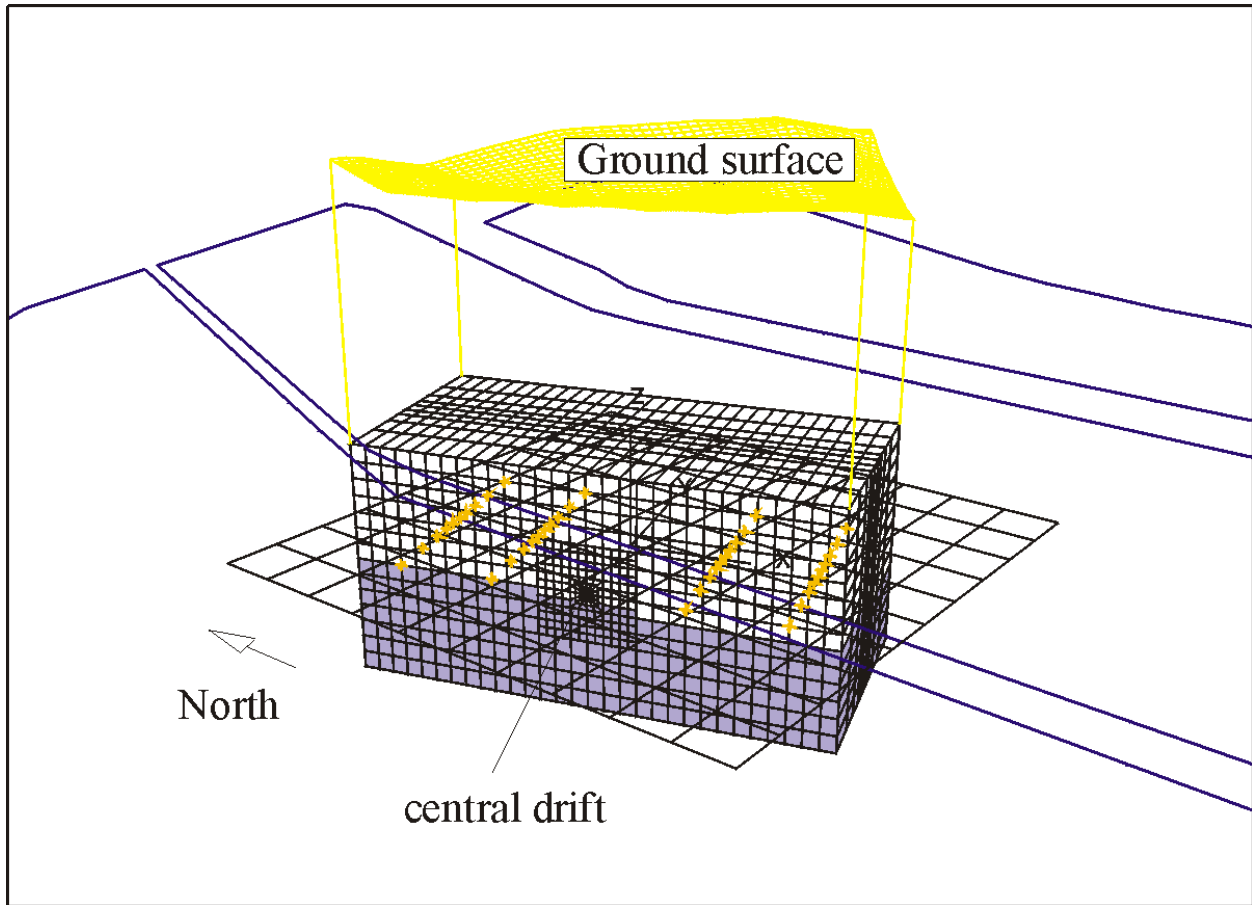


Figure C-2. Local (Large) Scale Calculation in the Central Part of the Repository

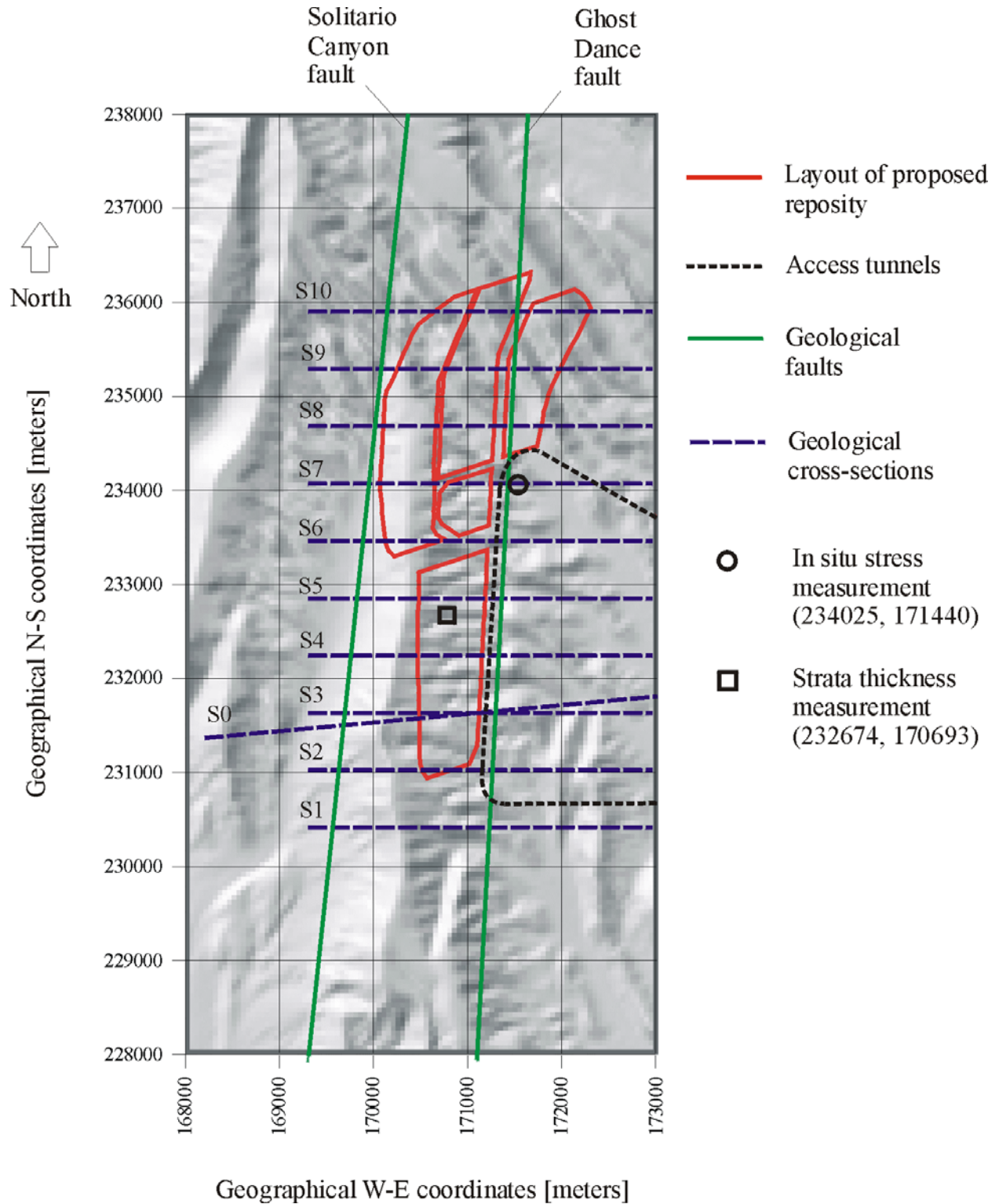


Figure C-3. Topographical Plan View of the Yucca Mountain Site and Main Elements Considered in the Regional Scale Calculation

Table C-1. Spatial Location of the Tectonic Faults Considered in the Analysis

<b>Name of the fault</b>	<b>Dip direction/Dip angle [degrees] (Direction measured from the North)</b>	<b>Coordinates of a point on the fault [meters] (coordinates are N-S, W-E and altitude)</b>
Solitario Canyon	276/60	(232000, 169730, 1084)
Ghost Dance	273/85	(232000, 171324, 1084)

Four mechanical units have been identified and used based on Ortiz et al. (1985 [DIRS 101280]). The units at the cross-sections S3, S7 and S10 in Figure C-3 are represented in Figures C-4a, C-4b, and C-4c, respectively. The spatial location of the geological units, as interpreted from geological maps, is indicated in Table C-2.

Table C-2. Spatial Location of the Stratigraphic Units Contracts Considered in the Calculation

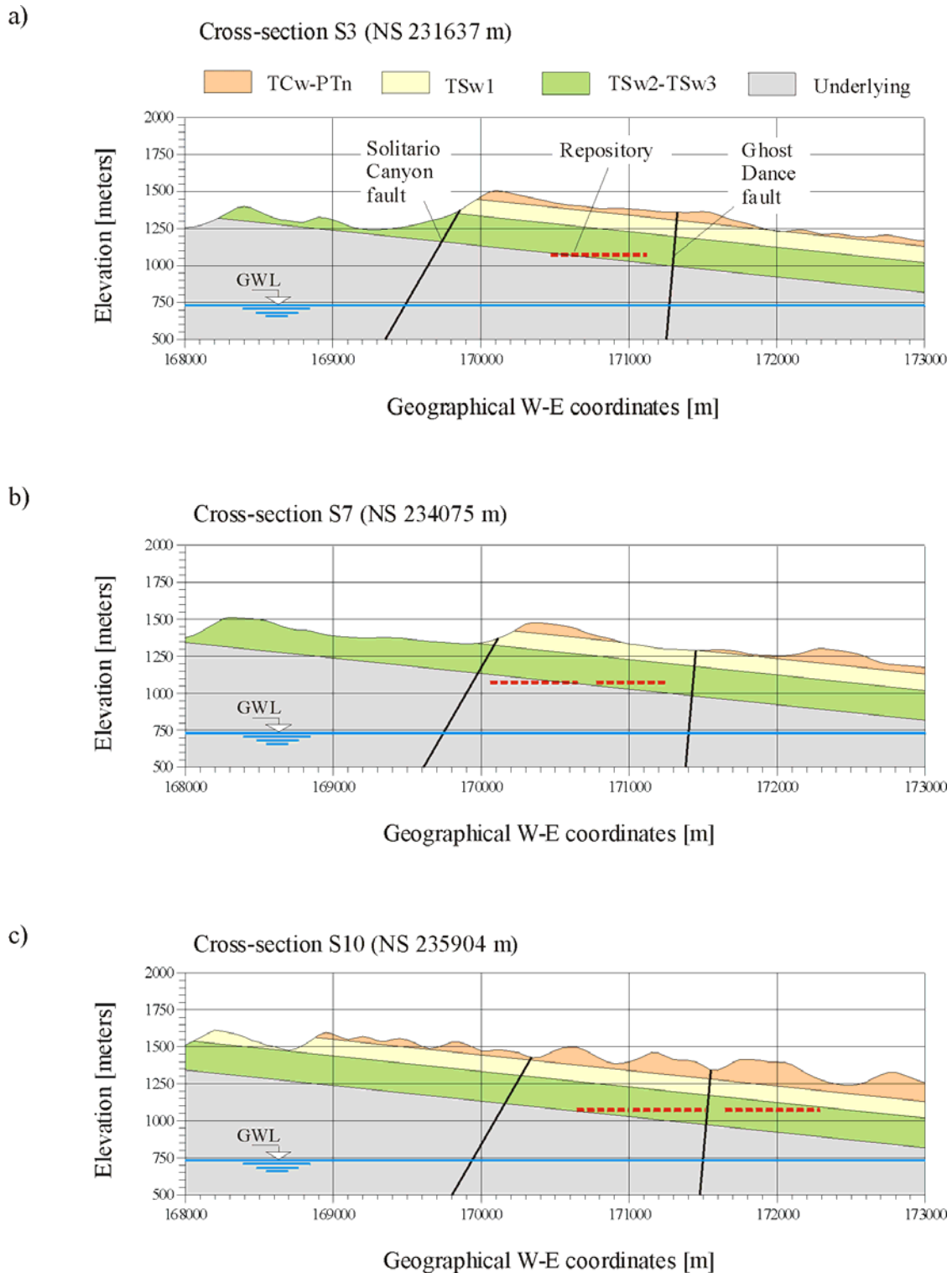
<b>Contact between units</b>	<b>Dip direction/Dip angle [degrees] (Direction from North)</b>	<b>Coordinates of a point on the contact [m] (coordinates are N-S, W-E and altitude)</b>
TCw-PTn & TSw1	090/06	(232674, 170693, 1372)
TSw1 & TSw2-TSw3	090/06	(232674, 170693, 1260)
TSw2-TSw3 & Underlying Strata	090/06	(232674, 170693, 1060)

The cross-sections in Figure C-4 indicate that the repository level (i.e., at the elevation 1073 meters) lies mostly in the TSw2-TSw3 unit.

Figure C-5 shows the FLAC3D regional scale calculation constructed based on the basis of the information described above. Figures C-5a and C-5b correspond to the sections S3 and S10 in Figures C-4a and C-4c. Figure C-5c is a N-S cross-section along the E-W coordinate 170500 in Figure C-3.

Figure C-6, shows a vertical cross-section at the N-S coordinate 232000 meters and a plan view of the FLAC3D calculation at the repository level (i.e., at the elevation 1073 meters). The calculation consists of three regions of decreasing zone density. A “near” region where the repository is located is made up of zones of characteristic length 75 meters in both the North-South and East-West directions and 50 meters in the vertical direction (the near region has 110,592 zones). The “middle” region is made up of zones that have twice the characteristic length as those in the near region and the “far” region has zones that are twice the characteristic length of those in the “middle” region (the middle region has 51,840 zones and the far region has 72,912 zones; the regional scale calculation has 235,344 zones). The two faults (Solitario Canyon fault on the west and Ghost Dance fault on the east) are represented as interfaces.

The mechanical properties considered for the four units (TCw-PTn, TSw1, TSw2-TSw3, and underlying strata indicated in Figure C-4) were computed based on *Ground Control for Emplacement Drifts for SR* (BSC 2001 [DIRS 155187], Section 4.1). The original mechanical properties (available for every stratigraphic unit at Yucca Mountain) have been averaged based on the thickness of the different units included in each of the four units considered in this calculation (Figure C-4). The properties are summarized in Table C-3.



NOTE: Fault displacements are not shown on the simplified cross-sections depicted in this figure. Detailed cross-sections including fault displacements are provided in Appendix M.

Figure C-4. Cross-Sections Showing the Four Thermal-Mechanical Units and Faults at the Locations Indicated as S3, S7, and S10 in Figure C-3



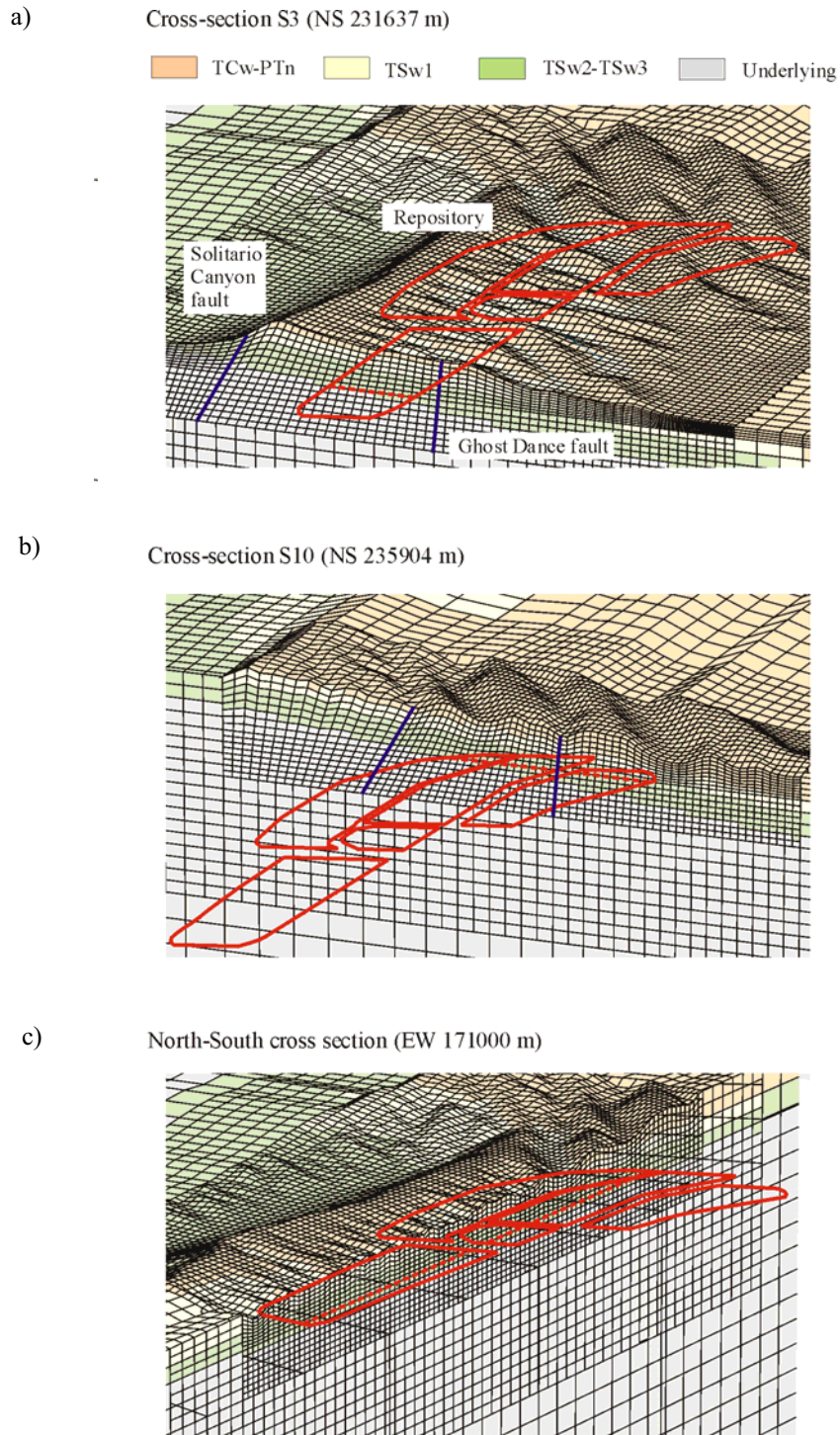
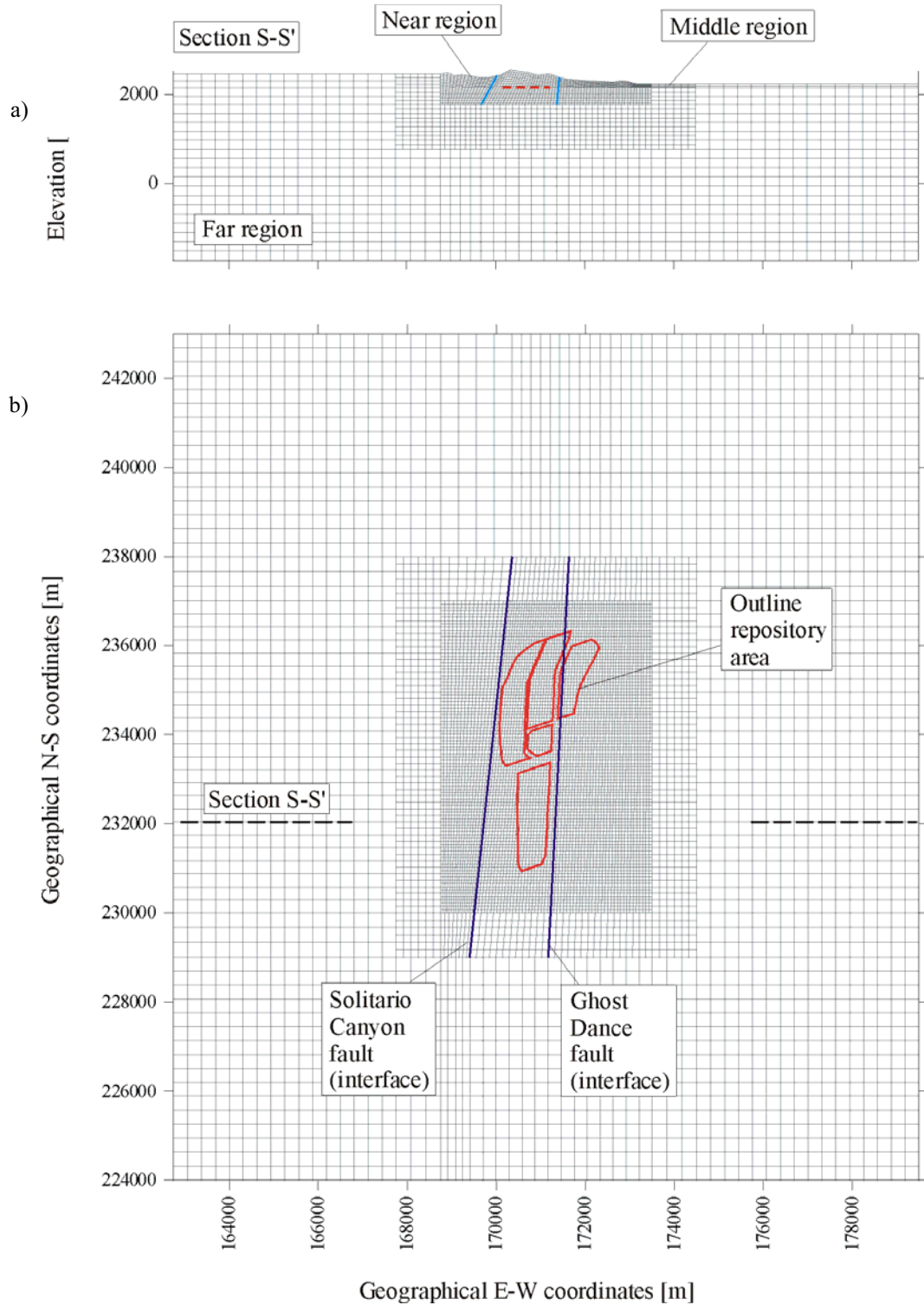


Figure C-5. E-W Cross-Sections S3 and S10 of Figures C-3 and C-4 and N-S Cross-Section Through the FLAC3D Calculation



NOTE: a) Cross-Section at the North Coordinate 232,000 Meters.

b) Plan View of the FLAC3D Calculation at the Elevation 1073 Meters.

Figure C-6. Repository Grid

Table C-3. Mechanical Properties Considered for the Rock Mass in the Regional and Local Scale Calculations

Property	TCw-PTn	TSw1	TSw2-TSw3	Underlying
Young Modulus [MPa]	2540	15210	15840	15840
Poisson's ratio	0.2	0.2	0.2	0.2
Density [kg/m <sup>3</sup> ]	1613	1983	2086	1545

NOTE: These data are based on preliminary results that are similar to the information provided in Appendix E (Tables E-1 and E-16). The results from the thermal-mechanical calculation presented in this appendix are not sensitive to minor changes in mechanical properties.

The fault interfaces are calculated as cohesion-less Coulomb contacts. The friction angle is considered to be 34° (Bauer et al. 1992 [DIRS 162227]) and the stiffness (in both normal and shear directions) is computed, based on the characteristic size of the surrounding zones, so as to simulate the effect of a highly “stiff” contact. Values of 275 MN/m have been considered for the “stiff” contact based on Equation 3.4 of Theoretical Background Manual of the FLAC3D (Itasca Consulting Group 2002 [DIRS 160331]).

The thermal properties considered for the four units (TCw-PTn, TSw1, TSw2-TSw3, and underlying strata indicated in Figures C-4 and C-5) were also computed by taking averages from the detailed stratigraphic unit information (Appendix E, Section E5). The thermal properties are listed in Table C-4. The specific heat values between 95°C and 114°C are exceptionally high compared to the values of other temperature ranges (Table C-4). The high specific heat values are based on the analytical solutions presented by Nimick and Connolly (1991 [DIRS 100690]). The primary NUFT thermal calculation that is used to support the drift degradation analyses (presented in Section 6.2) does not use the high specific heat values, since consideration of latent heat effects above the boiling point is built into the NUFT code.

Table C-4. Thermal Properties Considered for the Rock Mass in the Regional and Local Scale Calculations

Property	Condition	TCw-PTn	TSw1	TSw2-TSw3	Underlying
Conductivity $k$ [W/m°C]	<100°C	1.015	1.771	1.925	1.201
	≥ 100°C	0.525	1.220	1.328	0.581
Specific heat $C_v$ [J/kg °C]	< 95°C	1,158	939	937	1,304
	95°C ≤ $C_v$ < 114°C	11,135	5,791	5,714	15,775
	≥ 114°C	1,010	991	990	1,016
Thermal expansion $\alpha_t$ [1/°C]	<50°C	4.46x10 <sup>-6</sup>	6.56x10 <sup>-6</sup>	7.14x10 <sup>-6</sup>	7.14x10 <sup>-6</sup>
	50°C ≤ $\alpha_t$ < 75°C	4.46x10 <sup>-6</sup>	6.56x10 <sup>-6</sup>	7.47x10 <sup>-6</sup>	7.47x10 <sup>-6</sup>
	75°C ≤ $\alpha_t$ < 100°C	4.46x10 <sup>-6</sup>	6.56x10 <sup>-6</sup>	7.46x10 <sup>-6</sup>	7.46x10 <sup>-6</sup>
	≥ 100°C	4.46x10 <sup>-6</sup>	6.56x10 <sup>-6</sup>	9.07x10 <sup>-6</sup>	9.07x10 <sup>-6</sup>

The heat capacity data used in the thermal property calculation (Table C-4) were preliminary data superseded by DTN: SN0307T0510902.003 [DIRS 164196] (Table E-19). Therefore, an impact analyses was conducted regarding the preliminary data and presented in Appendix Q2. The impact analyses indicates there are insignificant impacts on the below 95°C and over 114 °C ranges, and only minor impact on the 95 to 114°C range for the local scale thermal-mechanical calculation (Section C3). An additional local scale calculation is not necessary since the local

scale calculation was only used to support the main thermal-mechanical calculation in Section 6.2. Both an initial state of stress and an initial state of temperature are considered for the regional scale calculation. The initial temperature in the rock mass is needed to compute the temperature-dependent thermal properties listed earlier.

The vertical component of in situ stress is considered to be a major principal stress,  $\sigma_1$  (see Section 6.3.1.1). It is considered to be lithostatic (i.e., computed as the weight of the overburden from the topography and density values described earlier). Figure C-7 shows contours of vertical stress in a cross-section of NS coordinate 232000 meters. The intermediate and minor principal stresses ( $\sigma_2$  and  $\sigma_3$  respectively) are horizontal (see Section 4, Table 4-1). The direction of the intermediate principal stress  $\sigma_2$  is N15°E. The ratio of intermediate to major principal stress is taken to be  $\sigma_2/\sigma_1 = 0.617$  based on the data developed in Section 6.3.1.1. This is based on values of the in situ stresses measured at the location shown in Figure C-3 (see Section 6.3.1.1). The direction of the minor principal stress  $\sigma_3$  is N105°E (or E15°S). The ratio of minor to major principal stress is taken  $\sigma_3/\sigma_1 = 0.361$  (also from the values of measured in situ stresses provided in Section 4, Table 4-1, and developed in Section 6.3.1.1).

The initial state of temperature is considered to vary linearly with depth below the surface (i.e., as defined by the topography shown in Figure C-1). The initial temperature is considered to be fixed and equal to 18°C at ground surface and equal to 34°C at the level of the permanent groundwater table. At the elevations of 1231 and 730 meters, time-averaged temperatures based on *UZ Flow Models and Submodels* [BSC 2004 [DIRS 169861], Section 6.3]) were considered. Note the temperature values are different from the boundary temperatures of the NUFT thermal calculation in the Section 6.2 (16.9°C for the ground surface and 29.2°C for the water table temperature), since the initial temperature is considered for the entire repository layout (BSC 2004 [DIRS 169861], Section 6.3). For points above the water table, the initial temperature is linearly interpolated from the fixed values at the ground surface and water table level. For points below the water table, the initial temperature is considered to be constant and equal to 34°C.

Thermal loading of the repository area is considered to be the only source of stress redistribution and induced displacement within the rock mass (the regional scale calculation does not take into account the excavation of drifts within the repository area). This thermal load is considered to be uniformly distributed within the boundary limits of the repository. In the present calculation, all panels comprising the repository (see Figure C-3) are considered to be activated at once (i.e., the calculation assumes an “instantaneous” emplacement of the waste in all panels of the repository; see Section 5.1).

The thermal load is computed considering a linear heat power source equal to 1450 W/m that acts along each drift and a separation between the axes of adjacent drifts of 81 meters (i.e., the value of distributed heat power, before any correction is made due to radioactive decay and ventilation, is equal to  $q_o = 1450/81 = 17.9 \text{ W/m}^2$ ).

The heat output is considered to vary in time according to the following equation, which is derived directly from fundamental physics:

$$q(t) = \delta(t) \times [1 - \phi_{ve}(t)] q_0 \quad (\text{Eq. C-1})$$

where  $t$  is the time in years,  $\delta(t)$  is a radioactive decay correction factor, and  $\phi_{ve}(t)$  is a correction factor for ventilation.

The graphical representation of the function  $\delta(t)$ , calculated from *D&E / PA/C IED Typical Waste Package Components Assembly* (BSC 2004 [DIRS 167369]), is shown in Figure C-8a.

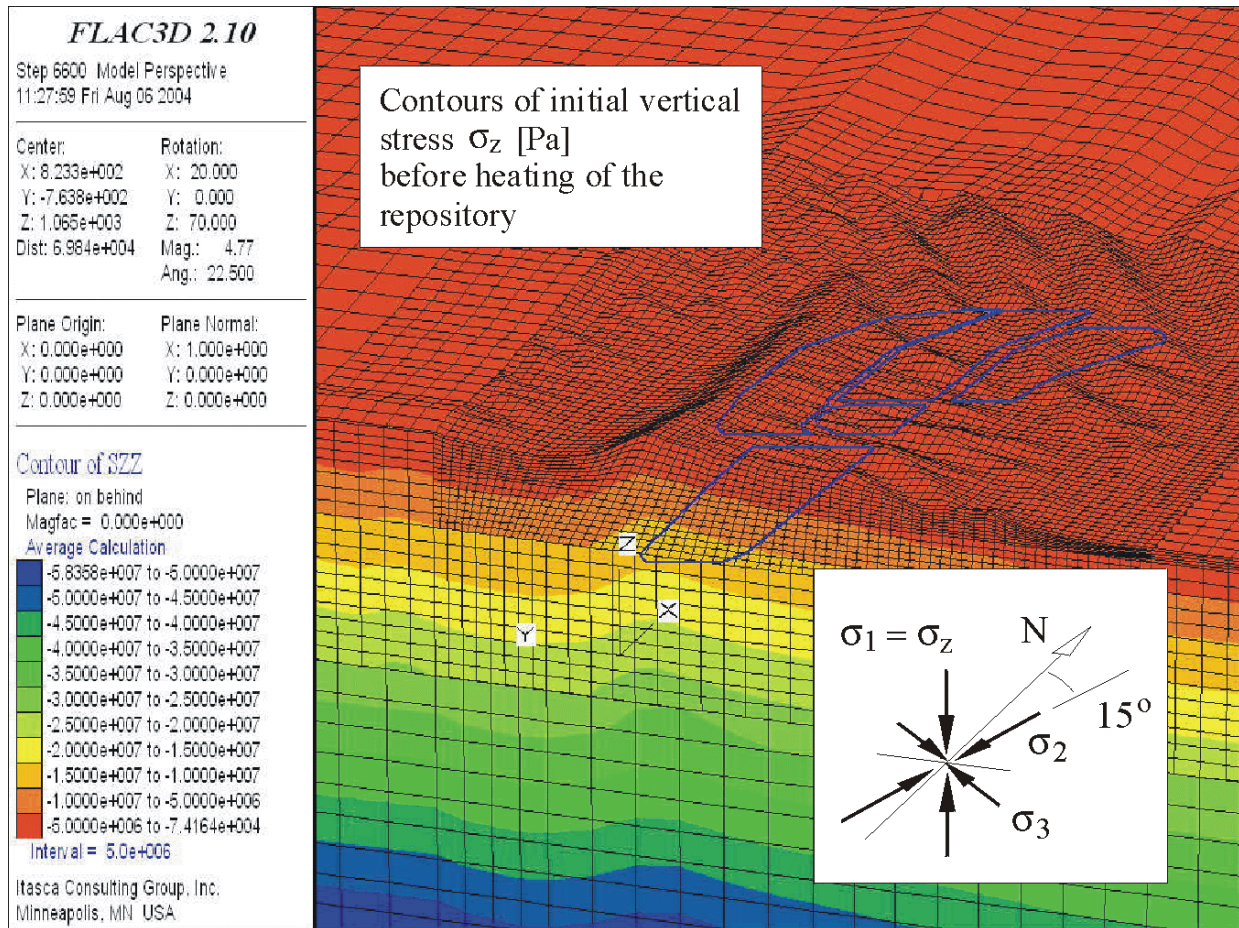


Figure C-7. Contours of the In Situ Vertical Stress  $\sigma_2 = \sigma_1$  and Direction of the Horizontal (Principal) Stresses  $\sigma_2$  and  $\sigma_3$

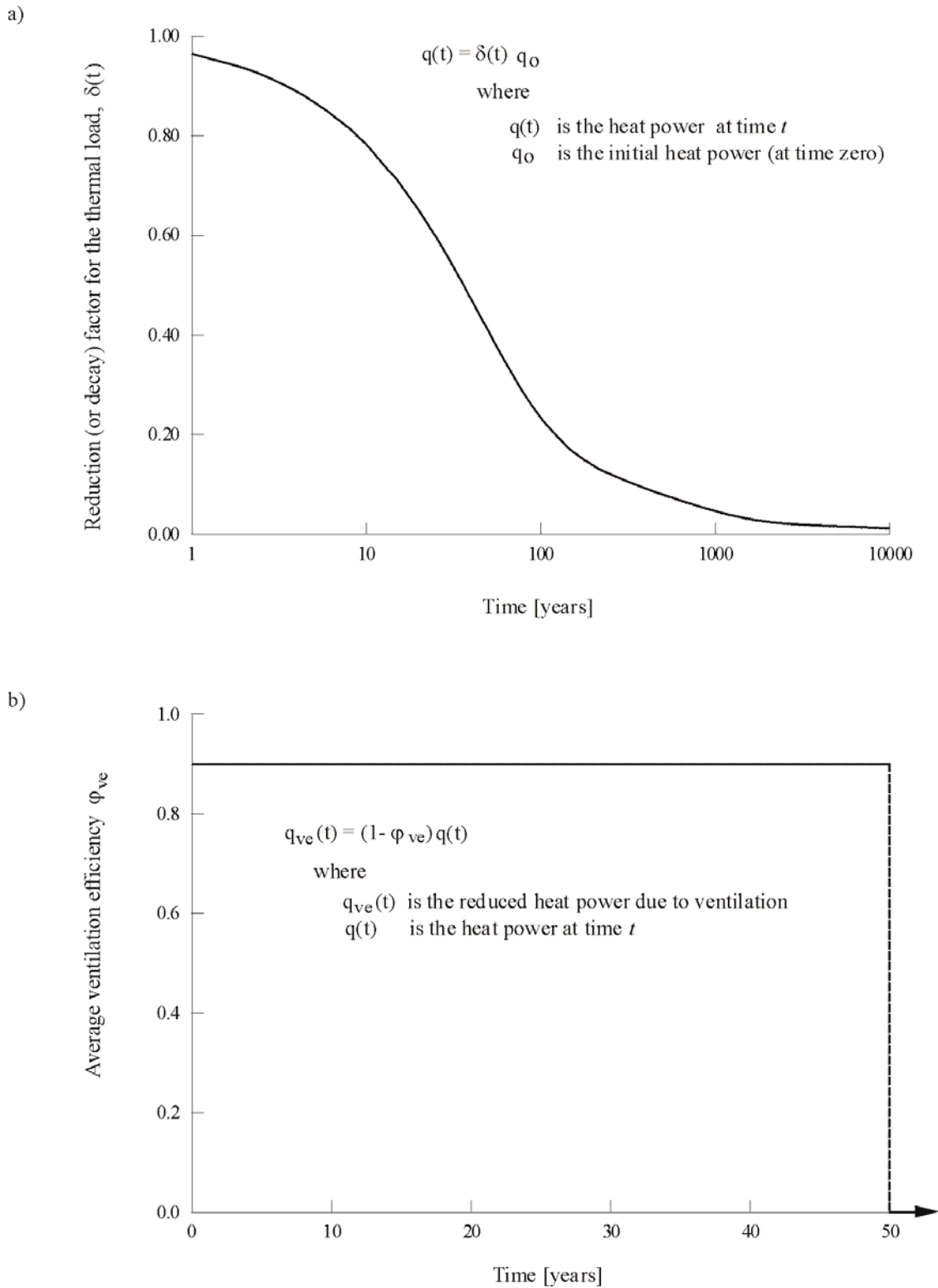


Figure C-8. Heat Source Correction Functions for a) Radioactive Decay and b) Ventilation

The graphical representation of the function  $\phi_{ve}(t)$  is shown in Figure C-8b. Note that forced ventilation is considered for a pre-closure period of 50 years. Throughout this period of time, ventilation efficiency is constant and equal to 90 percent.

Values of temperature change at specific points within thermal sectors have been determined (the points are indicated by the small circles ‘g1’ through ‘g5’ in Figure C-9). Figure C-10 shows the evolution of temperature at these points after 10,000 years of heating. Figure C-10a shows temperature as a function of time, and Figure C-10b presents the same results using a logarithmic time scale.

Heating of the repository area induces changes in stresses (with respect to the initial stresses described earlier) and displacements. Changes in stresses and displacements have been recorded for different stages of heating in the regional calculation (information is available for the sequence 1, 10, 20, 50, 100, 200, 300, 400, 500, 750, 1000, 2000, 3000, 4000, 5000, 7500, and 10,000 years).

For example, Figures C-11 and C-12 show the change in temperature along a cross-section of the calculation after 10, 100, 1000 and 10,000 years.

Figures C-13a and C-13b show contours of magnitude of induced displacement after 100 and 1000 years of heating.

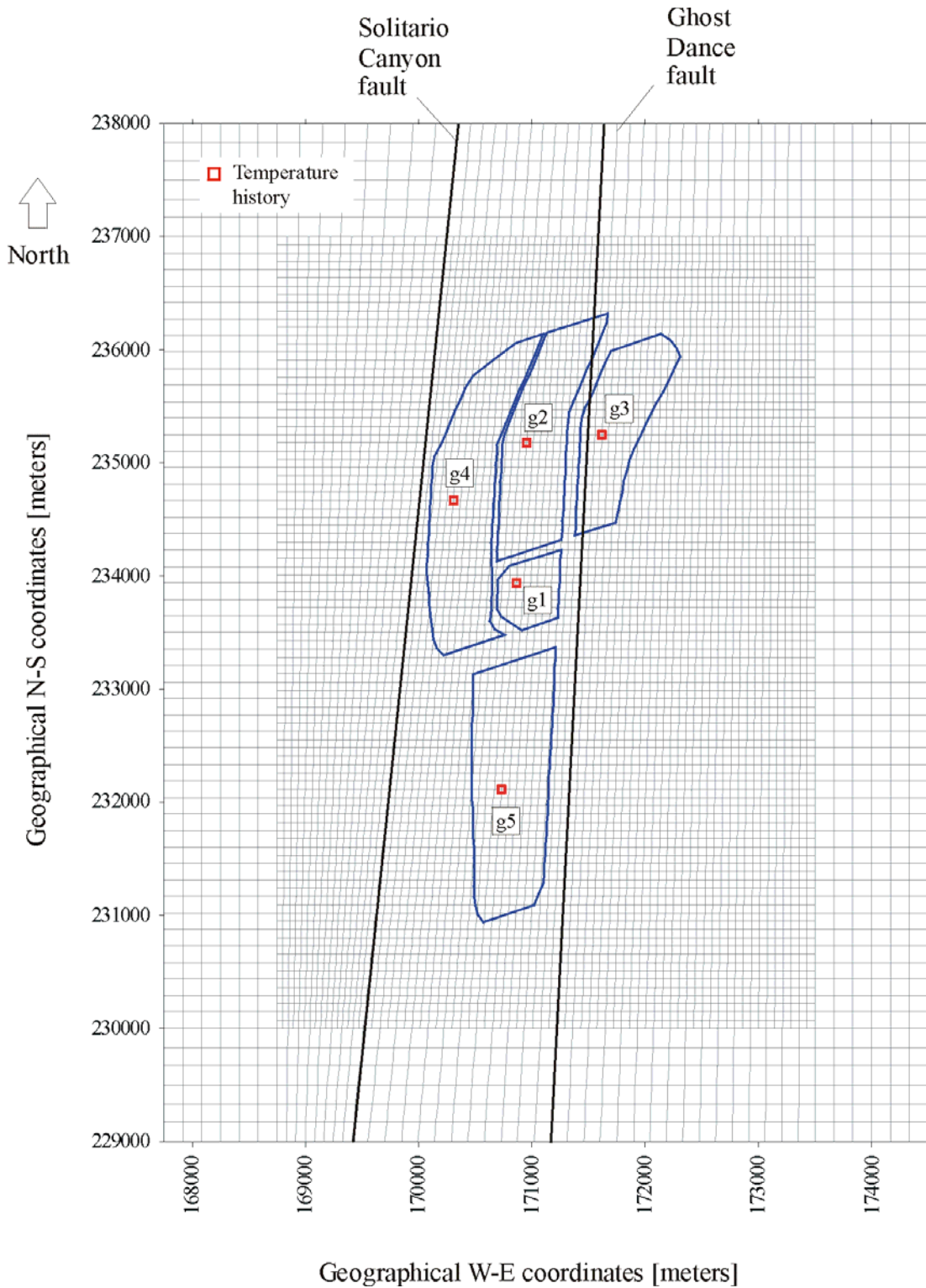
### **C3. DESCRIPTION OF THE LOCAL (LARGE) SCALE CALCULATIONS**

The purpose of the local-scale calculation is to analyze the effect of heating at a drift scale.

The locations of the local-scale calculation seen in Figure C-14 are with respect to the regional calculation. The center of the calculation is located at coordinates 170730, 234913, 1073 (W-E, N-S, and altitude in meters), while the edge of the calculation is at coordinates 170126, 233439, 1073 (W-E, N-S, and altitude in meters). The axes of the drifts in Figure C-14 are oriented N72°E with respect to the North. The center location is considered to be the hottest location of the calculation.

A plan view of the local-scale seen in Figure C-15 “center” calculation is at the repository level. The figure also shows two vertical cross-sections taken parallel and perpendicular to the axis of the drift. From Figure C-15, it is seen that the local scale calculation extends 200 meters vertically, 200 meters horizontally along the axes of the drifts, and 404 meters horizontally perpendicular to the axes of the drifts. From the vertical cross-sections, it is seen that the central drift (radius 2.75 meters) is simulated explicitly as a tunnel of this dimension. The surrounding drifts, separated a distance of 81 meters from the central drift and from each other, are not represented as voids, but rather as linear sources subject to thermal load. The local-scale “edge” calculation is similar to the center calculation except consideration of the repository edge location.

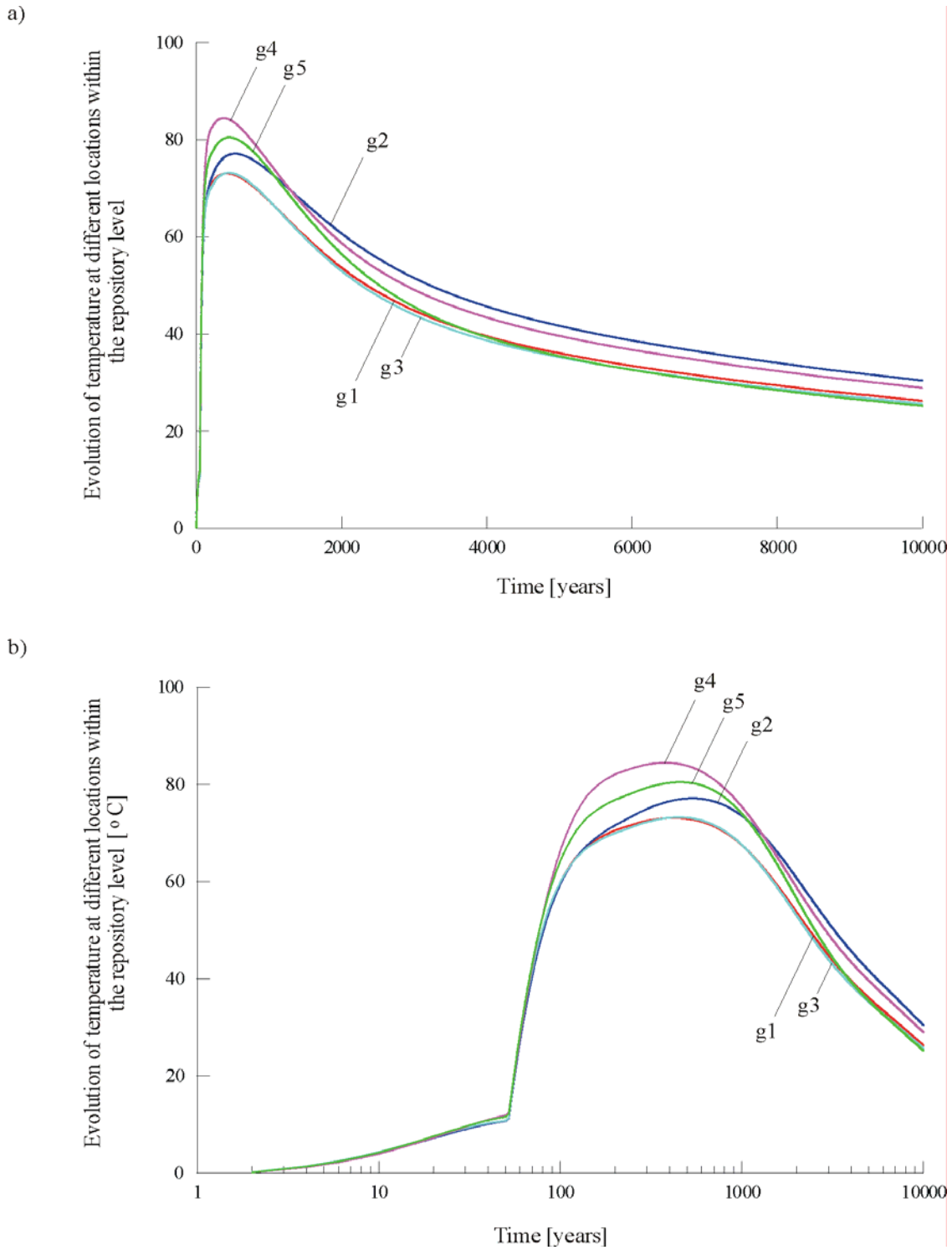
The local-scale calculation shown in Figures C-15 works in “coordination” with the regional-scale calculation described earlier. Thermal-mechanical properties, in situ temperatures and stresses, thermal loads, decay and ventilation functions are considered to be the same as those used in the regional scale calculations.



NOTE: Points 'g1' through 'g5' indicate the location where temperatures have been recorded in the calculation. These points do not relate to repository emplacement panel nomenclature.

Figure C-9. Plan View of the Repository Area Showing Boundaries of Uniformly Distributed Heating Sections

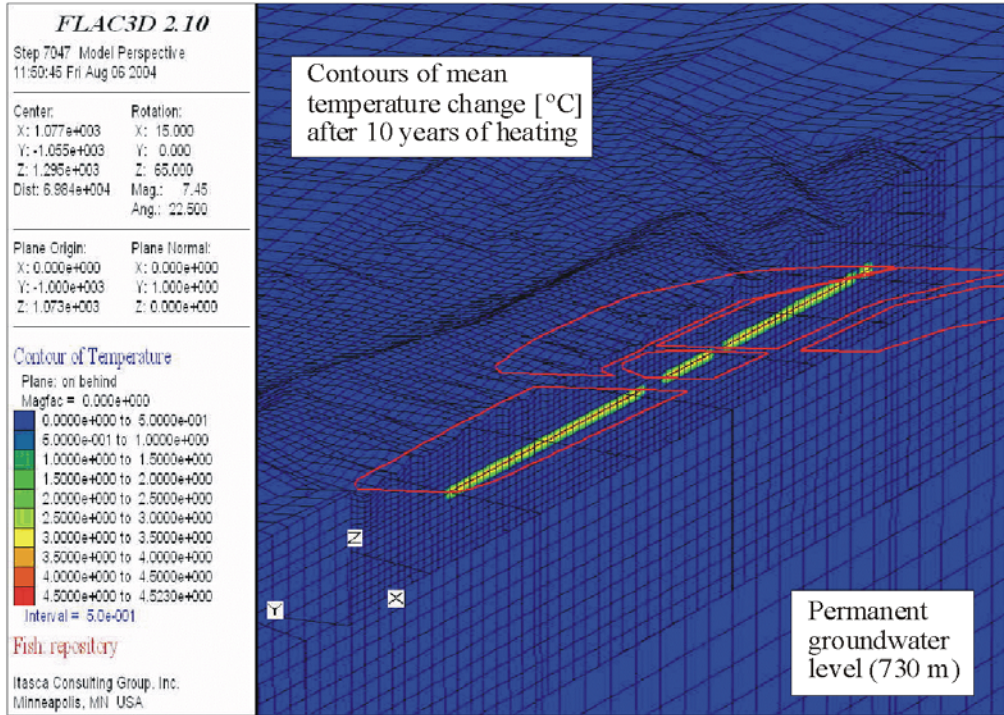




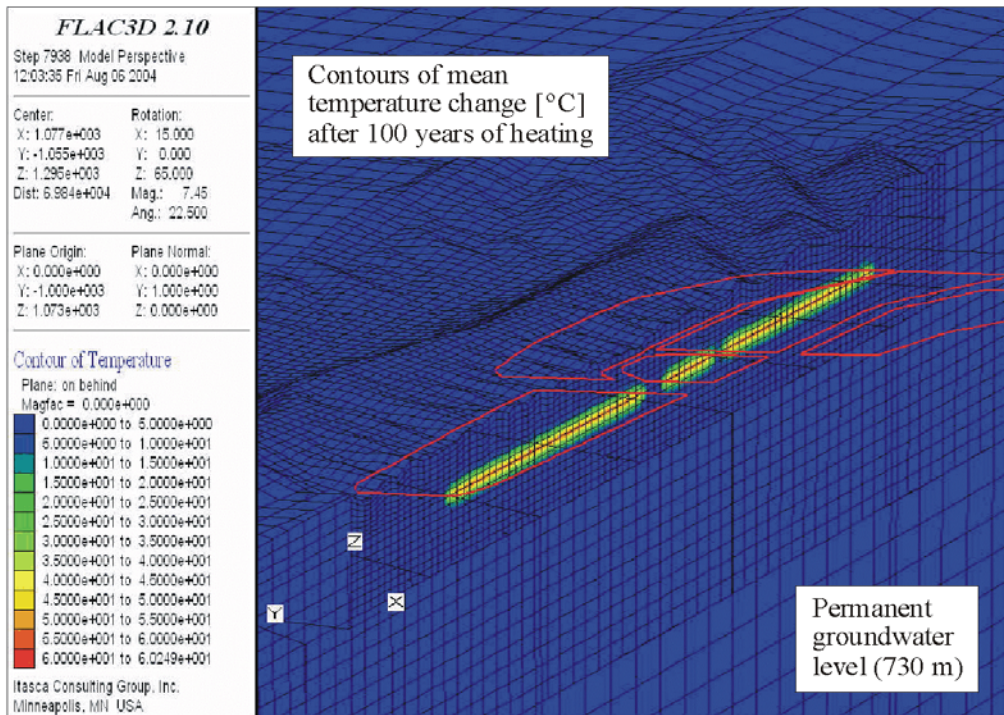
NOTE: a) Time in Years; b) Logarithm of Time in Years, for the Locations 'g1' through 'g5' Indicated in Figure C-9.

Figure C-10. Evolution of Temperature Increase as a Function

a)



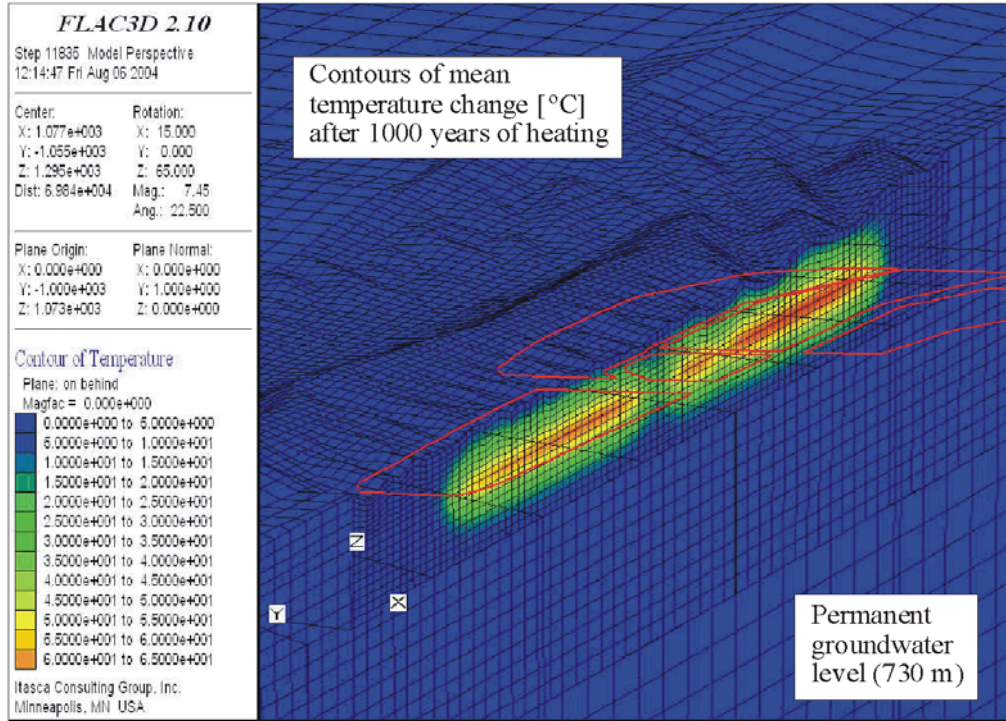
b)



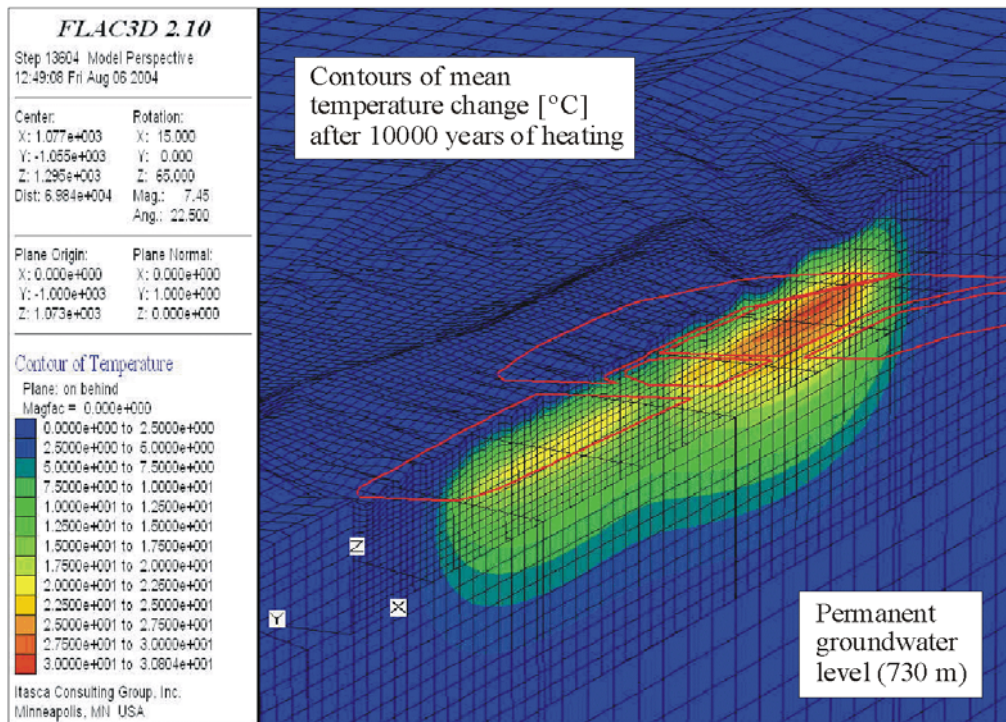
NOTE: a) after 10 years of heating; b) after 100 years of heating.

Figure C-11. Contours of Mean Temperature Change ( $\leq 100$  Years)

a)

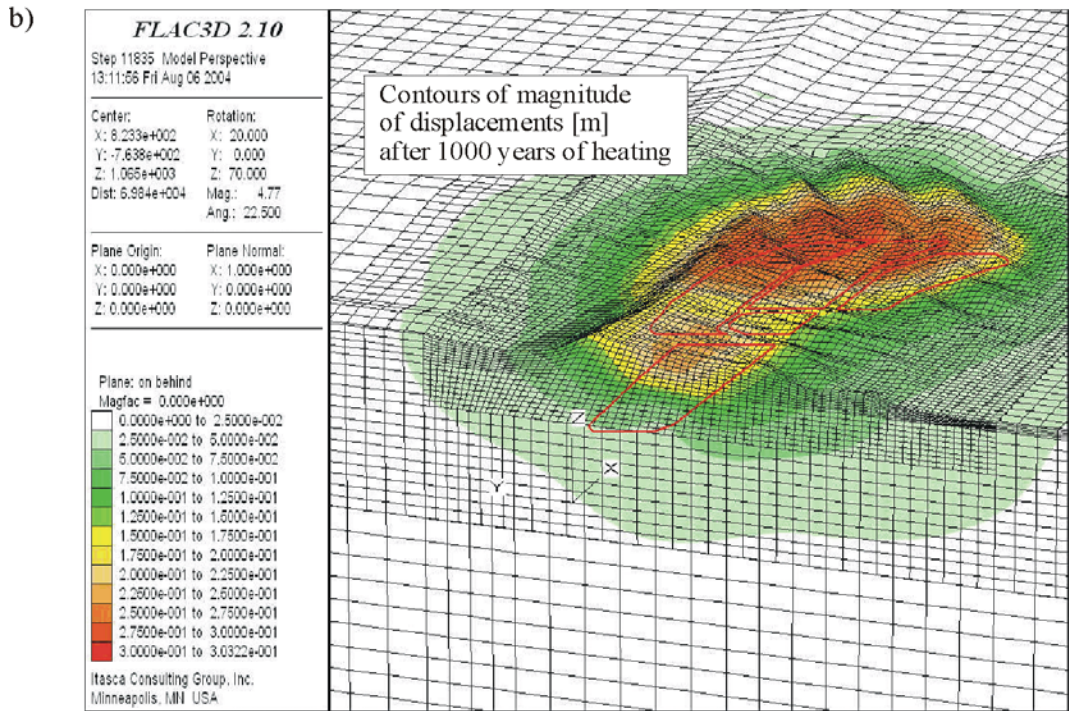
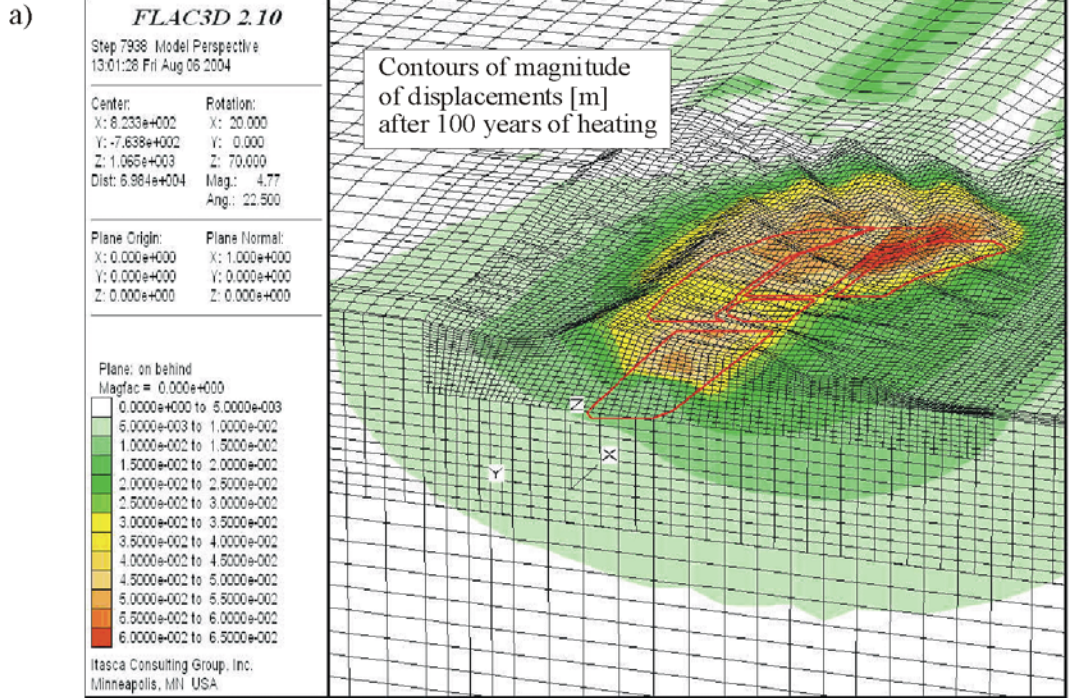


b)



NOTE: a) after 1,000 years of heating; b) after 10,000 years of heating.

Figure C-12. Contours of Mean Temperature Change ( $\geq 1,000$  Years)



NOTE: a) after 100 years of heating; b) after 1000 years of heating.

Figure C-13. Contours of Magnitude of Induced Displacements ( $\geq 100$  Years)

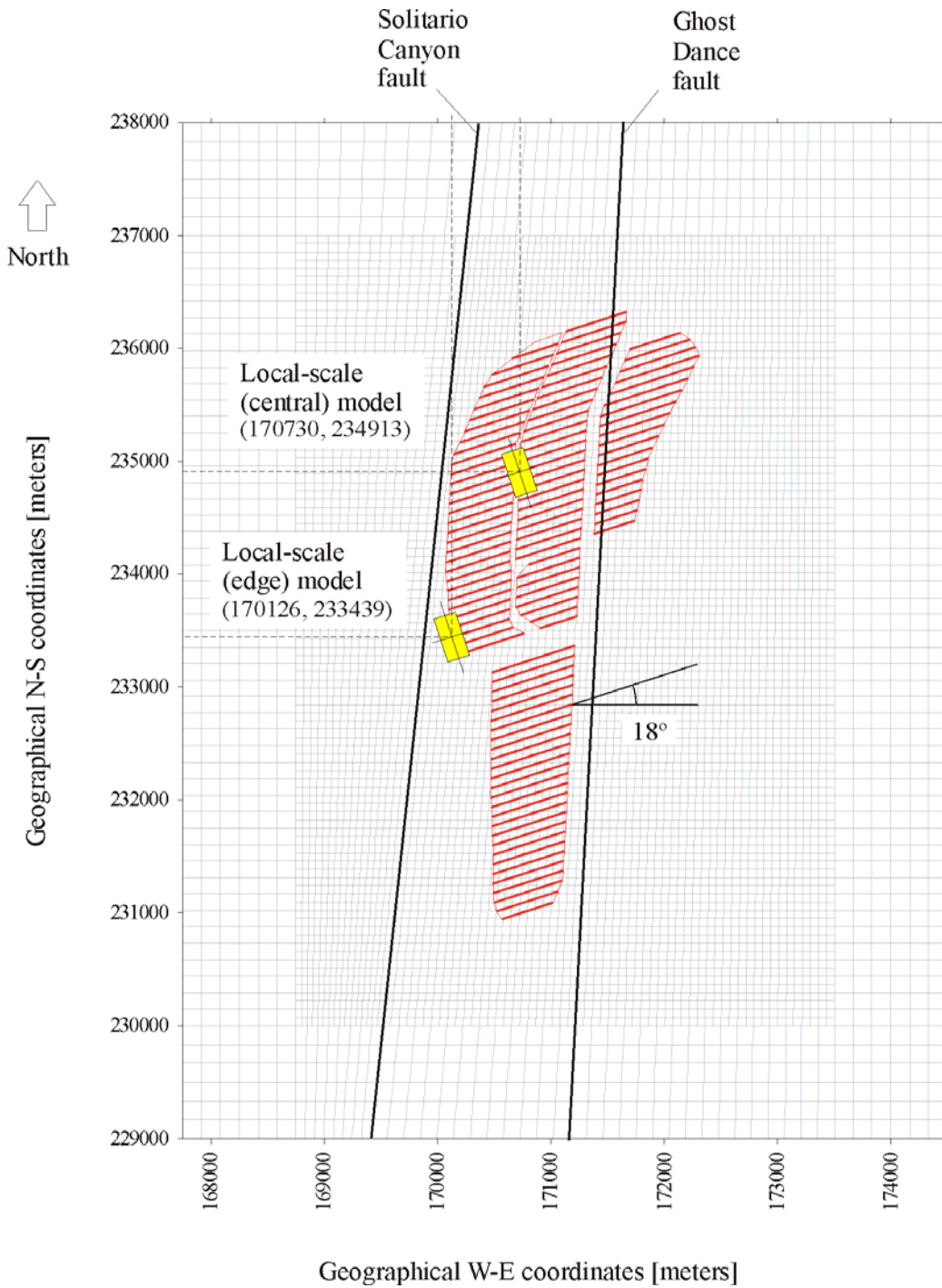


Figure C-14. Geographical Location of the Local Scale Calculation

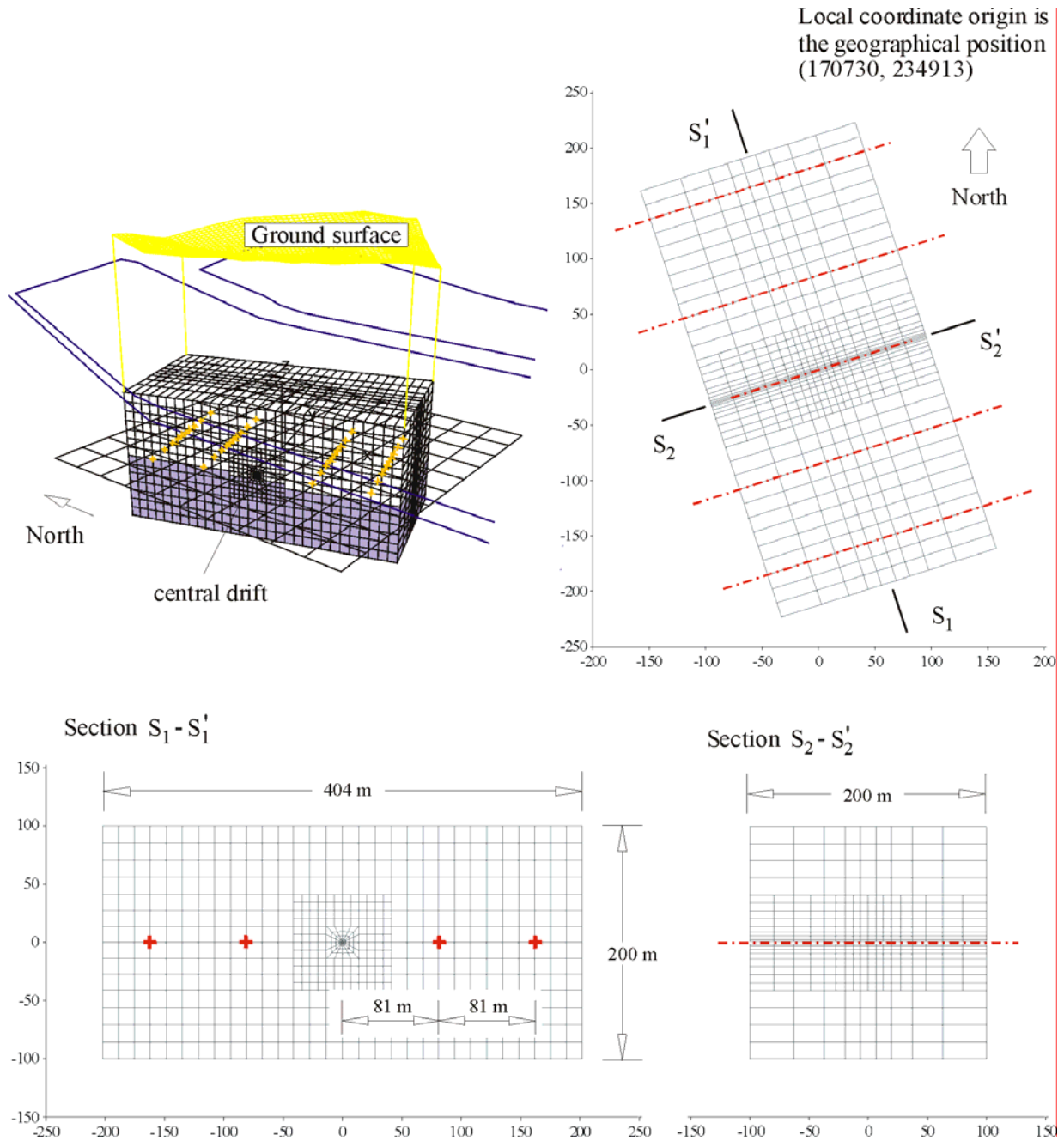


Figure C-15. Isometric and Plan View, and Cross-Sections of the Local Scale Center Calculation

The regional scale calculations provide the boundary conditions (i.e., temperature and stresses at the boundaries) needed to run the thermal-mechanical simulation. Transfer of temperatures and stresses from the regional-scale calculation to the local-scale calculations are performed by a series of interpolation functions. These functions compute the values of temperatures and stresses at the grid points and the zones of the regional scale calculation at specified times in the simulation (e.g., 1, 10, 100, 200, 300 . . . 10,000 years) and interpolate these to the grid points and zones of the local scale calculations.

The thermal-mechanical simulation at the local-scale is intended to determine the distribution of temperatures and stresses around the central drift (see Figure C-15). A linear thermal load of 1450 W/m (the same as used in the regional scale calculation) with the decay and ventilation functions shown in Figure C-8 is applied along the drifts represented in the calculations.

Results for the local-scale center calculation are represented in Figures C-16 through C-18. Figure C-16 represents the evolution of temperature at points surrounding the drifts on a vertical plane that passes through the center of the calculation and runs perpendicular to the axis of the drift (i.e., it has a direction of 162° from the North). Figure C-17 shows contours of temperature on this plane after 50 and 500 years of heating. Figure C-18 shows contours of the vertical stress  $\sigma_z$  after 50 and 500 years of heating.

Results for the local-scale edge calculation are also represented in Figures C-19 through C-21. Figure C-19 represents the evolution of temperature at points surrounding the drifts on a vertical plane that passes through the center of the calculation and runs perpendicular to the axis of the drift. Figure C-20 shows contours of temperature on this plane after 50 and 500 years of heating. Figure C-21 shows contours of the vertical stress  $\sigma_z$  after 50 and 500 years of heating.

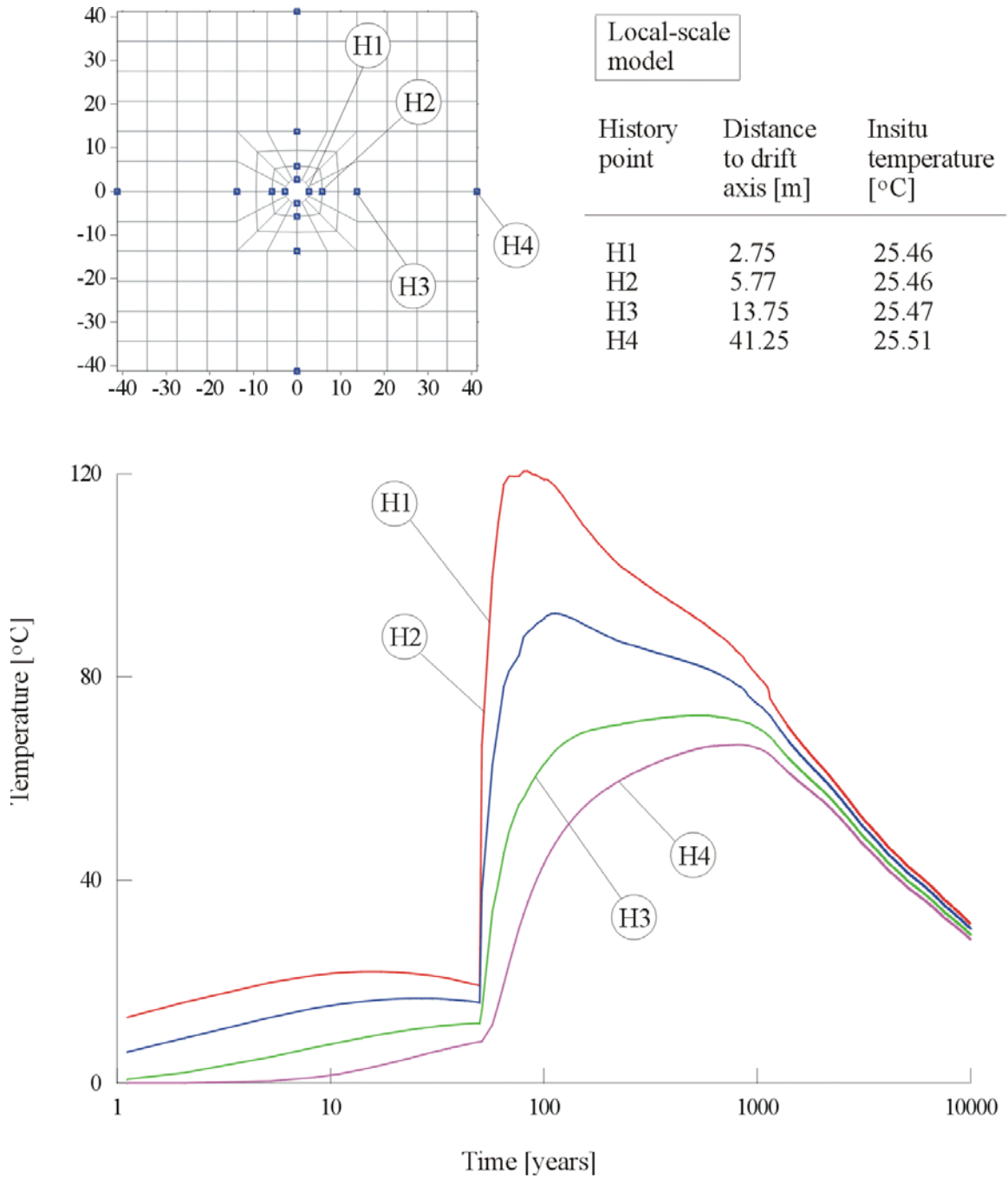
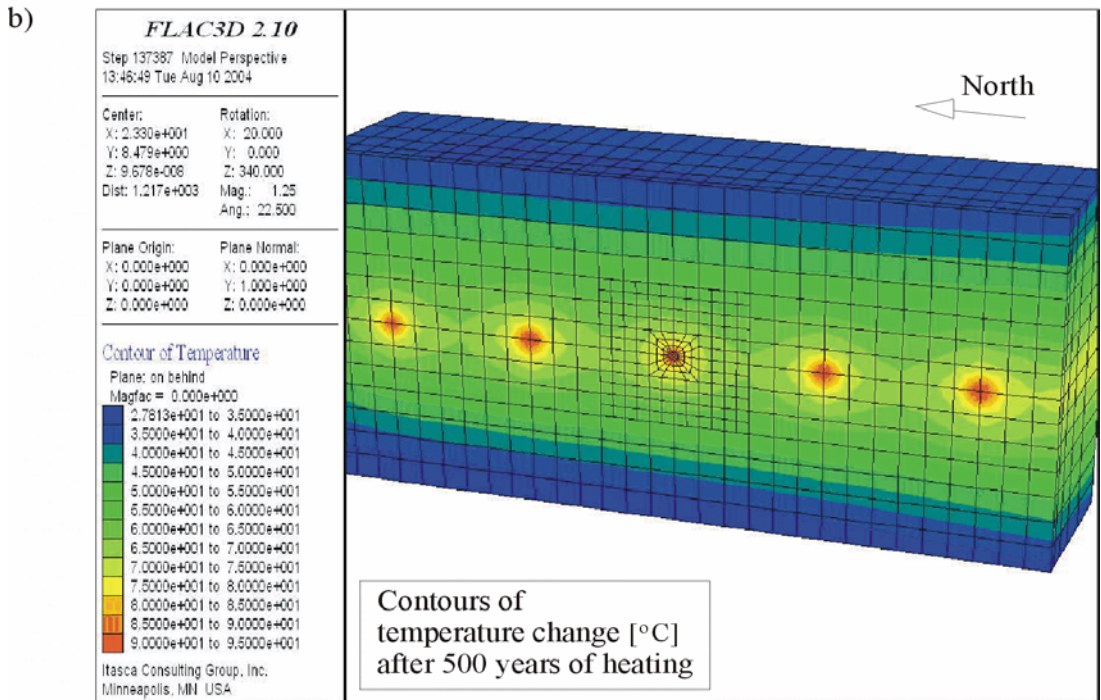
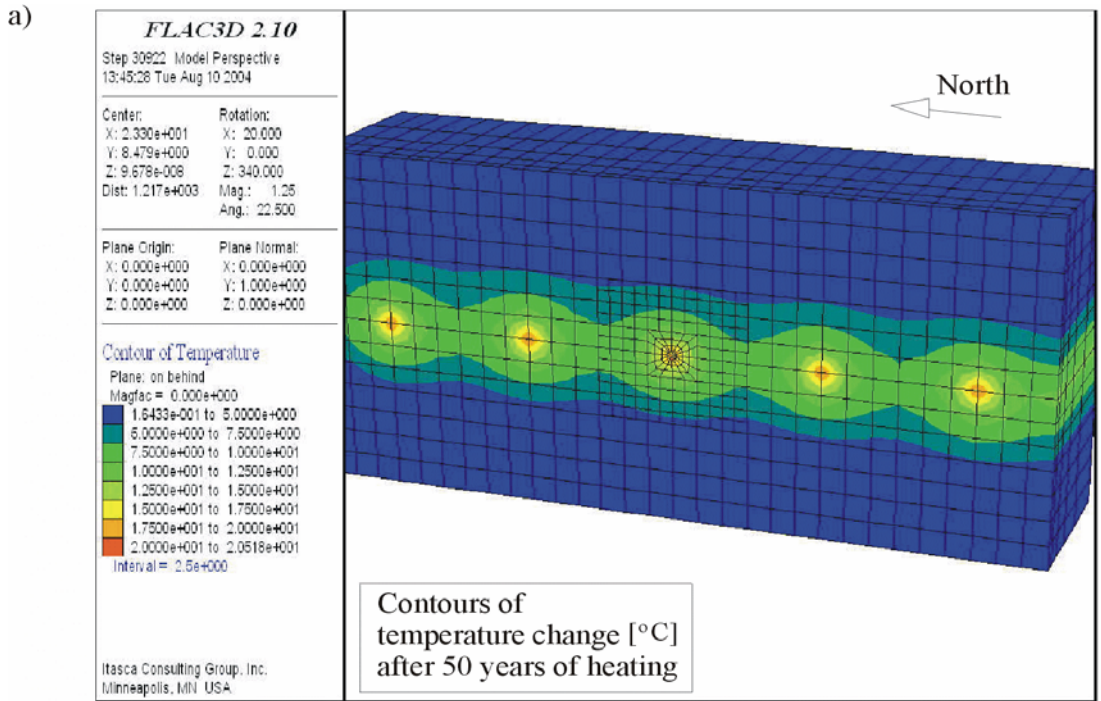


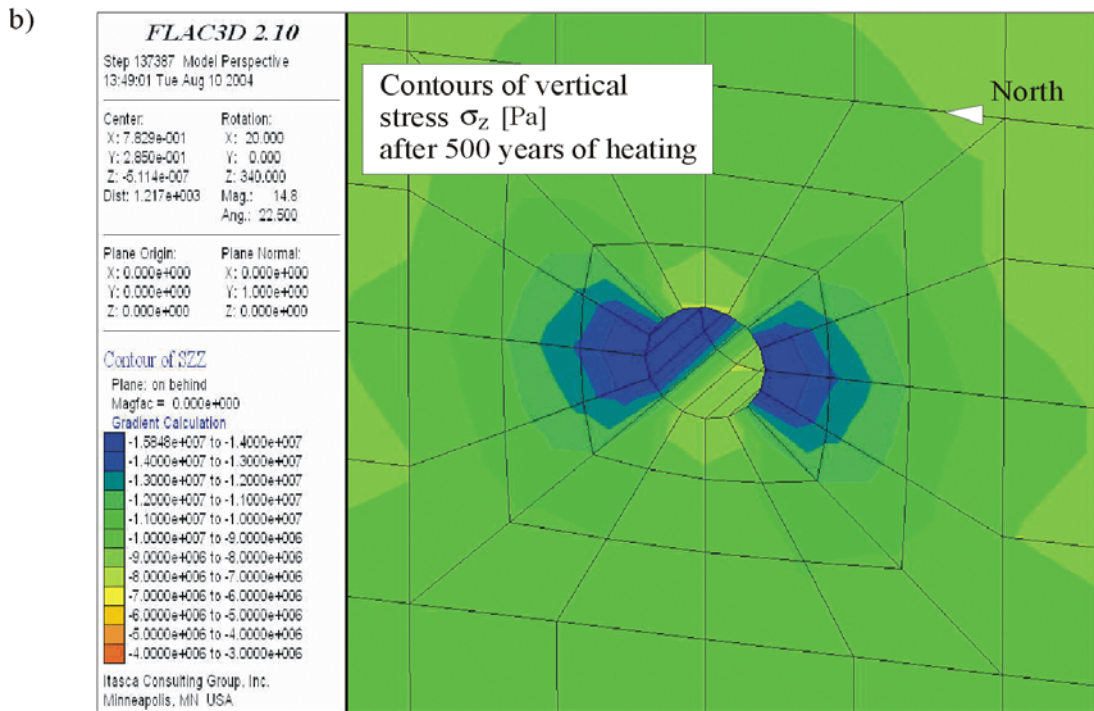
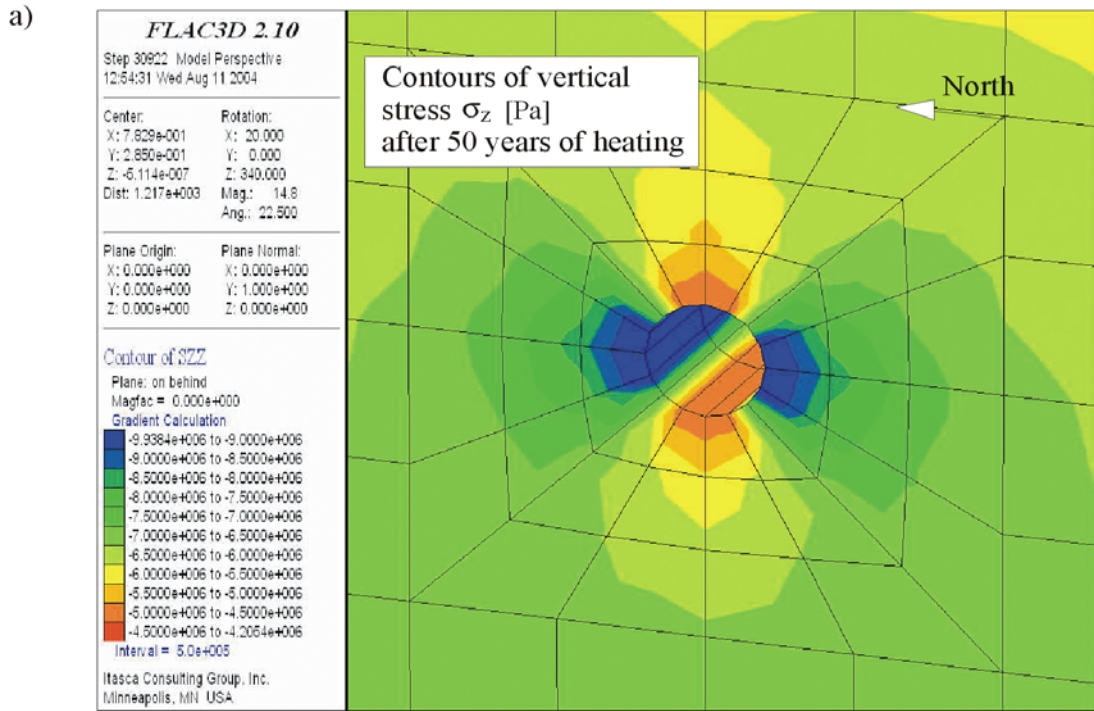
Figure C-16. Evolution of (Induced) Temperatures at Different Locations Around the Central Drift in the Local Scale Center Calculation





NOTE: Years of heating: a) 50 years; b) 500 years.

Figure C-17. Contours of Induced Temperatures in the Local Scale Center Calculation on Heating



NOTE: Years of heating: a)50 years; b) 500 years.

Figure C-18. Contours of Induced Vertical Stress  $\sigma_z$  for the Local Scale Center Calculation on Heating

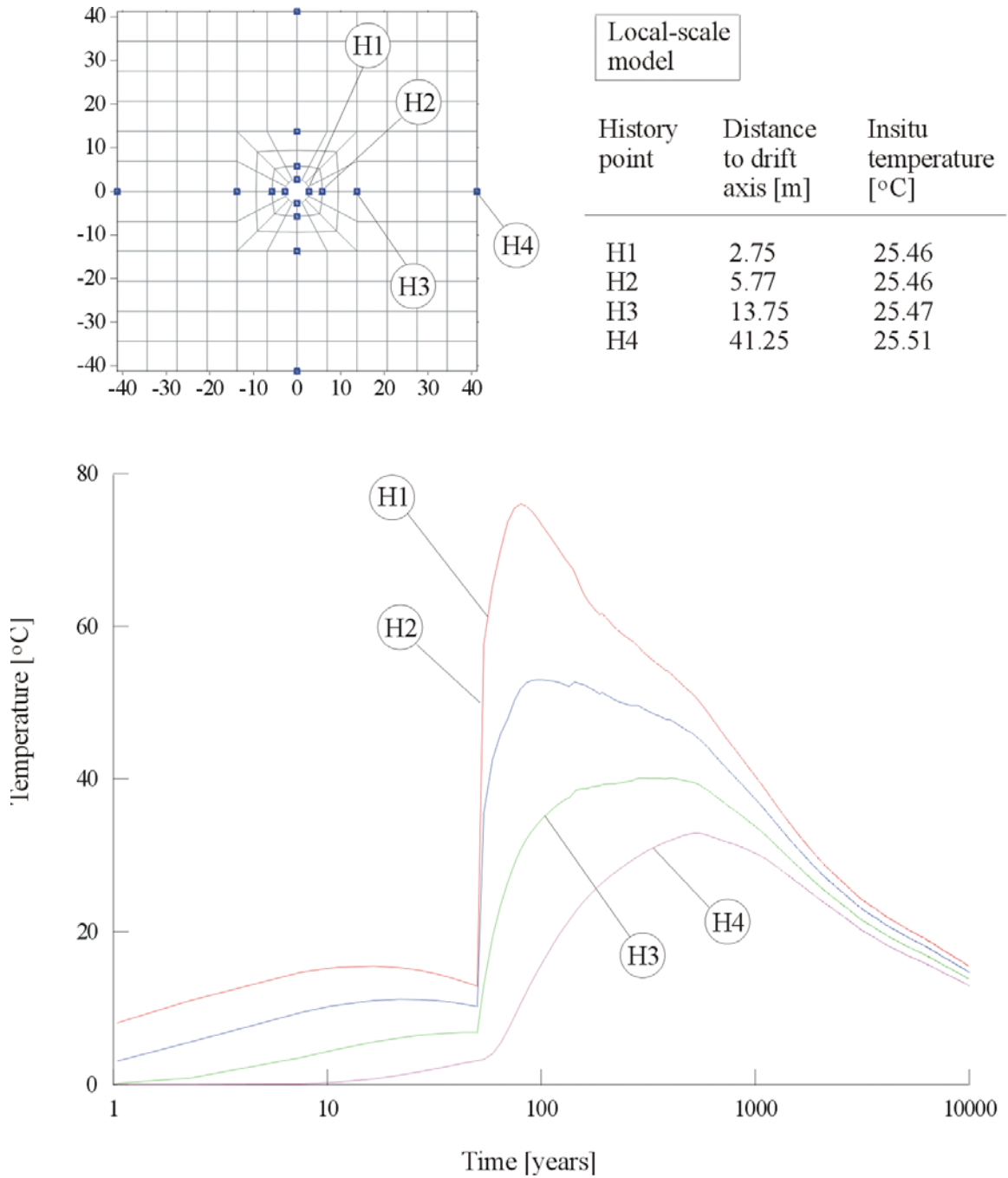
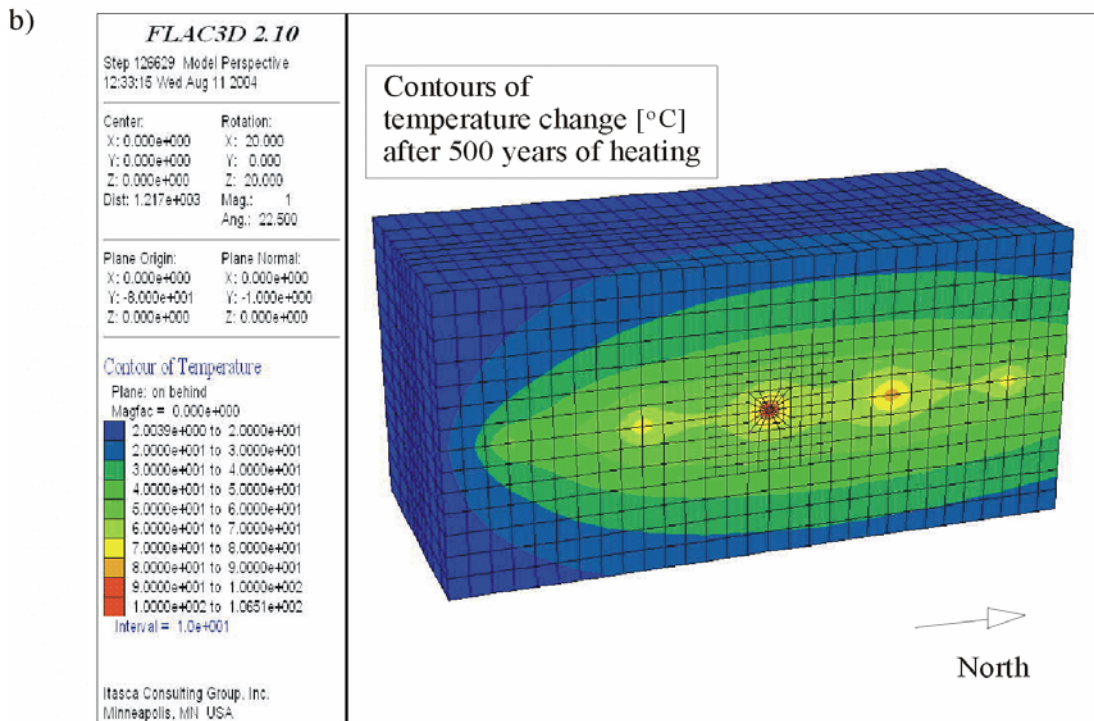
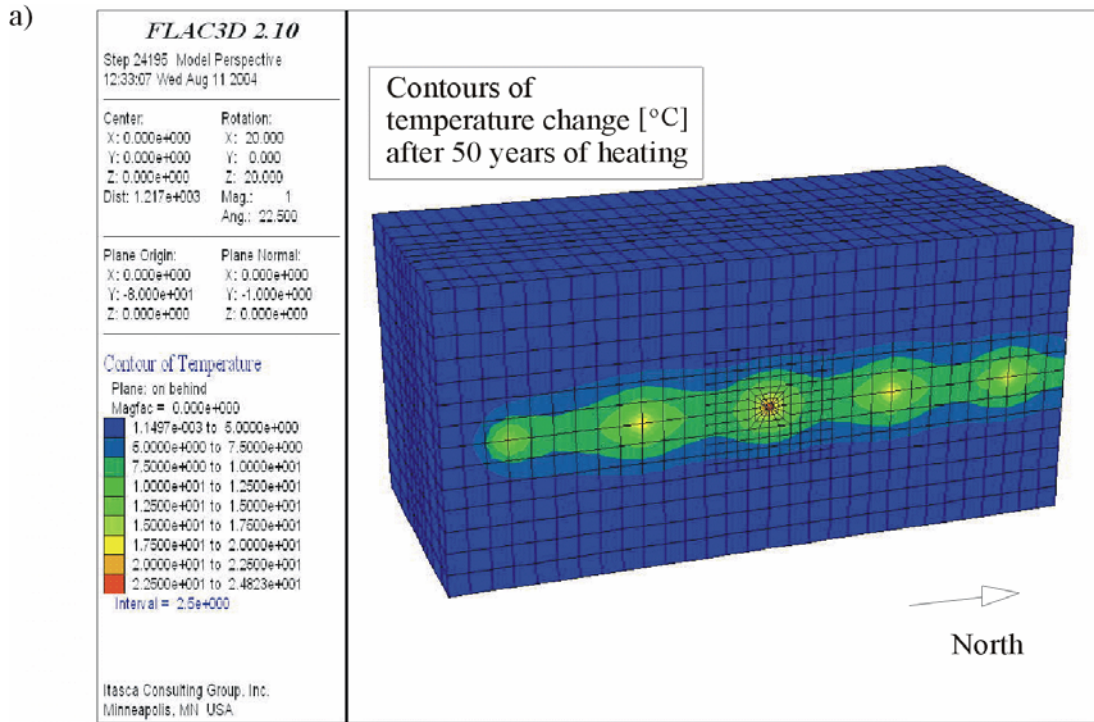
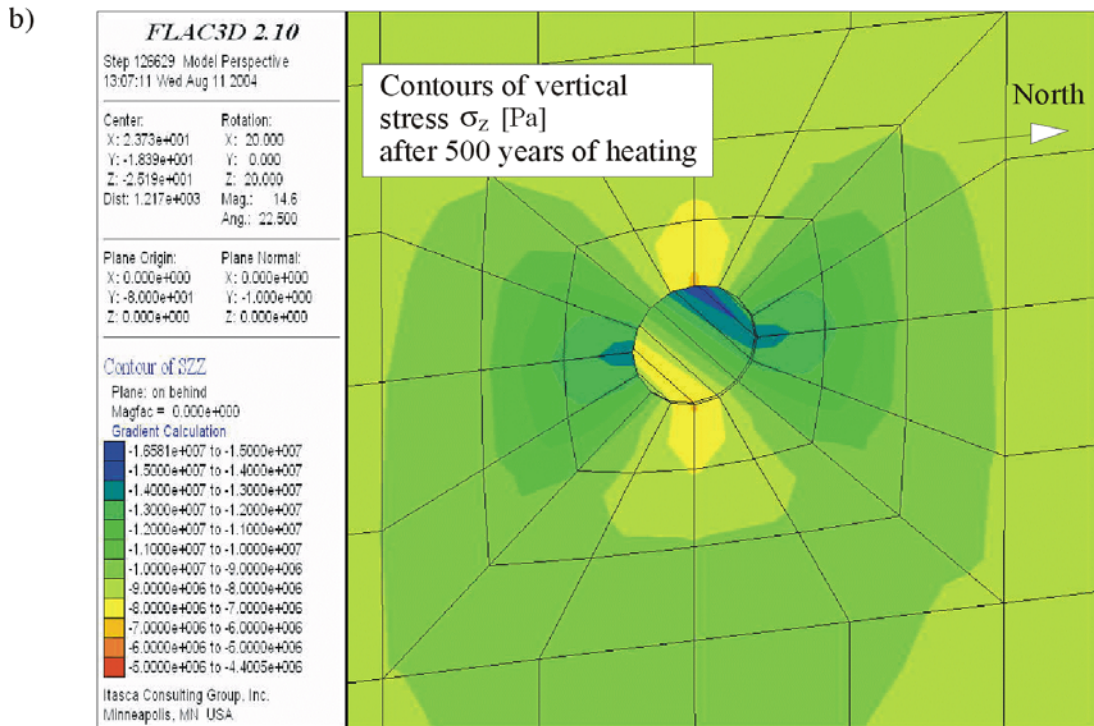
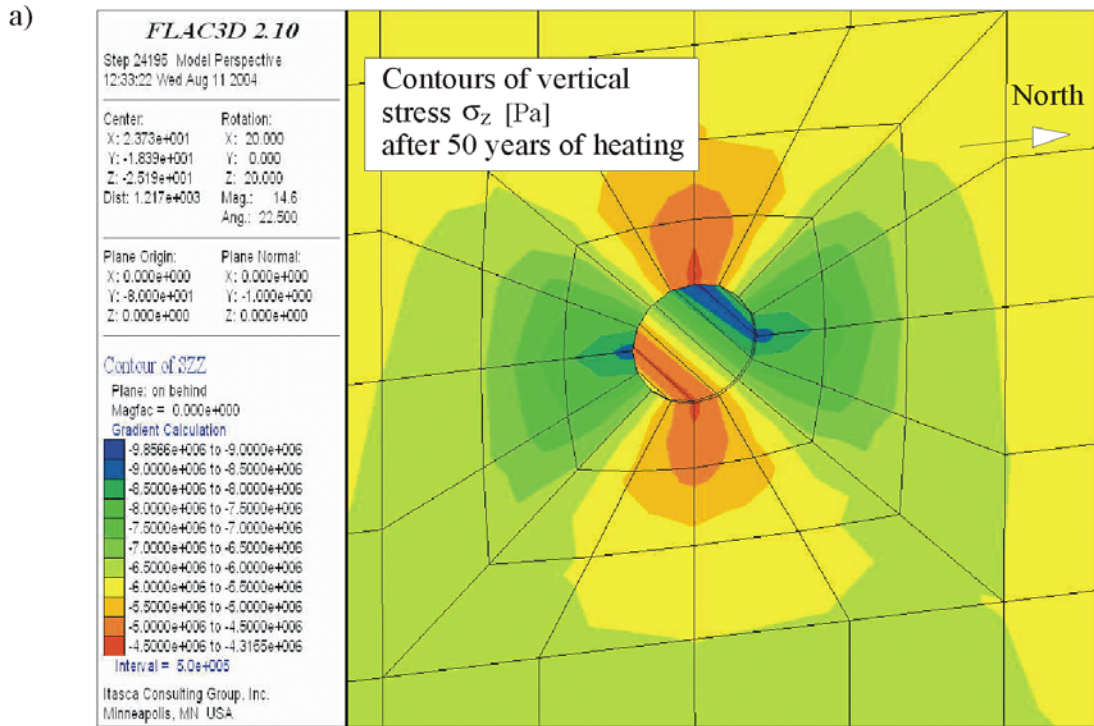


Figure C-19. Evolution of (Induced) Temperatures at Different Locations Around the Drift in the Local Scale Edge Calculation



NOTE: After heating: a) 50 years; b) 500 years.

Figure C-20. Contours of Induced Temperatures in the Local Scale Edge Calculation on Heating



NOTE: After heating: a) 50 years; b) 500 years of heating.

Figure C-21. Contours of Induced Vertical Stress  $\sigma_z$  for the Local Scale Edge Calculation on Heating

INTENTIONALLY LEFT BLANK

**APPENDIX D**  
**DRKBA ANALYSIS OF NONLITHOPHYSAL ROCK**





## DRKBA ANALYSIS OF NONLITHOPHYSAL ROCK

The DRKBA analysis approach involves the use of probabilistic key-block theory through the numerical code, DRKBA V3.31 (see Section 3.1). This method is based on an industry-accepted approach for analyzing geotechnical problems. Prior to initially purchasing the DRKBA software, technical literature sources were reviewed for the purpose of determining the most appropriate approach to be used in the development of a key-block analysis for the YMP. In summary, the issue of key-block analysis in underground excavations located in jointed rock masses has been considered in a number of design situations. Deterministic methods of block theory in rock engineering were advanced by Warburton (1981 [DIRS 150093]) and Goodman and Shi (1985 [DIRS 150094]). The UNWEDGE software (UNWEDGE V2.3, 30053 V2.3) is an example of a deterministic method that calculates the maximum block size given the spacing and orientation of three joint sets, and the excavation size and orientation. Subsequently Hoerger and Young (1990 [DIRS 151814]), Tyler et al. (1991 [DIRS 151818]), Kuzmaul and Goodman (1995 [DIRS 151816]) and Stone et al. (1996 [DIRS 150437]) have been orientated toward probabilistic risk assessment of key-block failure. Stone et al. (1996 [DIRS 150437]) reports on the use of DRKBA. These latest methods are considered suitable for the analysis of densely jointed and faulted rock masses where planar joint surfaces can reasonably be considered. These conditions typically exist at the YMP.

### D1. DRKBA APPROACH

DRKBA is a commercially available acquired software product (described in Section 3). The software simulates structural discontinuities as circular discs placed in the rock mass according to probabilistic distributions determined from tunnel mapping data. Joint planes are simulated by a Monte Carlo technique from probability distributions representing the orientation, spacing, and trace length of the corresponding joint set. DRKBA determines where joint planes intersect to form blocks, and then analyzes these blocks to determine if they are geometrically feasible (i.e., the shape of the block is such that it is physically possible to slide or fall into the tunnel opening). If the blocks are geometrically feasible, DRKBA then determines if they are mechanically stable (i.e., the gravitational forces that cause the block to move into the tunnel opening are less than the frictional forces on the block sliding surfaces). DRKBA does not include a ground support element.

A probabilistic key-block analysis using DRKBA requires four sets of data. The required data are stored in data files having extensions *.mkg*, *.exc*, *.den*, and *.prb*, and contain information for the grid, excavation, rock density, and joint sets, respectively. The make grid file (*.mkg*) includes the information required for building a grid of nodal points for the mesh. The excavation data file (*.exc*) contains the information for defining an excavation in three-dimensional space. The density file (*.den*) holds the information for the rock density data. The probabilistic joint data file (*.prb*) includes the required information for generating fracture space from the given fracture probability distributions.

The DRKBA software employs a bipolar Watson distribution for joint orientation data. The principal axis orientation and a concentration factor  $k$  are the required inputs for the bipolar Watson distribution. The concentration factor  $k$  is an index of the concentration. The larger the value of  $k$ , the more the distribution is concentrated towards the principal axis orientation. Joints

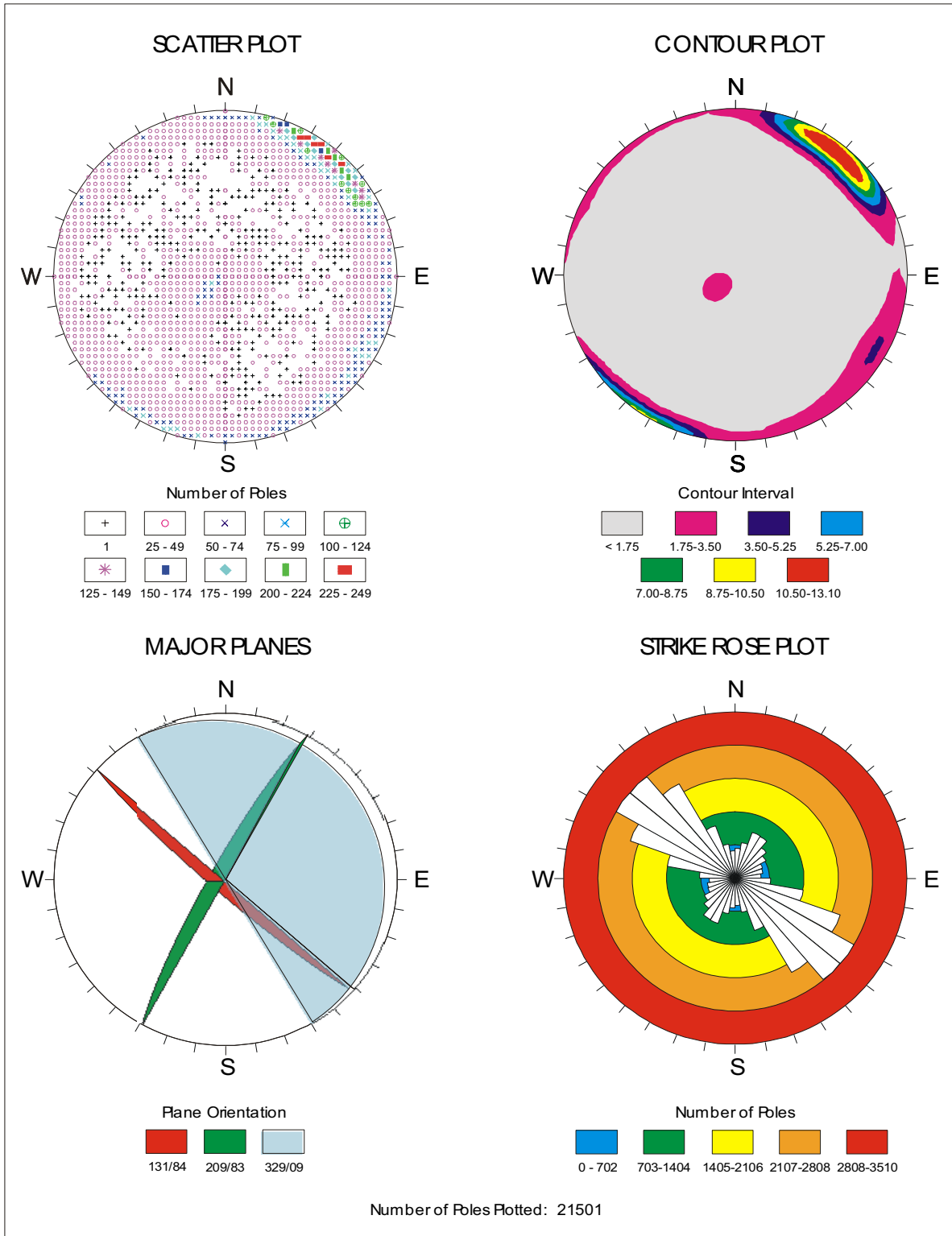
are represented as circular discs in the DRKBA analysis. Joint radii, spacings, and positioning are simulated with beta distributions. The beta distribution is a four-parameter distribution with the parameters  $a$ ,  $b$ ,  $p$ , and  $q$ . Parameters  $a$  and  $b$  represent the ends of the closed interval upon which the beta distribution is defined. The parameters  $p$  and  $q$  determine the shape of the distribution curve, their values were calculated from the mean and standard deviation of the transformed data. The transformed data were obtained by normalizing the data with the maximum value. The cohesion and friction angle of the joints are simulated as a bivariate normal distribution. Inputs for the mean and standard deviation of the joint strength parameters are required.

## D2. STATISTICAL REPRESENTATION OF JOINT DATA

The DRKBA software uses joint geometry inputs provided in Table 4-1, and which are described in *Fracture Geometry Analysis for the Stratigraphic Units of the Repository Host Horizon* (CRWMS M&O 2000 [DIRS 152286]). These developed fracture data include joint set orientation, joint spacing, joint trace length, and joint offset from the detailed line survey. Joint sets were identified in *Fracture Geometry Analysis for the Stratigraphic Units of the Repository Host Horizon* (CRWMS M&O 2000 [DIRS 152286], Section 6.4.1) based on clustering of the data from joint normal vectors plotted on stereonet as shown in Figure D-1 for the Tptpmn unit. A scatter plot, contour plot, strike rosette, and major planes are included in this figure. The major joint plane is expressed using the strike/dip format in this figure. The joint orientation is expressed in dip direction/dip format in Table D-1. In addition to the primary joint sets listed in Table D-1, a random joint set has also been simulated to account for any joint that is present in the rock mass but not accounted for in the primary sets. The dispersion of the individual joints about their associated joint set axes was modeled by a Watson bipolar distribution for axial data. This probability distribution is characterized by a unit normal vector representing the mean direction about which the data is clustered and a concentration factor  $k$  representing the degree to which the data is clustered about the mean direction. The concentration factors were calculated based on the eigenvalues and eigenvectors of the orientation matrix (Fisher et al. 1987 [DIRS 108447]). The calculated concentration factors are also listed in Table D-1. The process to calculate the concentration factors is included in the electronic files, *New-K-Tptpmn V1.mcd* and *K-small scale.mcd* (DTN: MO0408MWDDDMIO.002).

Joint radii, spacings, and positioning (see Section 5.2.1) are simulated with beta distributions. The offset measured from the center of the trace length to the scan line was used as the positioning parameter. The parameters  $a$ ,  $b$ ,  $p$  and  $q$  for the Tptpmn unit are listed in Table D-2, with the details for the calculation of each parameter provided in the electronic files, *New-Beta-Tptpmn V1.xls* and *Beta-small scale.xls* (DTN: MO0408MWDDDMIO.002). An example for calculating the distribution parameters with the fracture data of the first joint set for Tptpmn unit is provided in Section D6.

Cohesion and friction angle of the joints are simulated with the bivariate normal distribution. The laboratory shear strength tests indicate the mean cohesion value of 0.6 MPa with a range of 0.2 to 0.9 MPa (Appendix E, Section E2). Due to the wide range of values, the joint cohesion used in the nonlithophysal rockfall models is conservatively initialized as 0.1 MPa, resulting in increased rockfall.



Source: CRWMS M&O 2000 [DIRS 152286], Figure III-2.

Figure D-1. Determination of Primary Joint Sets, Tptpmn

Table D-1. Joint Set Orientation Data and Concentration Factors<sup>a</sup>

Lithologic Unit	Joint Set Number	Mean Dip Direction <sup>b</sup> (degrees)	Mean Dip <sup>b</sup> (degrees)	Concentration Factor k
Tptpmn	1	221	84	31.586
	2	299	83	26.143
	3	59	9	18.210
	Random (> 1-m trace)	267	79	2.896
	Random (< 1-m trace)	293	64	1.833

<sup>a</sup> Calculation details provided in DTN: MO0408MWDDDMIO.002, files *New-K-Tptpmn V1.mcd* and *K-small scale.mcd* and described in Section D7.

<sup>b</sup> The derivation of the joint set orientation data is shown in Figure D-1. The joint set orientation data for small trace length fractures (i.e., < 1 m trace) is documented in the file, *small scale filtering.xls* (DTN: MO0408MWDDDMIO.002) as the mean of the azimuth and dip data.

Table D-2. Beta Distribution Parameters for Tptpmn Unit<sup>a</sup>

Joint Set Number	Parameters	a (m)	b (m)	p	q
1	Spacing	0.0008	13.9199	0.2322	5.1372
	Radius	1.8200	108.0000	0.6554	20.7171
	Positioning	0.0000	9.1500	0.7569	10.2825
2	Spacing	0.0033	16.5306	0.4098	3.0879
	Radius	1.6400	141.0600	0.2024	7.2515
	Positioning	0.0000	9.1500	0.3292	4.0327
3	Spacing	0.0018	15.2606	0.2010	5.2988
	Radius	0.3200	101.6000	0.5503	8.5360
	Positioning	0.0150	9.1500	0.6369	4.6763
Random (> 1 m trace)	Spacing	0.0100	15.1900	0.5279	7.6008
	Radius	1.3000	60.6000	0.6333	9.2812
	Positioning	0.0000	9.1500	0.5735	7.6186
Random (< 1 m trace)	Spacing	0.0100	0.9900	0.5119	3.9947
	Radius	0.3000	1.9400	0.3850	1.3472
	Positioning	0.0050	0.4550	0.8316	3.0687

<sup>a</sup> Calculation details provided in DTN: MO0408MWDDDMIO.002, files *New-Beta-Tptpmn V1.xls* and *Beta-small scale.xls* are described in Section D7.

### D3. EXCAVATION MODELING

The excavation in this analysis is a horizontal 5.5 m diameter emplacement drift trending 75° in accordance with the repository design description (BSC 2003 [DIRS 165572], Sections 5.1.4 and 8.7). It should be noted that the actual emplacement drift azimuth is 72°. This 3° difference between the modeled and actual drift alignment is acceptable since given the variability of joint set orientations captured in the model, the alignment difference does not significantly affect the results from this analysis.

For each Monte Carlo simulation, a 24.4 m long (80-ft) tunnel has been modeled in a three-dimensional space. A circular tunnel opening without backfill was modeled using 18 plane equations to describe the circumference of the circular tunnel, and 2 plane equations were used to describe each end of the tunnel. The selection for the length of the tunnel modeled and the number of planes for simulation of the circular opening were based on the computer run time and the accuracy of the simulation. Calculations for the plane equations are included in the electronic file, *exca vectors V2.xls* (DTN: MO0408MWDDDMIO.002). The region around the excavation has been modeled with a grid consisting of 681,472 nodes. The nodes are spaced 0.3 m (1 ft) apart, with each node representing 0.028 cubic meters (1 cubic foot) of the rock mass.

#### D4. SEISMIC CONSIDERATION

Natural analogues for the effect of seismic events on rockfall are provided in Appendix G. Underground openings are constrained by the surrounding medium, and it is unlikely that underground openings could move to any significant extent independently of the medium or be subjected to vibration amplification. Two potential causes of block movement during seismic events were observed. The first is related to the differential acceleration in the rock blocks surrounding the tunnel due to seismic excitation (Dowding 1979 [DIRS 101977], p. 19). The second cause is the increase of the tangential force from seismic loading along the sliding surfaces of the rock block (Kaiser et al. 1996 [DIRS 108453], p. 8-3).

A high-frequency seismic wave is required for the possibility of block movement due to differential acceleration (Dowding 1979 [DIRS 101977], p. 19). For a case with shear wave velocity of 2000 m/sec intersecting a 5.5 m diameter drift in the repository host rock, the frequency that would produce the differential acceleration was calculated to be approximately 90 Hz. This frequency of concern is very high compared to the principal frequencies (1 to 10 Hz) with major earthquakes. Block movement due to differential acceleration is therefore not considered in this analysis.

With a relatively high ratio of wavelength to opening diameter, the surrounding rock mass and the opening itself move nearly as a rigid body with free-field acceleration. A simplified quasi-static approach was used in this analysis to account for the increase of the force along the sliding surfaces. Due to the limitation of DRKBA, seismic loads cannot be directly applied to the opening in the numerical simulation. An alternative method with reduction of joint strength parameters was used to account for the seismic effect. The reduced joint strength parameters are listed in Table D-3.

The following equation was derived using basic laws of motion for a sliding block (Figure D-2), and used to calculate the reduced friction angle in the alternative method:

$$\Delta\phi = \text{atan}(PGA/1g) \quad (\text{Eq. D-1})$$

where  $PGA$  is the peak ground acceleration of the shear wave with unit in  $g$ . The tangential forces ( $T1$  and  $T2$ ) and normal forces ( $N1$  and  $N2$ ) in Figure D-2 are defined as follows:

$$T1 = Mg \times \sin\theta \quad (\text{Eq. D-2})$$

Table D-3. Reduced Joint Strength Parameters to Account for Seismic Effect

Loading Case	Peak Ground Acceleration (g)	Joint Cohesion (Pa)	Joint Friction Angle (degree)
Static	—	99,873	41
Seismic $1 \times 10^{-3}$	0.14	21,282	34
Seismic $1 \times 10^{-4}$	0.47	10,776	18

NOTE: Peak ground acceleration for  $1 \times 10^{-4}$  ground motion was selected based on DTN: MO0306SDSAVDTH.000 [DIRS 164033] (see Table 6-5). Peak ground acceleration for  $1 \times 10^{-3}$  ground motion was selected based on preliminary data and is used for comparison only. Static joint cohesion and friction angle values are provided in Appendix E (Section E2). Seismic joint cohesion and friction angle values are calculated as described in this section. Note that static joint cohesion is conservatively scaled down to 0.1 MPa from 0.6 MPa (see Section D2).

$$T2 = Ma \times \cos \theta \quad (\text{Eq. D-3})$$

$$N1 = Mg \times \cos \theta \quad (\text{Eq. D-4})$$

$$N2 = -Ma \times \sin \theta \quad (\text{Eq. D-5})$$

where  $M$ ,  $a$ ,  $g$ , and  $\theta$  are defined in Figure D-2. At the incipience of block sliding, the tangential force is equal to the resisting frictional force:

$$T1 + T2 = (N1 + N2) \times \tan \phi \quad (\text{Eq. D-6})$$

where  $\phi$  is defined in Figure D-2. Substituting Equations D-2 through D-5 into Equation D-6 yields

$$Mg \times \sin \theta + Ma \times \cos \theta = (Mg \times \cos \theta - Ma \times \sin \theta) \times \tan \phi \quad (\text{Eq. D-7})$$

Equation D-7 can be arranged to the following form:

$$\frac{a}{g} = \frac{\cos \theta \times \tan \phi - \sin \theta}{\cos \theta + \sin \theta \times \tan \phi} = \frac{\tan \phi - \tan \theta}{1 + \tan \theta \times \tan \phi} \quad (\text{Eq. D-8})$$

Equation D-8 can be rewritten based on the trigonometric relationship for the tangent function:

$$\frac{a}{g} = \tan(\phi - \theta) = \tan(\Delta \phi) \quad (\text{Eq. D-9})$$

Equation D-1 is therefore derived as:

$$\Delta \phi = \text{atan}\left(\frac{a}{g}\right) \quad (\text{Eq. D-10})$$

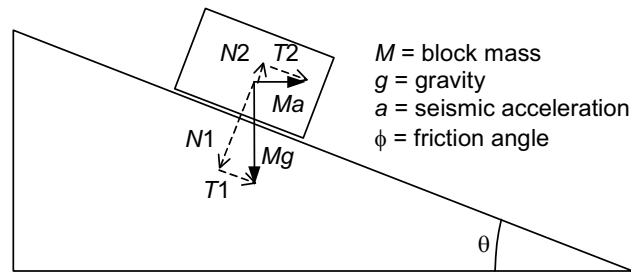


Figure D-2. Illustrative Example of Derivation of Equation D-1

where  $a = \text{PGA}$  in Equation D-1. Note that this approach is not applicable for large ground motions in which the PGA exceeds  $0.86\text{ g}$ , since with an initial static friction angle of  $41^\circ$ , Equation D-1 would produce negative friction angles.

This method is illustrated by the simple examples presented in Figure D-3. The stable joint plane example is presented in Figure D-3a. In this example, the alternative method (i.e., a reduced friction angle) predicts a stable condition, which is the same as the approach with the seismic load included. The unstable joint plane example is presented in Figure D-3b. The alternative reduced friction angle method is capable of predicting the unstable joint condition as shown.

#### D5. THERMAL AND FRACTURE - DEGRADATION CONSIDERATION

The induced thermal stress and the potential degradation of joint mechanical properties are the concerns for the thermal effect to the block movement. Due to the lateral confinement of the rock, the predicted thermal stress is highest in the horizontal direction. The high horizontal thermal stress provides a locking effect for the blocks formed by the predominant vertical joint sets during the heating period, thus preventing rockfall. Due to the limitation of the applying external loads using DRKBA, this locking effect, which reduces rockfall, was conservatively ignored in this analysis.

The site-specific time-dependent behavior of joint strength parameters for the host rock is not available at this time. An approach based on the time-dependent degradation work by Kemeny (1991 [DIRS 108455]) is used in this study. The approach considers that the degradation occurs mainly due to the reduction of joint cohesion. Joint cohesion exists due to the asperities along the joint surface. These asperities may shear off with time and they may shear off due to the increased shear stress caused by the thermal effect. By using the numerical analysis results for the thermally induced shear stress and some site-specific data, the joint cohesion degradation with time can be quantified based on the approach reported by Kemeny and Cook (1986 [DIRS 108454]).

The equation for the mode II stress intensity factor ( $K_{II}$ ) for a single asperity under shear and normal stresses can be expressed in the following (Kemeny and Cook 1986 [DIRS 108454]):

$$K_{II} = \frac{(\tau - \sigma_n \tan(\phi))2w}{\sqrt{\pi a(t)}} \quad (\text{Eq. D-11})$$

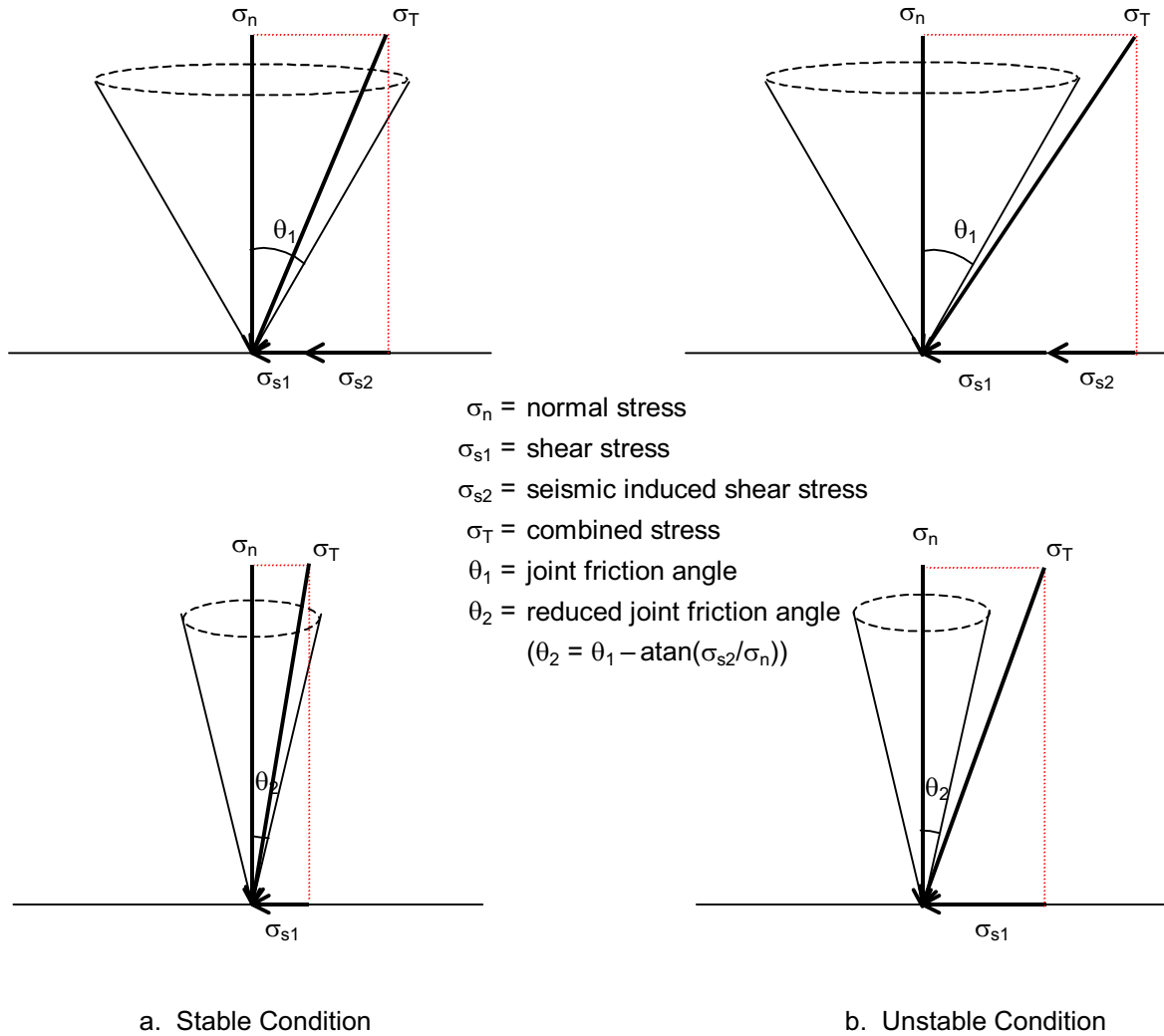


Figure D-3. Illustrative Examples for the Alternative Method to Account for Seismic Effect

where  $\tau$  is the shear stress,  $\sigma_n$  is the normal stress, and  $\phi$  is the friction angle. The geometrical parameters  $w$  and  $a$  are shown in Figure D-4.

Critical stress intensity factor of the mode II fracture,  $K_{IIC}$ , of  $0.5 \text{ MPa m}^{1/2}$  is selected based on data from the direct shear tests (Table E-3) and the Linear Elastic Fracture Mechanics (LEFM) theory. In the LEFM, the  $K_{IIC}$  is (Jaeger and Cook 1979 [DIRS 106219]):

$$K_{IIC} = \sqrt{G_c E} \tag{Eq. D-12}$$

where  $G_c$  is the strain energy release rate ( $\text{J m}^{-2}$ ) and  $E$  is the Young's modulus (GPa). The strain



energy release rate,  $G_c$ , could be estimated from the energy stored during the direct shear tests:

$$G_c = \frac{1}{2} C_0 d_c \quad (\text{Eq. D-13})$$

where  $C_0$  is the cohesion (peak shear strength at zero normal stress), and  $d_c$  is the displacement at the peak shear strength. While  $d_c$  is considered as 0.5 mm from the displacement at the peak shear strength of the lowest normal stress, 2.5 MPa (see the first row of Table E-3 and Figure 6 of Olsson and Brown 1997 [DIRS 106453]), cohesion and Young's modulus are utilized as 0.1 MPa (Section D.2) and 33.6 GPa (Table E-6), respectively. The resulting  $K_{IIC}$  value is  $0.92 \text{ MPa m}^{1/2}$ . However, a value of  $0.5 \text{ MPa m}^{1/2}$  is selected for this analysis, since the Young's modulus varies from 13.4 to 47.3 GPa (Table E-6) and the resulting  $K_{IIC}$  varies from 0.58 to  $1.09 \text{ MPa m}^{1/2}$ . The selected value is conservative, since the input cohesion and Young's modulus values are conservative.

It is considered that shear crack growth will occur when the mode II stress intensity factor,  $K_{II}$  reaches the  $K_{IIC}$ . Setting  $K_{II} = K_{IIC}$  and rearranging Equation D-11 for  $\tau$  gives the following:

$$\tau = \frac{K_{IIC} \sqrt{\pi a}}{2w} + \sigma_n \tan \phi \quad (\text{Eq. D-14})$$

Equation D-14 is the failure criterion for the discontinuity, and is made up of two terms, a cohesion term and a frictional term. The first term on the right hand side of the equation is the joint cohesion due to the asperity:

$$C_0 = \frac{K_{IIC} \sqrt{\pi a(t)}}{2w} \quad (\text{Eq. D-15})$$

where  $C_0$  is the joint cohesion.

The cohesion of 0.1 MPa is predicted using the parameters  $K_{IIC} = 0.5 \text{ MPa m}^{1/2}$ ,  $w = 0.5 \text{ m}$ , and  $a_0$  is equal to 0.0127 m. These parameters are therefore used as the initial parameters before time-dependent crack growth occurs. As the asperity size decreases due to time-dependent crack growth, the cohesion will decrease as given by Equation D-15.

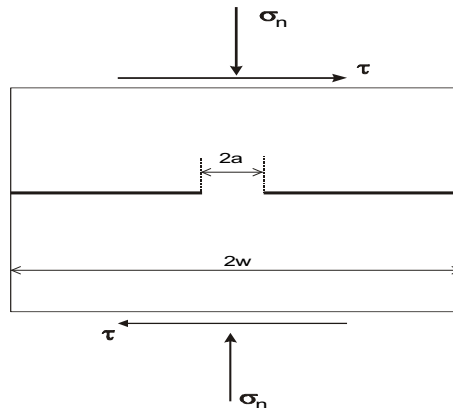


Figure D-4. Parameters Used for Calculation of Mode II Stress Intensity Factor

The time-dependent crack growth can be expressed using the following equation (Kemeny 1991 [DIRS 108455]):

$$\frac{d(a(t))}{dt} = A \left[ \frac{K_{II}}{K_{IIC}} \right]^n \quad (\text{Eq. D-16})$$

where  $A$  and  $n$  are subcritical crack growth parameters.

Combining Equations D-11 and D-16, the time-dependent crack growth can be written as:

$$\frac{d(a(t))}{dt} = 2^n A \pi^{-n/2} \left[ \frac{w(\tau - \sigma_n \tan(\phi))}{\sqrt{a(t)} K_{IIC}} \right]^n \quad (\text{Eq. D-17})$$

Previous studies of the Yucca Mountain area have used  $n = 25$  and  $A$  ranging from  $10^{-6}$  to  $10^{-4}$  m/sec (Kessler et al. 1996 [DIRS 100558]). A value for  $A$  of  $10^{-5}$  m/sec is used in this analysis.

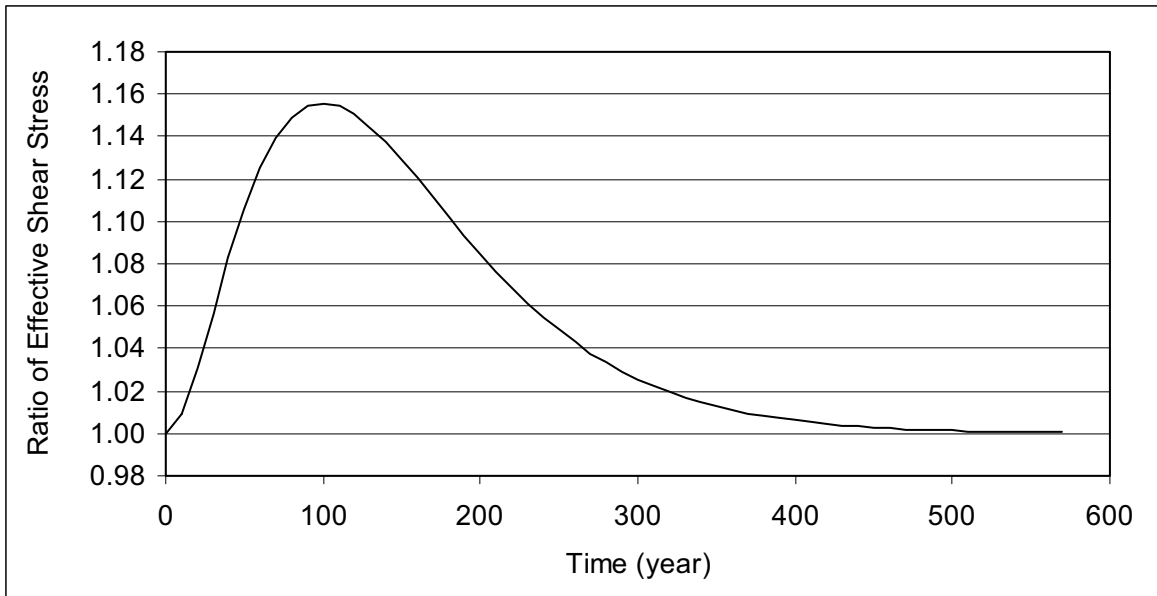
The effective shear stress,  $(\tau - \sigma_n \tan\phi)$ , is time-dependent due to the thermal loading by the canisters. The thermal loading can cause horizontal stresses as high as 50 MPa in the backs of the underground drifts, decreasing the stability of some joints and increasing the stability of others. On average, it is found that the effective shear stress along the joints  $(\tau - \sigma_n \tan\phi)$  increases by as much as 16 percent in the time period where heating of the rock occurs. The curve-fit function used to describe the additional effective shear stress due to thermal heating is as follows:

$$f(t) = 1 + 0.00001044556 * e^{(120-t)/50} t^2 \quad (\text{Eq. D-18})$$

This function is presented graphically in Figure D-5. The figure shows that the shear stresses are increased by approximately 10 percent in the period between 50 and 200 years. Adding this function to Equation D-17, the time-dependent crack growth expression is now:

$$\frac{d(a(t))}{dt} = 31536000 * 2^n A \pi^{-n/2} \left[ \frac{w(\tau - \sigma_n \tan(\phi))(1 + 0.00001044556 * e^{(120-t)/50} t^2)}{\sqrt{a(t)} K_{IIC}} \right]^n \quad (\text{Eq. D-19})$$

The nonlinear differential equation was solved numerically using the fourth order Runge-Kutta method in Mathcad (file: *Time thermal cohesion degradation V1.mcd*). The calculation results in an asperity versus time relationship. This relationship is then used in conjunction with Equation D-15 to obtain the cohesion values for various times (Table A-1, file: *Time thermal cohesion degradation V1.mcd*).



Appendix A-1, file *Thermal curve V1.xls*

Figure D-5. Function of the Additional Shear Stress Due to Thermal Loading

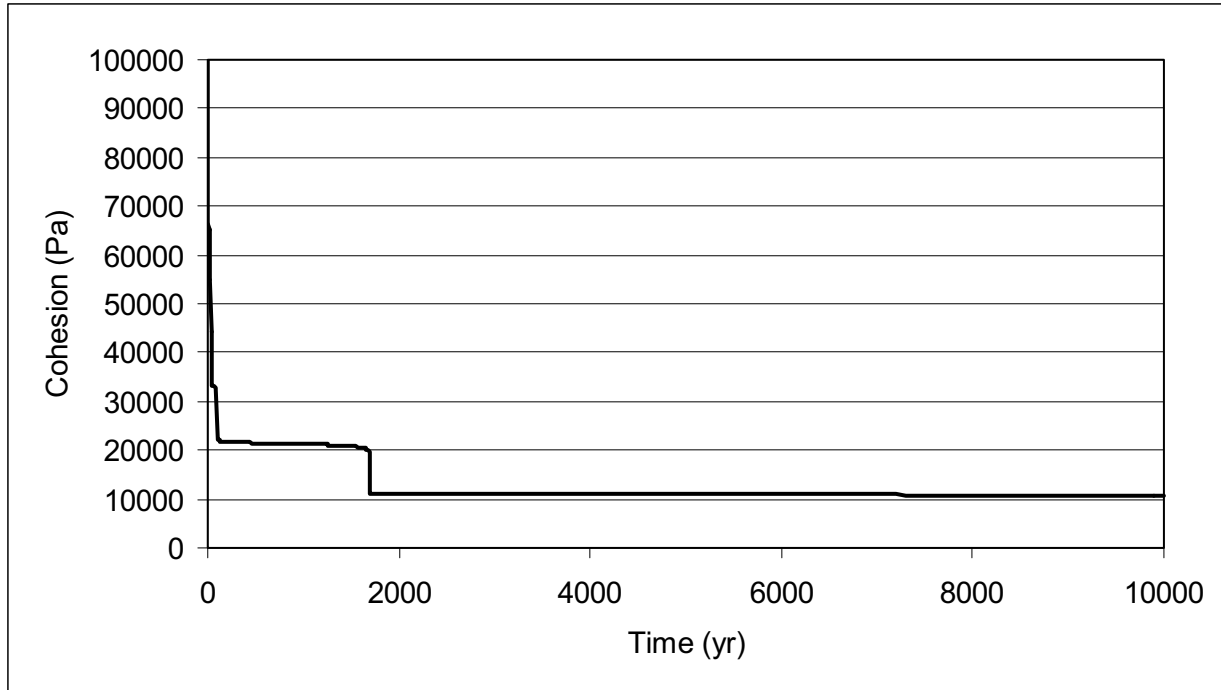
Numerical analysis made for the in situ stress state give a range of effective shear stresses ( $\tau - \sigma_n \tan\phi$ ) that range from 0.04 to 0.06 MPa. Calculations were made with effective shear stresses of 0.04, 0.0425, 0.045, 0.0475, 0.05, 0.0525, 0.055, 0.0575, and 0.06 MPa, and the results were averaged. This approach results in a stepped cohesion reduction over time as shown in Figure D-6.

## D6. ANALYSIS RESULTS

The prediction of key blocks forming at the emplacement drifts located in the Tptpmn unit is presented in this section. The results are presented for both a static key-block assessment and a quasi-static key-block assessment to account for seismic, thermal, and time effects on key-block development.

In the DRKBA analysis, random joint patterns are generated with joint centers positioned in three-dimensional space, considering each joint set in sequence for each Monte Carlo simulation. The forming of key blocks is therefore different in each Monte Carlo simulation. Test runs were conducted to determine an adequate number of Monte Carlo simulations for the analyses as described in Section D8. Based on the test run results, 400 Monte Carlo simulations are adequate for the Tptpmn unit.

The method used for the quasi-static analysis to simulate the seismic effect is described in Section D4. Two levels of earthquake representing a 1,000-year event ( $1 \times 10^{-3}$ ) and a 10,000 year event ( $1 \times 10^{-4}$ ) are considered. An emplacement drift orientation with an azimuth of  $75^\circ$  is the primary orientation for the quasi-static analysis. The inputs and outputs related to the quasi-static analysis are listed in Table A-1.



Source: Table A-1, file Cohesion Degradation V1.xls.

Figure D-6. Degradation of Joint Cohesion with Respect to Time

Figure D-7 presents the key-block size distribution for a 5.5 m diameter emplacement drift with a 75°-drift orientation. The cumulative frequency of occurrence corresponding to 50, 75, 90, 95, and 98 percentile block volume for each unit is listed in Table D-4. The maximum block size predicted from the analyses is included in this table. Additional details for the calculation of block size distribution data based on DRKBA output data are provided in Section D11.

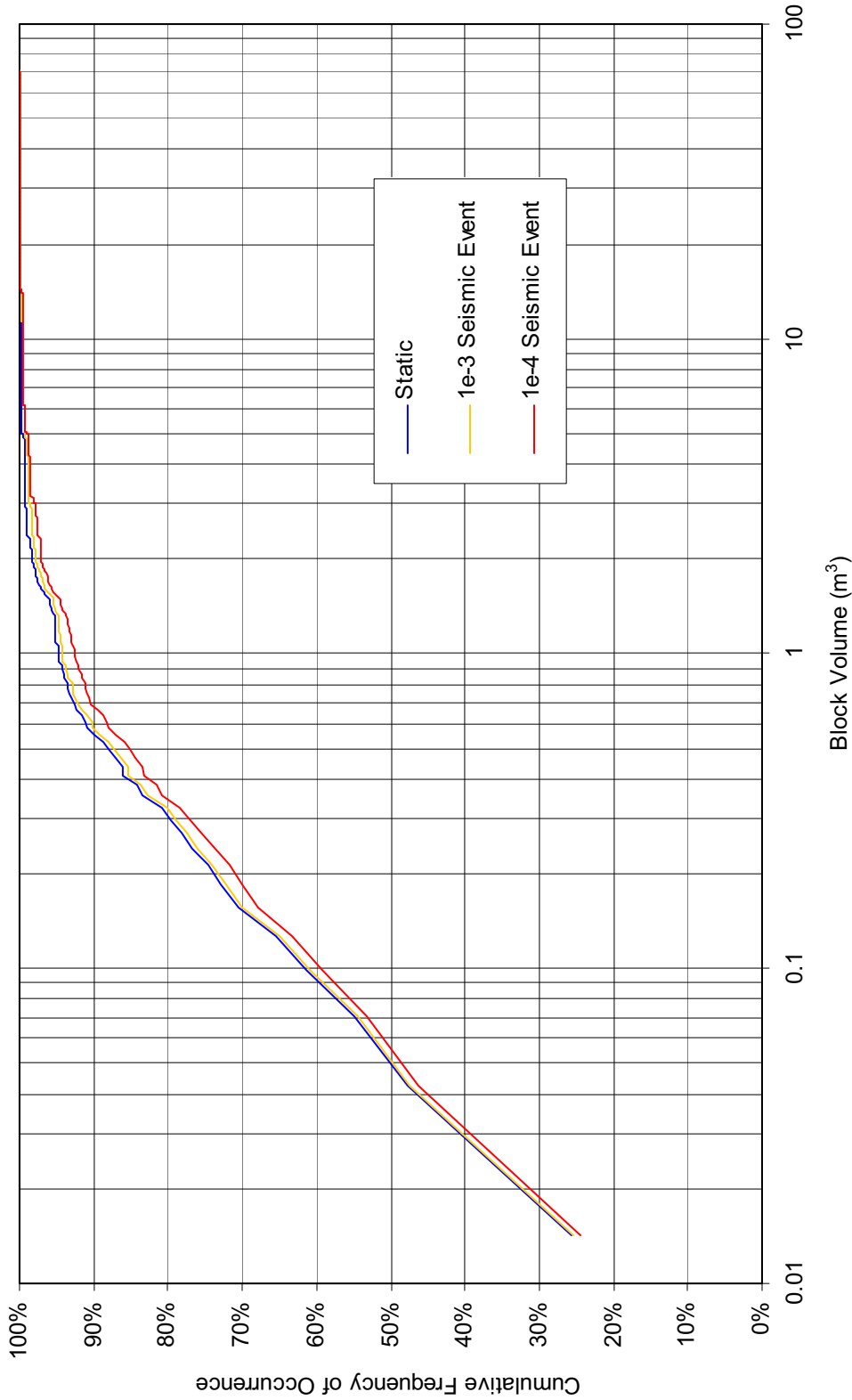
The predicted number of key blocks per unit length of drift is listed in Table D-5. The results show that there is an insignificant impact for a 1,000-year event earthquake ( $1 \times 10^{-3}$ ) on the number of rockfalls, and only a minor impact for a 10,000-year event ( $1 \times 10^{-4}$ ).

Table D-4. Block Volume Corresponding to Various Levels of Predicted Cumulative Frequency of Occurrence, 75°-Azimuth Emplacement Drift in Tptpmn Unit, with Seismic Consideration

Cumulative Frequency of Occurrence (%)	Static	Static Plus Seismic (m <sup>3</sup> )	
		1000-Year ( $1 \times 10^{-3}$ )	10,000-Year ( $1 \times 10^{-4}$ )
50%	0.04	0.04	0.04
75%	0.21	0.21	0.24
90%	0.55	0.55	0.67
95%	1.06	1.35	1.51
98%	1.85	2.31	2.99
maximum	14.29	14.29	14.29

Source: Table A-1, file: *tptmn seismic 75 res v2.xls*.

NOTE: in cubic meters.



Source: Table A-1, file: *tpmn seismic 75 res v2.xls*.

Figure D-7. Cumulative Key-block Size Distribution for Seismic Consideration in the Tptpmn Unit, 75°-Azimuth

Table D-5. Predicted Number of Key Blocks per Unit Length (km) Along 75°-Azimuth Emplacement Drift, with Seismic Consideration

Lithologic Unit	Static	Static Plus Seismic	
		1000-Year (1×10 <sup>-3</sup> )	10,000-Year (1×10 <sup>-4</sup> )
Tptpmn	50	51	55

Source: Table A-1, file: *tpmn seismic 75 res v2.xls*.

### D7. CALCULATION EXAMPLE FOR JOINT PARAMETERS USED IN DRKBA ANALYSIS (TPTPMN, JOINT SET 1)

An example is provided in this appendix to describe the process of calculating the required joint geometrical parameters. These parameters include the concentration factor *k* of a bipolar Watson distribution for joint set orientation and *a*, *b*, *p*, and *q* parameters of the beta distribution for joint radii, spacings, and positioning. The first joint set identified in the Tptpmn unit is used as the example.

The joint spacing, radii (two times the mapped trace lengths), and positioning (offset) were first sorted in the fracture database. Parameters *a* and *b* represent the ends of the closed interval upon which the beta distribution is defined. The smallest and largest joint parameters observed were assigned as *a* and *b* parameters. The values of *p* and *q* were calculated based on the technique presented by Derman et al. (1973 [DIRS 108444], pp. 398 to 403). In order to determine *p* and *q*, the joint data were transformed to the unit interval [0,1] by interpolation between the smallest and largest values encountered. The parameters *p* and *q* were then calculated from the mean and standard deviation of the transformed data by means of the following equations:

$$p = \mu [ \mu(1-\mu) / \sigma^2 - 1 ] \quad (\text{Eq. D-20})$$

$$q = (1-\mu) [ \mu(1-\mu) / \sigma^2 - 1 ] \quad (\text{Eq. D-21})$$

where  $\mu$  is the mean of the transformed data and  $\sigma^2$  is the variance of the transformed data. The calculations are included in Table D-6.

To calculate the concentration factor, the orientation matrix of the joint data has to be first determined (Fisher et al. 1987 [DIRS 108447], pp. 33, 175, and 176). The orientation matrix *T* is defined in the following:

$$T = \begin{bmatrix} \sum x_i^2 & \sum x_i y_i & \sum x_i z_i \\ \sum x_i y_i & \sum y_i^2 & \sum y_i z_i \\ \sum x_i z_i & \sum y_i z_i & \sum z_i^2 \end{bmatrix} \quad (\text{Eq. D-22})$$

where (*x<sub>i</sub>*, *y<sub>i</sub>*, *z<sub>i</sub>*) is the unit normal vector of a joint plane and *i* ranges from 1 to *n* (the number of fractures collected in the joint sets). The components of the orientation matrix are calculated in Table D-7.

Table D-6. Calculation of the a, b, p, and q Parameters for Joint Spacing, Radii, and Positioning

Joint Set #1	Dip= 84		Dip Direction = 221							
	Sorted Joint Spacing (m)	Sorted Trace Length (m)	Joint Offset (m)	Joint Offset (all positive, m)	Sorted Joint Offset (m)	Joint Radius (m)	Transformed Spacing	Transformed Radius	Transformed Offset	
	13.92	54.00	-0.65	0.65	9.15	108.00	1.0000	1.0000	1.0000	
	13.60	25.54	-0.04	0.04	9.15	51.08	0.9773	0.4639	1.0000	
	12.44	23.16	-1.30	1.30	9.15	46.32	0.8938	0.4191	1.0000	
	12.40	22.85	0.11	0.11	9.15	45.70	0.8910	0.4133	1.0000	
	11.22	20.74	0.02	0.02	8.87	41.48	0.8063	0.3735	0.9694	
	11.02	17.90	0.21	0.21	8.34	35.80	0.7915	0.3200	0.9115	
	10.73	17.70	0.11	0.11	8.05	35.40	0.7707	0.3163	0.8798	
	10.14	17.32	0.78	0.78	7.49	34.64	0.7284	0.3091	0.8186	
	9.97	17.17	-0.37	0.37	7.38	34.34	0.7163	0.3063	0.8060	
	9.81	17.02	0.41	0.41	6.90	34.04	0.7046	0.3034	0.7536	
	9.79	17.00	-0.85	0.85	6.50	34.00	0.7035	0.3031	0.7104	
	9.71	16.71	-0.72	0.72	6.48	33.42	0.6979	0.2976	0.7077	
	9.43	15.60	-0.01	0.01	6.42	31.20	0.6776	0.2767	0.7011	
	9.10	15.60	0.36	0.36	6.15	31.20	0.6538	0.2767	0.6721	
	8.97	15.25	-0.16	0.16	5.98	30.50	0.6442	0.2701	0.6530	
	8.93	14.90	-0.69	0.69	5.65	29.80	0.6416	0.2635	0.6169	
	8.87	14.60	-0.64	0.64	5.15	29.20	0.6374	0.2579	0.5628	
	8.75	14.21	0.60	0.60	5.00	28.42	0.6283	0.2505	0.5464	
	8.64	14.20	-0.26	0.26	4.90	28.40	0.6204	0.2503	0.5355	
	8.54	13.42	-0.09	0.09	4.73	26.84	0.6135	0.2356	0.5164	
	8.53	13.31	0.12	0.12	4.64	26.62	0.6126	0.2336	0.5071	
	8.46	13.05	-0.75	0.75	4.63	26.10	0.6075	0.2287	0.5060	
	8.37	12.05	-0.34	0.34	4.60	24.10	0.6013	0.2098	0.5027	
	7.99	11.56	-0.73	0.73	4.20	23.12	0.5742	0.2006	0.4590	
	7.96	11.52	-0.64	0.64	4.20	23.04	0.5719	0.1998	0.4590	
	7.90	10.99	0.36	0.36	4.15	21.98	0.5674	0.1899	0.4530	
	7.70	10.91	0.32	0.32	4.06	21.82	0.5533	0.1884	0.4437	
	<i>Data truncated — see DTN MO0408MWDDDMIO.002, file: "New-Beta-Tptpmn V1.xls", for complete data set</i>									
	0.00	1.00	4.15	4.15	0.00	2.00	0.0000	0.0017	0.0000	
	0.00	1.00	0.02	0.02	0.00	2.00	0.0000	0.0017	0.0000	
	0.00	0.94	0.54	0.54	0.00	1.88	0.0000	0.0006	0.0000	
		0.91	1.53	1.53	0.00	1.82		0.0000	0.0000	
Mean	0.60	2.54	—	—	0.63	5.08	0.0433	0.0307	0.0686	
Standard Deviation	1.12	1.94	—	—	0.67	3.87	0.0806	0.0365	0.0728	
Minimum (a)	0.00	0.91	—	—	0.00	1.82	—	—	—	
Maximum (b)	13.92	54.00	—	—	9.15	108.00	—	—	—	
p	—						0.2322	0.6554	0.7569	
q	—						5.1372	20.7171	10.2825	

Table D-7. Calculation of the Components for the Orientation Matrix

Station (m)	Azimuth	Dip	Dip Vector Component		Strike Vector Component			Pole Vector Component			x <sub>i</sub> x <sub>i</sub>	x <sub>i</sub> y <sub>i</sub>	x <sub>i</sub> z <sub>i</sub>	y <sub>i</sub> y <sub>i</sub>	y <sub>i</sub> z <sub>i</sub>	z <sub>i</sub> z <sub>i</sub>							
			xd	yd	zd	xs	ys	zs	xi	yi							zi						
2723.27	129	85	-0.055	-0.068	-0.996	-0.777	0.629	0.000	0.627	0.774	-0.087	0.3930	0.4854	-0.0546	0.5994	-0.0675	0.0076						
2723.85	142	81	-0.123	-0.096	-0.988	-0.616	0.788	0.000	0.778	0.608	-0.156	0.6058	0.4733	-0.1218	0.3698	-0.0951	0.0245						
2730.01	116	81	-0.069	-0.141	-0.988	-0.899	0.438	0.000	0.433	0.888	-0.156	0.1875	0.3844	-0.0677	0.7881	-0.1389	0.0245						
2733.73	124	72	-0.173	-0.256	-0.951	-0.829	0.559	0.000	0.532	0.788	-0.309	0.2828	0.4193	-0.1643	0.6217	-0.2436	0.0955						
2735.12	129	86	-0.044	-0.054	-0.998	-0.777	0.629	0.000	0.628	0.775	-0.070	0.3941	0.4867	-0.0438	0.6010	-0.0541	0.0049						
2735.56	299	84	0.051	0.091	-0.995	0.875	-0.485	0.000	-0.482	-0.870	-0.105	0.2325	0.4194	0.0504	0.7566	0.0909	0.0109						
2736.15	148	83	-0.103	-0.065	-0.993	-0.530	0.848	0.000	0.842	0.526	-0.122	0.7085	0.4427	-0.1026	0.2766	-0.0641	0.0149						
2738.56	141	87	-0.041	-0.033	-0.999	-0.629	0.777	0.000	0.776	0.628	-0.052	0.6023	0.4877	-0.0406	0.3950	-0.0329	0.0027						
2742.16	124	76	-0.135	-0.201	-0.970	-0.829	0.559	0.000	0.543	0.804	-0.242	0.2944	0.4365	-0.1313	0.6471	-0.1946	0.0585						
2742.34	137	79	-0.140	-0.130	-0.982	-0.682	0.731	0.000	0.718	0.669	-0.191	0.5154	0.4806	-0.1370	0.4482	-0.1277	0.0364						
2743.08	119	87	-0.025	-0.046	-0.999	-0.875	0.485	0.000	0.484	0.873	-0.052	0.2344	0.4229	-0.0253	0.7629	-0.0457	0.0027						
2753	115	88	-0.015	-0.032	-0.999	-0.906	0.423	0.000	0.422	0.906	-0.035	0.1784	0.3826	-0.0147	0.8204	-0.0316	0.0012						
2756.75	117	83	-0.055	-0.109	-0.993	-0.891	0.454	0.000	0.451	0.884	-0.122	0.2030	0.3985	-0.0549	0.7821	-0.1078	0.0149						
2759.11	295	75	0.109	0.235	-0.966	0.906	-0.423	0.000	-0.408	-0.875	-0.259	0.1666	0.3574	0.1057	0.7664	0.2266	0.0670						
2762.21	138	90	0.000	0.000	-1.000	-0.669	0.743	0.000	0.743	0.669	0.000	0.5523	0.4973	0.0000	0.4477	0.0000	0.0000						
2767.3	138	72	-0.230	-0.207	-0.951	-0.669	0.743	0.000	0.707	0.636	-0.309	0.4995	0.4498	-0.2184	0.4050	-0.1967	0.0955						
2768.07	118	77	-0.106	-0.199	-0.974	-0.883	0.469	0.000	0.457	0.860	-0.225	0.2093	0.3935	-0.1029	0.7401	-0.1935	0.0506						
2772.04	145	84	-0.086	-0.060	-0.995	-0.574	0.819	0.000	0.815	0.570	-0.105	0.6637	0.4647	-0.0852	0.3254	-0.0596	0.0109						
2774.87	127	76	-0.146	-0.193	-0.970	-0.799	0.602	0.000	0.584	0.775	-0.242	0.3410	0.4525	-0.1413	0.6005	-0.1875	0.0585						
2775.37	138	88	-0.026	-0.023	-0.999	-0.669	0.743	0.000	0.743	0.669	-0.035	0.5516	0.4967	-0.0259	0.4472	-0.0233	0.0012						
2777.34	124	76	-0.135	-0.201	-0.970	-0.829	0.559	0.000	0.543	0.804	-0.242	0.2944	0.4365	-0.1313	0.6471	-0.1946	0.0585						
2777.59	119	82	-0.067	-0.122	-0.990	-0.875	0.485	0.000	0.480	0.866	-0.139	0.2305	0.4158	-0.0668	0.7501	-0.1205	0.0194						
<i>Data truncated — see DTN MO0408MWDDDMIO.002, file: Orient-Tpptom V1.xls, for complete data set</i>																							
1437.69	115	86	-0.029	-0.063	-0.998	-0.906	0.423	0.000	0.422	0.904	-0.070	0.1777	0.3812	-0.0294	0.8174	-0.0631	0.0049						
1440.02	125	86	-0.040	-0.057	-0.998	-0.819	0.574	0.000	0.572	0.817	-0.070	0.3274	0.4676	-0.0399	0.6677	-0.0570	0.0049						
1441.27	128	73	-0.180	-0.230	-0.956	-0.788	0.616	0.000	0.589	0.754	-0.292	0.3466	0.4437	-0.1721	0.5679	-0.2203	0.0855						
1442.28	123	80	-0.095	-0.146	-0.985	-0.839	0.545	0.000	0.536	0.826	-0.174	0.2877	0.4430	-0.0931	0.6822	-0.1434	0.0302						
															SUM	2075.5	2290.83	-360.26	2803.2	-402.52	103.36		



The solution for the concentration factor  $k$  can be approximated based on the largest eigenvalue ( $\tau_3$ ) of the orientation matrix  $T$  (Fisher et al. 1987 [DIRS 108447], pp. 175 and 176). The solution is:

$$k = \begin{cases} 3.75 \times (3\tau_3 - 1) & \text{if } 0.333 < \tau_3 \leq 0.38 \\ 3.34 \times (3\tau_3 - 1) & \text{if } 0.38 < \tau_3 \leq 0.65 \\ 0.7 + 1/(1 - \tau_3) & \text{if } 0.65 < \tau_3 \leq 0.99 \\ 1/(1 - \tau_3) & \text{if } \tau_3 \geq 0.99 \end{cases}$$

Calculations of the eigenvalues and  $k$  factor were conducted using Mathcad and are presented in Table D-8.

#### **D8. DETERMINATION OF THE NUMBER OF DRKBA MONTE CARLO SIMULATIONS**

In the DRKBA analysis, random joint patterns are generated with joint centers positioned in three-dimensional space, considering each joint set in sequence for each Monte Carlo simulation. The forming of key blocks is therefore different in each Monte Carlo simulation. To determine the adequate number of Monte Carlo simulations for the analyses, test runs were first conducted. The criteria used to determine the adequate number of Monte Carlo simulations include: (1) consistent prediction of the block size distribution, (2) consistent prediction of the number of blocks per 10 simulations, and (3) consistent prediction of the maximum block size.

For the Tptpmn unit, test runs with 100, 200, 400, 600, and 800 Monte Carlo simulations were conducted. Figure D-8 shows the block size distribution curves for the five cases. The prediction of block size distribution for 200 simulations is similar to the results from 400 simulations. The predicted numbers of blocks per 10 simulations for the five cases are presented in Figure D-9. The results show that the number of blocks increases with the number of simulations until 400 simulations is reached. For 400 simulations or higher, the predicted numbers of blocks per 10 simulations converges to about 12 and remains fairly constant. The maximum block sizes predicted for the five cases are shown in Figure D-10. The maximum blocks predicted for 400, 600, and 800 simulations are identical. It was determined that 400 simulations are adequate for the DRKBA analyses for Tptpmn unit.

Table D-8. Calculation of the Concentration Factor k for Joint Orientation

Concentration Factor (k) Calculation for Watson Bipolar Distribution:  
(xx, xy,xz,yy,yz,zz calculated in EXCEL worksheet  
**Orient-Tptpmn V1.xls**)

Tptpmn, Joint Set 1

$$xx := 2075.455$$

$$xy := 2290.832$$

$$xz := -360.263$$

$$yy := 2803.184$$

$$yz := -402.518$$

$$zz := 103.3607$$

$$T := \begin{pmatrix} xx & xy & xz \\ xy & yy & yz \\ xz & yz & zz \end{pmatrix}$$

$$c := \text{eigenvals}(T) \quad c = \begin{pmatrix} 121.739 \\ 39.566 \\ 4.821 \times 10^3 \end{pmatrix}$$

$$n := c_0 + c_1 + c_2$$

$$cn := \frac{c}{n} \quad cn = \begin{pmatrix} 0.024 \\ 7.942 \times 10^{-3} \\ 0.968 \end{pmatrix} \quad \tau_3 := \max(cn)$$

$$k1 := 3.75(3\tau_3 - 1) \quad k2 := 3.34(3\tau_3 - 1)$$

$$k3 := 0.7 + \frac{1}{(1 - \tau_3)} \quad k4 := \frac{1}{(1 - \tau_3)}$$

$$k := \begin{cases} k1 & \text{if } 0.333 < \tau_3 \leq 0.38 \\ k2 & \text{if } 0.38 < \tau_3 \leq 0.65 \\ k3 & \text{if } 0.65 < \tau_3 \leq 0.99 \\ k4 & \text{if } \tau_3 \geq 0.99 \end{cases} \quad k = 31.586$$

NOTE: New-K-Tptpmn V2.mcd.

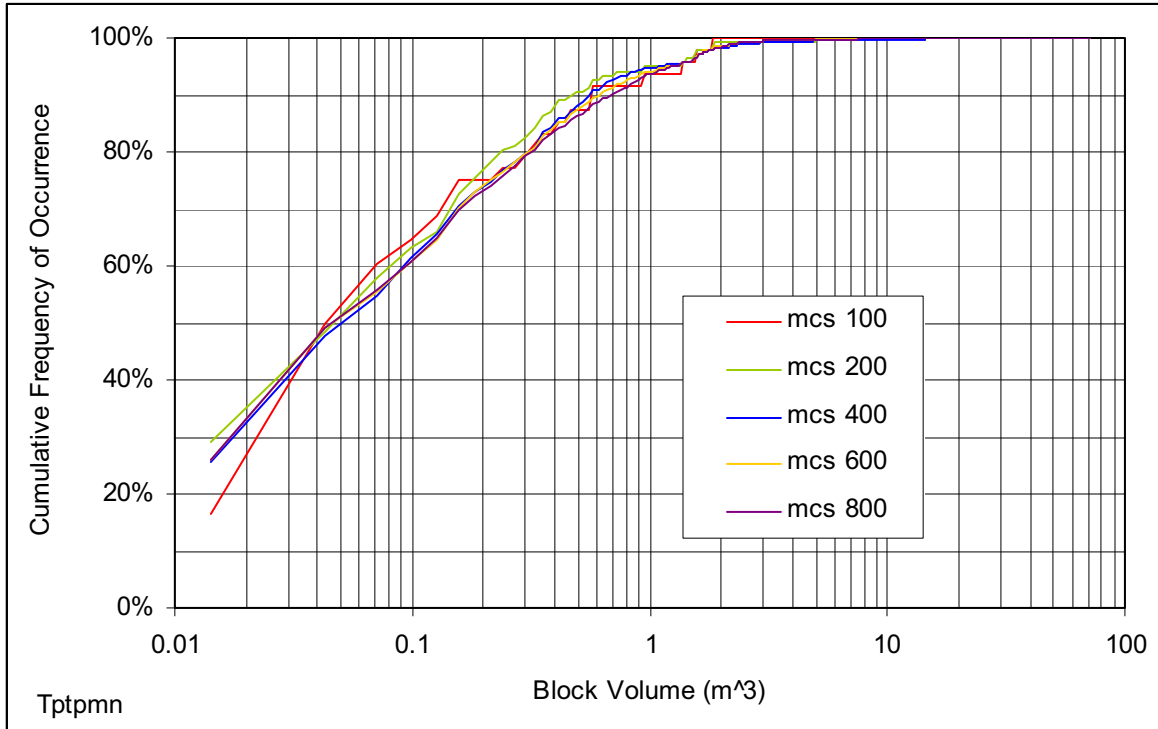


Figure D-8. Block Size Distributions for the Test Runs, Tptpmn Unit

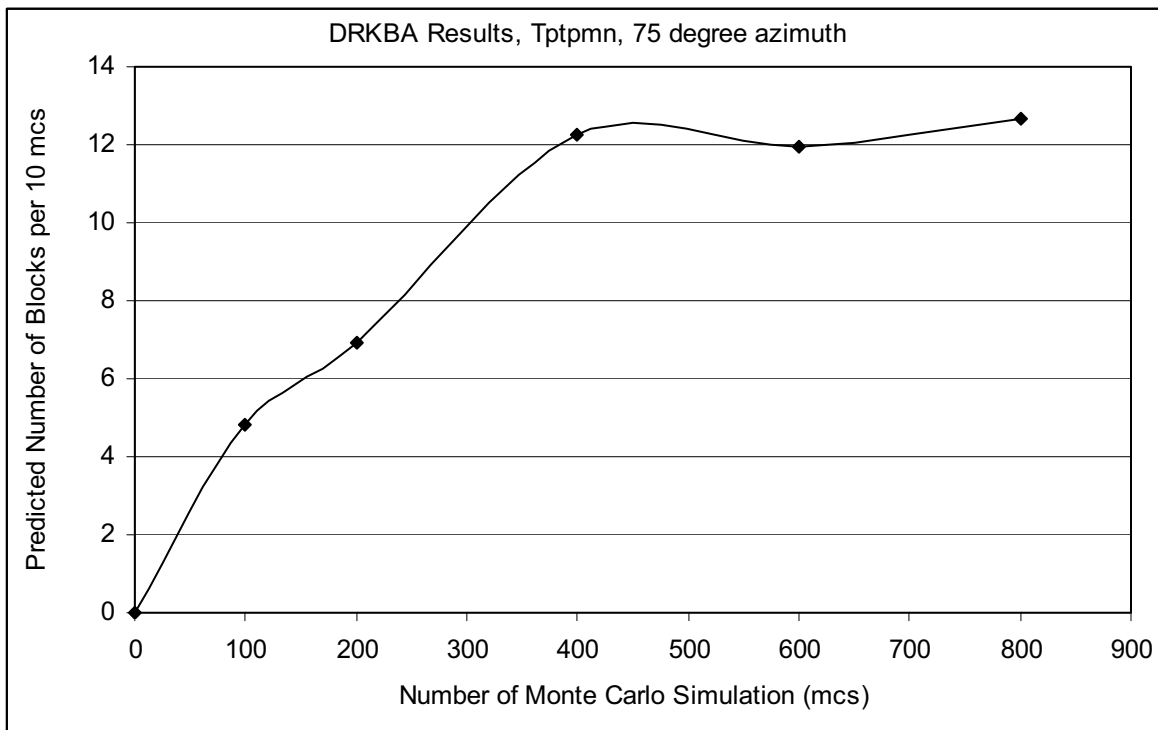


Figure D-9. Predicted Number of Key Blocks Per 10 Monte Carlo Simulations, Tptpmn Unit

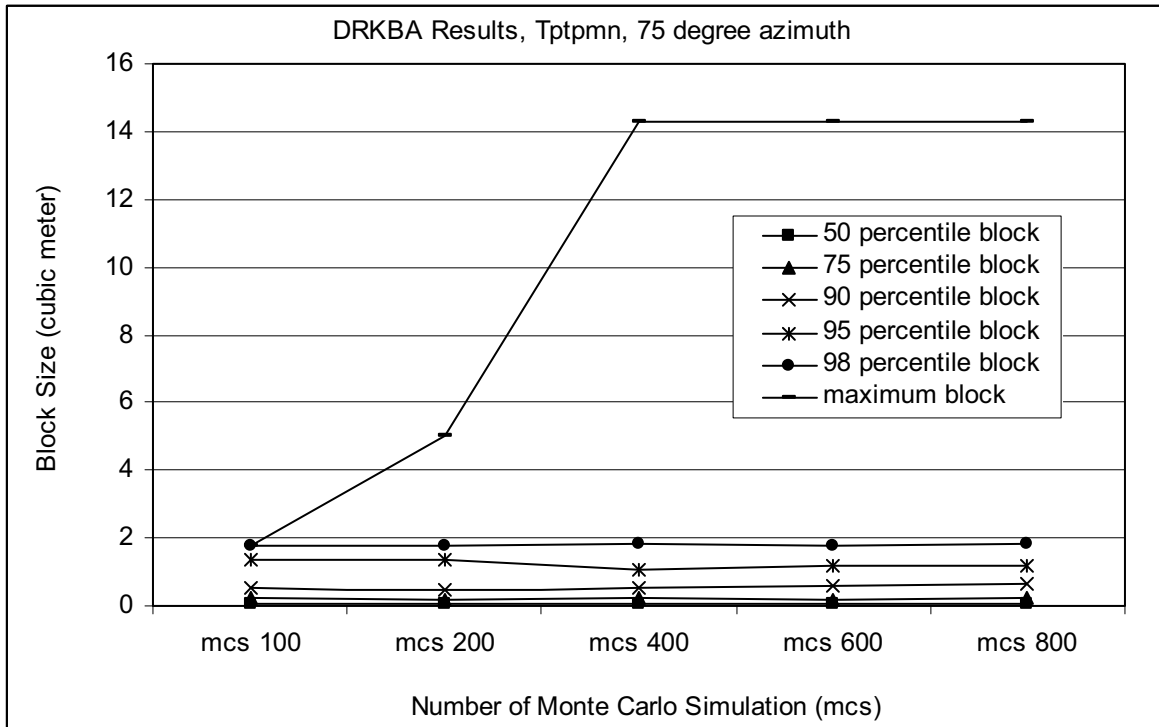


Figure D-10. Predicted Number of Maximum Block Size, Tptpmn Unit

## D9. ASSESSMENT OF JOINT PLANE REPRESENTATION IN THE DRKBA ROCKFALL MODEL

This section presents the results of a sensitivity calculation for the extent of the modeled joint plane based on the mapped joint trace length. It is recognized that the actual extent of a joint plane cannot be fully known based on field mapping data. The mapped trace length of a joint represents some portion of the overall joint plane. Under representing the extent of the joint plane would not be conservative in a key-block analysis. Since the underrepresented joint planes may not extend or connect to adjacent joint planes, under representation would limit the number of blocks otherwise generated in the model. Conversely, overstating the extent of the joint plane would increase connectivity among joint planes, thus creating more blocks in the model and resulting in an increased, or conservative, estimate of block development. However, infinite joint planes would not be an accurate representation of the jointed rock mass. This appendix develops the basis to sufficiently model the extent of the joint plane based on the available field data.

Joint planes are represented as circular discs in the DRKBA rockfall model with the radius of the joint plane equal to twice the mapped trace length. Figure D-11 shows a top view of a circular fracture disc intersecting an opening. Figure D-11 depicts three parameters used for the sensitivity calculation, including joint trace length ( $T$ ), joint radius ( $R$ ), and the shortest distance ( $Z$ ) from the center of the joint disc to the fracture trace.

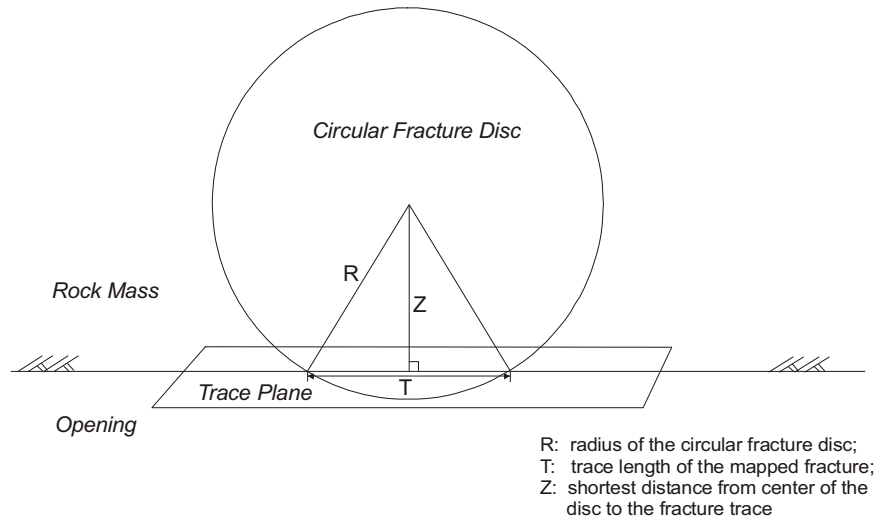


Figure D-11. Top View of a Circular Fracture Disc Intersecting an Opening

The multiplier,  $M$ , is used to obtain the radius of the circular fracture disc from the trace length, such that the radius parameter,  $R$ , as depicted in Figure D-11, is defined as:

$$R = M * T \tag{Eq. D-23}$$

Based on standard trigonometric relationships for triangles, the shortest distance from the center of the disc to the fracture trace can be derived as follows:

$$Z = (R^2 - (T/2)^2)^{1/2} = (M^2 - 1/4)^{1/2} * T \tag{Eq. D-24}$$

It is reasoned that the location where the circular disc intersects the opening (i.e., the intersection point of line  $Z$  and trace  $T$ ) is uniformly distributed at any point from the center of disc to the periphery of the disc. In other words, the opening can be located with equal probability to intersect any points of the disc. Therefore, the probability for the radius of the disc to be larger than the value derived from Equation D-14 can be simply expressed as a function of  $Z/R$ , such that:

$$P = 100\% - Z / R = 100\% - (M^2 - 1/4)^{1/2} / M \tag{Eq. D-25}$$

where  $P$  is the probability that  $R > M \times T$ .

The probabilities for various multipliers,  $M$ , are listed in Table D-9. For a circular joint plane described using a radius equal to twice the mapped trace length (i.e.,  $M=2$ ) as used in this analysis, there is an approximate 3 percent probability that the actual joint radius is greater than the modeled value. Therefore, the use of a multiplier,  $M$ , of 2 in this analysis is conservative.

Table D-9. Probability of  $R > M \times T$  for Various Multipliers

Multiplier (M)	0.5	0.6	0.7	0.8	1	1.5	2	3	5
Probability of $R > M \times T$	100.0%	44.7%	30.0%	21.9%	13.4%	5.7%	3.2%	1.4%	0.5%

## D10. CALCULATION OF THE PLANE EQUATIONS TO DESCRIBE THE EXCAVATION OPENING AS INPUT TO DRKBA

The method employed by the DRKBA code to represent excavation openings involves specification of sets of infinite planes that approximate the opening geometry. The infinite planes are defined using unit normal vectors and the shortest distance from the origin. For a circular opening without backfill (*exca vectors V2.xls*), a total of 20 planes were used to represent an 80-ft long cylinder as shown in Figure D-12.

Inputs for the calculation include the azimuth of tunnel axis (Cell D1, *exca vectors V2.xls*) and angle measured from horizontal axis for each plane (Cells P5 to P22, *exca vectors V2.xls*).

The equations for the rotation of unit vectors and axes presented in Fisher et al. (1987 [DIRS 108447], p. 32) were used to calculate the unit normal vector for each plane. The rotation matrix A is shown below:

$$A(\theta, \phi) = \begin{pmatrix} a11 & a12 & a13 \\ a21 & a22 & a23 \\ a31 & a32 & a33 \end{pmatrix} = \begin{pmatrix} \cos \theta \cos \phi & \cos \theta \sin \phi & -\sin \theta \\ -\sin \phi & \cos \phi & 0 \\ \sin \theta \cos \phi & \sin \theta \sin \phi & \cos \theta \end{pmatrix} \quad (\text{Eq. D-26})$$

where  $(\theta, \phi)$  are the polar coordinates of a unit vector measured relative to a pole in the direction  $(0,0)$ . The rotation of the tunnel axis sets  $\phi$  equal to the azimuth and  $\theta$  as 0. Cells contained in Columns F to N are the elements of the rotation matrix. Calculation of the unit vector of the infinite plane on the local coordinate (coordinate axes shown in Figure D-12) is based on the following equation:

$$u_i = \begin{pmatrix} x \\ y \\ z \end{pmatrix} = \begin{pmatrix} \sin \alpha_i \\ 0 \\ \cos \alpha_i \end{pmatrix} \quad (\text{Eq. D-27})$$

The x, y, and z components of the unit vector are calculated in Columns Q to S. Finally, the rotated unit normal vector on the global coordinate (East as x' axis and North as y' axis) are computed using the equation

$$\begin{pmatrix} x' \\ y' \\ z' \end{pmatrix} = A(\theta, \phi) \begin{pmatrix} x \\ y \\ z \end{pmatrix} \quad (\text{Eq. D-28})$$

The x', y', and z' components are calculated in Columns U to W. The last two rows in Columns U to W are for the end plane (shown in Figure D-12). The end plane normal vector is in the horizontal direction with x' equal to  $\sin \phi$  and y' equal to  $\cos \phi$ .

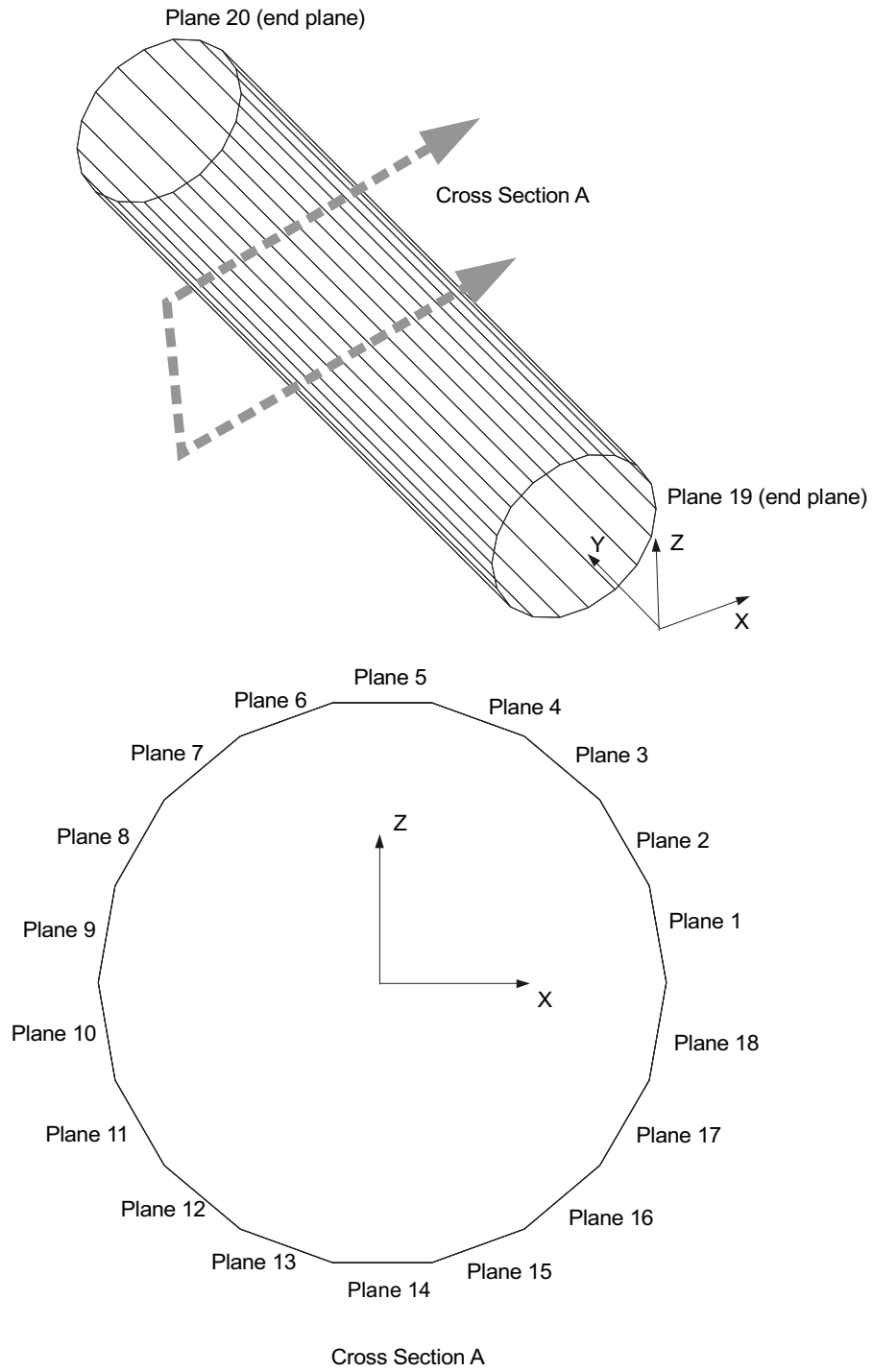


Figure D-12. Opening Representation - No Backfill

## D11. CALCULATION OF KEY-BLOCK SIZE DISTRIBUTION

The key-block output files *\*.bsd* (DTN: MO0408MWDDDMIO.002) from DRKBA contain the information on key-block size distribution in a histogram format which provides the number of blocks in each bin the user specified in the DRKBA input files. Two spreadsheet files (files *tpmn seismic 75 res v2.xls* and *small scale fractures results.xls*, DTN: MO0408MWDDDMIO.002) were generated to provide the key-block distribution in cumulative frequency of occurrence format presented in Sections D6 and 6.3.3.

There are three calculation worksheets contained in each of the two spreadsheet files. The worksheets are entitled “*results*”, “*cum*”, and “*percentile*”. The first worksheet “*results*” includes the imported block size data from DRKBA output files and the calculated percentage results within each block size bin. The second worksheet “*cum*” calculates the cumulative percentage corresponding to the various block sizes. The third worksheet “*percentile*” provides the results for the 50 percentile, 75 percentile, 90 percentile, 95 percentile, 98 percentile, and maximum size blocks.

Column A of the “*results*” worksheet lists the bin value for the block volume in cubic meters. These values are the converted values from the English unit outputs of DRKBA. The number of blocks predicted in DRKBA for each block volume bin is listed in the columns of the “*results*” worksheet identified in Table D-10. The values are imported from the *\*.bsd* output files of the DRKBA analysis. The total number of blocks was calculated in Row 6 using the Microsoft Excel *sum* function for each case. The percentage columns adjacent to the input block number columns listed in Table D-10 were then calculated using the individual block number in each bin and the total number of blocks. The values in the percentage columns represent the probabilistic density of rockfall within each block size bin.

Table D-10. Structure of Spreadsheet Files for Key-Block Size Distribution

File	Column		
	B	D	F
tpmn seismic 75 res v2.xls	Static	Seismic Level $1 \times 10^{-3}$	Seismic Level $1 \times 10^{-4}$
small scale fractures results.xls	Without Small-Scale	With Small-Scale	Not applicable

Worksheet “*cum*” was constructed from worksheet “*results*” by changing the columns identified in Table D-10 from number of blocks to cumulative number of blocks. The iterative formula to calculate the cumulative number of block is given below:

$$CNB_i = CNB_{i-1} + NB_i \quad (\text{Eq. D-29})$$

where

- $CNB_i$  = the cumulative number of block at block size bin  $i$
- $CNB_{i-1}$  = the cumulative number of block at block size bin  $i-1$
- $NB_i$  = the number of block at block size bin  $i$ .



The cumulative percentage was then obtained from the cumulative number of blocks and the total number of blocks. Same as in worksheet “*results*”, the total number of blocks is recorded in Row 6.

In order to locate the 50 percentile, 75 percentile, 90 percentile, 95 percentile, 98 percentile, and maximum size blocks efficiently, the Microsoft Excel *vlookup* function was used in worksheet “*percentile*”. Cells C8 to G2509 for file *tpmn seismic 75 res v2.xls* and cells C8 to E2509 for *small scale fractures results.xls* were set up as the *table\_array* for the *vlookup* function. The cumulative percentage values in these cells are the replicate of cells in the worksheet “*cum*”. The block sizes are expressed in cubic feet in the *table\_array*. The blocks for the cumulative frequency of occurrence at 50, 75, 90, 95, and 98 percent, and the maximum blocks (in cubic feet) are calculated in Cells C2517 to E2522 for file *tpmn seismic 75 res v2.xls* and Cells L5 to O10 for file *small scale fractures results.xls*. The block sizes were converted to cubic meter in Cells C2526 to E2531 for file *tpmn seismic 75 res v2.xls* and Cells Q5 to T10 for file *small scale fractures results.xls*.

The number of blocks per kilometer is calculated by dividing the total number of key blocks by the total simulated length. The total simulated length is determined as the number of simulations (i.e., 400 simulations) times the length of simulation (e.g., 80 ft/simulation  $\times$  0.0348 m/ft  $\times$  0.001 km/m).

INTENTIONALLY LEFT BLANK

**APPENDIX E**  
**CALCULATION OF ROCK PROPERTIES**



## CALCULATION OF ROCK PROPERTIES

This appendix documents the calculation of rock property values based on source data provided in the TDMS. The rock properties include density, joint strength properties, intact rock properties, rock mass strength properties, and thermal properties. The use of these properties in this analysis is described in Section 4.1.

### E1. ROCK DENSITY

The rock densities used in the thermal mechanical calculation of stresses at Yucca Mountain due to heating and cooling of the repository (Section 6.2) are provided in Table E-1. These data include dry bulk density values for the various lithostratigraphic and thermal-mechanical units of the Yucca Mountain rock strata. The mean values for thermal-mechanical units are determined by averaging the densities of the lithostratigraphic units within each thermal-mechanical unit, weighted according to the thickness of each lithostratigraphic unit. Additional details are provided in the Microsoft Excel file "*thermal properties TM units v2.xls*" (Table A-1).

For conservatism, saturated bulk density data from the Tptpln unit have been used in rockfall modeling (see Section 4.1.3). The saturated bulk density data are provided in Table E-2. The mean density value for these data is 2410 kg/m<sup>3</sup>.

### E2. JOINT STRENGTH PROPERTIES

Data from rotary shear stress experiments using core from the nonlithophysal units (i.e., Ttpm and Tptpln) are provided in Table E-3. These data include pairs of normal stress ( $\sigma$ ) and shear stress ( $\tau_p$ ) values determined from shear testing of various core specimens. The data pairs were plotted (Figure E-1) and a linear fit of the data was determined. The calculation of the linear fit is documented in Microsoft Excel file "*joint strength v2.xls*" (Table A-1). The equation for the linear fit is:

$$\tau_p = \tan\phi_j \sigma + C_j \quad (\text{Eq. E-1})$$

where

$\tau_p$	=	peak shear stress (MPa),
$\tan\phi_j$	=	coefficient of friction,
$\phi_j$	=	joint friction angle (degree),
$\sigma$	=	normal stress (MPa), and
$C_j$	=	joint cohesion (MPa).

Based on this linear fit, the following joint strength parameters were determined:

- Joint cohesion = 0.6 MPa
- Coefficient of friction = 0.90
- Joint friction angle = 42°.

Table E-1. Density Data for Various Thermal Mechanical Units and Associated Lithostratigraphic Units

Thermal Mechanical Unit	Stratigraphic Unit	Thickness <sup>a</sup> (m)	Dry Bulk Density (kg/m <sup>3</sup> )	DTN <sup>b</sup>
TCw / PTn	Tpcpv3	0.0	2310	SN0303T0503102.008 [DIRS 162401]
	Tpcpv2	5.1	1460	
	Tpcpv1	2.4	1460	
	Tpbt4	0.5	1460	
	Tpy	3.8	1460	
	Tpbt3	3.8	1460	
	Tpp	5.1	1460	
	Tpbt2	8.3	1460	
	Tptrv3	1.9	1460	
	Tptrv2	1.2	1460	
	Mean (weighted by unit thickness)			
TSw1	Tptrv1	1.2	2310	SN0404T0503102.011 [DIRS 169129]
	Tptrn	35.6	2190	
	Tptrl	6.1	2190	
	Tptpul	66.8	1834	
	Mean (weighted by unit thickness)			
TSw2 / TSw3	Tptpmn	38.3	2148	SN0303T0503102.008 [DIRS 162401]
	Tptpll	95.6	1979	
	Tptpln	55.1	2211	
	Tptpv3	12.0	2310	
	Mean (weighted by unit thickness)			
CHn1 / CHn2	Tptpv2	4.7	1460	SN0303T0503102.008 [DIRS 162401]
	Tptpv1	15.4	1460	
	Tpbt1	2.0	1460	
	Calico	45.5	1670	
	Calicobt	15.9	1670	
	Mean (weighted by unit thickness)			

<sup>a</sup> Thickness of units extracted from DTN: MO0012MWDGFM02.002 [DIRS 153777]. The details of this extraction are provided in Appendix M.

<sup>b</sup> Mean values are calculated in this report and not provided by the DTNs listed in this table. Data extracted from DTN: SN0404T0503102.11 [DIRS 169129] are summarized in BSC 2004 [DIRS 169854], Table 7-10. Data extracted from DTN: SN0303T0503102.008 [DIRS 162401] are summarized in BSC 2004 [DIRS 170033], Table 6-13.

Table E-2. Density Data from the Tptpln Unit

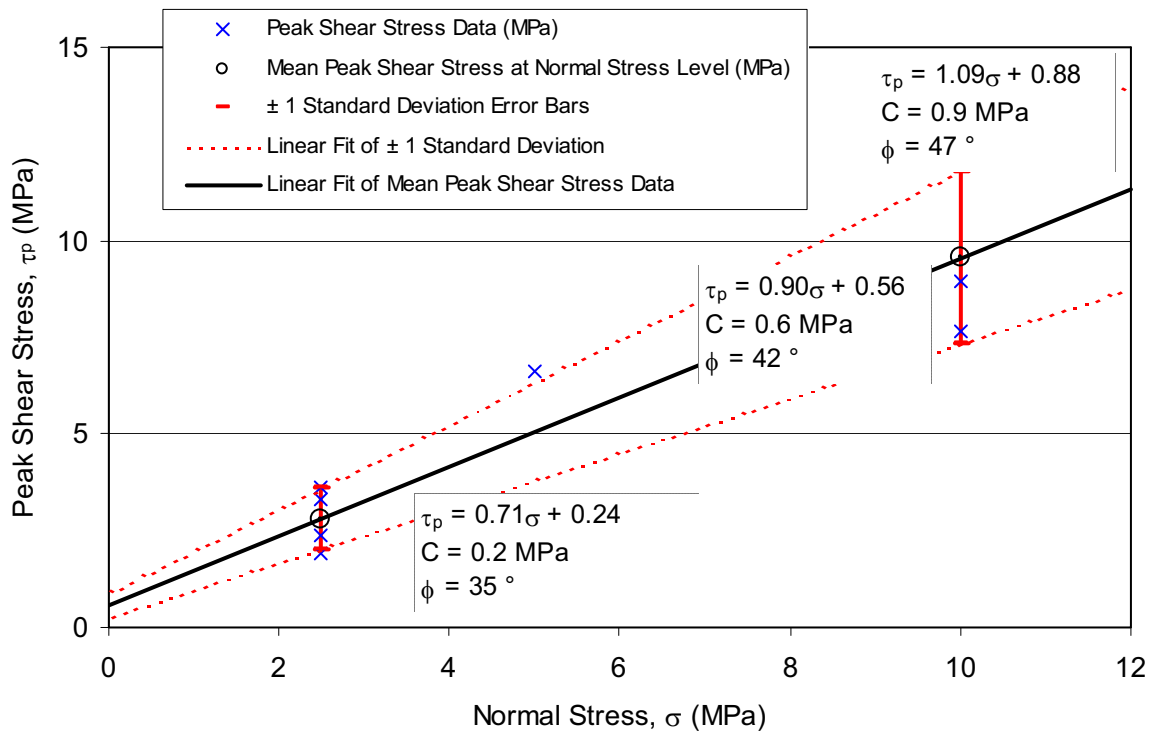
Borehole	Sample Number	Saturated Bulk Density (kg/m <sup>3</sup> )
NRG-7a	NRG-7a-1230.2-SNL	2395
NRG-7a	NRG-7a-1236.7-SNL	2393
NRG-7a	NRG-7a-1252.3-SNL	2369
NRG-7a	NRG-7a-1257.8-SNL	2421
NRG-7a	NRG-7a-1259.1-SNL	2420
NRG-7a	NRG-7a-1265.2-SNL	2426
NRG-7a	NRG-7a-1314.8-SNL	2418
NRG-7a	NRG-7a-1399.1-A-SNL	2409
NRG-7a	NRG-7a-1400.5-B-SNL	2428
NRG-7a	NRG-7a-1230.2-SNL	2339
NRG-7a	NRG-7a-1263.7-SNL	2416
NRG-7a	NRG-7a-1263.7-SNL	2396
NRG-7a	NRG-7a-1263.7-SNL	2421
NRG-7a	NRG-7a-1307.0-SNL	2414
NRG-7a	NRG-7a-1307.0-SNL	2411
NRG-7a	NRG-7a-1348.8-SNL	2440
NRG-7a	NRG-7a-1348.8-SNL	2424
NRG-7a	NRG-7a-1353.7-SNL	2388
NRG-7a	NRG-7a-1363.5-SNL	2442
NRG-7a	NRG-7a-1385.0-SNL	2424
NRG-7a	NRG-7a-1385.0-SNL	2419
NRG-7a	NRG-7a-1402.7-SNL	2358
NRG-7a	NRG-7a-1409.0-SNL	2450
SD-12	SD-12-1073.3-SNL	2415
SD-12	SD-12-1077.1-SNL	2426
SD-12	SD-12-1107.1-SNL	2416
SD-12	SD-12-1112.1-SNL	2400
SD-12	SD-12-1118.9-SNL	2372
SD-12	SD-12-1209.0-SNL	2423
SD-9	NRG-SD-9-1243-SNL	2418
SD-9	NRG-SD-9-1298-SNL	2439
SD-9	NRG-SD-9-1346.5-SNL	2419
Mean Density Value		2411

Source: DTN: SNL02030193001.027 [DIRS 108410].

Table E-3. Data from Shear Stress Experiments on Natural Fractures from the Nonlithophysal Units of the Repository Horizon

Source DTN	Specimen Number (also referred to as Sample Number)	Lithostratigraphic Unit	Normal Stress, $\sigma$ (MPa)	Peak Shear Stress, $\tau_p$ (MPa)	Joint Dilatation (deg)	Source Reports <sup>a</sup>
SNL02112293001.003 [DIRS 108412]	NRG-6-782.3-782.6-SNL	Tptpmn	2.5	1.9	1.1	Olsson and Brown 1997 [DIRS 106453] (Table 1)
SNL02112293001.005 [DIRS 108413]	SD-9-1254.7-1255.2-A	Tptpln	10.0	7.7	33.4	SNL1996 [DIRS 165408] (Tables 1 and 3)
	SD-9-1255.9-1256.3	Tptpln	2.5	2.4	8.5	
	SD-9-1254.7-1255.2-B	Tptpln	10.0	9.0	18.4	
SNL02112293001.007 [DIRS 108414]	SD-12-688.4-688.7	Tptpmn	2.5	3.6	14.2	SNL 1996 [DIRS 165410] (Tables 1 and 3)
	SD-12-1072.5-1073.0-A	Tptpln	2.5	3.3	13.7	
	SD-12-1072.5-1073.0-B	Tptpln	5.0	6.6	15.1	
	SD-12-778.1-780.0	Tptpmn	10.0	12.0	17.7	

<sup>a</sup> Data can be accessed through the source reports available via Records Processing Center Packages linked to the Source DTN.



Source: Data provided in Table E-3.

Figure E-1. Plot of Shear Strength Test Data from the TSw2 Thermal Mechanical Unit



To determine the range of the joint strength parameters (cohesion and friction angle), a statistical analysis was conducted as documented in file “*joint strength v2.xls*” (Table A-1). The mean shear stress was calculated at each normal stress level. A linear fit of the  $\pm$  one standard deviation about the mean data was used to determine the range of cohesion and friction angle (Figure E-1). Cohesion ranges from 0.2 to 0.9 MPa, while friction angle varies from 35° to 47°.

Joint dilation data from rotary shear tests for the nonlithophysal units are presented in Table E-3. The mean joint dilation is 15.3°, with a standard deviation of 9.2°. The range of joint stiffness data from rotary shear tests is presented in Table E-4 together with the mean values. The joint stiffness data presented are consistent with *Subsurface Geotechnical Parameters Report* (BSC 2003 [DIRS 166660], Tables 8-50 and 8-51).

Direct shear test data have recently been collected as documented in the *Subsurface Geotechnical Parameters Report* (BSC 2003 [DIRS 166660], Tables 8-47 and 8-52). For these tests, cooling joints have been distinguished from vapor phase partings. Results for cohesion, friction angle, dilation, and shear stiffness are shown in Table E-5. With the exception of the shear stiffness, the direct shear results (Table E-5) are similar to the rotary shear results (Tables E-3, E-4, and Figure E-1). Shear stiffness values determined from the direct shear tests are similar to the empirical estimations of joint shear stiffness (Duan 2003 [DIRS 163586], Tables 5.2 and 5.3). Normal joint stiffness values from direct shear tests were not available.

### E3. INTACT ROCK PROPERTIES FOR NONLITHOPHYSAL ROCK

Elastic rock properties data for nonlithophysal rock (i.e., the Ttpmn and Ttpln units), including Young’s modulus,  $E$ , and Poisson’s ratio,  $\nu$ , from laboratory tests on core specimens are shown in Table E-6. The mean Young’s modulus from this data is 33.6 GPa, and the mean Poisson’s ratio is 0.20. Bulk modulus,  $K$ , and shear modulus,  $G$ , are calculated as follows (Jaeger and Cook 1979 [DIRS 106219], p. 111):

$$K = \frac{E}{3 \cdot (1 - 2\nu)} \quad (\text{Eq. E-2})$$

$$G = \frac{E}{2 \cdot (1 + \nu)} \quad (\text{Eq. E-3})$$

Plugging the mean values of  $E$  and  $\nu$  into Equations E-2 and E-3 results in a bulk modulus value of 18.7 GPa, and a shear modulus value of 14.0 GPa.

Tensile strength data for the TSw2 unit were obtained from indirect tensile strength tests performed by the Brazilian Test method using core specimens as shown in Table E-7. The mean tensile strength from this data for the nonlithophysal units is 10.9 MPa for the Ttpmn and 7.9 MPa for the Ttpln. The lower lithophysal unit (i.e., Ttpll) has a mean tensile strength of 8.3 MPa. For the small Brazilian test samples, lithophysal cavities are not represented. The matrix rock material for the Ttpmn, Ttpll, and Ttpln Brazilian samples is therefore the same, and has a mean tensile strength of 8.9 MPa (Table E-7).

Table E-4. Normal and Shear Stiffness Data from Shear Stress Experiments on Natural Fractures from the Nonlithophysal Units of the Repository Horizon <sup>a</sup>

Source DTN	Specimen Number (also referred to as Sample Number)	Lithostratigraphic Unit	Test ID	Tangent Normal Stiffness at 5 MPa (MPa/mm)	Tangent Shear Stiffness (Maximum) (MPa/mm)	Source Reports <sup>a</sup>
SNL02112293001.003 [DIRS 108412]	NRG-6-782.3-782.6-SNL	Tptpmn	YM9	NA	45	Olsson and Brown 1997 [DIRS 106453], Figure 6
SNL02112293001.005 [DIRS 108413]	SD-9-1254.7-1255.2-A	Tptpln	YM23	105	100	SNL 1996 [DIRS 165408], p. A-2
	SD-9-1255.9-1256.3	Tptpln	YM24	NA	145	SNL 1996 [DIRS 165408], p. A-5
	SD-9-1254.7-1255.2-B	Tptpln	YM25	115	180	SNL 1996 [DIRS 165408], p. A-8
SNL02112293001.007 [DIRS 108414]	SD-12-688.4-688.7	Tptpmn	YM33	NA	45	SNL 1996 [DIRS 165410], p. A-2
	SD-12-1072.5-1073.0-A	Tptpln	YM34	NA	23	SNL 1996 [DIRS 165410], p. A-4
	SD-12-1072.5-1073.0-B	Tptpln	YM35	90	115	SNL 1996 [DIRS 165410], p. A-6
	SD-12-778.1-780.0	Tptpmn	YM36	65	120	SNL 1996 [DIRS 165410], p. A-8
<i>Mean</i>				94	97	—
<i>Standard Deviation</i>				22	55	

<sup>a</sup> Data can be accessed through the source reports available via Records Processing Center Packages linked to the source DTN.

Table E-5. Summary Statistics of Direct Joint Shear Test Results

Property	Statistic	Vapor Phase Parting	Cooling Joint
Joint Cohesion (MPa)	Mean	0.7	0.0
	Standard Deviation	0.1	0.1
	Minimum	0.7	-0.0
	Maximum	0.8	0.1
	Count	3	2
Joint Friction Angle (degree)	Mean	44	33
	Standard Deviation	2	0
	Minimum	42	33
	Maximum	46	34
	Count	3	2
Joint Dilatation (degree)	Mean	14	2
	Standard Deviation	2	4
	Minimum	12	-1
	Maximum	16	4
	Count	3	2
Joint Shear Stiffness (MPa/mm)	Mean	13	11
	Standard Deviation	6	6
	Minimum	8	7
	Maximum	20	15
	Count	3	2

Source: BSC 2003 [DIRS 166660], Tables 8-47 and 8-52.

Table E-6. Elastic Properties Data from the Nonlithophysal Units of the Repository Horizon <sup>a</sup>

Litho-stratigraphic Unit	Location	Specimen Number (also referred to as Sample Number)	Young's Modulus (GPa)	Poisson's Ratio	Original Source DTN
Tptpmn	Busted Butte	10/AE/2/Z	28.7	0.17	SNSAND85076200.000 [DIRS 160024]
		10/AE/46/Z	34.2	0.18	
		10/AE/9/Z	31.5	0.20	
		10-AE-3Y	18.6	0.07	
		10-AE-6X	28.6	0.14	
		10-AE-8X	21.7	0.11	
		10X12	34.6	0.21	SNSAND85070900.000 [DIRS 160022]
		10Y47	35.9	0.20	
		10Z15	37.4	0.20	
		12A2	45.8	0.22	
		12A3	44.2	0.21	
		13A2	34.9	0.21	
		26A1	45.7	0.20	
		26B1	34.6	0.21	
		26C1	47.3	0.19	
		26D1	42.5	0.14	
	26E1	47.2	0.19		
	28A2	34.6	0.20		
	USW G-4	G4-686.6-A	36.2	0.18	SNSAND84110100.000 [DIRS 160016]
		G4-686.6-D	40.7	0.17	
		G4-686.6-G	33.1	0.21	
		G4-742.75-E	35.6	0.21	
		G4-742.75-F	36.8	0.21	
		G4-742.75-G	34.6	0.21	
		G4-748.6-A	32.2	0.16	
		G4-748.6-B	32.3	0.21	
		G4-749.0-A	33.5	0.29	
		G4-749.0-B	34.1	0.27	
USW GU-3	GU-3 760.9/1A	30.2	0.19	SNSAND83164600.000 [DIRS 160009]	
	GU-3 760.9/1B	28.6	0.29		
	GU-3 760.9/2A	29.0	0.22		
	GU-3 760.9/2B	30.2	0.22		

Table E-6. Elastic Properties Data from the Nonlithophysal Units of the Repository Horizon (Continued)<sup>a</sup>

Litho-stratigraphic Unit	Location	Specimen Number (also referred to as Sample Number)	Young's Modulus (GPa)	Poisson's Ratio	Original Source DTN
Tptpmn	USW GU-3	GU-3 760.9/3A	30.6	0.23	SNSAND83164600.000 [DIRS 160009]
		GU-3 760.9/3B	30.8	0.21	
		GU-3 760.9/4A	29.3	0.19	
		GU-3 760.9/4B	28.1	0.16	
		GU-3 760.9/5A	30.7	0.22	
		GU-3 760.9/5B	30.0	0.21	
	UE-25 NRG #5	NRG-5-847.2-SNL-A	35.2	0.21	SNL02030193001.012 [DIRS 108416]
		NRG-5-849.4-SNL-A	37.0	0.19	
		NRG-5-861.2-SNL-A	17.1	0.23	
		NRG-5-873.4-SNL-A	13.4	0.30	
		NRG-5-887.2-SNL-A	40.5	0.20	
		NRG-5-888.8-SNL-A	39.4	0.19	
		NRG-5-891.9-SNL-A	38.3	0.15	
	USW NRG-6	NRG-5-896.5-SNL-A	39.1	0.10	SNL02030193001.004 [DIRS 108415]
		NRG-6-720.7-SNL-A	37.1	0.19	
		NRG-6-742.3-SNL-A	30.6	0.20	
		NRG-6-742.9-SNL-A	32.4	0.22	
		NRG-6-762.9-SNL-A	29.2	0.18	
		NRG-6-773.5-SNL-A	36.2	0.23	
		NRG-6-784.8-SNL-A	29.7	0.17	
		NRG-6-785.6-SNL-A	30.1	0.16	
	USW NRG-7a	NRG-6-806.8-SNL-A	31.7	0.16	SNL02030193001.019 [DIRS 108431]
		NRG-7/7A-777.0-SNL-A	32.9	0.22	
		NRG-7/7A-806.3-SNL-A	36.7	0.19	
		NRG-7/7A-818.5-SNL-A	33.1	0.20	
		NRG-7/7A-859.2-SNL-A	38.8	0.20	
		NRG-7/7A-865.4-SNL-I	34.3	0.20	
		NRG-7/7A-865.4-SNL-J	33.5	0.19	
		NRG-7/7A-865.4-SNL-K	34.9	0.22	
	USW SD-12	NRG-7/7A-865.4-SNL-L	35.7	0.21	SNL02030193001.023 [DIRS 108435]
SD-12-734.7-SNL-B		31.9	0.18		
USW SD-9	SD-12-781.1-SNL-B	36.7	0.21	SNL02030193001.026 [DIRS 108436]	
	SD-9-761.5-SNL-A	33.9	0.21		
	SD-9-768.7-SNL-A	36.9	0.20		
	SD-9-771.7-SNL-A	34.8	0.19		
	SD-9-774.6-SNL-B	16.8	0.19		
	SD-9-826.7-SNL-A	31.9	0.21		
	SD-9-832.8-SNL-C	29.8	0.19		
Tptpln	USW G-4	SD-9-842.1-SNL-E-1	36.3	0.20	SNSAND84110100.000 [DIRS 160016]
		G4-1307.2-A	30.2	0.23	
		G4-1307.2-C	22.8	0.20	

Table E-6. Elastic Properties Data from the Nonlithophysal Units of the Repository Horizon (Continued)<sup>a</sup>

Litho-stratigraphic Unit	Location	Specimen Number (also referred to as Sample Number)	Young's Modulus (GPa)	Poisson's Ratio	Original Source DTN
Ttptln	USW G-4	G4-1307.2-D	20.0	0.30	SNSAND84110100.000 [DIRS 160016]
		G4-1307.2-E	16.6	0.24	
		G4-1307.2-F	34.9	0.20	
	USW GU-3	GU-3 1050.4/1	35.5	0.18	SNSAND83164600.000 [DIRS 160009]
		GU-3 1050.4/2	36.1	0.19	
		GU-3 1050.4/3	36.3	0.19	
		GU-3 1067.8/3	32.7	0.24	
		GU-3 1067.8/4	32.1	0.24	
	USW NRG-7a	NRG-7/7A-1265.2-SNL-A	40.7	0.21	SNL02030193001.020 [DIRS 108432]
		NRG-7/7A-1257.8-SNL-A	41.8	0.20	
		NRG-7/7A-1259.1-SNL-A	40.6	0.21	
		NRG-7/7A-1314.8-SNL-A	37.7	0.21	
		NRG-7/7A-1252.3-SNL-A	30.4	0.14	
	USW SD-12	SD-12-1107.1-SNL-B	34.5	0.23	SNL02030193001.023 [DIRS 108435]
		SD-12-1209.0-SNL-B	31.9	0.28	
	USW SD-9	SD-9-1243.0-SNL-A	35.9	0.19	SNL02030193001.026 [DIRS 108436]
		SD-9-1298.0-SNL-A	39.9	0.25	
SD-9-1346.5-SNL-A		44.4	0.25		
Mean property values			33.6	0.20	—

<sup>a</sup> Elastic properties data are qualified and summarized in DTN: MO0402DQRIRPPR.003 [DIRS 168901]. The data can be found by downloading the data file from this DTN, and searching for the data using the Specimen Number. The elastic properties data have been selected according to test conditions to provide a consistent data set. Data with the following test conditions were selected: ambient temperature conditions, saturated samples, unconfined (confining pressure = 0 or 0.1 MPa), nominal strain rate of  $10^{-5} \text{ s}^{-1}$ , with sample diameters ranging from 25.4 to 50.8 mm.

Table E-7. Tensile Strength Data from the TSw2 Thermal Mechanical Unit<sup>a</sup>

Borehole	Specimen Number (also referred to as Sample Number)	Tensile Strength (MPa)	Original Source DTN	Lithostratigraphic Unit
NRG-5	NRG-5-788.6-SNL-A	4.3	SNL02030193001.009 [DIRS 109614]	Ttptmnn
	NRG-5-832.9-SNL-A	7.7		
	NRG-5-847.2-SNL-B	5.7		
	NRG-5-887.2-SNL-B	16.8		
	NRG-5-888.8-SNL-B	15.9		
	NRG-5-891.9-SNL-B	12.9		
NRG-6	NRG-6-742.3-SNL-B	14.5	SNL02030193001.004 [DIRS 108415]	
	NRG-6-742.9-SNL-B	13.0		
	NRG-6-773.5-SNL-B	7.9		
	NRG-6-784.8-SNL-B	12.5		
	NRG-6-785.6-SNL-B	14.1		

Table E-7. Tensile Strength Data from the TSw2 Thermal Mechanical Unit (Continued)<sup>a</sup>

Borehole	Specimen Number (also referred to as Sample Number)	Tensile Strength (MPa)	Original Source DTN	Lithostratigraphic Unit
NRG-7a	NRG-7/7A-762.1-SNL-A	9.3	SNL02030193001.019 [DIRS 108431]	Tptpmn
	NRG-7/7A-828.4-SNL-A	6.1		
	NRG-7/7A-855.0-SNL-A	11.6		
<i>Mean</i>		10.9	<i>Summary Statistics for Tptpmn</i>	
<i>Count</i>		14		
<i>Standard Deviation</i>		4.0		
<i>Minimum</i>		4.3		
<i>Maximum</i>		16.8		
NRG-6	NRG-6-848.0-SNL-B	7.9	SNL02030193001.004 [DIRS 108415]	
	NRG-6-908.2-SNL-A	8.8		
	NRG-6-934.0-SNL-A	10.8		
	NRG-6-934.0-SNL-B	4.0		
	NRG-6-956.8-SNL-A	5.3		
	NRG-6-963.3-SNL-B	3.2		
	NRG-6-969.3-SNL-A	7.5		
NRG-7a	NRG-7/7A-879.2-SNL-A	14.3	SNL02030193001.019 [DIRS 108431]	Tptpll
	NRG-7/7A-879.2-SNL-B	11.0		
	NRG-7/7A-881.0-SNL-A	12.1		
	NRG-7/7A-958.7-SNL-A	11.2	SNL02030193001.020 [DIRS 108432]	
	NRG-7/7A-958.7-SNL-B	11.5		
	NRG-7/7A-976.4-SNL-A	5.5		
	NRG-7/7A-976.4-SNL-B	6.3		
	NRG-7/7A-979.6-SNL-A	5.2		
	NRG-7/7A-1046.8-SNL-A	6.2		
	NRG-7/7A-1090.3-SNL-A	10.4		
	NRG-7/7A-1090.3-SNL-B	10.2		
	NRG-7/7A-1098.3-SNL-A	6.6		
	NRG-7/7A-1129.3-SNL-A	7.0		
	NRG-7/7A-1180.0-SNL-A	5.3		
	NRG-7/7A-1188.7-SNL-A	8.6		
NRG-7/7A-1230.2-SNL-B	9.2			
<i>Mean</i>		8.3	<i>Summary Statistics for Tptpll</i>	
<i>Count</i>		24		
<i>Standard Deviation</i>		2.9		
<i>Minimum</i>		3.2		
<i>Maximum</i>		14.3		
NRG-7a	NRG-7/7A-1263.7-SNL-A	13.7	SNL02030193001.020 [DIRS 108432]	Tptpln
	NRG-7/7A-1263.7-SNL-B	9.9		
	NRG-7/7A-1263.7-SNL-C	9.0		

Table E-7. Tensile Strength Data from the TSw2 Thermal Mechanical Unit (Continued)<sup>a</sup>

Borehole	Specimen Number (also referred to as Sample Number)	Tensile Strength (MPa)	Original Source DTN	Lithostratigraphic Unit
NRG-7a	NRG-7/7A-1307.0-SNL-A	10.9	SNL02030193001.020 [DIRS 108432]	Tptpln
	NRG-7/7A-1307.0-SNL-B	8.8		
	NRG-7/7A-1348.8-SNL-A	4.8		
	NRG-7/7A-1348.8-SNL-B	5.9		
	NRG-7/7A-1353.7-SNL-A	7.6		
	NRG-7/7A-1363.5-SNL-A	7.6		
	NRG-7/7A-1385.0-SNL-A	6.1		
	NRG-7/7A-1385.0-SNL-B	6.3		
	NRG-7/7A-1402.7-SNL-A	4.8		
	NRG-7/7A-1409.0-SNL-A	7.6		
<i>Mean</i>		7.9	<i>Summary Statistics for Tptpln</i>	
<i>Count</i>		13		
<i>Standard Deviation</i>		2.5		
<i>Minimum</i>		4.8		
<i>Maximum</i>		13.7		
<i>Mean</i>		8.9	<i>Summary Statistics for TSw2</i>	
<i>Count</i>		51		
<i>Standard Deviation</i>		3.3		
<i>Minimum</i>		3.2		
<i>Maximum</i>		16.8		

<sup>a</sup> Tensile strength data are qualified and summarized in DTN: MO0401DQIRIRPTS.003 [DIRS 168905].

The tensile strength of intact rock material is typically an order of magnitude lower than its compressive strength (compare the mean tensile strength of 10.9 MPa for the Tptpmn unit [Table E-7] to the mean compressive strength of 188.8 MPa for the Tptpmn unit [see Section E4.2, Table E-14]). The tensile strength of a rock mass is often considered to be zero since discontinuities offer little or no resistance to tensile stresses. However, compressive stresses are most prevalent in geotechnical problems, so the emphasis in geotechnical design is typically placed on the compressive and shear strength of rock (Brady and Brown 1985 [DIRS 126811], pp. 86-87).

Triaxial strength data (Table E-8) are used to calculate intact cohesion and friction angle of the nonlithophysal rocks. The triaxial data includes sets of confining pressure data paired with the corresponding axial stress at failure, as plotted in Figures E-2 and E-3. The Mohr-Coulomb approach for calculating cohesion and friction angle is used (Jaeger and Cook 1979 [DIRS 106219], pp. 87 to 93). A least-square linear fit of the axial stress ( $\sigma_1$ ) and the confining



pressure ( $\sigma_3$ ) data sets was performed (Figure E-2) and plotted in the form:

$$\sigma_1 = N \sigma_3 + \sigma_C \quad (\text{Eq. E-4})$$

where  $\sigma_1$  = axial stress, or the strength of the rock at failure,  
 $\sigma_3$  = confining pressure,  
 $\sigma_C$  = unconfined compressive strength,  
 $N$  = confinement factor.

The relationship between the linear equation above and the Mohr-Coulomb parameters, cohesion ( $C$ ) and friction angle ( $\phi$ ), is given by the following (Jaeger and Cook 1979 [DIRS 106219], p. 93):

$$\tau = C + \sigma_n \tan \phi \quad (\text{Eq. E-5})$$

where  $\tau$  = shear stress,  
 $C$  = cohesion,  
 $\sigma_n$  = normal stress  
 $\phi$  = friction angle.

Cohesion and friction angle are calculated based on their relationship to  $N$  and  $\sigma_c$  as follows (Jaeger and Cook 1979 [DIRS 106219], pp. 88 to 91):

$$C = \frac{\sigma_c}{2 \cdot \sqrt{N}} \quad (\text{Eq. E-6})$$

$$\phi = 2 (\tan^{-1} \sqrt{N} - 45^\circ). \quad (\text{Eq. E-7})$$

The calculation of cohesion and friction angle using the approach described above is documented in Microsoft Excel file, *intact strength nonlith v2.xls* (Table A-1), resulting in a mean cohesion of 36 MPa and a friction angle of 50° for the Tptpmn unit from borehole samples located near the ESF (Table E-8). The mean value of cohesion and friction angle is within the range of the values provided in the *Subsurface Geotechnical Parameters Report* (BSC 2003 [DIRS 166660], Table 8-40).

To evaluate the range of the intact strength parameters, cohesion and friction angle, using the data from Table E-8, a statistical analysis was conducted as documented in Table A-1, file: *intact strength nonlith v2.xls*. The mean axial stress was calculated at each confining stress level. A linear fit of the  $\pm$  one standard deviation about the mean data was used to determine the range of cohesion and friction angle. Cohesion ranges from 32 to 40 MPa, while friction angle varies from 41° to 56° (Figure E-2).

Table E-8. Uniaxial and Triaxial Test Data from the Tptpmn Lithostratigraphic Unit<sup>a</sup>

Location	Specimen Number (also referred to as Sample Number)	Confining Pressure, $\sigma_3$ (MPa)	Ultimate Differential Strength (also referred to as Compressive Strength) (MPa)	Axial Stress <sup>b</sup> , $\sigma_1$ (MPa)	Original Source DTN
USW GU-3	GU-3 760.9-1A	0	210.3	210.3	SNSAND83164600.000 [DIRS 160009]
	GU-3 760.9-1B	0	234.4	234.4	
	GU-3 760.9-2A	0	215.5	215.5	
	GU-3 760.9-3A	0	245.2	245.2	
	GU-3 760.9-5A	0	229.7	229.7	
	GU-3 760.9-5B	0	226.4	226.4	
	GU-3 760.9-2B	0	221.4	221.4	
	GU-3 760.9-3B	0	222.2	222.2	
	GU-3 760.9-4A	0	205.2	205.2	
	GU-3 760.9-4B	0	183.5	183.5	
UE-25 NRG #5	NRG-5-847.2-SNL-A	0	84.2	84.2	SNL02030193001.012 [DIRS 108416]
	NRG-5-849.4-SNL-A	0	240.8	240.8	
	NRG-5-861.2-SNL-A	0	55.3	55.3	
	NRG-5-873.4-SNL-A	0	38.4	38.4	
	NRG-5-887.2-SNL-A	0	240.9	240.9	
	NRG-5-888.8-SNL-A	0	288.9	288.9	
	NRG-5-891.9-SNL-A	0	253.5	253.5	
	NRG-5-896.5-SNL-A	0	184.7	184.7	
USW NRG-6	NRG-6-720.7-SNL-A	0	235.5	235.5	SNL02030193001.004 [DIRS 108415]
	NRG-6-742.3-SNL-A	0	162.3	162.3	
	NRG-6-742.9-SNL-A	0	212.8	212.8	
	NRG-6-762.9-SNL-A	0	112.1	112.1	
	NRG-6-773.5-SNL-A	0	117.4	117.4	
	NRG-6-784.8-SNL-A	0	223.0	223.0	
	NRG-6-785.6-SNL-A	0	218.6	218.6	
USW NRG-7a	NRG-7/7A-777.0-SNL-A	0	143.8	143.8	SNL02030193001.019 [DIRS 108431]
	NRG-7/7A-800.2-SNL-A	0	179.2	179.2	
	NRG-7/7A-806.3-SNL-A	0	225.4	225.4	
	NRG-7/7A-818.5-SNL-A	0	126.3	126.3	
	NRG-7/7A-859.2-SNL-A	0	118.8	118.8	
	NRG-7/7A-865.4-SNL-I	0	215.8	215.8	
	NRG-7/7A-865.4-SNL-J	0	232.0	232.0	
	NRG-7/7A-865.4-SNL-K	0	239.1	239.1	
NRG-7/7A-865.4-SNL-L	0	248.5	248.5		
USW SD-12	SD-12-734.7-SNL-B	0	193.3	193.3	SNL02030193001.023 [DIRS 108435]
	SD-12-781.1-SNL-B	0	198.2	198.2	
USW SD-9	SD-9-761.5-SNL-A	0	231.5	231.5	SNL02030193001.026 [DIRS 108436]
	SD-9-768.7-SNL-A	0	254.5	254.5	
	SD-9-771.7-SNL-A	0	160.8	160.8	
	SD-9-774.6-SNL-B	0	60.1	60.1	

Table E-8. Uniaxial and Triaxial Test Data from the Tptpmn Lithostratigraphic Unit (Continued)<sup>a</sup>

Location	Specimen Number (also referred to as Sample Number)	Confining Pressure, $\sigma_3$ (MPa)	Ultimate Differential Strength (also referred to as Compressive Strength) (MPa)	Axial Stress <sup>b</sup> , $\sigma_1$ (MPa)	Original Source DTN
USW SD-9	SD-9-826.7-SNL-A	0	224.9	224.9	SNL02030193001.026 [DIRS 108436]
	SD-9-832.8-SNL-C	0	183.3	183.3	
	SD-9-842.1-SNL-E-1	0	208.9	208.9	
USW G-4	G4-686.6-G	0.1	180.0	180.1	SNSAND84110100.000 [DIRS 160016]
	G4-749.0-A	0.1	268.0	268.1	
	G4-749.0-B	0.1	188.0	188.1	
	G4-686.6-A	0.1	270.0	270.1	
	G4-686.6-D	0.1	326.0	326.1	
	G4-742.75-E	0.1	235.0	235.1	
	G4-742.75-F	0.1	256.0	256.1	
	G4-742.75-G	0.1	279.0	279.1	
	G4-748.6-B	0.1	190.0	190.1	
	G4-748.6-A	0.1	196.0	196.1	
	G4-686.6-B	5	156.0	161.0	
USW NRG-7a	NRG-7/7A-865.4-SNL-C	5	254.8	259.8	SNL02030193001.019 [DIRS 108431]
	NRG-7/7A-865.4-SNL-F	5	317.3	322.3	
	NRG-7/7A-865.4-SNL-G	5	250.1	255.1	
	NRG-7/7A-865.4-SNL-H	5	226.6	231.6	
	NRG-7/7A-861.7-SNL-A	5	245.8	250.8	
USW SD-12	SD-12-745.6-SNL-B	5	330.7	335.7	SNL02030193001.023 [DIRS 108435]
USW G-4	G4-686.6-C	10	344.0	354.0	SNSAND84110100.000 [DIRS 160016]
	G4-686.6-F	10	360.0	370.0	
USW NRG-7a	NRG-7/7A-865.4-SNL-A	10	315.2	325.2	SNL02030193001.019 [DIRS 108431]
	NRG-7/7A-865.4-SNL-B	10	344.0	354.0	
	NRG-7/7A-865.4-SNL-D	10	225.5	235.5	
	NRG-7/7A-865.4-SNL-E	10	306.7	316.7	
	NRG-7/7A-805.6-SNL-A	10	137.1	147.1	
USW SD-12	NRG-7/7A-827.4-SNL-A	10	125.3	135.3	SNL02030193001.021 DIRS 108433]
	SD-12-762.6-SNL-B	10	272.8	282.8	

<sup>a</sup> Uniaxial and triaxial test data are qualified and summarized in DTN: MO0311RCKPRPCS.003 [DIRS 166073]. The data can be found by downloading the data file from this DTN, and searching for the data using the Specimen Number. The uniaxial and triaxial test data have been selected according to test conditions to provide a consistent data set. Borehole data with the following test conditions were selected: ambient temperature conditions, saturated samples, nominal strain rate of  $10^{-5} \text{ s}^{-1}$ , with sample diameters ranging from 25.4 to 50.8 mm.

<sup>b</sup> Axial Stress ( $\sigma_1$ ) is not provided in the DTN. Axial Stress =  $\sigma_1 = \sigma_3 + \text{Ultimate Differential Strength}$ .

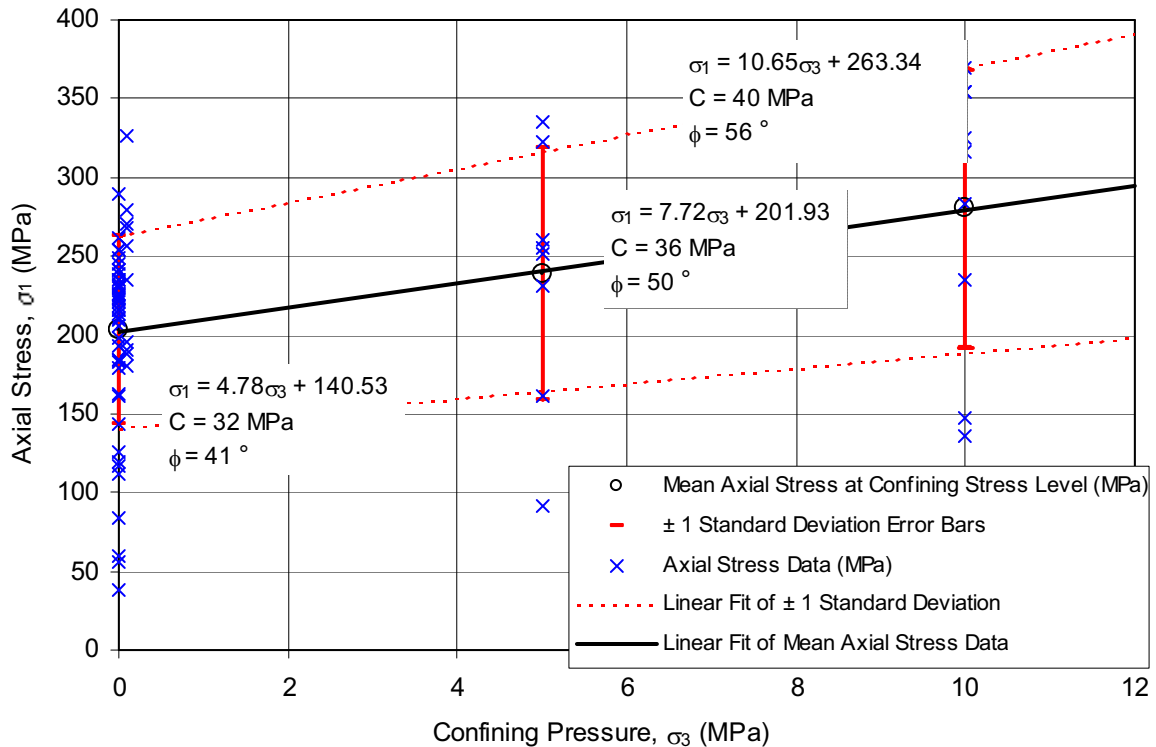


Figure E-2. Uniaxial and Triaxial Test Data from Borehole Samples Near the ESF for the Tptpm Lithostratigraphic Unit

## E4. ROCK MASS PROPERTIES

### E4.1 ASSESSMENT OF LITHOPHYSAL ROCK STRENGTH

#### E4.1.1 Introduction

The following section provides a discussion of the development of estimates of the rock mass mechanical properties of the lithophysal units of the Topopah Spring tuff. A description of the small and large core laboratory testing database is provided. The large core mechanical testing (including room dry and saturated conditions) was used to relate strength and modulus to lithophysal porosity, which is the primary factor in control of variability of mechanical properties in this rock. An initial set of base case strength and modulus values (termed rock strength “categories”) are developed as from the most-recent large core testing that span the entire range of lithophysal porosity conditions observed in the ECRB Cross-Drift. These base case values are used as a basis for a series of parametric analyses of emplacement drift stability under in situ, thermal and seismic loading described in Section 6.4. These analyses consider homogenous rock properties for each rock strength category with the lower strength categories leading to conservative results. Additional discussion on lithophysal rock strength is provided in *Lithophysal Rock Mass Mechanical Properties of the Repository Host Horizon* (BSC 2004 [DIRS 168970]).

The large core laboratory data set is necessarily limited in scope due to the variability and difficulty in sampling and testing large volume samples of the lithophysal rock mass. Therefore, discontinuum numerical models (PFC and UDEC), calibrated to reproduce the basic mechanical response of the laboratory test results, are used here to supplement the data base and clarify understanding of the mechanical response of lithophysal rock. The PFC model is used to explore the impact of lithophysal porosity, size, shape and distribution on the variability of mechanical properties, and thus establish upper and lower property bounds. The UDEC model is used to conduct drift-scale simulated compression analyses to examine the effect of spatial variability of in situ lithophysal porosity on rock mass strength variability. Conclusions are given as to the base case mechanical properties data set and the variability of the rock mass mechanical properties for use in performance analyses.

#### **E4.1.2 Small Core Mechanical Properties Data Base**

A large number of compression and tension tests have been conducted on small diameter (1-in to 2-in [25 mm to 50 mm]) cores from the Tptpul and Tptpll. This data is described in detail in the *Subsurface Geotechnical Parameters Report* (BSC 2003 [DIRS 166660]), and the results reviewed here.

Testing on small cores from the Topopah Spring subunits indicates a distinct control of both compressive strength and elastic modulus based on the total porosity of the sample (Figure E-3). The total porosity of these samples, due to their small size, is primarily composed of matrix ground mass porosity<sup>1</sup>. On the scale of the emplacement drifts, the total porosity is the sum of the matrix porosity (approximately 10 percent) plus lithophysal void porosity (approximately 10 to 25 percent). The additional porosity of vapor phase altered material may form rims or fill lithophysal voids (generally less than 5 percent). Estimates of the component porosity within the Tptpll derived from field mapping in the ECRB Cross-Drift are discussed in Appendix O. The impact of lithophysal voids (and the inability to sample them) with small core samples is evident as the maximum total lithophysal porosities are typically less than 20 percent (see Figure O-15).

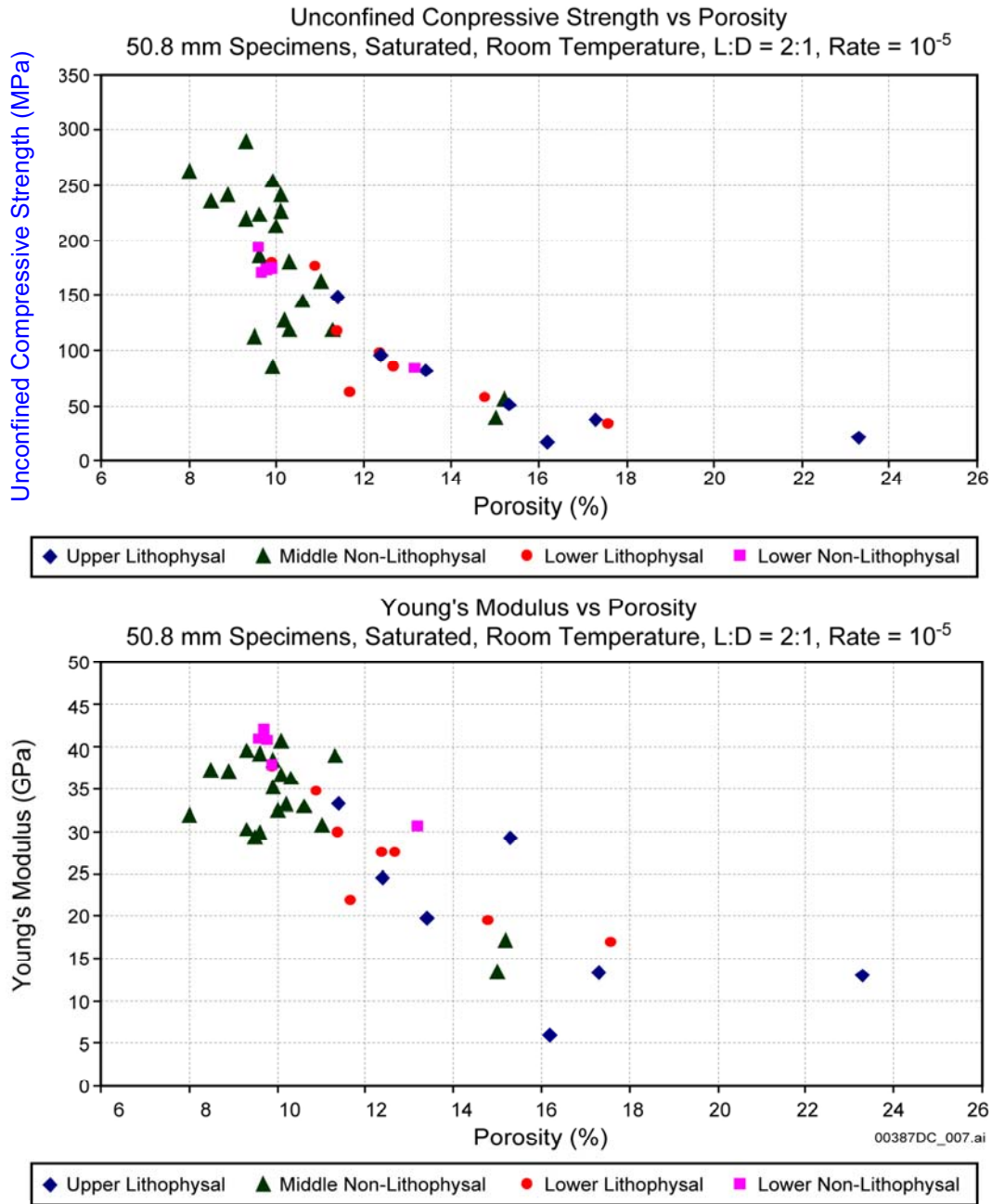
#### **E4.1.3 Large Core Unconfined Compression Testing**

##### **E4.1.3.1 Sample Gathering**

The small diameter cores (e.g., 1-in or 2-in diameter) do not accurately reflect the true strength or elastic properties of the lithophysal rock since the diameter precludes a reasonable sampling of the lithophysal voids. Therefore, reliance is placed on measurements from large diameter core samples that contain multiple lithophysal cavities in a given sample. To this end, an extensive drilling program was undertaken in the ESF main loop and ECRB Cross-Drift in 2002 to provide large-diameter (11.5-in.) core samples of lithophysal rock from the Tptpul and Tptpll that contain a reasonable lithophysal sampling.

---

<sup>1</sup> Matrix groundmass porosity is that pore space generally less than 2 $\mu$ m in size, and totaling approximately 10 percent of volume in densely welded tuffs (BSC 2003 [DIRS 166660], Section 8.2.3.2, p. 8-9). This porosity is considered to be an intrinsic property of the matrix groundmass for the subunits of the Topopah Spring, and is distinguished from lithophysal porosity, which is formed from gas collection in the matrix during the cooling process.



Source: BSC 2003 [DIRS 166660] (Figures 8-22 and 8-11).

NOTE: Porosity is composed of matrix and lithophysal porosity. The measurements are from a 50.8 mm diameter core. Note that small cores from lithophysal zones generally contain only small amounts of lithophysal porosity, and thus the above tests are not indicative, in general, of properties of the lower and upper lithophysal units.

Figure E-3. Intact Uniaxial Compressive Strength and Young's Modulus for Topopah Spring Subunits as a Function of Effective Porosity for 50.8 mm Diameter Samples

Figure E-4 shows a plan view of the ESF main loop and ECRB Cross-Drift and the locations from which core samples were retrieved (see Figure 7-1 for a photograph of one of the core lengths obtained from the Tptpll in the ECRB Cross-Drift). A total of nineteen 11.5-in. (290 mm) cores at least 12 in. (304 mm) in length was obtained. Of these, 13 had a length to diameter (L:D) ratio of 1.7 or greater, with one additional sample with L:D of 1.5. These were felt to be sufficiently close to the recommended 2:1 length-to-diameter ratio to allow for unconfined compression testing. Figure E-5 shows a photograph of some of the large cores and an unconfined compression test in progress. The remaining core sections were under-cored to provide sixteen additional 5.7-in. (146 mm) test samples. Although these samples are not judged to be sufficiently large to represent in situ properties, the data is, nonetheless useful as additional information for establishing the impact of porosity on strength and modulus and for estimating sample size effects. This data was supplemented by previous testing by Price et al. (1985 [DIRS 106602]) on 10.5-in. (267 mm) diameter cores taken from an outcrop of the Ttpul at Busted Butte (directly adjacent to and south of Yucca Mountain).

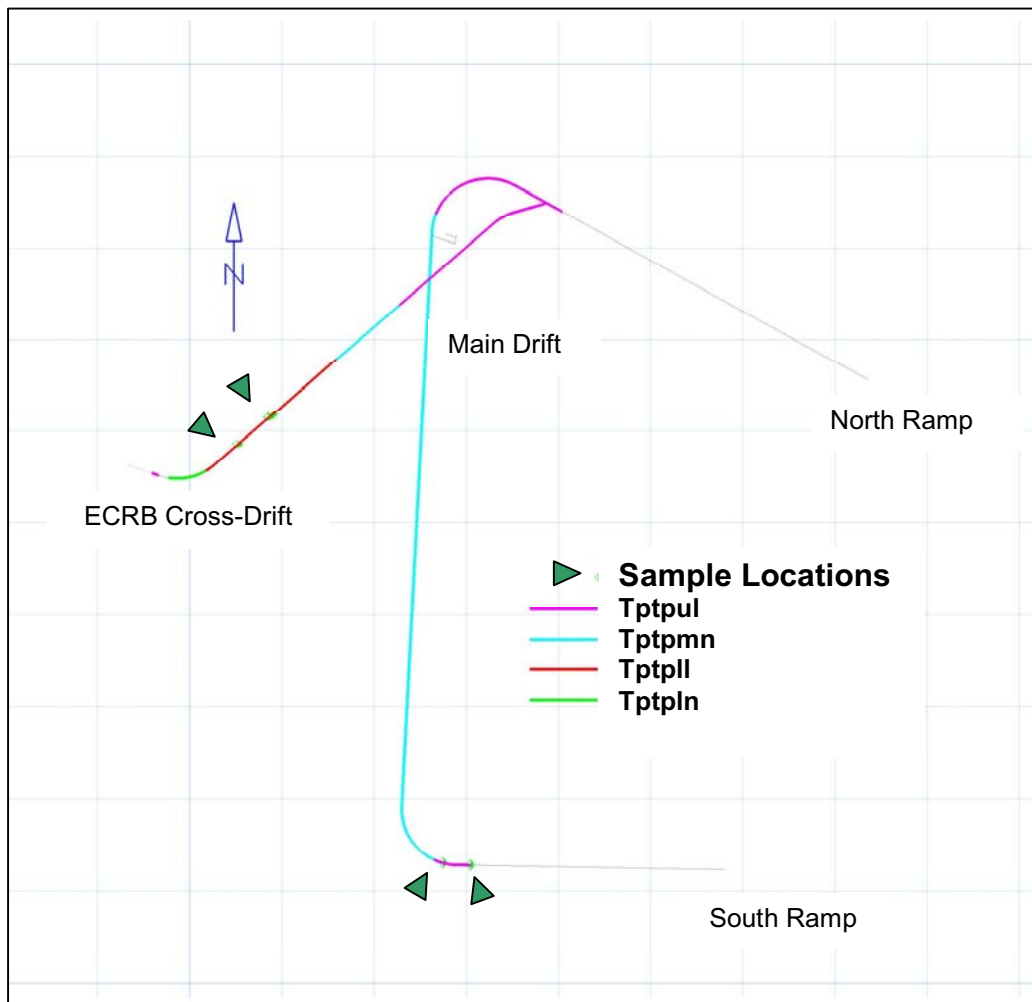
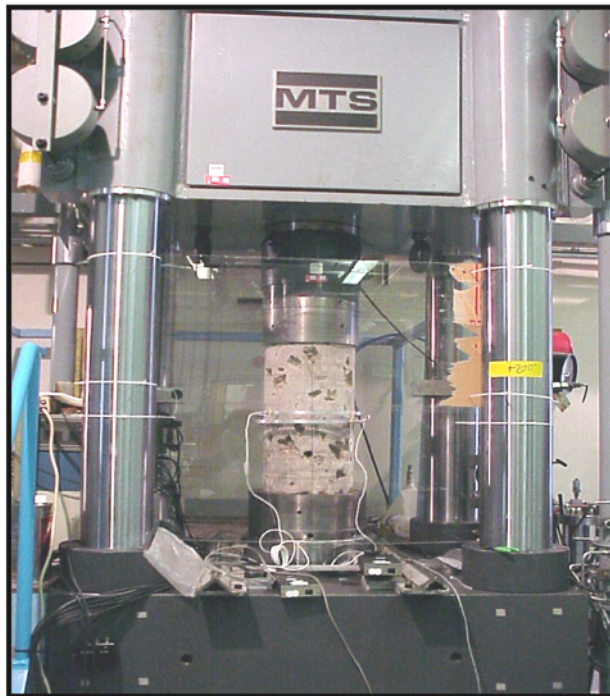


Figure E-4. Plan View of the ESF Main Loop and ECRB Cross-Drift Showing the Topopah Spring Rock Units and Location of 11.5-in Core Samples Taken in the Ttpul and Tptpll

(a)



(b)



00387DC\_012.ai

NOTE: a) from the Tptpll and Ttpul; b) a sample in unconfined compression.

Figure E-5. Photographs of Large Lithophysal Core Samples (290-mm/11.5-in. Diameter)

A program of laboratory compression testing to examine the matrix properties of the Tptpll (and comparison to previous testing in the Ttpmn) was undertaken as well. A large boulder from the lower portion of the Tptpll, containing few lithophysae, was collected and cut into samples of varying size (see Section E4.1.4.3). These samples were used for size effect and anisotropy examination in the Tptpll matrix material.



A primary source document that compiles the testing data on Topopah Spring tuff is the *Subsurface Geotechnical Parameters Report* (BSC 2003 [DIRS 166660]). Some of the specific data sources used here on lithophysal rock include:

- Uniaxial compression and Brazilian tensile strength tests on 2-in (50 mm) cores from North Ramp geotechnical boreholes (DTNs: SNL02030193001.004 [DIRS 108415]; SNL02030193001.019 [DIRS 108431]; SNL02030193001.020 [DIRS 108432])
- Uniaxial compression tests on 10.5-in (267-mm) diameter core samples of Tptpul from Busted Butte (Price et al. 1985 [DIRS 106602]) (DTN: MO0311RCKPRPCS.003 [DIRS 166073])
- Uniaxial compression tests on 11.5-in (290 mm) and 5.7-in. (146 mm) diameter core samples from the Tptpul and Tptpll drilled from exposures in the ESF main loop and ECRB Cross-Drift (Table E-9) (DTNs: SN0208L0207502.001 [DIRS 161871]; SN0211L0207502.002 [DIRS 161872]; SN0302L0207502.003 [DIRS 165014]; SN0305L0207502.004 [DIRS 165013])
- Uniaxial compression tests on 1, 2, 3.2 and 4.7-in (26, 51, 82, and 121 mm) diameter samples of the Tptpll from a Busted Butte outcrop boulder (DTN: SN0306L0207502.008 [DIRS 165015])
- Uniaxial compression experiments on wire-sawed samples (8-in square [200 mm] parallelepipeds) from a non-lithophysal boulder of Tptpll obtained from Busted Butte (DTN: SN0306L0207502.008 [DIRS 165015]).

#### **E4.1.3.2 Large Core Test Results and Analysis of Data**

The results of compression testing on 11.5-in. samples from the Tptpul and Tptpll from the ESF main loop and ECRB Cross-Drift (described above) and 10.5-in. samples from the Tptpul at Busted Butte form the basis for the development of mechanical property ranges. The data from these tests are provided in Table E-9.

Unconfined compression strength and Young's modulus as functions of approximate lithophysal porosity for the 10.5 and 11.5-in. samples of the Tptpll and Tptpul are shown in Figure E-6. Although significant scatter exists in the data, a best-fit exponential function has been superimposed on the data for room dry and saturated sample conditions. The data shows little average impact of saturation level on Young's Modulus, but results in a general reduction in unconfined compressive strength (UCS) as would be expected. Histograms of the distribution of UCS and Young's Modulus, given in Figure E-7, show a mean strength of 18.0 MPa and a mean modulus of 12.3 GPa for the samples.

It is useful to define the relationship of the UCS and Young's Modulus in a fashion that is independent of the lithophysal porosity. The UCS and Young's Modulus are the primary mechanical input properties, and representing their interrelationship on a single diagram allows one to more easily develop a base set of input properties that will define the pairing of these parameters across the entire range of potential in situ porosity conditions. Each of the mechanical properties pairs (UCS and Young's Modulus) can be related to an approximate

lithophysal porosity range, which can, in turn, be related to field mapping in the ESF main loop and ECRB Cross-Drift.

Table E-9. Mechanical Properties of Lithophysal Tuff from Large-Diameter Samples

Test ID	Lithostratigraphic Unit	L:D Ratio <sup>a</sup>	Saturation	Temperature (°C)	Ultimate Strength (MPa)	Young's Modulus (GPa)	Poisson's Ratio	Estimated Lithophysal Porosity <sup>c</sup>	DTN <sup>b</sup>
YMPLL49A	Tptpll	1.1 : 1	Dry	195	32.2	7.1	—	11.7	SN0211L0207502.002 [DIRS 161872]
YMPLL43A	Tptpll	1.1 : 1	Dry	200	31.1	6.5	—	20.3	SN0211L0207502.002 [DIRS 161872]
YMPLL23A	Tptpll	1.8 : 1	Room Dry	24	28.7	9.2	—	19.2	SN0211L0207502.002 [DIRS 161872]
YMPLL24A	Tptpll	1.8 : 1	Room Dry	24	13.3	5.0	—	22.2	SN0211L0207502.002 [DIRS 161872]
YMPLL46A	Tptpll	1.8 : 1	Room Dry	24	21.7	8.5	—	28.4	SN0211L0207502.002 [DIRS 161872]
YMPLL87A	Tptpll	1.9 : 1	Saturated	24	15.7	5.3	—	14.5	SN0211L0207502.002 [DIRS 161872]
YMPUL59B	Tptpul	1.2 : 1	Dry	190	19.6	7.3	—	39.4	SN0208L0207502.001 [DIRS 161871]
YMPUL67A	Tptpul	1.3 : 1	Dry	190	34.8	9.9	—	6.2	SN0208L0207502.001 [DIRS 161871]
YMPUL62B	Tptpul	1.0 : 1	Dry	200	37.0	13.7	—	19.3	SN0208L0207502.001 [DIRS 161871]
YMPUL50A	Tptpul	1.5 : 1	Room Dry	24	22.1	14.9	0.21	28.5	SN0211L0207502.002 [DIRS 161872]
YMPUL59A	Tptpul	2.0 : 1	Room Dry	24	13.5	5.8	0.39	30.3	SN0208L0207502.001 [DIRS 161871]
YMPUL61A	Tptpul	1.9 : 1	Room Dry	24	17.7	8.8	—	23.9	SN0208L0207502.001 [DIRS 161871]
YMPUL62A	Tptpul	1.8 : 1	Room Dry	24	25.9	13.7	—	12.7	SN0208L0207502.001 [DIRS 161871]
YMPUL64A	Tptpul	1.7 : 1	Room Dry	24	33.5	20.5	—	12.8	SN0208L0207502.001 [DIRS 161871]
YMPUL65A	Tptpul	2.0 : 1	Room Dry	24	26.2	19.5	—	11.9	SN0208L0207502.001 [DIRS 161871]
YMPUL66A	Tptpul	1.7 : 1	Room Dry	24	16.5	12.4	—	16.7	SN0208L0207502.001 [DIRS 161871]
YMPUL60A	Tptpul	1.8 : 1	Saturated	24	12.7	6.7	—	18.6	SN0208L0207502.001 [DIRS 161871]
YMPUL63A	Tptpul	1.9 : 1	Saturated	24	9.4	5.0	0.24	20.0	SN0208L0207502.001 [DIRS 161871]

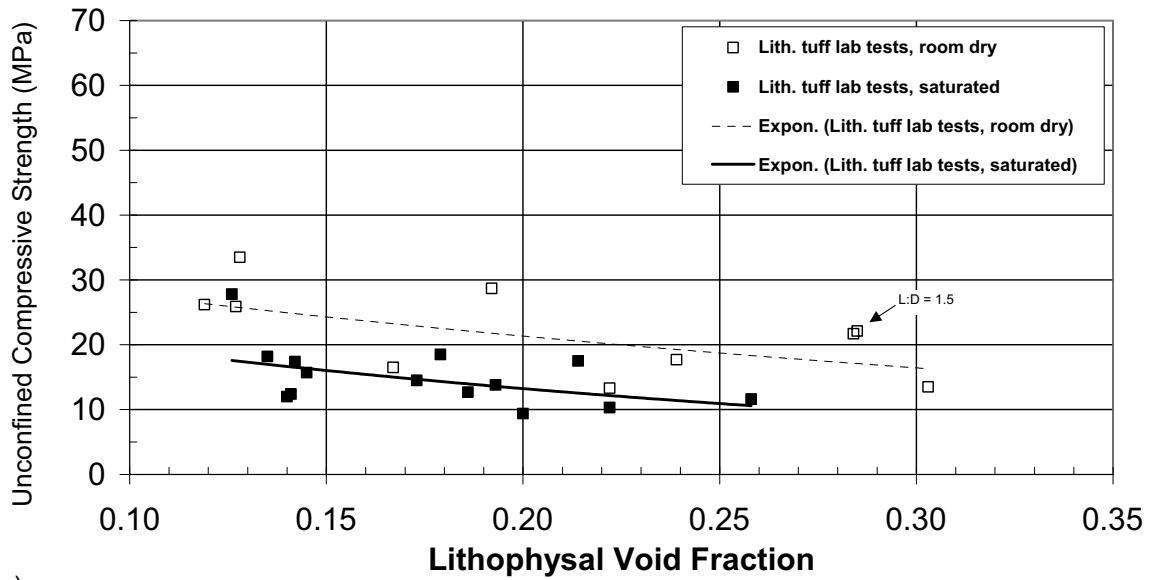
Table E-9. Mechanical Properties of Lithophysal Tuff from Large-Diameter Samples (Continued)

Test ID	Lithostratigraphic Unit	L:D Ratio <sup>a</sup>	Saturation	Temperature (°C)	Ultimate Strength (MPa)	Young's Modulus (GPa)	Poisson's Ratio	Estimated Lithophysal Porosity <sup>c</sup>	DTN <sup>b</sup>
YMPUL68A	Ttpul	2.1 : 1	Saturated	24	11.6	5.9	0.03	25.8	SN0208L0207502.001 [DIRS 161871]
1B	Ttpul	2.0 : 1	Saturated	22	14.5	14.2	—	17.3	MO0311RCKPRPCS.003 [DIRS 166073]
1D	Ttpul	2.0 : 1	Saturated	22	10.3	10.9	—	22.2	MO0311RCKPRPCS.003 [DIRS 166073]
2A	Ttpul	2.0 : 1	Saturated	22	12.4	11.9	—	14.1	MO0311RCKPRPCS.003 [DIRS 166073]
3A	Ttpul	2.0 : 1	Saturated	22	12.0	12.9	—	14.0	MO0311RCKPRPCS.003 [DIRS 166073]
8A	Ttpul	2.0 : 1	Saturated	22	18.2	16.6	—	13.5	MO0311RCKPRPCS.003 [DIRS 166073]
8B	Ttpul	2.0 : 1	Saturated	22	17.4	16.8	—	14.2	MO0311RCKPRPCS.003 [DIRS 166073]
8C	Ttpul	2.0 : 1	Saturated	22	18.5	15.8	—	17.9	MO0311RCKPRPCS.003 [DIRS 166073]
8D	Ttpul	2.0 : 1	Saturated	22	17.5	18.3	—	21.4	MO0311RCKPRPCS.003 [DIRS 166073]
8E	Ttpul	2.0 : 1	Saturated	22	13.8	15.8	—	19.3	MO0311RCKPRPCS.003 [DIRS 166073]
8F	Ttpul	2.0 : 1	Saturated	22	27.8	21.5	—	12.6	MO0311RCKPRPCS.003 [DIRS 166073]

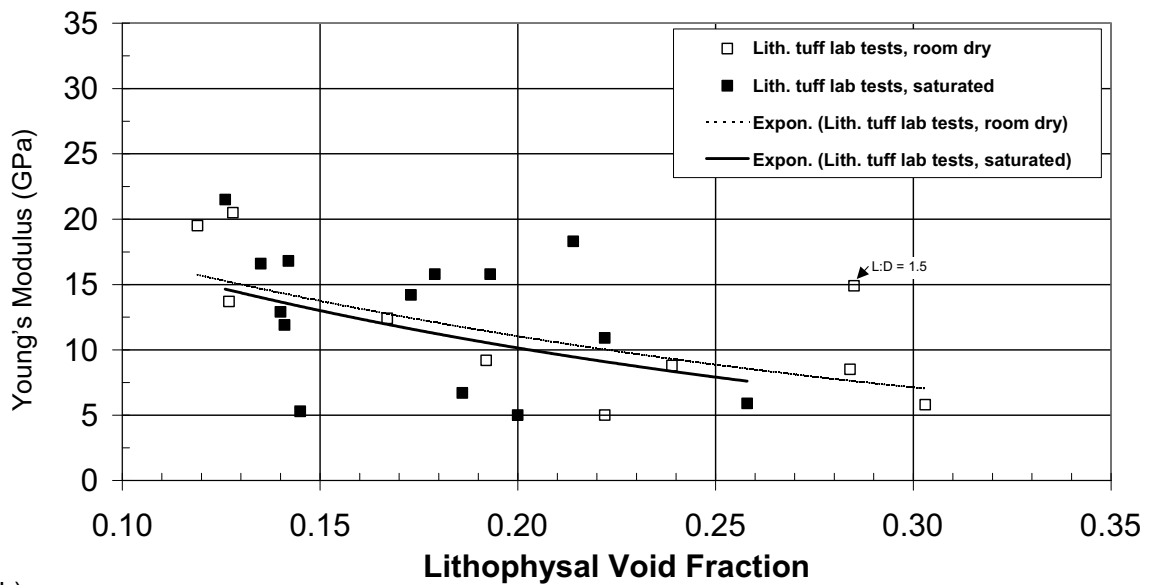
<sup>a</sup> Specimen length-to-diameter ratio.

<sup>b</sup> Specific data are located in rows 737 to 746 from DTN: MO0311RCKPRPCS.003 [DIRS 166073]. Additional test descriptions for the data in DTN: MO0311RCKPRPCS.003 [DIRS 166073] are provided by Price et al. (1985 [DIRS 106602]).

<sup>c</sup> Lithophysal porosity data for tests documented in DTNs SN0208L0207502.001 [DIRS 161871] and SN0211L0207502.002 [DIRS 161872] are provided by DTN: SN0305L0207502.005 [DIRS 163373]. Lithophysal property data for tests documented in DTN: MO0311RCKPRPCS.003 [DIRS 166073] are provided by Price et al. (1985 [DIRS 106602], Table 4).



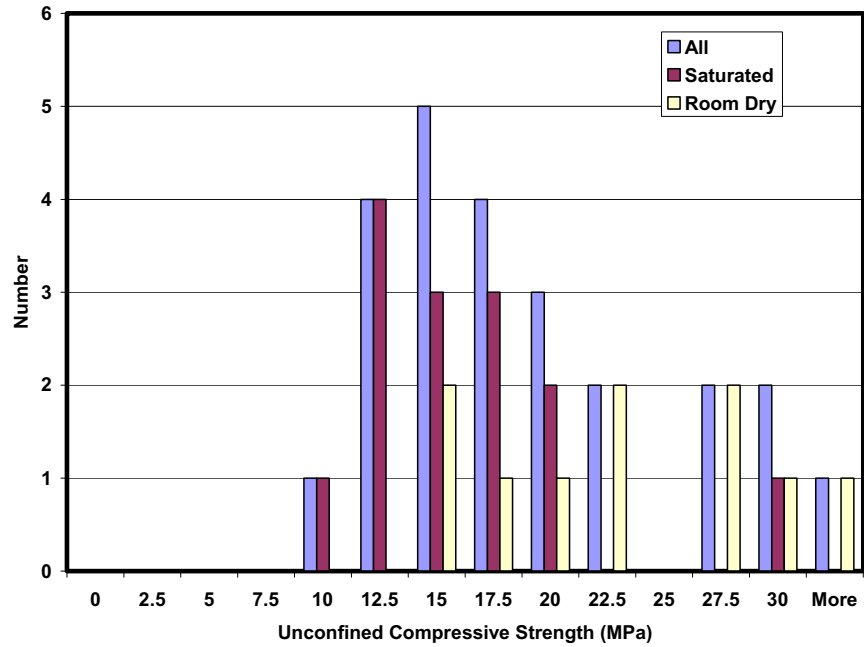
(a)



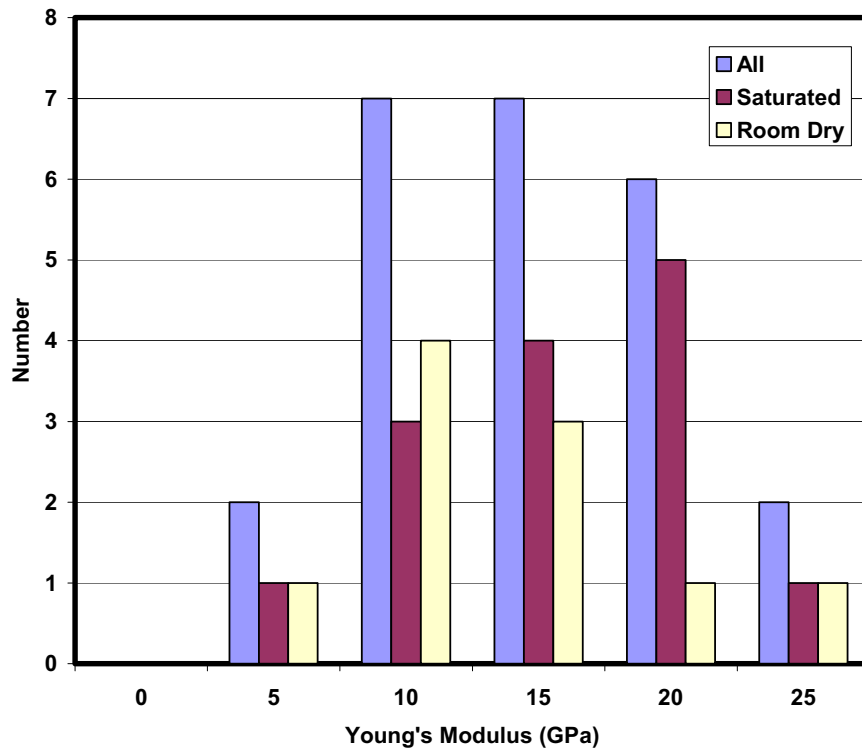
(b)

NOTE: (a) Unconfined Compressive Strength; (b) Young's Modulus as a Function of the Lithophysal Void Fraction and Saturation Level for 10.5-in. and 11.5-in.

Figure E-6. Variation in Diameter Cores from the Ttpul and TtpII



(a)



(b)

NOTE: (a) Unconfined Compressive Strength; (b) Young's Modulus for the 10.5-in. and 11.5-in.

Figure E-7. Histograms of Diameter Core Samples of Lithophysal Tuff

The UCS and modulus data for each large core test, presented in Figure E-6, is plotted in the form of UCS versus Young's modulus in Figure E-8. The data shows that a reasonably linear relationship exists between these mechanical properties. The large core data has been subdivided into two sets — the 11.5-in. data (room-dry and saturated) collected in 2002 and the 10.5-in. saturated samples from Busted Butte — and linear relations fit to each set. As seen in this plot, the saturated samples tend to form a lower bound to the room dry strengths.

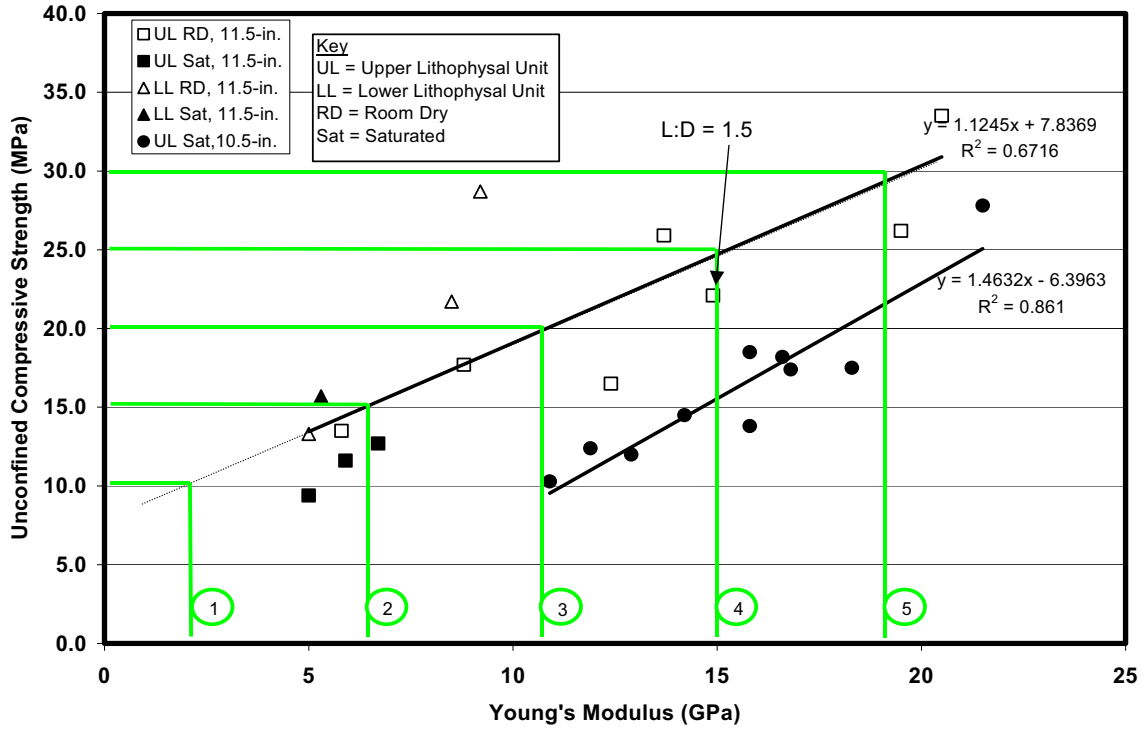
A parametric bounding analysis approach is developed initially in which the base case set of the 11.5-in. values of UCS and Young's modulus are defined from the linear fit to the data as shown in Figure E-8. The entire range of UCS is subdivided into a series of five evenly-distributed rock mass strength "categories" that reflect the approximate range of lithophysal porosity as observed in the field mapping (Table E-10 and Figure E-9). The categories encompass the range in UCS values from 10 MPa (lowest) to 30 MPa (highest). The modulus corresponding to each strength value is determined from the linear fit of the 11.5-in. data as shown. The initial or base case analysis of emplacement drift stability in lithophysal rock, as discussed in Section 6.4 of this document, use these rock strength categories and the consideration of a homogeneous rock mass for the parametric analyses. As discussed later, analyses are presented in which the impact of estimated in situ lithophysal porosity spatial variability on rock mass properties and drift stability is examined. The results are used to verify the conservative nature of the homogeneous rock mass consideration and the bounding calculation approach.

An estimate of the overall distribution of these rock mass strength categories within the Tptpll can be obtained from the lithophysal porosity mapping studies conducted in the ECRB Cross-Drift (see Appendix O, Figure O-15). The histogram given in Figure E-10 shows the abundance (frequency) and cumulative frequency distributions of lithophysal porosity, averaged over 5 m intervals in the ECRB Cross-Drift from stations 14+44 to 23+26 (essentially the top to bottom of the Tptpll). This plot subdivides the abundance of lithophysal porosity into 5-percent intervals that roughly correspond to those lithophysal porosity ranges for the various rock mass categories given in Table E-10. It is seen that the most abundant rock mass lithophysal porosity ranges found in situ are 10 to 20 percent, or corresponding roughly to rock mass strength Categories 3 and 4. Observations in the range of 10 to 15 percent lithophysal porosity are most common, and correspond to the Category 4 range. Observations of lithophysal porosity above 20 percent (Categories 1 and 2) are uncommon, representing about 10 percent of the entire Tptpll. Observations of lithophysal porosities greater than 20 percent are most common near the top of the Tptpll, around stations 15+50 to 16+00 (Figure 6-12).

Using the calculated Young's modulus values in Table E-10, corresponding values of bulk modulus,  $K$ , and shear modulus,  $G$ , were calculated according to Equations E-2 and E-3. A Poisson's ratio value of 0.2 was used for these calculations, which is based on both the laboratory test data (Table E-9) and data from the in situ slot tests (DTNs: SN0208F4102102.002 [DIRS 161874]; SN0212F4102102.004 [DIRS 161875]; SN0301F4102102.006 [DIRS 161876]). Cohesion (Table E-10) was calculated for a range of

friction angles using Equations E-6 and E-7, such that

$$C = \frac{0.5 \cdot \sigma_c}{\tan\left(\frac{\phi}{2} + 45^\circ\right)} \quad (\text{Eq. E-8})$$



NOTE: Source DTNs are provided in Table E-9. The 11.5-in. room-dry sample data has been subdivided into a series of categories for base-case calculations.

Figure E-8. Relationship of Unconfined Compressive Strength to Young's Modulus for Room-Dry and Saturated 10.5-in. and 11.5-in. Core Samples from the Ttpul and Ttpil

Table E-10. Suggested Range of Mechanical Properties Developed from 11.5-in. Core Testing, Selected for Base-Case Design and Performance Analyses

Rock Mass Category	Unconfined Compressive Strength (MPa)	Estimated Young's Modulus <sup>a</sup> (GPa)	Cohesion <sup>c</sup> (MPa)			Bulk Modulus <sup>c</sup> , K (GPa)	Shear Modulus <sup>c</sup> , G (GPa)	Approximate Lithophysal Porosity From Laboratory Tests <sup>b</sup> (%)
			$\phi=50$	$\phi=45$	$\phi=40$			
1	10	1.9	1.82	2.07	2.33	1.07	0.80	35 ± 8
2	15	6.4	2.73	3.11	3.50	3.54	2.65	28 ± 6
3	20	10.8	3.64	4.14	4.66	6.01	4.51	21 ± 4
4	25	15.3	4.55	5.18	5.83	8.48	6.36	13 ± 5
5	30	19.7	5.46	6.21	7.00	10.95	8.21	7 ± 7

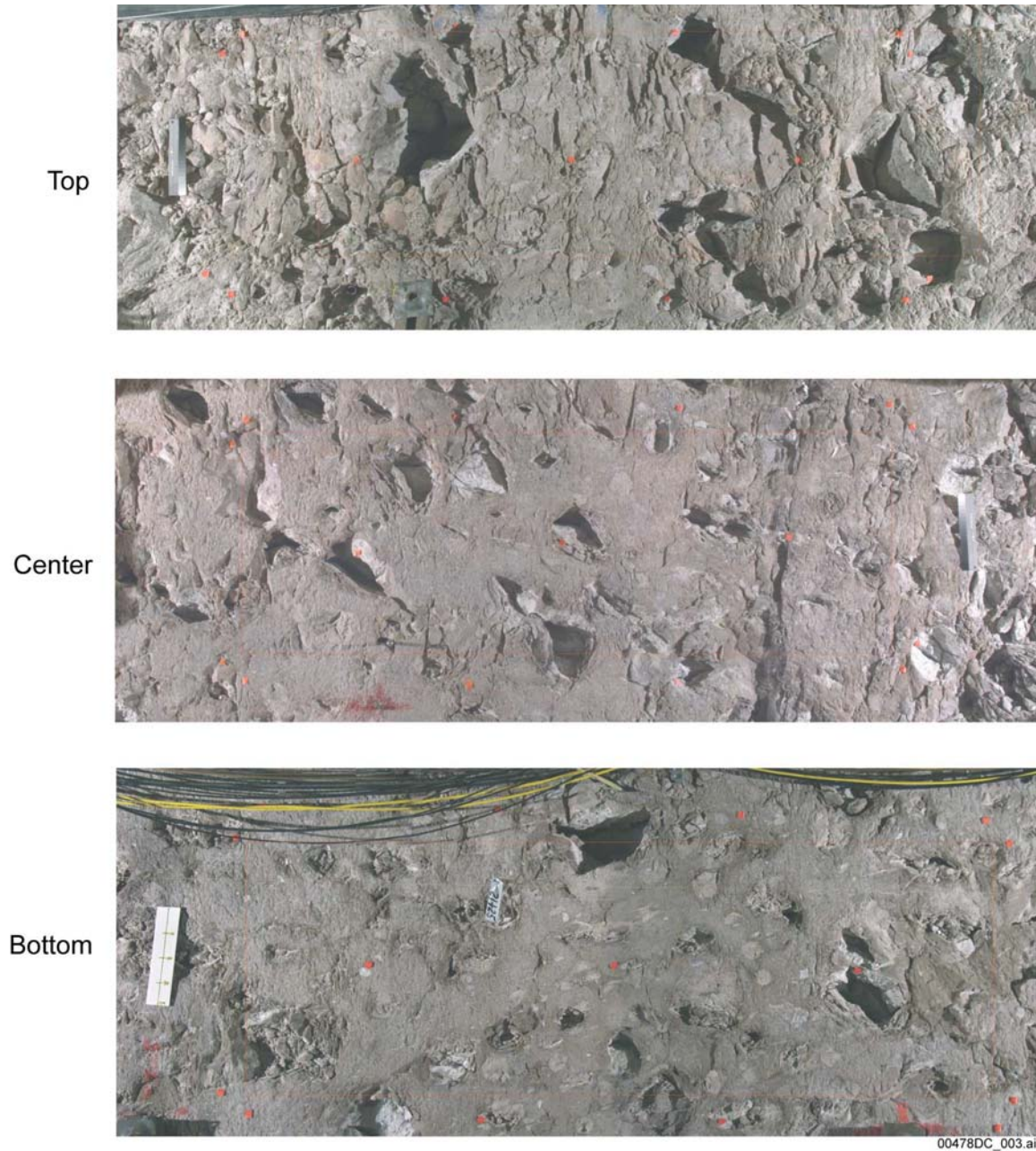
Source: DTNs provided in Table E-9.

<sup>a</sup> Young's Modulus estimated from linear fit to 11.5-in. core data given in Figure E-8.

<sup>b</sup> Approximated lithophysal porosity and ranges are from BSC 2004 [DIRS 168970], Table 6.6-1.

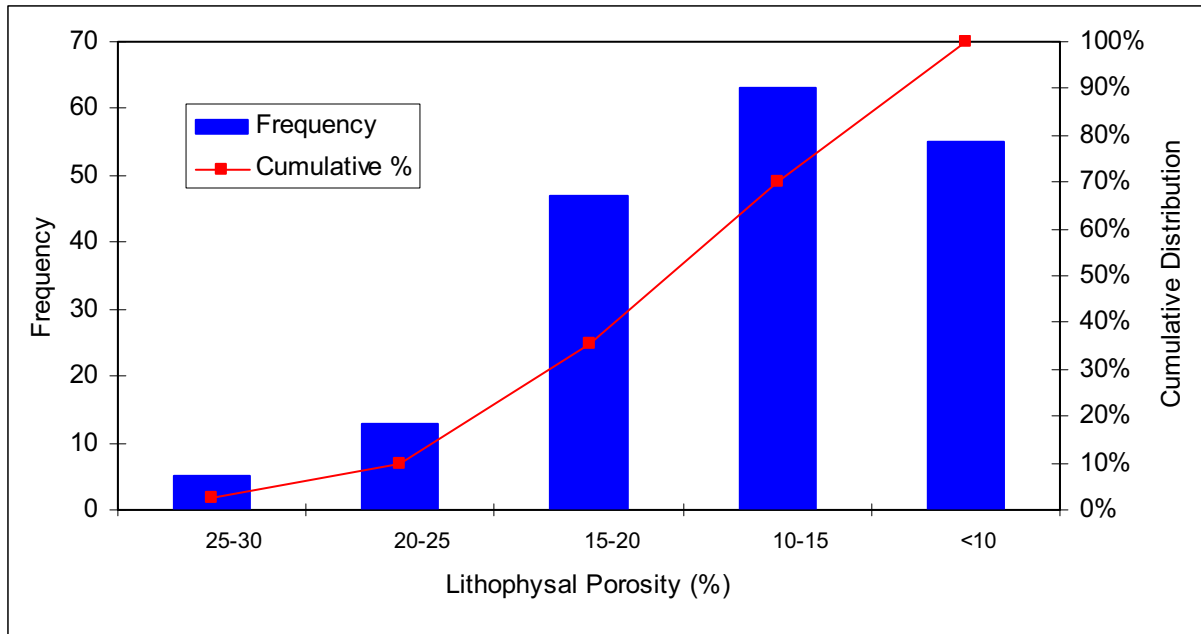
<sup>c</sup> Cohesion is calculated using Equation E-8. Bulk and shear modulus values are calculated based on Equations E-2 and E-3.





NOTE: Section 16+41 (top), Section 14+93 (center) and Section 21+24 (bottom). (see Appendix O): Category 3 (Top) With Lithophysal Porosity of Approximately 19 Percent, Category 4 (Center) With Lithophysal Porosity of 13.3 Percent, and Category 5 (Bottom) With Lithophysal Porosity of 8.5 Percent.

Figure E-9. Examples of Approximate Rock Strength Category Levels Taken from 1x3-m Panel Maps



NOTE: Lithophysal porosity data are from ECRB Cross-Drift station 14+44 to 23+26 (Appendix O, Section O6.6; see Microsoft Excel file, *Drift Deg AMR AF T-A-P Fit.xls*, worksheet "Volume Percent - Stats", which can be accessed through the TDMS using DTN: MO0408MWDDDMIO.002).

Figure E-10. Distribution of Lithophysal Porosity Abundance (Frequency) for the Tptpl in the Enhanced Characterization of the Repository Block Cross-Drift

#### E4.1.4 Investigation of Impact of Lithophysal Variability on Rock Mass Properties

The Tptpl rock mass is characterized by lithophysal porosity that varies with position in the rock mass. The Topopah Spring unit was laid down rapidly in thin, but laterally-extensive sheets. The formation of lithophysae, which is a phenomenon resulting from movement of vapor within the rock mass during the cooling process, results in a similar layering effect of lithophysal porosity. The mapping presented in Appendix O and analysis of spatial variability presented in Appendix T shows that the lithophysal porosity occurs in thin, laterally-extensive sheets with variability occurring primarily within the plane perpendicular to dip of the units. The approach to assessment of drift stability described in Section 6.4.2 uses parametric analyses based on the consideration of a homogenous rock mass characterized by constant rock properties. To represent the inherent variability of the rock mass, a series of discrete constant property levels, linked to lithophysal porosity, are used to represent (approximately) the lowest, highest and median in situ conditions. The likelihood of occurrence of these particular conditions is based on the percentage of a given strength category to exist in the Tptpl. This simplistic approach (as opposed to attempting to model spatial variability directly) was taken to facilitate modeling.

The rock mass porosity is, in reality, spatially-variable over a relatively small length scale (on the order of meters – see Appendix O). Therefore, the rock mass rarely consists of uniformly weak or strong material, but consists of small regions of varying strength and modulus. Appendix T presents a model that produces a synthetic representation of the spatial variability of the lithophysal porosity in the Tptpl, based on field mapping as described in Appendix O. Therefore, the consideration of a homogenous rock mass will tend to over predict the failure

potential of drifts in the weakest rock mass classifications and will under predict the yield in the highest rock mass classifications. The impact of actual lithophysae geometry and spatial variability on the rock mass properties and the relation to conservatism in the strength category bounding methodology is discussed below.

#### **E4.1.4.1 Effect of Variability of Lithophysal Porosity, Size and Shape on Mechanical Properties – Estimation of Upper and Lower Bounds for Lithophysal Mechanical Properties**

The large core laboratory testing is a relatively small sampling of the lithophysae conditions that exist in the field, although the approximate porosities of the cores encompass the range of most field-measured conditions. To extend the laboratory data base to account for the in situ variability in lithophysal porosity (i.e., shape, size, and distribution) a numerical study was conducted using the calibrated Particle Flow Code (PFC) model. The basic calibration and validation of the PFC model is described in Section 7.5 of this document. In this calibration, lithophysae were represented in simulated tuff samples as circular holes that were randomly distributed to produce a given porosity. It was shown that the numerical model was able to reasonably account for the failure mechanisms of lithophysal and nonlithophysal rock specimens as observed in the laboratory, and could reproduce the general effect of lithophysal porosity on UCS and Young's Modulus.

The same calibrated model is used here to conduct a “shape study” in which the impacts of lithophysal porosity, shape, size and distribution on rock property variability were examined.<sup>2</sup> In this study, simulated samples of the lithophysal rock mass were developed directly from field panel map lithophysae distributions (Appendix O) by overlaying (stenciling) the panel map directly onto the PFC model to create the void geometry. Figure E-11 shows an example of the result of simulated UCS tests on two “samples” of PFC models with stenciled lithophysae distributions. The figures show the tensile cracking between lithophysae at failure, and the impact of the specific distribution on failure mechanism and the associated stress-strain behavior.

Approximately 80 simulated unconfined compression cases of actual lithophysae distributions were modeled, and the results in terms of UCS and Young's Modulus as functions of the lithophysal porosity given in Figure E-12. The results are compared to the 11.5-in. laboratory test data as well as the previous PFC modeling using idealized circular lithophysae. The introduction of actual lithophysae shapes and distributions has two distinct effects with regard to the use of circular voids.

- The actual lithophysae shapes and distributions introduce significant variability into the strength or modulus for a given porosity. This variability is a function of the distribution of solid bridge length between lithophysae, which are, in turn, a function of the porosity and nature of the distribution of that porosity.
- The actual lithophysae shapes and distributions provide a lower bound to the strength and modulus to that given by the circular lithophysae shapes and to the laboratory data.

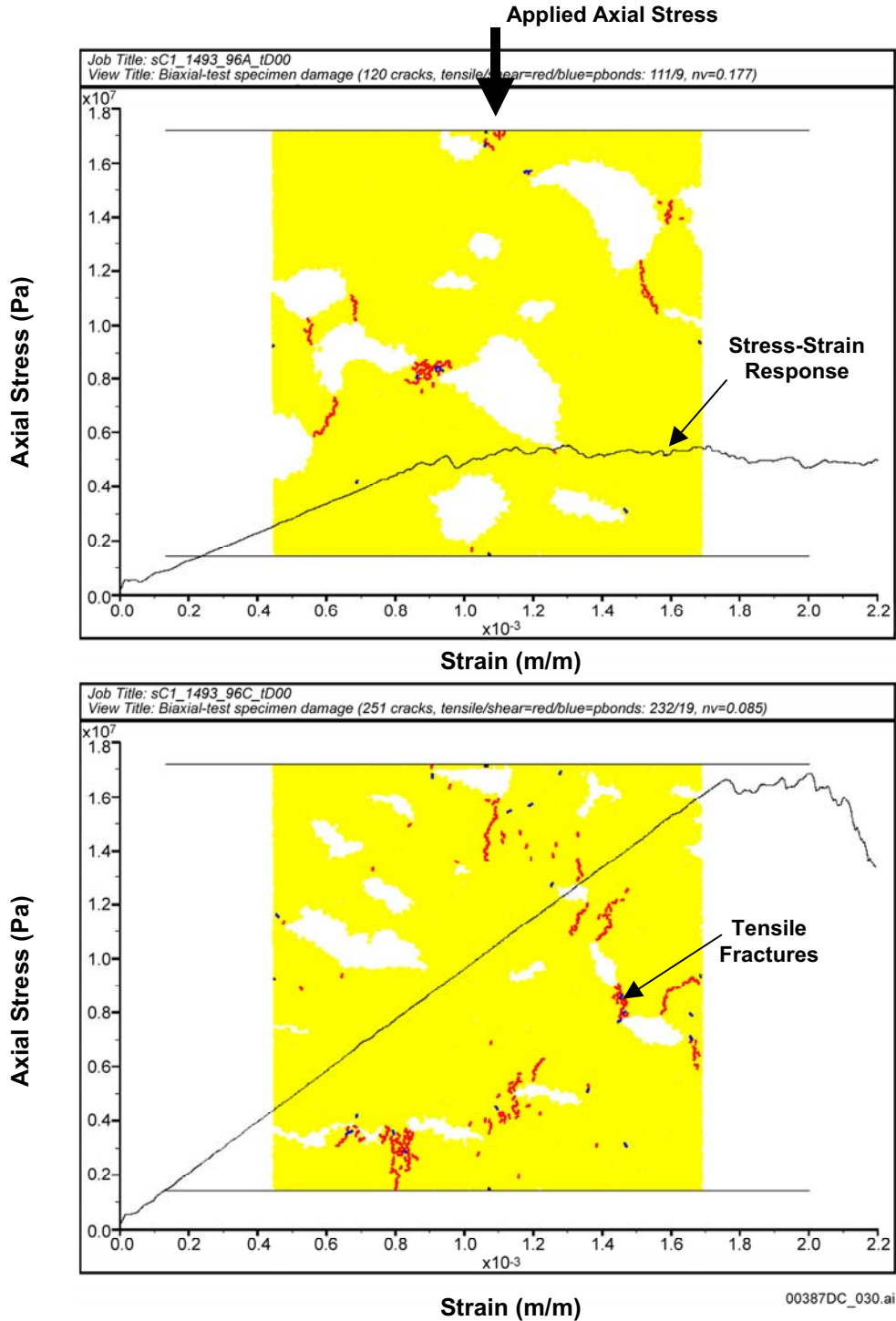
---

<sup>2</sup>This study is documented in detail in the *Subsurface Geotechnical Parameters Report* (BSC 2003 [DIRS 166660], Section 9.1).

The PFC shape study extrapolations are superimposed on the previous figure (Figure E-8) of UCS vs. Young's Modulus to estimate bounding values (Figure E-13). Upper and lower bounds to the data are estimated, and a mean value between these bounds shown which falls approximately along the original base case linear extrapolation for the 11.5-in. test results. The portion of the bounding curves that fall outside (below) the laboratory measurement range is dashed indicating that this extrapolation is not based on measurements. The base case rock mass property categories are shown in Figure E-13, illustrating the estimated upper and lower bounding values of UCS associated with each value of Young's Modulus.

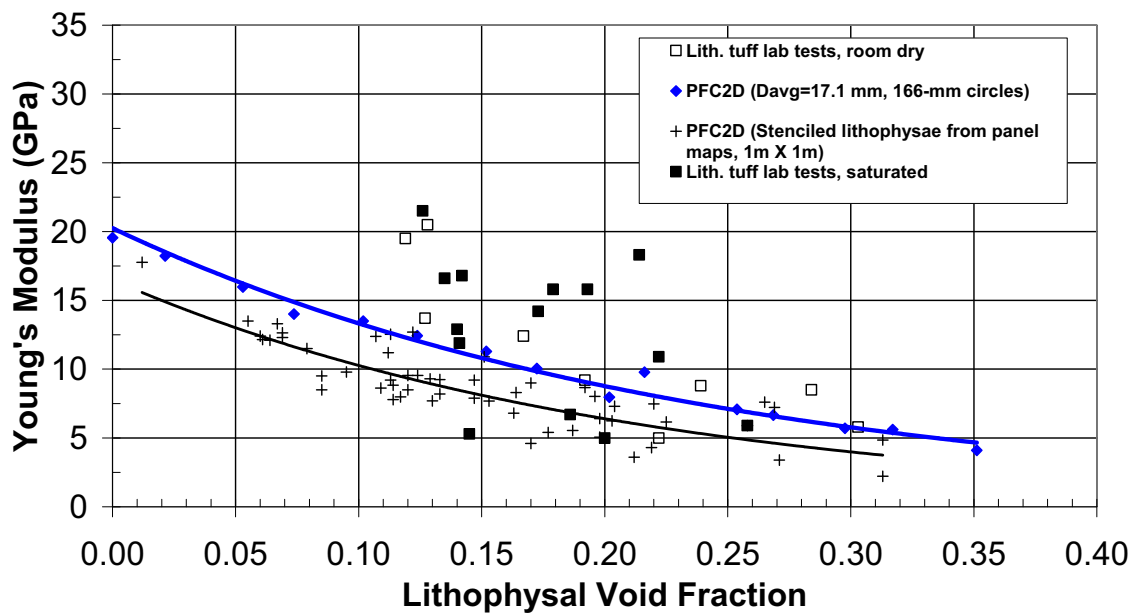
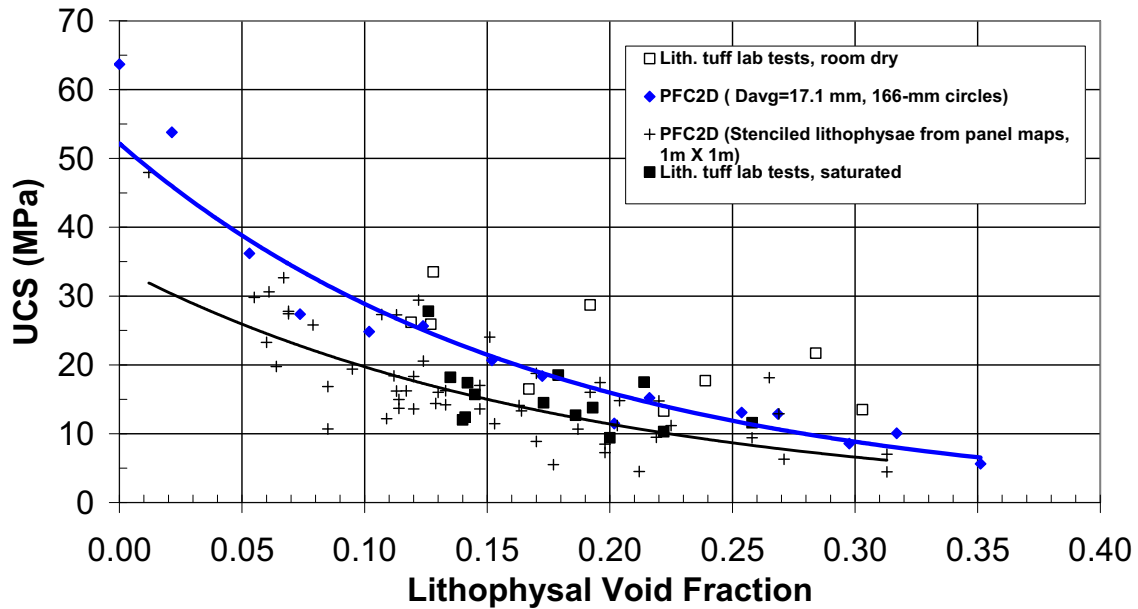
The impact of the bounding values on yield and performance are discussed in Section 6.4. In these studies, the rock mass was considered to be homogeneous with constant rock mass mechanical properties consisting of the lower bound of strength at the respective values of Young's Modulus (i.e., the intersection of the vertical category bar and the lower bound line in Figure E-13). The analyses involved examine stability of the emplacement drifts under in situ and thermal loading for the lower bound values for the categories. This modeling showed that UCS values less than approximately 10 MPa (i.e., the lower bound of Categories 1 and 2) result in predicted extensive sidewall failure of emplacement tunnels under in situ stresses only (Figure E-14). This is obviously not observed in the ECRB Cross-Drift or ESF main loop where tunnels are in stable and excellent condition with minimal ground support in the crown and generally no ground support in the sidewalls. The laboratory database shows that minimum UCS values, even for lithophysal porosities in excess of 30 percent, are approximately 10 MPa.

An explanation of why the rock mass UCS may have a lower bound of approximately 10 MPa is the inherent spatial variability of lithophysal porosity, and thus local variability in rock mass mechanical properties. The consideration of a homogeneous, high porosity rock mass, as used in the Category 1 and 2 cases, is conservative since spatial variability of porosity will result in a higher rock mass strength.



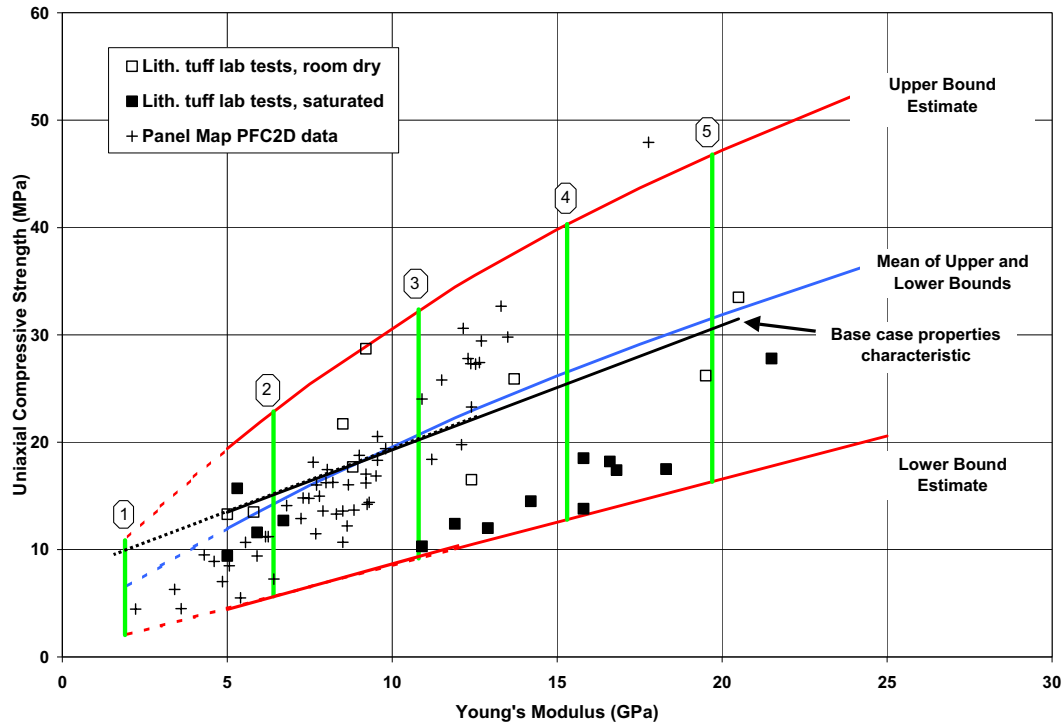
NOTE: Specimen is composed of several thousand bonded particles. Red lines are tensile fractures that have propagated between lithophysae to ultimately form a failure mechanism. Superimposed stress-strain curve illustrates impact of lithophysae distribution on strength, modulus and post-peak failure mechanism. Vertical axis is axial stress in Pa; horizontal axis is strain in m/m.

Figure E-11. Examples of Particle Flow Code Compression Tests Using Simulated Rock Specimens Developed by “Stenciling” Field Panel Maps in the Enhanced Characterization of the Repository Block



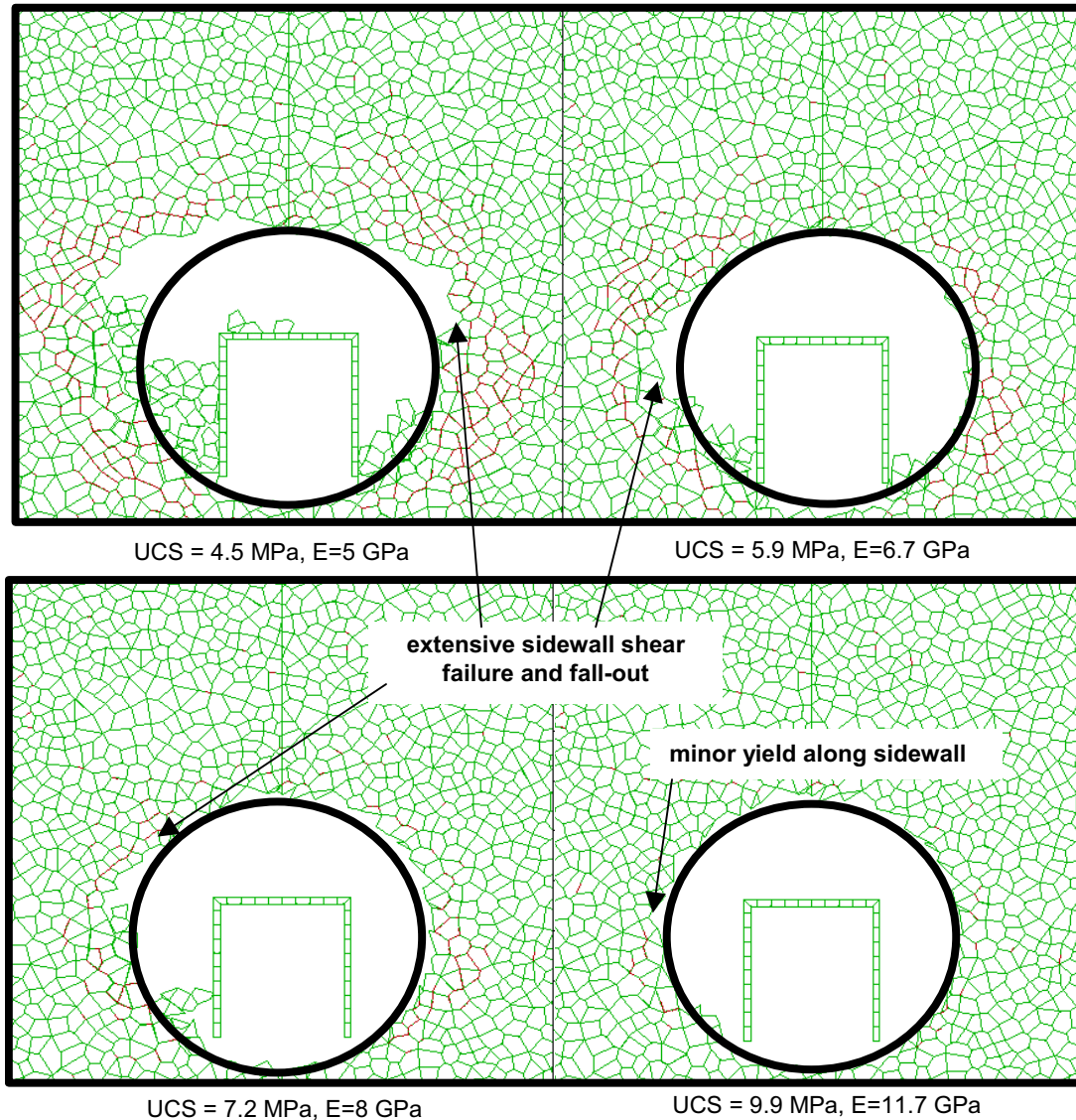
NOTE: Test data from large-core lithophysal tests -Table E-9.

Figure E-12. Plots Showing Data from Large Core Compression Testing of Tptpul and Tptpll Compared to Particle Flow Code Simulations Using Circular and Triangular Shaped Lithophysae as Well as Actual "Stenciled" Shapes from Enhanced Characterization of the Repository Block Panel Maps



NOTE: Approximate upper and lower bounds are shown.

Figure E-13. Unconfined Compressive Strength Versus Young's Modulus Showing Large Core Data and Results from PFC Panel Map Lithophysae Shape Study



NOTE: Drift exhibits extensive sidewall failure under in situ load only for UCS values less than approximately 10 MPa. This behavior is not observed in the ESF main loop or ECRB Cross-Drift and lower bound properties (UCS < approximately 10 MPa) under predict in situ strength values. See Figure E-13.

Figure E-14. Emplacement Drift Stability Analysis Under In Situ Loading for Combinations of UCS and Young's Modulus Along the Lower Bound Properties Line

#### E4.1.4.2 Investigation of Lithophysal Porosity Spatial Variability on Rock Mass Properties

To investigate the impact of spatial variability of porosity on the lower bound and mean rock mass properties, a numerical investigation was carried out using the calibrated UDEC Voronoi drift scale model<sup>1</sup>. The purpose of the analyses is to determine the rock mass stress-strain response for an inhomogeneous rock mass composed of spatially-varying lithophysal porosity,

<sup>1</sup> See Section 7.6.4 for details of UDEC model calibration methodology and Section 6.4.1 for resulting calibrated rock mass properties by strength category.

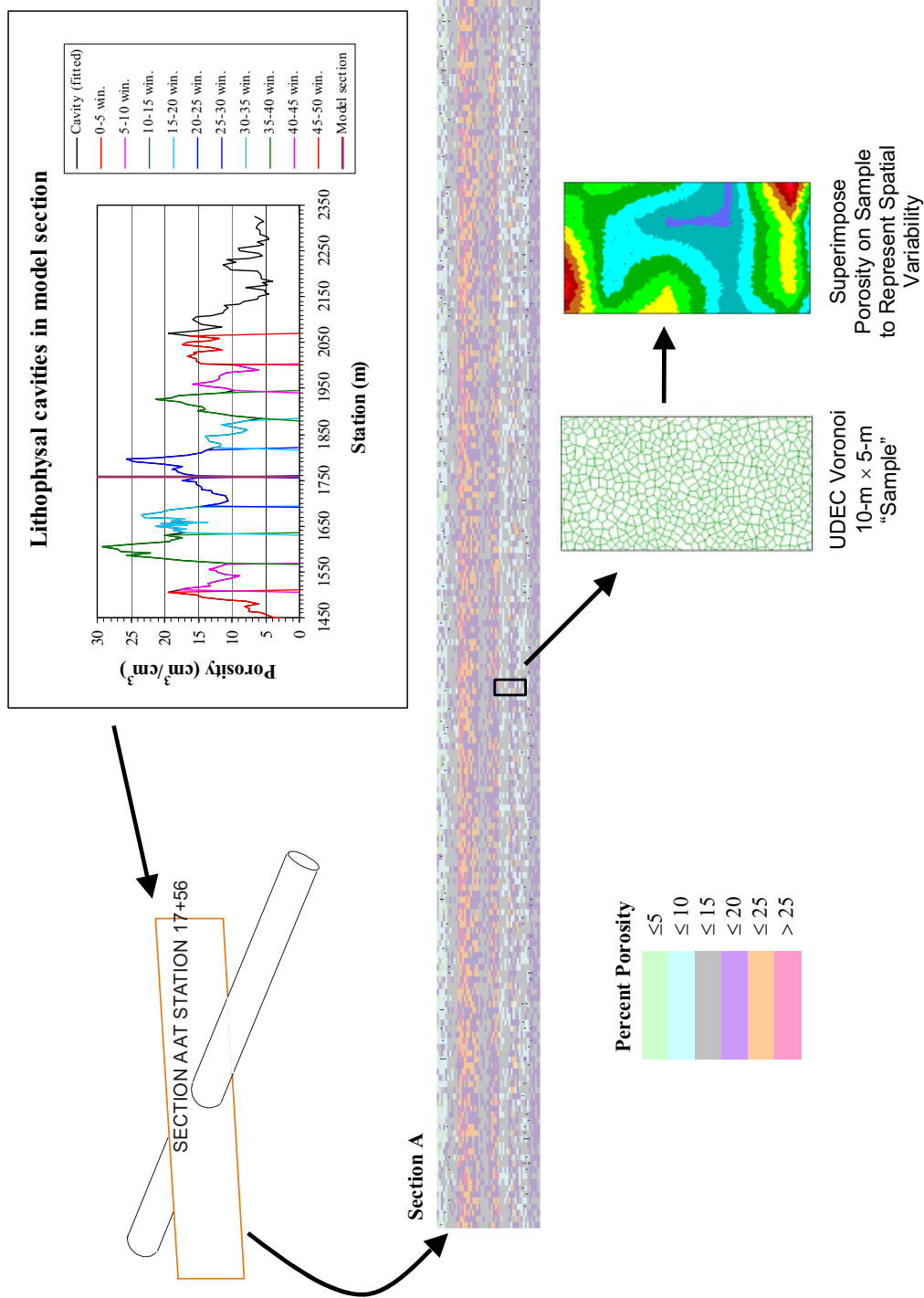


and thus spatially-varying rock mass UCS and Young's Modulus. The goal of the modeling is to conduct numerical compression tests on simulated rock mass "samples" that are sufficiently large to contain the variability of lithophysal porosity that will affect the emplacement drift scale. This requires a geometric model of the spatial variability of lithophysal porosity as a function of position within the Tptpll as well as the UDEC model.

Appendix T of this document presents a methodology for simulating the spatial variability of lithophysal porosity based on field measurements in the Tptpll in the ECRB Cross-Drift. The model is used to statistically represent lithophysal porosity in a series of 40 m long (along the axis of the ECRB Cross-Drift) by 50 m high (vertical) by 200 m wide parallelepipeds along the ECRB Cross-Drift axis from top to bottom of the Tptpll. The parallelepipeds are subdivided into a number of small (meter-scale) cubical grids within which the lithophysal porosity is estimated as a function of vertical and horizontal position. Figure T-5 (reproduced below in Figure E-15) presents examples of two vertical planes perpendicular to the drift axis centered at locations in the upper and lower portions of the Tptpll. These two planes correspond to the higher porosity zones at the top of the Tptpll and the lower porosity material near the contact with the Tptpln. Thirty rock mass "samples" measuring 10 m high by 5 m wide (drift scale) were randomly selected both vertically and horizontally within each of the parallelepipeds. Each of the porosity grids of the parallelepiped that are found within the boundaries of each of these 10 m × 5 m rock mass samples have a value of lithophysal porosity associated with them. This porosity is used to assign the associated rock mass category and, in turn, its associated UCS and modulus (and the calibrated cohesion<sup>2</sup>, friction angle and stiffness representing the strength and modulus) to the elements within that particular grid. The resulting sample thus contains spatially variable UCS and modulus that represents the in situ variability of lithophysal porosity. Figure E-15 shows an example of the geometry of one of the 10 m × 5 m UDEC "samples" composed of Voronoi blocks and the contours of the resulting lithophysal porosity captured from the simulated Tptpll parallelepipeds. The mean, maximum and minimum lithophysal porosities in each of the samples are plotted in Figure E-16, showing that the samples from the upper block, as expected, contain a greater proportion of lithophysal material with porosities in excess of 25 percent. The means of the samples show an average lithophysal porosity for the upper block of 15.3 percent and 12.8 percent for the lower block. These are consistent with the field measurements presented in Appendix O.

---

<sup>2</sup> See Table E-11 for relationship of approximate lithophysal porosity to rock mass category and Table 6-43 for calibrated rock mass Mohr-Coulomb properties for each rock mass category.



NOTE: A series of 10 m x 5 m test "sample" locations are chosen randomly in three-dimensional space. Spatial variability of porosity within the sample is overlaid onto the UDEC Voronoi test specimen and material properties associated with porosities are assigned to model elements to represent spatial variability of properties. Compression testing is performed to estimate the impact of spatial variability on UCS and Young's modulus. See Appendix T for details of the porosity model. Presented in Appendix T.

Figure E-15. Schematic Illustration of the Process of Sampling and Modeling Spatial Variability Using Lithophysical Porosity Simulation Model

UDEC simulations of compression tests were conducted for 30 samples from each of the upper and lower cross sections. For each sample, for rock mass strengths for each strength category were defined by two sets of values – the base case properties, and the lower bound rock mass properties, both illustrated in Figure E-16 and summarized in Table E-11. The upper bound values are not examined as they are irrelevant since the base case analyses of drift stability presented in Section 6.4 are conservative – higher strengths will only result in greater stability.

Table E-11. Base Case and Lower Bound Strength Values for Rock Categories Used in UDEC Analyses of Spatial Variability

Rock Mass Category	Unconfined Compressive Strength (MPa)		Estimated Young's Modulus <sup>a</sup> (GPa)	Approximate Lithophysal Porosity From Laboratory Tests <sup>b</sup> (%)
	Base Case	Lower Bound		
1	10	2.0	1.9	35 ± 8
2	15	5.6	6.4	28 ± 6
3	20	9.2	10.8	21 ± 4
4	25	12.8	15.3	13 ± 5
5	30	16.3	19.7	7 ± 7

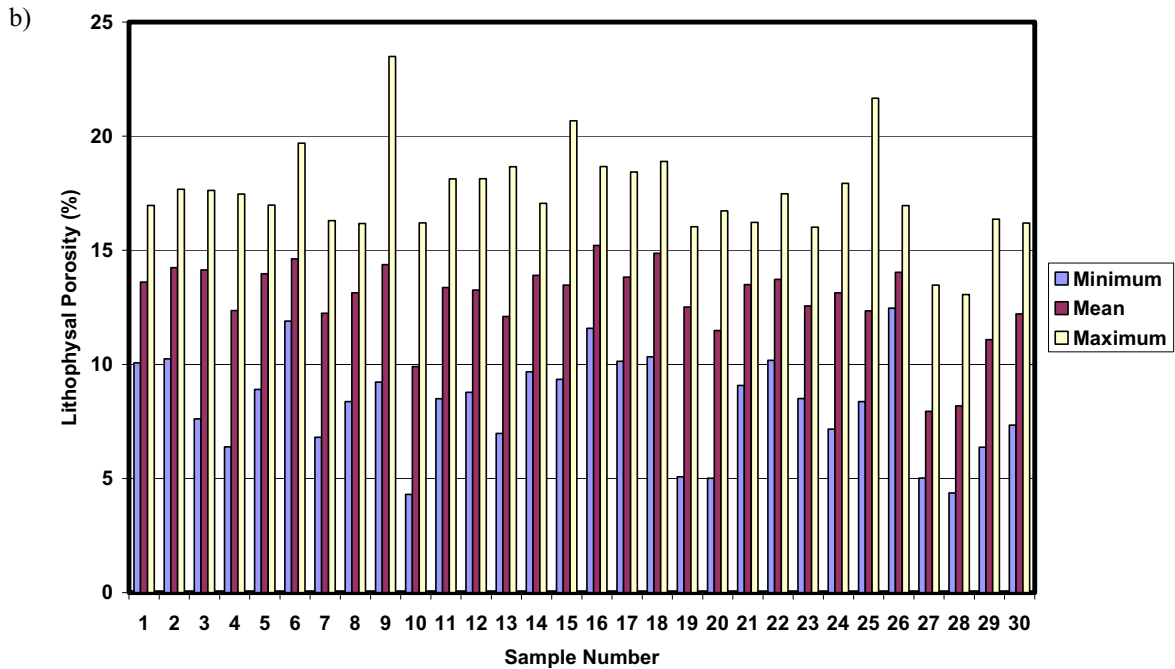
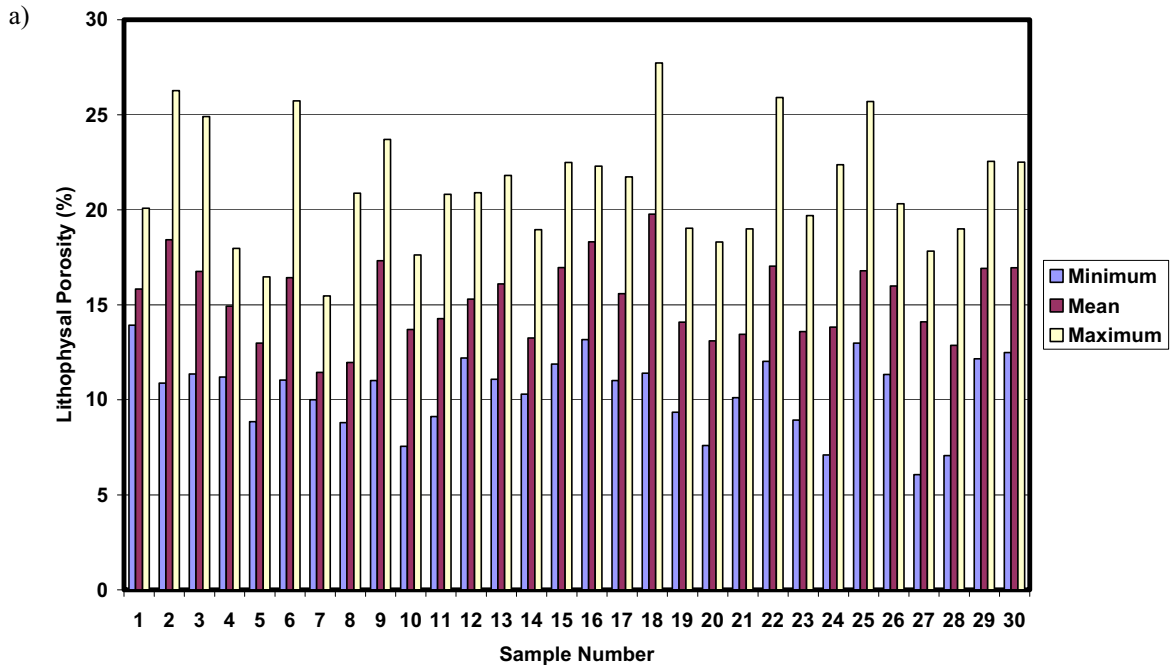
Source: DTNs provided in Table E-9.

<sup>a</sup> Young's Modulus estimated from linear fit to 11.5-in. core data given in Figure E-8

<sup>b</sup> Estimated from correlations of strength and modulus to lithophysal porosity in Figure E-6. Porosity ranges are based on BSC 2004 [DIRS 168970], Table 6.6-1.

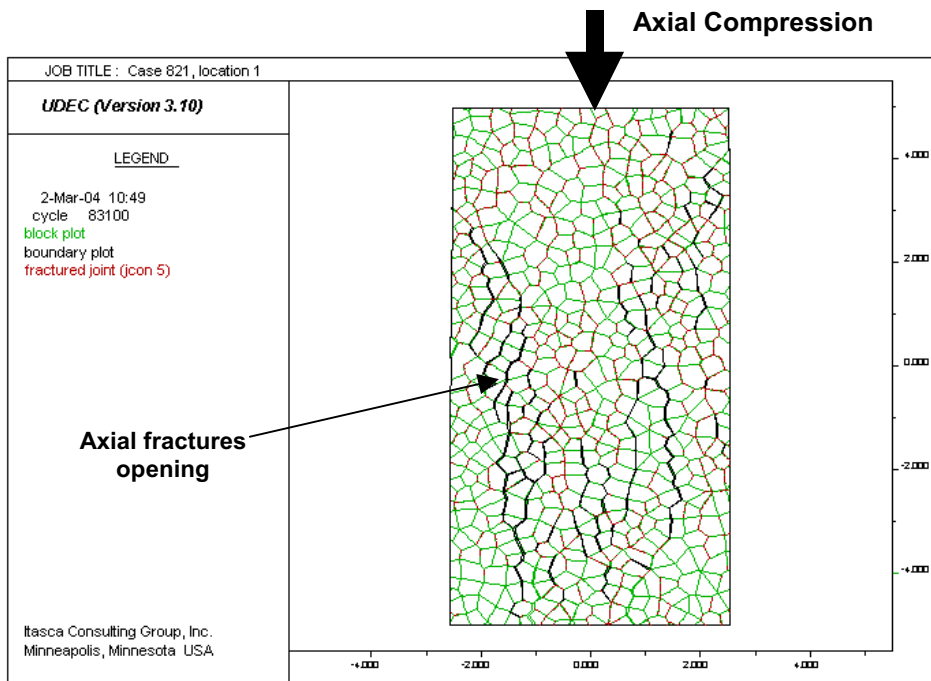
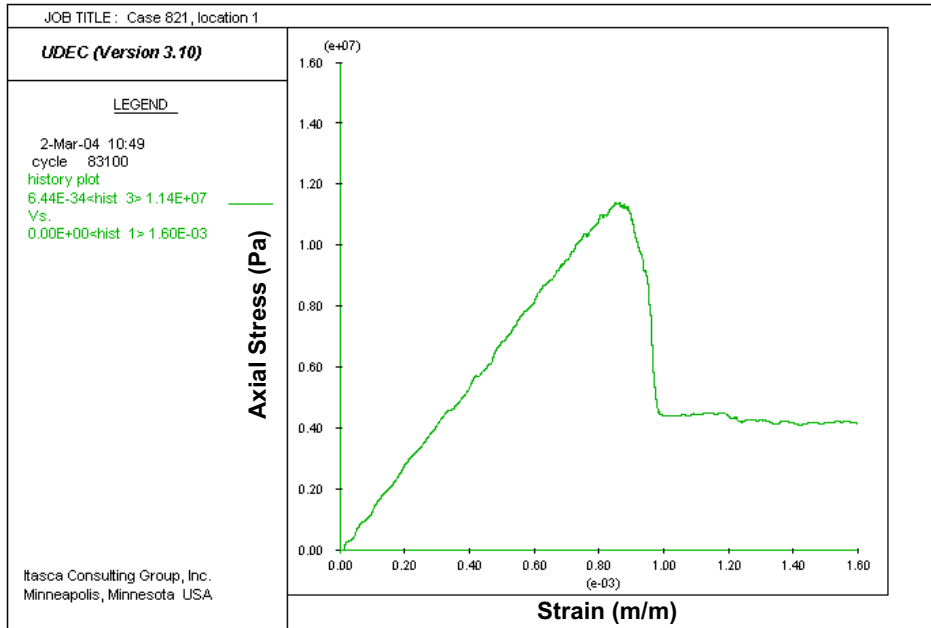
The numerical compression tests typically show that the samples fail as expected in an axial splitting mode (Figure E-17). The results of these analyses are summarized in Figure E-18 in terms of the relationship of UCS and Young's Modulus. Here, the laboratory and PFC shape study analyses are plotted along with the results of the numerical compression experiments for base case and lower bound properties. Several conclusions from this work can be made, including:

1. The variability in porosity distribution inherent in the samples results in UCS values that roughly equal or exceed 10 MPa. As seen in Figure E-18, the spatial variability in rock mass strength naturally results in sample strengths that gravitate toward that of the average porosity (i.e., around 15 percent). It is difficult, considering variable rock mass porosity, to produce average rock mass strength values that are at the low end of the category range. This agrees with observations in the ESF main loop and ECRB Cross-Drift of stable, lightly supported excavations in the lithophysal units that show little or no signs of instability.



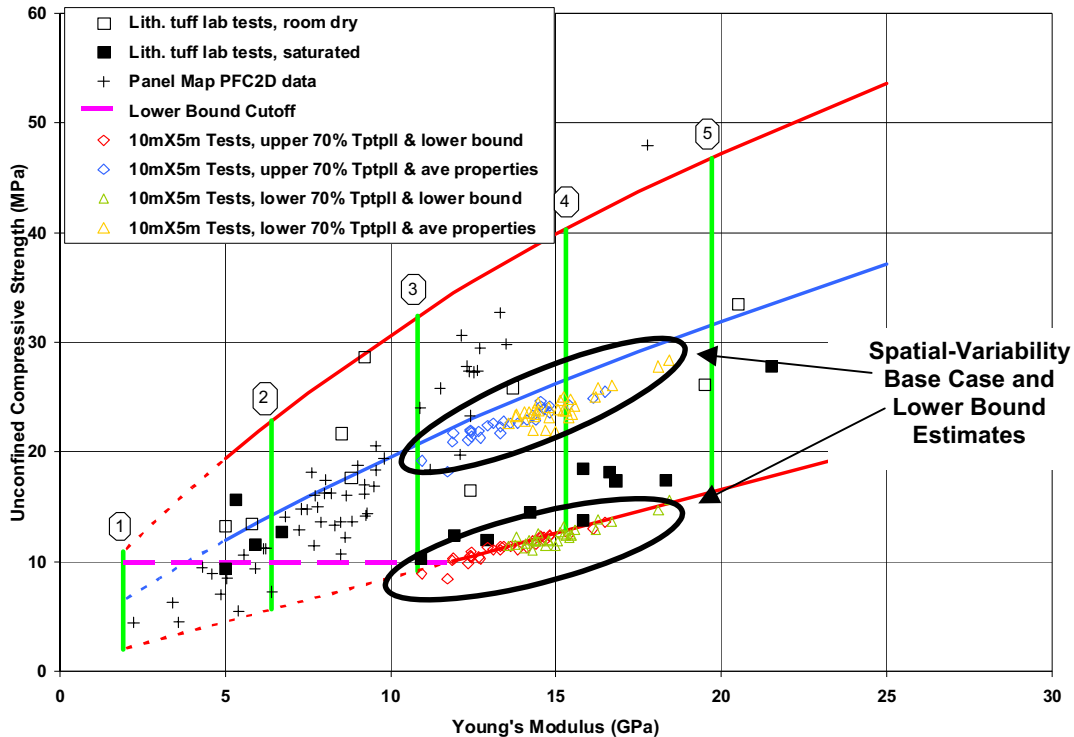
NOTE: Mean, minimum, and maximum refer to those values of lithophysal porosity in the particular sample. (a) the upper cross-section; (b) the lower cross-section of the Ttpll.

Figure E-16. Spatial Variability in Lithophysal Porosity in Each of 30 Samples Taken



NOTE: Estimated modulus and peak strength are determined from stress-strain curve. Sample is same as shown in Figure E-18. Sample fails in axial splitting mode as seen by black, axially oriented macro-fractures. Red block contacts indicate yield in either tension or shear.

Figure E-17. Example of Unconfined Compression Test Results on 10 m × 5 m Rock Mass Sample Containing Spatially Variable Lithophysal Porosity



NOTE: The results derived from base case and lower bound rock properties estimates. Note that a lower bound strength cut-off exists at approximately 10 MPa as a result of spatial variability of porosity.

Figure E-18. Relationship of UCS to Young's Modulus Showing the Results of Modeling Estimates of Properties for Spatially-Variable Lithophysal Rock Mass

2. The distribution of sample UCS and moduli for both base case and lower bound properties naturally fall within the range of rock mass strength categories 3 to 4. This is in agreement with the in situ distribution of lithophysal porosities (e.g., Figure O-15) that show the most common values lie in the Category 3 to 4 range. This confirms the consideration that the typical rock mass properties for the lithophysal units lie in the Category 3 to 4 range, and that the occurrence of Category 1 or 2 rocks is typically as localized regions of high porosity, potentially accompanied by large lithophysae.
3. The results verify that the consideration of homogenous rock mass properties used in the base case rock strength categories is conservative in nature.

Based on these calculations, the range of lithophysal rock mass properties are considered to have a lower bound strength of 10 MPa, with the lower bound following the saturated rock strength estimate for strengths greater than 10 MPa.

#### E4.1.4.3 Size Effect and Anisotropy of the Matrix of the Lithophysal Rock

To further explore the effect of sample size for nonlithophysal material, a single large block of material from the nonlithophysal section of the Tptpl near its lower boundary with the Tptpln was obtained from Busted Butte (Figure E-19).

A total of 110 samples with sizes ranging from 1-in to 8.8-in. (26 mm to 223 mm) diameter were cut and tested to examine both size effect and mechanical anisotropy. The mechanical anisotropy studies included testing of 2-in to 2.4-in. (51 mm to 62 mm) samples drilled at three mutually perpendicular directions from the same block of material. The results of the sample size on UCS are shown in Figure E-20. In this figure, the UCS is plotted as a function of the sample volume (as a log-log plot), and is compared to the test data for the Tptpmn given in Price 1986 [DIRS 106589]. The vertical offset of the two lines is indicative of the slightly different average strength of the Tptpll and Tptpmn matrix material, although the size effect is virtually identical. The mechanical anisotropy is demonstrated in terms of the average values for the Young's moduli from each of the perpendicular orientations. As seen in Figure E-21, there is a maximum anisotropy of approximately 10.6 percent in the average matrix moduli, which is considered to be a second order effect in comparison to lithophysal and fracturing effects.



00387DC\_009.ai

NOTE: Block from nonlithophysal portion of the Tptpll near its lower boundary with the Tptpln, Busted Butte.

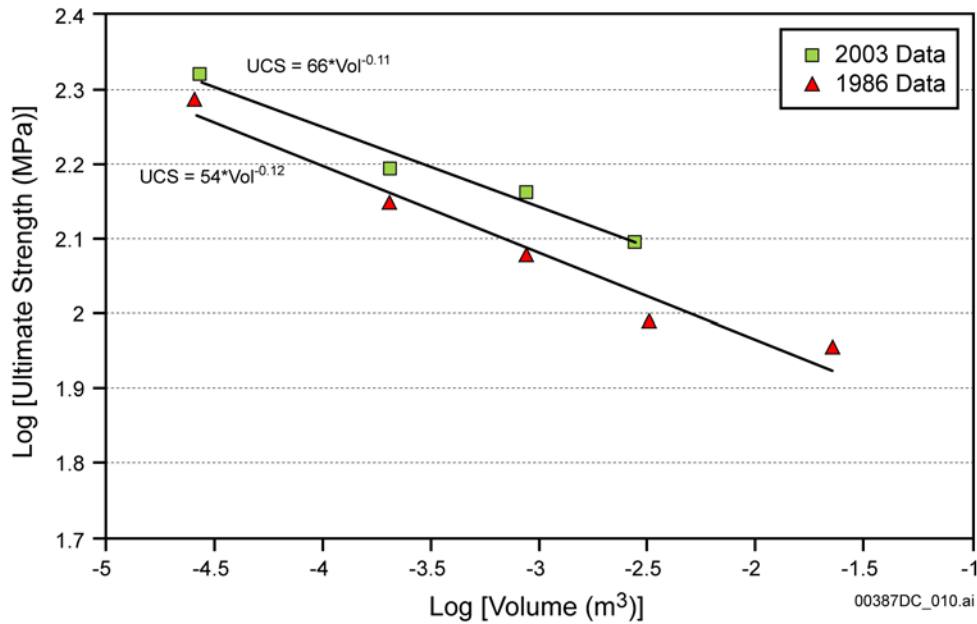
Figure E-19. Development of Rectangular Specimens for Matrix Size Effect and Anisotropy Study

A series of tests were run on 2-in. (51 mm) nonlithophysal Tptpll samples from the same outcrop boulder to examine the impact of saturation level on uniaxial compressive strength. It is impossible to accurately control moisture content at specific levels of saturation for a rock sample, so a number of tests aimed at fully drying and saturating and allowing the samples to equilibrate at room humidity conditions were run as shown in Table E-12. As seen in this table, the presence of moisture has a significant effect on compressive strength, particularly whether the samples are under heated-dry or exposed to humid air conditions. Complete drying of samples increases the mean strength of the samples tested by approximately 20 percent. This strength decrease in the presence of moisture is consistent with other testing of silicic rocks and is typical stress-corrosion mechanism involving chemical alterations due to moisture in flaws within the samples. The compression test data reported here is, unless otherwise noted, at room humidity conditions. Following a conservative design approach, performance calculations performed for ground support or postclosure effects consider average strength conditions from room temperature testing, with data ranges to cover fully saturated conditions.

Table E-12. Impact of Moisture Conditions on Uniaxial Compressive Strength of Nonlithophysal Tptpll Samples

Test Condition	Moisture Condition	Mean Strength (MPa)
1	Samples dried by slow heating to 200°C, tested at 200°C	213
2	Samples dried by slow heating to 200°C, then slowly cooled in dry environment, exposed to room humidity for about 30 minutes and tested at room temperature	176
3	Samples allowed to equilibrate with room humidity, tested at room temperature	158
4	Samples water saturated, tested at room temperature	149

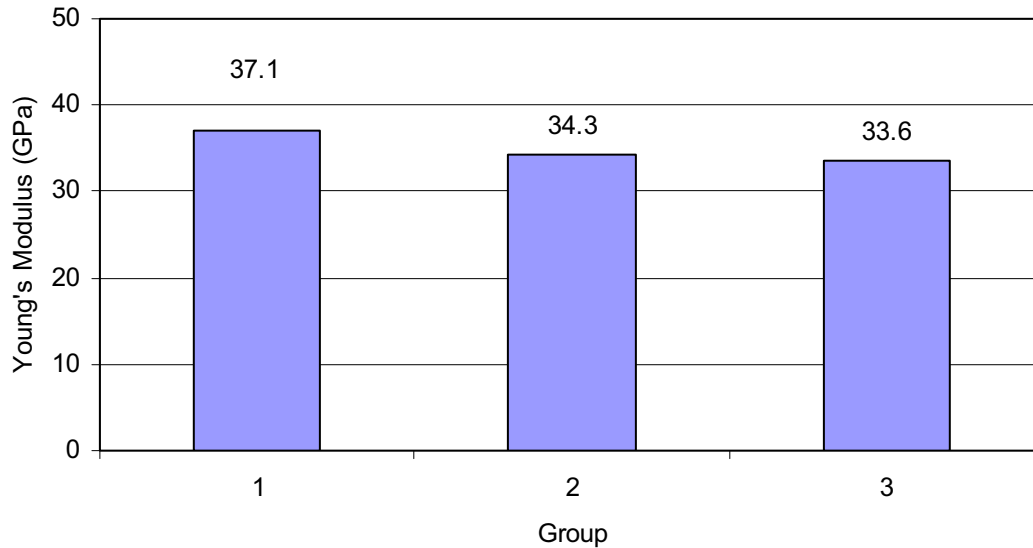
NOTE: Strengths are mean values from testing of 51 mm diameter samples at each moisture condition.



NOTE: Results from the 2003 testing of Tptpln/Tptpll samples (DTN: SN0306L0207502.008 [DIRS 165015]) are compared to previous testing of samples from the Tptpmn (Price 1986 [DIRS 106589]).

Figure E-20. Results of Size Effect Study Showing Variation in Sample Uniaxial Compressive Strength as a Function of Sample Volume





Source: Developed from source data provided by DTN: SN0306L0207502.008.

NOTE: Four block samples were used in the mechanical anisotropy study (see Figure E-19), including a total of 57 specimens cored from these samples in three mutually perpendicular directions. For each of the four blocks, an average Young's modulus was determined for each direction. This provides the orientation with the largest, medium, and smallest Young's modulus value for each block. Group 1 is the average of the largest values from each block, Group 2 is the average of the medium values from each block, and Group 3 is the average of the smallest values from each block. The averages of the 57 specimens show a maximum of 10.6 percent anisotropy in the average Young's modulus.

Figure E-21. Anisotropy in Young's Modulus of Nonlithophysal Tptpl Matrix for Three Mutually Perpendicular Coring Directions

## E4.2 ASSESSMENT OF ROCK MASS PROPERTIES FOR THE HEATED DRIFT

The calculation of rock mass properties for the Heated Drift in the ESF is described in this section, and also documented in the Microsoft Excel file, *rock mass strength v2.xls*, worksheet "Heated Drift" (Table A-1). Rock mass properties are calculated using the Hoek-Brown failure criterion (Hoek et al. 2002 [DIRS 162204], Section 2), which is expressed as

$$\sigma_1 = \sigma_3 + \sigma_{ci} \left( m_b \frac{\sigma_3}{\sigma_{ci}} + s \right)^a \quad (\text{Eq. E-9})$$

where  $\sigma_1$  and  $\sigma_3$  are the major and minor effective principle stresses at failure  
 $\sigma_{ci}$  is the uniaxial compressive strength of the intact rock material  
 $m_b$ ,  $s$ , and  $a$  are material constants.

This approach uses the Geological Strength Index (GSI) to characterize rock mass strength (Hoek et al. 2000 [DIRS 160539], pp. 91 to 97). Rock mass classification data using the Q system has been collected in the Heated Drift (Table E-13). To apply Q system data to estimate the strength of jointed rock masses, the Q system parameters related to stress (i.e.,  $J_w$  and  $SRF$ )

should be set equal to 1, which is equivalent to a dry rock mass subjected to medium stress conditions (Hoek et al. 2000 [DIRS 160539], pp. 96 to 97), such that:

$$GSI = 9 \ln Q' + 44 \quad (\text{Eq. E-10})$$

where

$$Q' = \left( \frac{RQD}{J_n} \right) \times \left( \frac{J_r}{J_a} \right) \quad (\text{Eq. E-11})$$

$RQD$  = rock quality designation

$J_n$  = joint set number

$J_r$  = joint roughness number

$J_a$  = joint alteration number.

The material constants  $m_b$ ,  $s$ , and  $a$  are given by

$$m_b = m_i \exp\left(\frac{GSI - 100}{28 - 14D}\right) \quad (\text{Eq. E-12})$$

$$s = \exp\left(\frac{GSI - 100}{9 - 3D}\right) \quad (\text{Eq. E-13})$$

$$a = \frac{1}{2} + \frac{1}{6} \left( e^{-GSI/15} - e^{-20/3} \right) \quad (\text{Eq. E-14})$$

where  $m_i$  is the value of  $m_b$  for intact rock and is determined based on laboratory triaxial test data, and  $D$  is a factor that depends on the degree of disturbance to which the rock mass has been subjected by blast damage and stress relaxation.  $D$  is 0 for the mechanically excavated tunnels in the ESF.

Following the approach by Hoek et al. (2002 [DIRS 162204], Section 3), the rock mass modulus of deformation is given by

$$E_m = \left(1 - \frac{D}{2}\right) \cdot 10^{(GSI-10)/40} \text{ for } \sigma_{ci} > 100 \text{ MPa} \quad (\text{Eq. E-15})$$

$$E_m = \left(1 - \frac{D}{2}\right) \sqrt{\frac{\sigma_{ci}}{100}} \cdot 10^{(GSI-10)/40} \text{ for } \sigma_{ci} \leq 100 \text{ MPa} \quad (\text{Eq. E-16})$$

where  $E_m$  is the rock mass modulus of deformation in GPa.

The global rock mass strength is determined as

$$\sigma_{cm} = \sigma_{ci} \cdot \frac{(m_b + 4s - a(m_b - 8s)) \left( \frac{m_b}{4} + s \right)^{a-1}}{2(1+a)(2+a)}. \quad (\text{Eq. E-17})$$

Table E-13. Q System Rock Mass Classification Data from the Heated Drift

Tunnel Station Interval (m)	Lithostratigraphic Unit	Thermal-Mechanical Unit	Q System Parameters			
			RQD	Jn	Jr	Ja
0   5	Tptpmn	TSw2	80	12	3	2
5   10	Tptpmn	TSw2	Not rated due to plate loading niche.			
10   15	Tptpmn	TSw2	78	9	1	2
15   20	Tptpmn	TSw2	69	12	1	2
20   25	Tptpmn	TSw2	90	12	3	2
25   30	Tptpmn	TSw2	76	9	3	2
30   35	Tptpmn	TSw2	77	9	3	2
35   40	Tptpmn	TSw2	67	9	3	2
40   45	Tptpmn	TSw2	83	15	3	2
45   50	Tptpmn	TSw2	58	15	3	2
50   55	Tptpmn	TSw2	59	15	2	2
55   60	Tptpmn	TSw2	54	15	2	2

Source: DTN: GS970608314224.007 [DIRS 158430].

NOTE: Q system parameters can be accessed through USGS 1997 [DIRS 169040], which is linked to the Source DTN.

The calculation of the mean intact rock strength,  $\sigma_{ci}$ , is documented in Table E-14. The value of the material constant for intact rock,  $m_i$ , is 33.87, which is documented in the *Subsurface Geotechnical Parameters Report* (BSC 2003 [DIRS 166660], Table 8-39).

The results of the calculation of rock mass properties for the Heated Drift using the approach described above are provided in Table E-15, with additional documentation provided in the Microsoft Excel file, *rock mass strength v2.xls* (Table A-1).

Table E-14. Intact Compressive Strength Data for the Tptpmn Unit <sup>a</sup>

Number	Specimen Number (also referred to as Sample Number)	Ultimate Differential Strength (also referred to as Compressive Strength) (MPa)	Original Source DTN
1	NRG-6-720.7-SNL-A	235.5	SNL02030193001.004 [DIRS 108415]
2	NRG-6-742.3-SNL-A	162.3	
3	NRG-6-742.9-SNL-A	212.8	
4	NRG-6-762.9-SNL-A	112.1	
5	NRG-6-773.5-SNL-A	117.4	

Table E-14. Intact Compressive Strength Data for the Tptpmn Unit<sup>a</sup> (Continued)

Number	Specimen Number (also referred to as Sample Number)	Ultimate Differential Strength (also referred to as Compressive Strength) (MPa)	Original Source DTN
6	NRG-6-784.8-SNL-A	223.0	SNL02030193001.004 [DIRS 108415]
7	NRG-6-785.6-SNL-A	218.6	
8	NRG-6-806.8-SNL-A	261.9	
9	NRG-5-847.2-SNL-A	84.2	SNL02030193001.012 [DIRS 108416]
10	NRG-5-849.4-SNL-A	240.8	
11	NRG-5-861.2-SNL-A	55.3	
12	NRG-5-873.4-SNL-A	38.4	SNL02030193001.012 [DIRS 108416]
13	NRG-5-887.2-SNL-A	240.9	
14	NRG-5-888.8-SNL-A	288.9	
15	NRG-5-891.9-SNL-A	253.5	
16	NRG-5-896.5-SNL-A	184.7	
17	NRG-7/7A-777.0-SNL-A	143.8	SNL02030193001.019 [DIRS 108431]
18	NRG-7/7A-800.2-SNL-A	179.2	
19	NRG-7/7A-806.3-SNL-A	225.4	
20	NRG-7/7A-818.5-SNL-A	126.3	
21	NRG-7/7A-859.2-SNL-A	118.8	
22	NRG-7/7A-865.4-SNL-I	215.8	
23	NRG-7/7A-865.4-SNL-J	232.0	
24	NRG-7/7A-865.4-SNL-K	239.1	
25	NRG-7/7A-865.4-SNL-L	248.5	
26	SD-12-734.7-SNL-B	193.3	SNL02030193001.023 [DIRS 108435]
27	SD-12-781.1-SNL-B	198.2	SNL02030193001.026 [DIRS 108436]
28	SD-9-761.5-SNL-A	231.5	
29	SD-9-768.7-SNL-A	254.5	
30	SD-9-771.7-SNL-A	160.8	
31	SD-9-774.6-SNL-B	60.1	
32	SD-9-826.7-SNL-A	224.9	
33	SD-9-832.8-SNL-C	183.3	
34	SD-9-842.1-SNL-E-1	208.9	
35	GU-3 760.9/1A	210.3	
36	GU-3 760.9/1B	234.4	
37	GU-3 760.9/2A	215.5	
38	GU-3 760.9/2B	221.4	
39	GU-3 760.9/3A	245.2	
40	GU-3 760.9/3B	222.2	
41	GU-3 760.9/4A	205.2	
42	GU-3 760.9/4B	183.5	
43	GU-3 760.9/5A	229.7	
44	GU-3 760.9/5B	226.4	
45	10/AE/2/Z	109.0	SNSAND85076200.000

Table E-14. Intact Compressive Strength Data for the Tptpmn Unit<sup>a</sup> (Continued)

Number	Specimen Number (also referred to as Sample Number)	Ultimate Differential Strength (also referred to as Compressive Strength) (MPa)	Original Source DTN
46	10/AE/46/Z	143.0	[DIRS 160024]
47	10/AE/9/Z	153.0	
48	10-AE-3Y	53.7	
49	10-AE-6X	107.0	
50	10-AE-8X	62.4	
51	G4-686.6-A	270.0	
52	G4-686.6-D	326.0	
53	G4-686.6-G	180.0	SNSAND84110100.000 [DIRS 160016]
54	G4-742.75-E	235.0	
55	G4-742.75-F	256.0	
56	G4-742.75-G	279.0	
57	G4-748.6-A	196.0	
58	G4-748.6-B	190.0	
59	G4-749.0-A	268.0	
60	G4-749.0-B	188.0	
61	10X12	126.8	SNSAND85070900.000 [DIRS 160022]
62	10Y47	143.2	
63	10Z15	158.4	
64	12A2	203.2	
65	12A3	132.2	
66	13A2	113.3	
67	26A1	200.5	
68	26B1	111.7	
69	26C1	274.3	
70	26D1	198.6	
71	26E1	241.3	
72	28A2	104.3	
<i>Mean</i>		188.8	—
<i>Standard Deviation</i>		63.7	

<sup>a</sup> Intact compressive strength data are qualified and summarized in DTN: MO0311RCKPRPCS.003 [DIRS 166073]. The data can be found by downloading the data file from this DTN, and searching for the data using the Specimen Number. The intact compressive strength data from the Tptpmn unit have been selected according to test conditions to provide a consistent data set. Data with the following test conditions were selected: ambient temperature conditions, saturated samples, nominal strain rate of  $10^{-5} \text{ S}^{-1}$ , with sample diameters ranging from about 25.4 mm to 50.8 mm.

Table E-15. Calculated Rock Mass Properties for the Heated Drift

Tunnel Station Interval (m)		Lithostratigraphic Unit	Thermal-Mechanical Unit	Mean Intact Unconfined Compressive Strength <sup>a</sup> (MPa)	Intact Material Constant <sup>b</sup>	Q'	GSI	Rock Mass Material Constants			Global Rock Mass Compressive Strength (MPa)	Rock Mass Modulus of Deformation (GPa)
								$m_b$	$s$	$a$		
0	5	Tptpmn	TSw2	189	33.87	10.00	64.7	9.61	0.02	0.50	80.03	23.34
5	10	Tptpmn	TSw2	189	33.87	Not rated due to plate loading niche.						
10	15	Tptpmn	TSw2	189	33.87	4.33	57.2	7.34	0.01	0.50	68.83	15.13
15	20	Tptpmn	TSw2	189	33.87	2.88	53.5	6.44	0.01	0.50	63.99	12.24
20	25	Tptpmn	TSw2	189	33.87	11.25	65.8	9.98	0.02	0.50	81.78	24.81
25	30	Tptpmn	TSw2	189	33.87	12.67	66.9	10.37	0.03	0.50	83.59	26.38
30	35	Tptpmn	TSw2	189	33.87	12.83	67.0	10.41	0.03	0.50	83.80	26.56
35	40	Tptpmn	TSw2	189	33.87	11.17	65.7	9.96	0.02	0.50	81.67	24.71
40	45	Tptpmn	TSw2	189	33.87	8.30	63.0	9.05	0.02	0.50	77.35	21.19
45	50	Tptpmn	TSw2	189	33.87	5.80	59.8	8.07	0.01	0.50	72.51	17.60
50	55	Tptpmn	TSw2	189	33.87	3.93	56.3	7.12	0.01	0.50	67.65	14.39
55	60	Tptpmn	TSw2	189	33.87	3.60	55.5	6.92	0.01	0.50	66.60	13.75
Average Rock Mass Properties for the Heated Drift											75.25	20.01

<sup>a</sup> Mean intact compressive strength is from Table E-14.

<sup>b</sup> The intact material constant,  $m_i$ , is from the *Subsurface Geotechnical Parameters Report* (BSC 2003 [DIRS 166660], Table 8-39).

### E4.3 ASSESSMENT OF ROCK MASS ELASTIC PROPERTIES FOR THERMAL MECHANICAL UNITS

Rock mass modulus of deformation was calculated using the approach described above (Section E4.2), with the rock mass modulus calculated using either Equation E-15 or E-16, depending on the intact rock strength. The thermal-mechanical units evaluated include the TCw, PTn, TSw1, and TSw2. The required input data include Q system input parameters  $RQD$ ,  $J_n$ ,  $J_r$ , and  $J_a$ . These data were collected in five-meter intervals throughout the ESF, and are documented in the Microsoft Excel file, *rock mass strength v2.xls*, in worksheet "Spatial Data" (Table A-1). The mean intact unconfined compressive strength  $\sigma_{ci}$  is used to determine the appropriate equation for rock mass modulus (see Equations E-15 and E-16). The calculation of mean intact unconfined compressive strength values for each thermal-mechanical unit is documented in the Microsoft Excel file, *rock mass strength v2.xls*, in worksheet "Intact Strength" (Table A-1). The calculation of rock mass modulus of deformation for each five-meter tunnel interval throughout the ESF is documented in the Microsoft Excel file, *rock mass strength v2.xls*, in worksheet "Spatial Data" (Table A-1). Using the standard data functions of Microsoft Excel, these data were sorted by thermal-mechanical unit, rank-ordered by rock mass modulus, and placed in the worksheet, "Sorted by TM Unit". The cumulative frequency of occurrence was

calculated in this worksheet, and five rock mass quality categories were identified for each thermal-mechanical unit to represent the range of property values, corresponding to cumulative frequencies of occurrence of 5, 20, 40, 70, and 90 percent. The calculated rock mass modulus values for each thermal-mechanical unit are summarized in Table E-16. The rock mass modulus data in Table E-16 were adjusted so that the upper bound limit did not exceed the mean intact Young's modulus. Mean intact Young's modulus values for thermal-mechanical units are calculated in the Microsoft Excel file, *rock mass strength v2.xls*, in worksheet "Intact Strength" (Table A-1). Rock mass modulus values corresponding to rock mass category 3 were selected for use in the thermal-mechanical assessment of stress within the rock mass (Section 6.2).

Empirical relationships to estimate rock mass Poisson's ratio from rock mass classification data are not available, and in situ test Poisson's ratio data are limited. It is considered that the mean values for intact rock from each thermal-mechanical unit are representative of the rock mass Poisson's ratio (Table E-16).

#### E4.4 ASSESSMENT OF BLOCK STRENGTH FOR NONLITHOPHYSAL ROCK

The strength of large-scale intact rock block material (i.e., between joints) for nonlithophysal rock is calculated based on available size-effect laboratory compression test data from Price (1986 [DIRS 106589]). The size-effect data are presented in Table E-17, and plotted in Figure E-22. Figure E-22 also shows a best-fit curve of the size effect data developed by Price (1986 [DIRS 106589], p. 7) together with the Hoek and Brown (1982 [DIRS 120981], p. 156) relationship between unconfined compressive strength and specimen diameter. The equation by Price (1986 [DIRS 106589]) for the best-fit curve was used to extrapolate the size-effect data to a sample size of 3 m (Figure E-22). Based on this extrapolation, a strength of 70 MPa was selected as representative of the large-scale intact rock block material for nonlithophysal rock.

Table E-16. Rock Mass Poisson's Ratio and Modulus of Deformation Values for Thermal Mechanical Units

Thermal-Mechanical Unit	Rock Mass Poisson's Ratio <sup>a</sup>	Rock Mass Modulus of Deformation (GPa)	Data Range	
			Rock Mass Modulus of Deformation, Em (GPa)	Rock Mass Quality Category
TCw	0.22	16.1	7.3	1
			12.9	2
			16.1	3
			23.2	4
			27.8	5
PTn	0.23	2.2	2.2	1
			2.2	2
			2.2	3
			2.2	4
			2.2	5

Table E-16. Rock Mass Poisson's Ratio and Modulus of Deformation Values for Thermal Mechanical Units (Continued)

Thermal-Mechanical Unit	Rock Mass Poisson's Ratio <sup>a</sup>	Rock Mass Modulus of Deformation (GPa)	Data Range	
			Rock Mass Modulus of Deformation, Em (GPa)	Rock Mass Quality Category
TSw1	0.25	17.3	8.6	1
			12.8	2
			17.3	3
			23.5	4
			23.5	5
TSw2	0.21	15.8	9.4	1
			12.9	2
			15.8	3
			21.5	4
			28.0	5

<sup>a</sup> Recent field test data in the Tptpl that indicate a mean rock mass Poisson's ratio of 0.2 (DTN: SN0208F4102102.002 [DIRS 161874]) compared to a mean intact Poisson's ratio of 0.21 (CRWMS M&O 1997 [DIRS 103564], Table 5-27). Therefore, rock mass Poisson's ratio values in this table are based on laboratory test data. The calculation of mean Poisson's ratio values is documented in the Microsoft Excel file, *rock mass strength v2.xls*, in worksheet "Intact Strength" (Table A-1).

Table E-17. Size-Effect Laboratory Compression Test Data for Nonlithophysal Rock

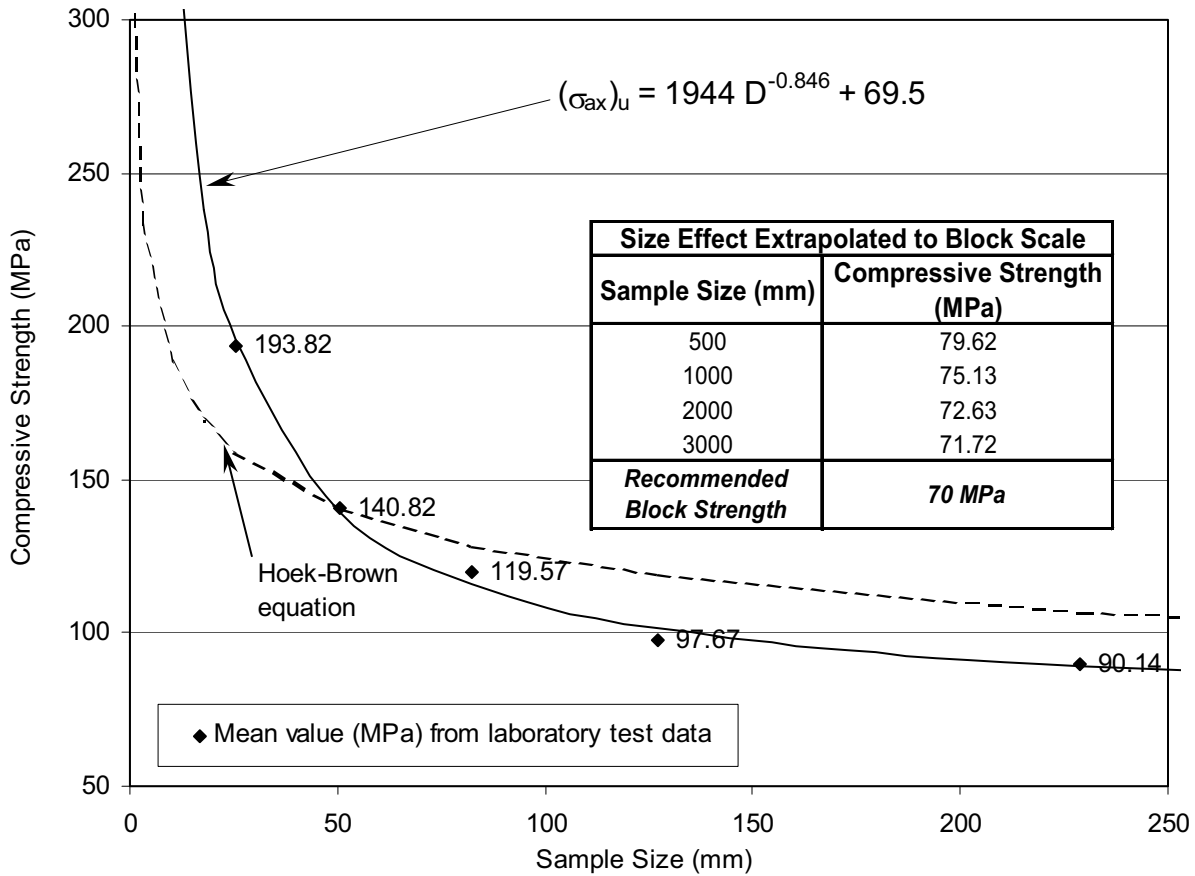
Row #	Test	Specimen Number	Specimen Diameter (mm)	Uniaxial Compressive Strength, ( $\sigma_{ax}$ ) <sub>u</sub> (MPa)
1	1	12A2	25.4	203.2
2	1	12A3	25.4	132.2
3	1	13A2	25.4	113.3
4	2	26C1	25.4	274.3
5	2	26D1	25.4	198.6
6	2	26E1	25.4	241.3
Mean value				193.82
7	1	10X12	50.8	126.8
8	1	10Y47	50.8	143.2
9	1	10Z15	50.8	158.4
10	2	26A1	50.8	200.5
11	2	26B1	50.8	111.7
12	2	28A2	50.8	104.3
Mean value				140.82
13	1	10E3	82.6	141.7
14	1	10E4	82.6	99.8
15	1	11A1	82.6	130.6
16	1	11A2	82.6	87.7



Table E-17. Size-Effect Laboratory Compression Test Data for Nonlithophysal Rock (Continued)

Row #	Test	Specimen Number	Specimen Diameter (mm)	Uniaxial Compressive Strength, ( $\sigma_{ax}$ ) <sub>u</sub> (MPa)
17	1	11C1	82.6	124.3
18	1	11D1	82.6	131.8
19	2	211	82.6	160.7
20	2	231	82.6	140.7
21	2	271	82.6	58.9
Mean value				119.57
22	1	10A1	127.0	59.9
23	1	10A2	127.0	84.3
24	1	10C1	127.0	92.4
25	1	10C2	127.0	98.2
26	1	10D1	127.0	89.8
27	1	10D2	127.0	69.7
28	2	221	127.0	134.3
29	2	234	127.0	85.8
30	2	261	127.0	170.8
31	2	281	127.0	90.4
32	2	282	127.0	98.8
Mean value				97.67
33	2	222	228.6	86.9
34	2	282	228.6	93.4
Mean value				90.14

Source: DTN: MO0311RCKPRPCS.003 [DIRS 166073] (see native data file, *DTN SEP data file revised2.xls*, rows 519-528, 532-533, and 542-563, from worksheet "basic data DTN").



Source: Laboratory test data provided in Table E-17. Hoek-Brown equation based on Hoek and Brown (1982 [DIRS 120981], p. 156).

Figure E-22. Sample Size Effect on Compressive Strength Based on Laboratory Test Data for Nonlithophysal Rock

### E5. THERMAL PROPERTIES

The thermal properties used in the thermal mechanical calculation of stresses at Yucca Mountain due to heating and cooling of the repository (Section 6.2), are provided in this section. These data include thermal conductivity (Table E-18), specific heat (Table E-19), and thermal expansion for saturated rock (Table E-20) for the various lithostratigraphic and thermal-mechanical units of the Yucca Mountain rock strata. The mean values for thermal-mechanical units are determined by averaging the thermal properties of the lithostratigraphic units within each thermal-mechanical unit, weighted according to the thickness of each lithostratigraphic unit. Additional details are provided in the Microsoft Excel file, *thermal properties TM units v2.xls* (Table A-1).

Table E-18. Thermal Conductivity for Various Thermal Mechanical Units and Associated Lithostratigraphic Units

Thermal Mechanical Unit	Stratigraphic Unit	Thickness <sup>a</sup> (m)	Thermal Conductivity <sup>b</sup> (W/m <sup>2</sup> K)		DTN <sup>c</sup>
			T ≤ 100° C	T > 100° C	
TCw / PTn	Tpcpv3	0.0	0.80	0.69	SN0303T0503102.008 [DIRS 162401]
	Tpcpv2	5.1	1.06	0.49	
	Tpcpv1	2.4	1.06	0.49	
	Tpbt4	0.5	1.06	0.49	
	Tpy	3.8	1.06	0.49	
	Tpbt3	3.8	1.06	0.49	
	Tpp	5.1	1.06	0.49	
	Tpbt2	8.3	1.06	0.49	
	Tptrv3	1.9	1.06	0.49	
	Tptrv2	1.2	1.06	0.49	
		<i>Mean (weighted by unit thickness)</i>	1.06	0.49	
TSw1	Tptrv1	1.2	0.80	0.69	SN0404T0503102.011 [DIRS 169129]
	Tptrn	35.6	1.81	1.30	
	Tptrl	6.1	1.81	1.30	
	Tptpul	66.8	1.77	1.18	
			<i>Mean (weighted by unit thickness)</i>	1.77	
TSw2 / TSw3	Tptpmn	38.3	2.07	1.42	SN0303T0503102.008 [DIRS 162401]
	Tptpll	95.6	1.89	1.28	
	Tptpln	55.1	2.13	1.49	
	Tptpv3	12.0	0.80	0.69	
			<i>Mean (weighted by unit thickness)</i>	1.92	
CHn1 / CHn2	Tptpv2	4.7	1.06	0.49	SN0303T0503102.008 [DIRS 162401]
	Tptpv1	15.4	1.06	0.49	
	Tpbt1	2.0	1.06	0.49	
	Calico	45.5	1.26	0.60	
	Calicobt	15.9	1.26	0.60	
			<i>Mean (weighted by unit thickness)</i>	1.21	

<sup>a</sup> Thickness of units extracted from DTN: MO0012MWDGFM02.002 [DIRS 153777]. The details of this extraction are provided in Appendix M.

<sup>b</sup> T = temperature.

<sup>c</sup> Mean values are calculated in this report and not provided by the DTNs listed in this table. Data extracted from DTN: SN0404T0503102.11 [DIRS 169129] are summarized in BSC 2004 [DIRS 169854], Table 7-10. Data extracted from DTN: SN0303T0503102.008 [DIRS 162401] are summarized in BSC 2004 [DIRS 170033], Table 6-13.

Table E-19. Specific Heat for Various Thermal Mechanical Units and Associated Lithostratigraphic Units

Thermal Mechanical Unit	Stratigraphic Unit	Thickness <sup>a</sup> (m)	Specific Heat <sup>b</sup> (J/kg°K)			DTN <sup>c</sup>
			T ≤ 95°C	95°C < T < 114°C	T > 114°C	
TCw / PTn	Tpcpv3	0.0	1.2E+03	8.4E+03	1.0E+03	SN0307T0510902.003 [DIRS 164196]
	Tpcpv2	5.1	1.2E+03	8.4E+03	1.0E+03	
	Tpcpv1	2.4	1.3E+03	9.1E+03	1.0E+03	
	Tpbt4	0.5	1.3E+03	9.1E+03	1.0E+03	
	Tpy	3.8	1.3E+03	9.1E+03	1.0E+03	
	Tpbt3	3.8	1.3E+03	9.1E+03	1.0E+03	
	Tpp	5.1	1.3E+03	9.1E+03	1.0E+03	
	Tpbt2	8.3	1.3E+03	9.1E+03	1.0E+03	
	Tptrv3	1.9	1.3E+03	9.1E+03	1.0E+03	
	Tptrv2	1.2	1.3E+03	9.1E+03	1.0E+03	
	<i>Mean (weighted by unit thickness)</i>			1.3E+03	9.0E+03	
TSw1	Tptrv1	1.2	8.9E+02	1.8E+03	9.9E+02	SN0307T0510902.003 [DIRS 164196]
	Tptrn	35.6	8.9E+02	2.7E+03	9.9E+02	
	Tptrl	6.1	8.9E+02	2.7E+03	9.9E+02	
	Tptpul	66.8	9.4E+02	3.6E+03	9.9E+02	
	<i>Mean (weighted by unit thickness)</i>			9.2E+02	3.2E+03	
TSw2 / TSw3	Tptpmn	38.3	9.1E+02	3.0E+03	9.9E+02	SN0307T0510902.003 [DIRS 164196]
	Tptpll	95.6	9.3E+02	3.3E+03	9.9E+02	
	Tptpln	55.1	9.0E+02	2.8E+03	9.9E+02	
	Tptpv3	12.0	9.1E+02	1.7E+03	1.0E+03	
	<i>Mean (weighted by unit thickness)</i>			9.1E+02	3.0E+03	
CHn1 / CHn2	Tptpv2	4.7	1.1E+03	5.1E+03	1.0E+03	SN0307T0510902.003 [DIRS 164196]
	Tptpv1	15.4	1.2E+03	6.4E+03	1.1E+03	
	Tpbt1	2.0	1.2E+03	6.4E+03	1.1E+03	
	Calico	45.5	1.4E+03	9.8E+03	1.1E+03	
	Calicobt	15.9	1.2E+03	7.6E+03	1.1E+03	
	<i>Mean (weighted by unit thickness)</i>			1.3E+03	8.4E+03	

<sup>a</sup> Thickness of units provided in Appendix M.

<sup>b</sup> T = temperature.

<sup>c</sup> Mean values are calculated in this report and not provided by the DTNs listed in this table.

Table E-20. Thermal Expansion for Various Thermal Mechanical Units

Thermal Mechanical Unit	Thermal Expansion Coefficient (1/°C)			
	25°C < T ≤ 50°C	50°C < T ≤ 75°C	75°C < T ≤ 100°C	100°C < T ≤ 125°C
TCw	7.09×10 <sup>-6</sup>	7.62×10 <sup>-6</sup>	8.08×10 <sup>-6</sup>	10.34×10 <sup>-6</sup>
PTn	4.46×10 <sup>-6</sup>	4.28×10 <sup>-6</sup>	-1.45×10 <sup>-6</sup>	-30.42×10 <sup>-6</sup>
TSw1	6.56×10 <sup>-6</sup>	7.32×10 <sup>-6</sup>	6.83×10 <sup>-6</sup>	6.92×10 <sup>-6</sup>
TSw2	7.14×10 <sup>-6</sup>	7.47×10 <sup>-6</sup>	7.46×10 <sup>-6</sup>	9.07×10 <sup>-6</sup>

T = temperature

NOTE: Source data provided by DTN: SNL01B05059301.006 [DIRS 129168]. Thermal expansion data are for saturated rock. The calculation of mean data is documented in Brodsky et al. (1997 [DIRS 100653], Table 4-4).

**APPENDIX F**

**FIELD OBSERVATION OF KEY BLOCKS IN THE ECRB CROSS-DRIFT**



## FIELD OBSERVATION OF KEY BLOCKS IN THE ECRB CROSS-DRIFT

This appendix documents the observation of key blocks in the ECRB Cross-Drift, including the Tptpul unit (Stations 0+00 to 10+15), the Tptpmn unit (Stations 10+15 to 14+44), the Tptpll unit (Stations 14+44 to 23+26), and the Tptpln unit (Stations 23+26 to 25+85) (Mongano et al. 1999 [DIRS 149850], pp. 105 and 106). Additional descriptions of key blocks in the ECRB Cross-Drift are provided in Section 6.1.5. Portions of the full periphery geologic maps containing key blocks are presented in Figures F-1 through F-14. An explanation of symbols on the full periphery geologic maps is provided in Figure F-1. The potential key blocks are identified on these maps as exposed fracture faces bounded by joints. The number of blocks per kilometer observed in the ECRB Cross-Drift (Table F-1) was determined by identifying the number of key blocks in each lithologic unit as indicated in Figures F-2 through F-14 over the total length of drift in the unit.

Table F-1. Number of Key Blocks Observed in the ECRB Cross-Drift

<b>Lithologic Unit</b>	<b>Metric Stationing<sup>a</sup> (m)</b>	<b>Length of Drift<sup>b</sup> (km)</b>	<b>Number of Blocks<sup>c</sup></b>	<b>Blocks per Kilometer</b>
Tptpul	0+00 to 10+15	1.02	3	3
Tptpmn	10+15 to 14+44	0.43	17	40
Tptpll	14+44 to 23+26	0.88	0	0
Tptpln	23+26 to 25+85	0.26	2	8

<sup>a</sup> Mongano et al. (1999 [DIRS 149850], pp. 105 and 106).

<sup>b</sup> Based on metric stationing (e.g., for the Tptpmn unit, length = (1444 m - 1015 m) / 1000 = 0.43 km).

<sup>c</sup> The observation of key blocks is documented in Figures F-2 through F-14.

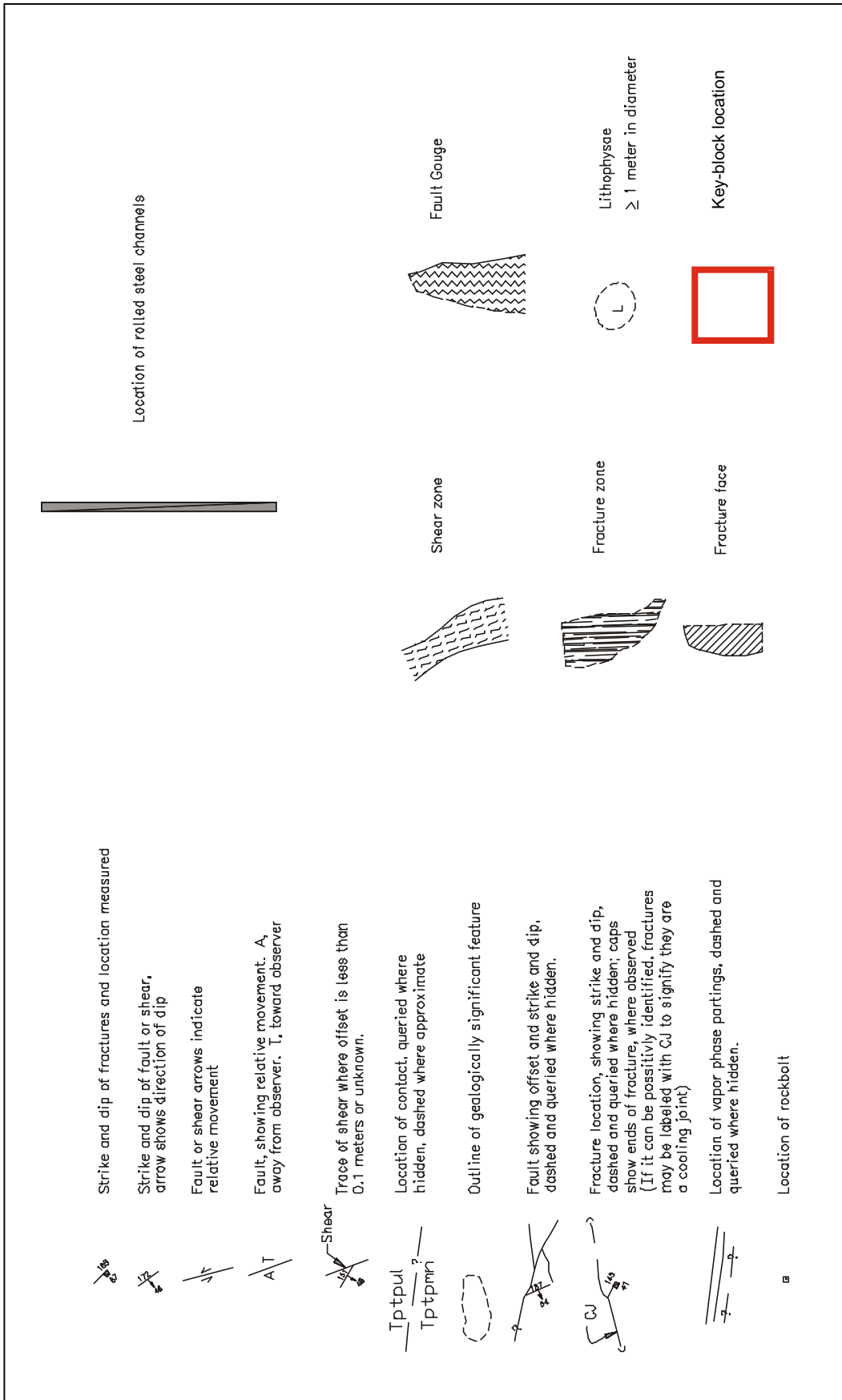
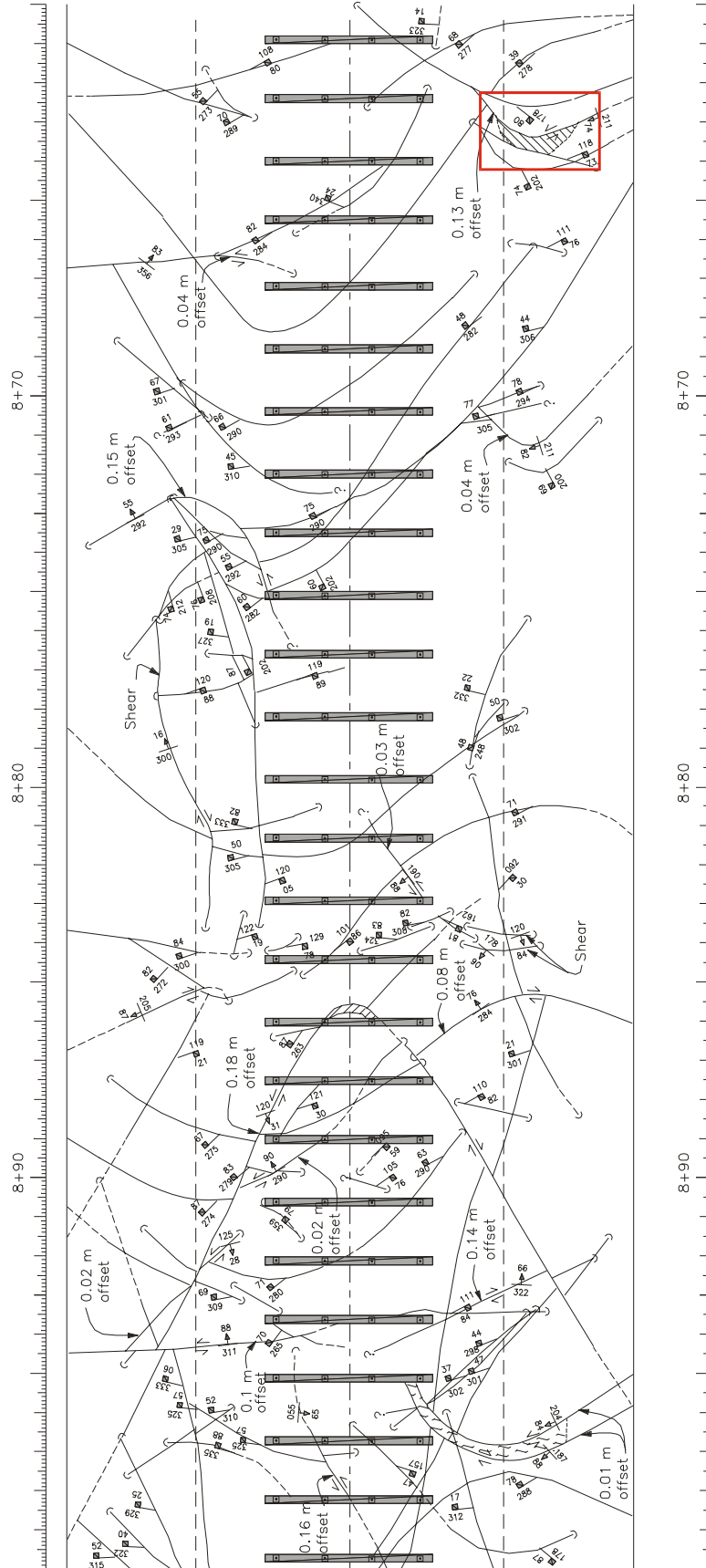


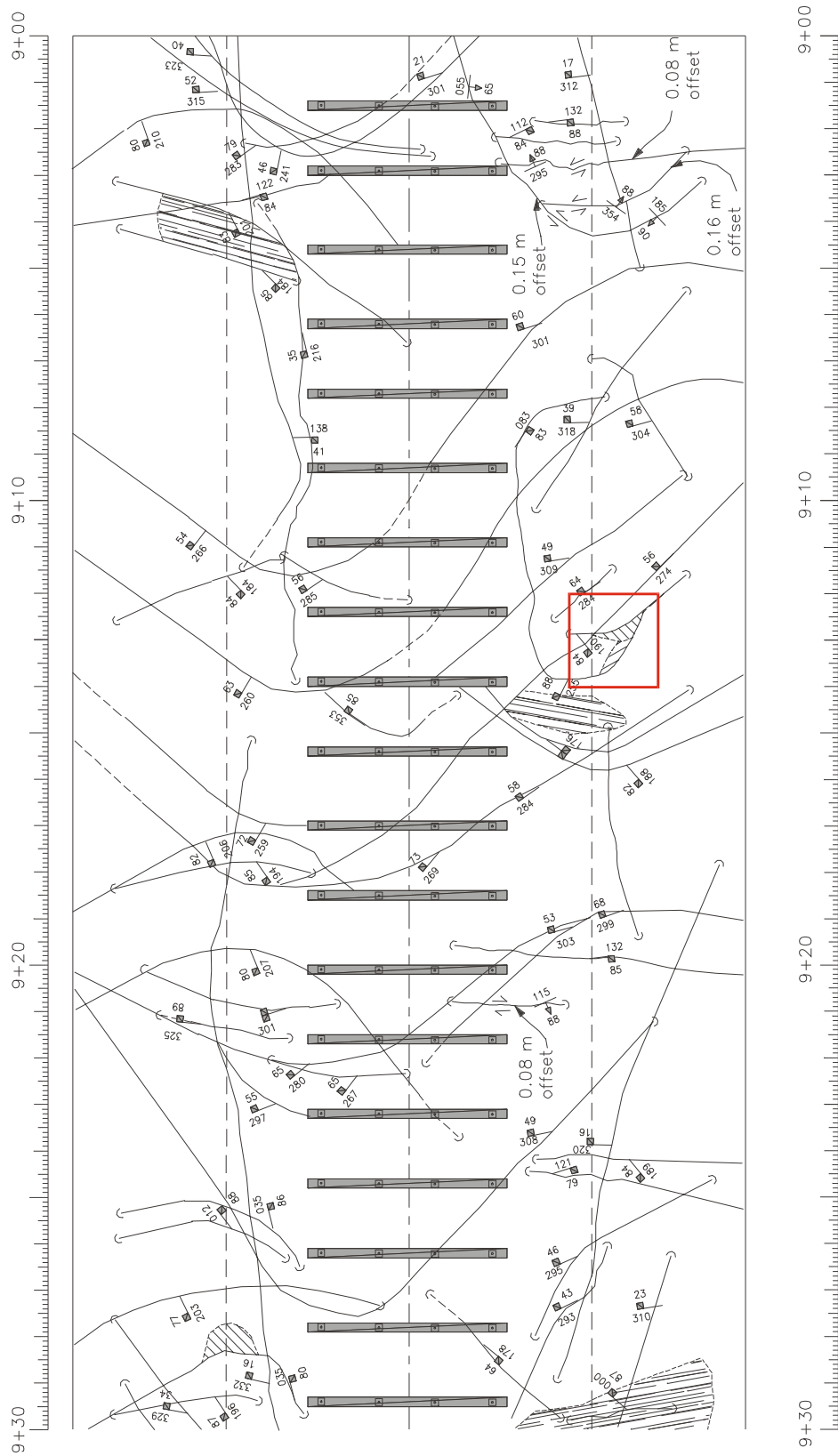
Figure F-1. Explanation of Symbols on Full Periphery Geologic Maps





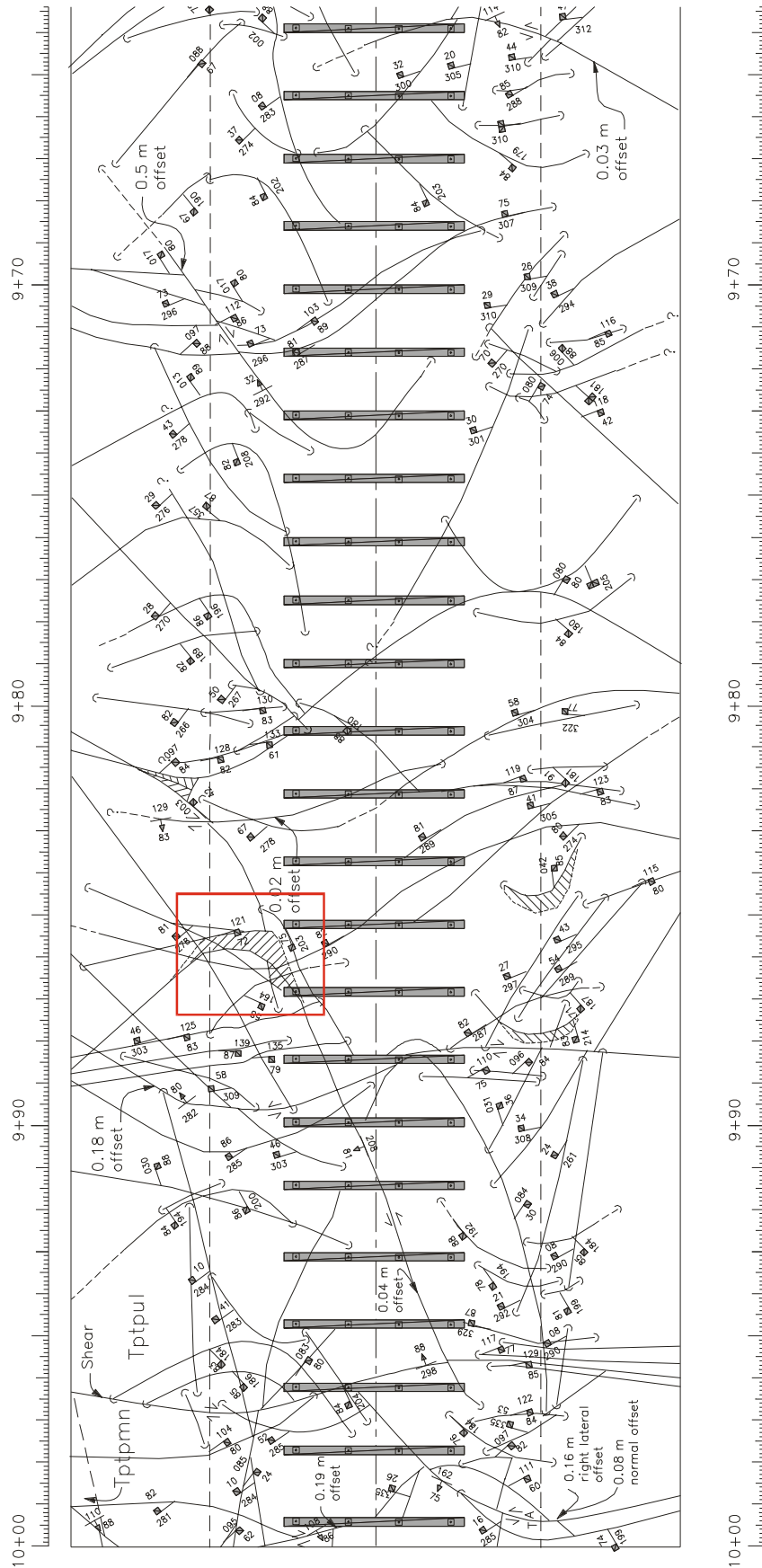
Source: GS990408314224.003 [DIRS 108404].

Figure F-2. Key-Block Location, Tptpul Unit, ECRB Cross-Drift Stations 8+60 to 9+00

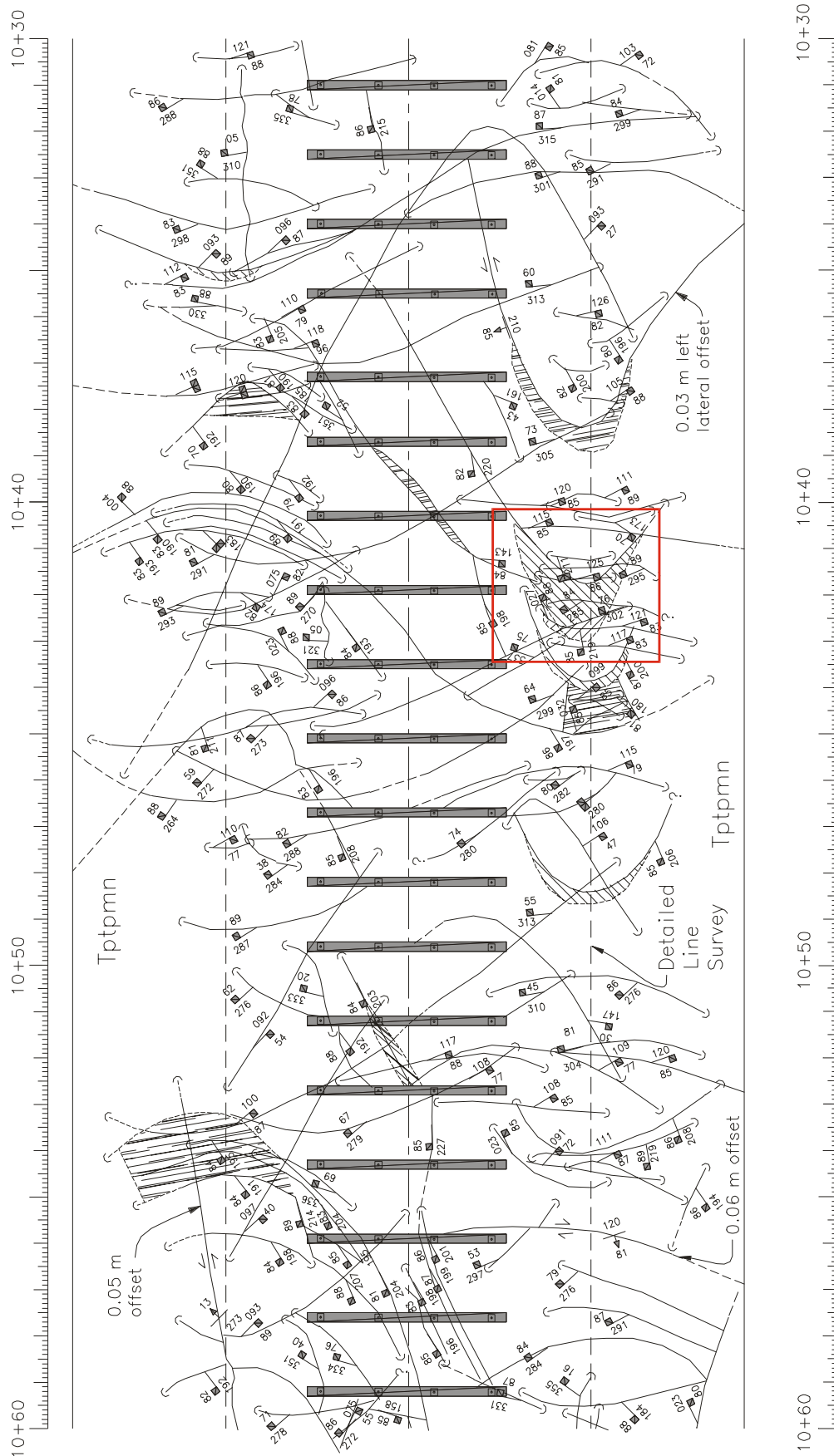


Source: GS990408314224.003 [DIRS 108404].

Figure F-3. Key-Block Location, Tptpul Unit, ECRB Cross-Drift Stations 9+00 to 9+30

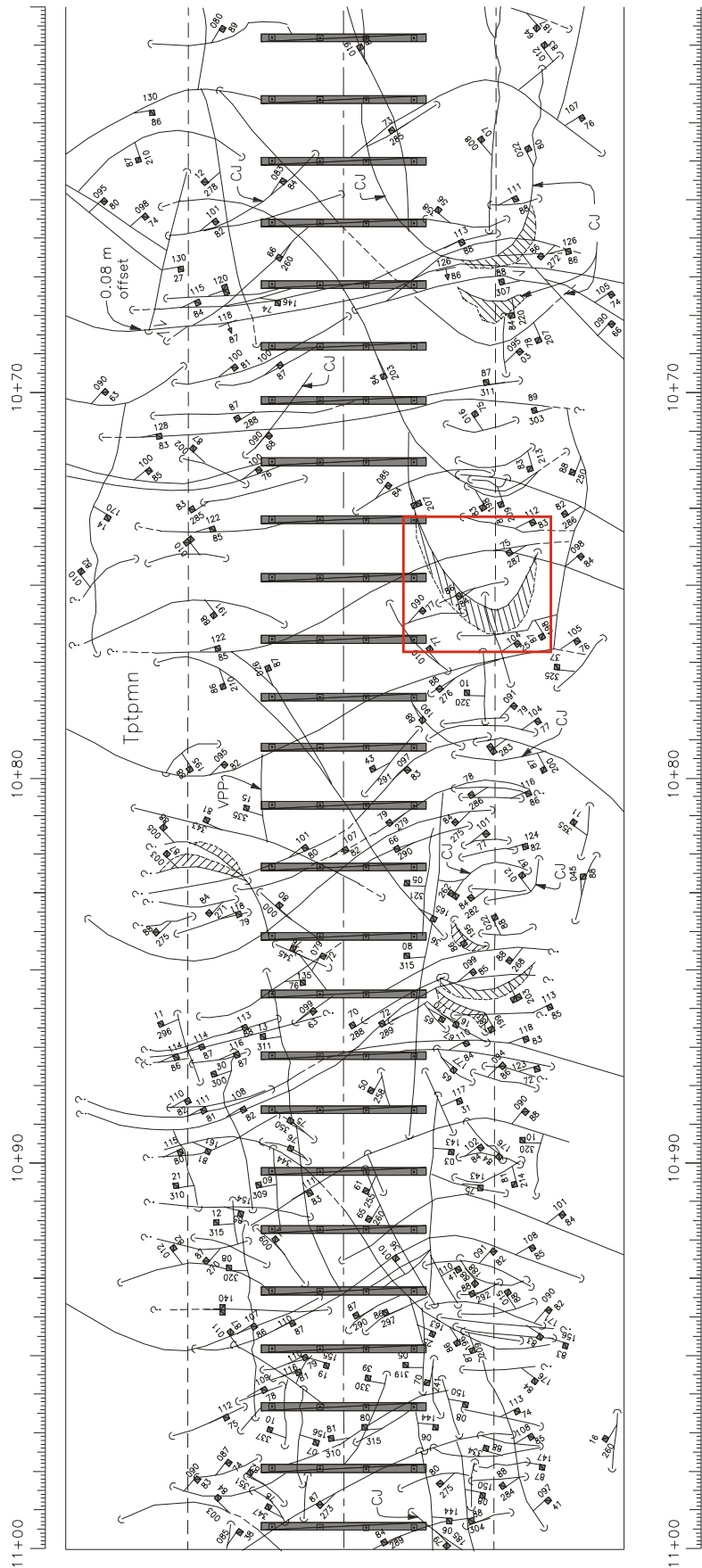


Source: GS990408314224.003 [DIRS 108404].  
Figure F-4. Key-Block Location, Tptpul Unit, ECRB Cross-Drift Stations 9+64 to 10+00



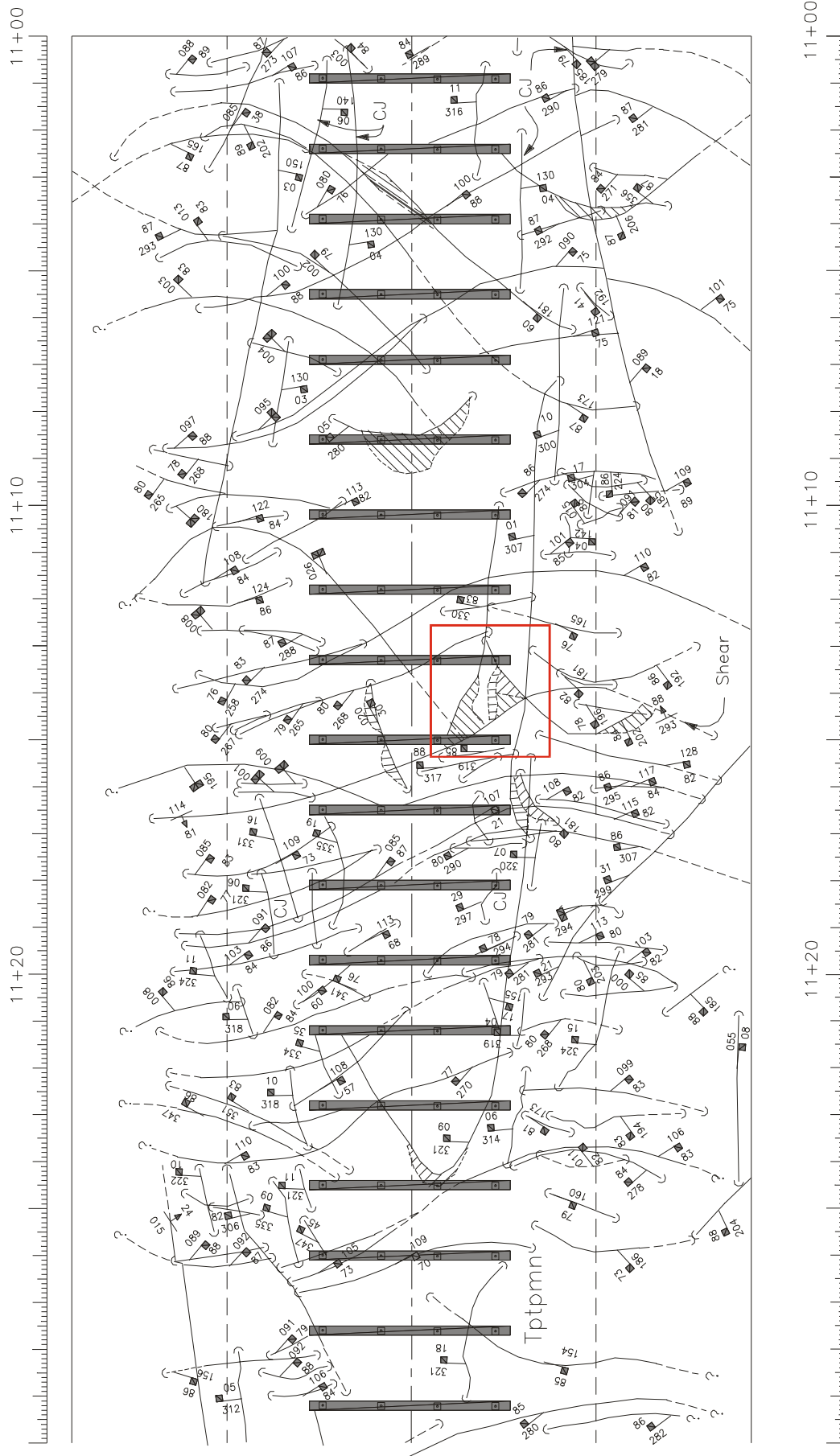
Source: GS990408314224.004 [DIRS 108405].

Figure F-5. Key-Block Location, Tptpm Unit, ECRB Cross-Drift Stations 10+30 to 10+60



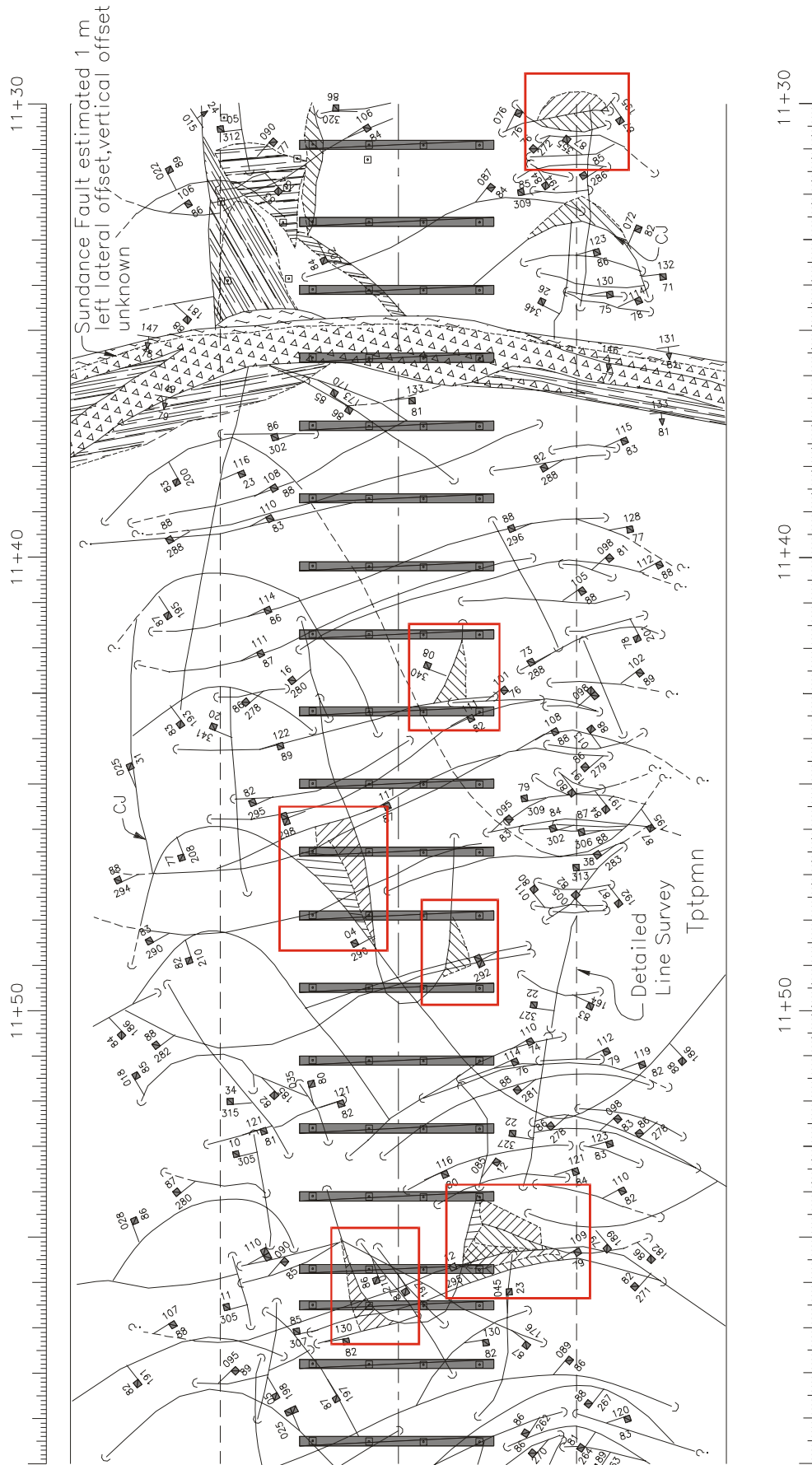
Source: GS990408314224.004 [DIRS 108405].

Figure F-6. Key-Block Location, Tptpmn Unit, ECRB Cross-Drift Stations 10+60 to 11+00



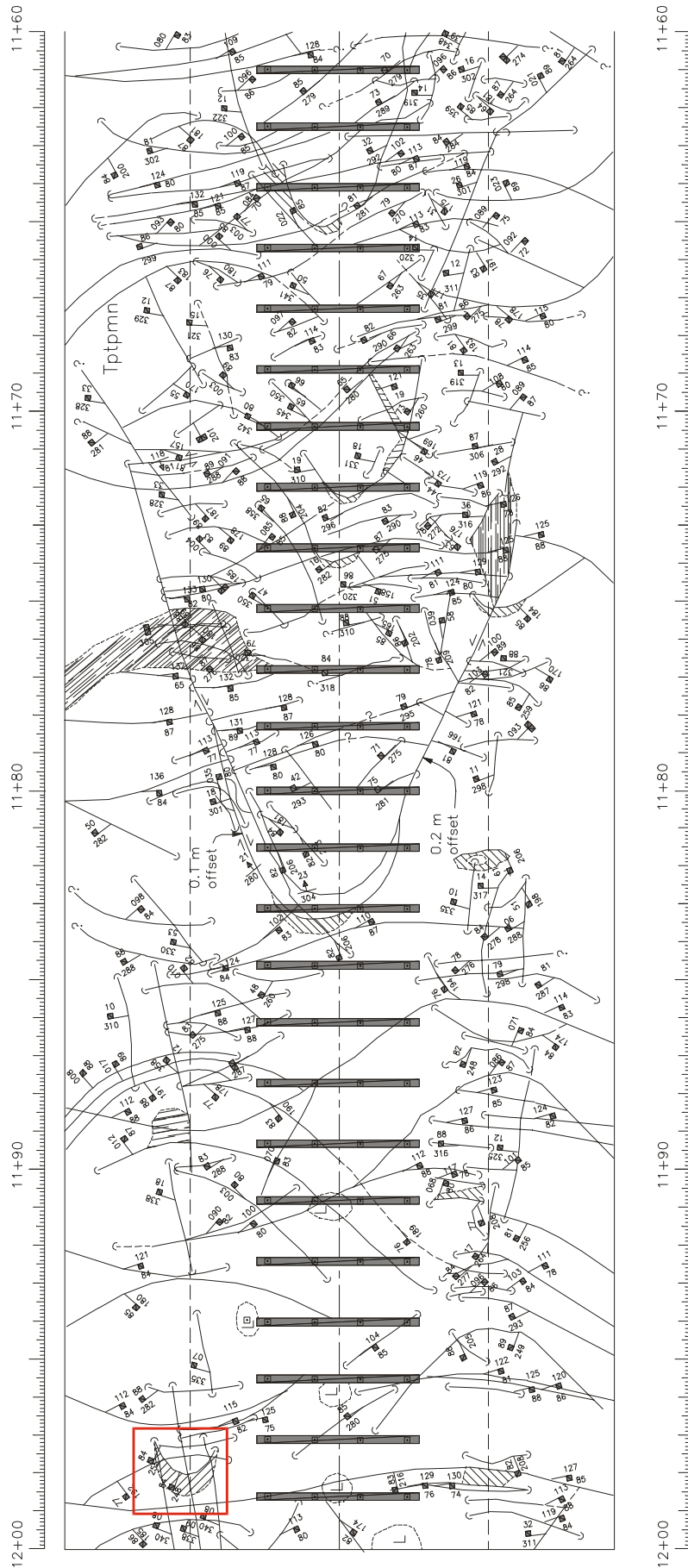
Source: GS990408314224.004 [DIRS 108405].

Figure F-7. Key-Block Location, Tptpmn Unit, ECRB Cross-Drift Stations 11+00 to 11+30



Source: GS990408314224.004 [DIRS 108405].

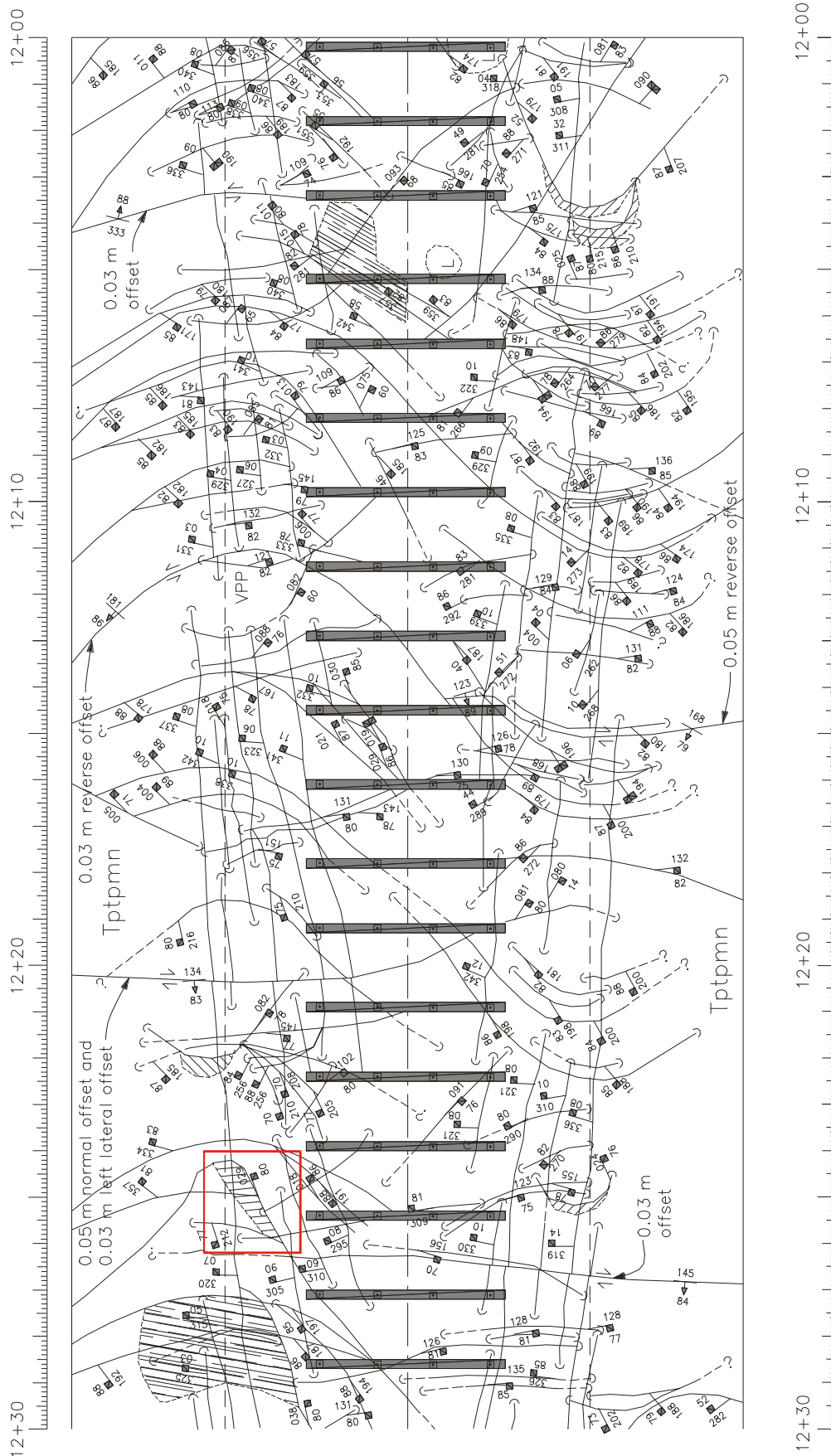
Figure F-8. Key-Block Location, Tptpmn Unit, ECRB Cross-Drift Stations 11+30 to 11+60



Source: GS990408314224.004 [DIRS 108405].

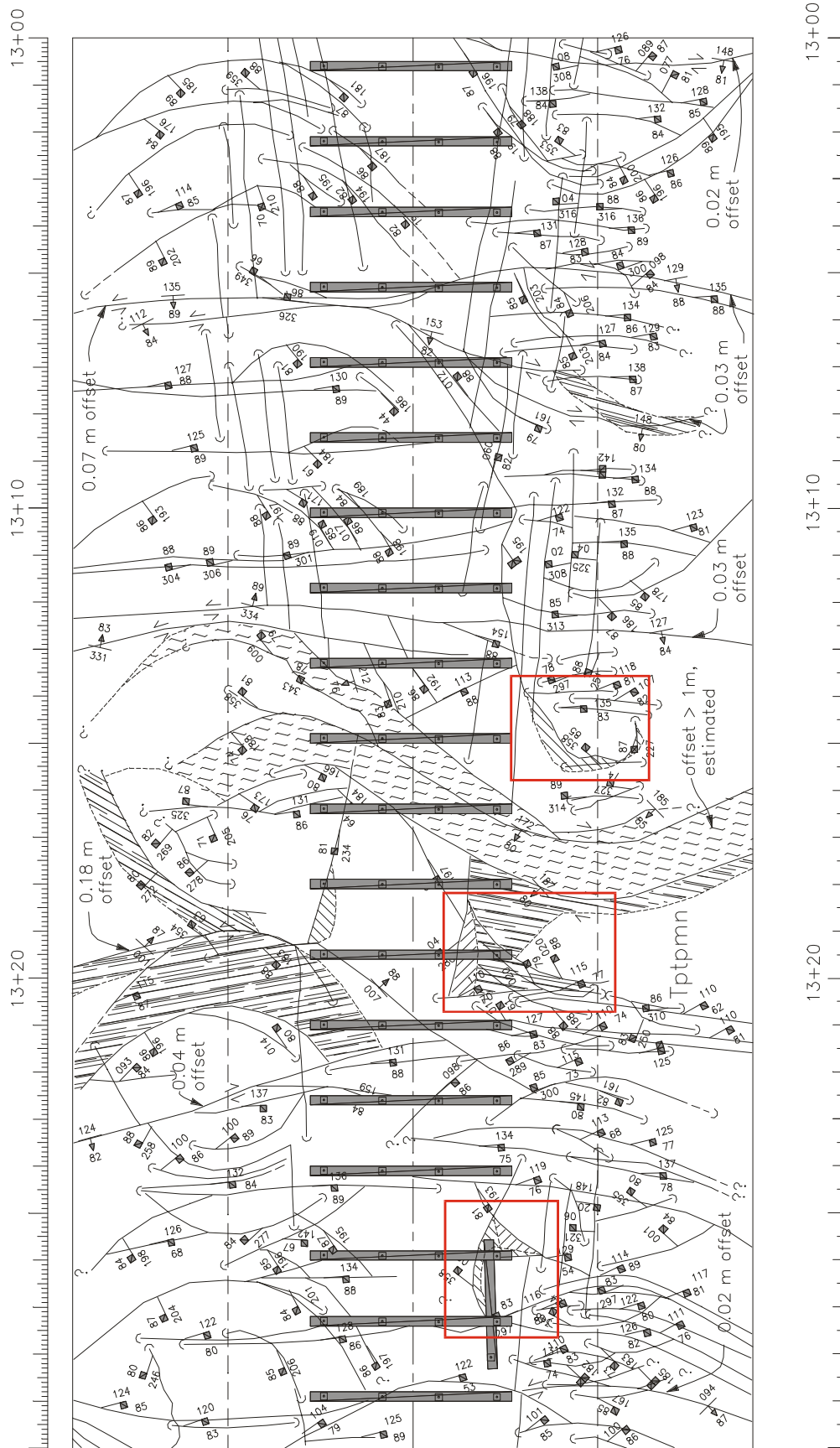
Figure F-9. Key-Block Location, Tptpmn Unit, ECRB Cross-Drift Stations 11+60 to 12+00





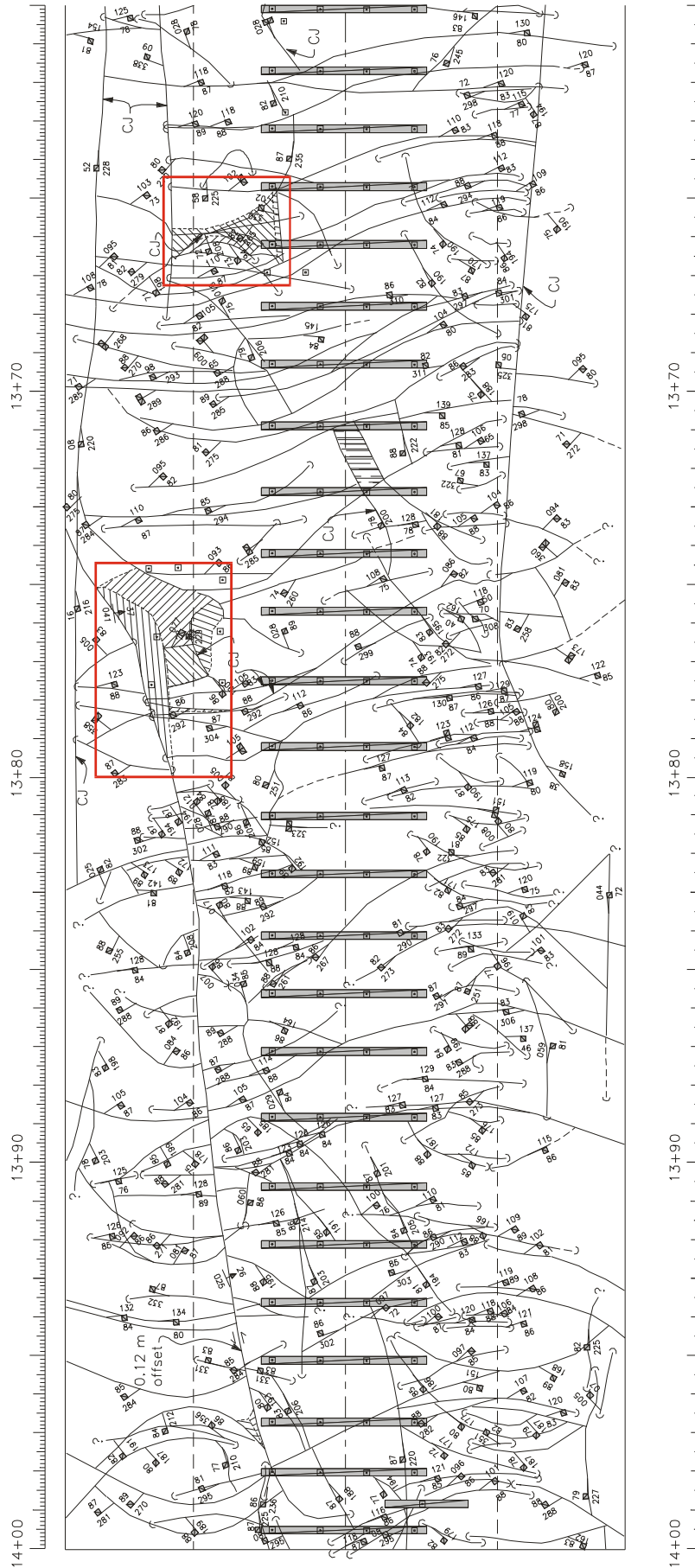
Source: GS990408314224.004 [DIRS 108405].

Figure F-10. Key-Block Location, Tptpmn Unit, ECRB Cross-Drift Stations 12+00 to 12+30



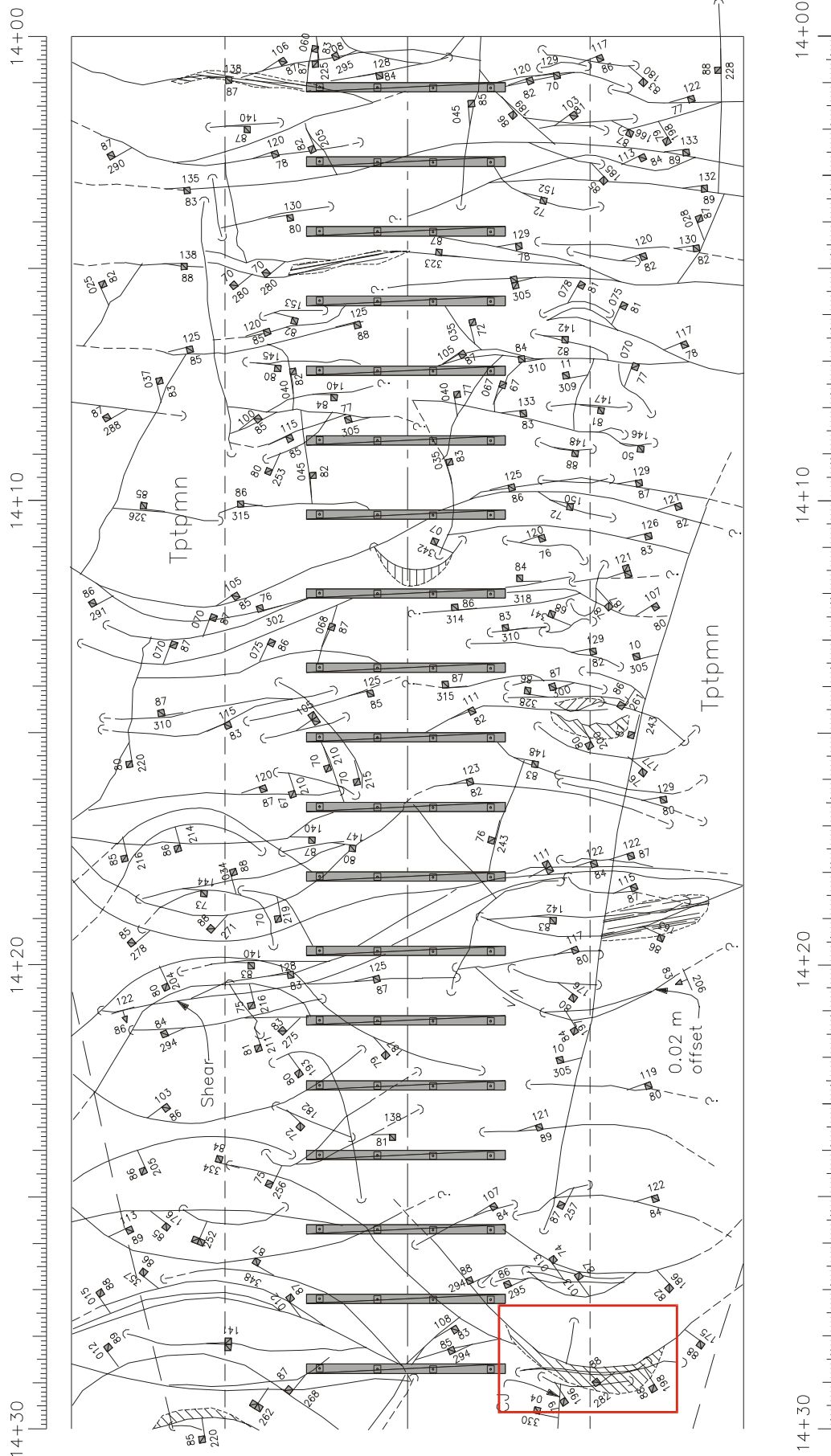
Source: GS990408314224.004 [DIRS 108405].

Figure F-11. Key-Block Location, Tptpmn Unit, ECRB Cross-Drift Stations 13+00 to 13+30



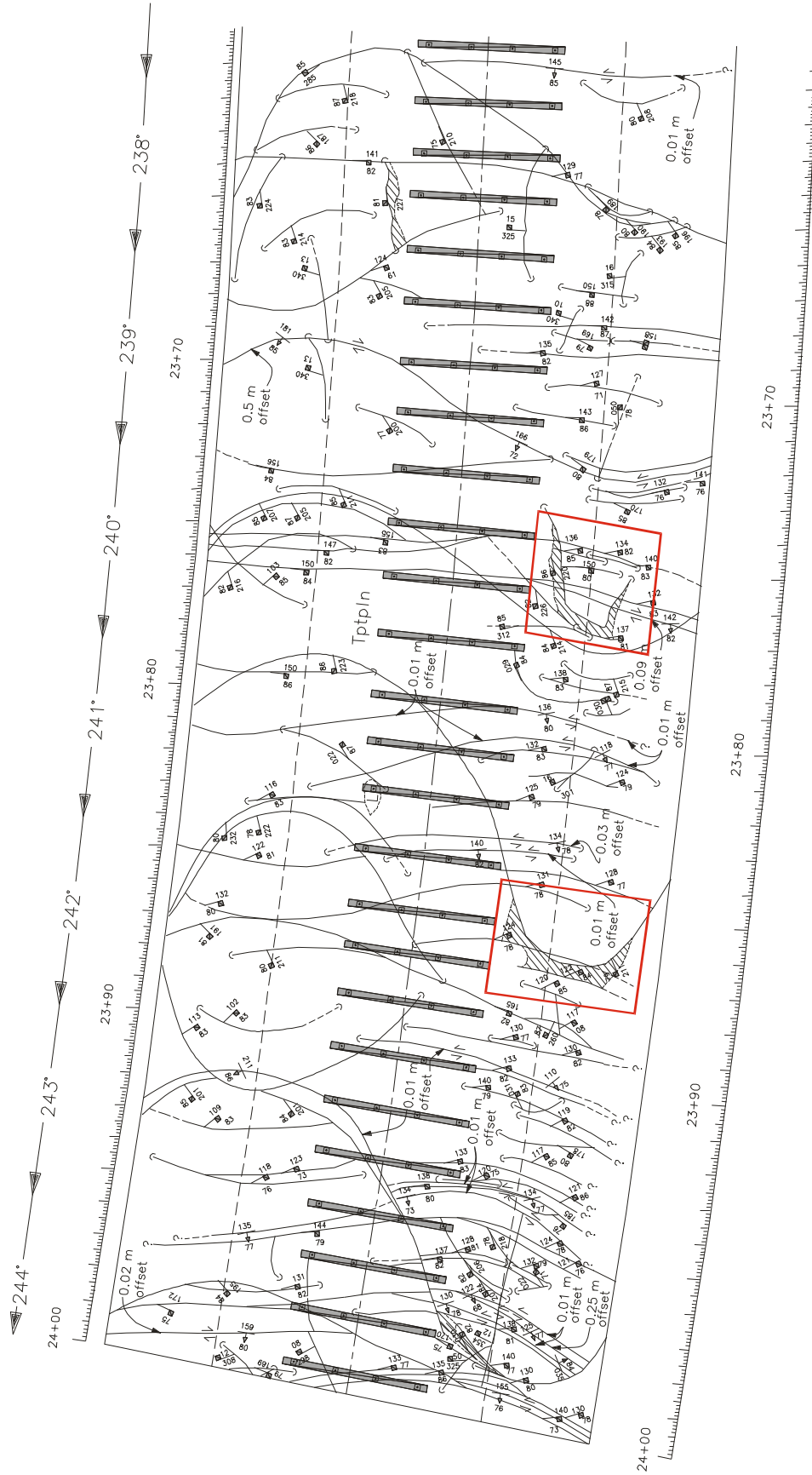
Source: GS990408314224.004 [DIRS 108405].

Figure F-12. Key-Block Location, Tptpmn Unit, ECRB Cross-Drift Stations 13+60 to 14+00



Source: GS990408314224.004 [DIRS 108405].

Figure F-13. Key-Block Location, Tptpmn Unit, ECRB Cross-Drift Stations 14+00 to 14+30



Source: GS990408314224.006 [DIRS 108409].

Figure F-14. Key-Block Location, Tptpln Unit, ECRB Cross-Drift Stations 23+65 to 24+00

INTENTIONALLY LEFT BLANK

**APPENDIX G**

**NATURAL ANALOGUES OF THE EFFECT OF SEISMIC EVENTS ON THE  
DEGRADATION OF UNDERGROUND STRUCTURES**





## **NATURAL ANALOGUES OF THE EFFECT OF SEISMIC EVENTS ON THE DEGRADATION OF UNDERGROUND STRUCTURES**

### **G1. ANALOGUES OF MAJOR EARTHQUAKES**

On July 28, 1976, a magnitude 7.8 earthquake occurred in Tang-Shan, China, a city with both substantial mining and industrial facilities. Surface shaking intensities at Tang-Shan were such that in the area where the strongest shaking occurred, 80 to 90 percent of the surface structures collapsed. However, for important engineered structures immediately below the surface, there was generally no serious damage regardless of the depth or size of the structure (Wang 1985 [DIRS 151821], p. 741).

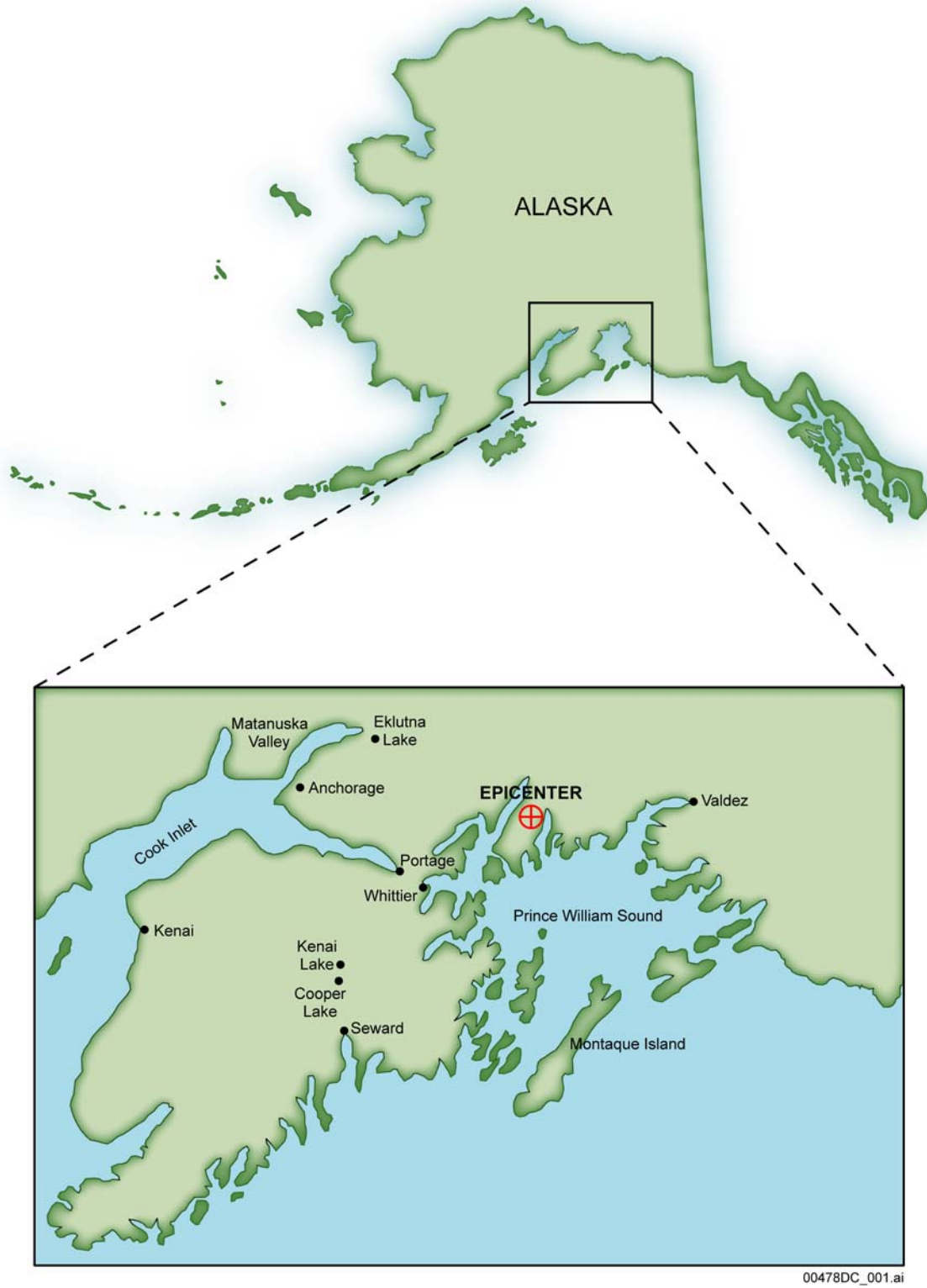
The USGS reported in the lessons and conclusions of the Alaskan earthquake on March 28, 1964 that no significant damage was reported to underground facilities, including mines and tunnels, as a result of the earthquake, although some rocks were shaken loose in places. The epicenter of the earthquake is shown in Figure G-1. Included in this analysis were studies of the coal mines in the Matanuska Valley, which were undamaged; the railroad tunnels near Whittie; the tunnel and penstocks at the Eklutna Hydroelectric Project; and the Chugach Electric Association tunnel between Cooper Lake and Kenai Lake. There were also no reports of damage to the oil and gas wells in and along Cook Inlet. The reports of no damage from the Alaskan earthquake are significant. With a moment magnitude is 9.2 (Kanamori 1977 [DIRS 167797], p. 2982), this earthquake was one of the largest to occur in this country, and surface damage was extreme (Pratt et al. 1978 [DIRS 151817], p. 32).

### **G2. ANALOGUE OF A RECENT EARTHQUAKE**

An example of a more recent earthquake can be found in the January 16, 1995, earthquake in Kobe, Japan, which had a magnitude of 6.9 (Bolt 1997 [DIRS 167798], p. 273). In this earthquake, tunnels in the epicentral region experienced no major damage (partial or total collapse) for peak ground accelerations measured at the surface of approximately 0.6 g (Savino et al. 1999 [DIRS 148612]).

### **G3. ANALOGUE OF A SITE-SPECIFIC EARTHQUAKE**

On June 29, 1992, a magnitude 5.6 earthquake occurred at Little Skull Mountain about 20 km from Yucca Mountain. Within days of the earthquake, a team of scientists examined the interior of the tunnel 125 meters deep in the epicentral region of the earthquake. The team reported no evidence of damage in the tunnel that could be associated with the earthquake (Savino et al. 1999 [DIRS 148612]).



00478DC\_001.ai

Source: Eckel 1970 [DIRS 157493].

Figure G-1. Epicenter of the 1964 Alaskan Earthquake

#### G4. DISCUSSION

Underground facilities in general are less prone to seismic damage than surface facilities. In fact, earthquake design features are low on the list of design priorities for underground construction projects (Rowe 1992 [DIRS 156898]). Nevertheless, case studies where underground facilities subjected to earthquake received significant damage have been reported (Sharma and Judd 1991 [DIRS 154505]; Rowe 1992 [DIRS 156898]; Raney 1988 [DIRS 147173]). These cases are in general characterized by either shallow overburden (Sharma and Judd 1991 [DIRS 154505]), poor ground condition (Rowe 1992 [DIRS 156898]), fault intersection (Stevens 1977 [DIRS 154501]; Rowe 1992 [DIRS 156898]), or are near the epicenter (Stevens 1977 [DIRS 154501]; Raney 1988 [DIRS 147173]). Sharma and Judd (1991 [DIRS 154505]) generated an extensive database of seismic damage to underground structures using 192 case histories. They reported that there is considerably less damage at depths greater than 50 m, and no heavy damage below 300 m. Rowe (1992 [DIRS 156898]) stated that total collapse of a civil engineering tunnel is invariably associated with the movement of an intersecting fault, and tunneling in soft, poor-quality ground is more susceptible to damage from earthquakes than those constructed in hard, competent rock. Stevens (1977 [DIRS 154501]) concluded that severe damage is inevitable when a mine or tunnel intersects a fault along which movement occurs and mines in the epicentral region of strong motions may suffer severe damage by shaking. Raney (1988 [DIRS 147173]) reported the effects of selected earthquakes in the western North American intermontane region and provided the observation of subsurface damages for 28 earthquakes. No damage was reported in 22 earthquakes and minor damage with spalling reported for 3 earthquakes. For the 3 cases with reporting damage, a “considerable portion of mine tunnels” was caved at Kennedy, Nevada near the epicenter for the 1915 Pleasant Valley, Nevada earthquake. No details were provided for the other 2 cases: the Quality Mine after the 1934 Excelsior Mountains earthquake (southeast of Hawthorne, Nevada) and Kraken Hill Mine after the 1983 Borah Peak, Idaho earthquake.

INTENTIONALLY LEFT BLANK

**APPENDIX H**  
**3DEC PROGRAM MODIFICATION AND MODEL OPTIMIZATION**  
**FOR ROCKFALL ANALYSIS**



## **3DEC PROGRAM MODIFICATION AND MODEL OPTIMIZATION FOR ROCKFALL ANALYSIS**

### **H1. INTRODUCTION**

Although 3DEC is fully capable for dynamic rockfall calculations, program modifications and optimization of the computer model are required in order to solve complex rockfall problems within a reasonable time frame. The complexity of the rockfall problems includes:

- Incorporating field fracture geometries with relatively short trace length
- Subjecting the rock mass to postclosure ground motion time histories
- Subjecting the rock mass to thermal stresses induced from emplaced waste
- Conducting a large number of analyses to obtain a statistically meaningful rockfall frequency and size distribution.

### **H2. 3DEC PROGRAM MODIFICATION**

Modifications of the 3DEC program for rockfall analyses include: (1) free-field boundaries, (2) partial density scaling for dynamic analysis, and (3) variable mechanical properties within a contact. A detailed description of the implementation and verification of these enhancements is provided by Lemos and Damjanac (2002 [DIRS 162058]). These modifications are included in the qualified version of 3DEC (Version 2.01). The areas of modification were validated during software qualification process. This appendix provides a brief description of these modifications and their relevance to rockfall analyses.

#### **H2.1 FREE-FIELD BOUNDARIES**

The free-field boundaries ensure that plane waves propagating upward suffer no distortion at the boundary because the free-field grid supplies conditions that are identical to those in an infinite model. In order to apply a free-field boundary in 3DEC, the model must be oriented such that the base is horizontal and its normal is in the direction of the y-axis, and the sides are vertical and their normals are in the direction of either the x-axis or z-axis.

The free-field model consists of four plane free-field grids on the side boundaries of the model and four column free-field grids at the corners. The four corner free-field columns act as free-field boundaries for the plane free-field grids. The plane free-field grids are two-dimensional models that consider infinite extension in the direction normal to the plane. The column free-field grids are one-dimensional models that consider infinite extension in both horizontal directions. Both the plane and column grids consist of standard 3DEC zones, which have gridpoints constrained in such a way to achieve the infinite extension consideration. The zoning of free-field blocks is similar to the model side faces. The side free-field blocks have two gridpoints across the thickness that are linked to move together. The corner free-field meshes have four gridpoints at each elevation, also linked to move together.

## H2.2 PARTIAL DENSITY SCALING FOR DYNAMIC ANALYSIS

Density scaling is a technique used in 3DEC in quasi-static calculations that substantially improves the efficiency of obtaining solutions. For the case of complex jointing models, zones with edge lengths much smaller than the average zone edge length are created during the automatic meshing procedure. These zones require very small time steps for numerical stability of the explicit algorithm. The critical time step is proportional to the smallest zone edge length. This makes the dynamic solution extremely time consuming. Density scaling only for those very small zones (a couple of orders of magnitude smaller than the average zone size) for dynamic analysis eliminates the very small time steps. The accuracy of the solution is preserved by keeping the change of the system inertia negligible. This scheme of partial density scaling is implemented in 3DEC in such a way that the user controls the amount of scaling to be introduced.

## H2.3 VARIABLE MECHANICAL PROPERTIES WITHIN A CONTACT

A contact between two blocks in 3DEC is subdivided into a number of sub-contacts if the blocks involved in the contact are deformable. The sub-contacts are determined based on discretization of the block faces that create the contact. Discretization of contact into sub-contacts allows representation of variation of contact forces and deformation in the plane. In earlier versions of 3DEC, mechanical properties (e.g., normal and shear stiffness, shear strength) of sub-contacts were assigned based on material properties of the contact they belong to. A modification of the code allows assignment of material properties to the sub-contacts independent of the material properties of the contact (to which sub-contact belongs to). This capability allows the program to model the finite trace length fractures from FracMan. Figure H-1 shows an example of the finite trace length fractures with extension of the rock bridges (i.e., the dashed lines in Figure H-1) to form the distinct blocks in 3DEC.

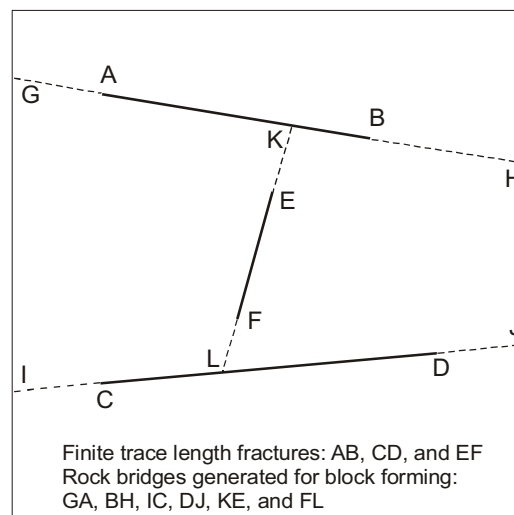


Figure H-1. Block Forming with Finite Trace Length Fractures and Rock Bridges in 3DEC



### H3. 3DEC MODEL OPTIMIZATION

Model optimization involves two aspects: reducing the model size and increasing the time step. 3DEC is based on a dynamic (time domain) algorithm that solves the equations of motion of the block system by an explicit finite difference method. A time step must be chosen that is smaller than some critical time step but is reasonable for solution time.

#### H3.1 REDUCING THE MODEL SIZE

The following methods are used to reduce the model size:

- A. Joints are generated within a limited domain as a representative volume around the drift. The representative volume extends one diameter at the side and two diameters on the top of the opening as shown in Figure 6-34 in Section 6.3.1.1. A sensitivity study of the size of the representative volume to rockfall prediction is presented in Section 6.3.1.6.5.
- B. Only blocks intersected by circular joints are cut during joint generation. Joints are sorted based on their trace length in a descending order. An algorithm is placed in the block cutting process to hide the blocks that are not intersected by the joint considered.
- C. Blocks that have face-face contact and their contact properties are completely solid are joined. That is, several blocks are merged to one if their contacts are solid. Blocks that have partial cracks between them are not joined. This approach allows for an analysis of the potential for crack extension.

#### H3.2 INCREASING THE TIME STEP

3DEC is based on a dynamic (time domain) algorithm that solves the equations of motion of the block system by an explicit finite difference method. The solution scheme used for the distinct element method is conditionally stable if the selected limiting time step satisfies both the stability criterion for calculation of internal block deformation as well as that for inter-block relative displacement. Even though explicit calculations execute very rapidly per time step, some way of increasing the time step is desirable in order to reduce computer time.

The following methods are used to increase the time step:

- A. Calculation of the time steps is a function of the minimum length (zone edge length) and stiffness (Itasca Consulting Group 2002 [DIRS 160331], Manual/3DEC). Cutting blocks with random joints results in very small block edge lengths. Blocks with a small volume (i.e., less than  $0.01\text{m}^3$ ) are deleted in the model to eliminate part of the blocks with small zone edge lengths. However, blocks of large volume may contain one or two small edges. An algorithm was developed that alters the geometry of these blocks and removes small edges less than 10 cm in length. The blocks were first detected and their geometry is stored in a data structure before they were deleted. New blocks are constructed within the bounds of the original blocks. In most cases, two close vertices are contracted into a single vertex. Faces that have both vertices lose one vertex. If the face already has only three vertices, then the entire face is

deleted. On faces that have only one of two vertices, a new face with co-planarity of vertices is created. The flow chart for the algorithm is shown in Figure H-2.

- B. The method of partial density scaling was adopted for dynamic analysis. Partial density scaling was implemented for dynamic analysis in 3DEC as described in Section H2.2. A time step of  $3 \times 10^{-5}$  seconds is set for the analysis, which satisfies the stability criteria for calculation and provides a solution in a reasonable time. This results in an increase of system mass ranging from 1 to 4 percent. The amount of increase is consistent with the verification problem provided by Lemos and Damjanac (2002 [DIRS 162058]). The accuracy of the solution is therefore preserved by keeping the change of the system inertia negligible.

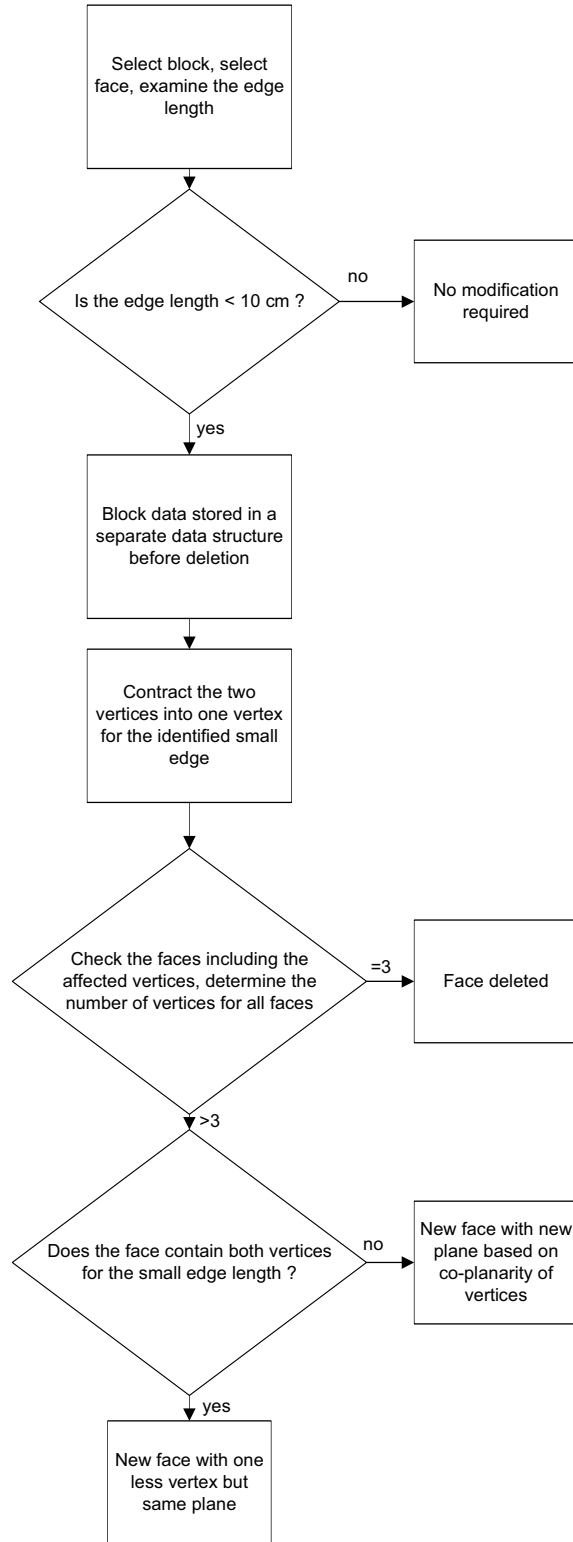


Figure H-2. Flow Chart for Treating the Small Edge Length Block

INTENTIONALLY LEFT BLANK

**APPENDIX I**  
**BLOCK SIZE GEOMETRY**



## **BLOCK SIZE GEOMETRY**

The predicted rock blocks impacting the drip shield have many different sizes and shapes. Since the block geometry information is mainly used for drip shield impact calculations, the geometry of large blocks is provided in this appendix. A total of 7 blocks with volume greater than 2.5 m<sup>3</sup> (6 metric tons) was selected for presentation. Blocks with high impact energy were considered during the selection process. The block geometric information for each individual block is presented in Figures I-1 to I-7 respectively. Six different views are provided for each block to illustrate the complex geometry observed for most large blocks. Most of the blocks consist of many surfaces and some of them have highly irregular shapes that are the end result of a non-persistent fracture network.

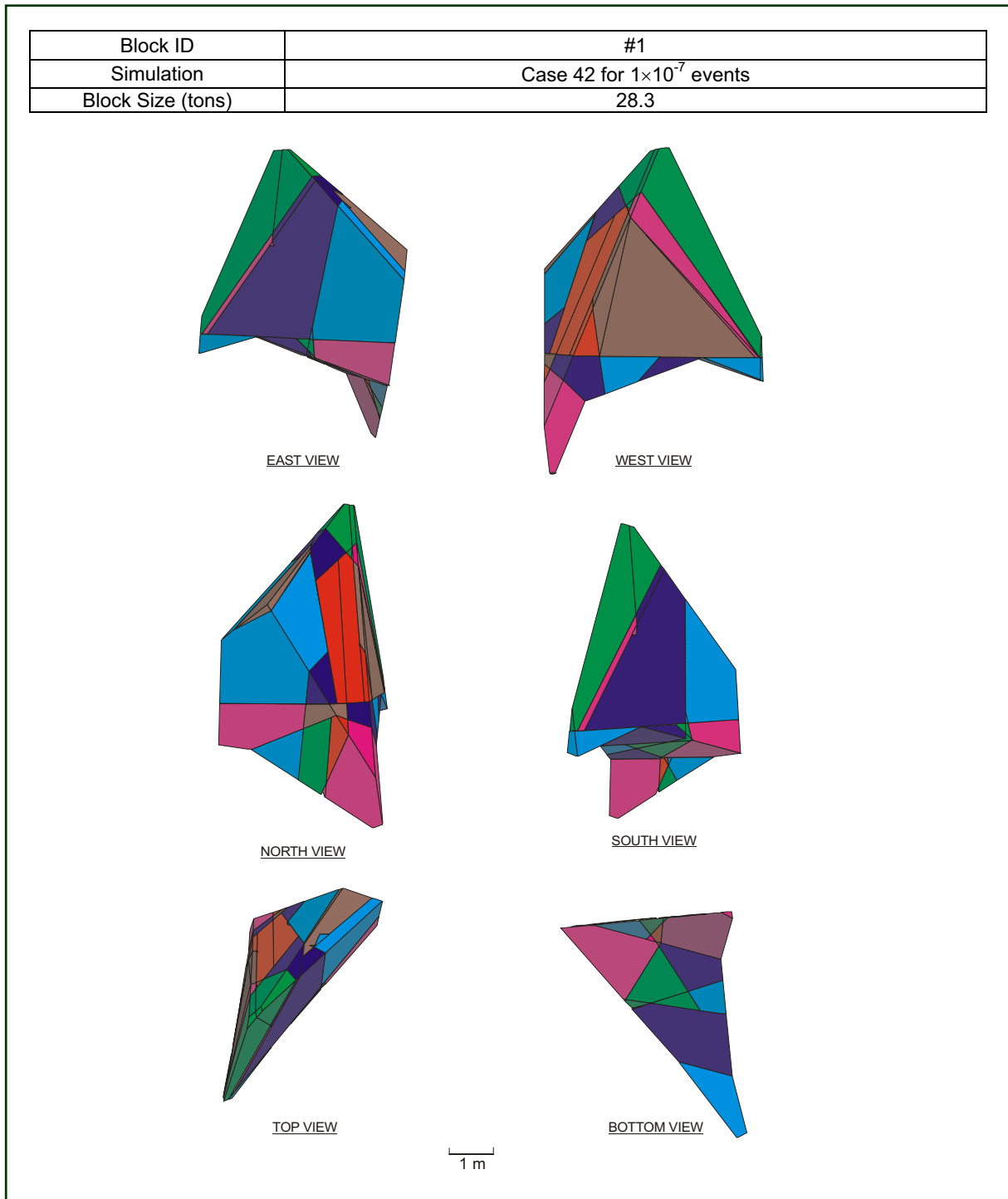


Figure I-1. Block Geometry Information for Block #1



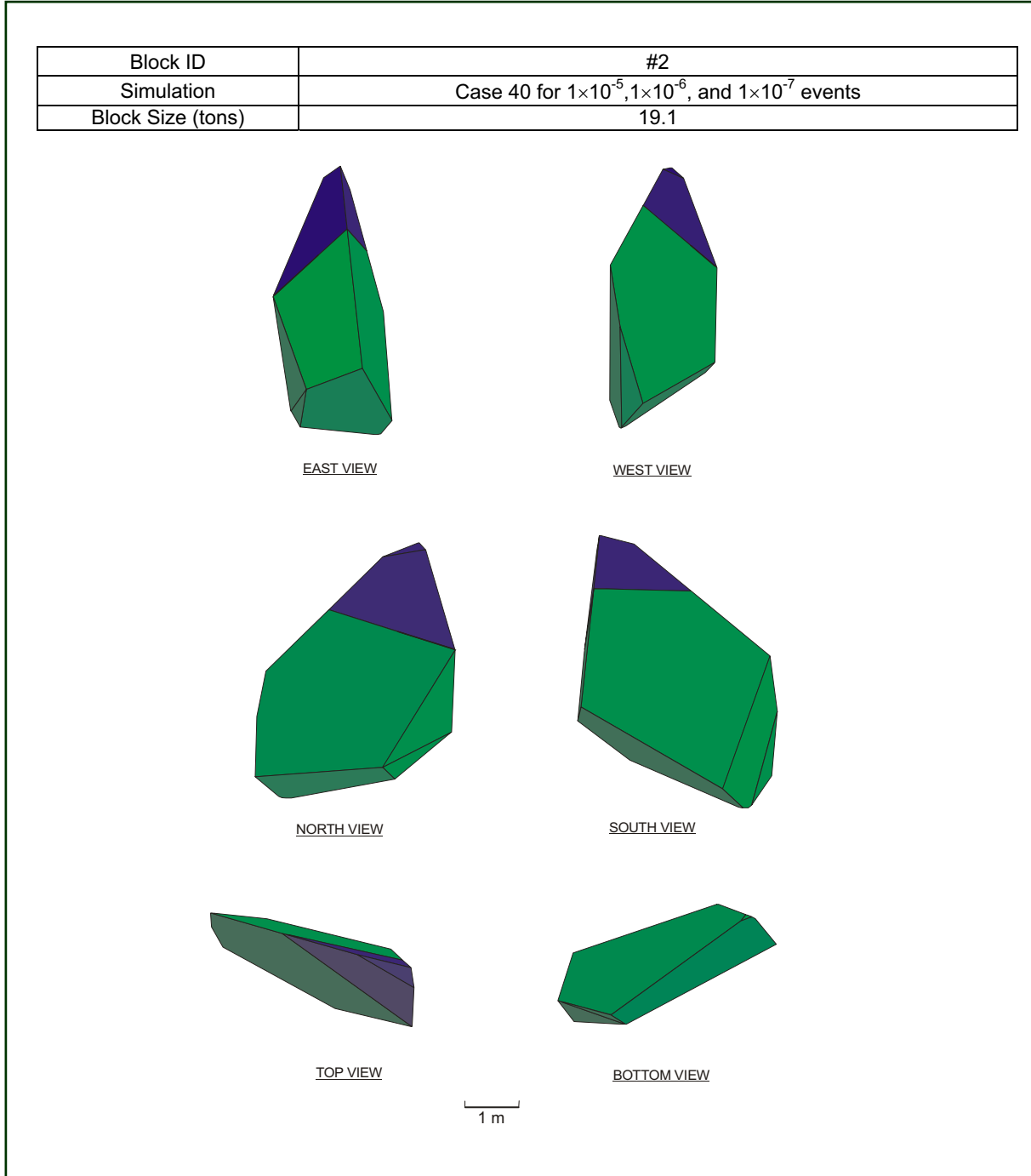


Figure I-2. Block Geometry Information for Block #2

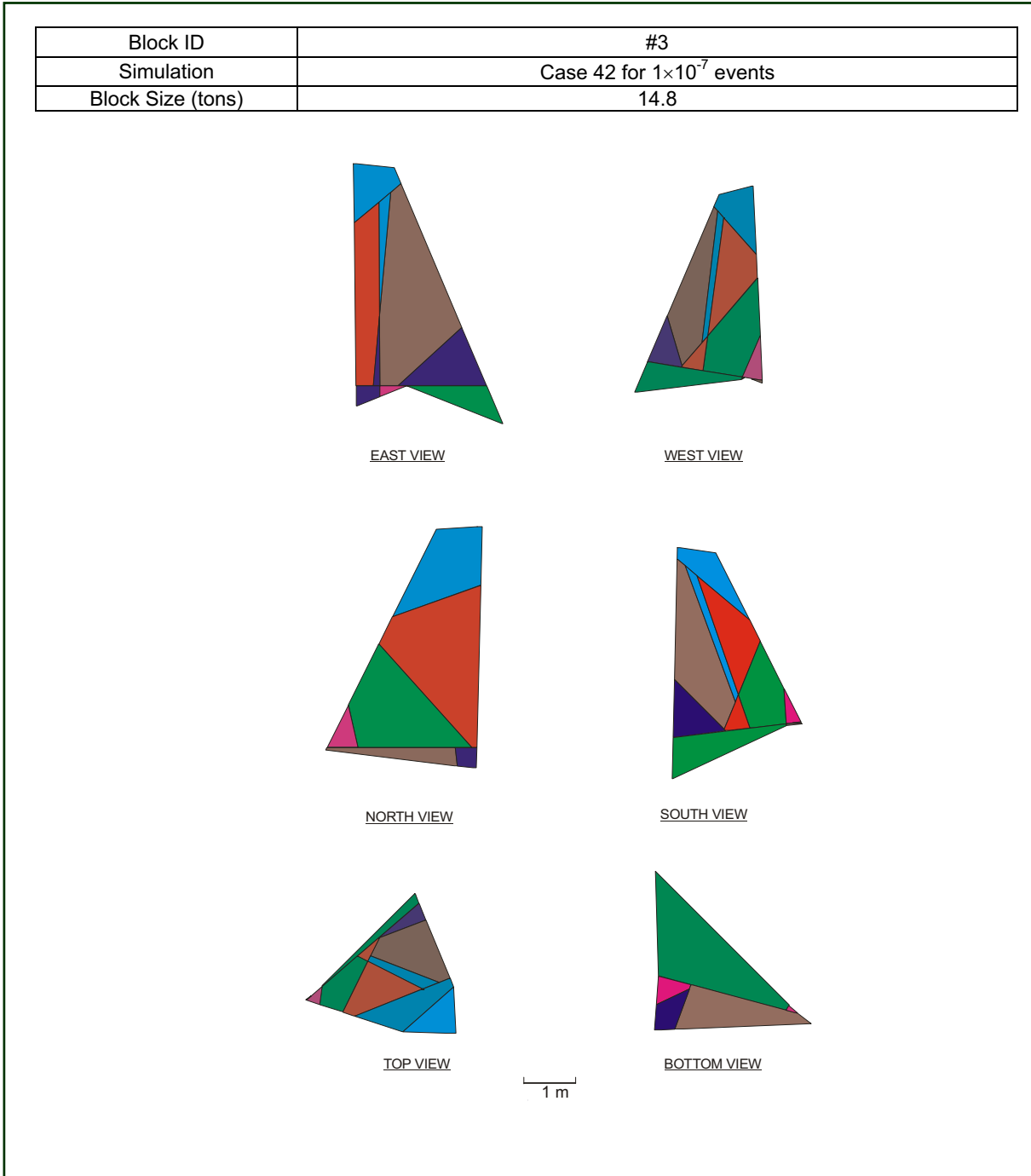


Figure I-3. Block Geometry Information for Block #3

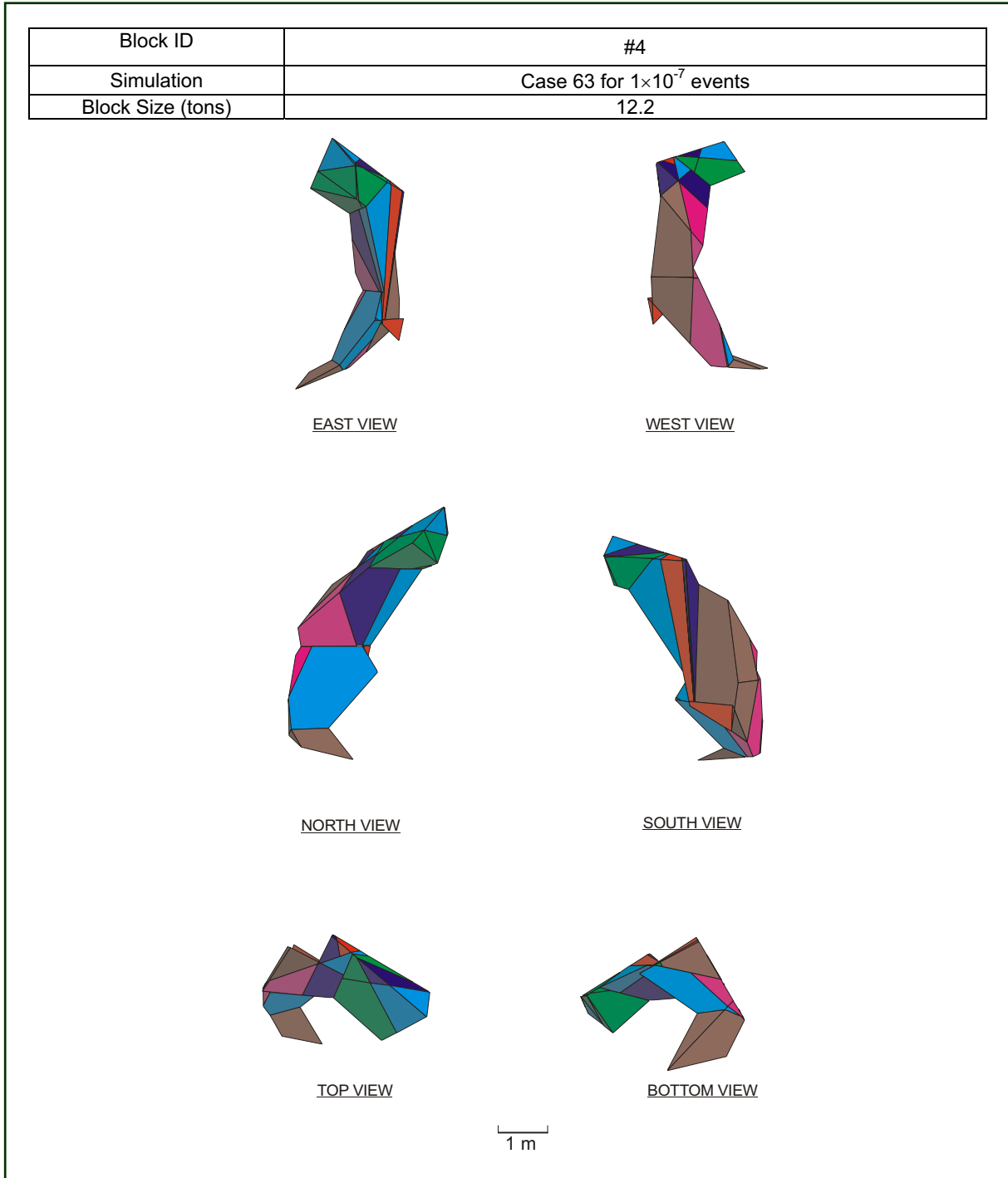


Figure I-4. Block Geometry Information for Block #4

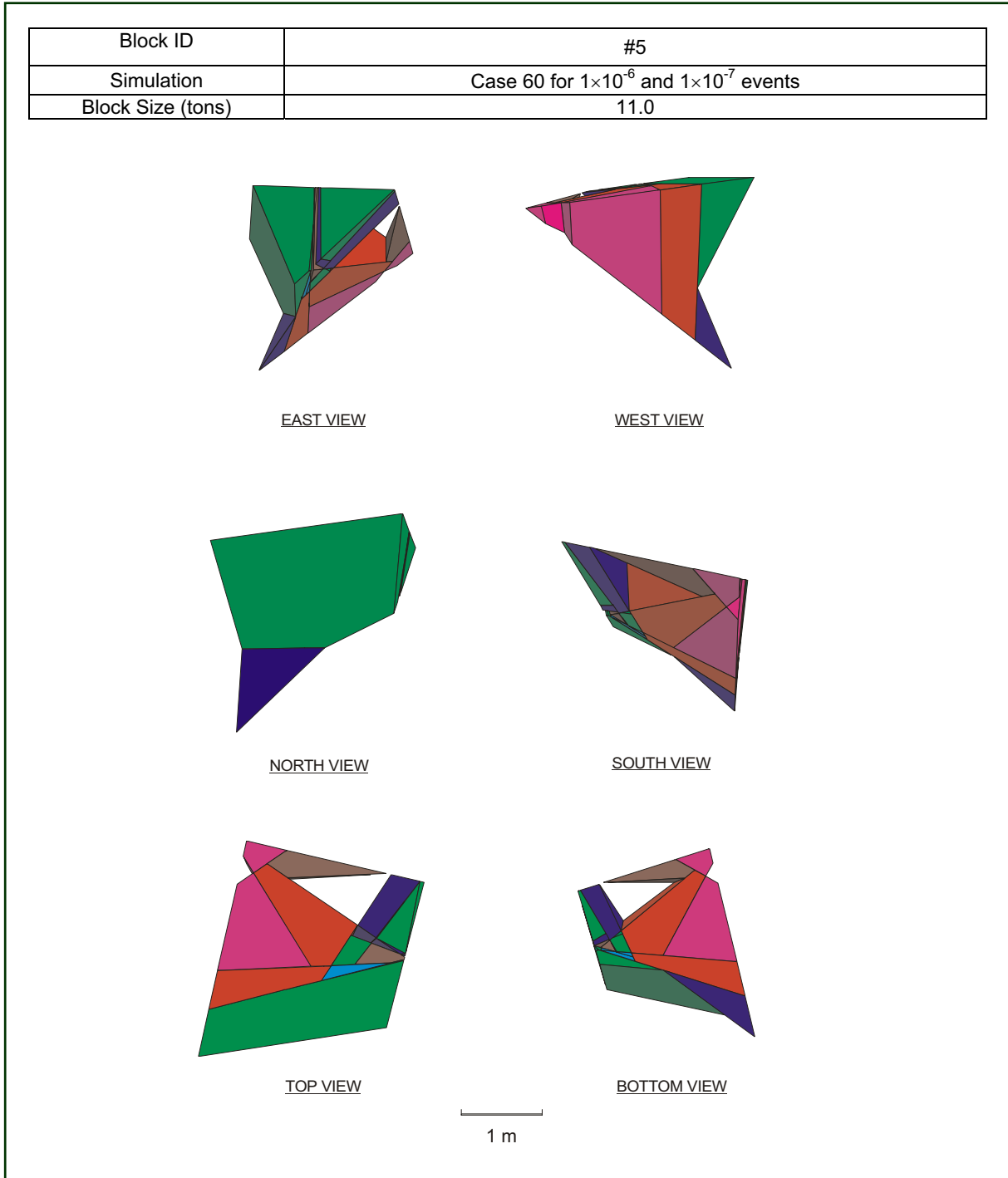


Figure I-5. Block Geometry Information for Block #5

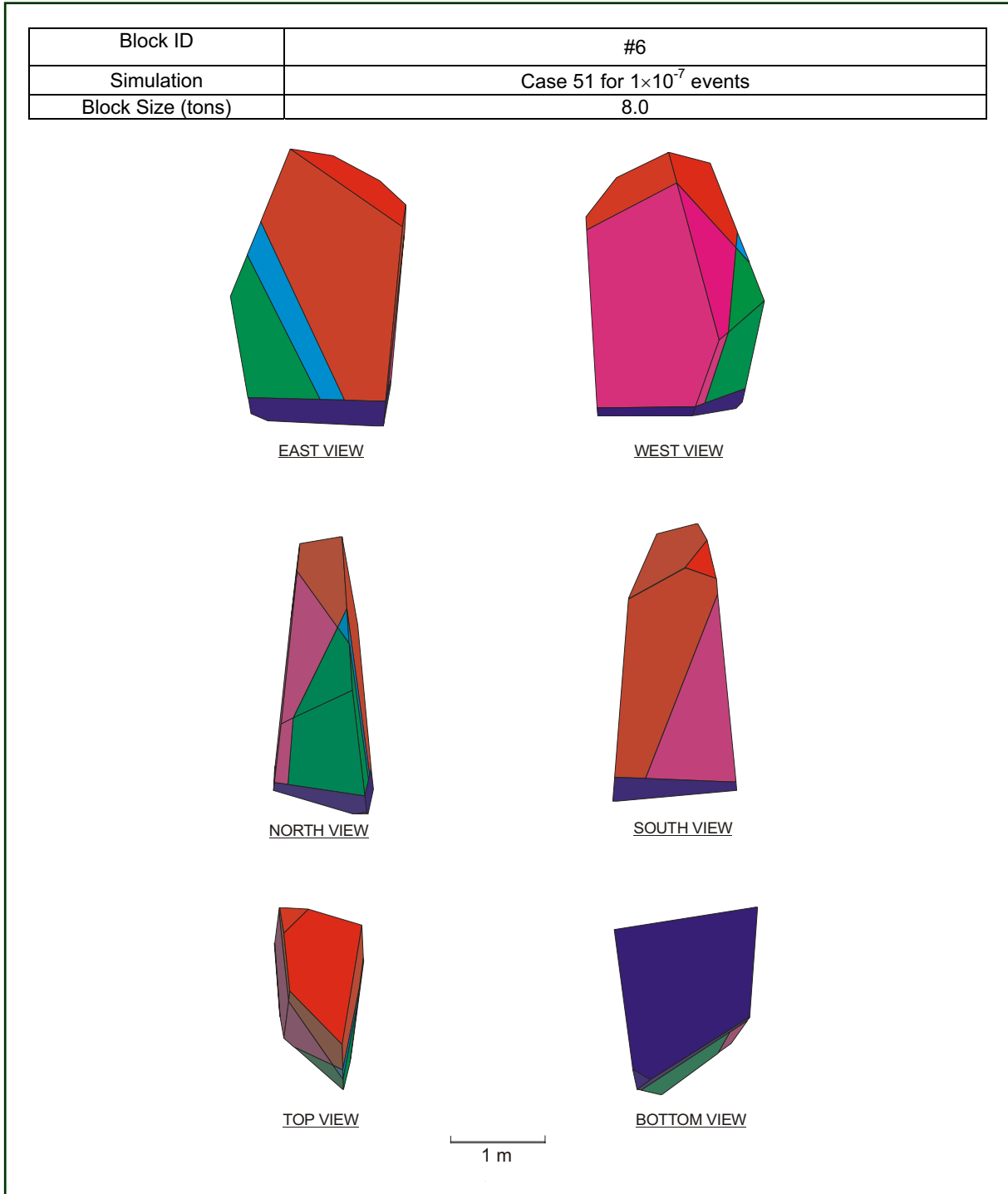


Figure I-6. Block Geometry Information for Block #6

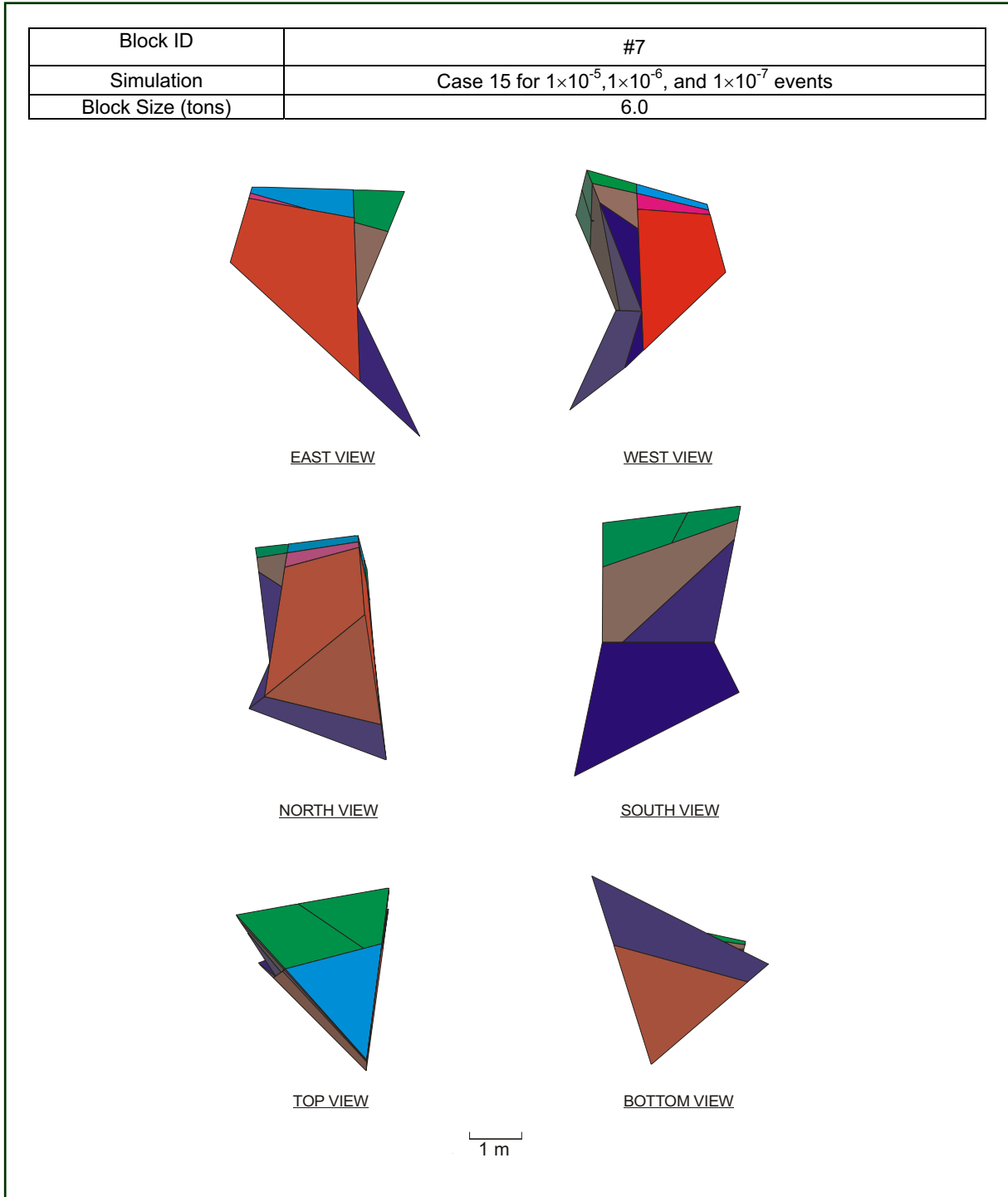


Figure I-7. Block Geometry Information for Block #7

**APPENDIX J**

**RANDOM SELECTION OF 3DEC MODELING REGION IN A 100-M CUBE  
FRACTURE NETWORK GENERATED BY FRACMAN**

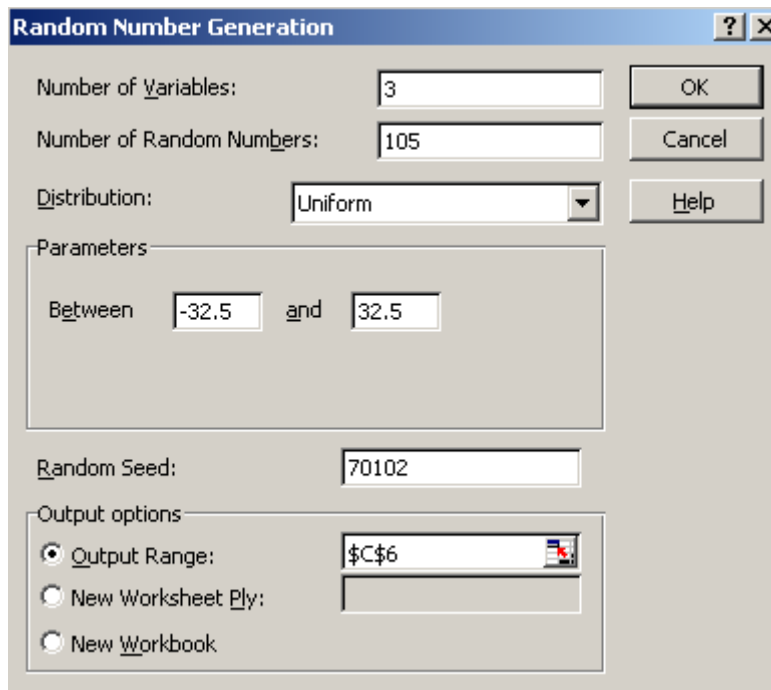




## RANDOM SELECTION OF 3DEC MODELING REGION IN A 100-M CUBE FRACTURE NETWORK GENERATED BY FRACMAN

A random selection of the 3DEC modeling region within a 100 m FracMan fracture network cube was conducted using the random number generation function provided in Microsoft Excel's spreadsheet analysis tools. Each 3DEC modeling region was uniquely determined by choosing the centroid of the modeling block. A random number generator with a uniform distribution in the range of -32.5 to 32.5 was used to generate the x-, y-, and z-coordinates. The range was selected so that the selected region was free of edge effects. The Microsoft Excel inputs for random number generation are shown in Figure J-1.

Table J-1 lists the 105 selected centroid locations. The centroids are projected to the X-Y, X-Z, and Y-Z planes as shown in Figures J-2 to J-4.



The screenshot shows the 'Random Number Generation' dialog box in Microsoft Excel. The dialog box has a title bar with a question mark and a close button. It contains several input fields and buttons. 'Number of Variables' is set to 3, 'Number of Random Numbers' is set to 105, and 'Distribution' is set to 'Uniform'. The 'Parameters' section shows 'Between -32.5 and 32.5'. The 'Random Seed' is set to 70102. The 'Output options' section has three radio buttons: 'Output Range' (selected), 'New Worksheet Ply', and 'New Workbook'. The 'Output Range' field is set to '\$C\$6'.

Figure J-1. Microsoft Excel Inputs for Random Number Generation

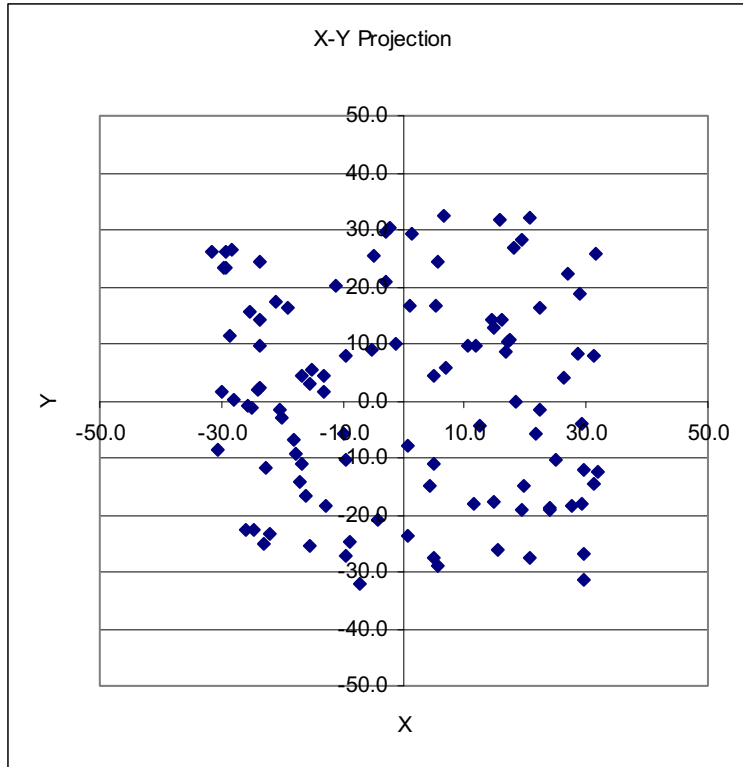


Figure J-2. Centroid Locations Projected to X-Y Plane

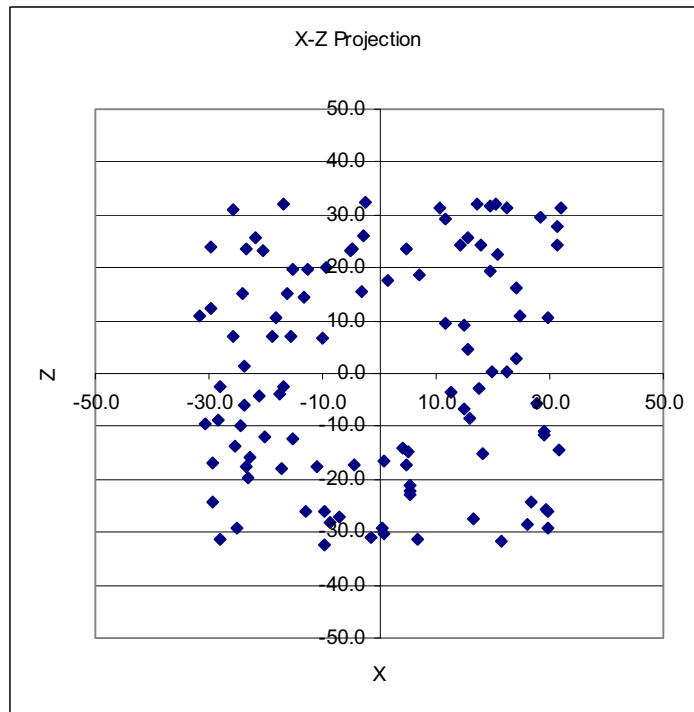


Figure J-3. Centroid Locations Projected to X-Z Plane

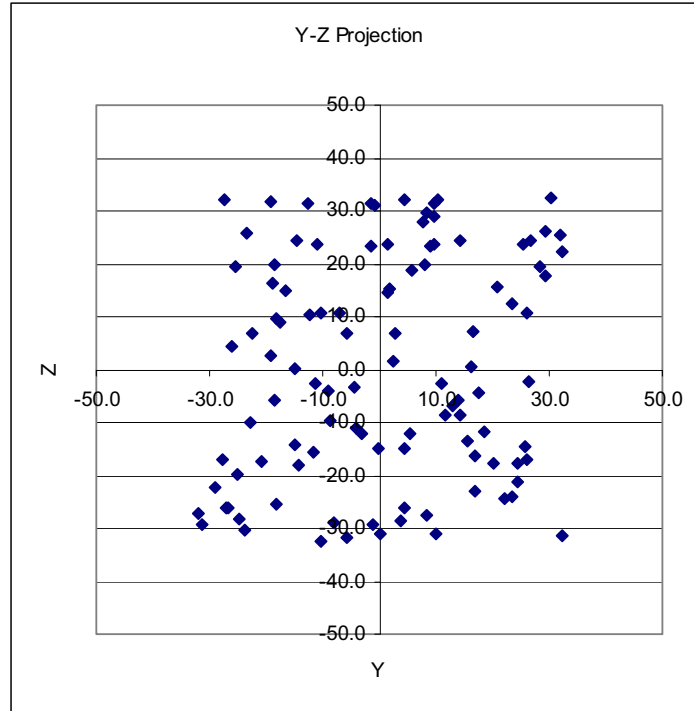


Figure J-4. Centroid Locations Projected to Y-Z Plane

Table J-1. Listing of Fracture Model Region Centroid Coordinates

Model Region	Centroid of Fracture Model Region		
	Xc	Yc	Zc
1	-2.8	29.5	26.0
2	-23.7	2.4	1.5
3	29.5	-26.7	-26.1
4	-16.7	4.5	32.2
5	28.5	8.3	29.6
6	-4.4	-20.8	-17.4
7	-20.2	-3.1	-12.1
8	-23.6	24.4	-17.7
9	-7.2	-32.0	-27.0
10	22.4	16.2	0.4
11	-17.2	-14.2	-18.1
12	-9.7	-27.1	-26.0
13	-21.1	17.5	-4.2
14	24.9	-10.4	10.8
15	19.5	28.3	19.4
16	-15.3	5.5	-12.3
17	-28.1	0.3	-31.2
18	10.6	9.8	31.5
19	-2.3	30.2	32.4

Table J-1. Listing of Fracture Model Region Centroid Coordinates (Continued)

Model Region	Centroid of Fracture Model Region		
	Xc	Yc	Zc
20	14.8	-17.7	9.0
21	-15.6	2.9	6.9
22	-25.3	15.5	-13.6
23	-16.8	-11.2	-2.6
24	18.3	0.0	-15.0
25	17.1	10.3	32.0
26	31.9	-12.6	31.3
27	27.6	-18.6	-5.8
28	21.6	-5.8	-31.9
29	-23.6	14.0	-5.9
30	6.6	32.3	-31.4
31	-3.1	20.7	15.4
32	-11.1	20.0	-17.7
33	-29.4	26.2	-16.9
34	-1.4	10.0	-31.0
35	-31.5	26.1	10.7
36	4.8	-11.1	23.7
37	6.9	5.7	18.8
38	29.6	-31.4	-29.3
39	-25.1	-1.1	-29.3
40	16.0	14.2	-8.6
41	29.2	-4.1	-11.0
42	26.8	22.2	-24.3
43	-13.3	1.5	14.4
44	14.4	14.2	24.3
45	-29.2	23.4	-24.2
46	5.5	24.4	-21.1
47	18.0	26.9	24.4
48	19.8	-14.9	0.3
49	-18.1	-6.9	10.6
50	14.9	12.9	-6.8
51	11.7	9.5	29.1
52	29.3	-18.2	-25.5
53	-15.3	-25.5	19.6
54	-29.5	23.5	12.3
55	-25.6	-1.0	30.9
56	4.3	-15.1	-14.1
57	16.7	8.5	-27.5
58	-22.7	-11.6	-15.7
59	15.7	31.8	25.6
60	0.6	-8.0	-29.1
61	-4.8	25.4	23.7

Table J-1. Listing of Fracture Model Region Centroid Coordinates (Continued)

Model Region	Centroid of Fracture Model Region		
	Xc	Yc	Zc
62	31.2	7.7	27.9
63	-16.1	-16.7	15.0
64	-9.6	-10.4	-32.4
65	-25.9	-22.5	6.9
66	29.0	18.6	-11.7
67	-23.0	-25.1	-19.7
68	1.0	16.8	-16.4
69	-20.6	-1.4	23.4
70	12.7	-4.4	-3.4
71	-9.8	-5.8	6.8
72	-8.8	-24.7	-28.2
73	-24.6	-22.7	-9.9
74	20.7	32.2	22.4
75	-19.0	16.4	7.1
76	23.9	-19.0	2.8
77	24.1	-18.8	16.3
78	-9.4	7.9	20.0
79	-24.1	1.9	15.2
80	26.2	3.9	-28.7
81	17.5	10.8	-2.7
82	-5.2	8.9	23.2
83	5.3	16.8	-23.1
84	19.4	-19.3	31.9
85	22.4	-1.6	31.4
86	20.6	-27.4	32.1
87	11.6	-18.2	9.5
88	-17.6	-9.2	-4.0
89	31.6	25.8	-14.4
90	31.2	-14.7	24.5
91	-28.5	11.6	-8.8
92	-30.6	-8.7	-9.7
93	29.7	-12.2	10.5
94	-28.2	26.5	-2.4
95	-13.0	4.3	-26.2
96	-29.8	1.6	23.9
97	15.5	-26.1	4.6
98	4.9	4.3	-14.7
99	1.4	29.3	17.8
100	4.8	-27.6	-17.1
101	-23.6	9.7	23.7
102	-12.7	-18.5	19.9
103	0.8	-23.8	-30.4

Table J-1. Listing of Fracture Model Region Centroid Coordinates (Continued)

<b>Model Region</b>	<b>Centroid of Fracture Model Region</b>		
	<b>Xc</b>	<b>Yc</b>	<b>Zc</b>
104	5.5	-29.0	-22.3
105	-22.0	-23.3	25.8

**APPENDIX K**

**SUFFICIENCY OF THE NUMBER OF 3DEC SIMULATIONS TO REPRESENT THE  
ROCKFALL CHARACTERISTICS**





## SUFFICIENCY OF THE NUMBER OF 3DEC SIMULATIONS TO REPRESENT THE ROCKFALL CHARACTERISTICS

This appendix addresses the issue on the sufficiency of the number of 3DEC simulations to represent the likely rockfall characteristics, such as block size, relative impact velocity, and impact energy of the rock to the drip shield. Summary statistics of the rockfall characteristics was compiled after each 5-run increment. The statistics, such as mean, median, maximum, and standard deviation, was then observed for the trend. The block size distribution was also observed to ensure the analyses results capture the proper rockfall size distribution.

Figures K-1 to K-3 shows the trend of the statistics for the analyses considering the  $1 \times 10^{-4}$  annual probability of exceedance ground motion with a total of 32 3DEC simulations. The corresponding numeric values for the statistics are tabulated in Tables K-1 to K-3. The maximum values of the block size, impact velocity, and impact energy occur between the 11<sup>th</sup> and 15<sup>th</sup> simulation. The trend shows that the statistics of rockfall characteristics approaches to asymptotic value approximately 15 to 20 runs of 3DEC simulation. Figure K-4 presents the block size cumulative distribution for the evolution of the analyses, the distribution also shows that approximately 15 to 20 runs of 3DEC simulation provide adequate representation of the size distribution.

Table K-1. Summary Statistics of Block Size (metric ton) for  $1 \times 10^{-4}$  Preclosure Ground Motion

Summary Statistics	1 <sup>st</sup> 5 runs	1 <sup>st</sup> 10 runs	1 <sup>st</sup> 15 runs	1 <sup>st</sup> 20 runs	1 <sup>st</sup> 25 runs	All 32 runs
Median	0.09	0.09	0.10	0.10	0.11	0.10
Mean	0.14	0.20	0.22	0.21	0.23	0.22
Maximum	0.69	2.04	2.72	2.72	2.72	2.72
Standard Deviation	0.14	0.29	0.35	0.33	0.35	0.33

Table K-2. Summary Statistics of Impact Velocity (m/sec) for  $1 \times 10^{-4}$  Preclosure Ground Motion

Summary Statistics	1 <sup>st</sup> 5 runs	1 <sup>st</sup> 10 runs	1 <sup>st</sup> 15 runs	1 <sup>st</sup> 20 runs	1 <sup>st</sup> 25 runs	All 32 runs
Median	2.40	2.30	2.36	2.22	2.36	2.25
Mean	2.51	2.47	2.58	2.47	2.57	2.43
Maximum	6.38	6.38	7.20	7.20	7.20	7.20
Standard Deviation	1.36	1.38	1.54	1.46	1.40	1.38

Table K-3. Summary Statistics of Impact Energy (J) for  $1 \times 10^{-4}$  Preclosure Ground Motion

Summary Statistics	1 <sup>st</sup> 5 runs	1 <sup>st</sup> 10 runs	1 <sup>st</sup> 15 runs	1 <sup>st</sup> 20 runs	1 <sup>st</sup> 25 runs	All 32 runs
Median	303	290	316	249	310	232
Mean	676	933	1196	1030	1161	1022
Maximum	6127	10304	20358	20358	20358	20358
Standard Deviation	1113	1828	2664	2424	2430	2224

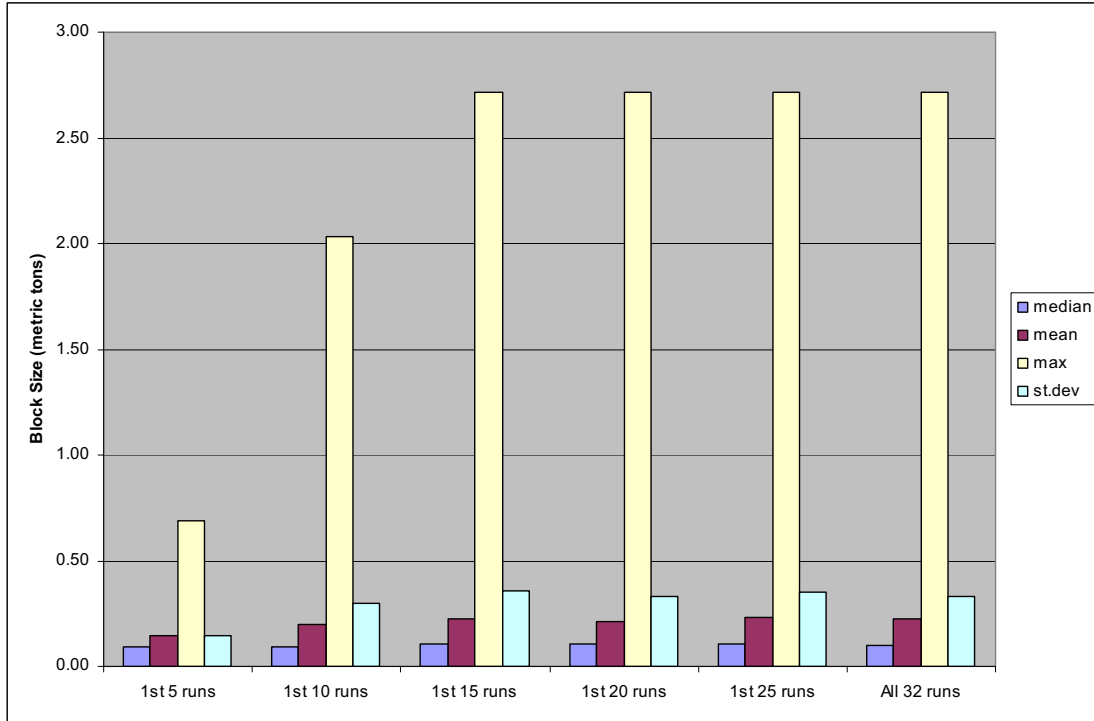


Figure K-1. Summary Statistics of Block Size (metric ton) for  $1 \times 10^{-4}$  Preclosure Ground Motion

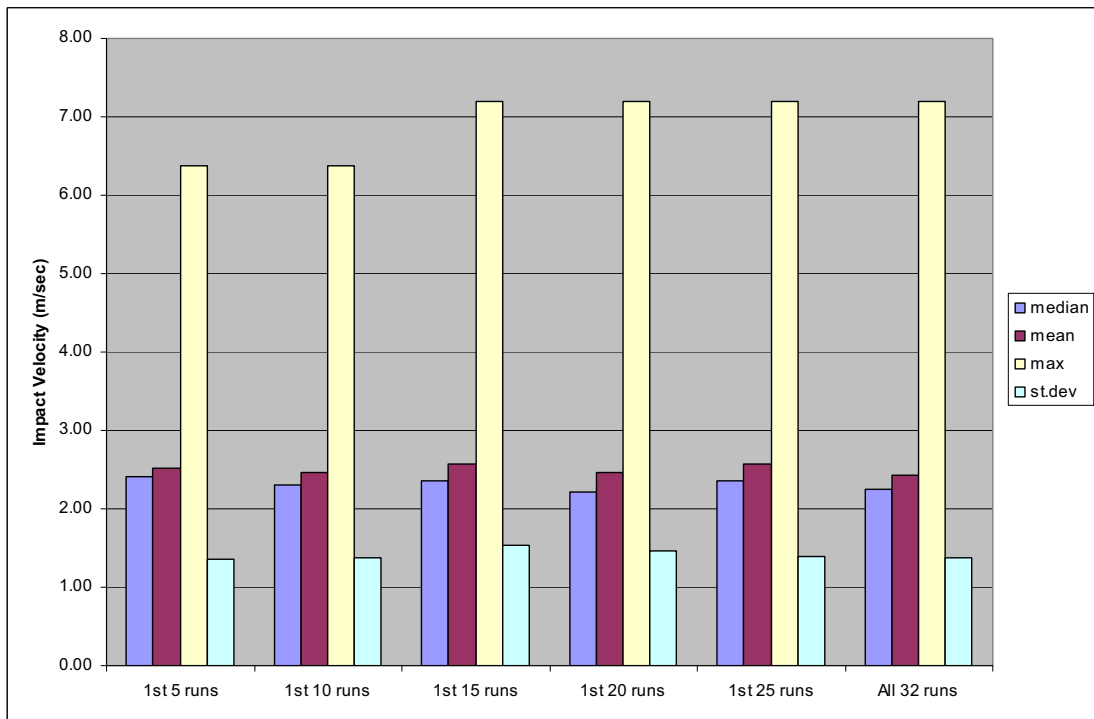


Figure K-2. Summary Statistics of Impact Velocity (m/sec) for  $1 \times 10^{-4}$  Preclosure Ground Motion

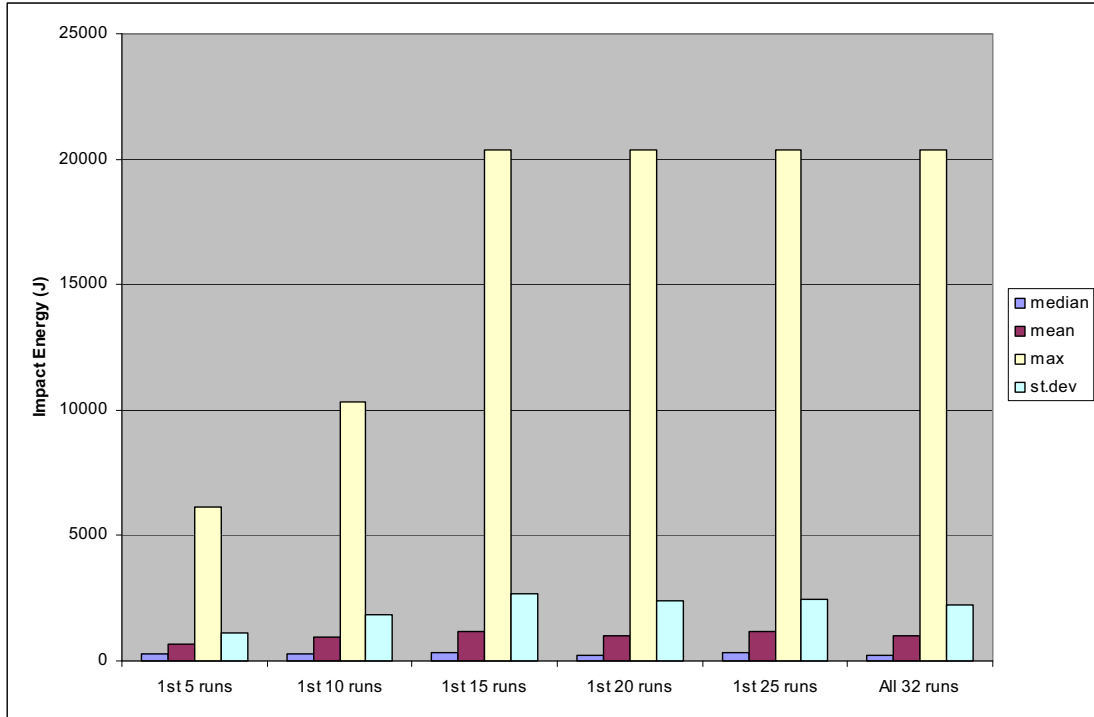


Figure K-3. Summary Statistics of Impact Energy (J) for  $1 \times 10^{-4}$  Preclosure Ground Motion

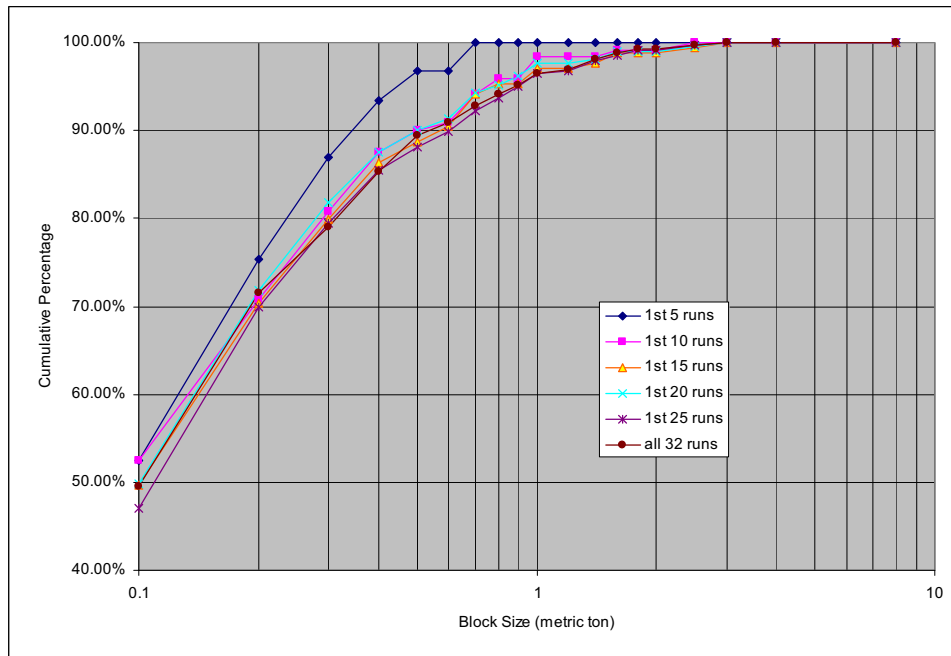


Figure K-4. Block Size Distribution for  $1 \times 10^{-4}$  Preclosure Ground Motion

Figures K-5 to K-7 shows the trend of the statistics for the analyses considering the  $1 \times 10^{-5}$  annual probability of exceedance ground motion with a total of 50 3DEC simulations. The corresponding numeric values for the statistics are tabulated in Tables K-4 to K-6. The maximum values of the block size, impact velocity, and impact energy occur between the 20<sup>th</sup> and 25<sup>th</sup> simulation. The trend shows that the statistics of rockfall characteristics approaches to asymptotic value approximately 25 to 30 runs of 3DEC simulation. Figure K-8 present the block size cumulative distribution for the evolution of the analyses, the distribution also shows that approximately 25 to 30 runs of 3DEC simulation provide adequate representation of the size distribution.

Table K-4. Summary Statistics of Block Size (metric ton) for  $1 \times 10^{-5}$  Ground Motion

<b>Summary Statistics</b>	<b>1<sup>st</sup> 5 runs</b>	<b>1<sup>st</sup> 10 runs</b>	<b>1<sup>st</sup> 15 runs</b>	<b>1<sup>st</sup> 20 runs</b>	<b>1<sup>st</sup> 25 runs</b>	<b>1<sup>st</sup> 30 runs</b>	<b>1<sup>st</sup> 35 runs</b>	<b>1<sup>st</sup> 40 runs</b>	<b>1<sup>st</sup> 45 runs</b>	<b>All 50 runs</b>
Median	0.09	0.10	0.12	0.11	0.13	0.12	0.12	0.12	0.12	0.12
Mean	0.26	0.26	0.31	0.30	0.40	0.37	0.37	0.36	0.35	0.35
Maximum	6.01	6.01	8.94	8.94	19.07	19.07	19.07	19.07	19.07	19.07
Standard Deviation	0.59	0.51	0.73	0.69	1.08	0.99	0.98	0.96	0.95	0.93

Table K-5. Summary Statistics of Impact Velocity (m/sec) for  $1 \times 10^{-5}$  Ground Motion

<b>Summary Statistics</b>	<b>1<sup>st</sup> 5 runs</b>	<b>1<sup>st</sup> 10 runs</b>	<b>1<sup>st</sup> 15 runs</b>	<b>1<sup>st</sup> 20 runs</b>	<b>1<sup>st</sup> 25 runs</b>	<b>1<sup>st</sup> 30 runs</b>	<b>1<sup>st</sup> 35 runs</b>	<b>1<sup>st</sup> 40 runs</b>	<b>1<sup>st</sup> 45 runs</b>	<b>All 50 runs</b>
Median	2.58	2.55	2.52	2.51	2.60	2.53	2.60	2.60	2.55	2.57
Mean	2.48	2.51	2.59	2.58	2.70	2.62	2.67	2.69	2.66	2.69
Maximum	5.35	5.81	9.05	9.05	9.42	9.42	9.42	9.42	9.42	9.42
Standard Deviation	1.22	1.22	1.48	1.43	1.50	1.50	1.43	1.45	1.44	1.48

Table K-6. Summary Statistics of Impact Energy (J) for  $1 \times 10^{-5}$  Preclosure Ground Motion

<b>Summary Statistics</b>	<b>1<sup>st</sup> 5 runs</b>	<b>1<sup>st</sup> 10 runs</b>	<b>1<sup>st</sup> 15 runs</b>	<b>1<sup>st</sup> 20 runs</b>	<b>1<sup>st</sup> 25 runs</b>	<b>1<sup>st</sup> 30 runs</b>	<b>1<sup>st</sup> 35 runs</b>	<b>1<sup>st</sup> 40 runs</b>	<b>1<sup>st</sup> 45 runs</b>	<b>All 50 runs</b>
Median	288	271	318	326	391	355	364	358	343	357
Mean	1005	1020	1190	1141	2260	2055	1899	1903	1839	1814
Maximum	17557	19410	20913	20913	435077	435077	435077	435077	435077	435077
Standard Deviation	2443	2356	2518	2414	16028	14585	12752	12346	12081	11430

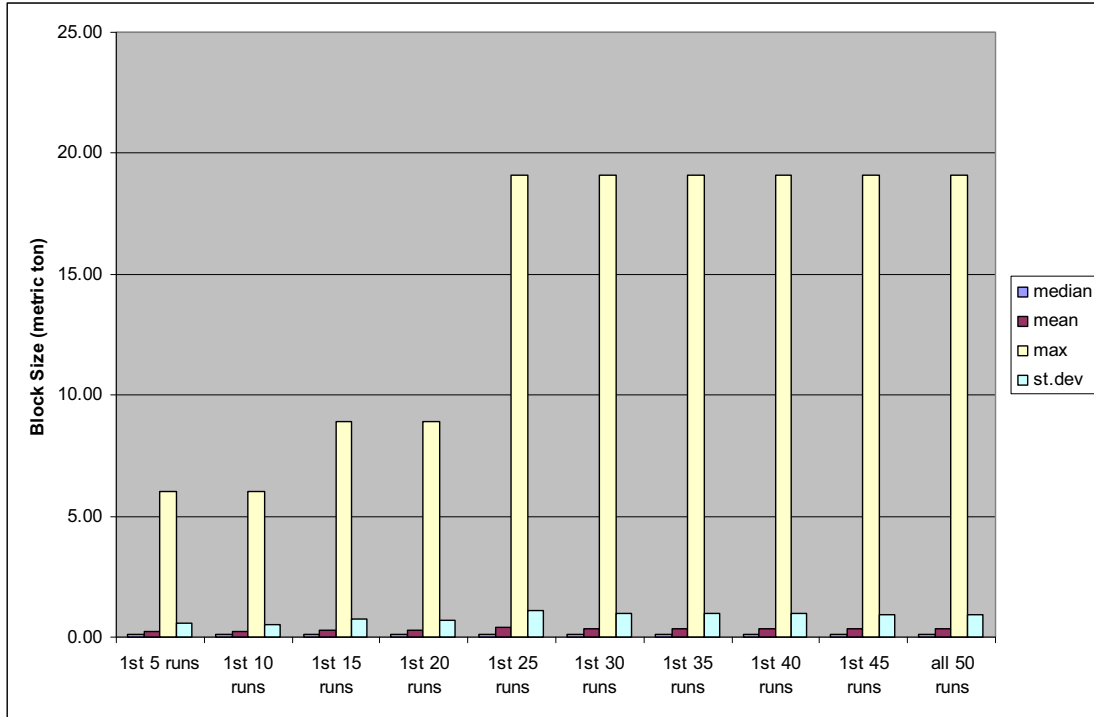


Figure K-5. Summary Statistics of Block Size (metric ton) for  $1 \times 10^{-5}$  Ground Motion

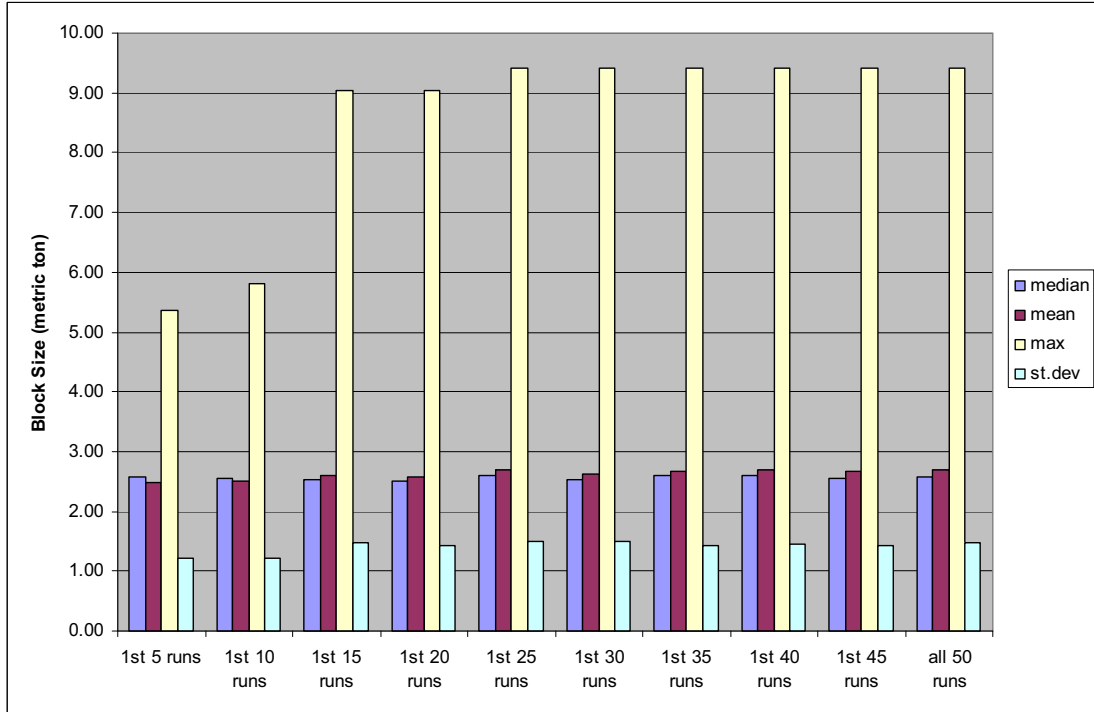


Figure K-6. Summary Statistics of Impact Velocity (m/sec) for  $1 \times 10^{-5}$  Ground Motion

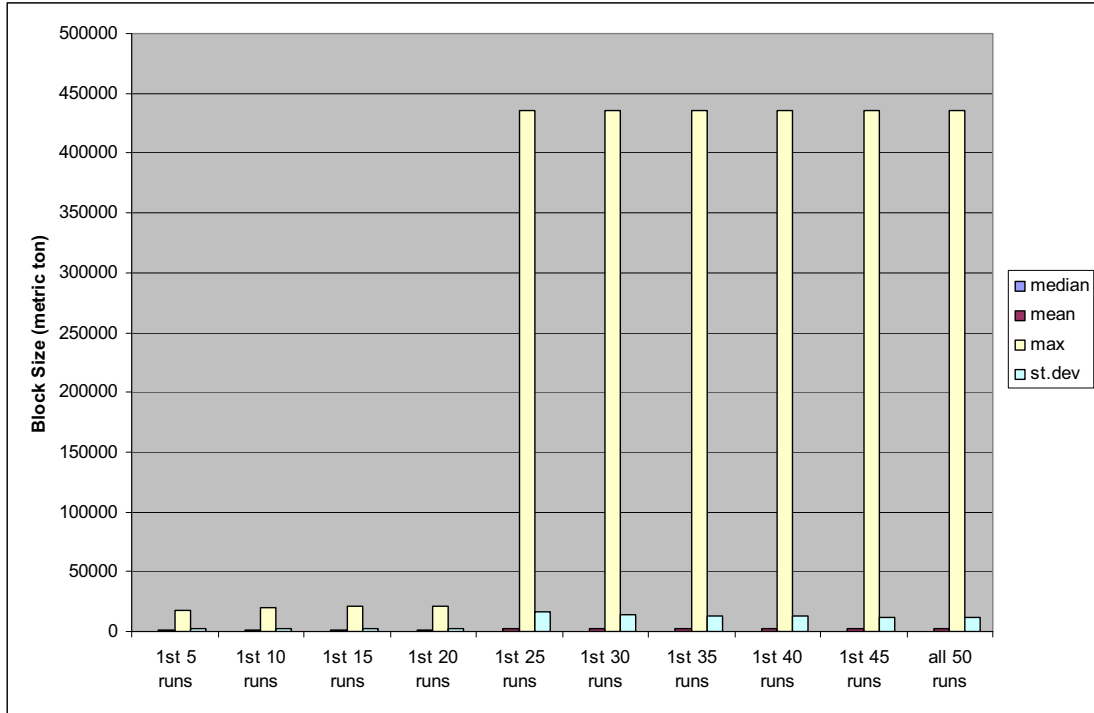


Figure K-7. Summary Statistics of Impact Energy (J) for  $1 \times 10^{-5}$  Ground Motion

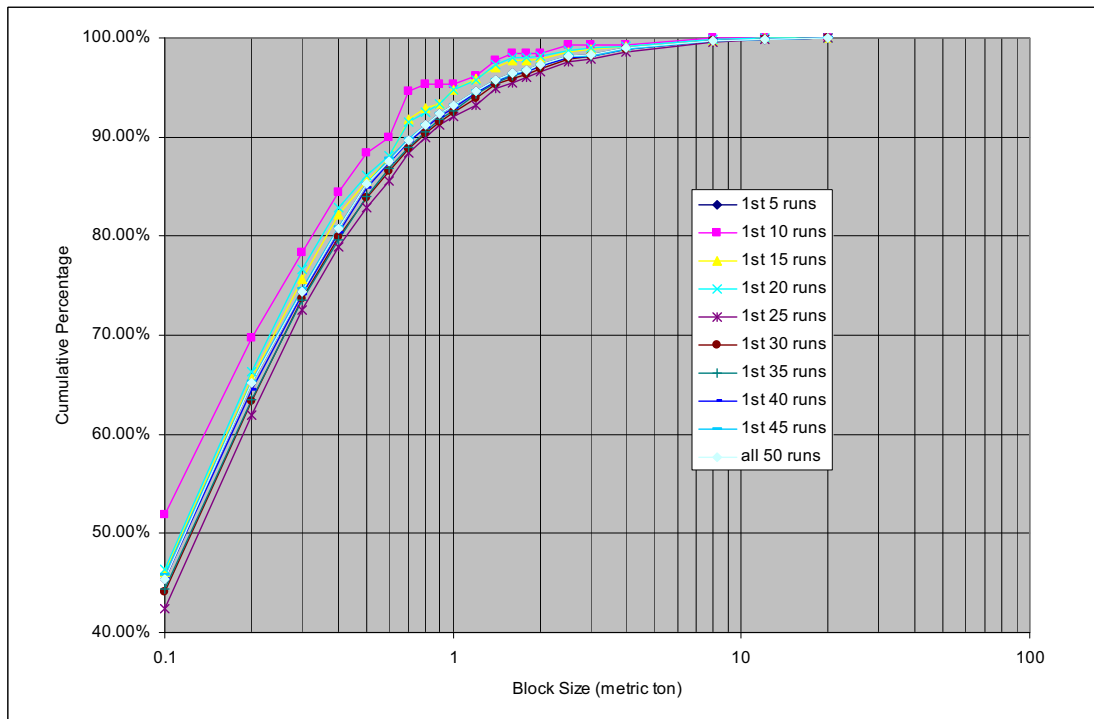


Figure K-8. Block Size Distribution for  $1 \times 10^{-5}$  Ground Motion

Figures K-9 to K-11 shows the trend of the statistics for the analyses considering the  $1 \times 10^{-6}$  annual probability of exceedance ground motion with a total of 50 3DEC simulations. The corresponding numeric values for the statistics are tabulated in Tables K-7 to K-9. The maximum block size occurs in between the 30<sup>th</sup> and 35<sup>th</sup> simulation, whereas the maximum impact velocity and impact energy occurs in between the 20<sup>th</sup> and 25<sup>th</sup> simulation. The trend shows that the statistics of rockfall characteristics approaches to asymptotic value approximately 30 to 35 runs of 3DEC simulation. Figure K-12 present the block size cumulative distribution for the evolution of the analyses, the distribution shows that approximately 25 to 30 runs of 3DEC simulation provide adequate representation of the size distribution.

Table K-7. Summary Statistics of Block Size (metric ton) for  $1 \times 10^{-6}$  Ground Motion

Summary Statistics	1 <sup>st</sup> 5 runs	1 <sup>st</sup> 10 runs	1 <sup>st</sup> 15 runs	1 <sup>st</sup> 20 runs	1 <sup>st</sup> 25 runs	1 <sup>st</sup> 30 runs	1 <sup>st</sup> 35 runs	1 <sup>st</sup> 40 runs	1 <sup>st</sup> 45 runs	All 50 runs
Median	0.09	0.10	0.12	0.12	0.13	0.13	0.13	0.12	0.12	0.13
Mean	0.35	0.34	0.35	0.36	0.44	0.41	0.43	0.43	0.43	0.43
Maximum	10.75	10.75	10.75	11.50	19.07	19.07	28.22	28.22	28.22	28.22
Standard Deviation	1.01	0.85	0.85	0.91	1.16	1.06	1.37	1.35	1.35	1.30

Table K-8. Summary Statistics of Impact Velocity (m/sec) for  $1 \times 10^{-6}$  Ground Motion

Summary Statistics	1 <sup>st</sup> 5 runs	1 <sup>st</sup> 10 runs	1 <sup>st</sup> 15 runs	1 <sup>st</sup> 20 runs	1 <sup>st</sup> 25 runs	1 <sup>st</sup> 30 runs	1 <sup>st</sup> 35 runs	1 <sup>st</sup> 40 runs	1 <sup>st</sup> 45 runs	All 50 runs
Median	2.97	3.01	3.10	3.06	3.11	3.02	2.97	2.98	2.98	2.97
Mean	3.08	3.17	3.30	3.27	3.36	3.26	3.23	3.22	3.21	3.23
Maximum	7.09	8.08	8.77	8.77	12.09	12.09	12.10	12.10	12.10	12.10
Standard Deviation	1.32	1.44	1.64	1.59	1.69	1.69	1.71	1.72	1.70	1.74

Table K-9. Summary Statistics of Impact Energy (J) for  $1 \times 10^{-6}$  Ground Motion

Summary Statistics	1 <sup>st</sup> 5 runs	1 <sup>st</sup> 10 runs	1 <sup>st</sup> 15 runs	1 <sup>st</sup> 20 runs	1 <sup>st</sup> 25 runs	1 <sup>st</sup> 30 runs	1 <sup>st</sup> 35 runs	1 <sup>st</sup> 40 runs	1 <sup>st</sup> 45 runs	All 50 runs
Median	407	475	582	563	678	574	556	550	548	576
Mean	1455	1625	1868	1974	2521	2368	2296	2275	2288	2350
Maximum	36584	36584	60585	60585	163657	163657	163657	163657	163657	163657
Standard Deviation	3428	3743	4277	4794	7788	7868	7600	7349	7786	7704

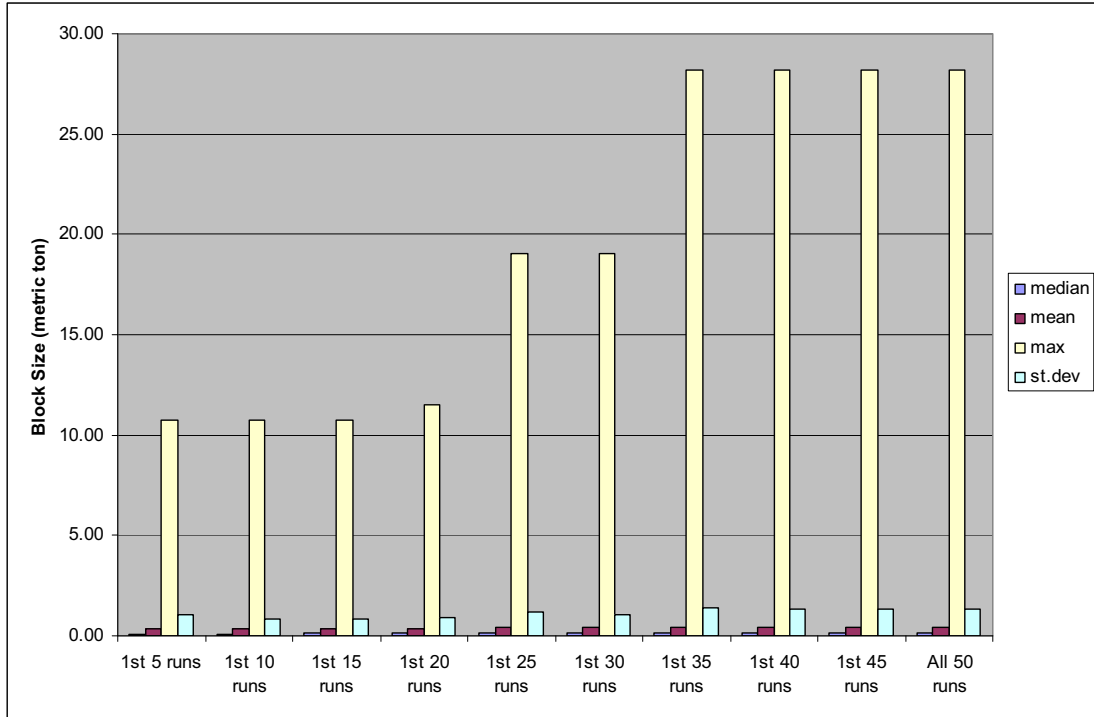


Figure K-9. Summary Statistics of Block Size (metric ton) for  $1 \times 10^{-6}$  Ground Motion

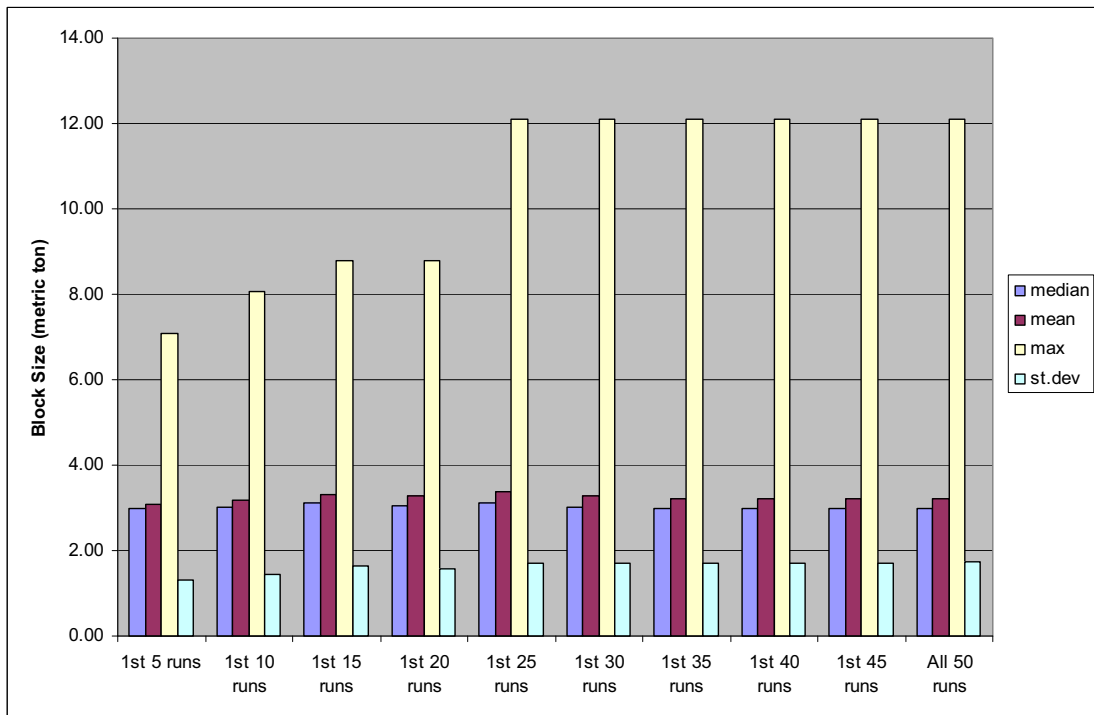
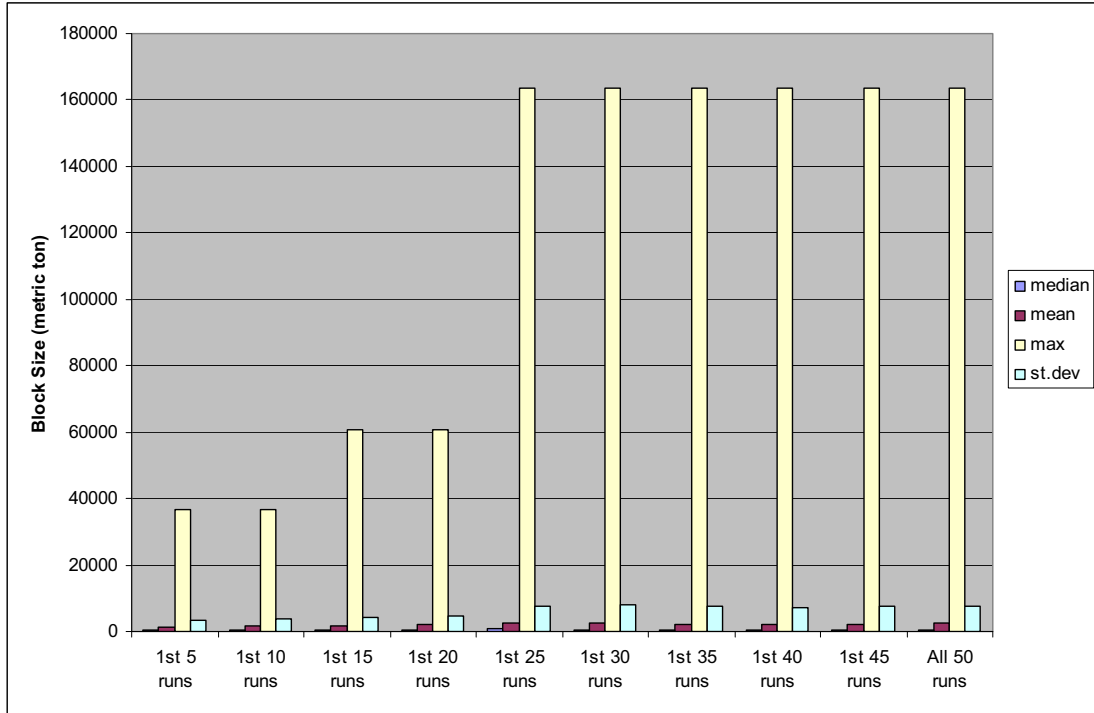


Figure K-10. Summary Statistics of Impact Velocity (m/sec) for  $1 \times 10^{-6}$  Ground Motion





NOTE: J = Joule.

Figure K-11. Summary Statistics of Impact Energy (J) for  $1 \times 10^{-6}$  Ground Motion

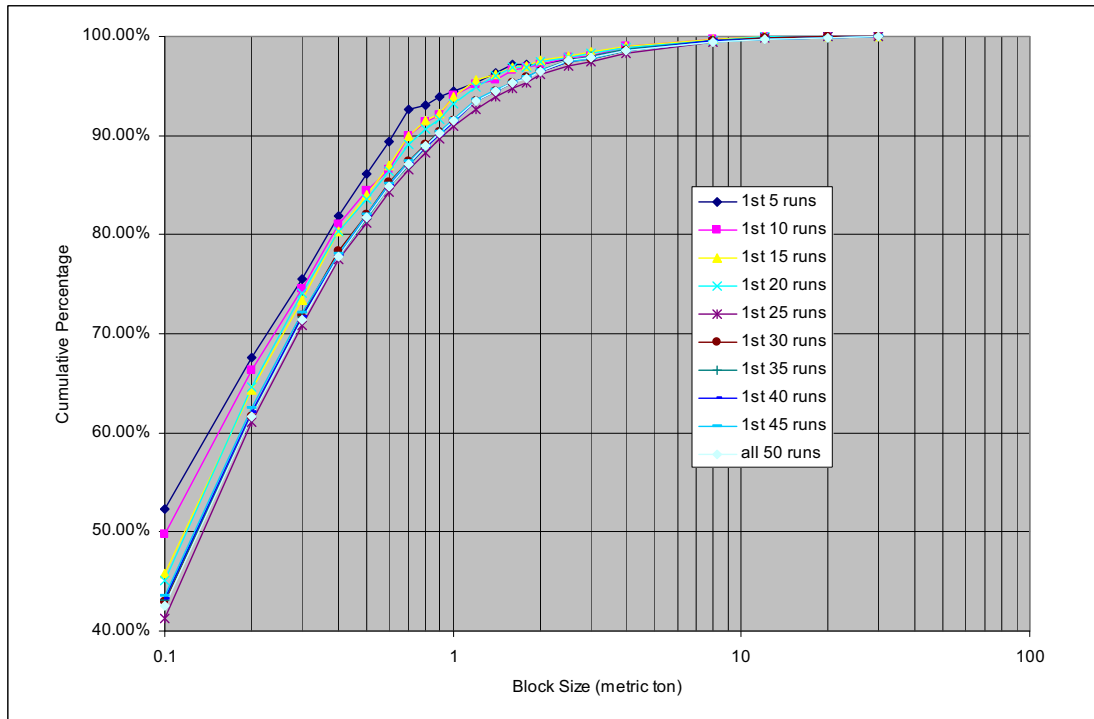


Figure K-12. Block Size Distribution for  $1 \times 10^{-6}$  Ground Motion

Figures K-13 to K-15 shows the trend of the statistics for the analyses considering the  $1 \times 10^{-7}$  annual probability of exceedance ground motion with a total of 44 3DEC simulations. The corresponding numeric values for the statistics are tabulated in Tables K-10 to K-12. The maximum block size and impact energy occurs in between the 20<sup>th</sup> and 25<sup>th</sup> simulation, whereas the maximum impact velocity occurs in between the 40<sup>th</sup> and 44<sup>th</sup> simulation. The trend shows that the statistics of rockfall characteristics approaches to asymptotic value approximately 30 to 35 runs of 3DEC simulation. Figure K-16 present the block size cumulative distribution for the evolution of the analyses, the distribution shows that approximately 20 to 25 runs of 3DEC simulation provide adequate representation of the size distribution.

Table K-10. Summary Statistics of Block Size (metric ton) for  $1 \times 10^{-7}$  Ground Motion

Summary Statistics	1 <sup>st</sup> 5 runs	1 <sup>st</sup> 10 runs	1 <sup>st</sup> 15 runs	1 <sup>st</sup> 20 runs	1 <sup>st</sup> 25 runs	1 <sup>st</sup> 30 runs	1 <sup>st</sup> 35 runs	1 <sup>st</sup> 40 runs	All 44 runs
Median	0.12	0.12	0.13	0.14	0.14	0.14	0.14	0.14	0.15
Mean	0.47	0.49	0.50	0.53	0.52	0.51	0.50	0.50	0.50
Maximum	14.58	14.58	14.58	19.05	28.29	28.29	28.29	28.29	28.29
Standard Deviation	1.29	1.25	1.29	1.39	1.57	1.50	1.44	1.44	1.43

Table K-11. Summary Statistics of Impact Velocity (m/sec) for  $1 \times 10^{-7}$  Ground Motion

Summary Statistics	1 <sup>st</sup> 5 runs	1 <sup>st</sup> 10 runs	1 <sup>st</sup> 15 runs	1 <sup>st</sup> 20 runs	1 <sup>st</sup> 25 runs	1 <sup>st</sup> 30 runs	1 <sup>st</sup> 35 runs	1 <sup>st</sup> 40 runs	All 44 runs
Median	4.35	4.16	4.11	3.75	3.97	3.85	3.82	3.83	3.78
Mean	4.38	4.25	4.31	4.04	4.26	4.18	4.19	4.17	4.17
Maximum	11.67	11.67	13.58	13.58	20.53	20.53	20.53	20.53	20.94
Standard Deviation	2.20	2.07	2.22	2.16	2.42	2.35	2.40	2.37	2.47

Table K-12. Summary Statistics of Impact Energy (J) for  $1 \times 10^{-7}$  Ground Motion

Summary Statistics	1 <sup>st</sup> 5 runs	1 <sup>st</sup> 10 runs	1 <sup>st</sup> 15 runs	1 <sup>st</sup> 20 runs	1 <sup>st</sup> 25 runs	1 <sup>st</sup> 30 runs	1 <sup>st</sup> 35 runs	1 <sup>st</sup> 40 runs	All 44 runs
Median	1163	1127	1176	981	1077	1020	1005	1004	1022
Mean	3786	3890	4005	3666	4301	4240	4099	4069	4146
Maximum	80283	80283	80283	80283	706914	706914	706914	706914	706914
Standard Deviation	8419	8294	8457	8003	20139	18558	17649	17526	16749

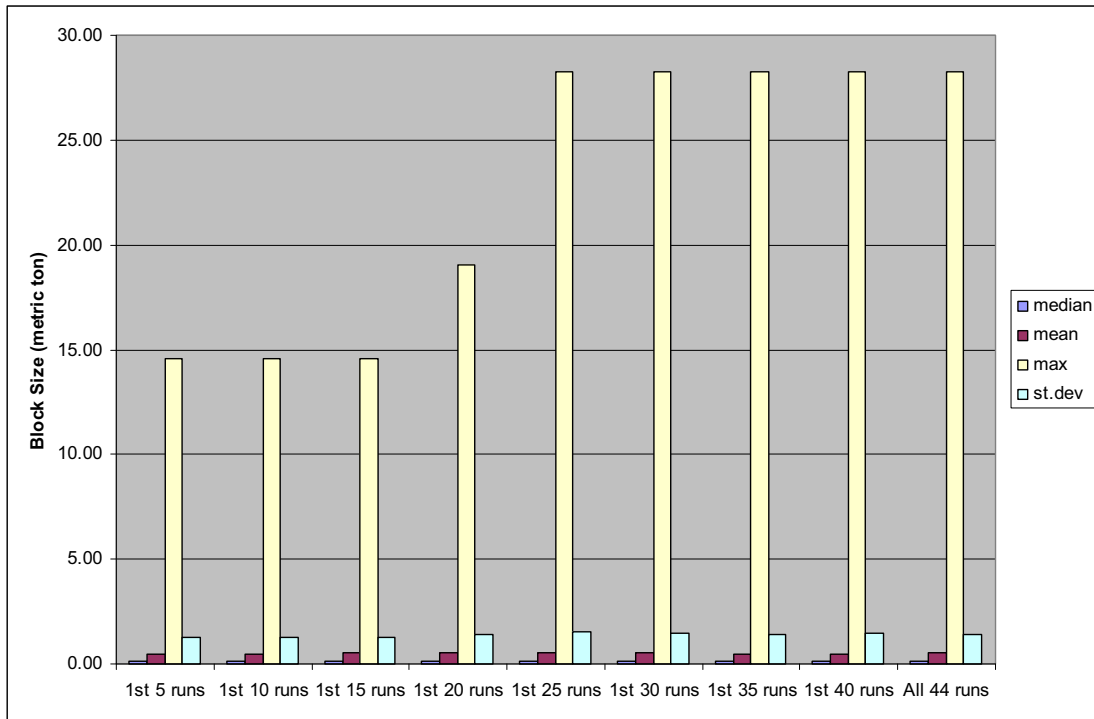


Figure K-13. Summary Statistics of Block Size (metric ton) for  $1 \times 10^{-7}$  Ground Motion

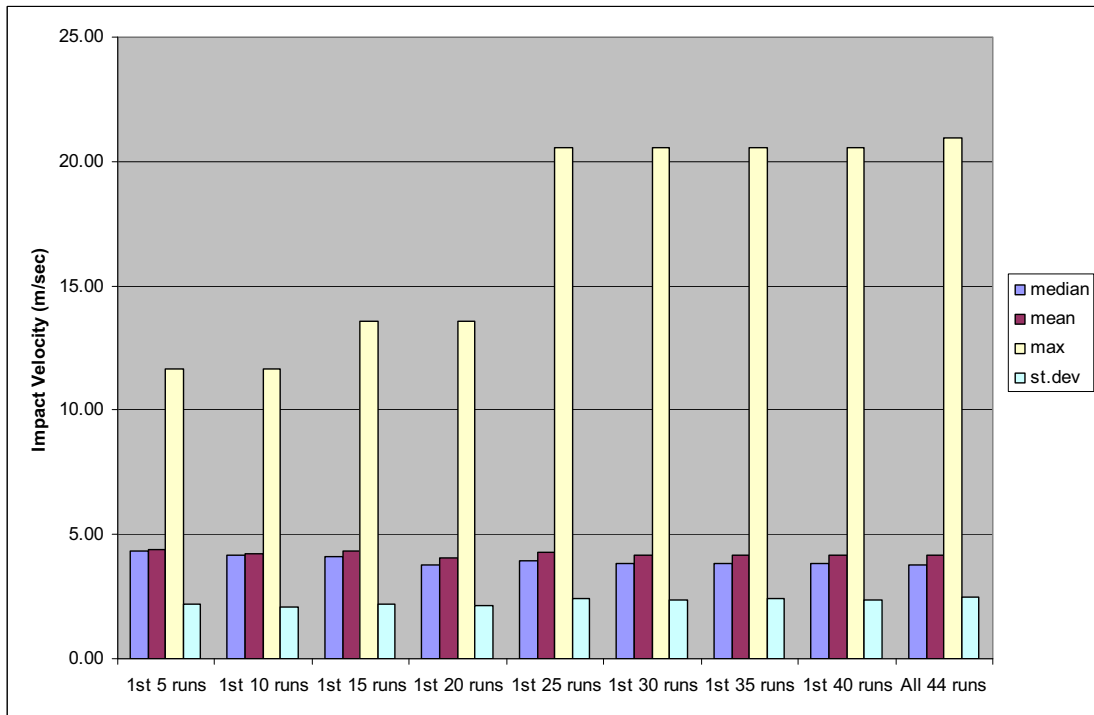
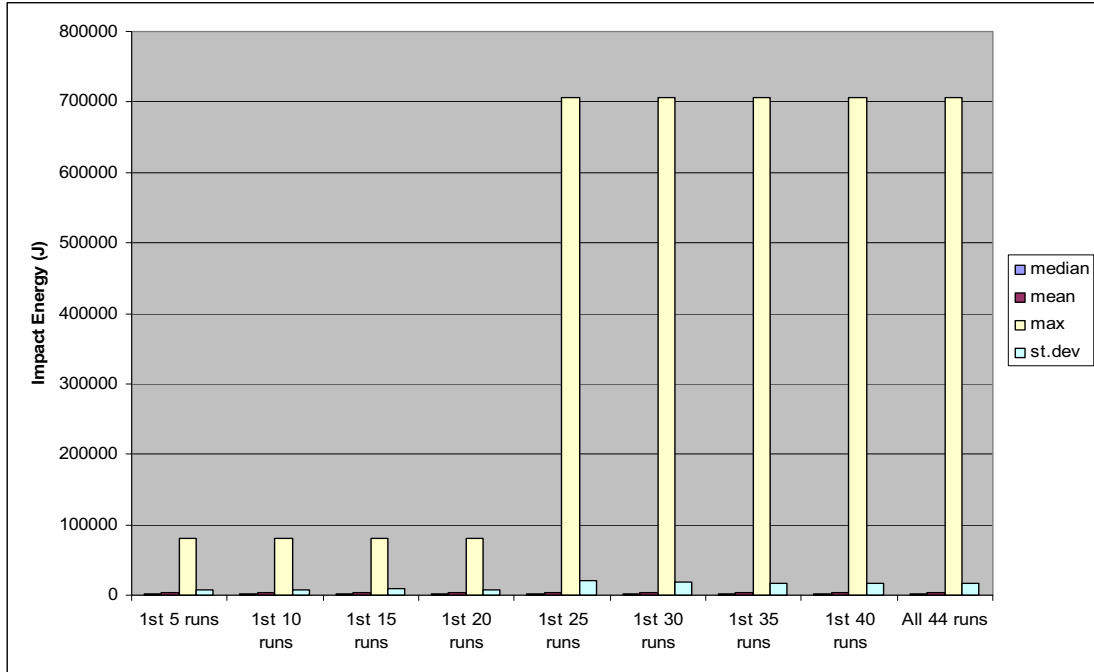


Figure K-14. Summary Statistics of Impact Velocity (m/sec) for  $1 \times 10^{-7}$  Ground Motion



NOTE: J = Joule.

Figure K-15. Summary Statistics of Impact Energy (J) for  $1 \times 10^{-7}$  Ground Motion

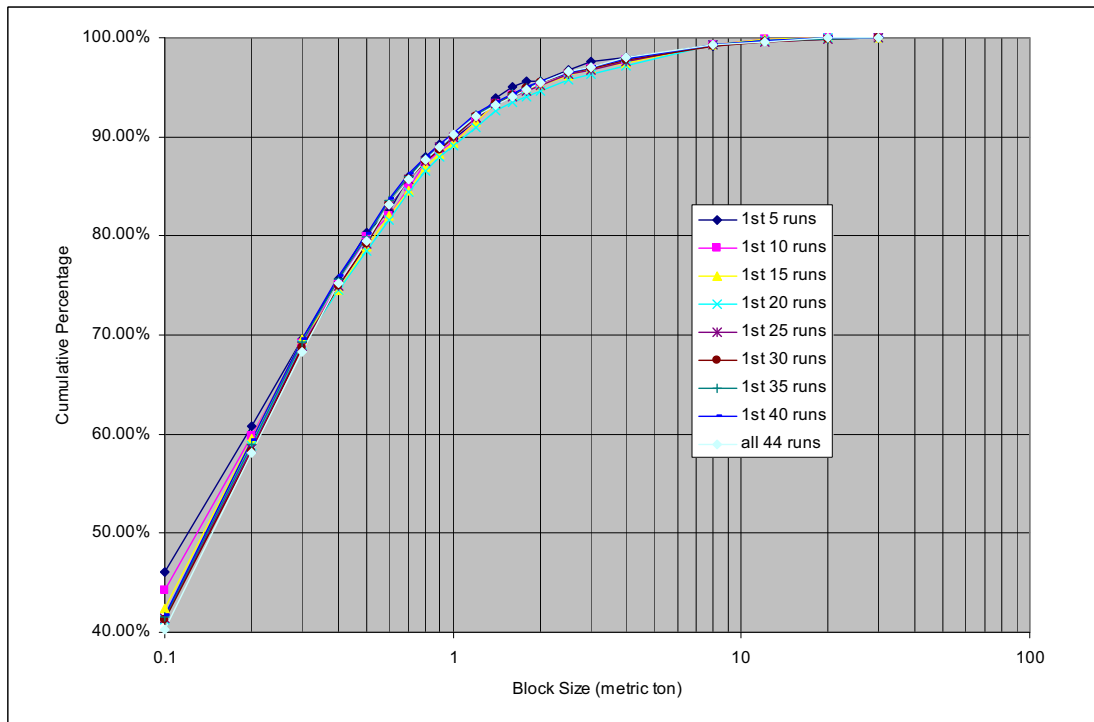


Figure K-16. Block Size Distribution for  $1 \times 10^{-7}$  Ground Motion

**APPENDIX L**

**CONVERSION OF FRACMAN FRACTURE OUTPUT TO 3DEC INPUT**



## CONVERSION OF FRACMAN FRACTURE OUTPUT TO 3DEC INPUT

The coordinate systems used for FracMan and 3DEC are shown in Figure L-1. The FracMan system is a right-hand system with North pointing to the negative x-axis, whereas the 3DEC system uses a left-hand system with North parallel to the z-axis. The conversion is accomplished by using the following equations:

$$X_{3DEC} = Y_{FracMan} \quad (\text{Eq. L-1})$$

$$Z_{3DEC} = -X_{FracMan} \quad (\text{Eq. L-2})$$

$$Y_{3DEC} = Z_{FracMan} \quad (\text{Eq. L-3})$$

This conversion was done in the Microsoft Excel spreadsheet files *3DEC-S1shtA\_TPO.xls*, *3DEC-S1shtB\_TPO.xls*, *3DEC-s2sht\_TPO.xls*, *3DEC-s3\_sht\_TPO.xls*, *3DEC-VPPLONG\_TPO.xls*, and *Tptpll- Fracman Generated Fracture Data.xls* (Table A-1). The x-, y-, and z-coordinates in worksheet “3DEC input” were obtained based on the original coordinate values in worksheet “Fracman output” and Equations L-1 to L-3. The dip, dip direction, and radius inputs in 3DEC were a direct copy from FracMan outputs. Additional worksheets, which sort the fracture data listing based on the descending order for radius, are included in the spreadsheet files. This sorted fracture data is used for 3DEC model optimization as described in Appendix H.

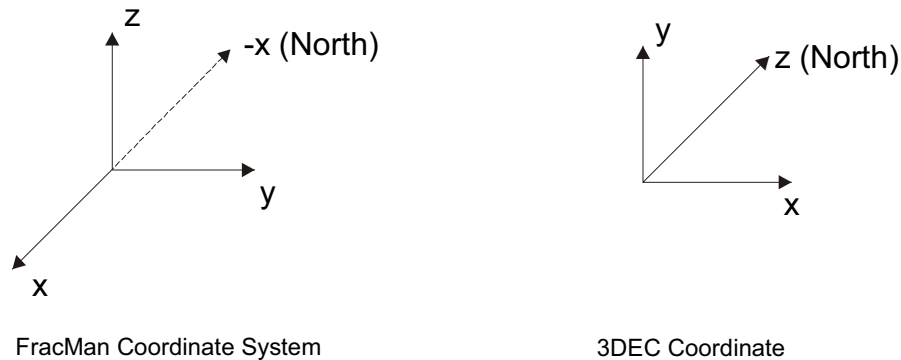


Figure L-1. Coordinate System Adopted in FracMan and 3DEC

INTENTIONALLY LEFT BLANK



**APPENDIX M**

**GFM2000 INPUT AND OUTPUT FILES FOR STRATIGRAPHIC  
UNIT THICKNESS DATA AND CROSS-SECTIONS**



## **GFM2000 INPUT AND OUTPUT FILES FOR STRATIGRAPHIC UNIT THICKNESS DATA AND CROSS-SECTIONS**

### **M1. INTRODUCTION**

Stratigraphic unit thickness and cross-sections for the thermal-mechanical calculation were extracted from DTN: MO0012MWDGFM02.002 [DIRS 153777]. The extracted stratigraphic unit thickness was used in calculating mean rock properties for the thermal-mechanical units, while the cross-sections were utilized to create three-dimensional mesh used in the thermal-mechanical calculation. The detailed calculation, data, and mesh description are presented in Appendices C and E.

The extraction of the unit thickness and cross-sections was conducted on the geologic data from the TDMS (DTN: MO0012MWDGFM02.002 [DIRS 153777]), using EarthVision V.5.1 software (see Section 3). The EarthVision V.5.1 software was qualified for three-dimensional geologic modeling and was used within its range of validation. The stratigraphic unit thickness was extracted at the location of NS 232674 m and WE 170693 m, which is approximately the center of the repository (Appendix C, Figure C-3), while the three cross-sections were extracted at the locations of NS 231637 m, NS 234075 m, and NS 235904 m (Appendix C, Figure C-3). An additional stratigraphic unit thickness was extracted at the location of NS 234025 m and WE 171440 m, which is the location of the in situ stress measurements (DTN: SNF37100195002.001 [DIRS 131356]) at borehole ESF-AOD-HDRFR#1 (Section 6.3.1.1 and Figure C-3). The unit thickness data were used to calculate the overburden stress at the depth of the in situ measurement from the surface.

All the input and output files from the EarthVision software for the extraction of the unit thickness and the cross-section are presented in the following sections.

### **M2. EARTHVISION INPUT AND OUTPUT FILES**

The input files (*central.dat*, *hope\_01.sh*, and *combine.sh*) and output file (*alldata\_01\_2.dat*) for the extraction of the unit thickness at the location of WE 170693 m and NS 232674 m are available in the TDMS (DTN: MO0408MWDDDMIO.002).

The input files for the extraction of the three cross-sections at the locations of NS 231637 m (S3), NS 234075 m (S7), and NS 235904 m (S10) are also available in the TDMS (DTN: MO0408MWDDDMIO.002). The resulting cross-sections (output files *s3.dxf*, *s7.dxf*, and *s10.dxf*) are shown in Figures M-1 to M-3.

The input files (*hldr1.dat*, *hope\_02.sh*, and *combine.sh*) and output file (*alldata.dat*) for the extraction of the unit thickness at the location of NS 234025 m and WE 171440 m are available in the TDMS (DTN: MO0408MWDDDMIO.002).

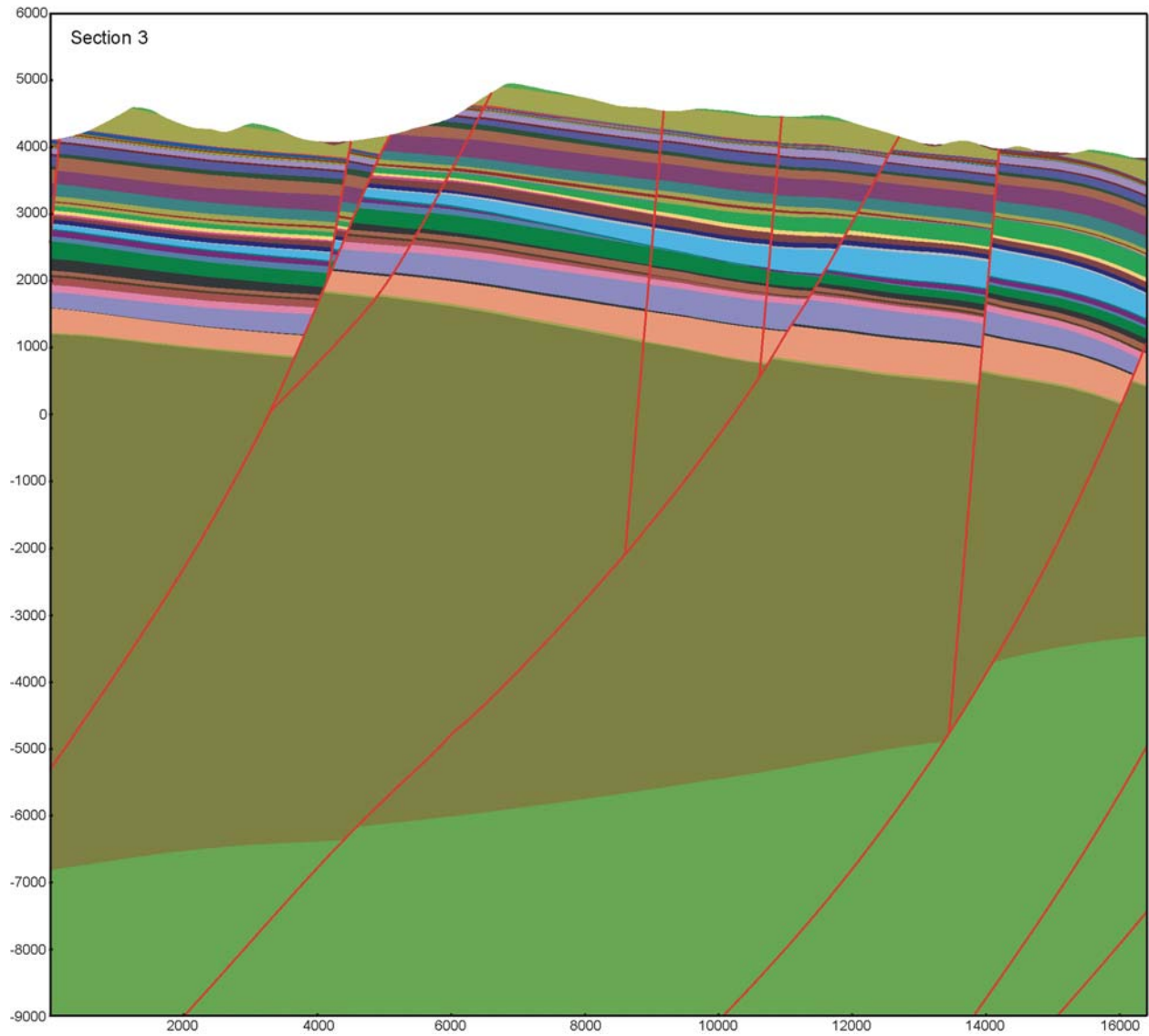


Figure M-1. Cross-Section Extracted at the Location of S3 (NS 231637 m), Using the EarthVision Software

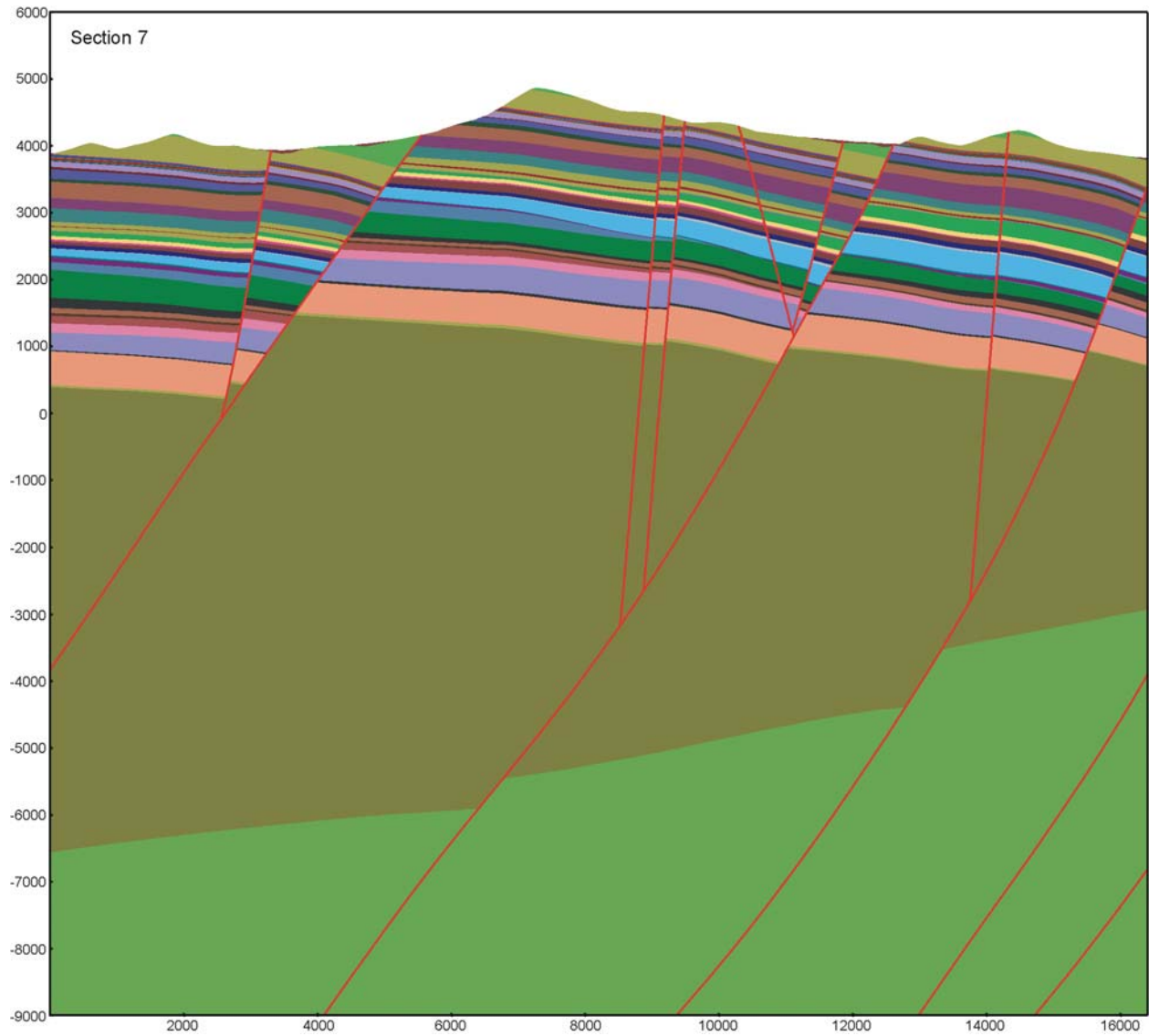


Figure M-2. Cross-Section Extracted at the Location of S7 (NS 234075 m), Using the EarthVision Software

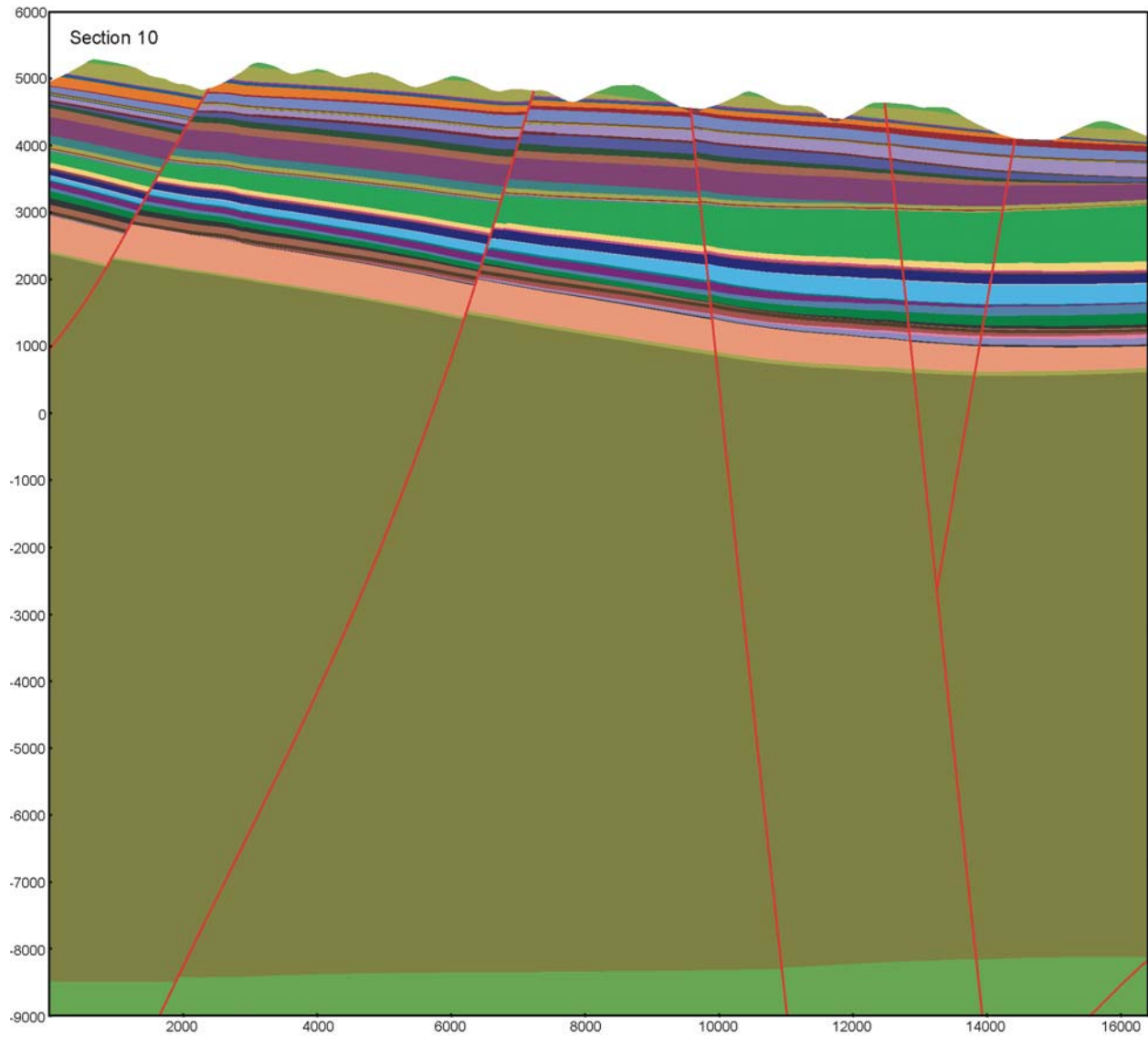


Figure M-3. Cross-Section Extracted at the Location of S10 (NS 235904 m), Using the EarthVision Software

### M3. OVERBURDEN STRESS AT THE DEPTH OF THE IN SITU TEST

The vertical stress due to the weight of overburden at the depth of the in situ test from the surface was calculated from the stratigraphic unit thickness at the in situ test location and the mean stratigraphic unit density presented in Table E-1 (i.e., vertical stress = overburden thickness [m]  $\times$  9.81 m/sec<sup>2</sup>  $\times$  density [kg/m<sup>3</sup>]). Based on the supporting information for DTN: SNF37100195002.001 [DIRS 131356], the elevation of the in situ measurement is 1033.3 m (CRWMS M&O 1997 [DIRS 147458], MOL.19970717.0008, Table 5). Details of the calculation and the resulting overburden load of 4.7 MPa are presented in Table M-1.

Table M-1. Overburden Load at the Depth of the In Situ Test

Unit	Thickness (m)	Elevation at Top (m)	Elevation at Bottom (m)	Density <sup>a</sup> (kg/m <sup>3</sup> )	Overburden Thickness <sup>b</sup> (m)	Overburden Load (MPa)
Tpcpv3	0.0	1285.1	1285.1	2310	0.0	0.0
Tpcpv2	4.9	1285.1	1280.2	1460	4.9	0.1
Tpcpv1	4.2	1280.2	1275.9	1460	4.2	0.1
Tpbt4	1.4	1275.9	1274.6	1460	1.4	0.0
Tpy	10.4	1274.6	1264.1	1460	10.4	0.1
Tpbt3	4.3	1264.1	1259.8	1460	4.3	0.1
Tpp	20.8	1259.8	1239.0	1460	20.8	0.3
Tpbt2	8.2	1239.0	1230.8	1460	8.2	0.1
Tptrv3	2.8	1230.8	1227.9	1460	2.8	0.0
Tptrv2	0.8	1227.9	1227.2	1460	0.8	0.0
Tptrv1	1.0	1227.2	1226.2	2310	1.0	0.0
Tptrn	54.4	1226.2	1171.8	2190	54.4	1.2
Tptrl	9.1	1171.8	1162.7	2190	9.1	0.2
Tptpul	74.8	1162.7	1087.9	1834	74.8	1.3
Tptpmn	36.8	1087.9	1051.1	2148	36.8	0.8
Tptpll	102.6	1051.1	948.5	1979	17.8	0.3
In Situ Vertical Stress						4.7

<sup>a</sup> The mean stratigraphic unit density is from Table E-1.

<sup>b</sup> The overburden thickness is from the elevation of the in situ test, which is 1033.3 m (CRWMS M&O 1997 [DIRS 147458], MOL.19970717.0008, Table 5).

INTENTIONALLY LEFT BLANK



**APPENDIX N**

**MODEL VALIDATION REVIEW — 3DEC MODELING OF  
SEISMIC GROUND MOTION-INDUCED ROCKFALL**



## **MODEL VALIDATION REVIEW — 3DEC MODELING OF SEISMIC GROUND MOTION-INDUCED ROCKFALL**

An outside expert technical review was conducted as a means of validating the 3DEC model for representation of nonlithophysal rock (see Section 7.7.6). Dr. John Tinucci of the PanTechnica Corporation in Minneapolis, Minnesota, was contracted for this purpose. Dr. Tinucci is a Professional Engineer and has a Ph.D. from the University of California, Berkeley, where his thesis research was in the area of analysis of the stability of blocky rock masses, and, in particular, in the development of key-block methods for tunnel stability assessment. He has extensive experience in the use of the 3DEC program for surface and underground stability assessment. Particularly valuable experience for the present application is his use of 3DEC to model dynamic stability of deep underground mine openings. Dr. Tinucci's review report is provided in this appendix.

Dr. Tinucci provides a summary of specific 3DEC model assumptions and abstractions, including recommendations for changes or other issues that should be considered (see "Recommendations" on p. 19/20 and Table 1, pp. 7/20 through 9/20, of the review report in this appendix). A response to Dr. Tinucci's recommendations is provided as follows:

- Recommendation #1 (from Table 1, p. 7/20): Reexamine the magnitude of input ground motions.
  - Response: A limitation study of ground motions is ongoing, which reexamines ground motion magnitudes. Any impacts to this report due to changes to ground motion data as a result of the limitation study would be documented in a future revision. The current input ground motions (see Section 4.1) are the best available source of site-specific ground motion data.
- Recommendation #2 (from Table 1, p. 7/20): Values of joint cohesion, joint friction, and joint dilation should depend on other joint strength parameters.
  - Response: Sensitivity analyses were conducted using three additional joint categories that consider a range of joint strength parameters (Section 6.3.1.6.2).
- Recommendation #3: Due to the complexity of the FISH functions within 3DEC model, it is highly recommended that the functions be independently checked by another engineer to ensure accuracy.
  - Response: FISH functions have been independently checked (by the technical checker) as part of the checking of the 3DEC input files.
- Recommendation #4 (from Table 1, p. 8/20): Compute blocks based on local spacing (approximately 0.5 m) to determine block volume change.
  - Response: The recommendation was provided for the original FracMan results. The synthetic fracture network from FracMan has since been revised to provide a better quantitative comparison with mapped fracture data (based on joint spacing, trace length, and orientation). The current synthetic FracMan fracture geometry provides a

relatively good fit of the underground mapping fracture geometry data, as shown in Table 6-2.

- Recommendation #5 (from Table 1, p. 8/20): Include references for other known studies that employ similar approaches.
  - Response: Additional validation based on data from a Defensive Nuclear Agency-sponsored explosive tunnel stability field experiment has been included, which builds confidence in the simulation of dynamic blocky systems (Section 7.7.4). Reference for other Yucca Mountain applications using FracMan have been added in Section 6.1.6.2.
- Recommendation #6 (from Table 1, p. 8/20): Include sensitivity runs for natural damping of the rock mass.
  - Response: Although damping is not explicitly specified in the 3DEC input, it is considered with the simulation of joint slip, joint separation, and bridge damage during seismic shaking. The current approach is considered reasonable and yet not overly conservative.
- Recommendation #7 (from Table 1, p. 8/20): Check sub-contacts for several cases for failure along bridges, and then re-assess the need for using finer discretization.
  - Response: Bridge damage during seismic shaking is discussed in Section 6.3.1. In general, less than 1 percent bridge area is damaged when subjected to  $1 \times 10^{-5}$  ground motions. Bridge area damage increases to about 4 percent with  $1 \times 10^{-6}$  ground motions, and 30 percent for  $1 \times 10^{-7}$  ground motions. Since only a relatively small portion of the surface area of the unstable blocks was formed by the damaged bridge, it was not necessary to conduct additional sensitivity studies using a more refined grid.
- Recommendation #8 (from Table 1, p. 8/20): Run one case with a much larger fractured volume including the floor.
  - Response: The sensitivity of model sizes is provided in Section 6.3.1.6.5. The base-case model (25 m  $\times$  25 m  $\times$  25 m) was determined to be adequate for rockfall prediction.
- Recommendation #9 (from Table 1, p. 9/20): Should qualitatively compare blocks formed with those formed from simulated fractures.
  - Response: The identification of blocks observed in the ECRB Cross-Drift is provided in Appendix F. For simulating an actual joint geometry using 3DEC, the difficulty of generating joints in the rock mass not exposed at the tunnel surface prevents a solution with credible geometry. The quantitative comparison of the joint geometrical parameters from mapping data and from FracMan as discussed in Section 6.1.6 provides a similar confirmation for the adequacy of the fracture system.

- Recommendation #10 (from Table 1, p. 9/20): De-emphasize DRKBA results in the final report.
  - Response: The DRKBA results have been de-emphasized, appearing primarily in Appendix D. This report focuses on the use of 3DEC and UDEC as documented in Sections 6.3 and 6.4. The DRKBA results are primarily used as confirmation for the 3DEC results (Section 7.7.5).

The following errata are provided for Dr. Tinucci's report:

- Page 1/20: The report was submitted to the “Engineered Barrier System Department.”
- Page 2/20: “G. Neider-Westerman, 2000” refers to CRWMS M&O 2000 [DIRS 152286].
- Page 2/20: “N. Barton, 2002” refers to Duan 2003 [DIRS 163586].
- Page 7/20: In Table 1, “Small Joints” are discussed on p. 11/20.
- Page 8/20: In Table 1, “Sub-horizontal Joint Spacing” is discussed on p. 12/20.
- Page 8/20: In Table 1, “Joint Strength Degradation” is discussed on p. 13/20.
- Page 8/20: In Table 1, “Fractured Rock Boundaries” are discussed on p. 14/20.
- Page 8/20: In Table 1, “Fractures in Floor” are discussed on p. 14/20.
- Page 9/20: In Table 1, “Event Orientation” is discussed on p. 15/20.
- Page 9/20: In Table 1, “Removing Unstable Blocks” is discussed on p. 15/20.
- Page 9/20: In Table 1, “Support System” is discussed on p. 17/20.
- Page 11/20: In the “Ground Motion” discussion, the three probable events are the 1 in 2000 year event, the 1 in 1 million year event, and the 1 in 10 million year event.



**MODEL VALIDATION REVIEW  
3DEC MODELING OF SEISMIC GROUND MOTION-INDUCED ROCKFALL**

**Submitted to**

Engineers Barrier Group  
Bechtel/SAIC

**Review by**

John P. Tinucci, PE, PhD  
PanTechnica Corporation

**INTRODUCTION**

The 3DEC program is currently being used for simulation of mechanical response of the Middle Non-Lithophysal unit to seismic shaking induced by seismic ground motions. The objective of this modeling is to provide estimates of the size, shape and number of rocks that may be dislodged and fall into the emplacement drifts as a function of the level of the estimated ground motions. The ground motions (for various annual exceedence probability levels) are supplied by others within the project. This review is to be used as a portion of the validation requirements for model analysis given in procedure AP-SIII.10Q

**Review Criteria**—The documentation regarding the use of the 3DEC program for representing rockfall work has been reviewed using the following criteria:

1. Is this information presented accurately using applicable methods, assumptions, and recognized techniques?
2. Does existing model documentation provide adequate confidence required by the model's relative importance to the potential performance of the repository system to support model validation for its intended purpose and stated limitations?

**Associated Documentation for Review**—The following documents have been provided for review. It is understood that several of these documents are work-in-progress whose final content will be different upon submittal.

1. 3DEC V2.01 software qualification reports and Itasca 3DEC V2.01 addendum.
2. PowerPoint presentations of rockfall analyses.

Prepared for  
Bechtel/SAIC on behalf of  
U.S. Department of Energy

1/ 20

19 February 2003



3. Geology of the ECRB Cross Drift–Exploratory Studies Facility, Yucca Mountain Project, Yucca Mountain, Nevada, Mongano, et al, 1999.
4. Fracture Geometry Analysis for the Stratigraphic Units of the Repository Host Horizon, G. Neider-Westerman, 2000.
5. Draft of preliminary work (draft report to date, Excel Spreadsheets for results summary, input files).
6. An Application of Rock Mass Characterization and Rock Joint Empirical Models at Yucca Mountain, To Assist in the Disposal Tunnel Design Studies, N. Barton, 2002

**Modeling Objectives**–The original *Drift Degradation Analysis* documentation for these analyses was reviewed by NRC in 2001. The NRC identified four items related to rockfall analysis that must be resolved to close the Repository Design and Thermal-Mechanical Effects key technical issue. The four items, in annotated form, are:

- Provide clarification for how reduction in cohesion adequately accounts for thermal effects.
- Analyze small trace-length fracture data from the ESF and ECRB to assess their effect on block development.
- Provide basis for effective maximum rock size including consideration of the effect of variation of the joint dip angle.
- 1) Revise DRKBA analyses using appropriate joints strengths accounting for their long-term degradation. 2) Analyze block sizes based on joint trace length data supplemented by available small joint trace length data. 3) Verify DRKBA analyses using (a) thermal and seismic boundary conditions, (b) fracture patterns simulations, (c) thermal and mechanical properties for rock blocks and joints, (d) long-term degradation of joint strength, and (e) site-specific ground motion.

The 3DEC analyses are intended to address several of these items and this review includes comments on the applicable portions. The stated objectives of the drift degradation analysis, in annotated form are to:

- model jointing around the drifts,
- provide a statistical description of block sizes around the drifts,
- estimate changes in drift profile resulting from deterioration of the drifts, and
- provide an estimate of the time required for significant drift deterioration to occur.

**Site Visit**–On January 28 -30, 2003, a site visit was made to both the Bechtel/SAIC facilities and ESF facilities. Time spent at the Bechtel/SAIC facilities was to review the input data, model setup and analysis results which had been performed to date. Engineers Mark Board, Ming Lin, Dwayne



Kicker and Rob Lung were involved in discussions. Part of one day involved an underground tour of the ESF facilities. The purpose of this trip was to examine actual rock conditions for which the 3DEC analyses were to represent. Both ESF and ECRB drifts were examined in the Lithophysal and Non-Lithophysal zones.

## **GENERAL OBSERVATIONS ON MODELING APPROACH**

The conceptual model that is used for these analyses is that a finite volume of rock containing the emplacement drift starts in an unsupported, equilibrium condition. Then a seismic event is applied to the model and blocks are shaken loose falling on the drip shield. Simulated fractures are used to compute blocks formed by their intersection and the rockmass is discretized in the numerical model. The program 3DEC is used to solve the system of equations. 3DEC uses a distinct element method to solve for the interaction between blocks. An explicit finite difference solution scheme is used to solve the equations of motion and deformability of the rock.

**Conceptual Model Components**—There are three key components of this conceptual model that have been included to represent realistic conditions. First the represented rock contains simulated fractures to capture the discontinuum behavior of the expected blocky rockmass. Second, the fractures have been generated using statistical data from mapped fractures, which produce realistic trace maps similar to traces mapped by the geologists underground. Finally, the in situ conditions of gravitational stresses, excavation-induced stresses and thermally-induced stresses have been included to represent static loading conditions, plus a stress wave is propagated through the model to represent dynamic loading conditions. These essential components define a model that is appropriate for the described purposes.

**Representation Accuracy**—As with any modeling analysis, the model is an accurate representation of actual expected rock behavior only when it represents conditions that lie within the known limitations. The mathematical tools employed (FRACMAN and 3DEC) are known to have limitations. However, upon review of the model, it does not appear that the conceptual model lies beyond the applicable mathematical representations of underground conditions and rock behavior. What has been implemented in these analyses is consistent with state-of-the-art numerical modeling techniques in the geomechanics industry.

Judging the accuracy of the model is very difficult because of the lack of measured data. The mathematical model only generally represents the underlying conceptual model. That is—there are no real underground drifts oriented the same as what was modeled to compare static results to. The fractures were only simulated since there is no way to map joints until the excavations are made. Rock and joint properties were only estimated from conditions with sufficient accuracy required to estimate the four objectives of the analysis: effects of jointing, statistical representation of block sizes, changes in drift profile, and time required for drift deterioration to occur. We may never know how accurate the model results are, however, we do know that the approach adopted has been known to produce reasonably accurate results for analyses for which accuracy is known.





The analyses have done a reasonable job of quantifying where accuracy is required when additional, more accurate, analyses are performed. The sensitivity study has identified that joint strength (especially dilation and cohesion), and joint frequency and orientation are critical parameters for predicting unstable block volumes. By identifying the sources of uncertainties and impacts of uncertainties on model output, the authors of this study are able to defend their current estimates and are knowledgeable about improving the model to reduce the uncertainties. More importantly, this study provides a basis for collecting additional field and laboratory data for resolving an important NRC key technical issue.

**Mathematical Model Confidence**—Due to the complexity of the analysis, the process used to establish confidence that the mathematical model produces reasonable results was broken down in parts. First the inputs, or initial conditions, were checked prior to simulating the seismic event. The volume of unstable blocks under ‘static’ conditions was examined for reasonableness. Since the analysis did not examine actual ESF or ECRB drift block geometries, it was not possible to compare the model results to unstable blocks observed underground. The next confidence check of the model was to pass a simple undamped wave to the model, applied at the bottom of the model. The output response at the top of the model was examined for reasonableness. This confirmed that the model was capable of passing waves without energy loss at boundaries and internally to the model. The model was then checked for result reasonableness by applying sequentially larger seismic events. This confirmed that larger seismic loading produced larger volumes of unstable blocks. Finally the sensitivity study was used to confirm the parameters having the greatest influence on the results. This was done to demonstrate the reasonableness of the base case conditions.

**Alternative Algorithms**—The overall approach of using FRACMAN to generate fracture, and 3DEC to compute the block and solve the equations of motions is not the only approach available for assessing block stability. There are alternative algorithms of simulating fractures, but none are known to so robustly address stochastic simulation, plus FRACMAN is the most widely used fracture simulation program in the petroleum, mining and nuclear waste industries. An alternative approach to simulating fractures was examined through the DRKBA rockfall analyses performed prior to this work. The simulation algorithm is not considered as robust as that implemented by FRACMAN. Similarly there are alternative block stability analysis methods available besides using the 3DEC program. The DRKBA program was used which makes use of limit equilibrium solution to stability. It is considered not as accurate as 3DEC since in situ stress, thermal stress, and seismic loading are not explicitly represented. An alternative numerical approach to 3DEC program is the 3-D DDA program. 3-D DDA is a distinct element method that solves the equations of motion and can account for in situ stress, thermal stress and seismic loading. Its limitation, as currently implemented is that blocks are simply deformable and the program has not been ‘qualified’ for use in the quality assurance aspects of nuclear waste program. Therefore, the overall approach to solving the mathematical models (i.e. FRACMAN and 3DEC combination) is the best that the geomechanics industry has to offer. The 3DEC program has been through the process of being ‘qualified’ for use from the quality assurance point of view.



**Input Data Reasonableness**—There are two classes of information used to develop the mathematical models: input data for assigning values to parameters and professional judgment for assembling the model. Great effort has been focused on using representative laboratory and field data to assign to parameters. A table in the report has been developed which identifies the source of inputs and how the magnitudes were determined. The only data that is unsubstantiated is the low probability seismic events (i.e.  $1e-6$ , 1). In the absence of historic data, it is my opinion that these motions are too large and it needs to be demonstrated that the ground can geologically store and release such energy.

**Model Abstractions**—There is no doubt that some of the professional judgments used to develop the model have influence on the results. These judgments are treated differently because they are not a statement that is taken to be true in the absence of confirming data, as an assumption would do. Rather, these judgments are made to simplify the mathematical model, and thus are abstractions. There are trade- offs between accuracy and simplifications in order to compute results. The central constraint on these analyses is that the numerical model required to accurately represent the conceptual model can be excessively large and computationally intensive. Significant effort has been placed on reducing the mathematical model to a manageable size while having minimal impact on the accuracy of results. Judgments were necessary to optimize the number of blocks, the number of finite different zones, the boundary distance from the tunnel, constitutive behavior of intact rock and joints, time-step for dynamic loading, etc. The professional judgments used to simplify the model to a manageable size are logical and not inconsistent with what is commonly practiced in modeling underground tunnels in blocky ground conditions. Several of the simplifications can be argued as to their impact on results accuracy. However, their impact is minimal compared to the impact of the assumptions, especially in regards to the assumed seismic ground motions.

**Intended Use of Results**—It is understood that the output data is intended to be used for two general purposes: to estimate the force magnitude and location of blocks impacting the drip shield, and the profile of the degraded drift. These results could only represent ‘typical best estimates’ given that none of the real drifts currently exist and the fractures have not been mapped. Collectively, the assumptions and simplifications serve to provide results that are thought to be conservative; that is one would expect that fewer blocks than are predicted by the model results would become unstable and fall when subjected to these conditions. However, these results are not considered to be ‘upper bound’ estimates because even more conservative assumptions and simplifications could be made and yet they would not be considered unreasonable. For example, it would have been reasonable to use 2-D UDEC models to provide estimates of unstable blocks. Therefore, the modeling approach adopted is reasonable (and rather novel) when compared to the intended use of the results.

**Appropriate Confidence Level**—Criteria for ensuring the appropriate level of confidence in the model results has been obtained is governed by two sets of criteria: appropriateness of the seismic events and appropriateness of the drift degradation analysis.



As mentioned before, I have serious concerns about the applicability of the low probability seismic records (i.e.  $1e-6$  and  $1e-7$  probability events) supplied as input to appropriately represent the expected ground motion. It has not been shown that such motions are sustainable by the geology, although the mathematical modeling techniques used to estimate the motion are consistent with common practice. Those techniques have not been shown to be applicable to low probability events. Other aspects of the seismic portion of the analysis (i.e. motion application, free field boundaries, event duration, etc.) appear to be appropriate. In order not to bias the results to an extreme type of seismic event, 17 real records were scaled to 3 expected magnitudes (i.e. 15 events implemented in combinations of various fracture realizations for a total of 105 simulations). This approach to examining various scenarios is appropriate given the lack of information on extremely infrequent historic seismic events.

Confidence in the other parts of the model related to simulating ground conditions (i.e. fracture simulation, application of various stress conditions, model discretization, removal of fallen blocks, etc.) are adequate given the intended use of the results. The criterion that data uncertainty be characterized and propagated through the model abstraction appears to be adequately addressed by the sensitivity studies. The need for the model to be compared to known conditions also appears to be adequately addressed by the fracture map comparisons, the pre-event conditions comparisons, and 3DEC results comparisons to DRKBA results. It is important to note that confidence in the model is based only on visual examination of expected conditions since no measurements or recordings were made as part of this analysis.

### **SPECIFIC OBSERVATIONS ON MODEL ASSUMPTIONS AND ABSTRACTIONS**

Given the above general discussion on the adequacy of the overall model results, there are aspects of the analysis that deserve specific comments. The purpose of this section is to address specific assumptions and abstractions that were necessary to assemble the conceptual and mathematical models.

Table 1 is a summary of each modeling issue. The table includes a summary of what aspect of that issue is important and the approach that was adopted in the analysis. Also tabulated is a summary of whether the approach is reasonable and any recommendations for changes or other issues that need to be considered.

Prepared for  
Bechtel/SAIC on behalf of  
U.S. Department of Energy

6/ 20

19 February 2003



Table 1. Summary Model Assumption and Abstraction Issues

Issue	Aspect	Approach	Approach Reasonableness	Recommendation	Page Discussed
Joint Cohesion	Assumption – Magnitude of values	Mean minus 1 std dev, Zero in sensitivity	Reasonable, sensitivity will likely over-predict unstable blocks	Values should depend on other joint strength parameters.	10
Joint Friction	Assumption – Peak vs. Residual values	Mean peak, Residual in sensitivity	Slightly conservative/slightly conservative	See above.	10
Joint Dilation	Assumption – not coupled w/ Friction	Zero, mean in sensitivity	Base case of zero combined with peak friction values is not reasonable	See above.	10
Joint Stiffness	Assumption – low normal & shear magnitudes	Similar normal & shear stiffness	Low values but acceptable since magnitude has minor impact on results		10
Intact Blocks Behavior	Abstraction – No rockmass failure	All elastic except 'glued' joints with high strength	Reasonable since inelastic blocks would not change results		11
Ground Motion	Assumption – extreme probabilities	Extrapolate using standard methods	$1e^{-6}$ and $1e^{-7}$ events appear unreasonably large, not completely rational	Reexamine the magnitude of input ground motions	11
Simulated Fracture Volume	Abstraction – Single realization in large volume	Random tunnel location within volume for different realizations	Reasonable given the limited of mapped data		11
Small Joints	Abstraction – small joints pulled from analysis database	Less than 1m length not included in statistics	Reasonable since they have low probability of forming blocks.		11
Non-Concave Blocks	Abstraction – Cutting non-joint area	Convex-blocks glued & given intact strength	Reasonable given that intact strength is much greater than joint strengths.		12
Fracture Size	Abstraction – Realness of simulation	Simulation based on area of joints per unit volume instead of length & spacing	Reasonable since samples from simulation compared well to maps.		12
Terezaghi Correction	Abstraction – Correct for joints sub-parallel to tunnel	Neglect correction	Reasonable given data collected from variable tunnel orientations & large tunnel size compared to joint spacing.		12



Issue	Aspect	Approach	Approach Reasonableness	Recommendation	Page Discussed
Sub-horizontal. Joint Spacing	Abstraction – Localized variations	Include all data to determine average	Locally not very conservative, but quite reasonable on overall repository scale.	Compute blocks on local spacing (~0.5m) to see block volume change – dynamic runs not necessary.	12
Damping	Abstraction – natural damping of rock mass	None, 5% in sensitivity study	Reasonable given real value is not known and jointing provides some motion damping	Include a couple sensitivity runs	13
Bridge Failure	Abstraction – Bridge is only inelastic portion of block	Joints used intact rock strengths	Reasonable given rock strength is much greater than induced stress field	Check sub-contacts for several cases for failure along bridge and then re-assess need for using finer discretization.	13
Joint Strength Degradation	Assumption – Previous seismic loading of joint system	No degradation, Residual friction. in sensitivity study	Unknown influence, but reasonable approach given sensitivity analysis is lower bound condition.		13
Similar Analysis Approach	Abstraction – Acceptableness of approach	None globally, Portions have been performed before	Collectively the approach is novel, but various parts are common to that done by others and thus overall approach is reasonable.	Include references for other known studies that employ similar approaches.	14
Fractured Rock Boundaries	Abstraction – Sufficient Block Volume	Identify blocks along tunnel surface 25m, 35, & 45m in sensitivity study	Unknown impact, but issue with low probability seismic events, which are already suspect.	Run one case with a much larger fractured volume including floor	14
Fractures in Floor	Abstraction – Tunnel Deformability	Neglect blocks in floor	Reasonable given size of model and interest focused on falling rocks.	See above.	15
In Situ Stress	Assumption – Lithostatic stress field	Mean values, high stress ratio in sensitivity study	Reasonable, little impact on results since stresses would need to be much lower.		15
Event Duration	Abstraction – Length of shaking motion	5%/95% energy cut off by time	Reasonable, little impact on results since significant energy would need to be excluded.		15

Prepared for  
Bechtel/SAIC on behalf of  
U.S. Department of Energy

8/ 20

19 February 2003



Table 1. Summary Model Assumption and Abstraction Issues (Continued)

Issue	Aspect	Approach	Approach Reasonableness	Recommendation	Page Discussed
Event Orientation	Abstraction – Compare to least stable block forces	Flip H1 & H2 along X&Y axes in sensitivity	Reasonable, little impact since horizontal components are similar in magnitude.		15
Removing Unstable blocks	Abstraction – Bulking stabilizes chain blocks	Deleted on contact, left in contact with drip shield in sensitivity study	Over predicts volume of unstable blocks, but provides a broader simulation of rockfall on drip shield		16
Comparison to Real Blocks	Abstraction – Observable validation	No comparisons made	Unknown impact since no real seismic response data exists	Should qualitatively compare blocks formed with those formed from simulated fractures.	16
DRKBA Analyses	Abstraction – Comparison to another approach	Of minor importance since analysis had major limitations	Stability part does not provide reliable comparison because no stress & no motion	De-emphasize DRKBA results in final report	16
Pore Pressures	Abstraction – Strength reduction during shaking	Neglect	Reasonable since not saturated		17
Thermal Stresses	Abstraction – Additional forces on blocks	Decoupled thermal and mechanical	Reasonable since boundary conditions for cooling are unknown		17
Reflecting Boundaries	Abstraction – Wave interference due to close boundaries	Implemented free-field non-reflecting boundaries	Reasonable		17
Support System	Abstraction – Effectiveness for additional support	Neglected	Reasonable since nobody knows how effective they will be in long-term		17

Prepared for  
Bechtel/SAIC on behalf of  
U.S. Department of Energy

9/ 20

19 February 2003



**Joint Cohesion**—The approach adopted for joint cohesive strength was to use the mean value minus one standard deviation from laboratory data. It is not clear for these calculations how much of the cohesion can be relied on in the long-term. For most dam stability analyses (USACOE & USBR) the designers would assume no long-term cohesion. However, during trip underground the joints were observed to be very tight, with the only observable open joints at the springline, most likely associated with tunnel excavation disturbance. Overall, this approach to cohesion is reasonable and yet not overly conservative. It is recommended that joint cohesion be considered in conjunction with the other joint strength parameters, per Barton’s recommendation. See Table 1.

**Joint Friction**—Friction angle values have been taken as mean peak total friction for the base calculations (while assuming dilation is zero). Residual friction values were used in the sensitivity studies. The combinations of cohesion, friction and dilation for estimating rock strength should all be inter-connected and not be treated as independent cases. The base case (i.e. fri. = peak fri. & dil. = 0) is not logical since laboratory tests did not show zero dilation when peak friction is attained. The case with residual friction and no dilation makes physical sense as a state that could exist after disturbance has occurred. It is recommended that joint friction be considered in conjunction with the other joint strength parameters. See Table 1.

**Joint Dilation**—Dilation angles other than zero were run in the sensitivity study. Results suggest dilation has a large influence on the stability of blocks. The laboratory values used for dilation are probably on the low side given the tightness of joints observed during the underground visit. Dilation plays an important role in these analyses partly because of the presence of low apex angle blocks formed by the intersection of the high angle joints. That is, the dominant joints intersect to form large sliver-shaped blocks whose apex angle is between 10° - 20°. Removable blocks require roughness (or dilation) angle if less than ½ the apex angle – in the range of 5° - 10° in order to be removable. This range is close to values reported for the laboratory tests. Therefore, by assuming dilation angle of zero would conservatively predict the number of removable blocks as well as a lower composite joint strength. It is recommended that joint dilation be considered in conjunction with the other joint strength parameters. See Table 1.

**Joint Stiffness**—Joint stiffness were taken as mean values from laboratory data. Shear stiffness normally is expected to be less than normal stiffness, by about 1-2 orders of magnitude. However, joint normal and shear stiffness were the same value in the analysis, which were 6 orders of magnitude less than the stiffness of the intact blocks. Their magnitude seems low given the tightness of joints. The implication of this is that most of the deformation around the tunnel will be taken up by the joint system. When combined with the low cohesion and medium friction angles used for joint strengths, much of the block deformation will be in the form of joint slip. Stiffer joints would mean more of the deformation would be from joint slip instead of slip. Stiffer joints would mean more of the deformation would be from joint slip instead of compression. The approach adopted to assign joint stiffness is not expected to have significant influence on the number of unstable blocks. Thus, the approach to adopting joint stiffness is reasonable and yet not overly conservative. See Table 1.



**Intact Blocks Behavior**—Elastic blocks have been assumed in this analysis. This implies that the intact rock is infinitely strong. Sidewall fractures near springline in the tunnel were observed in the lower non-lithophysal unit during the underground visit. However, beyond a distance of about  $\frac{1}{2}$  m the rock showed minimal observable damage, even in the jointing. The strength of the non-lithophysal rocks is estimated at about 70 MPa, yet the maximum stresses around the tunnel are about 21 MPa (i.e. 3 times  $\sigma_1$ ). During dynamic loading some localized sidewall spalling could be expected. By ignoring the energy loss associated with minor spalling more energy is transmitted to the joint system. This might slightly over estimate the number of unstable blocks. This approach to intact rock strength is quite reasonable, but might result in conservative results (i.e. too large unstable block volumes). It is recommended that a sensitivity case be run with inelastic blocks to see if the low probability seismic events produce stress spikes sufficient to local sidewall spalling. See Table 1.

**Ground Motion**—Ground motion input data represents three probable events: the 1 in 10,000 year event, the 1 in 1 million year event and the 1 in 10 million year event. Peak motions are reasonable for the  $5e-4$  event (PPV = 19 cm/s, PPA = 0.19 g). However, they appear high for the other 2 events ( $1e-6$  : PPV = 2.44 m/s, PPA = 10.46 g and  $1e-7$  : PPV = 5.35 m/s, PPA = 16.28 g). If such ground motions had been experienced underground, there is expected to be geologic evidence of damage, especially in the weaker lithophysal zone. Yet nothing has been reported by site geologists. When these large ground motions are input to the 3DEC model, the results indicate that all removable blocks become unstable. The results appear excessively conservative. See Table 1.

**Simulated Fracture Volume**—Simulated joints have been used to generate the jointing geometry that the blocks are computed from. Statistical parameters from scanline mapping data were computed and input to FRACMAN program to simulate a single realization of the 3-D joint system. The volume of rocks simulated was a 100 m x 100 m x 100 m cube oriented parallel the emplacement drifts (00/073 as X axis,). A 25m x 25m x 25m of rock surrounding the tunnel was then randomly located within the cube. The 3DEC model was “cut” depending on the relative location of joints within the volume. Given the lack of real data in the emplacement drifts (as they are unmined to date) this is a very reasonable approach to estimate the jointing that might be there when the tunnels are excavated. See Table 1.

**Small Joints**—It is understood that statistics were computed (length, spacing, dip, dip direction, termination, etc.) with only mapped joints longer than 1m. Ignoring small joints will have minimal impact on the stability results because 1) it can be shown that small joints have a low probability of intersecting to form blocks and 2) such small blocks have a high probability of being “nested” in larger removable blocks. Thus, the approach to neglecting short joints in the FRACMAN simulation is reasonable and does not produce overly conservative results. In fact the inclusion of such short joints is expected to produce a large number of “isolated” joints whose impact would be to soften the overall rockmass, likely reducing the number of unstable blocks for a given ground motion. This could be verified by making a sensitivity run but is not necessarily recommended at this time given the purpose of the analyses. See Table 1.





**Non-concave Blocks**—3DEC is limited to using non-concave blocks. When fractures are input they must “cut” completely through a given block. The approach adopted was to overcome this limitation by “gluing” joints back together for the portion of the joint beyond the radius of the simulated joint. Complex FISH functions were written to allow this on a block by block basis. Although this approach is quite clever, it is recommended that these functions be carefully checked for errors due to their complexity. This approach has been used by others in programs like UDEC; however, I am not aware of it being used in 3-D. Although “gluing” cut blocks using intact rock properties is a common practice in 3DEC analyses, this application of “gluing partially cut” blocks is novel. This approach is a very reasonable and is capable of producing realistic block geometries and fractured rockmass geometries. See Table 1.

**Fracture Size**—Fracture size is handled in FRACMAN by using trace length and spacing data to compute a statistical area of fractures required in the given volume of rock. The simulation generates a fracture radius and location for a given set while checking the area-to-volume ratio. Each set is simulated separately and then superimposed to compute truncations. The reasonableness of this approach is checked by generating unrolled simulated fracture maps of fractures as they intersect the tunnel walls. These maps were compared to actual unrolled fracture maps recorded underground. The FRACMAN results produce reasonable maps that look realistic when compared to recorded unrolled maps. See Table 1.

**Terezaghi Correction**—The FRACMAN analysis has made no adjustments in the data for fractures oriented sub-parallel to the tunnel. It is common for fractures mapped in smaller diameter openings, such as boreholes, to be biased in the number of fractures recorded sub-parallel to the opening. A Terezaghi correction would normally be applied to the data to correct for this. In the case of the ESF, there is a sub-horizontal joint set sub-parallel to the plunge of the tunnel. However, the project geologists that did the mapping felt that due to a) the large diameter of the tunnel when compared to the observed spacing of the sub-horizontal set and b) the mapped tunnels traversed a range of orientations, it is not likely that a significant number of sub-horizontal fractures were not accounted for in the overall database of joints. Thus, the approach of not applying a Terezaghi correction to the sub-horizontal joint set data is reasonable. See Table 1.

**Sub-Horizontal Joint Spacing**—The spacing of sub-horizontal jointing was observed to vary along the length of the tunnel in the non-lithophysal zone. In some locations it appeared to be on the order of ½ m spacing (longer joints) while in other areas it was in excess of 4m spacing (shorter joints).



Results from the joint statistics report an average spacing of 4.2 m. It is likely that the statistics “smear” the spacing to this larger value. It is this sub-horizontal plane that typically forms the release plane on blocks formed by the intersection on the other 3 joint sets. By not directly accounting for the ½m spacing long sub-horizontal joints, only very large blocks become removable. It is these large blocks where de-stressing around the tunnel has little impact on their stability. Had this closer spacing been used, more blocks nearer the tunnel surface would have been formed and thus a larger unstable volume predicted in certain areas of the tunnel. The approach adopted is reasonable on the scale of the repository, but might under predict unstable blocks locally. It is recommended that other FRACMAN simulations be performed to check the effect on the distribution of removable blocks. It is probably not necessary to perform additional dynamic analyses unless block size distributions are vastly different. See Table 1.

**Damping**—All of the dynamic analyses have been performed with a motion damping coefficient of zero. This implies that the only damping in the system is the energy loss due to interaction between blocks brought about by the open/close shaking of joints. It is common practice to use some minor amount of damping (2% - 5%) to account for natural damping of the rock mass. The impact of not damping the motion is expected to be more high-frequency energy being available at block boundaries and more “vibration” of the joints. This would lead to more joint slip and, thus, more unstable blocks. To neglect damping is reasonable and yet not overly conservative. It is recommended that a couple sensitivity runs be made to verify how conservative this assumption is. See Table 1.

**Bridge Failure**—The way blocks are formed in the model required that the joint extend beyond the simulated radius, but the “non-real” area of the joint was “glued” back using intact rock strengths (see item Non-Concave Blocks above). This glued area simulates an intact “bridge” of rock. When combined with the elastic blocks, any differential motion across the “isolated” joint will result in significant stress concentrations in the “glued” portion nearest the joint. Since the intact rock strength was used for simulate the gluing, this is the only place in the model where the intact rock could fail. Given a) the large strength difference between the joints and the intact rock, b) the rapid load change of the applied seismic event, and c) no applied damping in the system, there could be artificially high stresses generated at the glued contacts nearest the joint contacts. It is not known what percent of the reported unstable blocks had originally glued joints that had broken during the seismic event. The percentage of “unstable blocks with partially glued faces” might be sensitive to the number of sub-contacts along the glued joints. If this is the case, the reported volume of unstable blocks could be over estimated for a modeling discretization reasons. It is recommended that the unstable blocks from a few runs be checked to see if a large portion of their face area were from glued sub-contacts. If this is true, a sensitivity run should be made with a more finely discretized grid. See Table 1.



**Joint Strength Degradation**—The strength of joints were held constant for all seismic events. However, blocks exposed to low probability events will also have experienced higher probability events. This repetitive loading will result in shaking damage to the joint system (e.g., on average for every  $10^{-7}$  event the rock will have experienced 10 of the  $10^{-6}$  events). This shaking damage should manifest itself as a reduction in strength. This behavior was not simulated in the base case analysis. The sensitivity study includes a case with residual joint strengths, which would represent a lower bound condition for this behavior. It is unlikely that accounting for this behavior would improve the reliability of the results since no laboratory data is available to estimate the magnitude of joint strength degradation. Thus, the approach adopted of examining results from residual strength runs is reasonable. See Table 1.

**Similar Analysis Approach**—The entire analysis approach adopted for this study is thought to be unique. The reviewer knows of no other complete set of analyses that have been published in the literature that approach the magnitude or complexity of this study. However, others have adopted aspects of the analyses. For example, the use of FRACMAN to simulate a volume of fractures based on line mapping data has been documented. The same is true of the use of 3DEC to simulate seismic ground motion. The novel portions of the model development (i.e. gluing blocks in non-joint regions, selectively cutting blocks to minimize the numbers of blocks, etc.) is not unique and has been documented. However, it is their automation via FISH functions that has not been published else where to the reviewer's knowledge. Rockfall analyses of waste repository drifts have been studied in the Finish waste program, although the approach was to analyze block stability using static loading and limit equilibrium solutions. Dynamic analyses of rockfall conditions have been performed for South African deep-mining rockburst problems. Given the uniqueness of these analysis requirements, it is the reviewer's opinion, sufficient aspects of the adopted modeling techniques have been documented by other researchers that the overall approach to estimating seismic rockfall volumes is reasonable. All other known similar analyses would be sufficiently more conservative than those presented here. It is recommended that the final report contain references to known published analyses. See Table 1.

**Fractured Rockmass Boundaries**—A 25m x 25m x 25m volume of rock was used to compute discrete blocks in 3DEC, even though 100m x 100m x 100m was simulated in FRACMAN. The sensitivity of results to this volume has been examined by computing blocks in 35m x 35m x 35m volume and 45m x 45m x 45m volume. Results indicate less unstable blocks at 35m and more at 45m. The reason for this is not explained. The reason for using the original 25m was to keep the computations to a manageable size. In the reviewers opinion the sensitivity study does not address whether the 25m volume is adequate. It is recommended that one large block model (60m x 60m x 60m of fractured rocks) with the tunnel centered in the volume be computed with fine zone discretization. This model would simulate blocks more than 10 tunnel diameters extending beyond the major zone of excavation-induced stress region. See Table 1.



**Fractures in Floor**—The model did not simulate any blocks in the floor of the tunnel, yet fractures are known to exist there. The reason was that the analysis focuses on gravitational rockfall after being dislodged. The impact of neglecting fractures in the floor is less deformability of the tunnel and more motion-energy is likely transmitted to the joint system. This approach allows a reduction in the computational size of the model. The approach is reasonable, yet would produce a larger volume of unstable blocks than had the floor been represented as fractured. It is recommended one large block model be computed that includes fractures in the floor (see Fractured Rockmass Boundaries). See Table 1.

**In Situ Stress**—Pre-excavation in situ stresses used in the analyses were taken from mean measurement values. A sensitivity run was made with a higher stress ratio ( $\tau_h : \tau_v$ ). Given the small expected variations in the stress field, there is little influence on the results. In situ stress is considered a minor variable in the analyses and thus the approach adopted is reasonable. See Table 1.

**Event Duration**—The decision was made to truncate the duration of the seismic record due to excessive computational time required to complete the analysis. The approach was to compute the applied energy over time and cut the record duration so that the first 5% and last 5% of the energy was neglected. This is a common practice in numerical modeling of seismic events in such high strength materials because only small changes occur in the model with late-time motion. This would not be the case if pore pressure dissipation was thought to be an issue for block stability. An alternative approach that is used in similar analyses is to perform frequency filtering where high frequencies are filtered since they contain little energy. This was not necessary for these analyses for two reasons: a) the critical time-step is governed by the minimum block and zone sizes capable of transmitting the wave motion, and b) automatic inertial mass scaling was implemented into 3DEC. Additionally, the peak energy is applied early in the record so loose blocks will have had sufficient time to fall, and thus the length of the event is expected to have little impact on the final rockfall volume results. This approach to shorting the record duration is reasonable. See Table 1.

**Event Orientation**—Ground motion was applied to the model parallel the model boundaries with  $v_v$  vertically in Z axis,  $v_{H1}$  horizontally in X axis and  $v_{H2}$  horizontally in Y axis. In the sensitivity study H1 and H2 motion components were reversed. This method does not necessarily produce the worst case motion on individual blocks. However, the combination of forces critical for block stability will be different for each block since each block is comprised of joints of different orientations. Given the near random shape of blocks (and thus their critical force vector orientation) and the fact that H1 and H2 components are of similar magnitude, the net impact on the predicted volume of unstable blocks is expected to be minimal. Therefore the approach of performing a sensitivity computation where the H1 and H2 components are reversed is reasonable. See Table 1.



**Removing Unstable Blocks**—The base case analysis adopted the approach of removing blocks from the analysis after they had made contact with the simulated drip shield. This was done to estimate potential impact of subsequently unstable blocks that might hit the drip shield. In actuality, large blocks would likely stay in contact with the drip shield preventing other blocks from impacting it.

For large collapse zones, large blocks might even prevent other blocks from falling. The other blocks would loosen but not have space to fall freely. In the sensitivity analysis a case was run where no unstable blocks were deleted in order to check this approach. The approach of removing the blocks by deleting them after they contact the drip shield is reasonable. See Table 1.

**Comparison to Real Blocks**—All of the analyses were performed with block geometries determined from the FRACMAN-simulated joint volume. No real blocks in the underground tunnels were analyzed. Although the actual geometry is not known because they extend back into the Rockmass, fewer modeling assumptions are required to generate the blocks (i.e. their location, orientation and tunnel trace length are known). Such an analysis would provide a comparison between the volume of unstable simulated-blocks and the volume of unstable real-blocks. Comparisons of unstable blocks from real and simulated fracture sections are not expected to be the same; however, the ratio of stable to unstable volume of blocks should be similar. It is recommended for purposes of model calibration that 3DEC blocks be generated from the FRACMAN volume for comparison to specific sections of tunnel. If the block volumes are similar then there will be more confidence in the approach used to simulate blocks for emplacement drift orientations. There would be no need at this time to compute the seismic response unless the block volumes were vastly different. See Table 1.

**DRKBA Analyses**—The original rockfall study was comprised exclusively of results from DRKBA limit equilibrium analyses. Those analyses were limited by the following assumptions:

- In situ stresses were neglected.
- The seismic motion was represented by changing joint cohesive strengths.
- Thermal stresses were neglected.
- Fracture simulation was based on joint length and spacing only along tunnel surface and assumed infinite into the Rockmass.
- Small trace length data was included producing significantly more volume of small blocks

The first 3 of these are considered major limitations (the 2nd is considered not completely rational as it applies to resisting forces instead of driving forces). Although there are these limitations, the analyses results provide an alternative approach to the 3DEC numerical model results. It is recommended that the DRKBA results discussion in the original report on be moved to an attachment and they be de-emphasized. See Table 1.



**Pore Pressures**—Pore pressure in the rockmass generated as a result of the seismic shaking were neglected in these analyses. This is reasonable since the rock mass is only partly saturated and the build up of pore pressures is unlikely. See Table 1.

**Thermal Stresses**—Thermal strains induced by the waste heating the drifts will generally serve to increase the stresses on the blocks. As the repository cools over time, these stresses will dissipate. The cooling impact on the local joint system is unknown as joints may either stay closed in compression or open due to tension. Either way, this effect is expected to extend only locally around the peripheral of the drift where the radial stresses are low. Larger blocks would remain clamped by the thermal stresses. The approach adopted in the analysis was to decouple the thermal calculations from the mechanical calculations. This is reasonable since the rock is treated as elastic and all the strains (including thermally induced) are fully recoverable. The only irrecoverable deformations occur as joints slip. Thermal calculations were sequenced by computing: thermal equilibrium, static mechanical equilibrium, and then dynamic loading. This approach is reasonable because it allows the blocks to come to static equilibrium prior to seismic loading. See Table 1.

**Non-Reflecting Boundaries**—One of the problems in modeling seismic events is that the applied wave reaches the boundary of the model and is reflected back into the area of interest before the complete wave has passed through the area of interest. This would result in an amplification of the motion. The 3DEC program was modified specifically for these analyses to include non-reflecting boundaries. This prevents reflected motion from propagating back through the grid. It is reasonable that an equivalent dynamic stress was applied to the base of the model propagating upwards to simulate the seismic event. Vertical free-field boundaries were applied consisting of a row of zones that simulate non-reflecting boundaries. This approach is common for dynamic analyses. See Table 1.

**Support System**—No ground support was included in the model. Although support is expected to be installed in the drifts, it is reasonable to assume that they will not contribute significant support in the long-term. See Table 1.

## CONCLUSIONS

The modeling effort represented by this work is some of the most extensive rockfall analyses in blocky rockmass known to be performed to date. The mathematical model makes use of several novel techniques for representing fractures and then creating a blocky rockmass.

The simulation work done with FRACMAN is theoretically sound and produces a realistic fracture pattern similar to trace maps recorded by the geologists. Although local fracturing (i.e. lengths, spacing, orientation relative to the drift, etc.) might be different than average values computed from the entire database, the simulated fractures appear very reasonable. Even the technique of simulating one set of fractures in a large volume and then sampling from random locations within the volume to create the 3DEC block model is a rational approach,



The combination of joint strength properties (i.e. cohesion, friction angle and dilation angle) for the base case has not been considered collectively. Rather, as independent parameters they represent conditions that do not make sense (i.e. peak friction and no dilation).

Joint stiffness values are low but, since their magnitude has minor impact on results, the approach is acceptable. In agreeing with Dr. Barton (Introduction: Reference #6, above), the normal stiffness should be stiffer than the shear stiffness, although I am not sure I agree with Dr Barton on the orders of magnitude.

The low probability seismic events (i.e.  $1e-6$  and  $1e-7$ ) appear unreasonably large as input ground motion. It should be demonstrated that the geology can store such energy before such events are used in analysis. No geologic evidence, to the reviewer's knowledge, has been presented which suggests that such large events have occurred in the geologic past. There is no doubt that this is the single most influential parameter in the analysis due to the large range of acceleration and velocity variations.

The manner in which sub-horizontal fracture spacing was treated results in predications not very conservative on a local level where average spacing of long fractures is significantly less. However, on an overall repository scale the approach is reasonable because there are other local areas where the sub-horizontal fracture spacing is significantly more than average. This is another reason that the study results apply overall conditions and not locally.

The DRKBA stability analysis performed for the original rockfall study does not provide reliable comparison to these analyses because no stress was included nor was ground motion properly represented. However since there are not many other discontinuum block analyses techniques that can be use to compare the FRACMAN/3DEC analyses to, a summary of the DRKBA results should be left in the report because they are of comparison value.

Finally, it is important to note that the analyses presented in this study have been well conceived. Given the complexity of mathematical models and the limited data available, the team has developed an analysis procedure which is state-of-the-art. They have combined techniques in a way that provides realistic estimates of rockfall volumes and impact on the drip shield. Undoubtedly, as more data become available this approach can be refined to provide more accurate estimates. I do not believe it is worthwhile spending the effort to provide more accurate estimates at this time since data uncertainty is still large.

Prepared for  
Bechtel/SAIC on behalf of  
U.S. Department of Energy

18/ 20

19 February 2003



## Recommendations

There are several techniques that can be used to improve the accuracy of these analyses with the current uncertainty in data. The following recommendations should be considered as part of the work scope for producing a final document for this work. The recommendations are in order of decreasing importance.

1. As mentioned throughout this review the large seismic events are suspect. It is recommended that the input motions be reexamined. Although review of the seismology work was not part of this review scope, more convincing arguments need to be presented which demonstrates that the geology can actually store this energy and sustain such motion.
2. The base case values for joint strength parameters should be examined through a sensitivity study to be consistent with each of cohesion, friction angle and dilation angle.
3. Due to the complexity of the FISH functions within 3DEC model, it is highly recommended that all the functions be independently checked by another engineer to ensure accuracy. This might include more detailed comments/documentation of those functions.
4. A sensitivity case should be included where a block system is computed on local spacing (~0.5m) of sub-horizontal joints to see block volume change. It would not be necessary to perform the dynamic runs. This will provide a feel for variations in the unstable block volumes.
5. The documentation of these analyses should include references for other known studies that employ similar approaches to solving this type problem. This will significantly boost the reader's confidence that the adopted approach has been published elsewhere.
6. A sensitivity case should be included where several damping values are used to estimate the uncertainty in neglecting damping in the model.
7. Unstable blocks should be checked for sub-contacts to have been broken along the "bridge" portion of the block. The results should then be reassessed to see if a sensitivity case is needed with finer discretization provides the same results.
8. A sensitivity case should be developed that uses a much larger fractured volume which includes the floor. This will provide confidence that block stability is not biased by the limited number of blocks simulated in the model.





9. To provide confidence that the simulated fracture set provides stability results similar to that obtained from real mapped fractures, a sensitivity case should be run using specific jointing mapped in the ESF or ECRB drifts. This will qualitatively compare the volume of blocks formed with those formed from simulated fractures and provide confidence that the analyses are not excessively conservative in predicting unstable blocks.
10. The final documentation should de-emphasize DRKBA results by moving them to an attachment and provide a succinct summary of their results.

I hope that BSC finds this 3DEC modeling review to be beneficial. If you have questions on the findings I can be reached at 952-368-3079 or [jtinucci@pantechnica.com](mailto:jtinucci@pantechnica.com).

Respectfully submitted

John P. Tinucci, PE, PhD  
President PanTechnica Corporation

Prepared for  
Bechtel/SAIC on behalf of  
U.S. Department of Energy

20/ 20

19 February 2003

INTENTIONALLY LEFT BLANK

**APPENDIX O**

**DESCRIPTION OF LITHOPHYSAL ABUNDANCE AND LITHOPHYSAL  
CHARACTERISTICS IN THE ECRB CROSS-DRIFT**



## DESCRIPTION OF LITHOPHYSAL ABUNDANCE AND LITHOPHYSAL CHARACTERISTICS IN THE ECRB CROSS-DRIFT

With the large volume of the proposed repository located in the lower lithophysal zone, a detailed study of the lithostratigraphic features in the lower lithophysal zone exposed in the ECRB Cross-Drift has been completed (DTNs: GS021008314224.002 [DIRS 161910] and GS040608314224.001 [DIRS 171367]). The data package documents the distributions of size, shape, and abundance of lithophysal cavities, rims, spots, and lithic clasts, and these data can be displayed and analyzed as (1) local variations, (2) along the tunnel (a critical type of variation), and (3) as values for the total zone. The percent of lengths and areas of features on the tunnel wall are typically referred to as “abundance”. Because of the variations in scale of the features from lengths measured in millimeters to meters and variations in similar rock characteristics from tens to hundreds of meters, a variety of methods have been used to document the features in the rocks (Table O-1). Full Peripheral Maps, Detailed Line Surveys, and Small-Scale Fracture Surveys are primarily to document fractures, although lithophysae are described or annotated in some of these products.

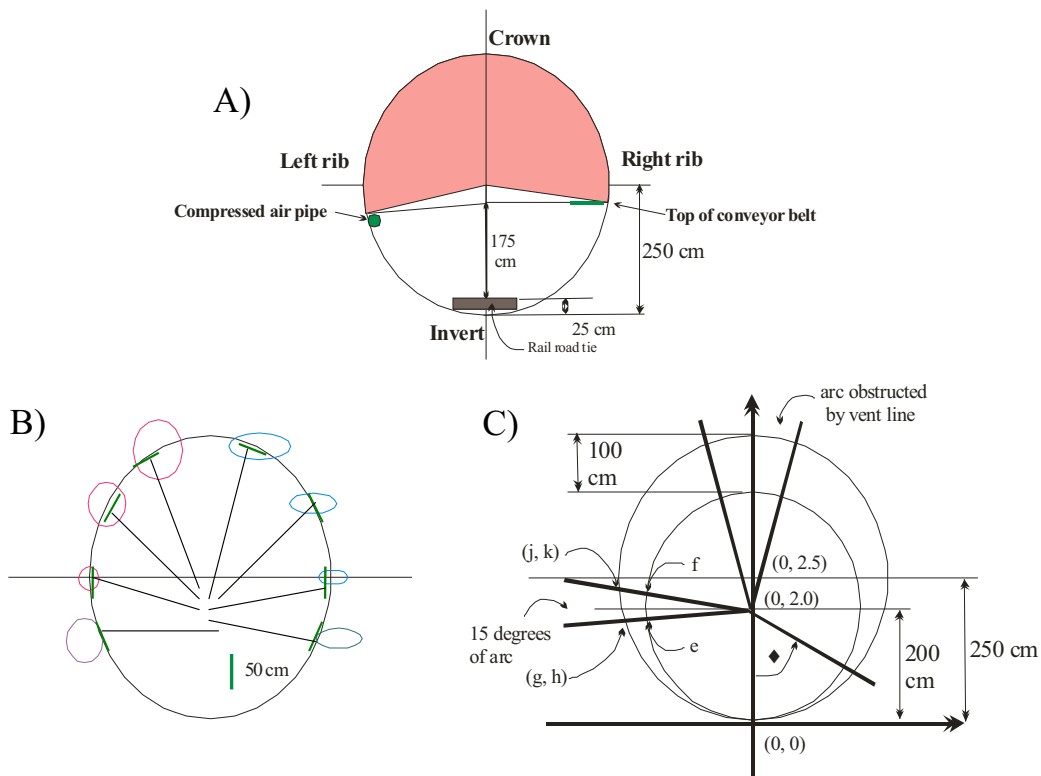
Table O-1. Methods Used to Document the Distribution of Lithostratigraphic Features in the Lower Lithophysal Zone of the Topopah Spring Tuff in the ECRB Cross-Drift

Method	Location	Procedure/Configuration	Data Collected
Full peripheral mapping	ECRB Cross-Drift, continuous (14+44 to 23+26)	Map visible tunnel surfaces	Discontinuities >1 m, contacts, tunnel supports
Detailed line surveys	ECRB Cross-Drift, continuous (14+44 to 23+26)	Tape line along one side of tunnel	Discontinuities >1 m
Small-scale fracture surveys	ECRB Cross-Drift, 6 selected locations (11+15 to 24+30)	Each 6 meter long horizontal traverse intersects three 2 meter long vertical traverses	Discontinuities <1 m
Panel maps	ECRB Cross-Drift, 18 selected locations (14+93 to 22+94)	1 x 3 meter maps, 1:10 scale, overlays on photographs	Lithophysae, rims, spots, lithic clasts
Tape traverses	ECRB Cross-Drift, 187 selected locations at 5 meter intervals (14+05 to 23+35)	Traverses across tunnel, measured with tape attached to pole	Lithophysae cavities only
Angular traverses	ECRB Cross-Drift, 22 selected locations (14+60 to 22+00)	Traverses across tunnel, laser-prism measurements with geometric solutions	Length of lithophysal cavities, rims, spots, stringers, lithic clasts, and matrix-groundmass
Large-lithophysae inventory	ECRB Cross-Drift, continuous (14+40 to 17+55)	528 Lithophysae with long axis 0.5 m and greater	Long axis, short axis, station, wall position

### O1. TAPE AND ANGULAR TRAVERSE DATA

Tape and angular traverses, which are variations in linear or one-dimensional measurement techniques, include data from the upper half of the tunnel (typically from the compressed air pipe on one side to the top of the conveyor belt on the other side, Figure O-1). In linear traverses,

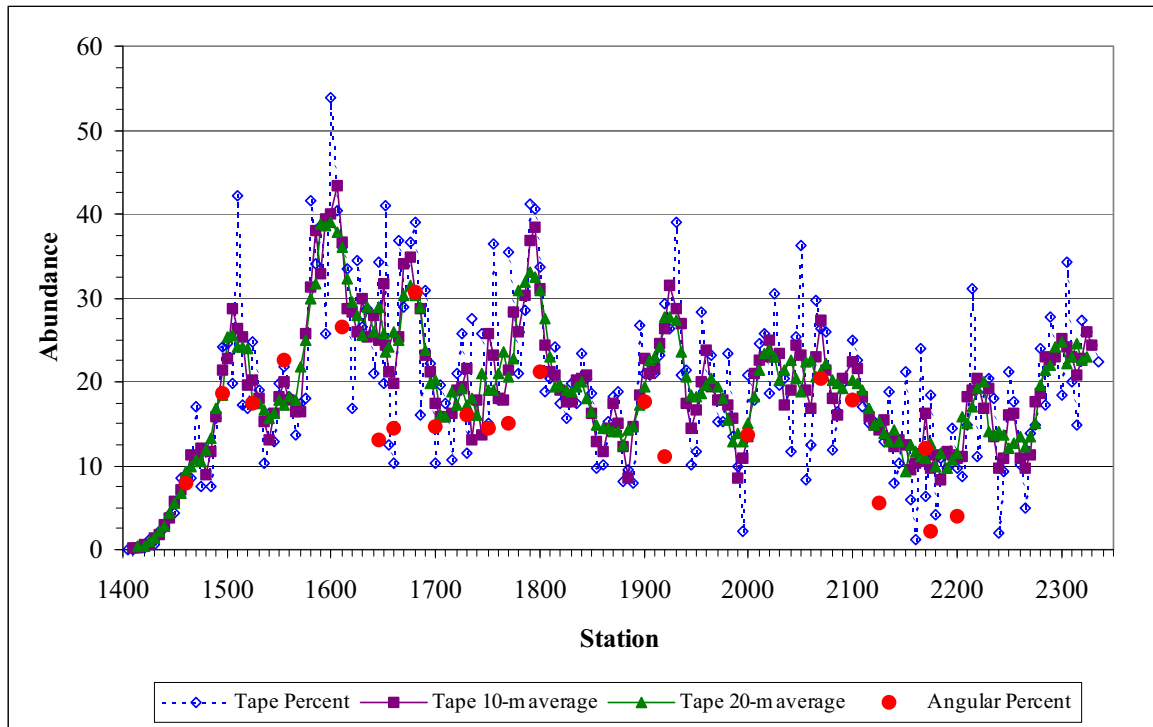
total abundance (percent) of a type of feature is the sum of lengths of the features divided by the total length of the traverse. Tape traverses include the measured length of lithophysal cavities along the traverse, length of the traverse, and a visual estimate of the abundance of rims and spots; therefore, tape data are discontinuous data (not all features are mapped). The advantage of tape traverses is that these data are every 5 m along the tunnel and indicate variations in the lithophysal cavity abundance along the tunnel (Figure O-2; see Section O6.3), but abundance values are typically greater than those documented with angular traverses and panel maps. There are 22 angular traverses, but they consist of continuous data (specific lengths of each lithophysal cavity, rim, spot, lithic clast, and matrix-groundmass), and measurements are to the nearest 5 to 10 mm. Angular traverses consist of continuous data (all features are mapped) and provide a similar resolution of data to that of panel maps. Abundance of lithophysal cavities determined in angular traverses is similar to, or slightly less than, the abundance determined with tape traverses (Figure O-2). Angular traverse data (Table O-2; see Section O6.2) can be used to adjust the lithophysal cavity, rim, and spot data from tape traverses (Section O6.6).



NOTE:

- A) Cross-section view of tunnel (looking toward the heading) showing parts of the tunnel (crown, ribs, and invert), positions of the compressed air pipe, conveyor belt, railroad ties, and position of the laser-prism (175 cm above railroad tie). The shaded area is the most typically measured part of the tunnel.
- B) Tape traverse data are discontinuous in that only the length of the lithophysal cavities is measured.
- C) Angular traverse data are continuous in that the edges of the features are measured and lengths are calculated with analytical geometric relations.

Figure O-1. Geometric Relations of Tape and Angular Traverse Data from the Tptpll



NOTE: Abundance (percent of traverse length) of cavities are from tape and angular traverse data. These data are from DTN: GS021008314224.002 [DIRS 161910] and have not been adjusted as they are in Figure O-9.

Figure O-2. Abundance of Lithophysal Cavities from Angular Traverse data and Tape Traverse Data Collected at 5 m Intervals from the Tptpl in the ECRB Cross-Drift with 10 m and 20 m Moving Averages

## O2. PANEL MAP DATA

In addition to the along-the-tunnel variation in the abundance of features such as lithophysae, there are variations in the sizes, shapes, and distances between features. These types of variations are most easily observed with the panel map data (Figures O-3 to O-8). Locations of the panel maps were positioned to capture representative variations in the rocks along the tunnel, and they were not positioned to capture a specific feature such as the largest lithophysae. The tunnel walls at panel map locations were washed prior to photographing and mapping the site. At each panel map location, three photographs were taken at 90° to the wall and with low-angle illumination to accentuate the relief of the wall caused by cavities (and fractures). The three photographs are merged (to form a mosaic) of an area about 1.6 × 4.3 m and the 1 × 3 m map area is positioned to minimize the number and amount of partially included features. The panel maps, which have a 1:10 scale, are two-dimensional, continuous data because the features are mapped and documented. Boundaries of the features were drawn on the photographs in the field. During the mapping, the mapper attempted to represent the projected intersection of the feature with the tunnel wall, so there might be a slight difference in the mapped shape of the feature compare to the perceived shape in the photograph. On the panel maps, the boundaries of lithophysal cavities, rims, spots, and lithic clasts are depicted with different colors (red, green, blue, and gold respectively) and the alphanumeric labels of the features are L (lithophysal cavities and rims), S (spots), and C (clasts).

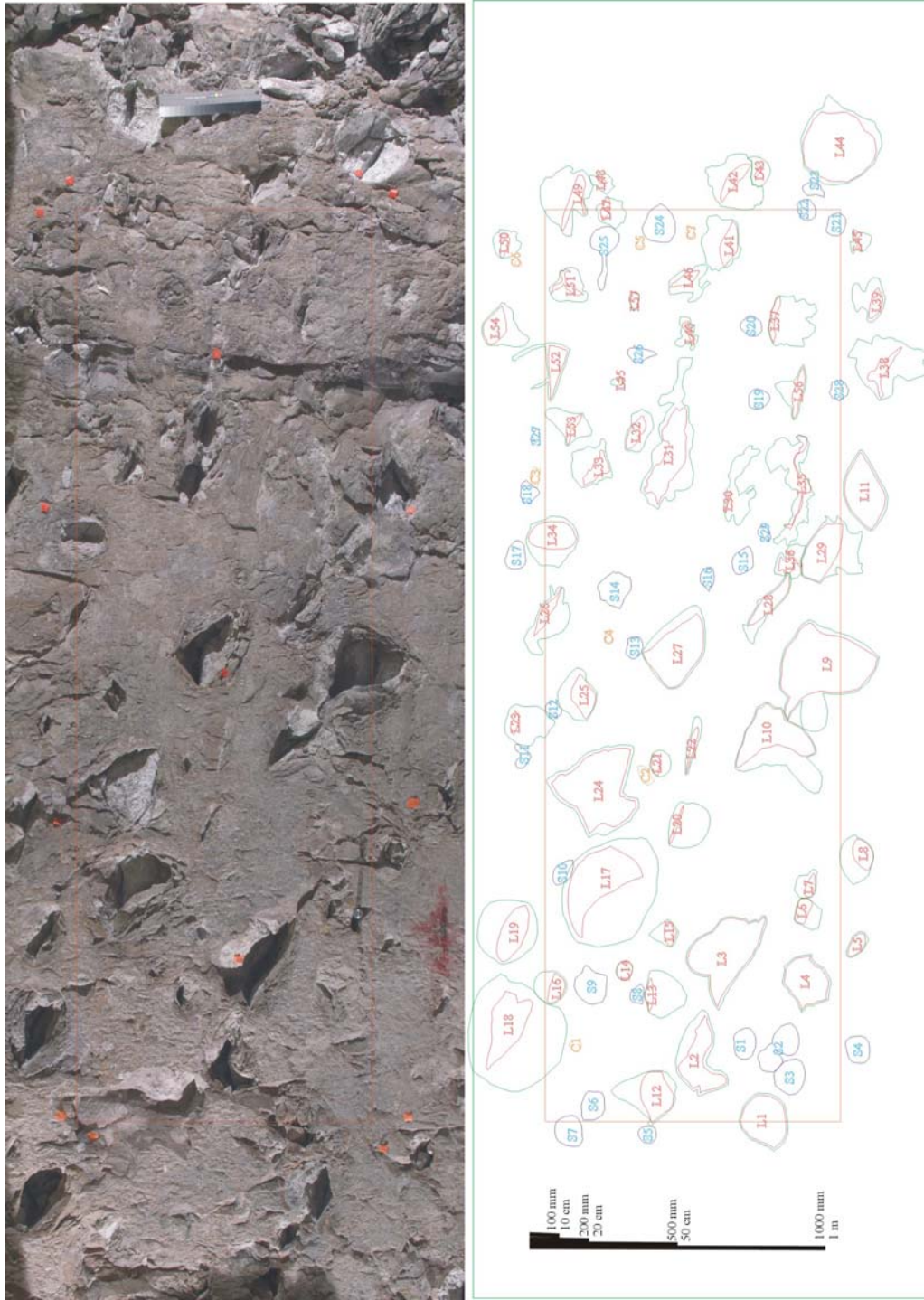
Table O-2. Summary of Traverse Lengths and Abundance (Percentage) of Lithophysal Cavities, Rims, Spots, Lithic Clasts and Matrix-Groundmass Based on Angular Traverses from Stations 14+60 to 22+00 in the ECRB Cross-Drift

Station (m)	Station (m) (numerical)	Total arc length of traverse (degrees)	Total length of traverse (mm)	Total length of visible traverse (mm)	Matrix-Groundmass (percent)	Lithophysal cavities (percent)	Rims (percent)	Spots (percent)	Lithic Clasts (percent)
14+60	1460	228.50	10851	7829	64.2	7.9	11.0	16.8	0.2
14+95	1495	232.33	11003	8967	62.0	18.7	7.2	12.1	0.0
15+25	1525	202.00	9784	7457	59.1	17.4	7.2	15.8	0.5
15+53	1553	202.08	9786	7759	59.9	22.5	8.0	9.6	0.0
16+10	1610	209.58	10095	7393	53.5	26.5	7.0	13.0	0.0
16+42	1642	360.00	15081	11614	70.7	13.1	6.3	8.8	1.1
16+58	1658	206.25	9960	7932	68.0	14.4	8.1	9.5	0.0
16+75	1675	192.25	9369	7316	49.6	30.7	13.7	6.0	0.0
17+00	1700	196.92	9569	7281	63.0	14.6	11.0	11.4	0.0
17+27	1727	208.33	10044	7958	68.2	16.1	8.0	7.7	0.0
17+50	1750	184.17	9016	6916	69.8	14.4	10.6	4.0	1.2
17+70	1770	233.67	10980	8989	74.9	15.0	6.9	3.2	0.0
18+00	1800	191.50	9292	7111	64.0	21.1	10.2	4.8	0.0
19+00	1900	195.08	9450	7046	60.8	17.7	13.9	6.6	1.0
19+20	1920	194.08	9404	7424	67.0	11.1	19.6	2.3	0.0
20+00	2000	192.25	9314	7353	70.3	13.7	6.4	7.2	7.2
20+70	2070	193.83	9387	7049	68.6	20.4	7.5	3.1	0.5
21+00	2100	180.08	9513	7367	66.1	17.8	10.5	5.5	5.5
21+25	2125	193.67	9372	7396	78.6	5.6	8.8	7.0	0.0
21+70 <sup>a</sup>	2170 <sup>a</sup>	176.67	8826	5731	57.9	12.0	5.7	24.3	0.0
21+75 <sup>a</sup>	2175 <sup>a</sup>	171.58	8532	6470	68.0	2.2	8.3	20.9	0.0
22+00	2200	198.00	9628	9196	67.2	3.9	4.8	23.5	0.6

Source: DTN: GS021008314224.002 [DIRS 161910] (Table from file *Tptpl Lithop SEP Data File.xls*, worksheet "SEP-Angular Trav. Data".)

<sup>a</sup> Only cavity data was collected in the angular traverse; however, the amounts of rims and spots were estimated in the field and the values were recalculated to 100 percent.

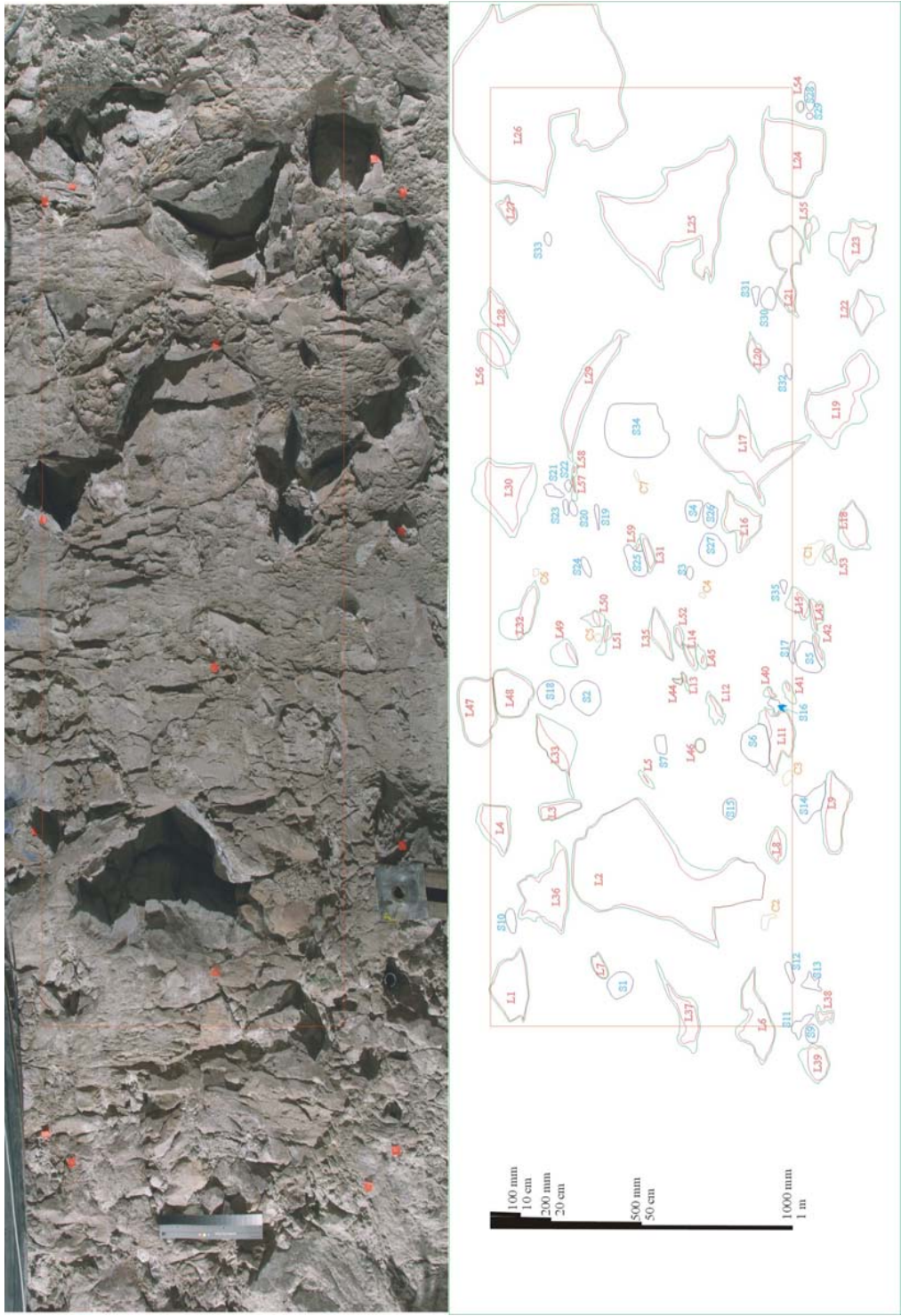




Source: Photograph and map are from DTN: GS021008314224.002 [DIRS 161910].

NOTE: Meter scale is on the left. Red rectangle is the 1x3 m panel map area. Lithophysae have red "L" identifiers with cavities outlined in red and rims in green. Spots have blue "S" identifiers with cyan outlines. Lithic clasts have orange "C" identifiers with gold outlines.

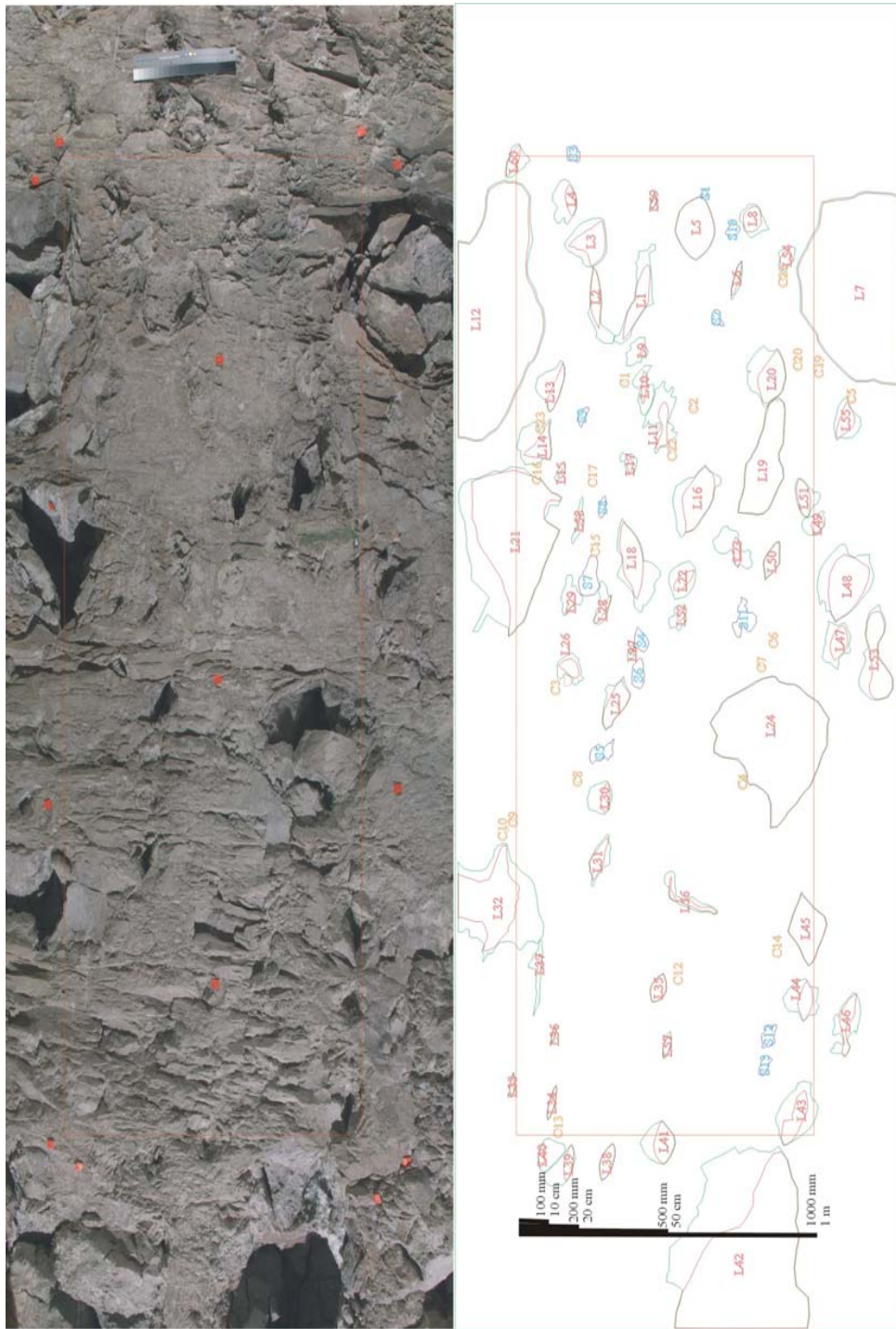
Figure O-3. Lithophysae, Spots, and Clasts of Tptpl located on the Right Rib from Station 14+93 to 14+96



Source: Photograph and Map are from DTN: GS021008314224.002 [DIRS 161910].

NOTE: Meter scale is on the left. Red rectangle is the 1x3 m panel map area. Lithophysae with cavities outlined in red and rims in green. Spots have blue "S" identifiers with cyan outlines. Lithic clasts have orange "C" identifiers with gold outlines.

Figure O-4. Lithophysae, Spots, and Clasts of Tptpll in Panel Map 1641 Located on the Left rib from Station 16+41 to 16+44

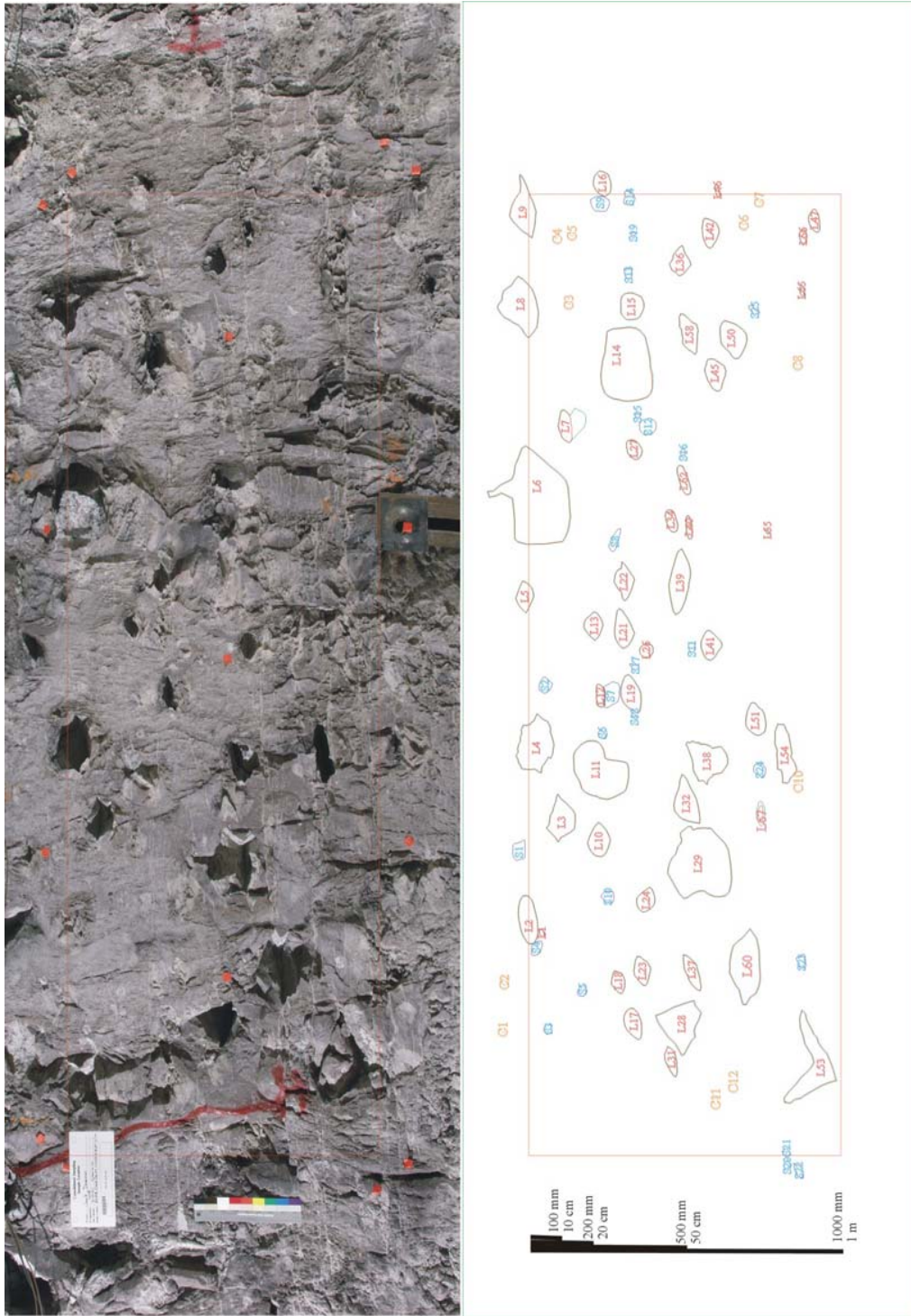


Source: Photograph and map are from DTN: GS021008314224.002 [DIRS 161910].

NOTE: Meter scale is on the left. Red rectangle is the 1x3 m panel map area. Lithophysae have red "L" identifiers with cavities outlined in red and rims in green.

Spots have blue "S" identifiers with cyan outlines. Lithic clasts have orange "C" identifiers with gold outlines.

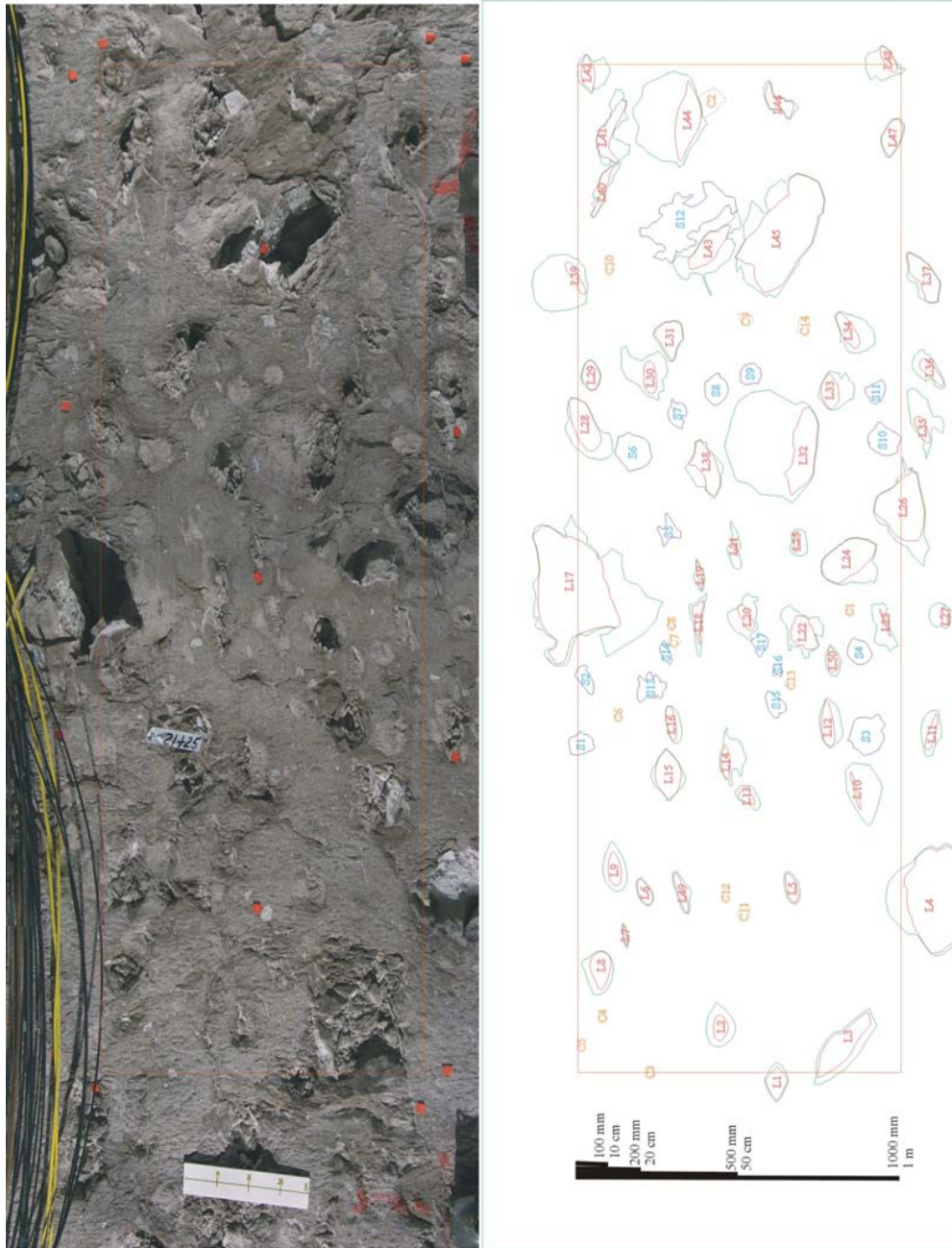
Figure O-5. Lithophysae, Spots, and Clasts of Tptpl in Panel Map 1641 Located on the Right Rib from Station 16+41 to 16+44



Source: Photograph and map are from DTN: GS021008314224.002 [DIRS 161910].

NOTE: Meter scale is on the left. Red rectangle is the 1x3 m panel map area. Lithophysae have red "L" identifiers with cavities outlined in red and rims in green. Spots have blue "S" identifiers with cyan outlines. Lithic clasts have orange "C" identifiers with gold outlines.

Figure O-6. Lithophysae, Spots, and Clasts of Tptpll in Panel Map 1726 Located on the Left Rib from Station 17+26 to 17+29



Source: Photograph and map are from DTN: GS021008314224.002 [DIRS 161910].

NOTE: Meter scale is on the left. Red rectangle is the 1x3 m panel map area. Lithophysae have red "L" identifiers with cavities outlined in red and rims in green. Spots have blue "S" identifiers with cyan outlines. Lithic clasts have orange "C" identifiers with gold outlines.

Figure O-7. Lithophysae, Spots, and Clasts of Tptpll in Panel Map 2124 Located on the Left Rib from Station 21+24 to 21+27



Source: Photograph and map are from DTN: GS021008314224.002 [DIRS 161910].

NOTE: Meter scale is on the left. Red rectangle is the 1x3 m panel map area. Lithophysae have red "L" identifiers with cavities outlined in red and rims in green. Spots have blue "S" identifiers with cyan outlines. Lithic clasts have orange "C" identifiers with gold outlines.

Figure O-8. Lithophysae, Spots, and Clasts of Tptpl Located on the Left Rib from Station 22+32 to 22+35

The selected panel maps (Figures O-3 to O-8) display good examples of many of the lithostratigraphic features. Some of these features are listed below.

- “Simple” lithophysae: L25, L26, and L34 on Figure O-3; L34 on Figure O-4; L4 and L41 on Figure O-6
- Merged lithophysae: L2 on Figure O-4
- Lithophysae with extension cracks where small cracks occur along the cavity wall: L44 on Figure O-3
- Extension-crack lithophysae where the expansion cracks dominate the geometry of the cavity wall: L17 and L25 on Figure O-4; L7, L12, L21, and L24 on Figure O-5
- Backfilled lithophysae (some partial): L26 on Figure O-4; L2 on Figure O-7
- Large-lithophysae (> 50 cm diameter): L2, L25, and L26 on Figure O-4; L7, L12, L21, L24, and L42 on Figure O-5
- Vapor-phase partings (and stringers): Figure O-6 (lower half)
- Spots: Any map, but especially Figure O-7 and Figure O-8
- Fractures mapped with detailed line survey: Red lines in Figure O-8
- Small-scale fractures: Any map, especially the left side of Figure O-5 and the right side of Figure O-6.

Panel maps provide 2-dimensional (area) data for specific features or as the total of the map area (DTN: GS021008314224.002 [DIRS 161910], Table O-3). Additionally, the “Data” files for the panel maps in the data package include 3-dimensional measurements (height, width, and depth) from which an equivalent ellipsoid can be calculated. The methods used in making panel maps and point-counting the areas of features result in values accurate to about 2 to 5 percent of the listed value (DTN: GS021008314224.002 [DIRS 161910]). To test the influence of positioning the map area, the panel map for 16+41 on the left wall was used to compare the reported values with values from four alternative positions. The descriptive statistics on the area percent determined from the five map positions indicate the matrix-groundmass and lithophysal cavities have 95 percent confidence levels of less than 4 percent and the rims, spots, and lithic clasts have 95 percent confidence levels of less than 0.5 percent (DTN: GS021008314224.002 [DIRS 161910], see data summary documentation in the records package).

Table O-3. Summary of Abundance (Percentage) of Lithophysal Cavities, Rims, Spots, and Matrix-Groundmass Based on Panel Maps in the ECRB CROSS-DRIFT from Stations 14+93 to 22+94

Station (m)	Station (m) (numerical)	Panel Maps	Matrix / Groundmass (percent)	Lithophysal Cavities (percent)	Rims (percent)	Spots (percent)	Lithic Clasts (percent)
14+93	1493	14+93L	69.5	13.3	13.3	3.7	0.2
15+51	1551	15+51L	77.3	15.8	3.6	2.0	1.3
16+10	1610	16+10R	78.2	15.3	3.6	2.8	0.1
16+24	1624	16+24R	72.6	13.4	11.3	2.6	0.1
16+41	1641	16+41L	71.6	19.0	5.7	3.5	0.1
16+41	1641	16+41R	80.4	12.6	5.9	1.0	0.1
16+56	1656	16+56L	75.6	13.2	7.3	3.7	0.1
17+26	1726	17+26L	81.9	16.4	0.9	0.7	0.0
17+68	1768	17+68L	83.2	13.6	2.1	0.9	0.1
17+68	1768	17+68R	84.5	10.1	4.6	0.6	0.1
18+05	1805	18+05L	76.7	14.0	5.6	3.5	0.2
18+86	1886	18+86L	73.8	17.4	5.4	3.0	0.3
19+19	1919	19+19L	83.6	12.8	2.1	1.3	0.3
20+18	2018	20+18L	77.5	15.3	4.9	2.1	0.2
20+69	2069	20+69L	83.8	9.2	3.9	3.0	0.2
21+24	2124	21+24L	78.2	8.5	9.7	3.2	0.5
22+32	2232	22+32L	62.4	5.3	7.4	24.6	0.2
22+94	2294	22+94L	86.1	7.5	0.3	5.7	0.4

Source: DTN: GS021008314224.002 [DIRS 161910].

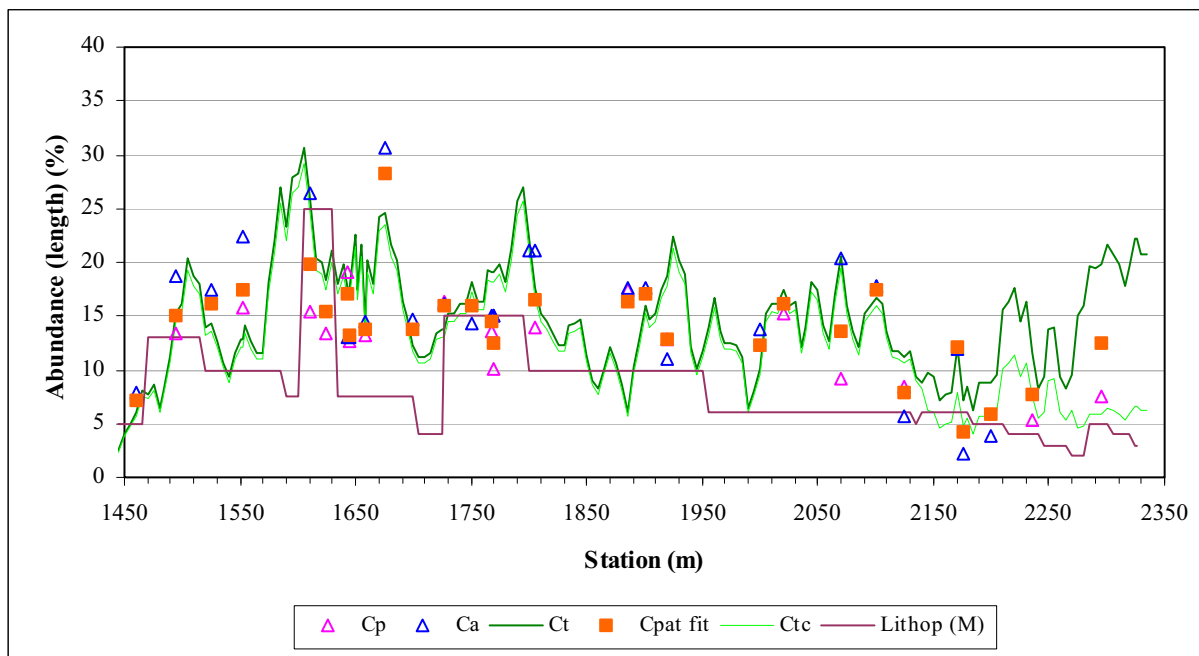
NOTE: Table is from file *Tptll Lithop SEP Data File.xls*, worksheet "SEP - Panel Map Data".

### 03. VARIATION IN ABUNDANCE IN LITHOPHYSAL CAVITIES, RIMS, AND SPOTS ALONG THE TUNNEL

The abundance of lithophysal cavities varies along the Cross-Drift partially from actual variations in the rocks and in part resulting from the methods used to collect the data (i.e., tape or angular traverses or panel maps) (Figure O-9). The abundance of cavities determined from the panel maps and angular traverses have not been adjusted. However, the original abundance values for lithophysal cavities from tape data (Figure O-2) have been corrected using a "typical" traverse length, a 15 m moving average, and a linear equation of correlation for collocated tape and angular traverse data (Sections O6.3 and O6.6). Numerous correlation equations were examined (Section O6.6), and a linear equation fitted to the collocated data and having an intercept at 0, with an  $R^2$  of 0.6204 was the best correlation and resulted in the corrected curve "Ct" in Figure O-9. A set of cavity values was calculated for each location with two or more types of data using the ratios 60:30:10 (panel:angular:tape) where the three data occur and 60:40 (panel:tape or angular:tape) where there are only two types of data ("Cpat fit" in Figure O-9). These weighting ratios are empirically determined based on the relative detail of each type of data. The tape data was corrected one last time using an empirically determined proportional adjustment (i.e., corrected value [Ctc] equals tape value [Ct] plus the tape value [Ct] times a percent) (Section O6.6). The percents used include -0.05 from 14+05 to 21+40, -0.35 from 21+45 to 22+70, and -0.70 from 22+75 to 23+35. These percents, especially the larger



amounts from 21+45 to 23+35, were used to correct large cavity abundance values inherited from the original tape data that resulted from initially identifying the abundant spots (some with thin veinlets in them) as lithophysal cavities. This correction of the tape data is warranted on the basis of comparisons with the angular traverse and panel map data (there are no angular traverse data from 22+00 to 23+35) and estimates of lithophysae described in Mongano et al. (1999 [DIRS 149850]) (Figure O-9; see Section O6.5).



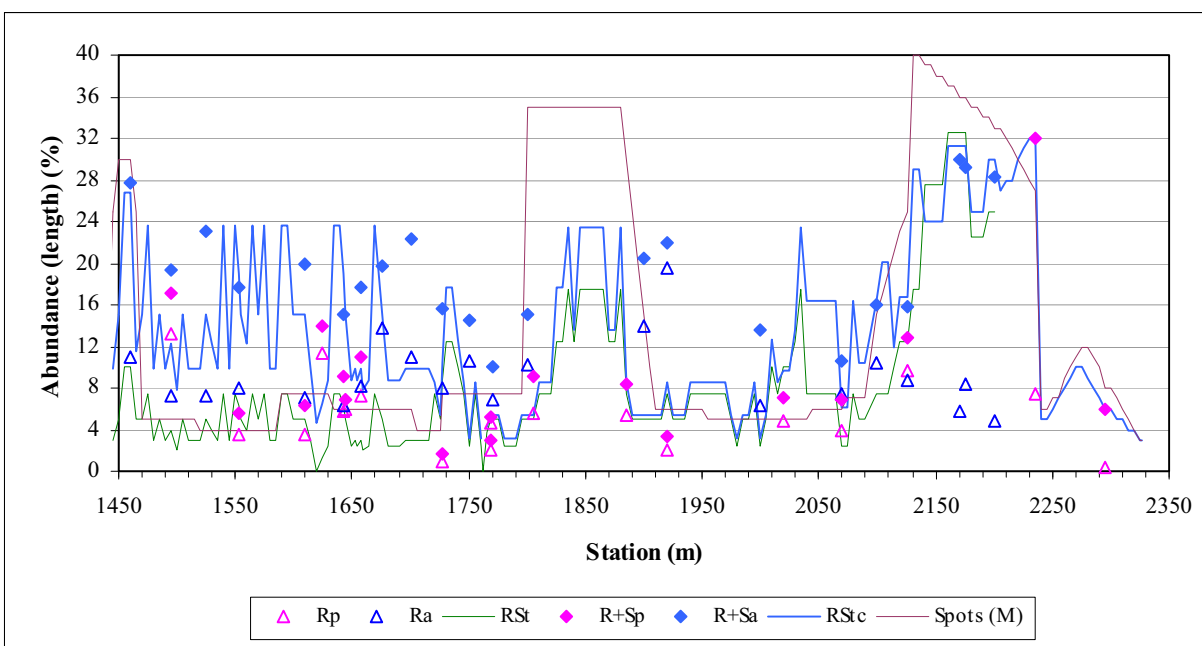
Source: DTN: GS021008314224.002 [DIRS 161910].

NOTE: "Ct" data has been corrected based on an equation for correlation of tape and angular data. "Cpat fit" is the calculated value where two or more types of data occur together (map, angular, or tape data). "Ctc" has been corrected, especially from Station 21+25 to 23+35, to emulate the smaller amounts of lithophysal cavities determined from panel maps and angular traverses. Correlations and calculations for Ct, Cpat fit, and Ctc are described in Section O6.6. The results are compared to the cavity values (Lithop M) from Mongano et al. (1999 [DIRS 149850]). The data and curves are presented in file *Drift Deg AMR AF T-A-P fit V1.xls*, worksheet "Length - Fit and Stats" (See Table A-1).

Figure O-9. Abundance of Lithophysal Cavities from Panel Maps (Cp) and Angular and Tape Traverses (Ca and Ct, Respectively)

Similar to the lithophysal cavity data, the abundance of rims and spots varies along the ECRB Cross-Drift partially from actual variations in the rocks and in part resulting from the methods used to collect the data (i.e., tape or angular traverses or panel maps) (Figure O-10). The abundance of rims and spots determined from the panel maps and angular traverses have not been adjusted. However, the original visual estimates of "rims plus spots" in the tape traverses (see Section O6.3 and "RSt" in Figure O-10) have been corrected using 5-m and a 2<sup>nd</sup>-order polynomial equation of correlation for collocated tape and angular traverse data (Section O6.6). Numerous correlation equations were examined, but in the end, a 2<sup>nd</sup>-order polynomial equation (which because of the very small  $x^2$  value approximates a linear equation) was fitted to the collocated data from 17+60 to 22+00, and although the Y-axis intercept is +11.086, the  $R^2$  is 0.7973 (Section O6.6). As with the lithophysal cavity data, a set of "rim+spot" values were

calculated for each location with two or more types of data using the empirically determined ratios of 60:30:10 (panel:angular:tape) where the three data occur and 60:40 (panel:tape or angular:tape) where there are only two types of data. These values were used during curve fitting, but are not displayed in Figure O-10. The totals of “rims plus spots” from the panel and angular data have been calculated and compare well to the corrected “rim plus spot:” tape values (R+Sp, R+Sa, and RStc, respectively in Figure O-10). There are no visual estimates of rims plus spots in the tape traverse data from 22+00 to 23+35, so these values are estimated from the panel map data and descriptions from Mongano et al. (1999 [DIRS 149850]) (Sections O6.3, O6.5, and O6.6). The sharp decrease in spots depicted in curves “RStc” and “Spot (M)” (Figures O-10 and O-11) result from changes in the abundance of spots across a fault at 22+38 (Mongano et al. 1999 [DIRS 149850]).

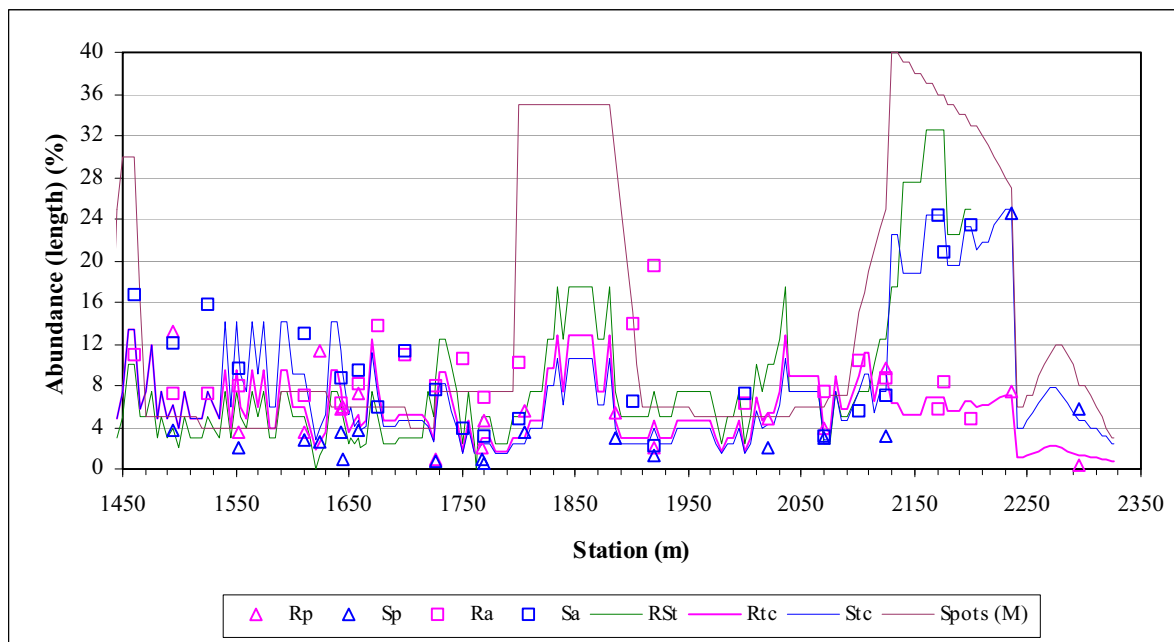


Source: DTN: GS021008314224.002 [DIRS 161910].

NOTES: “R+Sp” is rims plus spot values in panel maps. “R+Sa” is rims plus spot values in angular traverses. “RStc” is the corrected tape values based on an equation for correlation of tape and angular data. Correlations and calculations for R+Sp, R+Sa, and RStc are described in Section O6.6. Spot values from Mongano et al. (1999 [DIRS 149850]) are described in Section O6.5. The data and curves are presented in file *Drift Deg AMR AF T-A-P fit V1.xls*, worksheet “Length - Fit and Stats” (See Table A-1).

Figure O-10. Abundance of Rims From Panel Maps (Rp) and Angular (Ra) and the Combined Rim and Spot Values from Tape Traverses (Rt)

The “rim plus spot” values from the corrected tape data was separated into rim and spot values based on the general ratios of each feature in the panel and angular traverse data respectively. These proportions are not the same along the tunnel, so a series of proportions were empirically determined. The ratios of rims to spots include 0.50 from 14+45 to 15+35, 0.40 from 15+40 to 16+52, 0.53 from 16+55 to 17+35, 0.55 from 17+40 to 21+25, and 0.22 from 21+30 to 23+35. The total corrected “rim plus spot” (RStc) was multiplied by these ratios to calculate the amount of rims, and the amount of spots was determined by difference (Rtc and Stc, respectively in Figure O-11).



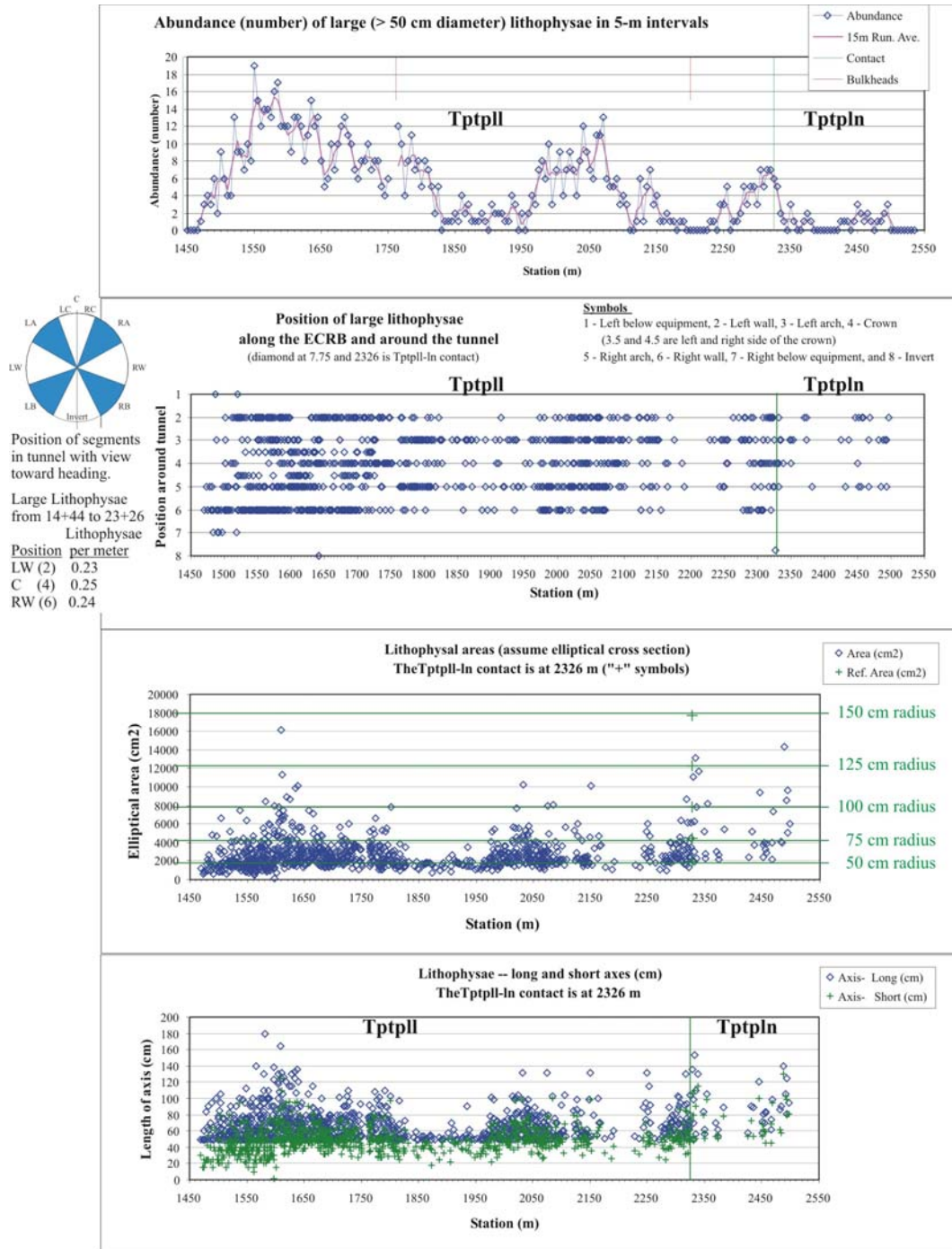
Source: DTN: GS021008314224.002 [DIRS 161910].

NOTE: "Rtc" represents fitted rim values from the corrected "RStc" (Figure O-10) based on the ratio of rim and spot values in panels and angular data. "Stc" represents fitted spot values from the corrected "RStc" (Figure O-10) based on the ratio of rim and spot values in panels and angular data. Correlations and calculations for Rtc and Stc are described in Section O6.6. Spot values from Mongano et al. (1999 [DIRS 149850]) are described in Section O6.5. The data and curves are presented in file *Drift Deg AMR AF T-A-P fit V1.xls*, worksheet "Length - Fit and Stats" (See Table A-1).

Figure O-11. Abundance of Rims and Spots from Panel Maps (Rp and Sp), Angular (Ra and Sa), and the Original Estimated Combined Rim and Spot Values from Tape Traverses (RSt)

#### O4. LARGE LITHOPHYSAE

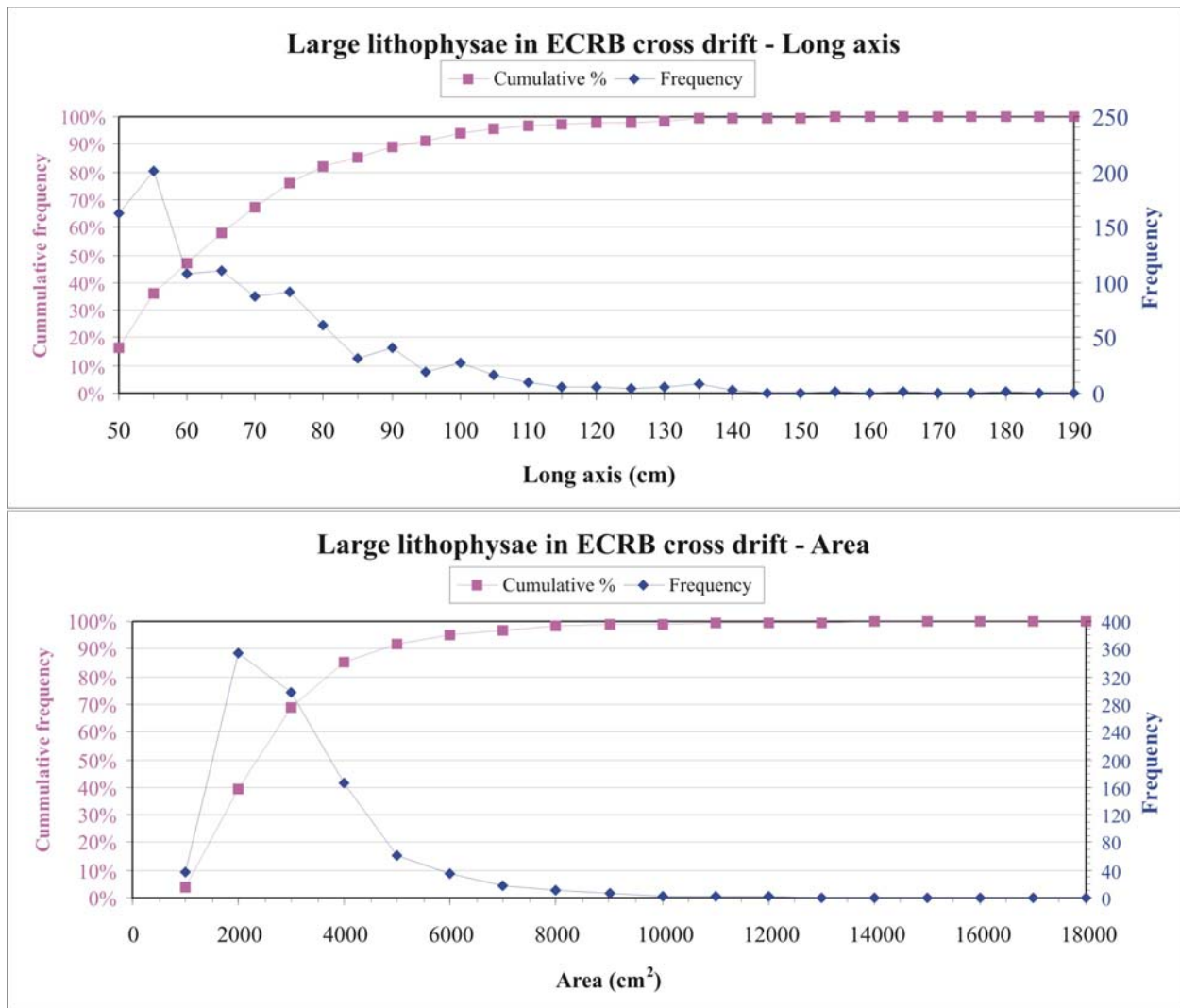
The large-lithophysae inventory was designed to document the large lithophysae (those with a minimum diameter of 50 cm) in the ECRB Cross-Drift from Station 14+00 to 17+56. The initial phase of the inventory stopped at 17+56 because of a closed bulkhead (DTNs: GS021008314224.002 [DIRS 161910]), and the second phase of the inventory was completed from 17+60 to 25+35 after the bulkhead was opened (GS040608314224.001 [DIRS 171367]). A few large lithophysae were documented (entirely or partially) in the tape and angular traverses and panel maps, but most were not included in these other techniques because of the scales and locations at which the other measurements were made. The long and short axis exposed on the wall of the tunnel was measured (with the same tape on a pole technique used in the tape traverses), and the station and position on the tunnel wall was recorded (DTNs: GS021008314224.002 [DIRS 161910]; GS040608314224.001 [DIRS 171367]). There are accurately surveyed station, northing, easting, and elevation values for the large lithophysae (DTNs: GS021008314224.002 [DIRS 161910]; GS040608314224.001 [DIRS 171367]). The large-lithophysae data can be displayed by station along the tunnel as discrete features and 5 m abundance (simply the number count) (Figure O-12), or a cumulative frequency and frequency plots of axis length and area (Figure O-13).



Source: DTNs: GS021008314224.002 [DIRS 161910]; GS040608314224.001 [DIRS 171367].

NOTE: Diagram of tunnel cross-section shows the nomenclature used to identify the position of large lithophysae. The small inserted table lists the average number of large lithophysae per meter of tunnel for the left and right walls (LW and RW, positions 2 and 6, respectively) and the crown (C, position 4) from Stations 14+70 to 17+56.

Figure O-12. Abundance (Number of Large Lithophysae) per 5 m Intervals, Locations, Areas, and Long and Short Axes of Large Lithophysae in the Tptpll and Tptpln from ECRB Cross-Drift Station 14+50 to 25+00



Source: DTNs: GS021008314224.002 [DIRS 161910]; GS040608314224.001 [DIRS 171367].

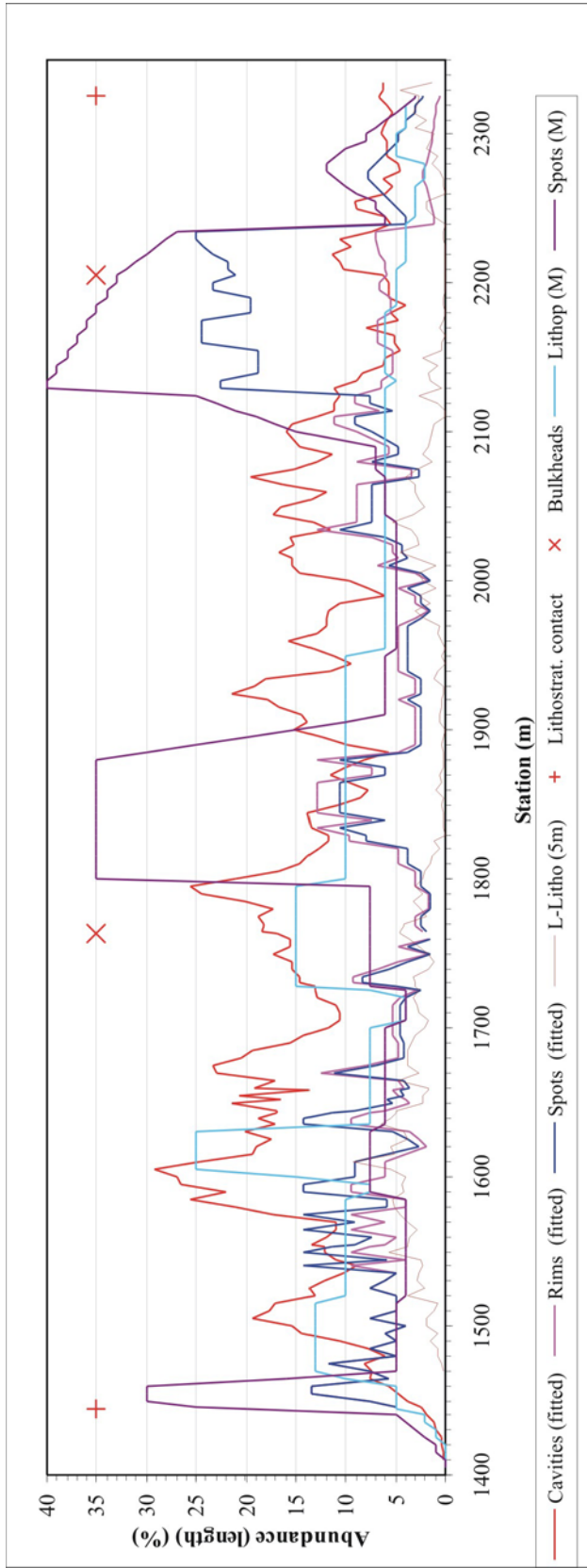
NOTE: The data and curves are presented in file *Drift Deg AMR AD L-Litho V1.xls*, worksheet "Tptll Large-Litho Sum Graphs" (See Table A-1).

Figure O-13. Frequency and Cumulative Frequency of the Long Axes and Areas of Large Lithophysae in the Tptll in the Cross-Drift

### O5. CALCULATED POROSITY OF LITHOPHYSAL CAVITIES, RIMS, SPOTS AND TOTAL POROSITY ALONG THE TUNNEL

The corrected tape traverse data for lithophysal cavities, rims, and spots results in "fitted" abundance curves and indicates substantial variations along the tunnel in these features (Figure O-14). Using these "fitted" abundance curves for lithophysal cavities, rims, and spots, and (by difference) the matrix-groundmass (and ignoring the trace amount of lithic clasts), the porosity of these features and the total porosity along the tunnel can be calculated (Figure O-15). The porosities of each of the component features are variably constrained. Lithophysal cavities have a porosity of 1.00 cm<sup>3</sup>/cm<sup>3</sup>. Samples from the upper and lower lithophysal zone in the ECRB Cross-Drift have been used to determine the porosities of the matrix-groundmass, rim, and spot features (DTN: GS030483351030.001 [DIRS 163440]). Measured porosity values of

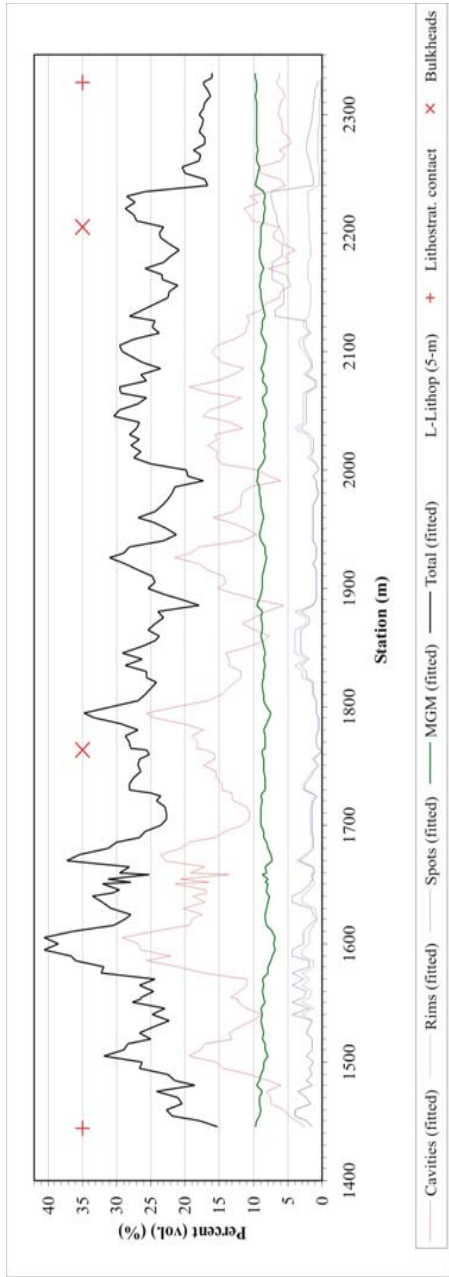
the matrix-groundmass in samples from the lower lithophysal zone in the ECRB Cross-Drift range from 0.09 to 0.14 cm<sup>3</sup>/cm<sup>3</sup>, and rims and spots in these same samples range from 0.23 to 0.37 cm<sup>3</sup>/cm<sup>3</sup>, so calculations of porosity in this report use a mean porosity of 0.104 cm<sup>3</sup>/cm<sup>3</sup> for matrix-groundmass and 0.30 cm<sup>3</sup>/cm<sup>3</sup> for rims and spots (Otto and Buesch 2003 [DIRS 170727]; DTN: GS030483351030.001 [DIRS 163440]). Additionally, inclusion of the large lithophysae can locally contribute as much as 9.4 percent to the total porosity (see station 16+10 in Figure O-15b). In several other sections of the tunnel, the large lithophysae contribute from 3 to 6 percent, with other sections having 0 to 2 percent (Figure O-15b). Although for many purposes it is appropriate to describe the distributions and porosities of each type of feature (lithophysal cavities, large-lithophysal cavities, rims, spots, and matrix-groundmass), these features can be combined into similar associations (small and large lithophysal cavities, rims plus spots, and matrix-groundmass) (Figure O-16).



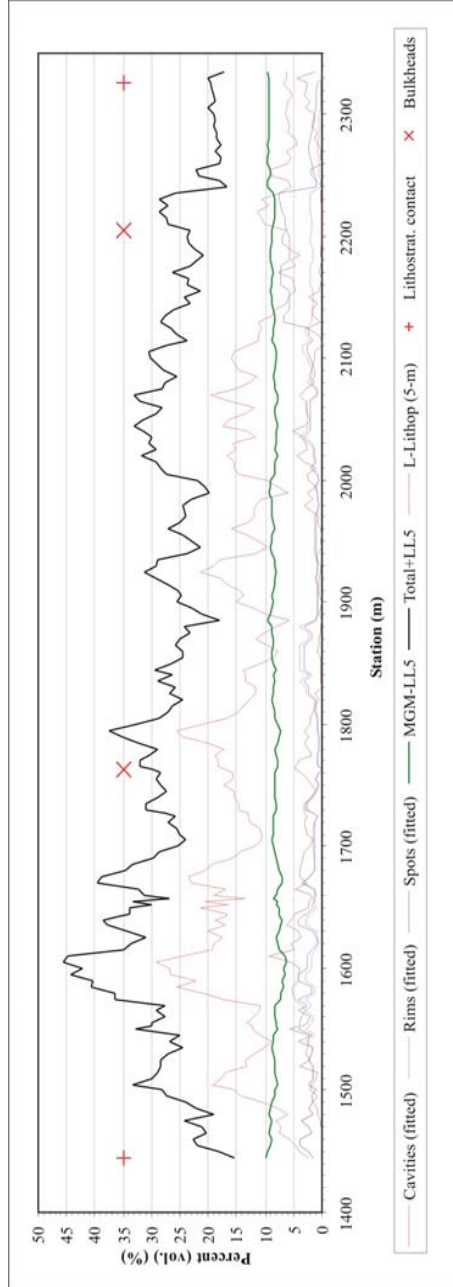
Source: DTNs: GS021008314224.002 [DIRS 161910]; GS040608314224.001 [DIRS 171367].

NOTE: Additional details provided in Section O6.6 and file *Drift Deg AMR AF T-A-P fit V1.xls*, worksheet "Length - Fit and Stats" (See Table A-1). Estimates of lithophysae (Lithop M) and spots (Spots M) are from Mongano et al. (1999 [DIRS 149850]).

Figure O-14. Abundance Curves of Lithophysal Cavities, Rims, and Spots (Determined by Combining Panel Map and Tape and Angular Traverse Data), Large-Lithophysae Based on 5 m Segments of the Tunnel, and Estimates of Lithophysae and Spots



a)



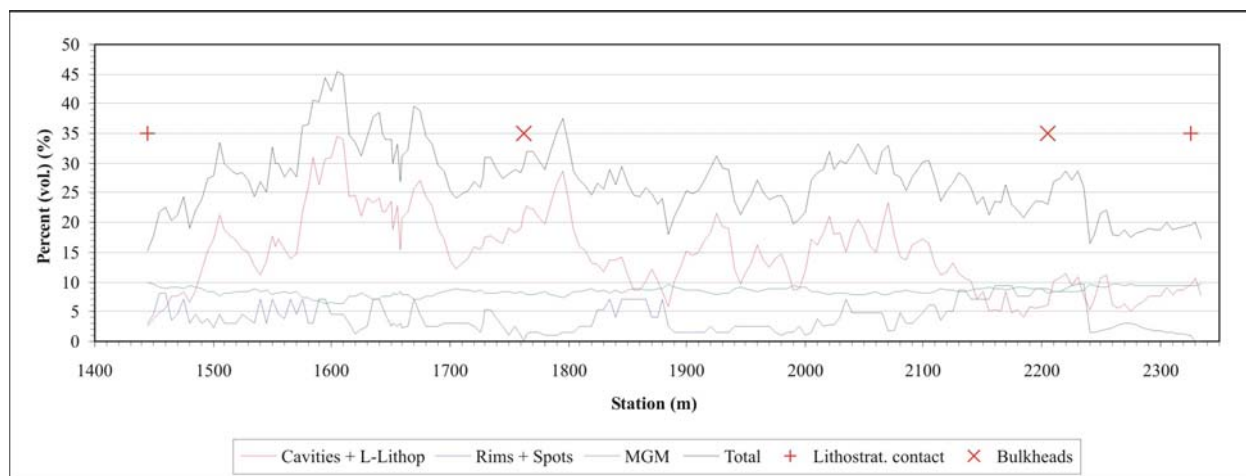
b)

Source: DTNs: GS021008314224.002 [DIRS 161910]; GS040608314224.001 [DIRS 171367].

NOTES: Porosity of the 5 m averaged large-lithophysae inventory is not included in the total in the upper graph (a). The large-lithophysae values are included in the lower graph (b). Additional details provided in Section O6.6 and file *Drift Deg AMR AF T-A-P fit V1.xls* (See Table A-1).

Figure O-15. Calculated Porosity of Lithophysal Cavities, Rims, Spots, Matrix-Groundmass, and the Total Porosity in the Tptpl Exposed Along the ECRB Cross-Drift





Source: DTNs: GS021008314224.002 [DIRS 161910]; GS040608314224.001 [DIRS 171367].

NOTE: Additional details provided in Section O6.6 and file *Drift Deg AMR AF T-A-P fit V1.xls*, worksheet "Volume Percent - Stats" (See Table A-1).

Figure O-16. Calculated Porosity of Lithophysal Cavities (Including Large Lithophysae), the Combination of Rims and Spots, Matrix-Groundmass (MGM), and the Total Porosity in the Tptpll Exposed in the ECRB Cross-Drift from Station 14+44 to 23+30

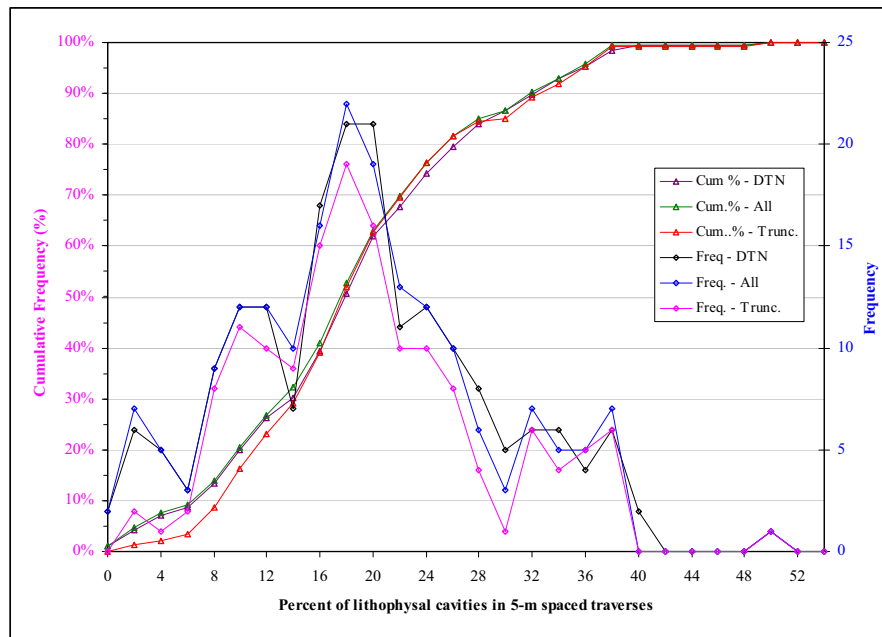
## O6. DESCRIPTIVE STATISTICS FOR THE TOTAL LOWER LITHOPHYSAL ZONE

In addition to the along-the-tunnel variations in abundance, size, and shape of lithophysal cavities, rims, and spots, the distributions of these features can be summarized for the total lower lithophysal zone. For example, using the tape traverse data, the abundance of cavities in each traverse has a mean of 18 to 19 percent depending on the length of tunnel used in the calculation (Table O-4, Figure O-17, and Section O6.3). The tape data used in this figure has been adjusted to the "typical traverse length" but has not been "corrected" with the several "correlation functions" described previously and in Section O6.6. Similarly, the abundance (percent) of individual lithophysal cavities within a traverse indicates most lithophysal cavities form about 2 percent of a traverse length (Table O-5, Figure O-18, and Section O6.3), and the typical length of lithophysal cavities along the traverses is about 150 mm (Table O-6, Figure O-19, and Section O6.3). Descriptive statistics comparing the 5 m traverse data with 10 m, 15 m, 20 m, 25 m, and 30 m "moving averages" indicates no effective change in the mean of 18.9 percent lithophysal cavities, but many of the statistics decrease with increasing length of the "moving average" (Table O-7 and Section O6.3). However, the most significant change in the statistics for the abundance of lithophysal cavities, especially in the standard deviation and sample variance, occurs from the 5 m to 10 m or 15 m data (Table O-7 and Section O6.3). The typical abundance of "rims plus spots" from the tape traverse data is about 8 percent depending on the length of tunnel used in the calculation (Table O-8 and Section O6.3).

Table O-4. Descriptive Statistics for the Abundance of Lithophysal Cavities in Individual Tape Traverses for Various Lengths of Tunnel in the Tptpl in the Cross-Drift

Statistic	Data Package	Revised			
		2335 to 1405	2326 to 1444	2320 to 1460	2200 to 1460
Stations	2335 to 1405	2335 to 1405	2326 to 1444	2320 to 1460	2200 to 1460
Length along tunnel (m)	930	930	882	860	740
Mean	19.4	18.0	18.7	18.9	18.9
Standard Error	0.7	0.7	0.7	0.7	0.7
Median	18.8	17.6	17.8	17.8	17.8
Mode	15.2	16.2	16.2	16.2	16.6
Standard Deviation	10.2	9.3	8.8	8.7	8.7
Sample Variance	103.3	86.7	76.9	74.8	75.4
Kurtosis	0.1	-0.1	0.0	0.1	0.2
Skewness	0.4	0.3	0.5	0.6	0.6
Range	53.9	48.4	47.2	47.2	47.2
Minimum	0.0	0.0	1.2	1.2	1.2
Maximum	53.9	48.4	48.4	48.4	48.4
Sum	3,608	3,355	3,298	3,254	2,793
Count	186	186	176	172	148
Confidence Level (95.0%)	1.5	1.3	1.3	1.3	1.4

NOTE: Data in "Data Package" column from DTN: GS021008314224.002 [DIRS 161910]. The Revised data are in *Drift Deg AMR AC T-Trav.xls*, worksheet "Tape data (mm)" (see Table A-1).



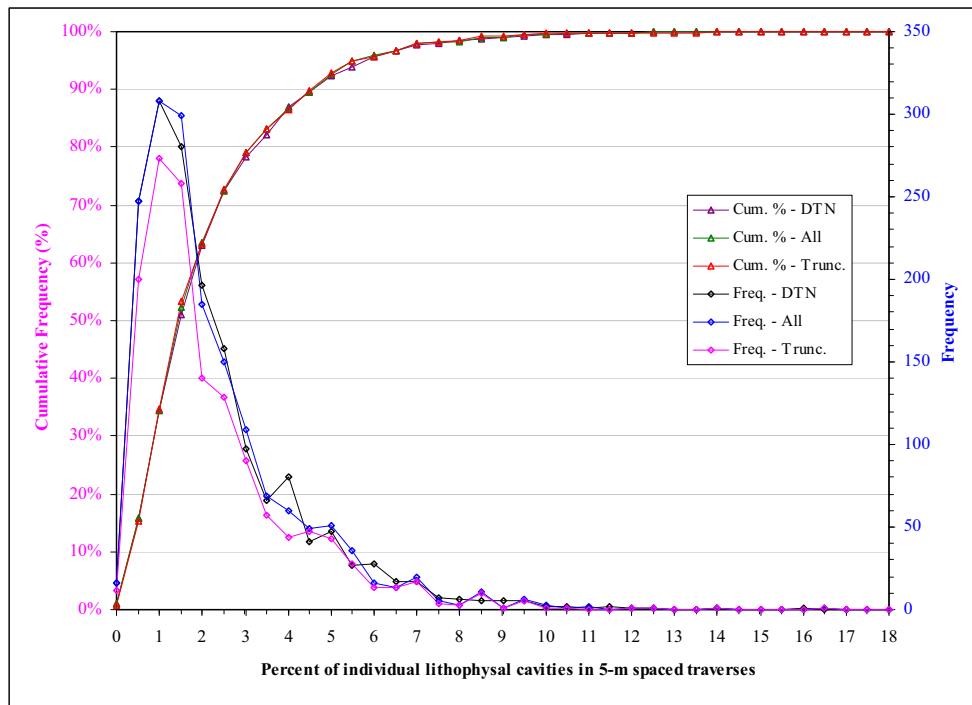
NOTE: Data submitted in the original data package (DTN: GS021008314224.002 [DIRS 161910]) is indicated by "DTN". The "All" and "trunc." data are from the adjusted length traverses (see Section O6.3 and file *Drift Deg AMR AC T-Trav.xls*, worksheet "Tape data (percent)" [Table A-1]). Truncated data designated as "Trunc."

Figure O-17. Frequency (Number) and Cumulative Frequency of the Abundance (Percent) Lithophysal Cavities from Tape Traverses in the Tptpl of the ECRB Cross-Drift from 14+05 to 23+35 (All) and 14+60 to 22+00 (Truncated Data)

Table O-5. Descriptive Statistics for the Abundance of Individual Lithophysal Cavities in Individual Tape Traverses for Various Lengths of Tunnel in the Tptpll in the Cross-Drift

Statistic	Data Package	Revised			
		2335 to 1405	2326 to 1444	2320 to 1460	2200 to 1460
Stations	2335 to 1405	2335 to 1405	2326 to 1444	2320 to 1460	2200 to 1460
Length along tunnel (m)	930	930	882	860	740
Mean	2.17	2.02	2.02	2.06	2.00
Standard Error	0.05	0.05	0.05	0.05	0.05
Median	1.49	1.34	1.34	1.46	1.34
Mode	1.49	1.33	1.33	1.33	1.33
Standard Deviation	1.99	1.85	1.83	1.82	1.84
Sample Variance	3.96	3.43	3.35	3.32	3.38
Kurtosis	6.32	6.05	6.13	6.16	6.34
Skewness	2.03	2.01	2.00	2.00	2.03
Range	17.91	16.09	16.09	16.09	16.09
Minimum	0.00	0.00	0.00	0.00	0.00
Maximum	17.91	16.09	16.09	16.09	16.09
Sum	3607.71	3355.24	3297.95	3254.38	2792.89
Count	1664	1664	1630	1583	1393
Confidence Level (95.0%)	0.10	0.09	0.09	0.09	0.10

NOTE: Data in "Data Package" column from DTN: GS021008314224.002 [DIRS 161910]. The Revised data are in *Drift Deg AMR AC T-Trav.xls*, worksheet "Tape data (percent)" (see Table A-1).



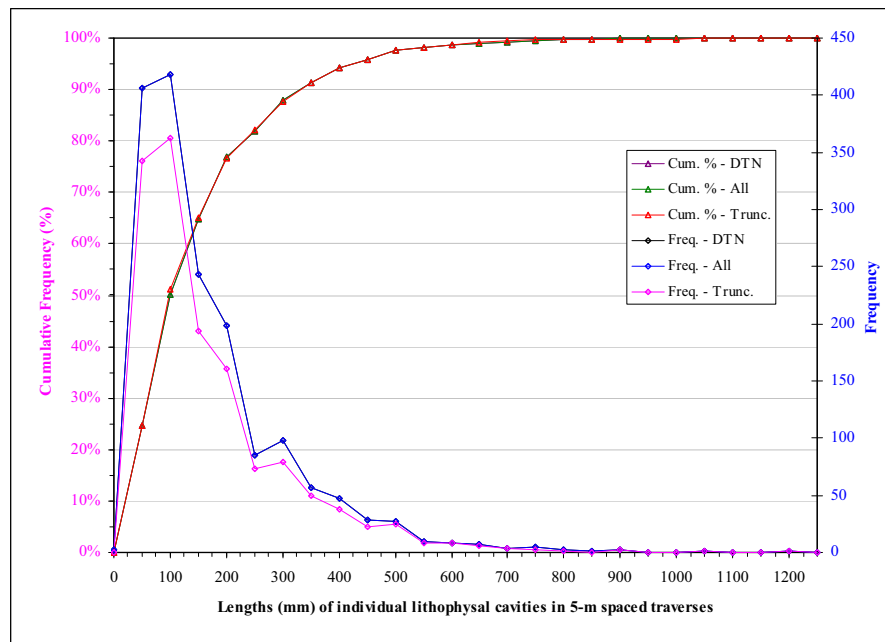
NOTE: Data submitted in the original data package (DTN: GS021008314224.002 [DIRS 161910]) is indicated by "DTN". The "All" and "Trunc." data are from the adjusted length traverses (see Section O6.3 and file *Drift Deg AMR AC T-Trav.xls*, worksheet "Tape data (percent)" [Table A-1]). Truncated data designated as "Trunc."

Figure O-18. Frequency (Number) and Cumulative Frequency of the Abundance (Percent) of Individual Lithophysal Cavities from Tape Traverses in the Tptpll in the Cross-Drift from 14+05 to 23+35 (All) and 14+60 to 22+00 (Truncated Data)

Table O-6. Descriptive Statistics for the Lengths (mm) of Individual Lithophysal Cavities in Individual Tape Traverses for Various Lengths of Tunnel in the Tptpll zone in the Cross-Drift

Statistic	Data Package	Revised			
		2335 to 1405	2326 to 1444	2320 to 1460	2200 to 1460
Stations	2335 to 1405	2335 to 1405	2326 to 1444	2320 to 1460	2200 to 1460
Length along tunnel (m)	930	930	882	860	740
Mean	152.6	152.6	152.9	155.4	151.6
Standard Error	3.4	3.4	3.4	3.4	3.7
Median	100	100	110	110	100
Mode	100	100	100	100	100
Standard Deviation	138.6	138.6	137.0	136.3	137.6
Sample Variance	19208.3	19208.3	18757.0	18586.5	18926.2
Kurtosis	6.0	6.0	6.1	6.1	6.3
Skewness	2.0	2.0	2.0	2.0	2.0
Range	1200	1200	1190	1190	1190
Minimum	0	0	10	10	10
Maximum	1200	1200	1200	1200	1200
Sum	251723	251723	247413	244143	209393
Count	1650	1650	1618	1571	1381
Confidence Level (95.0%)	6.69	6.69	6.67	6.74	7.26

NOTE: Data in "Data Package" column from DTN: GS021008314224.002 [DIRS 161910]. The Revised data are in *Drift Deg AMR AC T-Trav.xls*, worksheet "Tape data (mm)" (see Table A-1).



NOTE: Data submitted in the original data package (DTN: GS021008314224.002 [DIRS 161910]) is indicated by "DTN" The "All" and "Trunc." data are from the adjusted length traverses (see Section O6.3 and file *Drift Deg AMR AC T-Trav.xls*, worksheet "Tape data (mm)" [Table A-1]). Truncated data designated as "Trunc."

Figure O-19. Frequency (Number) and Cumulative Frequency of the Lengths (mm) of Individual Lithophysal Cavities from Tape Traverses in the Tptpll of the ECRB Cross-Drift from 14+05 to 23+35 (All) and 14+60 to 22+00 (Truncated Data)

Table O-7. Descriptive Statistics for the Abundance of Lithophysal Cavities in Tape Traverses Calculated with 10 m, 15 m, 20 m, 25 m, and 30 m “moving averages” for the Total Tptpll in the ECRB Cross-Drift

Statistic	Value					
	2200 to 1460					
Stations	2200 to 1460					
Length along tunnel (m)	5-m traverses	10-m average	15-m average	20-m average	25-m average	30-m average
Mean	18.9	18.9	18.9	18.9	18.9	18.9
Standard Error	0.7	0.6	0.5	0.5	0.5	0.5
Median	17.8	18.3	18.1	18.3	18.1	18.3
Mode	16.6	16.7	15.5	23.3	11.8	22.0
Standard Deviation	8.7	7.0	6.5	6.1	5.9	5.7
Sample Variance	75.4	48.6	41.8	37.6	35.3	33.0
Kurtosis	0.2	0.29	0.20	0.00	-0.15	-0.14
Skewness	0.6	0.55	0.59	0.56	0.49	0.48
Range	47.2	39.0	31.4	27.9	26.6	27.0
Minimum	1.2	3.4	7.6	8.9	8.4	8.1
Maximum	48.4	42.4	39.0	36.8	35.0	35.1
Sum	2,793	2,890.5	2,887.6	2,890.4	2,897.1	2,897.0
Count	148	153	153	153	153	153
Confidence Level (95.0%)	1.4	1.10	1.02	0.97	0.94	0.91

NOTE: Data in *Drift Deg AMR AC T-Trav.xls*, worksheet “Tape data (percent)” (see Table A-1).

Table O-8. Descriptive Statistics for the Abundance of “Rims Plus Spots” in Individual Tape Traverses for Various Lengths of Tunnel in the Tptpll of the ECRB Cross-Drift

Statistic	Data Package	Revised	
	2200 to 1405	2200 to 1405	2200 to 1460
Stations	2200 to 1405	2200 to 1405	2200 to 1460
Length along tunnel (m)	795	795	740
Mean	8.0	8.0	8.4
Standard Error	0.6	0.6	0.6
Median	5.0	5.0	7.5
Mode	7.5	7.5	7.5
Standard Deviation	7.1	7.1	7.1
Sample Variance	50.1	50.1	50.5
Kurtosis	3.3	3.3	3.1
Skewness	1.9	1.9	1.9
Range	32.0	32.0	31.5
Minimum	0.5	0.5	1.0
Maximum	32.5	32.5	32.5
Sum	1257	1257	1233
Count	157	157	146
Confidence Level (95.0%)	1.1	1.1	1.2

NOTE: Data in “Data Package” column from DTN: GS021008314224.002 [DIRS 161910]. The Revised data are in *Drift Deg AMR AC T-Trav.xls*, worksheet “Tape data (percent)” (see Table A-1).

Comparison of the descriptive statistics for abundance of lithophysal cavities, rims, and spots in panel maps, angular traverses, and corrected tape traverses in the lower lithophysal zone indicate the corrected tape values are consistent with the values determined from the other methods (Table O-9 and Section O6.6). These relations are also consistent for various lengths of the tunnel such as comparing the segments from 14+60 to 23+20 and 14+60 to 22+00 (Table O-9; Section O6.6). The “prime” section of the tunnel for the lower lithophysal zone is from 14+60 to 23+20 where the tunnel is entirely within the lower lithophysal zone (i.e., there is no “mixing” from the adjacent rock units). The more restricted section from 14+60 to 22+00 is better to use for many detailed descriptions and comparative statistics because there is good overlap of the various types of data (panel maps and angular and tape traverses) and there is minimal need to extrapolate and convert some of the data. The abundance values for each of the lithostratigraphic features can be converted into rock-mass porosity values (using the porosity values of each component). Using the porosities of  $1.00 \text{ cm}^3/\text{cm}^3$  for lithophysal cavities,  $0.25 \text{ cm}^3/\text{cm}^3$  for rims and spots, and  $0.13 \text{ cm}^3/\text{cm}^3$  for the matrix-groundmass (Flint 1998 [DIRS 100033], Table 7), the lower lithophysal zone (as a whole and not including the large lithophysae) averages 13.1 percent lithophysal cavities, 1.4 percent rims, 1.9 percent spots, and 10.9 percent matrix-groundmass for a total porosity of 27.3 percent (Table O-10). Alternatively, using the porosities of  $1.00 \text{ cm}^3/\text{cm}^3$  for lithophysal cavities,  $0.30 \text{ cm}^3/\text{cm}^3$  for rims and spots,  $0.104 \text{ cm}^3/\text{cm}^3$  for the matrix-groundmass (Otto and Buesch 2003 [DIRS 170727]), and including the large-lithophysal cavities, the lower lithophysal zone averages 13.1 percent lithophysal cavities, 2.0 percent large-lithophysal cavities, 1.7 percent rims, 2.3 percent spots, and 8.4 percent matrix-groundmass for a total porosity of 27.5 percent (Table O-11).

#### **O6.1 DESCRIPTIVE STATISTICS FOR LITHOPHYSAL CAVITIES, RIMS, SPOTS, AND LITHIC CLASTS IN PANEL MAPS IN THE Tptpll OF THE ECRB CROSS-DRIFT FROM STATIONS 14+93 TO 22+97**

The descriptive statistics for lithophysal cavities, rims, spots, and lithic clasts in panel maps in the Tptpll of the ECRB Cross-Drift from Stations 14+93 to 22+97 were determined to support the distribution of size and abundance of lithostratigraphic features as described in Sections O2 and O6.6. Descriptive statistics were determined using data provided in DTN: GS021008314224.002 [DIRS 161910] and are reproduced in Table A-1. Descriptive statistics are provided for the sizes (actually areas in  $\text{mm}^2$ ) and percent of the total area for lithostratigraphic features including lithophysal cavities, rims, spots, and lithic clasts. The descriptive statistics were determined with the standard functions of commercial off-the-shelf software Microsoft Excel 97 SR-2, and are documented in the Microsoft Excel file, *Drift Deg AMR AA PMap.xls* (Table A-1), which can be accessed through the TDMS (DTN: MO0408MWDDDMIO.002).

#### **O6.2 DESCRIPTIVE STATISTICS FOR LITHOPHYSAL CAVITIES, RIMS, SPOTS, AND LITHIC CLASTS IN ANGULAR TRAVERSES IN THE Tptpll OF THE ECRB CROSS-DRIFT FROM STATIONS 14+60 TO 22+00**

The descriptive statistics for lithophysal cavities, rims, spots, lithic clasts, and matrix-groundmass in angular traverses in the Tptpll of the ECRB Cross-Drift from Stations 14+60 to 22+00 were determined to support the distribution of size and abundance of lithostratigraphic features as described in Sections O1 and O6.6. Descriptive statistics were

determined on data provided in DTN: GS021008314224.002 [DIRS 161910], and were determined in support of this report. Descriptive statistics are provided for the sizes (actually lengths in mm) and percent of the total lengths for lithostratigraphic features including lithophysal cavities, rims, spots, lithic clasts, and the matrix-groundmass. The descriptive statistics were determined with the standard functions of commercial off-the-shelf software Microsoft Excel 97 SR-2, and are documented in the Microsoft Excel file, *Drift Deg AMR AB A-Trav.xls* (Table A-1), which can be accessed through the TDMS (DTN: MO0408MWDDDMIO.002).

Table O-9. Descriptive Statistics for Abundance of Lithophysal Cavities, Rims, and Spots in Panel Maps, Angular Traverses, and Corrected Tape Traverses in the Tptpl Exposed in the ECRB Cross-Drift from Stations 14+60 to 23+20 and 14+60 to 22+00

Descriptive Statistics	1460 to 2320 m					1460 to 2200 m			1460 to 2320 m			1460 to 2200 m		
	Cp	Ca	Ct	Ctc	LLm5	Ctc-m	Rp	Ra	Rtc	Rtc-m	Sp	Sa	Stc	Stc-m
Mean	12.9	15.5	15.0	13.1	1.9	14.0	5.4	9.1	5.6	6.0	3.8	10.1	7.8	7.4
Standard Error	0.8	1.2	0.4	0.4	0.1	0.4	0.8	0.7	0.2	0.2	1.3	1.4	0.5	0.5
Median	13.4	15.0	14.6	12.9	1.8	13.6	5.2	8.1	5.2	5.3	2.9	8.3	5.7	5.7
Mode	N/A	15.0	17.9	17.0	0.0	17.0	2.1	11.0	3.0	3.0	3.5	N/A	2.4	2.4
Standard Deviation	3.6	6.3	5.0	5.3	1.7	5.1	3.4	3.3	3.0	2.9	5.4	6.5	6.2	5.7
Sample Variance	12.9	39.8	24.7	28.6	2.8	26.0	11.9	11.2	9.2	8.5	28.7	42.3	38.4	32.4
Kurtosis	-0.1	0.8	0.1	-0.2	1.2	0.1	0.4	3.5	0.0	0.0	15.5	0.1	1.3	1.7
Skewness	-0.5	0.0	0.5	0.4	1.0	0.3	0.8	1.6	0.7	0.8	3.8	1.0	1.5	1.5
Range	13.7	28.5	24.7	25.2	9.4	25.2	13.0	14.8	12.5	11.7	24.0	22.0	23.5	23.0
Minimum	5.3	2.2	6.0	4.0	0.0	4.0	0.3	4.8	0.9	1.7	0.6	2.3	1.4	1.4
Maximum	19.0	30.7	30.7	29.2	9.4	29.2	13.3	19.6	13.4	13.4	24.6	24.3	25.0	24.4
Sum	232.7	418.7	2693.3	2352.8	329.8	2182.9	97.5	200.8	1005.7	934.8	68.1	223.1	1402.7	1151.6
Count	18	27	180	180	170	156	18	22	179	155	18	22	179	155
Confidence Level (95.0%)	1.7	2.4	0.7	0.8	0.3	0.8	1.6	1.4	0.4	0.5	2.5	2.7	0.9	0.9

"N/A" indicates "Not Applicable".

Source: DTNs: GS021008314224.002 [DIRS 161910]; GS040608314224.001 [DIRS 171367].

NOTE: Symbols Cp, Ca, Ct, Ctc are defined in the caption for Figure O-9. LLm5 is Large Lithophysae in 5-m intervals and Ctc-m is Cavities in the converted tape data in the main (or prime) part of the tunnel from 1460 to 2200 m. Symbols Rp, Ra, Rt, Rtc are defined in the caption for Figure O-11, and Rtc-m are the Rims in the converted tape data in the main (or prime) part of the tunnel from 1460 to 2200 m. Symbols Sp, Sa, St, Stc are defined in the caption for Figure O-11, and Stc-m are the Spots in the converted tape data in the main (or prime) part of the tunnel from 1460 to 2200 m. The data are presented in Drift Deg AMR AF T-A-P fit V1.xls (See Table A-1).



Table O-10. Descriptive Statistics for Porosity of Lithophysal Cavities, Rims, and Spots in Panel Maps, Angular Traverses and Corrected Tape Traverses in the Tptpl Exposed in the ECRB Cross-Drift from Stations 14+60 to 23+20 (without Large Lithophysae)

Descriptive Statistic	Cavities (panel)	Rims (panel)	Spots (panel)	Cavities (angular)	Rims (angular)	Spots (angular)	Cavities (tape)	Rim-Spot (tape)	MGM (fitted)	Cavities (fitted)	Rims (fitted)	Spots (fitted)	Total (fitted)
Mean	12.9	1.4	0.9	15.3	2.3	2.5	16.4	2.1	10.9	13.1	1.4	1.9	27.3
Standard Error	0.8	0.2	0.3	1.5	0.2	0.3	0.4	0.1	0.1	0.4	0.1	0.1	0.3
Median	13.4	1.3	0.7	14.8	2.0	2.1	16.0	1.6	10.8	12.9	1.3	1.4	27.4
Mode	N/A	0.5	0.9	N/A	2.8	N/A	16.2	1.3	10.5	17.0	0.7	0.6	30.0
Standard Deviation	3.6	0.9	1.3	6.9	0.8	1.6	4.8	1.7	0.7	5.3	0.8	1.6	4.5
Sample Variance	12.9	0.7	1.8	47.2	0.7	2.6	22.9	2.9	0.5	28.6	0.6	2.4	20.2
Kurtosis	-0.14	0.42	15.49	0.37	3.45	0.08	0.14	3.58	0.66	-0.17	0.00	1.26	0.66
Skewness	-0.51	0.76	3.82	0.10	1.63	0.98	0.44	1.99	-0.42	0.42	0.67	1.48	0.42
Range	13.7	3.2	6.0	28.5	3.7	5.5	27.0	7.8	3.5	25.2	3.3	6.2	23.2
Minimum	5.3	0.1	0.2	2.2	1.2	0.6	5.5	0.3	8.7	4.0	0.0	0.0	18.5
Maximum	19.0	3.3	6.2	30.7	4.9	6.1	32.5	8.1	12.2	29.2	3.3	6.2	41.7
Sum	232.7	24.4	17.0	336.8	50.2	55.8	2894.3	311.4	1955.9	2352.8	251.4	350.7	4910.7
Count	18	18	18	22	22	22	177	150	180	180	180	180	180
Confidence Level (95.0%)	1.7	0.4	0.6	2.9	0.3	0.7	0.7	0.3	0.1	0.8	0.1	0.2	0.7

"N/A" indicates "Not Applicable".

Source: DTN: GS021008314224.002 [DIRS 161910].

NOTE: Porosity of the Rim and Spot material was calculated with a mean values of 0.25 cm<sup>3</sup>/cm<sup>3</sup> and matrix-groundmass (MGM) was calculated with a mean value of 0.13 cm<sup>3</sup>/cm<sup>3</sup>, and Rim-Spot (tape data) is only from 14+60 to 22+00. The data are presented in file *Drift Deg AMR AF T-A-P fit V1.xls*, worksheet "Volume Percent - Stats" (See Table A-1).

Table O-11. Descriptive Statistics for Porosity of Lithophysal Cavities, Rims, and Spots in Panel Maps, Angular Traverses and Corrected Tape Traverses and the Large Lithophysae Inventory in the Tptpl Exposed in the ECRB Cross-Drift from Stations 14+60 to 23+20

Descriptive Statistic	Cavities (panel)	Rims (panel)	Spots (panel)	Cavities (angular)	Rims (angular)	Spots (angular)	Cavities (tape)	Rim-Spot (tape)	MGM (fitted)	Cavities (fitted)	Rims (fitted)	Spots (fitted)	L-Litho (5m)	Total (fitted)
Mean	12.9	1.6	1.1	15.3	2.7	3.0	15.0	4.0	8.4	13.1	1.7	2.3	2.0	27.5
Standard Error	0.8	0.2	0.4	1.5	0.2	0.4	0.4	0.2	0.0	0.4	0.1	0.1	0.1	0.4
Median	13.4	1.5	0.9	14.8	2.4	2.5	14.6	3.0	8.4	12.9	1.6	1.7	1.8	27.3
Mode	N/A	0.6	1.1	N/A	3.3	N/A	17.9	1.6	7.9	17.0	0.9	0.7	0.0	31.9
Standard Deviation	3.6	1.0	1.6	6.9	1.0	2.0	5.0	2.3	0.6	5.3	0.9	1.9	1.7	5.6
Sample Variance	12.9	1.1	2.6	47.2	1.0	3.8	24.7	5.2	0.4	28.6	0.8	3.5	2.9	31.3
Kurtosis	-0.14	0.4	15.5	0.37	3.5	0.1	0.1	-0.6	0.7	-0.2	0.0	1.3	0.9	0.7
Skewness	-0.51	0.8	3.8	0.10	1.6	1.0	0.5	0.7	-0.6	0.4	0.7	1.5	0.9	0.6
Range	13.7	3.9	7.2	28.5	4.4	6.6	24.7	9.4	3.3	25.2	4.0	7.5	9.4	28.9
Minimum	5.3	0.1	0.2	2.2	1.4	0.7	6.0	0.0	6.3	4.0	0.0	0.0	0.0	16.6
Maximum	19.0	4.0	7.4	30.7	5.9	7.3	30.7	9.4	9.7	29.2	4.0	7.5	9.4	45.4
Sum	232.7	29.2	20.4	336.8	60.2	66.9	2693.3	625.9	1514.8	2352.8	301.7	420.8	359.0	4949.1
Count	18	18	18	22	22	22	180	156	180	180	180	180	178.0	180.0
Confidence Level (95.0%)	1.7	0.5	0.7	2.9	0.4	0.8	0.7	0.4	0.1	0.8	0.1	0.3	0.3	0.8

N/A indicates "Not Applicable".

Source: DTN: GS021008314224.002 [DIRS 161910]; GS040608314224.001 [DIRS 171367].

NOTE: Porosity of the Rim and Spot material was calculated with a mean values of 0.30 cm<sup>3</sup>/cm<sup>3</sup> and matrix-groundmass (MGM) was calculated with a mean value of 0.104 cm<sup>3</sup>/cm<sup>3</sup> (Section O5 and O6.6), and Rim-Spot (tape data) is only from 14+60 to 22+00. The data are presented in file Drift Deg AMR AF T-A-P\_fit V1.xls, worksheet "Volume Percent - Stats" (See Table A-1).

### **O6.3 DESCRIPTIVE STATISTICS FOR LITHOPHYSAL CAVITIES, RIMS, SPOTS, AND LITHIC CLASTS IN TAPE TRAVERSES IN THE Tptpll OF THE ECRB CROSS-DRIFT FROM STATIONS 14+05 TO 23+35**

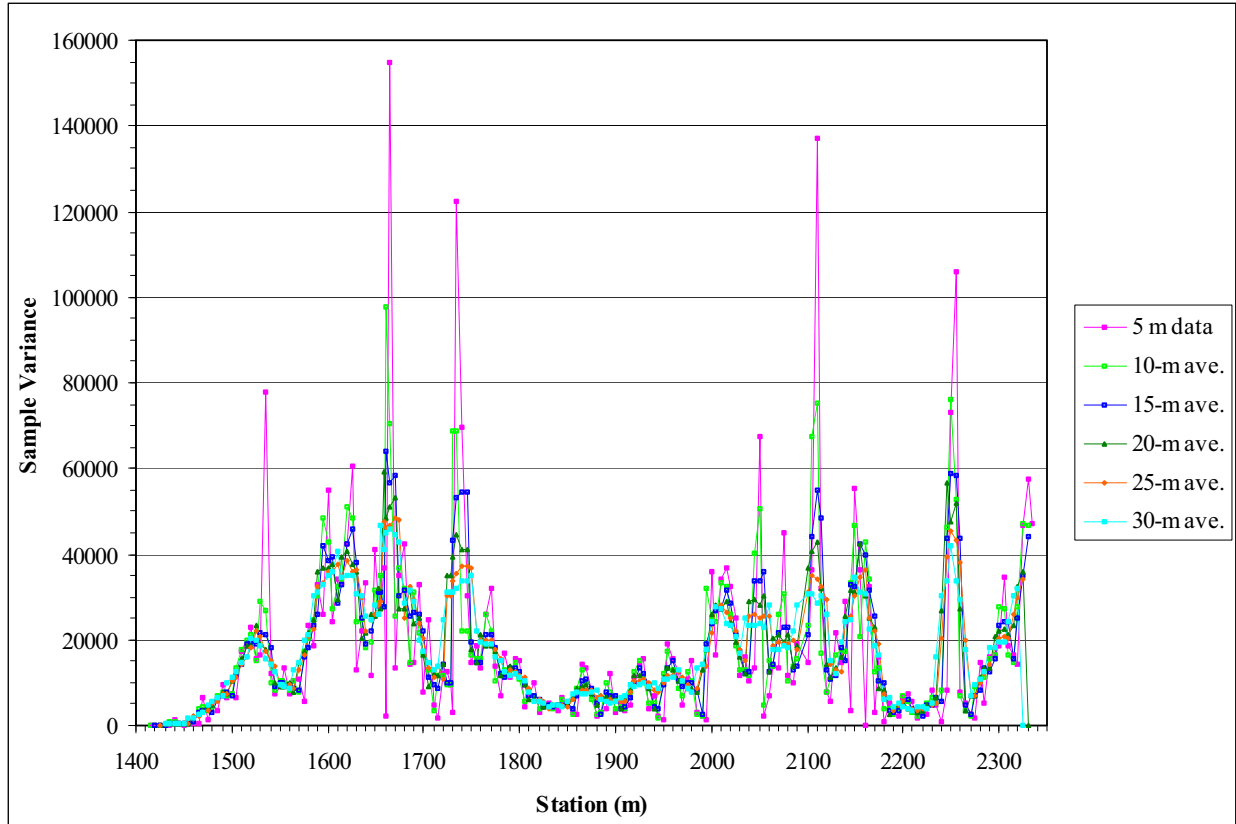
The descriptive statistics for lithophysal cavities, rims, spots, and lithic clasts in tape traverses in the Tptpll of the ECRB Cross-Drift from Stations 14+05 to 23+35 were determined to support the distribution of size and abundance of lithostratigraphic features as described in Sections O1 and O6.6. Descriptive statistics were determined on data provided in DTN: GS021008314224.002 [DIRS 161910], and were determined in support of this report. The lengths of the tape traverses in the original data package (DTN: GS021008314224.002 [DIRS 161910]) were longer or shorter than those determined at the same locations with the angular traverses, so the tape traverse lengths were corrected using the angular traverse lengths and resulted in “typical traverse lengths”. The “typical traverse lengths” used to determine the abundance of lithophysal cavities are 7.46 m from 14+20 to 17+55 (double vent line), and 7.53 m from 17+65 to 23+35 (single vent line). Descriptive statistics and histograms are provided for the sizes (actually lengths in mm) and percent of the individual and total lengths for lithophysal cavities and the total percent of the visually estimated amounts of rims plus spots. Descriptive statistics were determined for individual traverses, 10 m, 15 m, 20 m, 25 m, and 30 m “running averages” and for total lithophysal cavities. The descriptive statistics and histograms were determined with the standard functions of commercial off-the-shelf software Microsoft Excel 97 SR-2, and are documented in the Microsoft Excel file, *Drift Deg AMR AC T-Trav.xls* (Table A-1), which can be accessed through the TDMS (DTN: MO0408MWDDDMIO.002).

Adjustments were made to the tape data in the Microsoft Excel file, *Drift Deg AMR AC T-Trav.xls* (Table A-1), for the calculation of “moving averages” where there is a “gap” in the data. A gap occurs where a tape traverse was not made including the locations of a few panel maps. A description of the calculation of “moving averages” includes the following:

- A. Running averages of tape traverse data were made for 10, 15, 20, 25, and 30 meters. These cells (Microsoft Excel file, *Drift Deg AMR AC T-Trav.xls* [Table A-1]) have no color fill.
- B. The standard averaging practice includes:
  - 10 m: value averaged with next value below (“down” tunnel to next station)
  - 15 m: value averaged with value above and value below
  - 20 m: value averaged with value above and next 2 values below
  - 25 m: value averaged with 2 values above and 2 values below
  - 30 m: value averaged with 2 values above and next 3 values below.
- C. Where a gap in data occurs, the affected cell contains a comment, and may be color-coded. A gray color-coded cell indicates a null value was adjusted by averaging values of adjacent cells. Gray cells may indicate adjustments of null values on 5 m increments or on less than 5 m increments.

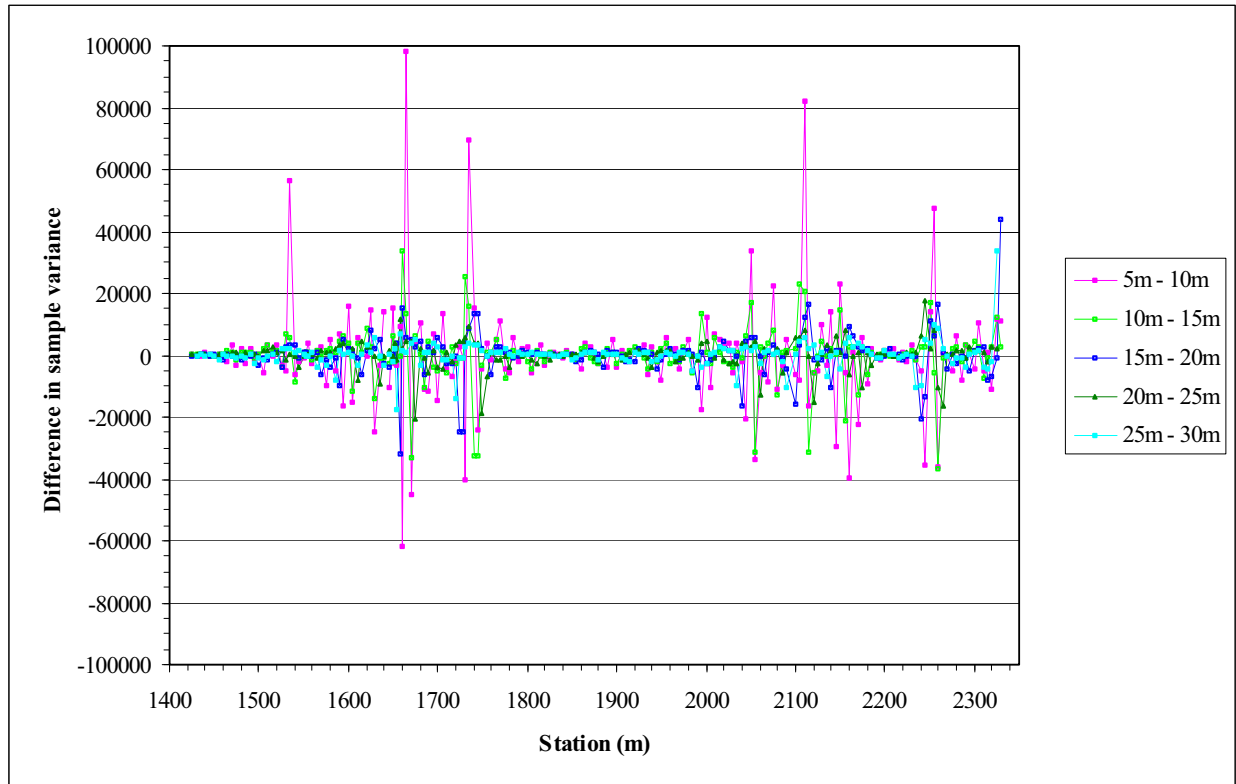
- D. In some cases where a gap in data occurs in an adjacent cell on an increment less than 5 m, the affected cell was not color coded, but a comment was included indicating a default to standard averaging practice using the next 5 m increment. Where a gap in data occurs on a 5 m increment, adjustments were made, and affected cells were colored light turquoise.
- E. The standard adjustment (rule 1) for data gaps consists of:
- 10 m: two values below null value averaged
  - 15 m: one value above and 2 values below null value are averaged
  - 20 m: one value above and 3 values below null value are averaged
  - 25 m: two values above and 3 values below null value are averaged
  - 30 m: two values above and 4 values below null value are averaged.
- F. A light yellow cell located in the first 12 rows indicates a gap in the data. A light yellow cell located in the running average section indicates a situation where rule 1 was altered to avoid using null values in adjacent cells. In an effort to lessen the effect of data spikes in the tape traverse data, the above procedure (rule 1) for adjustments was departed to capture a smaller value in place of a larger value where the choice was available. (light green cells).

Sample variance of the summed lengths of lithophysal cavities in the 5 m data and the 10 m to 30 m moving average data indicates (1) variations along the tunnel and (2) the most significant minimization in variance in the 10 m and 15 m moving average data. Sample variance is a measure of the variability of the values relative to the mean value, so variations in the variance provide insight into the internal lithostratigraphic features of the lower lithophysal zone. Sample variance along the tunnel indicates there are segments (from Stations 15+00 to 18+05 and 19+90 to 21+80) that have significantly greater amounts of cavities than is typical for the lithostratigraphic unit as a whole (Figure O-20). As discussed in Section O3, the amounts of lithophysal cavities measured behind the bulkhead at 22+01 are probably over estimates, so the larger variances from 22+45 to 23+35 must be viewed with caution. Comparison of the variance in the 5 m data and 10 m to 30 m moving average data provides a measure of length scales across which the data have large or small variations. The 5 m data has the largest variation in values and progressively longer moving average values have smaller variations, but regardless of moving average or not, the data maintain the along-the-tunnel variations in the abundance of lithophysal cavities (Figure O-20). Differences in sample variance pairs of data at each station indicate the greatest step in minimizing the variance is with the 10 m or 15 m moving averages (Figure O-21). For example, subtracting the 10 m moving average value from the 5 m data results in numerous values larger or small than  $\pm 4,000$ , and subtracting the 15 m moving average value from the 10 m moving average value results in only a few values larger or smaller than  $\pm 2,000$ .



NOTE: Data and graph are from the adjusted length traverses (see Table A-1, *Drift Deg AMR AC T-Trav.xls*, worksheet "Tape data (mm)").

Figure O-20. Sample Variance in the Summed Length of Lithophysal Cavities Based on 5 m Data and 10 m to 30 m Moving Average Data from Tape Traverses in the Tptpl of the ECRB Cross-Drift from 14+05 to 23+35



NOTE: Data and graph are from the adjusted length traverses (see Table A-1, *Drift Deg AMR AC T-Trav.xls*, worksheet "Tape data (mm)"). "5 m to 10 m" is the difference in sample variance at each station of the 5 m data minus the variance of 10 m data.

Figure O-21. Differences in Sample Variance in the Summed Length of Lithophysal Cavities with Pairs of Various Moving Average Data from Tape Traverses in the Ttptll of the ECRB Cross-Drift from 14+05 to 23+35

#### **O6.4 DESCRIPTIVE STATISTICS FOR LARGE LITHOPHYSAE FROM THE LARGE-LITHOPHYSAL INVENTORY IN THE Ttptll OF THE ECRB CROSS-DRIFT FROM STATIONS 14+50 TO 17+56**

The descriptive statistics for lithophysal cavities, rims, spots, and lithic clasts in large-lithophysal inventory in the Ttptll of the ECRB Cross-Drift from Stations 14+50 to 17+56 were determined to support the distribution of size and abundance of lithostratigraphic features as described in Sections O5 and O6.6. Descriptive statistics were determined on data provided in DTN: GS021008314224.002 [DIRS 161910], and were determined in support of this report. Descriptive statistics are provided for the sizes (actually areas in mm<sup>2</sup>) and percent of the individual and total area for lithophysal cavities for 5 m long and 10 m long tunnel segments. The descriptive statistics were determined with the standard functions of commercial off-the-shelf software Microsoft Excel 97 SR-2, and are documented in the Microsoft Excel file, *Drift Deg AMR AD L-Litho V1.xls* (Table A-1), which can be accessed through the TDMS (DTN: MO0408MWDDDMIO.002).

## **O6.5 DESCRIPTIVE STATISTICS FOR ABUNDANCE OF LITHOPHYSAE AND SPOTS IN THE Tptpll ALONG THE ECRB CROSS-DRIFT FROM STATIONS 14+05 TO 23+35**

The descriptive statistics for the abundance of lithophysae and spots in the Tptpll of the ECRB Cross-Drift from Stations 14+05 to 23+25 were compiled in support of the calculation of the distribution of the abundance of lithostratigraphic features as described in Sections O4 and O6.6. Descriptive statistics were determined from (and are consistent with) values described in Mongano et al. (1999 [DIRS 149850], Tables 3 and 4). The descriptions presented in Mongano et al. (1999 [DIRS 149850], Tables 3 and 4) are summarized in the Microsoft Excel file, *Drift Deg AMR AE Mongano.xls* (Table A-1), and specific values for drift segments presented in Tables 3 and 4 (Mongano et al. 1999 [DIRS 149850]) are listed in 5 m station increments to facilitate plotting of and determining descriptive statistics for the data. The estimated “median” and “maximum” values are summarized in Table O-12 where the “median” values do not include local maximum values and the “maximum” values include only the maximum values. The descriptive statistics were determined with the standard functions of commercial off-the-shelf software Microsoft Excel 97 SR-2. The Microsoft Excel file, *Drift Deg AMR AE Mongano.xls* (Table A-1), can be accessed through the TDMS (DTN: MO0408MWDDDMIO.002).

## **O6.6 CORRELATIONS AND CORRECTIONS TO TAPE TRAVERSE DATA AND DETERMINATION OF “BEST FIT” VALUES OF LITHOPHYSAL CAVITIES, RIMS, SPOTS, AND MATRIX-GROUNDMASS IN THE Tptpll ALONG THE ECRB CROSS-DRIFT**

To produce the “best fit” values for lithophysal cavities, rims, spots, and matrix-groundmass located every 5 m along the ECRB Cross-Drift, the tape traverse data output for cavities and “rims plus spots” were initially corrected to the angular traverse data, then panel map data, and finally with one more set of empirical correction factors. The panel map and angular traverse data are not corrected and are from the original lithophysal study data package (DTN: GS021008314224.002 [DIRS 161910]) and the tape traverse data are from the file *Drift Deg AMR AC T-Trav.xls* (Table A-1). The basic data including 10 m to 30 m moving averages of tape data, correlation equations, and empirical corrections are included in the Microsoft Excel file, *Drift Deg AMR AF T-A-P Fit V1.xls* (Table A-1), and can be accessed through the TDMS (DTN: MO0408MWDDDMIO.002). The descriptive statistics in the “Length - Fit and Stats” and “Volume Percent - Stats” worksheets were determined with the standard functions of commercial off-the-shelf software Microsoft Excel 97 SR-2. A description of the worksheets contained in *Drift Deg AMR AF T-A-P Fit V1.xls* (Table A-1) is provided as follows:

- A. The “T-A-P Cav Fit” worksheet contains lithophysal cavity data from the tape and angular traverses and panel maps, and compares and correlates the tape and angular traverse data using equations of correlation. The abundance of cavities is calculated using the tape data and correlation equation and results in values every 5 m along the tunnel (symbol “Ct”). The “Ct” values are used in the “Length - Fit and Stats” worksheet.

Table O-12. Descriptive Statistics for “Median” and “Maximum” Abundance (Percent) of Lithophysal Cavities and Spots in the Tptpll Exposed in the ECRB Cross-Drift from Stations 14+44 to 23+26

Descriptive Statistics		1444 to 2326			1460 to 2320		
		Lithop (M)	Spots (M)	Spot (M Por)	Lithop (M)	Spots (M)	Spot (M Por)
Estimated Mean Values	Mean	8.67	13.52	3.38	8.81	13.35	3.34
	Standard Error	0.33	0.89	0.22	0.34	0.90	0.23
	Median	7.50	7.00	1.75	7.50	7.00	1.75
	Mode	10.00	6.00	1.50	10.00	6.00	1.50
	Standard Deviation	4.56	12.15	3.04	4.57	12.14	3.03
	Sample Variance	20.82	147.63	9.23	20.84	147.31	9.21
	Kurtosis	3.21	-0.58	-0.58	3.18	-0.47	-0.47
	Skewness	1.53	1.09	1.09	1.52	1.14	1.14
	Range	23.00	37.00	9.25	23.00	36.00	9.00
	Minimum	2.00	3.00	0.75	2.00	4.00	1.00
	Maximum	25.00	40.00	10.00	25.00	40.00	10.00
	Sum	1612.00	2514.50	628.63	1586.00	2403.50	600.88
	Count	186	186	186	180	180	180
	Confidence Level(95.0%)	0.66	1.75	0.44	0.67	1.77	0.44
	Estimated Maximum Values	Mean	12.27	12.27	4.20	12.48	16.63
Standard Error		0.40	0.40	0.24	0.40	0.99	0.25
Median		10.00	10.00	2.50	10.00	10.00	2.50
Mode		15.00	15.00	1.75	15.00	7.00	1.75
Standard Deviation		5.39	5.39	3.33	5.35	13.27	3.32
Sample Variance		29.05	29.05	11.06	28.59	176.00	11.00
Kurtosis		1.78	1.78	-0.95	1.82	-0.86	-0.86
Skewness		1.13	1.13	0.87	1.15	0.92	0.92
Range		27.00	27.00	9.25	27.00	35.00	8.75
Minimum		3.00	3.00	0.75	3.00	5.00	1.25
Maximum		30.00	30.00	10.00	30.00	40.00	10.00
Sum		2283.00	2283.00	781.75	2247.00	2994.00	748.50
Count		186	186	186	180	180	180
Confidence Level(95.0%)		0.77	0.77	0.48	0.78	1.94	0.48

Source: Mongano et al. 1999 [DIRS 149850], Tables 3 and 4.

NOTE: Data from Mongano et al. 1999 [DIRS 149850] (Tables 3 and 4) utilized for 5 m station increments. See Drift Deg AMR AE Mongano.xls (Table A-1).

- B. The “T-A-P R-S Fit” worksheet contains estimated “rims plus spot” data from the tape traverses and angular traverse and panel map data, and compares and correlates the tape and angular traverse data using equations of correlation. The abundance of “rims plus spots” is calculated using the tape data and correlation equation and results in values every 5 m along the tunnel. These calculated tape values are adjusted to the angular traverse and panel map values by empirically determined correction factors and result in “best fit” values “Rims+Spots (tape-cor)”. The “Rims+Spots (tape-cor)” values are used in the “Length - Fit and Stats” worksheet.



- C. The “Length - Fit and Stats” worksheet summarize lithophysal cavity, rim, and spot data from the corrected tape traverses and the angular traverses and panel maps, and is used to develop “fitted” abundance along the tunnel. The “Ct” values are from the “T-A-P Cav Fit” worksheet, and the “Rims+Spots (tape-cor)” values are from the “T-A-P R-S Fit” worksheet. “Fitted” cavity, rim, and spot curves are developed using corrected tape values that are adjusted by to the angular traverse and panel map values with empirically determined correction factors. Descriptive statistics for abundance of cavities, rims, and spots are determined for data along the tunnel from Stations 14+60 to 23+20, the “best” technical data from 14+60 to 22+00, and as a “average” for the entire Tptpll zone.
- D. The “Volume Percent - Stats” worksheet replicates the “Length - Fit and Stats” worksheet, but the porosity is calculated every 5 m along the tunnel and is “averaged” for the total length of the Tptpll zone. The amount of matrix-groundmass is determined by difference (100 minus the sum of cavities, rims, and spots). Based on the description of lithostragraphic features related to lithophysae (Figure 6-3), the porosity of lithophysal cavities is considered to be 1.00 (cm<sup>3</sup>/cm<sup>3</sup>), rims and spots are 0.30 (cm<sup>3</sup>/cm<sup>3</sup>), and the matrix-groundmass is 0.104 (cm<sup>3</sup>/cm<sup>3</sup>). Descriptive statistics for the porosity of cavities, rims, and spots are determined for data along the tunnel from Stations 14+60 to 23+20, the “best” technical data from 14+60 to 22+00, and as an “average” for the entire Tptpll zone.

This report provides alternative methods for both the calculation of the porosity of features and the inclusion of the large lithophysal inventory data, and the differences in these approaches is shown by the “fitted” mean porosity values in Table O-13. Relative to Method A in Table O-13, an increase in mean porosity of the rims and spot material results in slight increases in the “fitted” rims and spots, and the decrease in the mean porosity of the matrix-groundmass material results in a decrease in the “fitted” matrix-groundmass. A cumulative effect of these changes in the mean porosity of the rim, spot, and matrix-groundmass materials is that the total “fitted” porosity decreased by 1.6 percent resulting primarily from the larger amount of matrix-groundmass than rim and spot materials (see Method B in Table O-13). The inclusion of the large lithophysal cavities slightly reduced the “fitted” matrix-groundmass to 8.4 percent because the large lithophysal cavity porosity is subtracted at each station and increased the total “fitted” porosity to 27.5 percent (see Method C in Table O-13).

Table O-13. Mean Porosity of Lithophysal Cavities, Large-Lithophysal Cavities, Rims, Spots, Matrix-groundmass, and Total Porosity in the Tptpl Exposed in the ECRB Cross-Drift from Stations 14+60 to 23+20 Using Three Methods

"Fitted" Features	Method A: Excluding Large Lithophysae (from Table O-10) <sup>a</sup>	Method B: Excluding Large Lithophysae with Modified Calculation of Porosity Features <sup>b</sup>	Method C: Including Large Lithophysae with Modified Calculation of Porosity Features (from Table O-11) <sup>c</sup>
Cavities	13.1	13.1	13.1
Large-lithophysae	N/A	N/A	2.0
Rims	1.4	1.7	1.7
Spots	1.9	2.3	2.3
Matrix-groundmass	10.9	8.6	8.4
Total	27.3	25.7	27.5

"N/A" indicates "Not Applicable".

<sup>a</sup> Mean porosity of the matrix-groundmass is 0.13 cm<sup>3</sup>/cm. The mean porosity of the rims and spots is estimated to range from 0.20 to 0.30 cm<sup>3</sup>/cm<sup>3</sup> (with a mean porosity of 0.25 cm<sup>3</sup>/cm<sup>3</sup>). The large lithophysae data are not included. The full table of descriptive statistics is provided in Table O-10.

<sup>b</sup> Mean porosity of the matrix-groundmass is 0.104 cm<sup>3</sup>/cm<sup>3</sup>. The mean porosity of the rims and spots is 0.30 cm<sup>3</sup>/cm<sup>3</sup>, and the large lithophysae data are included (DTN: MO0408MWDDDMIO.002, file *Drift Deg AMR AF T-A-P V1.xls*, worksheet "Volume Percent – Stats" (see Table A-1).

<sup>c</sup> Mean porosity of the matrix-groundmass is 0.104 (cm<sup>3</sup>/cm<sup>3</sup>). The mean porosity of the rims and spots is 0.30 cm<sup>3</sup>/cm<sup>3</sup>. The large lithophysae data are included. The full table of descriptive statistics is provided in Table O-11.

## O6.7 ACCURACY OF MEASURED AND CALCULATED VALUES

The accuracy of measured values must be understood in the context of three conditions: (1) the specific measurements made on features, (2) conditions that affect the measurements, and (3) how well the measurements and the summed and calculated values represent the three-dimensional distributions of the features.

**Accuracy of Measured Data for Each of the Four Data Collection Methods**—The panel maps are at a 1:10 scale and measurements are recorded to the nearest millimeter. Individual measurements in the panel maps can be accurate to 1 or 2 mm for small or narrow features; however, large, irregularly shaped objects (those with dimensions of several decimeters) can be accurate to 10 to 50 mm depending on how the data collector identifies the long and short axes.

Angular traverses are measured in degrees and minutes, and the recorded values are rounded to the nearest 5 minutes. In the ECRB Cross-Drift, an arc of 5 minutes calculates to about 4 mm on the tunnel wall, and this is also about the diameter of the laser beam. Pragmatically, the identification of the edge of a feature is a function of how sharp (or gradational) is the edge and the conditions in the tunnel. The edges of most features including lithophysal cavities, rims, and spots are relatively sharp (can be identified to less than 2 mm in width) with close examination. However for most features, the distance from the data collector to the tunnel wall was 1 to 3.5 m, so even with binoculars, the accuracy of the measurement is about 15 minutes (about 10 mm). The conditions in the tunnel during collection of the angular traverse data included the need to wear safety glasses (and at times a respirator), irregular distribution of tunnel illumination, dust cover on the tunnel walls, irregularities (breakouts) along the tunnel walls, and obstructions to

the line of sight and the need to estimate positions of features. With these various conditions, a practical accuracy is probably 5 to 40 minutes (about 4 to 30 mm) for any given measurement.

The tape (stadia rod) used for the tape traverses is divided into decimeters and centimeters, and the data can be recorded to the nearest 1 cm. However, based on the projection of the cavity walls to the tape, the difficulties in positioning the tape along the wall result in a practical accuracy of probably 2 to 10 cm for any given measurement.

Similar to the tape traverse measurements, the tape (stadia rod) used in the large-lithophysae inventory is divided into decimeters and centimeters, and the data can be recorded to the nearest 1 cm. However, based on the projection of the cavity walls to the tape, the difficulties in positioning the tape along the wall result in a practical accuracy probably 2 to 10 cm for any given measurement.

**Conditions that Affect the Accuracy and Use of Measurements**—In the panel maps there are three main conditions that can affect the accuracy of the values (others are described in the data package for DTN: GS021008314224.002 [DIRS 161910]):

1. The boundaries of features in the panel maps are based on photographic interpretation, hand-drawn maps compiled in the tunnel, and values measured in the tunnel and recorded in the Excel workbooks. Boundaries of features are typically sharp (as described above); however, the portrayal of the boundaries, regardless of being observations in the tunnel or as photographic interpretation, is a bit subjective; therefore, it can affect the accuracy of the feature boundaries. The subjective aspects typically arise where the edge of a feature does not occur on the tunnel wall (i.e., in a broken out lithophysal cavity or block bounded by fractures). The attempted balance used by the mapper is to project the contact to the plane of the tunnel wall, which is the plane on which the map is made, but also depict the contact where it “appears” to be on the photograph and would be viewed by other users. In part, this is an issue of perspective, but it does not affect the total percent of features by more than 1 to 3 percent.
2. A few of the panels from 17+63 to 23+00 were not washed as well as the ones from 14+90 to 17+63; therefore, the photographs of the tunnel walls were not as helpful for mapping the features. One result of the incomplete washing was that some of the features were more difficult to identify in the photograph than in other locations. A second result was that some of the lithophysal cavities that had been backfilled with rock flour from the tunnel boring machine were not cleaned out; therefore, they were excavated by hand and hammer. Because the photographs were taken before this additional excavation, the edges of the lithophysae were approximated and drawn on the photograph.
3. Rocks in the panel maps have distributions in the sizes and spatial positions of lithostratigraphic features; therefore, the position of the map-area (1x3 m) box can result in variations in areas. Panel map 1641-44L was used to compare the original position of the map area (that which is included in the data package) and four other alternative positions. The alternative positions were selected such that one position is

to the upper left of the original position, and the other alternative positions are to the upper right, lower right, and lower left (respectively) of the original position. Descriptive statistics on the percent areas determined from the five map positions indicate the matrix-groundmass and lithophysal cavities have 95 percent confidence levels of less than 4 percent and the rims, spots, and lithic clasts have 95 percent confidence levels of less than 0.5 percent (Table O-14).

Table O-14. Comparative Values from the Original Position of the Panel Map and Four Alternative-Position Maps

Map positions	No. of Objects	MGM %	L-cavities %	L-rims %	Spots %	C-Lithic %
OP	117	71.61	19.01	5.75	3.49	0.14
AP1	90	70.35	21.70	5.13	2.77	0.05
AP2	110	75.69	15.52	5.01	3.54	0.24
AP3	106	76.75	14.45	4.91	3.65	0.24
AP4	99	75.77	15.89	5.20	3.08	0.05
Descriptive statistics	No. of Objects	MGM %	L-cavities %	L-rims %	Spots %	C-Lithic %
Mean	104.40	74.03	17.31	5.20	3.31	0.15
Standard Error	4.63	1.28	1.33	0.15	0.17	0.04
Median	106.00	75.69	15.89	5.13	3.49	0.14
Standard Deviation	10.36	2.85	2.98	0.33	0.37	0.09
Sample Variance	107.30	8.15	8.89	0.11	0.14	0.01
Range	27.00	6.40	7.25	0.84	0.88	0.19
Minimum	90.00	70.35	14.45	4.91	2.77	0.05
Maximum	117.00	76.75	21.70	5.75	3.65	0.24
Confidence Level(95.0%)	12.86	3.54	3.70	0.40	0.46	0.12

Source: DTN: GS021008314224.002 [DIRS 161910], Table S03045\_001, file *Tptpll Lithop Data Sum Sheet 15Nov02.doc*.

NOTE: OP = original position, AP = alternative position, MGM = matrix-groundmass, L-cavities = lithophysal cavities, L-rims = rims on lithophysae, C-Lithic = lithic clasts.

In the tape traverse data there are three main conditions that can affect the accuracy of the values (others are described in the data package for DTN: GS021008314224.002 [DIRS 161910]):

1. In the data package, the amounts of lithophysal cavities in the tape traverses from 21+25 to 23+35 are greater than (and from 22+01 to 23+35 much greater than) those documented in panel maps and angular traverses. This segment of the tunnel was the first to have data collected and it contains abundant spots. Re-examination of the exposures from 21+25 to 22+01 indicates many of the initially identified lithophysae are spots, although some spots have a thin stringer or veinlet inside, and this appears to have lead to the identification as lithophysae.
2. Tape traverse data were collected by three collectors, and there appears to be a slight variation in the estimated amounts of rims and spots depending on the different collectors. There are slightly smaller estimates in the section from 14+00 to 17+63 compared to the section from 17+63 to 22+01. Additionally, some of the measurements of rims and spots from the panel maps and angular traverses in these

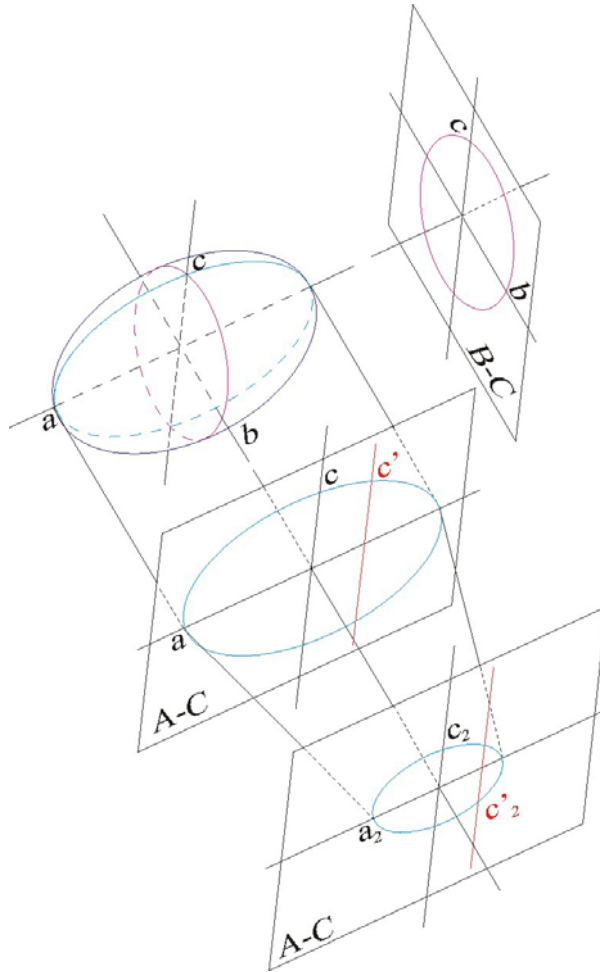
sections of the tunnel appear to confirm the smaller visual estimates determined in the tape traverse. However, other panel map and angular traverse data appears to indicate the visual estimates determined in the tape traverse are underestimated. Adjustments of the tape data are described in Sections O4 and O6.

3. In the tape traverse data, one component used in calculating the abundance of lithophysal cavities is the total length of the traverse. The length of the traverse results from the amount of construction materials in the tunnel and the height of the laser-prism above the invert (see Figure O-1 and the data package for DTN: GS021008314224.002 [DIRS 161910] for a detailed discussion). The traverses began at the top of the compressed air pipe and ended at the top of the conveyor belt, and the construction materials that affected the length include pipes, electrical lines, steel sets, vent lines, the conveyor belt and frame, and other equipment. Although the influence of the laser-prism height on the length was discussed by investigators, it was never specified and not explicitly recorded. Initially (from Station 22+00 to 19+80), the total and visible lengths were measured for each traverse with a wheel on the end of the extension rod/handle. At Station 19+80 the compiler determined that most measured lengths and tunnel conditions were similar enough that the visible length of 6.7 m was used as the standard value for the remainder of the traverses to Station 14+05. Some of the angular traverses were measured at the same locations as the tape traverses, and the calculated visible lengths vary from 7.0 to 7.8 m (these values do not include the traverses where there is no vent line or conveyor). This comparison indicates the 6.7 m visible length is probably too short for most of the tape traverses. The amount of difference in the calculated percent based on the total length of the traverse is proportional to the amount of cavities measured such that a traverse with only a few percent cavities is barely affected whereas the traverse with the most cavities is affected the most. For example, the greatest effect occurs in the traverse at 16+00 with 3.6 m length of cavities, so with a 6.7 m length, the cavities form 53.9 percent of the tunnel wall. If the visible length of the tape traverse is adjusted to 7.2 m, the calculated abundance of lithophysal cavities locally decreases by as much as 3.7 percent (a 6.9 percent decrease). Additionally, and if the adjusted visible length is 7.4 m, the cavity value decreases by as much as 5.8 percent (a 10.7 percent decrease). The correction of tape data is described more in Sections O4 and O6.

Qualitatively, there are reasonably good comparisons of values measured with different techniques, and some data can be compared quantitatively. Differences in the values measured by the three methods (panel maps, angular traverses, and tape traverses) are expected because of how the data are collected, and these relations are implicit in the need to design three methods of data collection. The lithophysal cavity values from the tape traverses tend to be 1 to 3 times greater than in adjacent or collocated panel map and/or angular traverse values. The angular traverse values (for lithophysal cavities, rims, spots, and clasts) tend to be slightly greater than those for the panel maps; however, locally the panel map values can be greater. The average lithophysal-cavity value that is fully within the lower lithophysal zone (from Station 14+60 to 23+20) is 18.9 percent from tape traverses (nonadjusted values from Table O-4) compared to 15.5 percent from angular traverses and 12.9 percent from panel maps (Table O-9).

**How Well Measurements Represent the Three-Dimensional Distributions of the Features—**

Determining the 3-dimensional size, shape, and distribution of features and objects is one of the ultimate results of the measurements described in this appendix. Most measurements in solid objects that cannot be disaggregated (such as rocks) are made with 2-dimensional cross sections and 1-dimensional traverses, so it is important to appreciate the geometric relations of the three-dimensional objects with respect to how they are measured. For example, an ellipsoid consisting of three axes (A is the longest, B is intermediate in length, and C is the shortest) can be cut along many planes to create various two dimensional cross-sections (Figure O-22). The smallest cross sectional area is for a plane through the B-C axes, an intermediate cross sectional area is through the A-C axes, and the maximum cross sectional area is through the A-B axes. An ellipsoid is a simplified rendition of many lithostratigraphic features, especially where a foliation is well developed such as rocks in the lower lithophysal zone exposed in the ECRB Cross-Drift. With respect to the lower lithophysal zone in the tunnel, the left and right ribs approximate cuts along planes parallel to the one that contains the A-C axes, and the crown and invert approximate cuts along planes parallel to the one that contain the A-B axes. Cross sections that contain the primary axes and transect the center of the ellipsoid have the maximum area (for example, a and c in Figure O-22). However, any plane cut parallel to the primary plane (for example A-C) that does not transect the center of the ellipsoid has the same cross sectional shape, but the axes are shorter (a<sub>2</sub> and c<sub>2</sub>) and the area is smaller. If a 1-dimensional linear traverse transects an object, then the maximum length of the intercept occurs only if the transect is along the primary axis (for example, c in Figure O-22). However, if the transect is parallel to the C axis, but does not intersect the center of the ellipsoid, then the length of the intercept is less than the length of the axis (for example, c' and c'<sub>2</sub> in Figure O-22). These relations are the basis of the observation in technical procedure, YMP-USGS-GP-20, R1 (*Estimating Abundance of Features in Core and in Outcrop, Including Lithophysae, Spots, Clasts, and Fractures*) that 2- and 1-dimensional measurements typically result in under estimates of the true measurements of a feature. This review of geometric relations of measurements indicates that even with the methods used and documentation of measurements and correlations of values between the various techniques, the actual values at a specific location or the descriptive statistics are judged to represent minimum values.



NOTE: The  $a$  axis is the longest axis, the  $b$  axis is the intermediate length, and the  $c$  axis is the shortest.

Figure O-22. Geometric Relations of Three-Dimensional Ellipsoid with Two-Dimensional Cross Sections and One-Dimensional Transects

INTENTIONALLY LEFT BLANK



**APPENDIX P**  
**PRESSURES ON THE DRIP SHIELD**  
**CALCULATED FROM THE DISCONTINUUM MODEL**



## **PRESSURES ON THE DRIP SHIELD CALCULATED FROM THE DISCONTINUUM MODEL**

### **P1. INTRODUCTION**

The drip shield loads (i.e., impact and static loads of the caved rock) in the lithophysal rock mass were first assessed considering that the drip shield is rectangular (with geometry approximately corresponding to the outline of the actual shape), rigid, and slaved to the free-field ground motion (i.e., the motion unaffected by interaction of the seismic waves with the drift). Those considerations were used in the initial analysis because they are conservative, resulting in overprediction of the caved rock-mass loads on the drip shield. The rectangular drip-shield shape reduces the potential for stress arching through the caved rock mass above the drip shield. Stress redistribution through the multi-component system is a function of ratios between stiffnesses of different components. If the drip shield is considered to be infinitely stiff, it certainly will reduce the positive stress arching in the caved rock mass, resulting in increased loads on the drip shield. In order to demonstrate the level of conservatism in those results and to obtain more realistic estimates of the drip shield loads, an improved model of the drip shield has been developed that includes better representation of geometry and has stiffness that approximates the actual drip-shield stiffness. (The model used in the UDEC drift collapse analysis is two-dimensional. The geometry of the drip shield is three-dimensional.) Development and validation of the drip-shield model is discussed in Appendix Y.

In Section P2, the effects of the shape and stiffness of the drip shield on the drip shield loads are analyzed for different loading conditions (i.e., seismic shaking and quasi-static drift collapse). Detailed analysis of the drip shield loads (using the new model) and the results are presented in Sections P3 to P5.

### **P2. EFFECT OF DRIP-SHIELD SHAPE AND STIFFNESS**

The effect of drip-shield stiffness and shape on the drip shield loads, both impact and static, due to rockfall is analyzed for seismic shaking with probability of annual recurrence of  $1 \times 10^{-5}$  and for quasi-static drift degradation. None of the actual static loads (e.g., in situ or thermal stresses) are expected to cause total drift collapse even for the long-term strength of the rock mass (i.e., accounting for time-dependent strength degradation). The quasi-static drift degradation is considered here to represent an extreme case of the static load on the drip shield. It is considered that the rock mass completely loses its cohesive strength and that total drift collapse takes place under the action of in situ stresses and gravitational forces.

#### **P2.1 SEISMIC SHAKING**

Case 11 (i.e., ground motion 9 and rock mass category 1, see Table 6-44) with  $1 \times 10^{-5}$  ground motion was used in this analysis since this case couples a high-energy ground motion (see Table 6-6) with the lowest strength rock category. The initial analyses were performed using the original drip-shield model (rectangular and rigid drip shield) shown in Figure P-1 and the model shown in Figure P-2, in which the drip shield has an arched top and is deformable, but pinned (i.e., free rotation, fixed translation) at the bottom of both sides. The pinned points are slaved to

the free-field motion in a similar way the entire drip shield was slaved in the original model. (The invert, the pallet, and the waste canisters are not represented in these two models.)

Figures P-1 and P-2 show the segment ID and the final configuration of the models when equilibrium is achieved after the shaking. This ground motion does not result in total drift collapse. The calculated loads on the drip shield, shown in Figure P-3, and the average pressures (for the sides and the top), listed in Table P-1, are fairly similar for these two cases and are insignificant with regard to the stability of the drip shield.

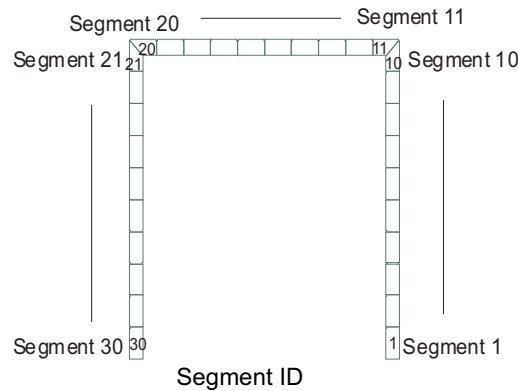
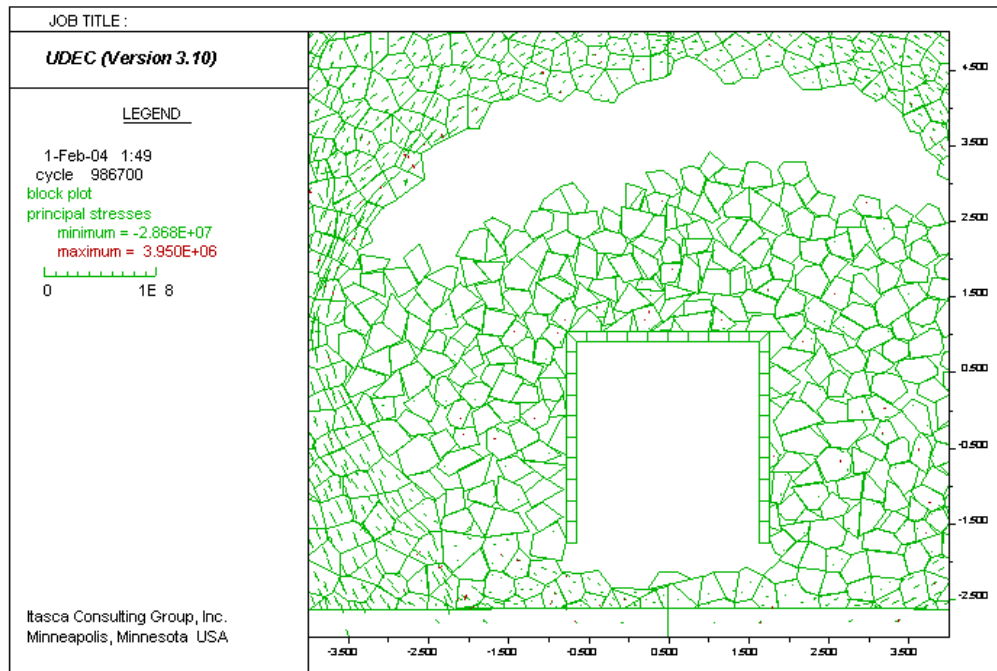


Figure P-1. Ground Motion  $10^{-5}$ , Case 11: Equilibrium State for Rigid, Rectangular Drip Shield

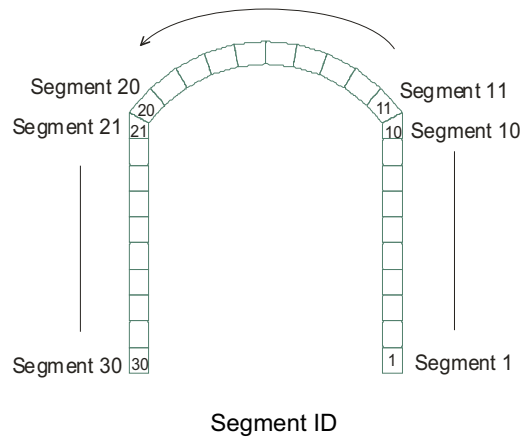
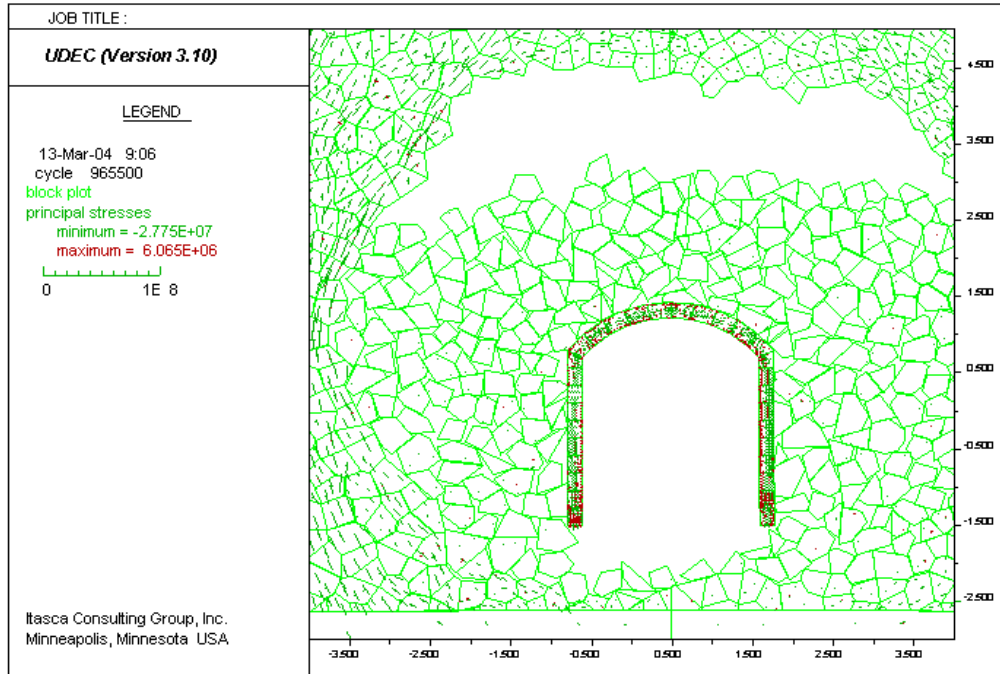


Figure P-2. Ground Motion  $10^{-5}$ , Case 11: Equilibrium State for Deformable Drip Shield With Arched Top, Pinned Bottom, No Invert

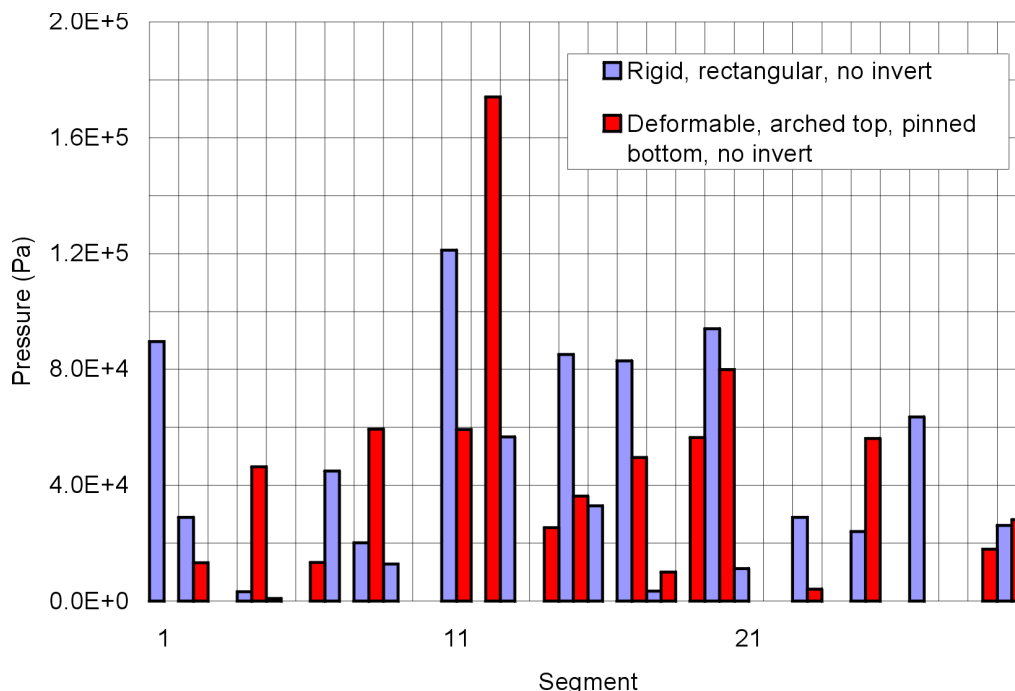


Figure P-3. Ground Motion  $10^{-5}$ , Case 11: Loads On the Drip Shield For Cases Without the Invert

Table P-1. Ground motion 10-5, Case 11: Average Loads On the Drip Shield For Cases Without the Invert

Case	Left	Top	Right
	$\text{kN/m}^2$	$\text{kN/m}^2$	$\text{kN/m}^2$
rigid, rectangular	15.4	47.63	20.03
deformable, arched top, pinned sides	10.62	49.13	13.25

The drip shield will rest on the invert under its own weight. The load by the rockfall, in addition to deforming it, may also move the entire drip shield by sliding it along the invert and by lifting it from the invert. Also, the inertial forces during seismic shaking can cause movement of the drip shield. It is expected that movement of the drip shield will have an effect on the load of the caved rock on the drip shield. For example, it is observed in the case of the rigid drip shield that there is often a significant imbalance between the horizontal forces acting on the drip shield. If the drip shield is free to move horizontally, the imbalance should be relatively small, less than the frictional force between the drip shield and the invert.

Case 11 was then run with the invert presented as a horizontal slab (shown in Figure P-4). It was considered in the simulations that the invert is rigid, slaved to the free-field motion of the rock mass. The friction angle between the drip shield and the invert is 22 degrees, which corresponds to the friction coefficient of 0.4. The pallet and the waste package also are included in the model and are modeled as rigid, slaved to the free-field motion of the rock mass. The presence of the invert affects the rockfall. The invert provides horizontal support at its elevation and affects the volume of the initial drift cross-section that can be filled with the caved rock, resulting in earlier build-up of the back-pressure by the caved rock, compared to the cases in which the caved rock

also fills the space below the invert (as shown in Figure P-2). Consequently, the results of the models with the invert cannot be compared with the results of the models without the invert. Three cases (all of which include the invert) are considered. The model shown in Figure P-4 (The model configuration in the equilibrium state after seismic shaking is shown.) is for a rigid drip shield slaved to the invert (i.e., the drip shield has the same motion as the free-field). In the model shown in Figure P-5, the drip shield can slide freely on the invert, but it cannot separate from the invert. The most realistic conditions of interaction between the drip shield and the invert are represented in the case shown in Figure P-6. In this case, the drip shield can slide, but it also can detach from the invert. (It is shown in Figure P-6 that the left side of the drip shield has lifted off the invert.)

The amount of the rockfall in the three cases is less than in the cases without the invert. The drip shield is not completely covered with caved rock. Therefore, the example is not good for assessing the effect of the deformability of the drip shield on the stress arching in the caved rock mass above the drip shield. The static loads on the drip shield (shown in Figure P-7 and summarized in Table P-2) are relatively small. However, the effect of the drip shield sliding on the invert on the horizontal forces acting on the drip shield can be noticed. The imbalance between the forces on the left and right sides of the drip shield is much smaller for the cases in which the drip shield is allowed to slide (Some imbalance still exists even for those two cases because of the frictional forces and the reaction between the drip shield and the pallet when the drip shield comes in the contact with the pallet, as shown in Figure P-6.). The histories of the impact loads during the rockfall for the case shown in Figure P-6 are shown in Figures P-8, P-9, and P-10 for the left side, the top, and the right side of the drip shield, respectively. Relatively large impact loads are recorded; in this case, the maximum impact pressures are of the order of 5 MPa.

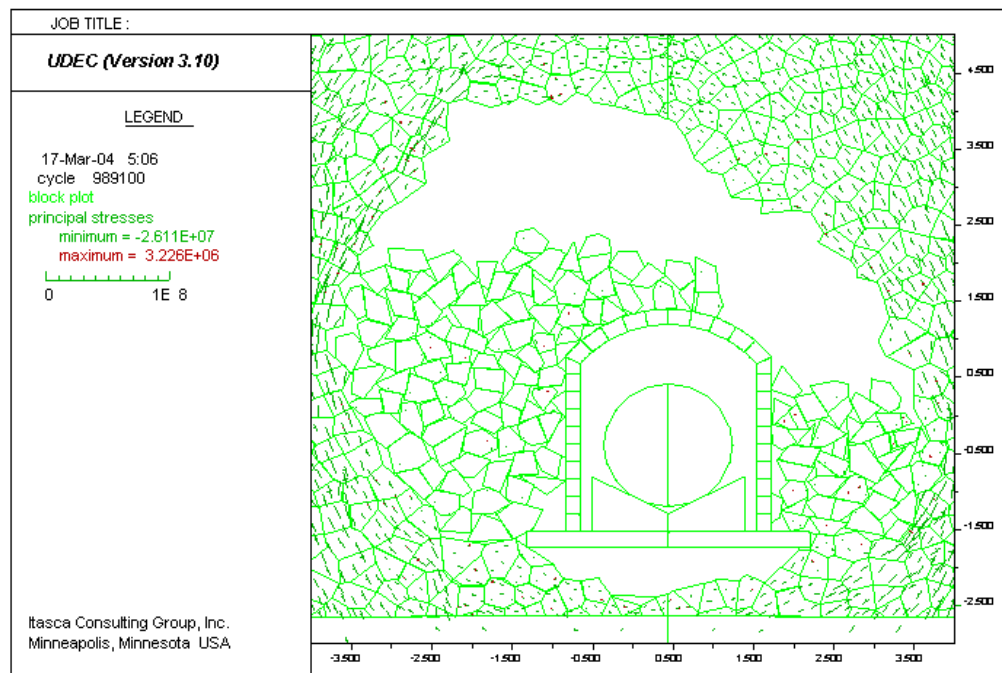


Figure P-4. Ground Motion  $10^{-5}$ , Case 11: Equilibrium State for Rigid Drip Shield With Arched Top, Bottom Fixed to the Invert

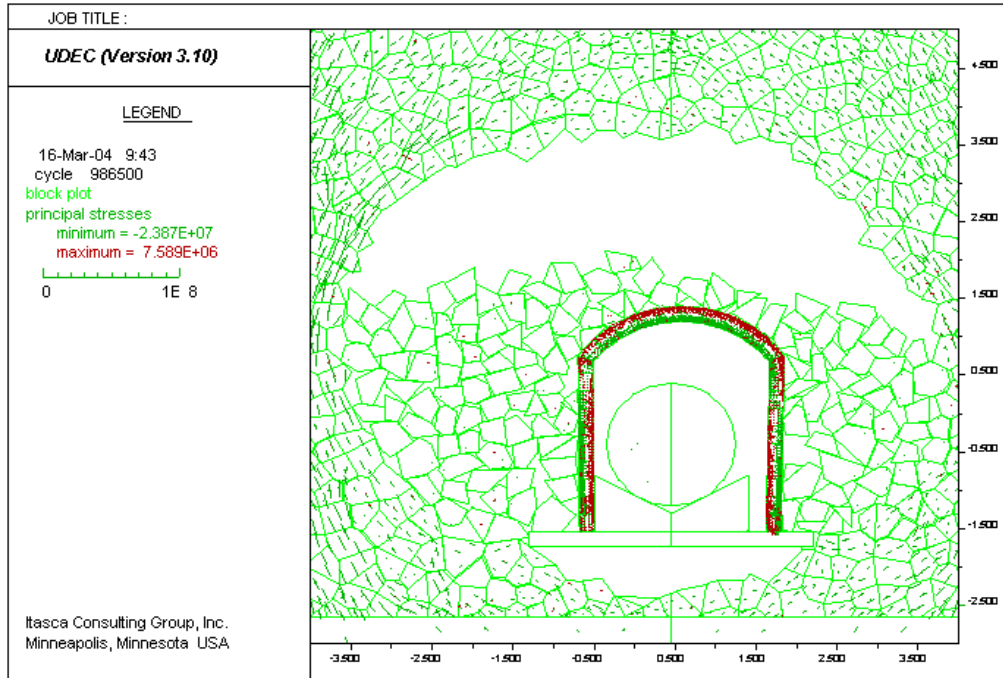


Figure P-5. Ground Motion  $10^{-5}$ , Case 11: Equilibrium State for Deformable Drip Shield With Arched Top, Bottom Slides On the Invert

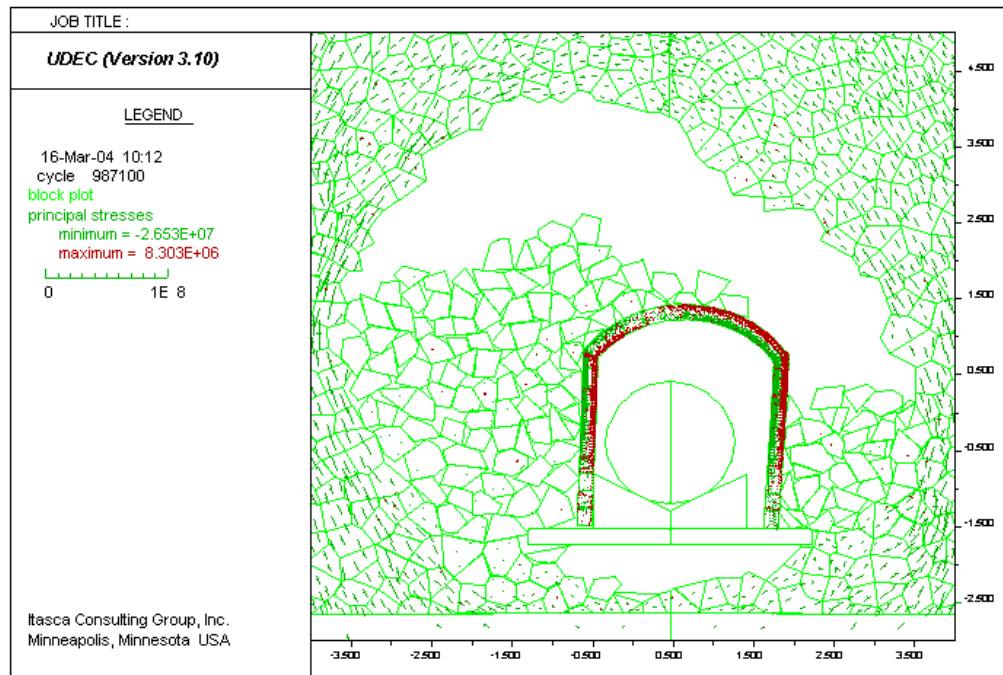


Figure P-6. Ground Motion  $10^{-5}$ , Case 11: Equilibrium State for Deformable Drip Shield With Arched Top, Bottom Rests On the Invert



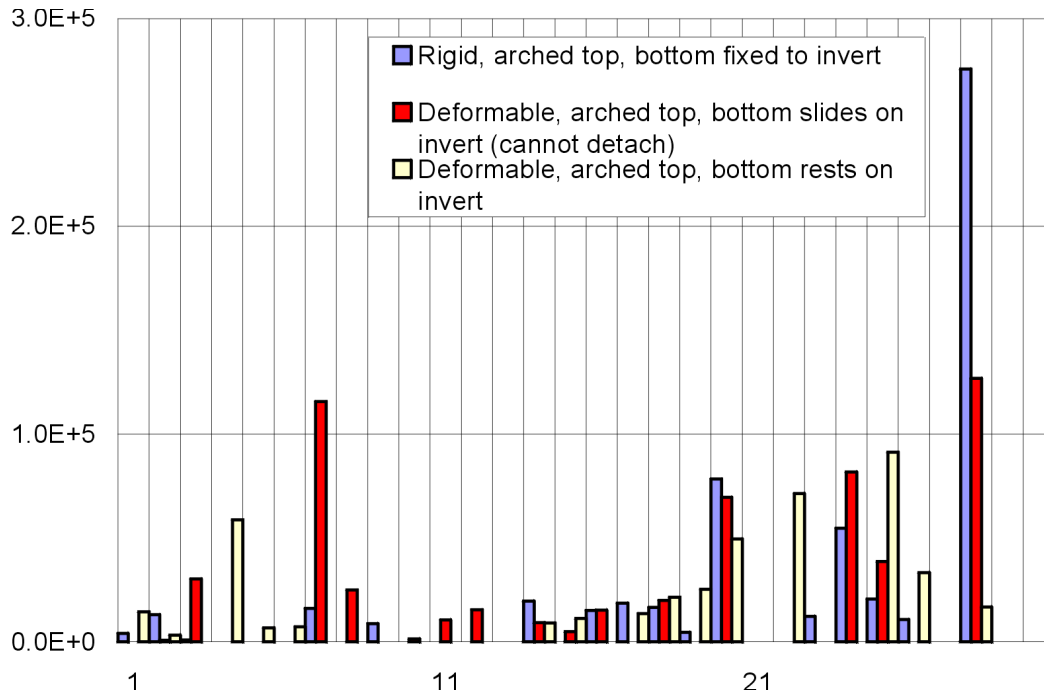


Figure P-7. Ground Motion 10<sup>-5</sup>, Case 11: Loads On The Drip Shield for Cases With the Invert

Table P-2. Ground Motion 10<sup>-5</sup>, Case 11: Average Loads On the Drip Shield for Cases With Invert

Case	Left kN/m <sup>2</sup>	Top kN/m <sup>2</sup>	Right kN/m <sup>2</sup>
rigid, arched top, bottom fixed to invert	37.40	15.25	4.28
deformable, arched top, bottom slides on invert	24.72	14.46	17.28
deformable, arched top, bottom rests on invert	21.26	12.99	9.00

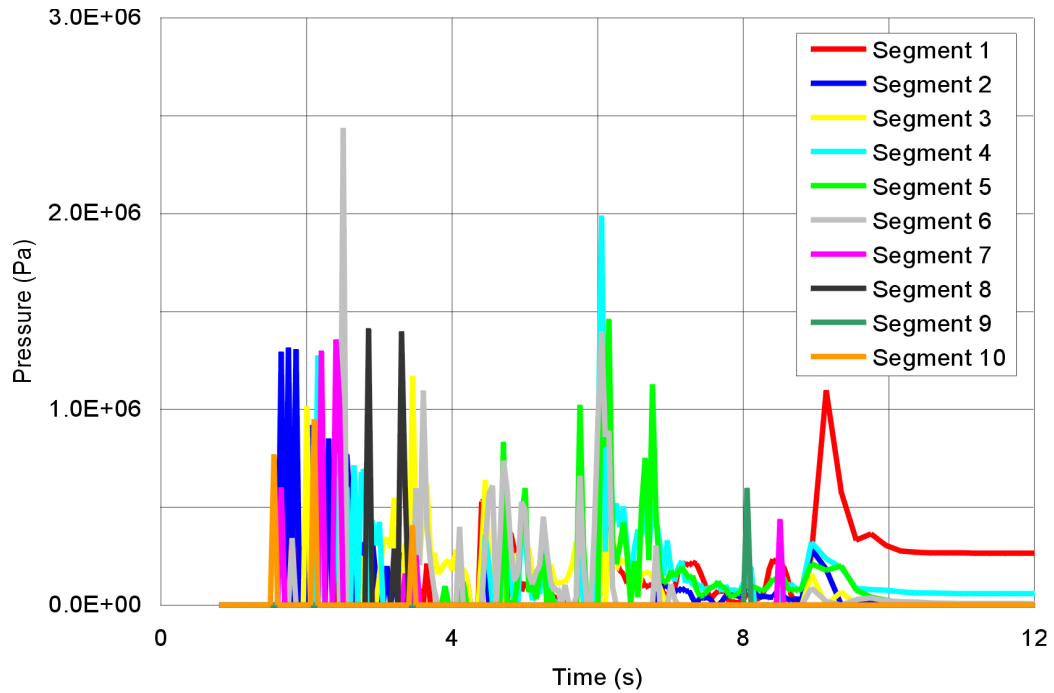


Figure P-8. Ground Motion  $10^{-5}$ , Case 11: Dynamic Loads On the Right Side for Deformable Drip Shield With Arched Top, Bottom Rests On the Invert

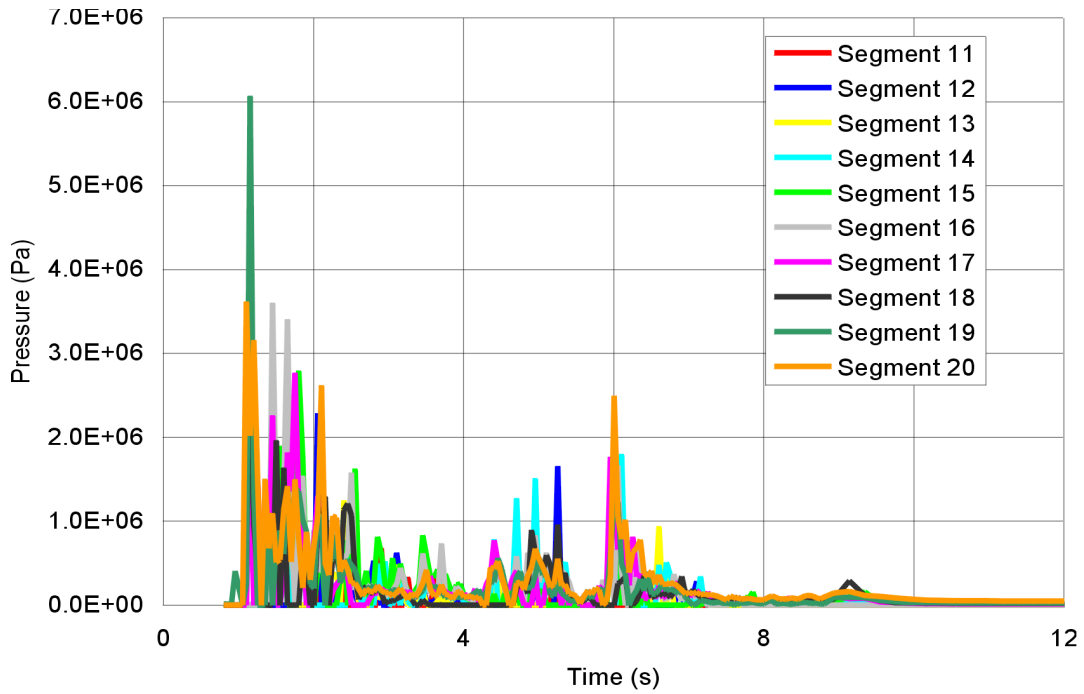


Figure P-9. Ground Motion  $10^{-5}$ , Case 11: Dynamic Loads On The Top for Deformable Drip Shield With Arched Top, Bottom Rests On the Invert

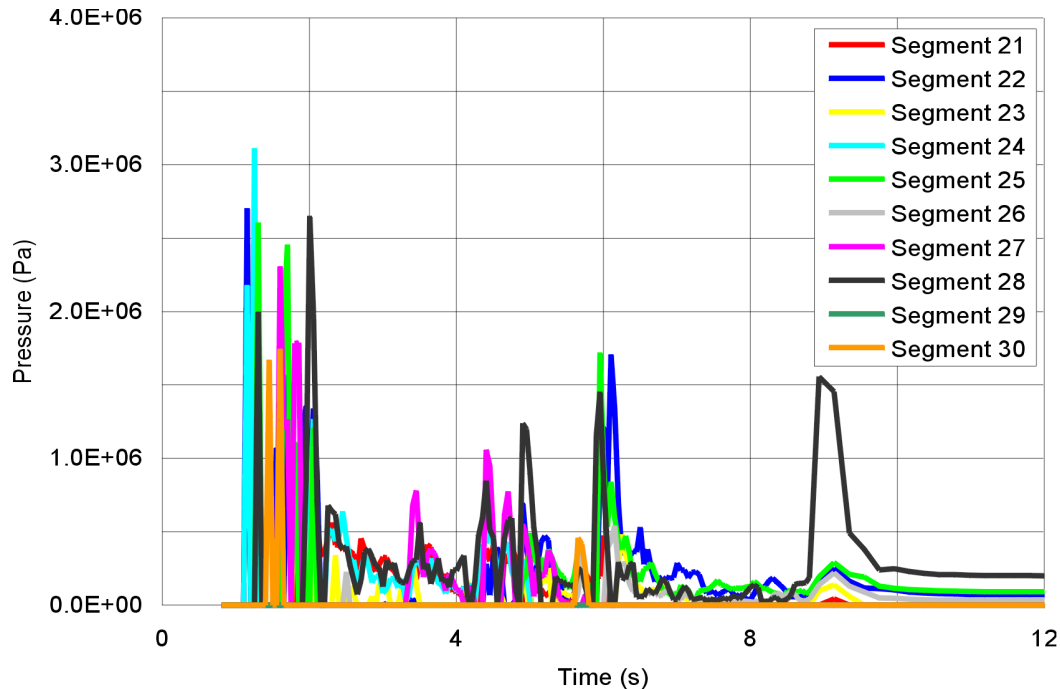


Figure P-10. Ground Motion  $10^{-5}$ , Case 11: Dynamic Loads On the Left Side for Deformable Drip Shield With Arched Top, Bottom Rests On the Invert

## P2.2 QUASI-STATIC DEGRADATION

The quasi-static drift degradation was analyzed for both 0.2-m and 0.3-m sizes of the Voronoi blocks.

### P2.2.1 Block Size 0.3 m

The final geometries of the models without the invert are shown for the rectangular, rigid drip shield in Figure P-11 and for the deformable drip shield pinned at the bottom of two sides in Figure P-12. The summary of the drip shield loads is provided in Figure P-13 and Table P-3. In this particular case deformability of the drip shield does not seem to have a significant effect on the vertical load on the drip shield. In fact, the load on the deformable drip shield is approximately 10 percent larger than on the rigid, rectangular drip shield (The increase in the load on the top is probably due to randomness in the response of this system.). However, the horizontal loads on the sides of the drip shield in the model with the deformable drip shield are much less than in the model with the rigid drip shield. The imbalance between the horizontal forces in the case of the deformable drip shield is because the bottom on both sides of the deformable drip shield is pinned. That boundary condition resulted in very large force at the lower left end (i.e., segment 30 in Figure P-13) of the drip shield.

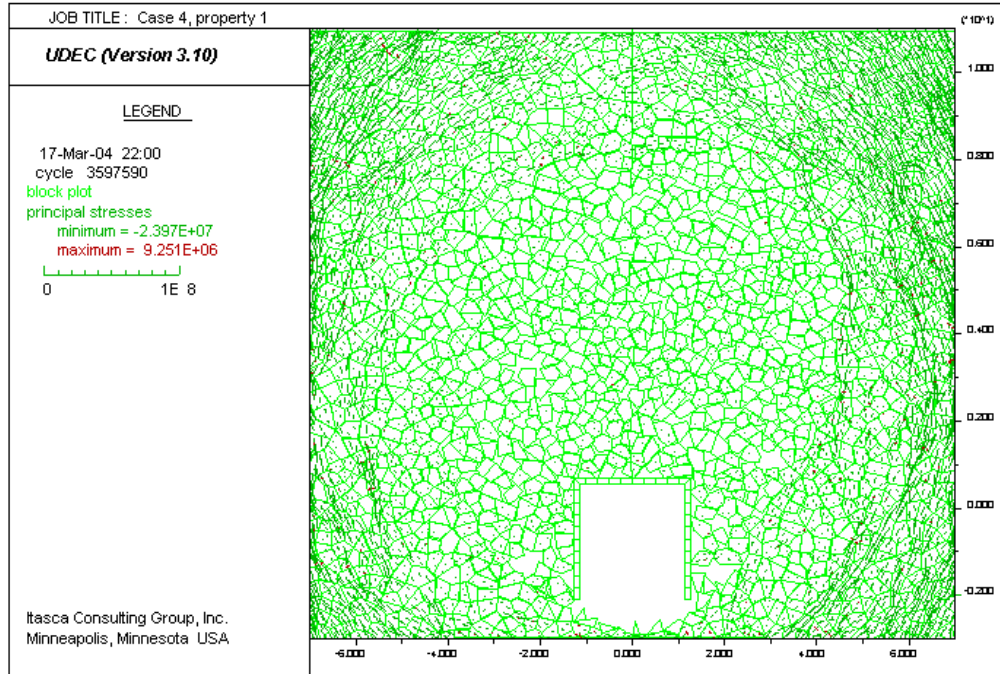


Figure P-11. Quasi-Static Drift Degradation, 0.3 m Block Size: Equilibrium State for Rigid, Rectangular Drip Shield

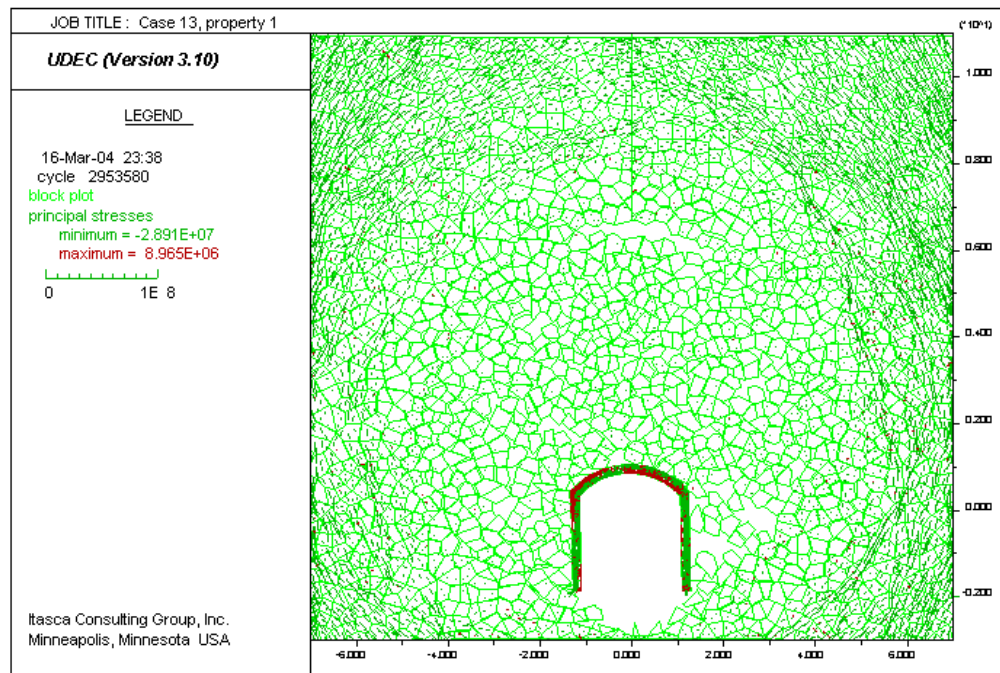


Figure P-12. Quasi-Static Drift Degradation, 0.3-m Block Size: Equilibrium State for Deformable Drip Shield With Arched Top, Pinned Bottom, No Invert

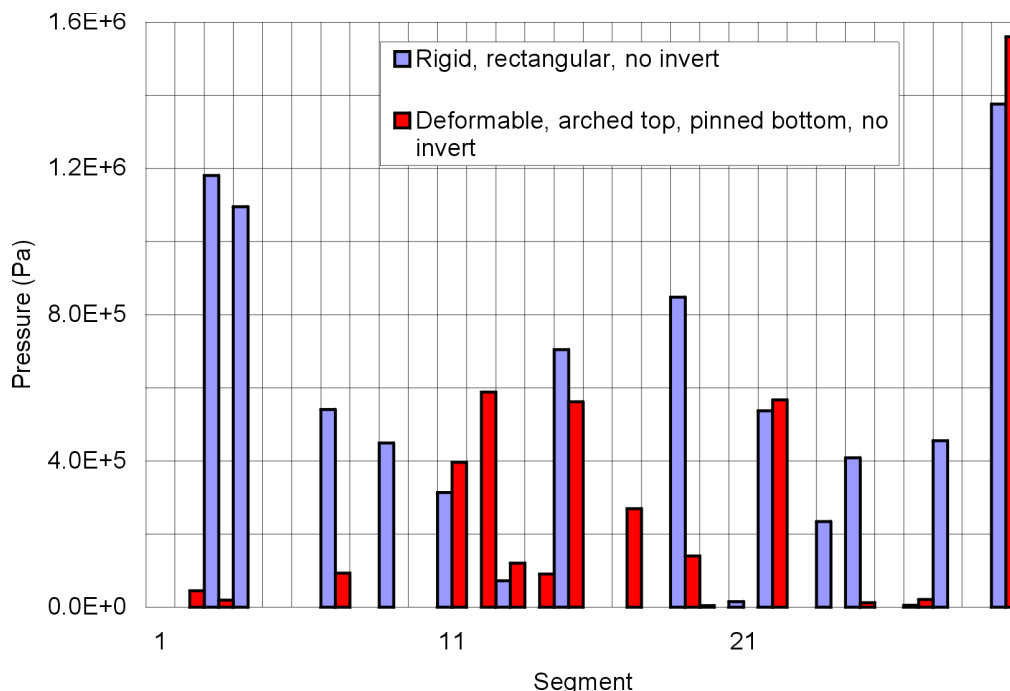


Figure P-13. Quasi-Static Drift Degradation, 0.3 m Block Size: Loads On the Drip Shield for Cases Without Invert

Table P-3. Quasi-Static Drift Degradation, 0.3 m Block Size: Average Loads On the Drip Shield For Cases Without the Invert

Case	Left kN/m <sup>2</sup>	Top kN/m <sup>2</sup>	Right kN/m <sup>2</sup>
rigid, rectangular	303.18	194.18	326.70
deformable, arched top, pinned sides	216.06	216.65	15.82

If the invert, the pallet, and the waste package are included in the model, the extent of the caved region is reduced as shown in Figures P-14 and P-15. Stable arches are formed, with a gap between the caved rubble and the stable rock mass, due to the finite size of the rock blocks considered here despite the fact that the cohesive strength of the joints (contacts between the blocks) is reduced to zero. Two cases are considered here. The case with the rigid drip shield is shown in Figure P-14; the case with the drip shield resting under gravity on the invert is shown in Figure P-15 (When resting under gravity, the drip shield is allowed to slide and detach from the invert.). The results for the drip shield loads (shown in Figure P-16 and Table P-4) are completely dominated by the reduced size of the cave above the emplacement drift. The pressures are relatively small, and the effect of deformability of the drip shield is not apparent.

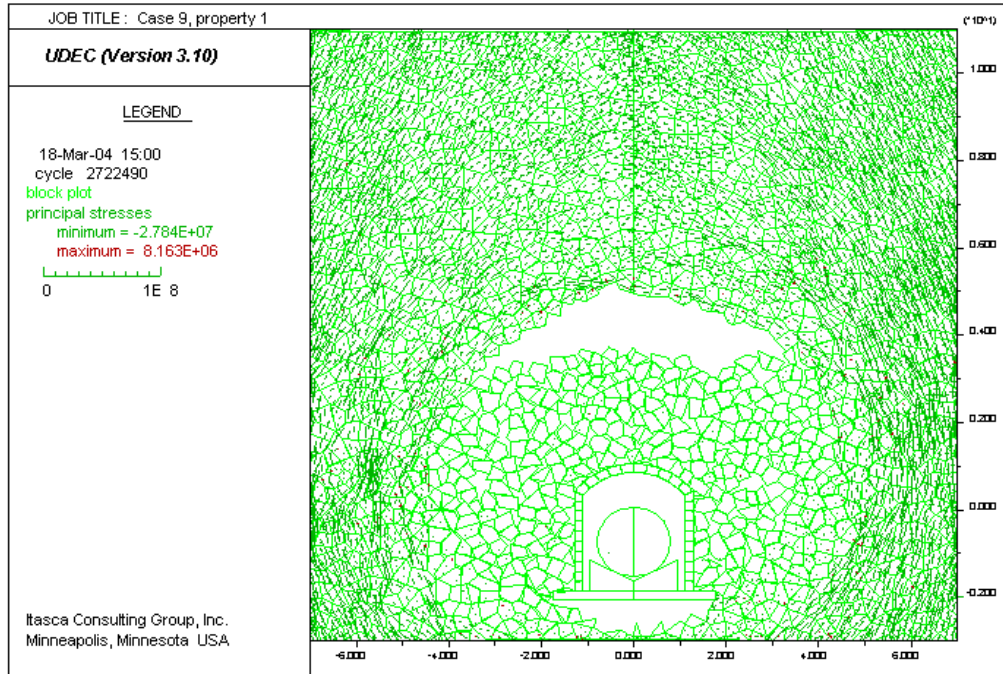


Figure P-14. Quasi-Static Drift Degradation, 0.3 m Block Size: Equilibrium State for Rigid Drip Shield With Arched Top, Bottom Fixed To the Invert

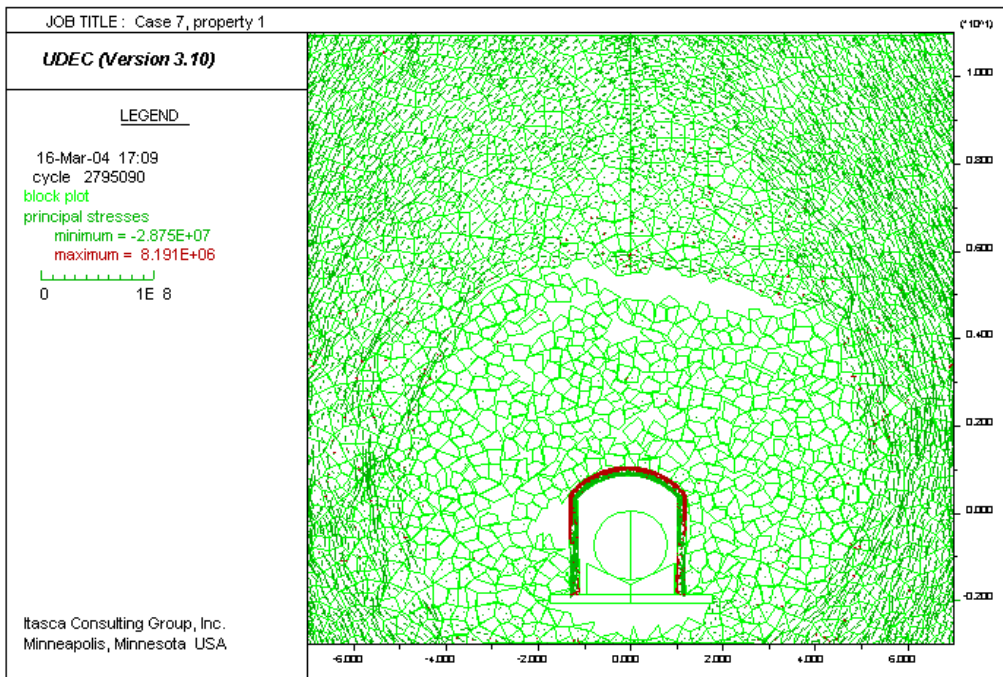


Figure P-15. Quasi-static Drift Degradation, 0.3 m Block Size: Equilibrium State for Deformable Drip Shield With Arched Top, Bottom Rests On the Invert

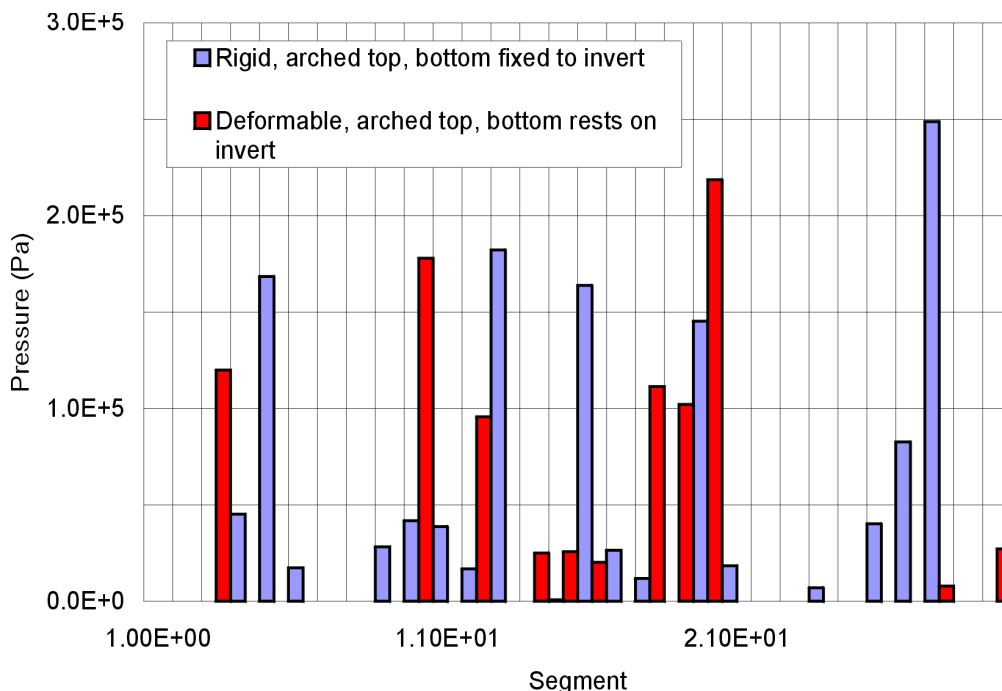


Figure P-16. Quasi-Static Drift Degradation, 0.3 m Block Size: Loads On the Drip Shield for Cases With the Invert

Table P-4 Quasi-Static Drift Degradation, 0.3 m Block Size: Average Loads On the Drip Shield For Cases With Invert

Case	Left kN/m <sup>2</sup>	Top kN/m <sup>2</sup>	Right kN/m <sup>2</sup>
rigid, arched top, bottom fixed to invert	39.70	58.56	30.09
deformable, arched top, bottom rests on invert	35.04	59.85	29.79

### P2.2.2 Block Size 0.2 m

Quasi-static drift degradation using the smaller, 0.2 m Voronoi block size, generally results in more conservative predictions of the load on the drip shield. The smaller block size yields better packing and smaller bulking of the caved rock. Also, the potential for formation of stable arches when the cohesive strength of the joints between the blocks is reduced to zero becomes smaller as the block size is decreased.

The equilibrium model configurations for the cases without the invert are shown for the rigid, rectangular drip shield in Figure P-17 and for the deformable drip shield pinned at the bottom in Figure P-18. The contours of displacement magnitudes, which indicate the extent of the caved rock, are shown in Figure P-19 for the model with deformable drip shield. The stress tensor field, shown in Figure P-20 for the same model, illustrates how the stress arches are formed in the caved rock above the drip shield. There is a significant component of randomness in the response of such systems. The correlation between the stress trajectories (shown in Figure P-20) and the static loads on the drip shield (shown in Figure P-21) can be established easily. The large drip shield loads for segments 3 and 13 are consequences of the localized stress trajectories

of large stress magnitudes directed toward segments 3 and 13. (The segments are numbered from the lower right corner of the drip shield in the counter-clockwise direction.)

The summary of the drip shield loads in Figure P-21 and Table P-5 indicates that the vertical load on the drip shield is reduced for the deformable drip shield. However, there is a significant component of the imbalance in the horizontal forces acting on the deformable drip shield because of the boundary condition used at the bottom of the drip shield.

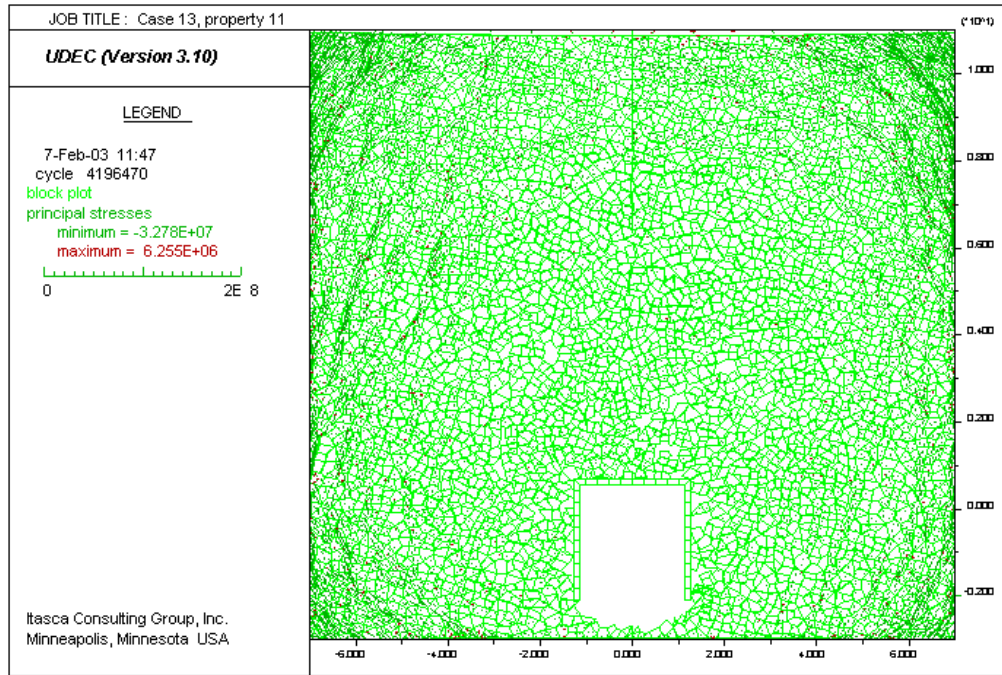


Figure P-17. Quasi-Static Drift Degradation, 0.2-m Block Size: Equilibrium State for Rigid, Rectangular Drip Shield



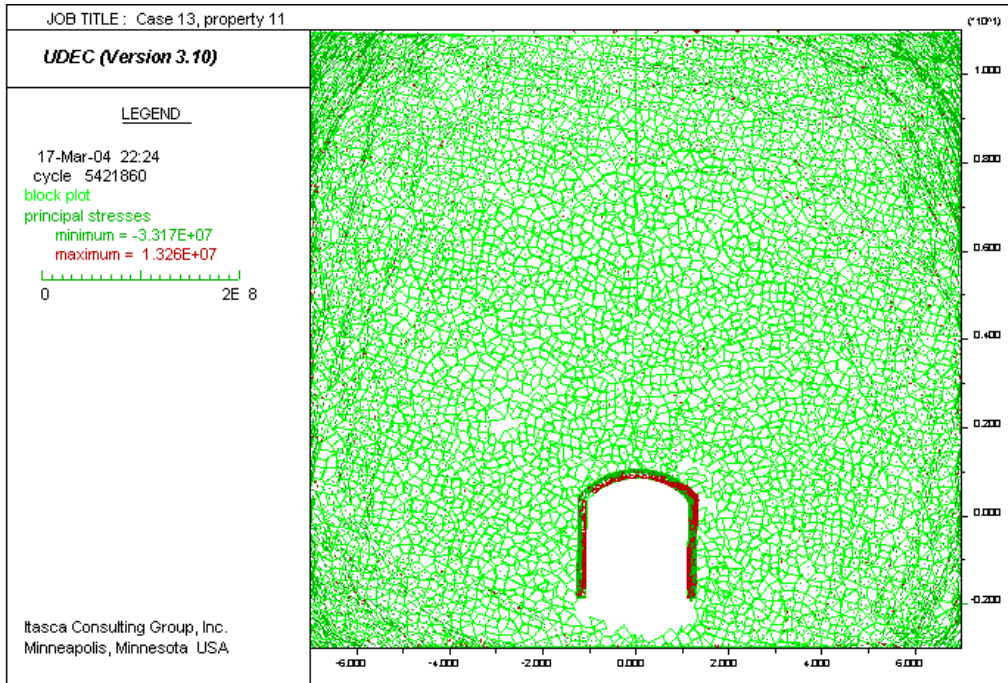


Figure P-18. Quasi-Static Drift Degradation, 0.2 m Block Size: Equilibrium State for Deformable Drip Shield With Arched Top, Pinned Bottom, No Invert

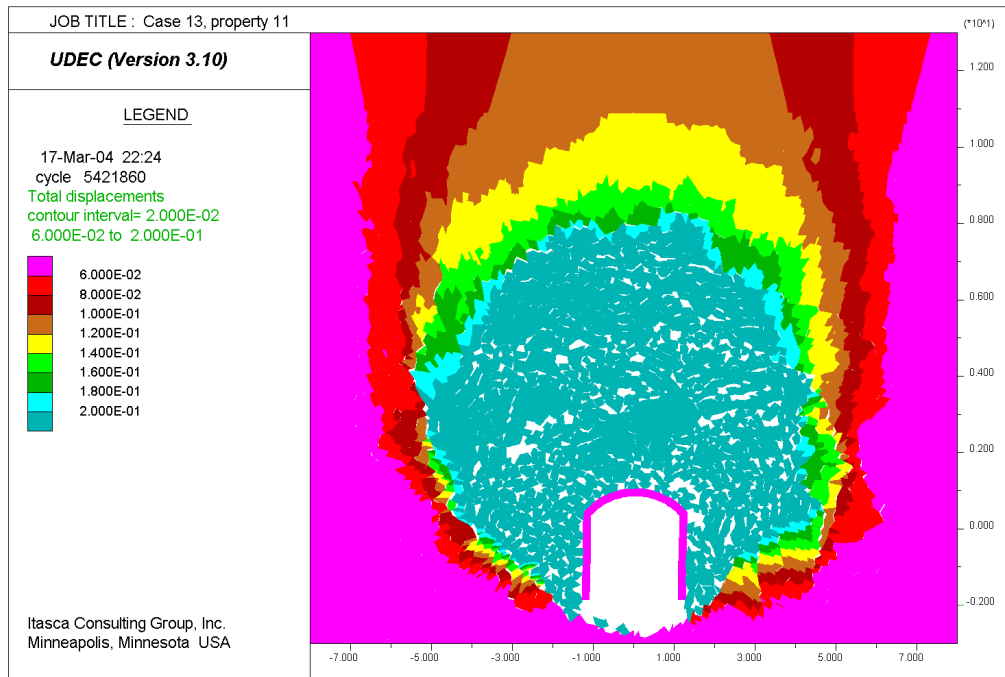
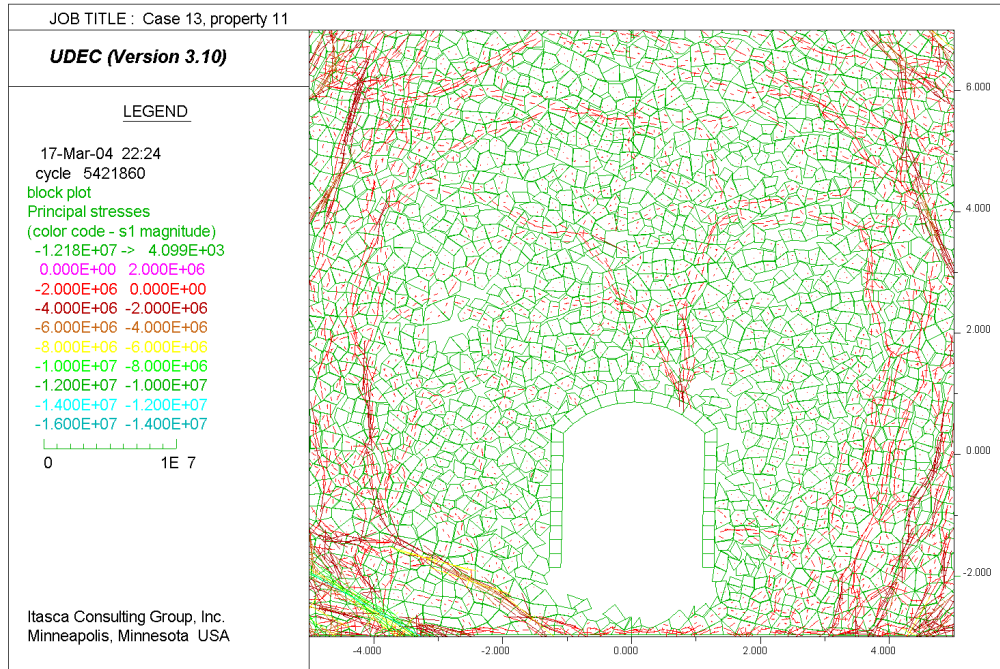


Figure P-19. Quasi-Static Drift Degradation, 0.2 m Block Size: Contours of Displacement (m) Magnitude for Deformable Drip Shield With Arched Top, Pinned Bottom, No Invert



NOTE: Pa = Pascal.

Figure P-20. Quasi-Static Drift Degradation, 0.2 m Block Size: Stress Tensor Field (Pa) for Deformable Drip Shield With Arched Top, Pinned Bottom, No Invert

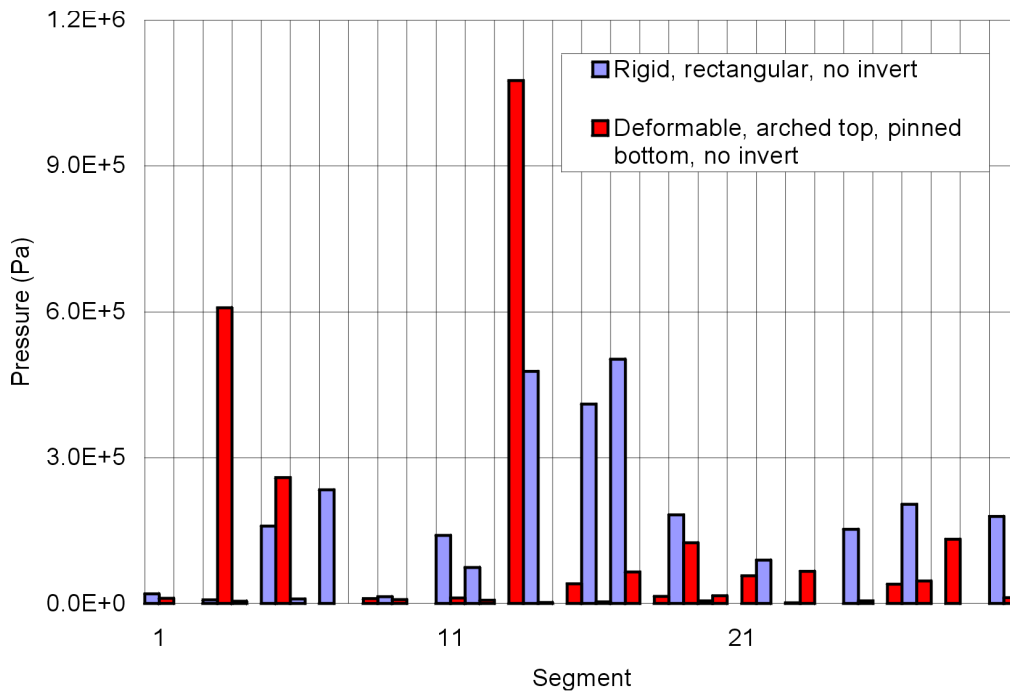


Figure P-21. Quasi-Static Drift Degradation, 0.2 m Block Size: Loads on the Drip Shield for Cases Without the Invert

Table P-5. Quasi-Static Drift Degradation, 0.2 m Block Size: Average Loads On the Drip Shield For Cases Without the Invert

Case	Left	Top	Right
	kN/m <sup>2</sup>	kN/m <sup>2</sup>	kN/m <sup>2</sup>
rigid, rectangular	62.61	179.16	44.78
deformable, arched top, pinned sides	35.75	136.04	89.52

The results for the cases with the invert, the pallet, and the waste packages included in the model are shown in Figures P-22 through P-26, and Table P-6. Two cases are considered: the rigid drip shield; and the deformable drip shield, free to slide and detach from the invert. The more realistic model of the drip shield results in reduction (approximately 25 percent) of the vertical load on the drip shield and more balanced horizontal loads (see Table P-6).

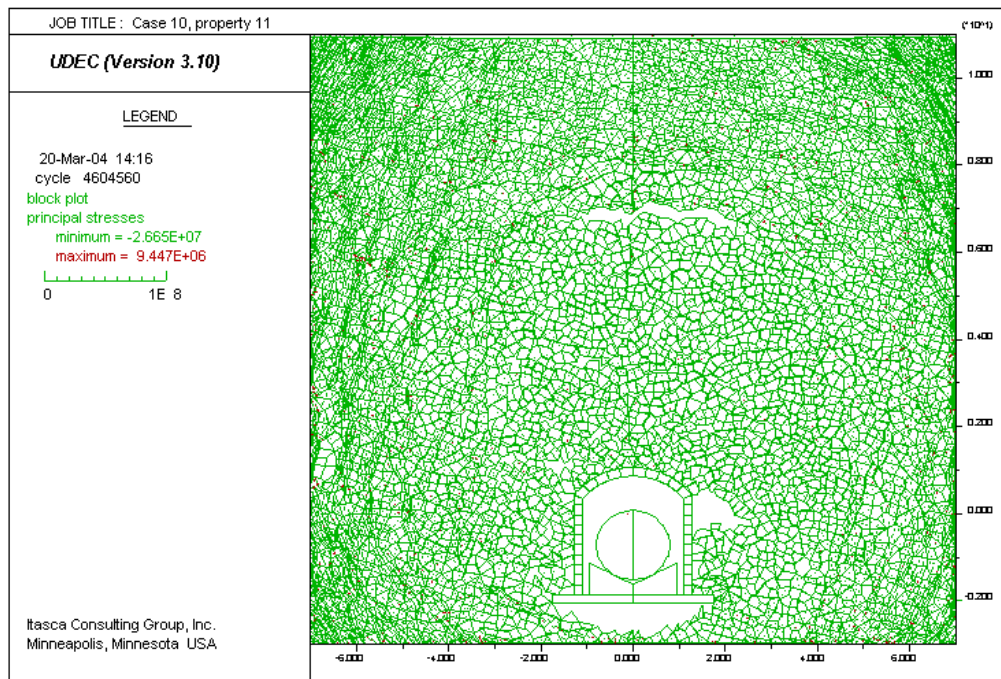


Figure P-22. Quasi-Static Drift Degradation, 0.2 m Block Size: Equilibrium State for Rigid Drip Shield With Arched Top, Bottom Fixed to the Invert

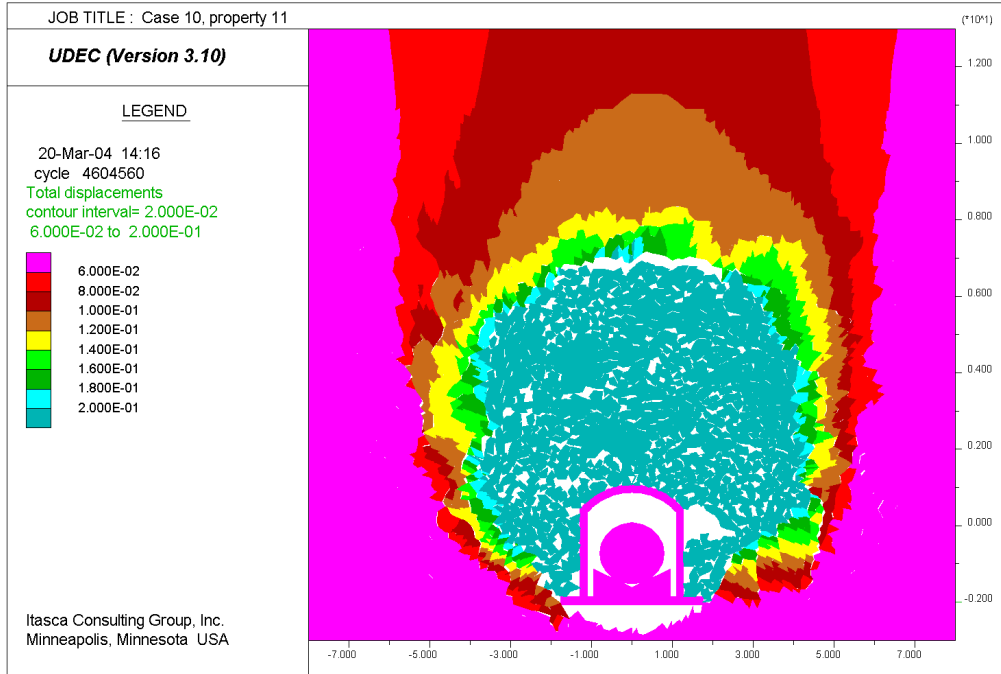


Figure P-23. Quasi-Static Drift Degradation, 0.2 m Block Size: Contours of Displacement (m) Magnitude for Rigid Drip Shield With Arched Top, Bottom Fixed to the Invert

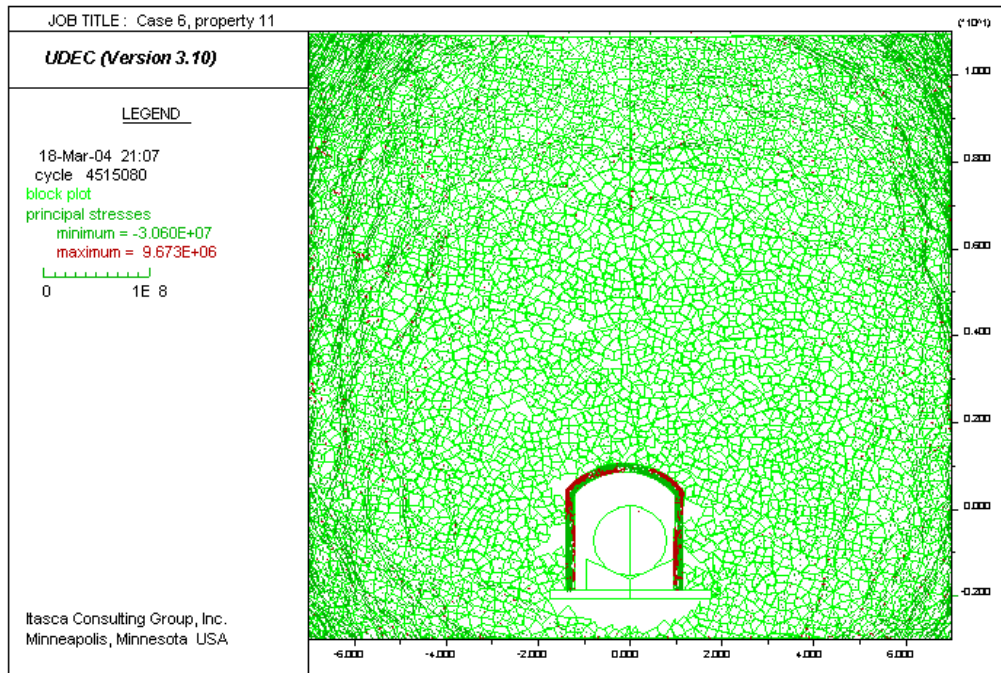


Figure P-24. Quasi-Static Drift Degradation, 0.2 m Block Size: Equilibrium State for Deformable Drip Shield With Arched Top, Bottom Rests On the Invert

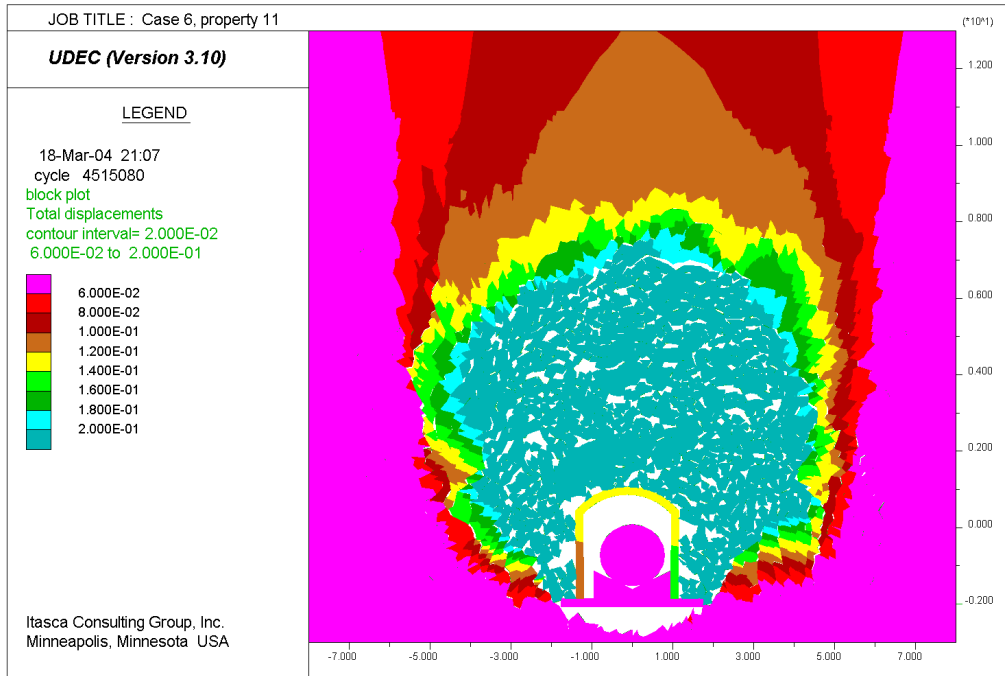


Figure P-25. Quasi-Static Drift Degradation, 0.2 m Block Size: Contours of Displacement (m) Magnitude for Deformable Drip Shield With Arched Top, Bottom Rests On the Invert

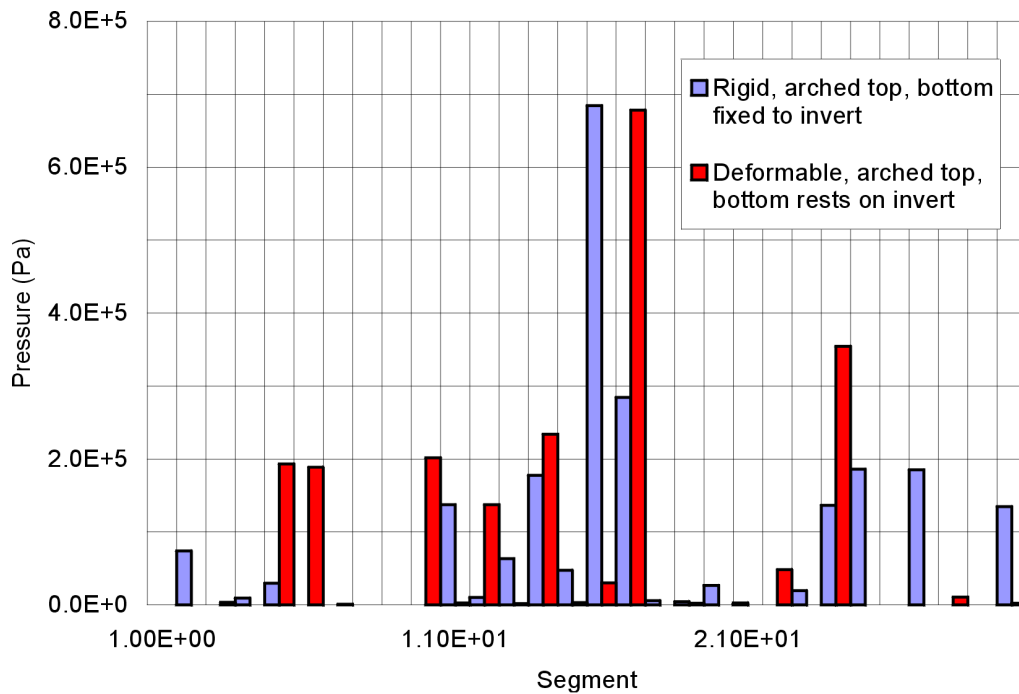


Figure P-26. Quasi-static Drift Degradation, 0.2 m Block Size: Loads On the Drip Shield for Cases With the Invert

Table P-6. Quasi-Static Drift Degradation, 0.2 m Block Size: Average Loads On the Drip Shield For Cases With Invert

Case	Left	Top	Right
	kN/m <sup>2</sup>	kN/m <sup>2</sup>	kN/m <sup>2</sup>
rigid, arched top, bottom fixed to invert	66.45	144.15	11.28
deformable, arched top, bottom rests on invert	41.54	108.92	58.76

### P3. IMPACT AND STATIC LOADS DUE TO STRONG GROUND MOTION SEISMIC SHAKING

Impact and static loads on the drip shield are assessed for ground motions with  $1 \times 10^{-6}$  and  $1 \times 10^{-7}$  probability of annual recurrence. Another objective of these simulations was to investigate if the drip shield could be overturned during strong ground motions. Ground motions 3, 7, 9, and 13 were analyzed for both levels of probability. Those particular ground motions were selected based on different criteria (i.e., peak ground velocity, total power in the velocity spectrum, Arias intensity) for intensity of ground motion, as the four strongest ground motions from the sets of 15 ground motions for both  $1 \times 10^{-6}$  and  $1 \times 10^{-7}$  levels of probability. Category 3 lithophysal rock mass was considered in the simulations.

Although the seismic shaking for 8 simulated ground motions causes large displacements of the entire model, and large displacement of the drip shield relative to its original position inside the emplacement drift (as shown in Figure P-27), the drip shield does not get overturned at the end of the simulations. The model equilibrium configurations for ground motion 3 from  $1 \times 10^{-6}$  and  $1 \times 10^{-7}$  sets are shown in Figures P-28 and P-33, respectively. The model reached the equilibrium configuration with drip shield in an upright position in both cases. For these strong ground motions, the collapse of the drift occurs very quickly—in some cases backfilling the drip shield within a second after the onset of strong ground motion (The strong ground motion for the model shown in Figure P-27 started at 1.75 s. At the state shown in Figure P-27, which is at 2.74 s, the drift is already backfilled.). Once the drip shield is backfilled, it is difficult to overturn it, because the caved rock provides the back-pressure and constrains the motion of the drip shield.

The pressure histories for the segments of the drip shield are shown in Figures P-29 through P-31 for  $1 \times 10^{-6}$  ground motion, and in Figures P-34 through P-36 for  $1 \times 10^{-7}$  ground motion. The maximum transient pressures are relatively large, up to 10 MPa for  $10^{-6}$  ground motion and up to 40 MPa for  $1 \times 10^{-7}$  ground motion. The average block mass in these simulations is approximately 200 kg. (The characteristic block size in the plane of the model is 0.3 m.) If the maximum impact velocity in the case of  $1 \times 10^{-6}$  ground motion is approximately 8 m/s, the maximum impact energy for a single block is 6.4 kJ/m. During these strong ground motions, the rock mass shatters before reaching the drip shield. Consequently, the drip shield is subjected to series of small energy impacts by small blocks, instead of impacts by large blocks (as is the case in the model of drift stability in the non-lithophysal rock mass). Duration of the impact by a single block in the case of  $1 \times 10^{-6}$  ground motion is of the order of one millisecond.

The static pressures on the drip shield are summarized in Figure P-32 and Table P-7 for  $1 \times 10^{-6}$  ground motion and in Figure P-37 and Table P-8 for  $1 \times 10^{-7}$  ground motion.

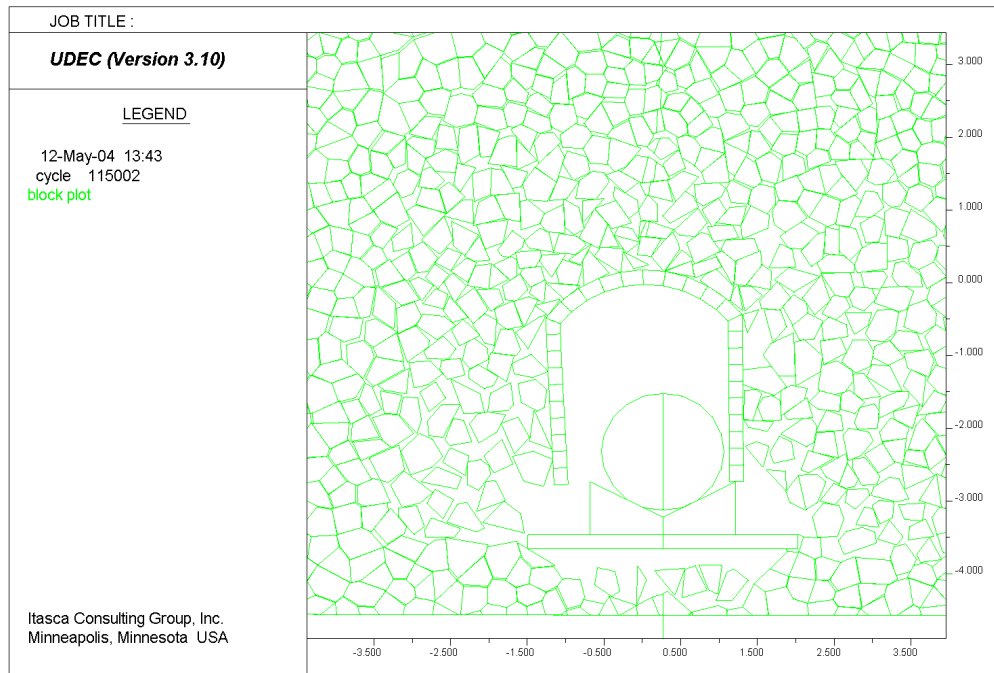


Figure P-27. Ground Motion  $10^{-6}$  Number 3: Model Configuration After 2.75 s of Shaking

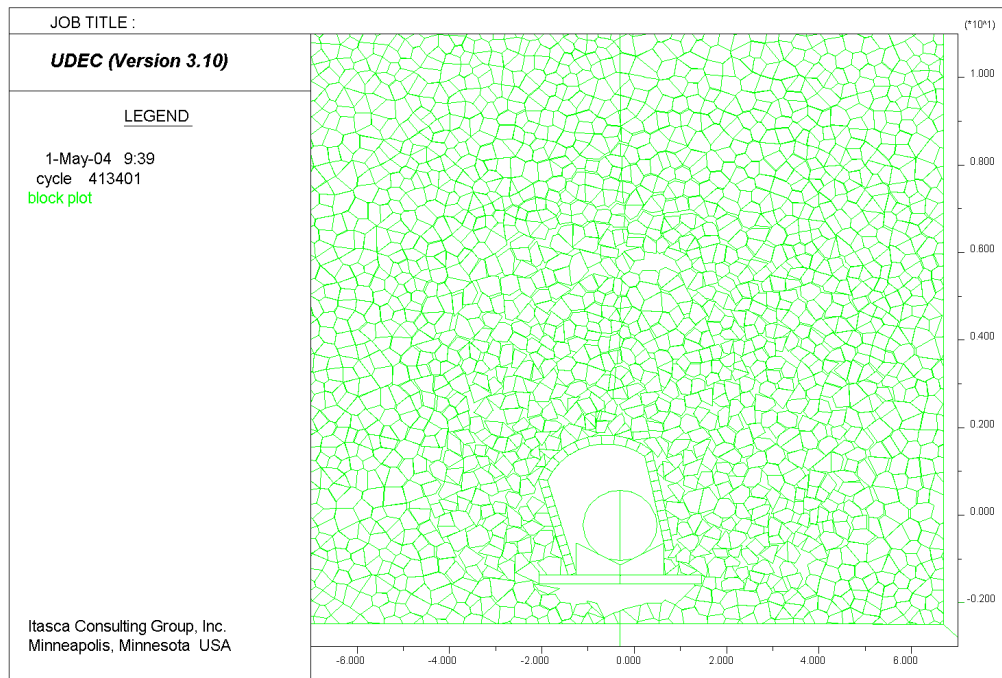


Figure P-28. Ground Motion  $10^{-6}$  Number 3: Model Configuration in the Equilibrium State After Shaking

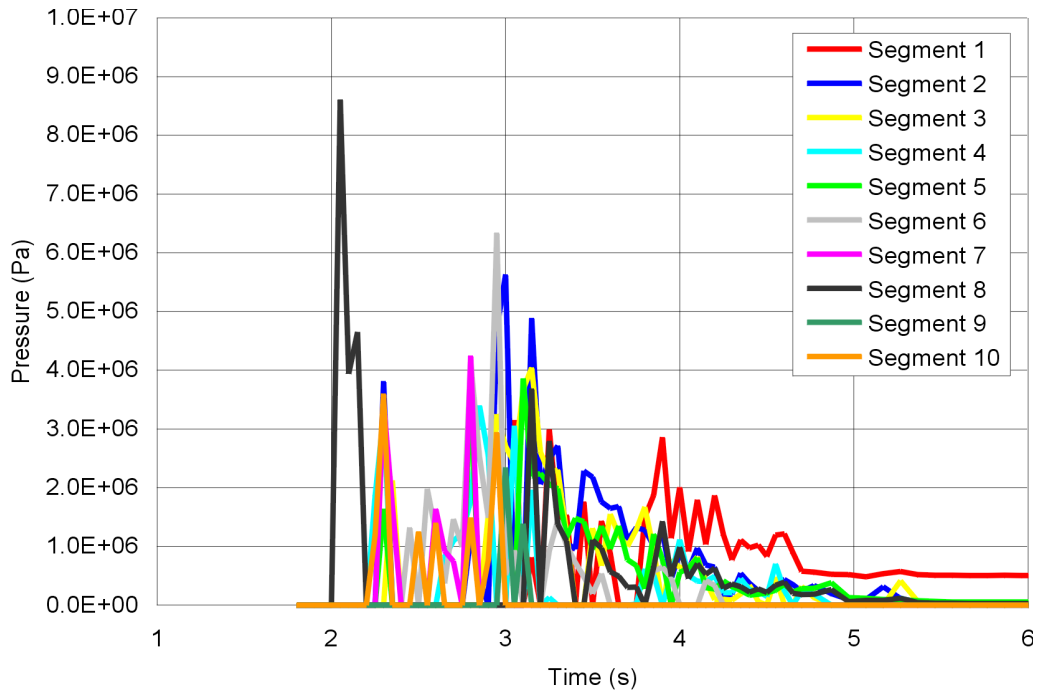


Figure P-29. Ground Motion  $10^{-6}$  Number 3: Dynamic Loads On the Right Side

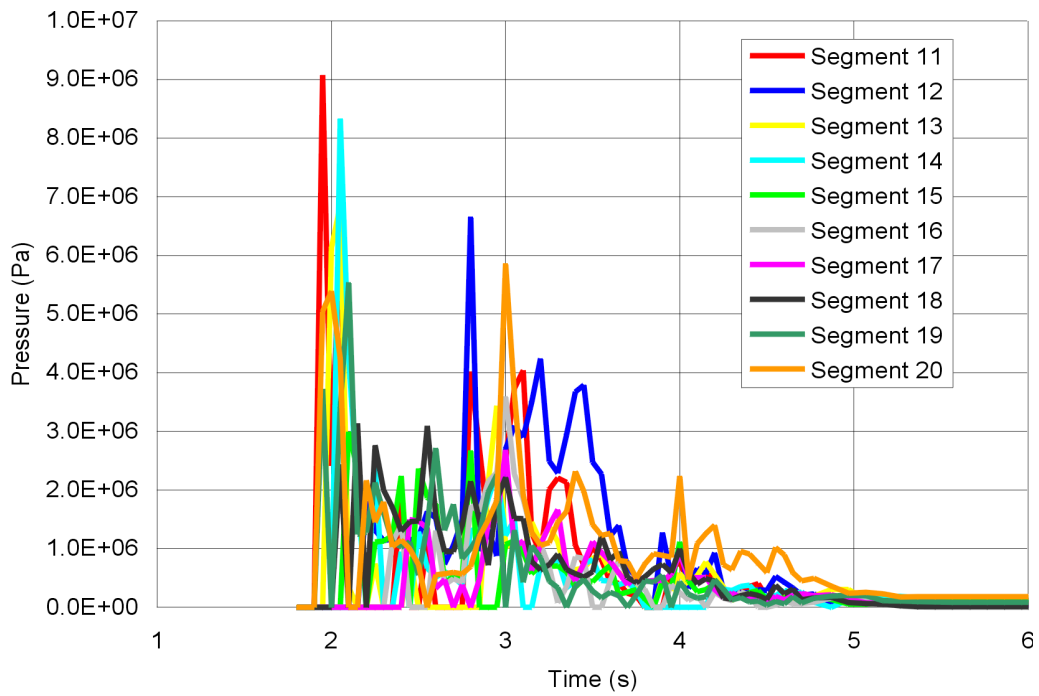


Figure P-30. Ground Motion  $10^{-6}$  Number 3: Dynamic Loads On the Top



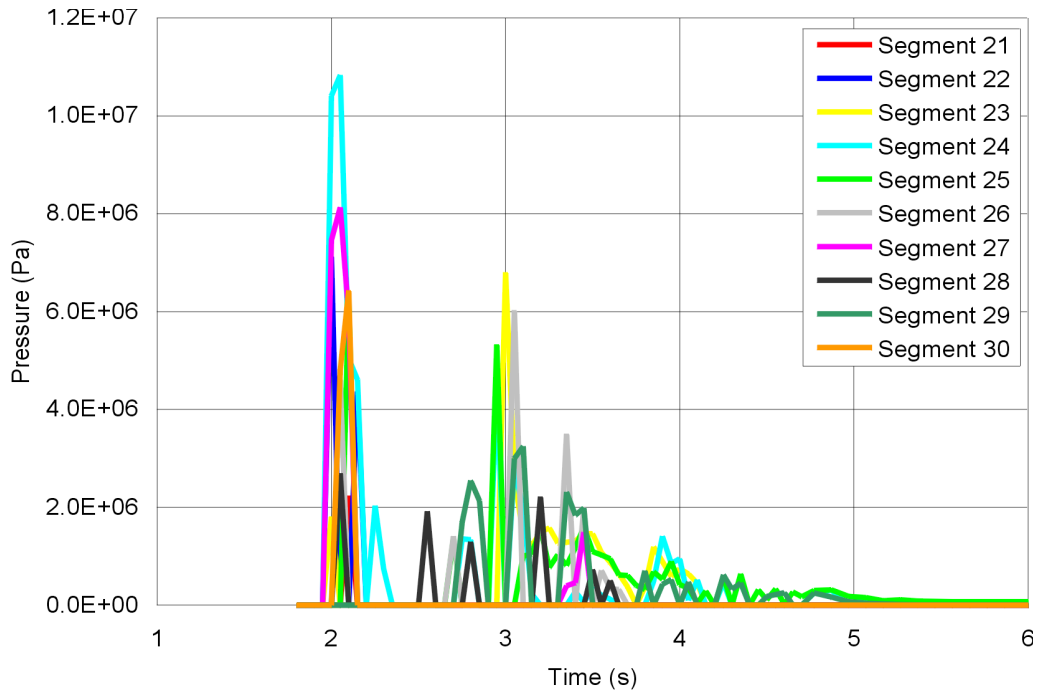


Figure P-31. Ground Motion  $10^{-6}$  Number 3: Dynamic Loads On the Left Side

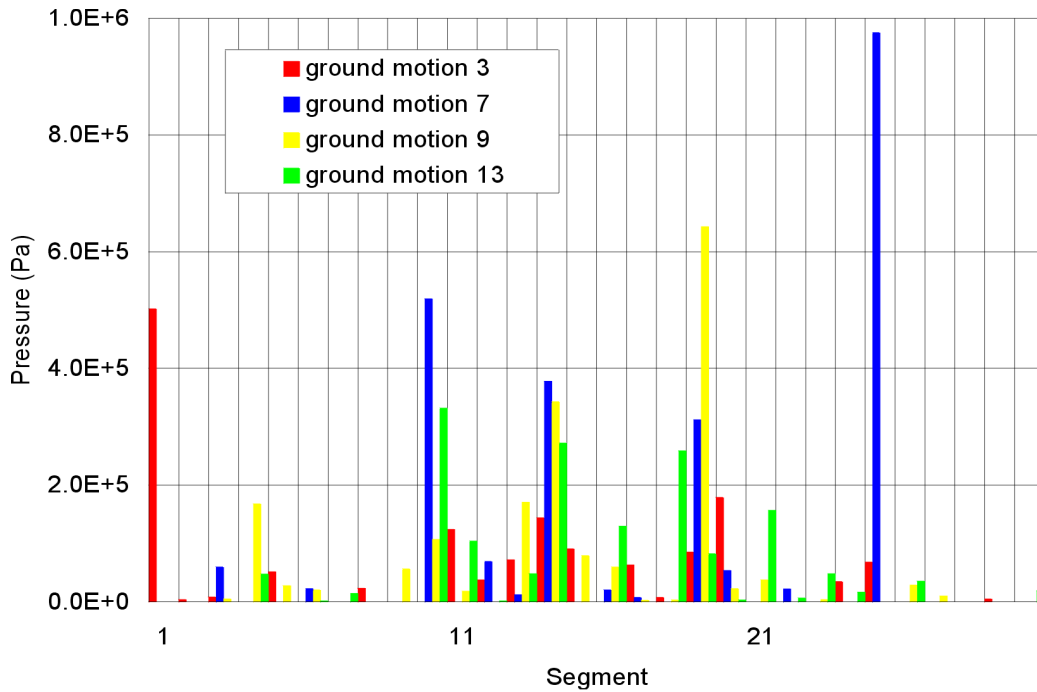


Figure P-32. Static Loads On The Drip Shield After Shaking With Four Different  $10^{-6}$  Ground Motions

Table P-7. Four Different  $10^{-6}$  Ground Motions: Average Loads On the Drip Shield

Ground motion	Left	Top	Right
	kN/m <sup>2</sup>	kN/m <sup>2</sup>	kN/m <sup>2</sup>
3	10.77	80.44	58.92
7	99.78	85.42	60.19
9	8.03	134.34	38.46
13	28.29	90.15	39.57

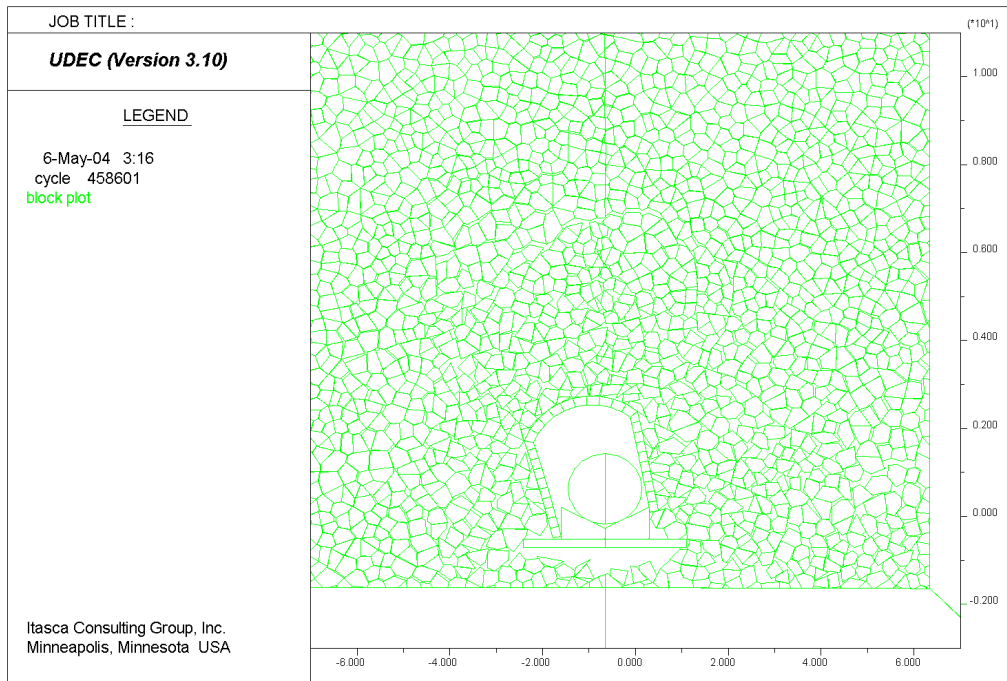


Figure P-33. Ground Motion  $10^{-7}$  Number 3: Model Configuration in the Equilibrium State After Shaking

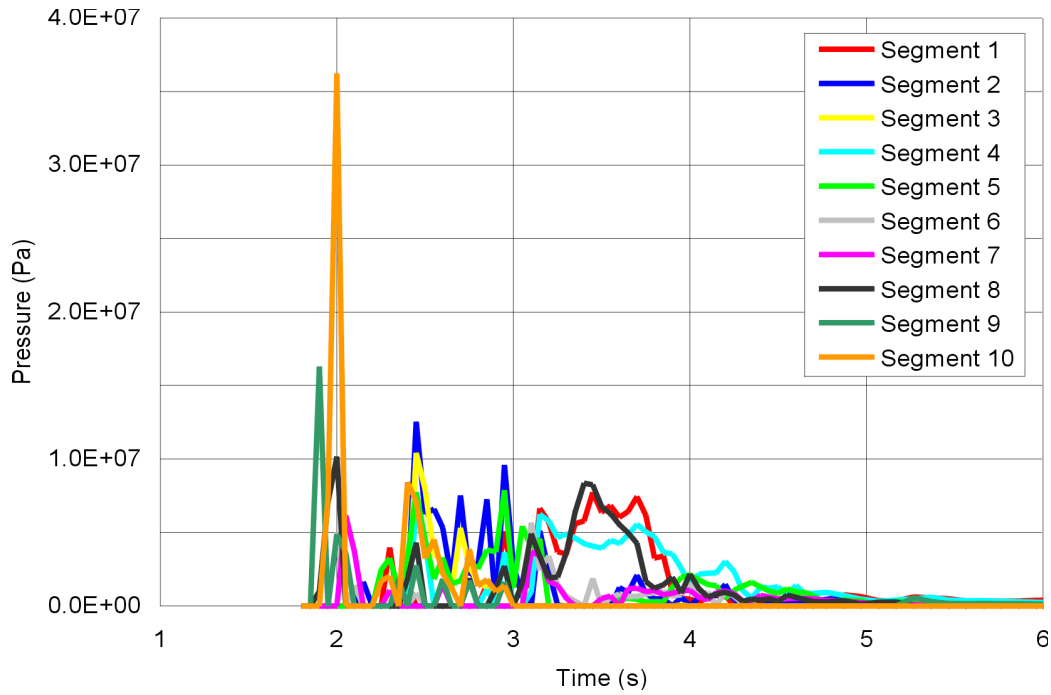


Figure P-34. Ground Motion  $10^{-7}$  Number 3: Dynamic Loads On the Right Side

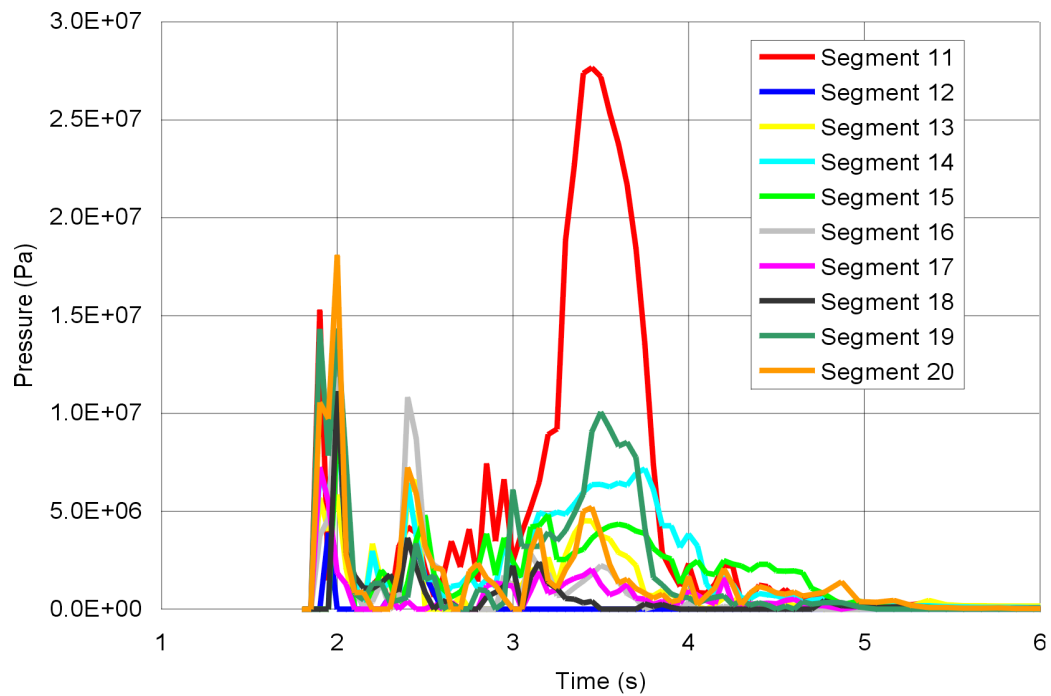


Figure P-35. Ground Motion  $10^{-7}$  Number 3: Dynamic Loads On the Top

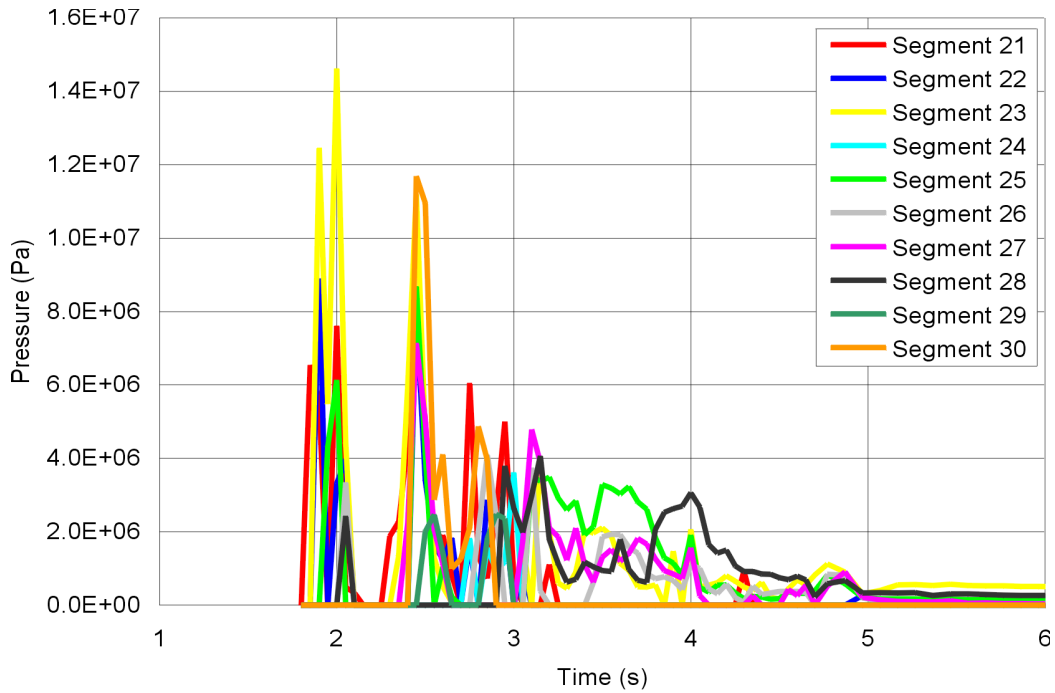


Figure P-36. Ground Motion  $10^{-7}$  Number 3: Dynamic Loads On the Left Side

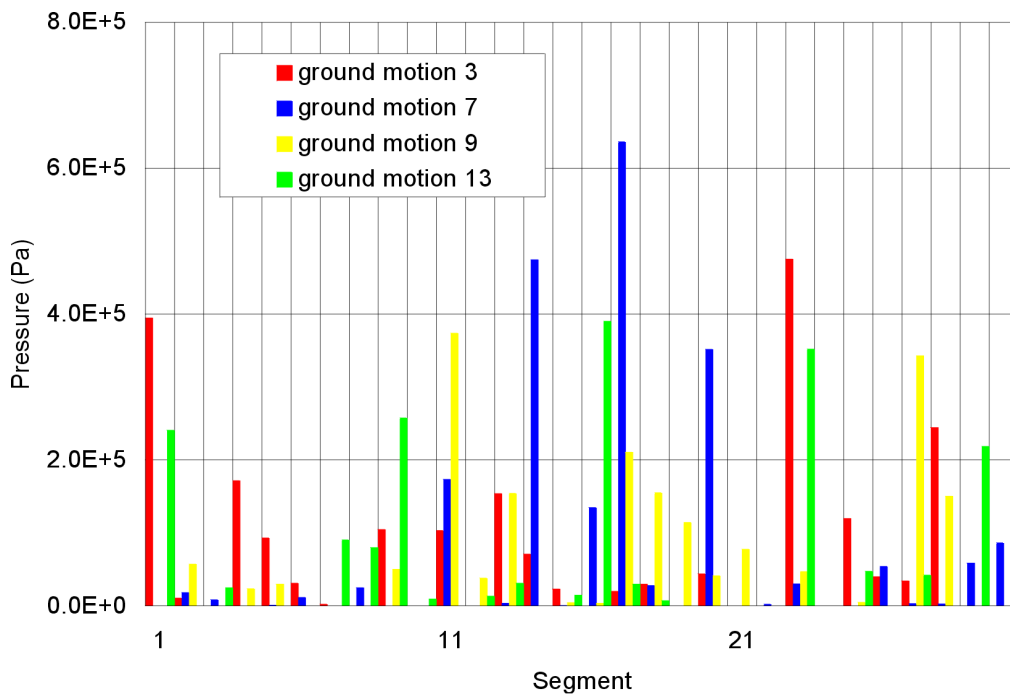


Figure P-37. Static Loads On the Drip Shield After Shaking With Four Different  $10^{-7}$  Ground Motions

Table P-8. Four Different  $10^{-7}$  Ground Motions: Average Loads On the Drip Shield

Ground motion	Left	Top	Right
	kN/m <sup>2</sup>	kN/m <sup>2</sup>	kN/m <sup>2</sup>
3	91.32	44.50	80.78
7	23.71	180.27	6.39
9	62.27	109.59	16.07
13	104.16	48.63	70.31

#### P4. MULTIPLE REALIZATIONS OF QUASI-STATIC DRIFT DEGRADATION

The drift collapse and the drip shield loads are expected to be random. The rockfall will vary considerably along the drifts, even within the same units, mostly because of variability in mechanical properties throughout the repository horizon. Even in the sections in which the emplacement drifts collapsed in a similar way, the load on the drip shield can vary significantly from one cross-section to another. The reason for this variability is the stochastic nature of rockfall, which involves formation of the blocks of irregular shapes and different sizes and their rockfall, during which the blocks undergo large translations and rotations. In such systems, a small change in the initial conditions or block geometry can result in a very different outcome of the rockfall in terms of position and orientation of the block. Consequently, the load on the drip shield will vary significantly (along the drip shield, but also in the cross-section). The UDEC model of drift stability mimics this variability in the rockfall and in loads on the drip shield. To assess dependence of the drip shield loads on the different realizations of Voronoi block geometry, the problem of quasi-static drift collapse was solved for five additional realizations. The base case, realization 1, is the model of the deformable drip shield resting on the invert and the particular realization of the Voronoi block geometry discussed in Section P2.2.2. The results for the six cases are summarized in Table P-9 and Figure P-38. The bulking factors for the caved rock mass are also calculated and listed in Table P-9. The variability of the load in the cross-section (for each realization and from one realization to another) is very large. The average pressure distribution is calculated for the six realizations and included as the solid line in Figure P-38. After averaging, the pressure variability in the cross-section is reduced. The average pressures on the top of the drip shield vary in the range between 110 kN/m<sup>2</sup> and 155 kN/m<sup>2</sup> (Table P-9).

Table P-9. Quasi-Static Drift Degradation, 0.2 m Block Size, Multiple Realizations of Voronoi Block Geometry: Average Loads On the Drip Shield

Realization	Left	Top	Right	Bulking factor
	kN/m <sup>2</sup>	kN/m <sup>2</sup>	kN/m <sup>2</sup>	
1	41.54	108.92	58.76	0.24
2	19.15	147.07	19.33	0.19
3	31.35	154.80	6.69	0.25
4	57.23	129.76	128.82	0.20
5	69.69	112.73	105.43	0.22
6	32.97	113.87	52.19	0.21

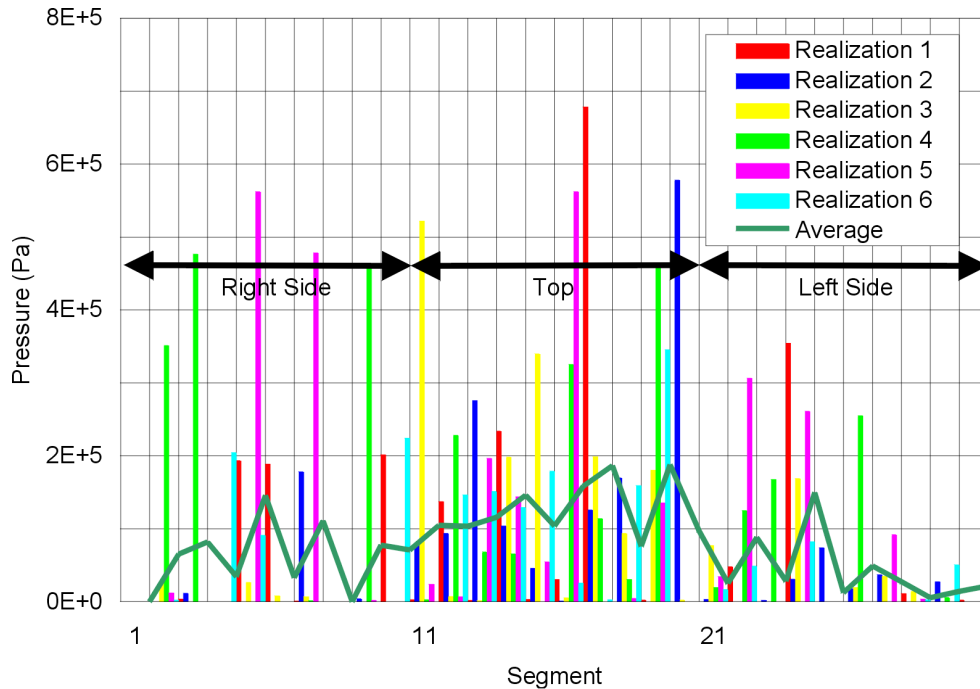


Figure P-38. Static Loads On The Drip Shield After Quasi-Static Drift Degradation For Six Realizations Of Voronoi Block Geometry

## P5. EFFECT OF SEISMIC SHAKING OF COLLAPSED DRIFT

The effect of seismic shaking of the collapsed drift on the drip shield loads in the case of the rigid, rectangular drip shield is presented in Appendix V. The same analysis is carried out again for the more realistic drip shield model described in Section P2, and for a wider range of ground motions—i.e., ground motions with  $1 \times 10^{-4}$ ,  $1 \times 10^{-5}$  and  $1 \times 10^{-6}$  probability of annual recurrence. Ground motions number 9, from the set of  $1 \times 10^{-5}$  ground motions, and number 1, from the set of  $1 \times 10^{-6}$  ground motions, were used in these simulations. The pressure (of the caved rock on the drip shield) histories for the segments during  $1 \times 10^{-4}$  and  $1 \times 10^{-6}$  ground shaking are shown in Figures P-39 through P-44. The static pressures on the drip shield after the models are equilibrated are summarized in Figure P-45 and Table P-10. The pressures on the drip shield vary during the shaking, sometimes resulting in transient pressures that are up to an order of magnitude larger than the original static pressures. For example, the static pressure for segment 10 in Figure P-42 is approximately 0.5 MPa, but it increases to approximately 5 MPa at 2.4 s of  $1 \times 10^{-6}$  ground motion. The static pressure in the equilibrium state after shaking increases compared to the static pressures in the equilibrium state before shaking. In Table P-10, the trend is apparent from the average pressures on the top of the drip shield. The average pressure increases for each level of ground motion, and the increase becomes larger for stronger ground motions. Associated with pressure increase is reduction in the bulking factor. The shaking results in compaction (i.e., irreversible volume reduction) of the caved rock. The bulking factor decreases more for stronger ground motions.

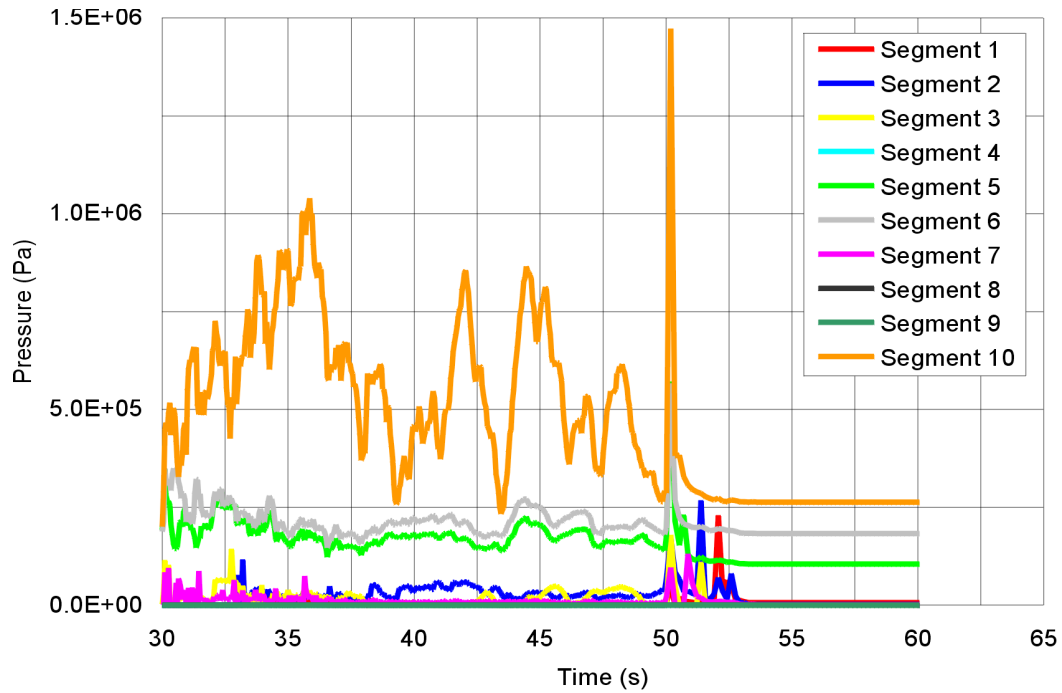


Figure P-39. Already Collapsed Drift, Ground Motion  $10^{-4}$ : Dynamic Loads On the Right Side

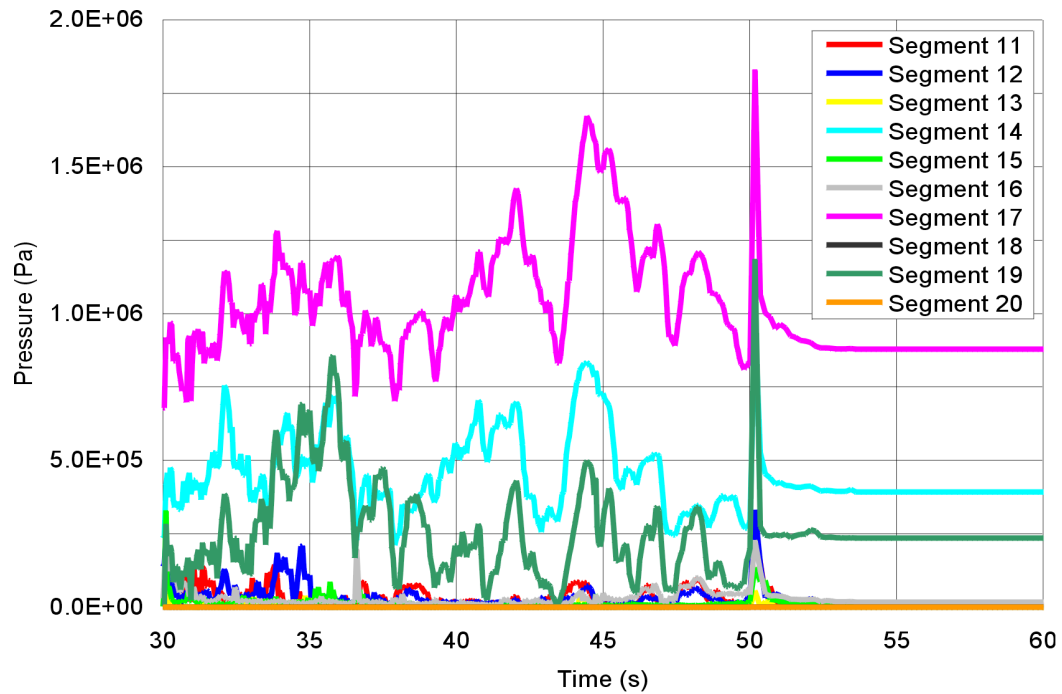


Figure P-40. Already Collapsed Drift, Ground Motion  $10^{-4}$ : Dynamic Loads On the Top

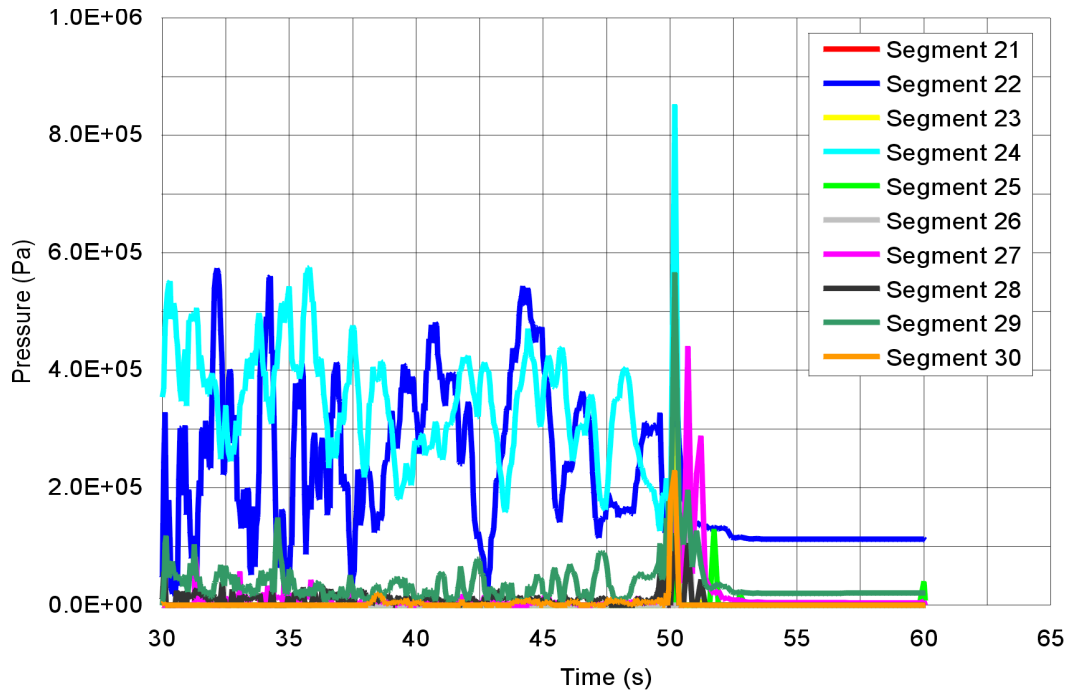


Figure P-41. Already Collapsed Drift, Ground Motion  $10^{-4}$ : Dynamic Loads On the Left Side

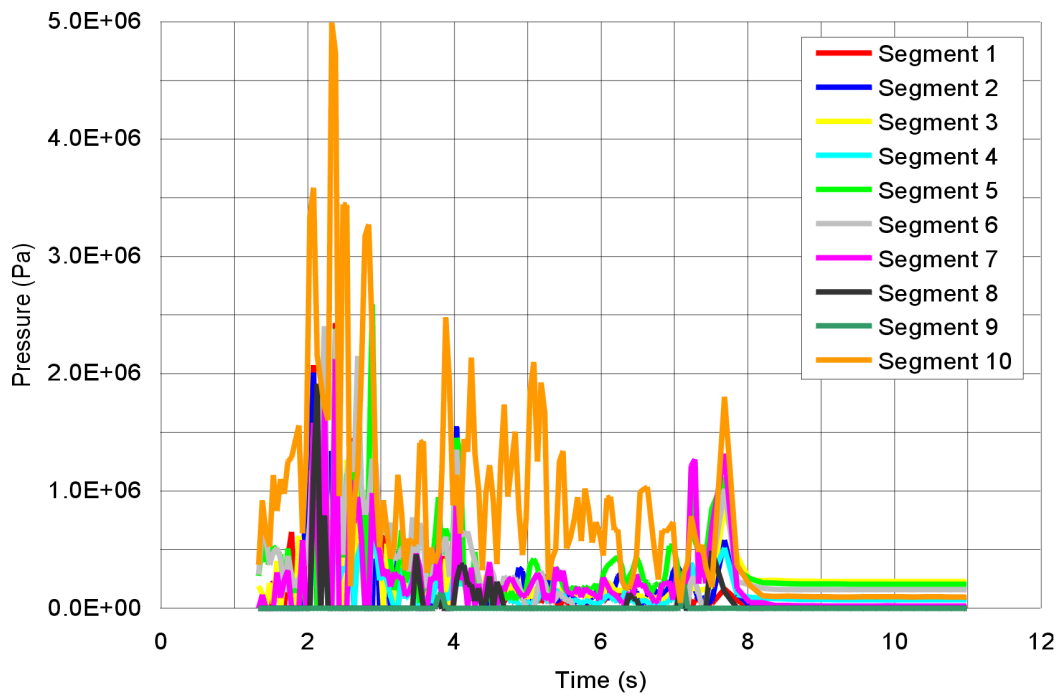


Figure P-42. Already Collapsed Drift, Ground Motion  $10^{-6}$  Number 1: Dynamic Loads On the Right Side



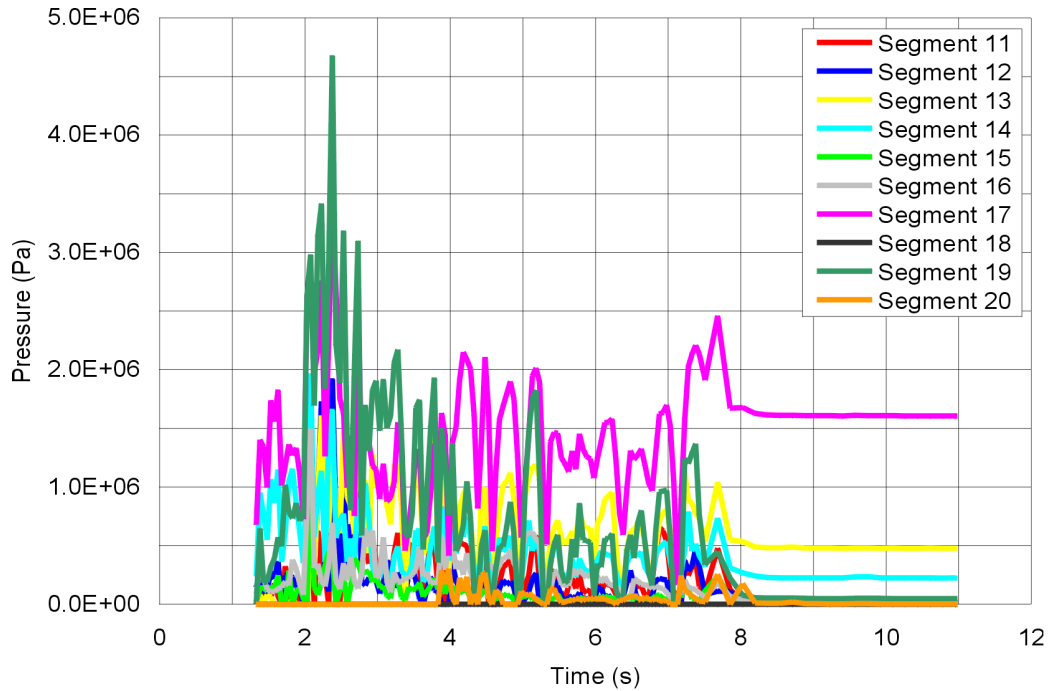
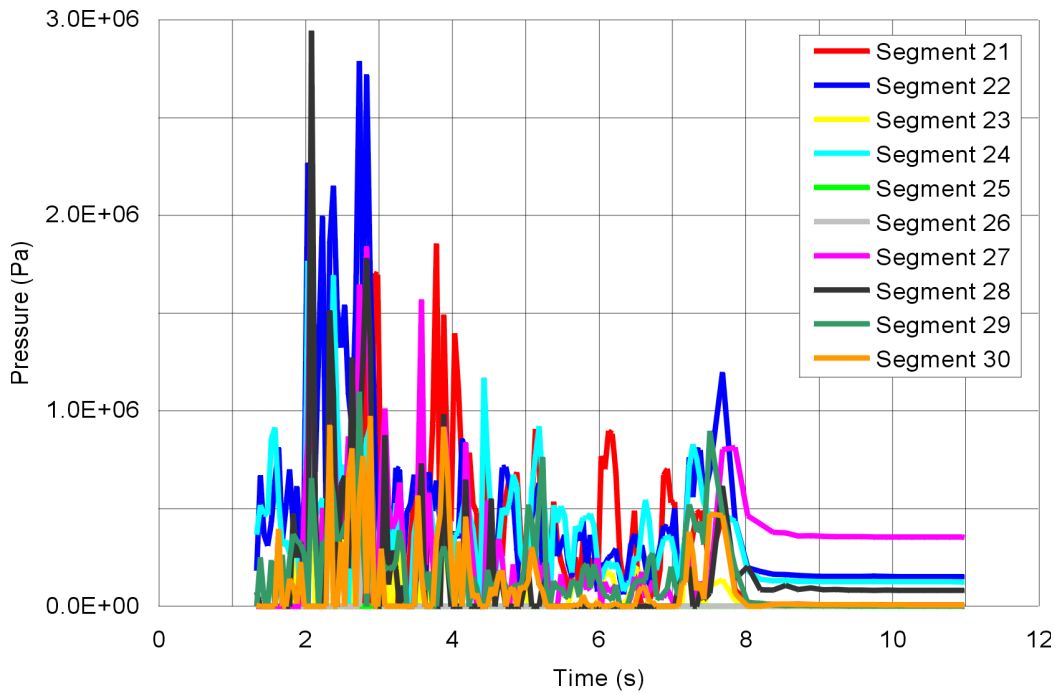
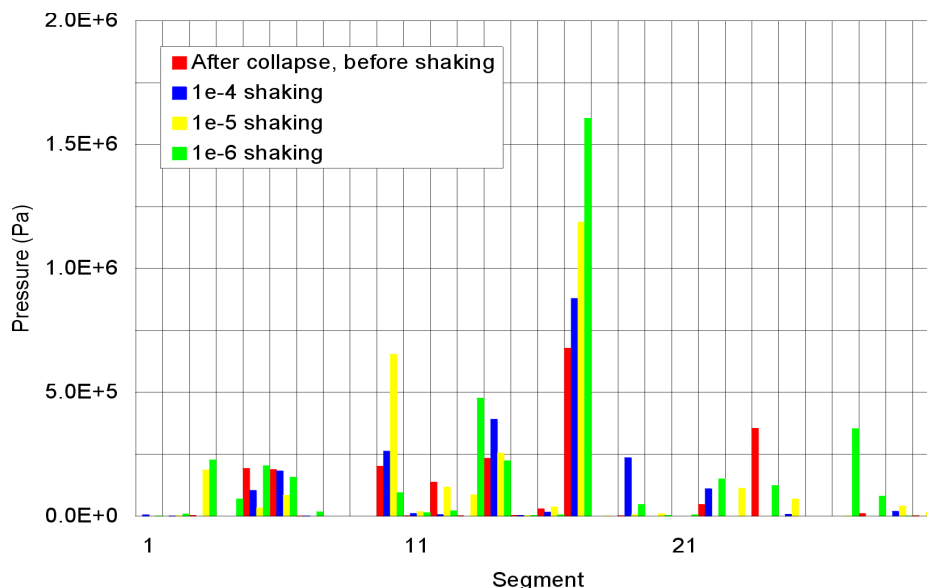


Figure P-43. Already Collapsed Drift, Ground Motion  $10^{-6}$  Number 1: Dynamic Loads On the Top



NOTE: Pa = Pascal.

Figure P-44. Already Collapsed Drift, Ground Motion  $10^{-6}$  Number 1: Dynamic Loads On The Left Side



NOTE: Pa = Pascal.

Figure P-45. Effect Of Seismic Shaking After Quasi-Static Collapse On Drip Shield Loads

Table P-10. Effect of Seismic Shaking After Quasi-Static Collapse: Average Loads On the Drip Shield

Case	Left	Top	Right	Bulking Factor
	kN/m <sup>2</sup>	kN/m <sup>2</sup>	kN/m <sup>2</sup>	
quasi-static collapse	41.54	108.92	58.76	0.24
10 <sup>-4</sup> shaking	13.94	154.39	55.90	0.20
10 <sup>-5</sup> shaking	24.08	172.32	96.08	0.14
10 <sup>-6</sup> shaking	72.18	240.05	78.14	0.10

## P6. CONCLUSION

The drip shield loads are estimated and compared using different models. The most realistic drip-shield model, which generally resulted in the smallest loads, is used for further investigations of drip shield loads for different conditions of drift collapse and seismic loading subsequent to the collapse. Strong ground motions with  $1 \times 10^{-6}$  and  $1 \times 10^{-7}$  probability of annual recurrence, cause drift collapse within a second after onset of strong ground motion. The caved rock backfills the drift, providing a constraint to the motion of the drip shield and preventing the drip shield from being overturned. The rock mass is fragmented into small pieces (The model predicts disintegration of the rock mass into the original Voronoi blocks.) before they impact the drip shield. Large blocks, of the size similar to the size of the block created in the non-lithophysal rock mass, are not expected to impact the drip shield located in lithophysal rock mass. However, the transient impact pressures can be quite large, of the order of tens of megapascals. The drip shield load after quasi-static drift collapse was estimated for six different realization of the Voronoi block geometry. The average pressures on the top of the drip shield vary in the range 110 kN/m<sup>2</sup> and 155 kN/m<sup>2</sup>. The seismic shaking subsequent to the drift collapse results in an increase of the load on the drip shield. For strong ground motions, that increase can be more than 100 percent.

**APPENDIX Q**  
**IMPACT ANALYSES**



## IMPACT ANALYSES

### Q1. IMPACT ANALYSES ON LDTH (LINE-AVERAGED HEAT SOURCE, DRIFT-SCALE, THERMOHYDROLOGIC) SUB-MODEL

An impact analysis was conducted for the drift-scale thermal calculation performed by the NUFT thermohydrology software employing a two-dimensional, line-averaged heat source, drift-scale, thermohydrologic (LDTH) sub-model. The LDTH sub-model is a part of the multiscale thermohydrologic model created by the NUFT software, which is described in *Multiscale Thermohydrologic Model* (BSC 2004 [DIRS 163056]). An LDTH sub-model, P2WR5C10 (coordinates: E 170730, N 234913), was selected from the new 108 LDTH sub-models (DTN: LL030808623122.036 [DIRS 165790]) for this impact review. The P2WR5C10 LDTH sub-model location selected has the following characteristics of interest compared to the L2C3 LDTH sub-model (Section 6.2):

- Approximately the geometric center of the license application reference repository layout (BSC 2003 [DIRS 164519]).
- The repository horizon is located approximately 310 m below the ground surface and 279 m above the water table. This elevation puts the repository horizon at approximately 1053 m above sea level (DTN: LL030808623122.036 [DIRS 165790]).
- The repository horizon is located in the Tptpll with approximately 45 m of Tptpll above the repository horizon and 59 m of Tptpll below the repository horizon (DTN: LL030808623122.036 [DIRS 165790]).
- The mean infiltration conditions have surface infiltration rates of 4.7 mm/year during the first 600 years of emplacement (present day climate), 14.6 mm/year from 600 years to 2000 years (monsoonal climate), and 22.1 mm/year from 2000 years on (glacial transition climate) (DTN: LL030808623122.036 [DIRS 165790]).
- The ground surface temperature is fixed at 16.9°C, and the water table temperature is fixed at 28.3°C (DTN: LL030808623122.036 [DIRS 165790]).

The preclosure forced ventilation has a varying heat removal capacity from the air inlet to exit of an emplacement drift due to temperature change of the airflow. The heat removal ratio is also a function of time as the waste package power output and rock mass temperature changes (BSC 2004 [DIRS 169862]). The heat removal ratio at 600 m from inlet<sup>1</sup>, as shown in Table Q-1, was obtained from DTN: MO0306MWDALAFV.000 [DIRS 163961] and was used for calculating temperature during the preclosure period.

---

<sup>1</sup> Emplacement drifts in the repository average approximately 600 m in length (BSC 2003 [DIRS 165572]).

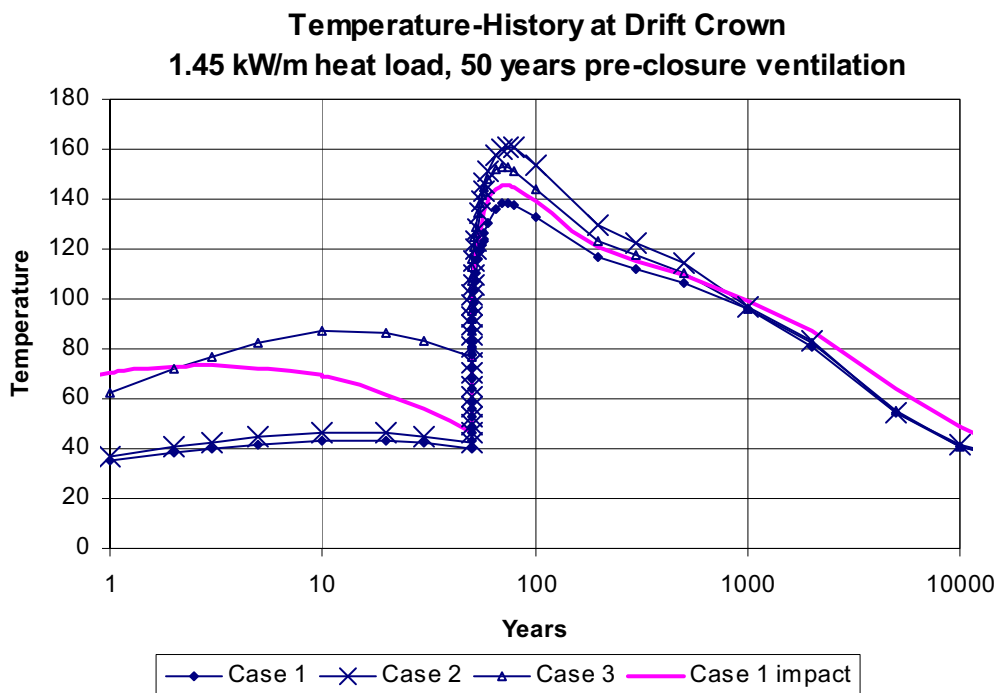
Table Q-1. Preclosure Ventilation Heat Removal Ratio at 600 m from Inlet

Time (year)	Heat Removal Ratio (%)
0.00	0.0
0.01	38.4
0.02	39.1
0.05	36.4
0.1	35.8
0.167	59.7
0.5	67.7
1	70.1
2	74.0
5	78.2
7	79.3
10	80.7
20	84.3
30	86.0
50	90.2

Source: DTN MO0306MWDALAFV.000 [DIRS 163961].

The temperature history at the drift crown from this thermal calculation based on the revised LDTH sub-model is presented in Figure Q-1, and is compared to the three cases of thermal calculations (Section 6.2) previously reported in this document. The new thermal calculation results (termed “Case 1 impact”) vary from the previous Case 1 base-case calculation, primarily in the preclosure period. Maximum temperature differences are about 35°C and 9°C for the preclosure and postclosure periods, respectively. The temperature increase during the preclosure period is caused by the time-dependent ventilation heat removal ratio (Table Q-1) that is lower than 90 percent (Section 5.1.2) used in the previous preclosure calculations. Note that the temperature from the revised thermal calculation is slightly higher than the three previous cases after 2000 years. The temperature increase is due to a lower seepage infiltration ratio of the new LDTH sub-model (see Section 6.2 and this appendix).

The primary impact of this change in temperature on drift degradation is the impact on thermally induced stresses in the near-field of the emplacement drift. A simple, yet conservative, estimate of the impact on thermal stresses can be made based on the maximum additional postclosure temperature in the revised analyses, the rock mass thermal expansion coefficient and the bulk modulus. The results of these calculations are presented in Table Q-2. The approximate thermal stress increase due to the revised thermal calculation is based on Equation 6-6 (Section 6.2) and on the maximum temperature increase of 9°C during the postclosure period (Figure Q-1). The bulk modulus,  $K$ , is calculated from rock mass Young’s modulus and Poisson’s ratio of the TSw2 thermal-mechanical unit based on Equation E-2 (Appendix E). The increase of thermal stress is about 1.5 MPa for the Ttppll Category 3 (Table E-10) that has a representative rock mass Young’s modulus and Poisson’s ratio, while the Ttpmnm from the Heated Drift (Table E-15) has a thermal stress increase of 2.8 MPa. The thermal stress increase of the Ttppll is less than 10 percent of the rock mass strength of the Ttppll Category 3 (20 MPa, Table E-10). Also, the thermal stress increase of the Ttpmnm is less than 10 percent of the rock mass strength of the Ttpmnm (75.25 MPa, Table E-15), which has a higher rock quality than the Ttppll.



File source: DTN: MO0408MWDDDMIO.002, file LA1450\_R5C10\_NUFT\_Temp\_crss-sctn.xls.

Figure Q-1. Temperature History at the Drift Crown up to 10000 Years

Table Q-2. Maximum Increase of Thermal Stress during the Postclosure

Rock Mass	Young's Modulus (Pa)	Poisson's Ratio <sup>c</sup>	Thermal Expansion Coefficient <sup>d</sup> (1/°C)	Bulk Modulus (Pa)	Maximum Temperature Increase (°C)	Increase of Thermal Stress (Pa)
Tptpll Category 3 <sup>a</sup>	1.08E+10	0.21	9.07E-06	6.21E+09	9	1.52E+06
TSw2 Category 5 <sup>b</sup>	2.01E+10	0.21	9.07E-06	1.16E+10	9	2.83E+06

<sup>a</sup> Obtained from Table E-10.

<sup>b</sup> Obtained from Table E-15.

<sup>c</sup> Obtained from Table E-16.

<sup>d</sup> Obtained from Table E-20; TSw2 and 100 °C < T ≤ 125 °C.

The thermal stress increase from the revised LDTH sub-model (Table Q-2), although it is less than 10 percent of the rock mass strength, could potentially have some impact on thermal degradation and thermal/seismic combined degradation. However, the revised thermal calculation for the postclosure period is bounded by the Case 2 and Case 3 sensitivity calculation (Figure Q-1). Based on the rockfall analysis for the nonlithophysal rock (Sections 6.3.1.3 and 6.3.1.4) and the lithophysal rock (Section 6.4.2.3), the Case 2 and Case 3 sensitivity calculation demonstrated that the temperature increase from the Case 1 base case did not induce any significant additional rockfall (Section 6.3.1.3 and Section 6.4.2.3), and even generated less rockfall for Tptpmn (Table 6-24). Therefore, the temperature increase from the revised LDTH sub-model during the postclosure period is already covered by the previous rockfall analysis,

and it is concluded that there is no impact to the rockfall prediction by using the new thermal calculation for the postclosure period. An additional analysis with thermal consideration, and combined thermal and seismic consideration for the drift degradation is not necessary for the postclosure period.

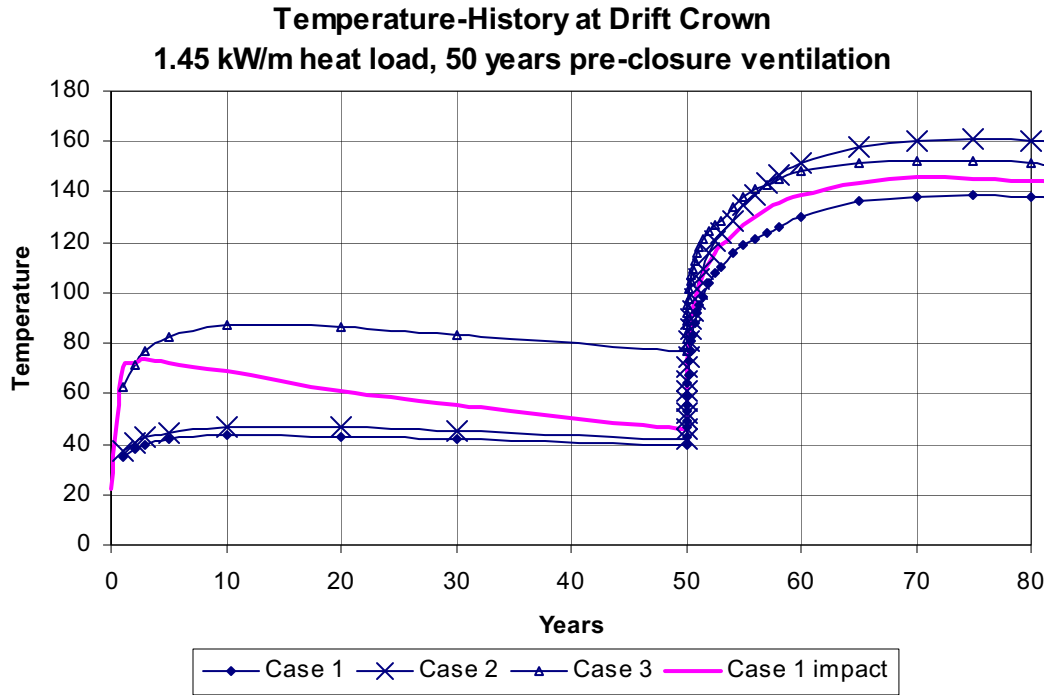
The temperature increase due to the revised LDTH sub-model during the preclosure period is much more significant than the postclosure period (Figure Q-2). However, the temperature itself is much lower compared to the postclosure period (below 75°C), and it is still bounded by the Case 3 sensitivity calculation. The rockfall analysis for the lithophysal rock (Section 6.4.2.3) considered the Case 3 sensitivity case, and concluded temperature increase from the Case 1 base case did not induce any significant additional rockfall (Section 6.4.2.3). Therefore, it is also concluded that the temperature increase from the new LDTH sub-model during the preclosure period has no impact on the rockfall prediction by using the new thermal calculation for the preclosure period.

Drift deterioration analysis due to the time-dependent rock mass degradation is presented in Section 6.4.2.4 and Appendix S. Combined effects of the thermal and time-dependent degradation are presented in Appendix S3.4.2 based on the Case 1 base-case calculation. The results show minor spalling around the drift (Figures S-42, S-43, and S-44) and only a small increase in spalling compared to the time-dependent consideration case (Figure S-38, S-39, and S-40). While the temperature effects combined with the time-dependant degradation accelerated and increased drift degradation especially after the emplacement drift closure (see 80 years plots in Figure S-42, S-43, and S-44), the amount of rockfall is still small and the damage is limited to vicinity of the emplacement drift. The increase of temperature due to the revised thermal calculation (Case 1 impact) could potentially result in some additional deterioration of emplacement drift.

Time-dependent strength degradation combined with revised thermal load was evaluated for the Category 2 and 5 lithophysal rocks (Figures Q-3 and Q-4). The impact runs considered the higher temperatures of the revised LDTH NUFT model (Figure Q-1) for both the preclosure and postclosure periods. The spalling and damage due to the revised thermal and time-dependent degradation were slightly different from the previous coupled thermal and time-dependent damage analysis (Figures S-42 and S-44). However, the amount of spalling and damage was generally remained same for the Category 2 and 5 rocks compared to the previous coupled thermal and time-dependent damage. Therefore, it is concluded that the temperature increase from the revised LDTH sub-model has no significant impact on the rockfall prediction of combined thermal and time-dependent effects.

Based on the previous observation, the same conclusion that there is no significant impact could be attained for the coupled seismic, thermal, and time-dependent damage analysis (Appendix S3.4.3), and an additional analysis for the coupled seismic, thermal, and time-dependent damage is not necessary.





Source: DTN: MO0408MWDDDMIO.002, file LA1450\_R5C10\_NUFT\_Temp\_crss-sctn.xls.

Figure Q-2. Temperature History at the Drift Crown up to 80 Years

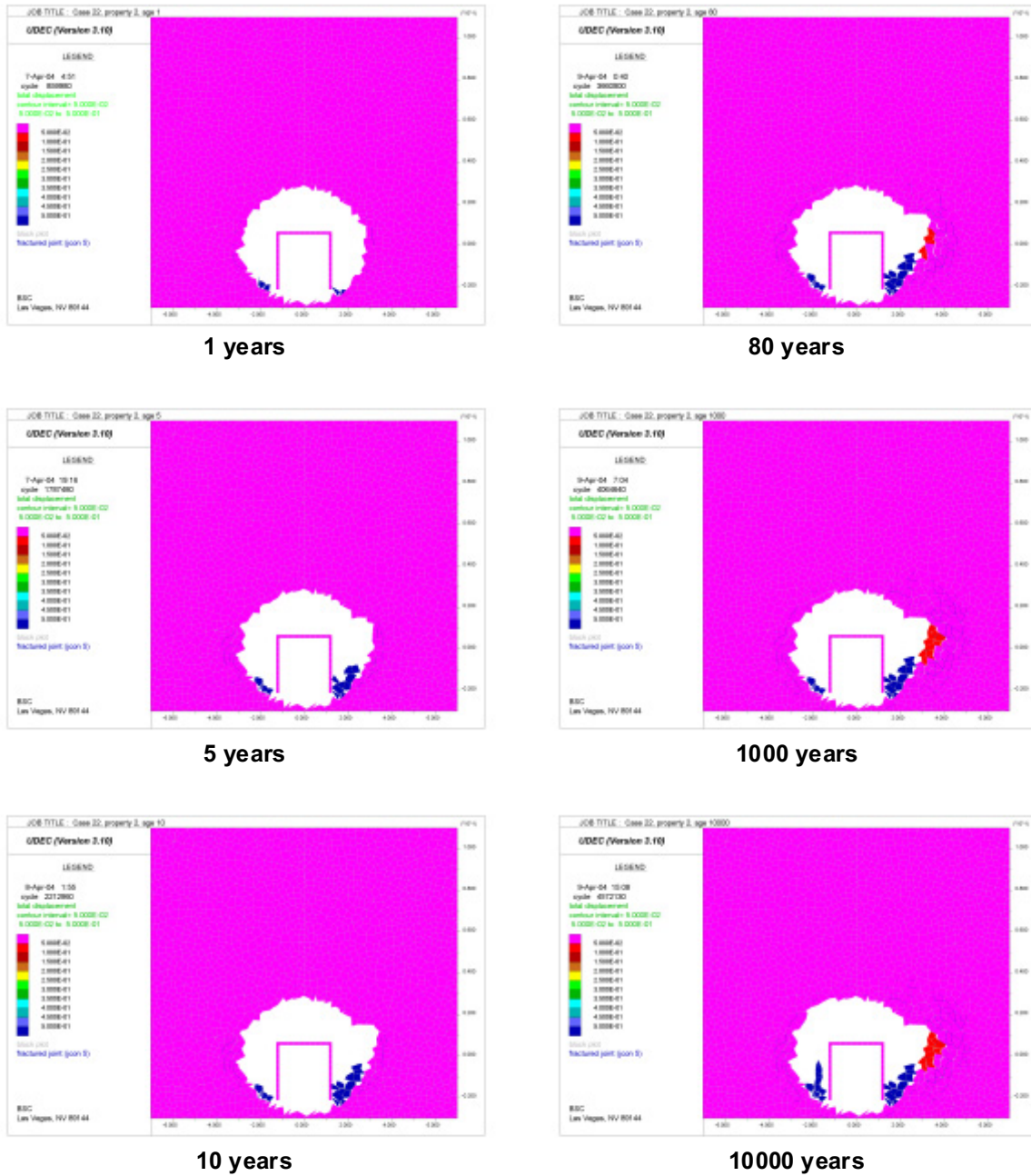


Figure Q-3. Evolution of Damage Due to Strength Degradation and with Revised Thermal Load for Category 2 – Tuff Best-fit Static-Fatigue Curve

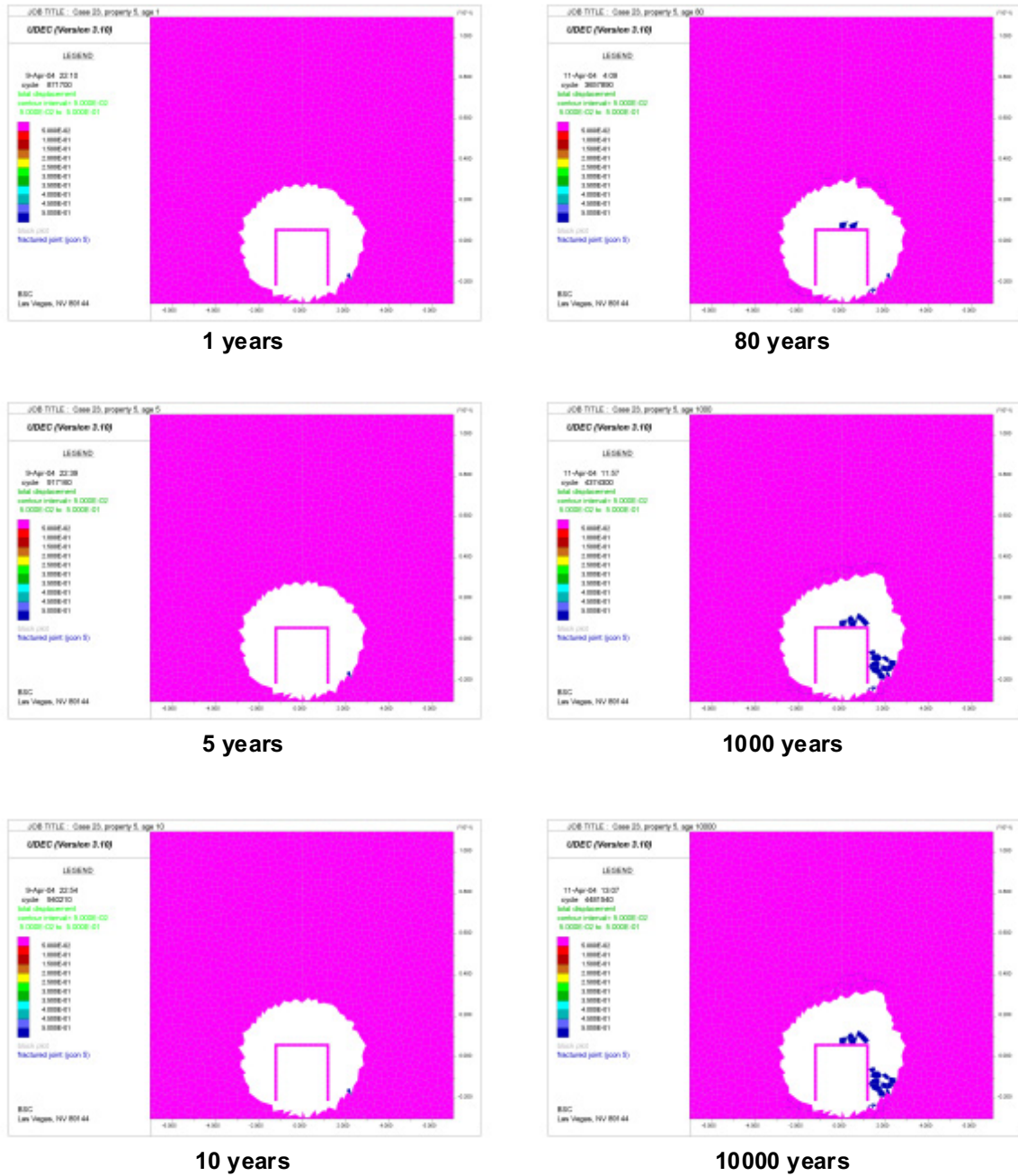


Figure Q-4. Evolution of Damage Due to Strength Degradation and with Revised Thermal Load for Category 5 – Tuff Best-fit Static-Fatigue Curve

## Q2. IMPACT ANALYSES ON HEAT CAPACITY

The regional and local scale thermal-mechanical calculations used the weight-averaged thermal property values for the four thermal-mechanical units (Table C-4). The heat capacity data used in the thermal property calculation were preliminary data superseded by DTN: SN0307T0510902.003 [DIR 164196] (Table E-19). The revised specific heat values for the thermal-mechanical units are presented in Table Q-3. Only small changes of the values occur in the below 95°C range, especially in the repository units (2 percent decrease in TSw1 and 3 percent decrease in TSw2-TSw3). The impacts of the thermal properties for the below 95°C range are estimated as minor for the FLAC3D thermal-mechanical calculation, since the value changes in the repository units (TSw1 and TSw2-TSw3) are less than 3 percent. Based on the equation defined heat capacity at constant pressure (Brodsky et al. 1997 [DIRS 100653], p. 20):

$$C_p = \frac{1}{m} \frac{\Delta Q}{\Delta T} \quad (\text{Eq. Q-1})$$

where  $m$  is the mass of the specimen (kg),  $\Delta Q$  is the increment of heat added to the subject (J), and  $\Delta T$  is the change of specimen temperature (K), the change of the temperature is also estimated to be about 3 percent.

The impact of the revised heat capacity for the over 114°C range is also considered insignificant since change of the heat capacity value is irrelevant (less than 0.2 percent) for the TSw2-TSw3 repository unit.

Large heat capacity value changes occur in the 95°C to 114°C range (almost 50 percent decrease in the TSw2-TSw3 unit, as shown in Table Q-3). The 95°C to 114°C range is not substantial for the regional scale FLAC3D thermal-mechanical calculation, since the calculated temperatures in Appendix C were well below 95°C (Figure C-10). For the local scale calculation, the resulting temperature and thermally induced stress using the revised specific heat should be under some impact as a result of its low heat capacity value, especially for the central drift (Figure C-16). However, the rock volume for temperatures over 95°C is localized adjacent to the drift wall, and the time duration over 95°C is also limited to several hundred years. Also, the local scale thermal-mechanical calculation was only served to support and add confidence to the main thermal-mechanical calculation presented in Section 6.2. The resulting data from Section 6.2 (not from Appendix C) were used in the subsequent analyses of this document. Therefore, an additional local scale thermal-mechanical calculation is not necessary.

Table Q-3. Specific Heat Considered for the Rock Mass in the Regional and Local Scale Thermal-Mechanical Calculations (Appendix C)

Property	Condition	TCw-PTn	TSw1	TSw2-TSw3	Underlying
Preliminary specific heat $C_v$ [J/kg °C]	< 95°C	1,158	939	937	1,304
	95°C ≤ $C_v$ < 114°C	11,135	5,791	5,714	15,775
	≥ 114°C	1,010	991	990	1,016
Updated specific heat <sup>a</sup> $C_v$ [J/kg °C]	< 95°C	1,300	920	910	1,300
	95°C ≤ $C_v$ < 114°C	9,000	3,200	3,000	8,400
	≥ 114°C	1,000	990	990	1,100

<sup>a</sup> The mean values are calculated from DTN: SN0307T0510902.003 [DIRS 164196].

### Q3. IMPACT ANALYSES FOR USE OF PFC2D AND PFC3D FISHTANK

PFC2D V.2.0 and PFC3D V.2.0 (Section 3.1) were used for the study of rock mass strength and long-term strength degradation in Section 7.6 and Appendix S.

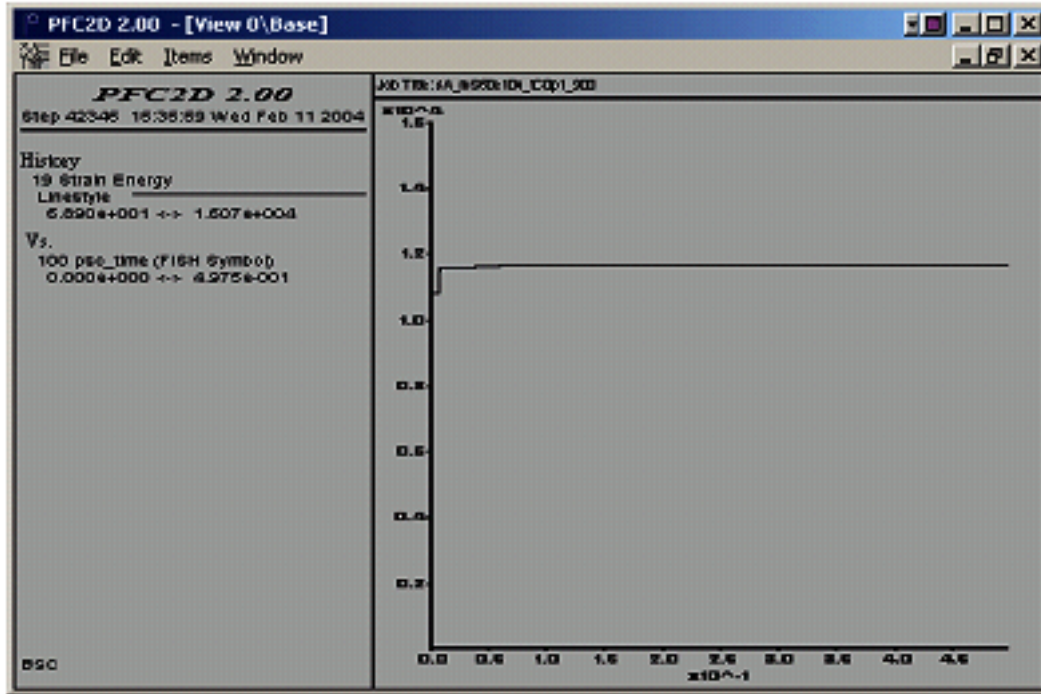
The PFC models of rock mass strength and long-term strength degradation used FishTank 04lb. FishTank is a library of Fish functions that is technically supported and updated by the PFC software vendor, Itasca. FishTank can be downloaded from the Itasca website ([www.itascacg.com](http://www.itascacg.com)). PFC2D V.2.0 and PFC3D V.2.0 install FishTank 03a and 04c automatically during the software installation, respectively. Since qualification of PFC2D and PFC3D did not specifically identify FishTank in their qualification processes, the usage of FishTank 04lb is outside of the range of PFC2D and PFC3D software validation.

PFC2D V.2.0 and PFC3D V.2.0 with FishTank 04lb (STN: 10828-2.0-01 and 10830-2.0-01 respectively) were qualified in accordance with LP-SI.11Q-BSC, *Software Management*, and LP-SI-12Q-BSC, *Qualification of Level A Software*. An impact review was conducted on the PFC models in the Section 7.6 and Appendix Q using the newly qualified PFC2D and PFC3D software.

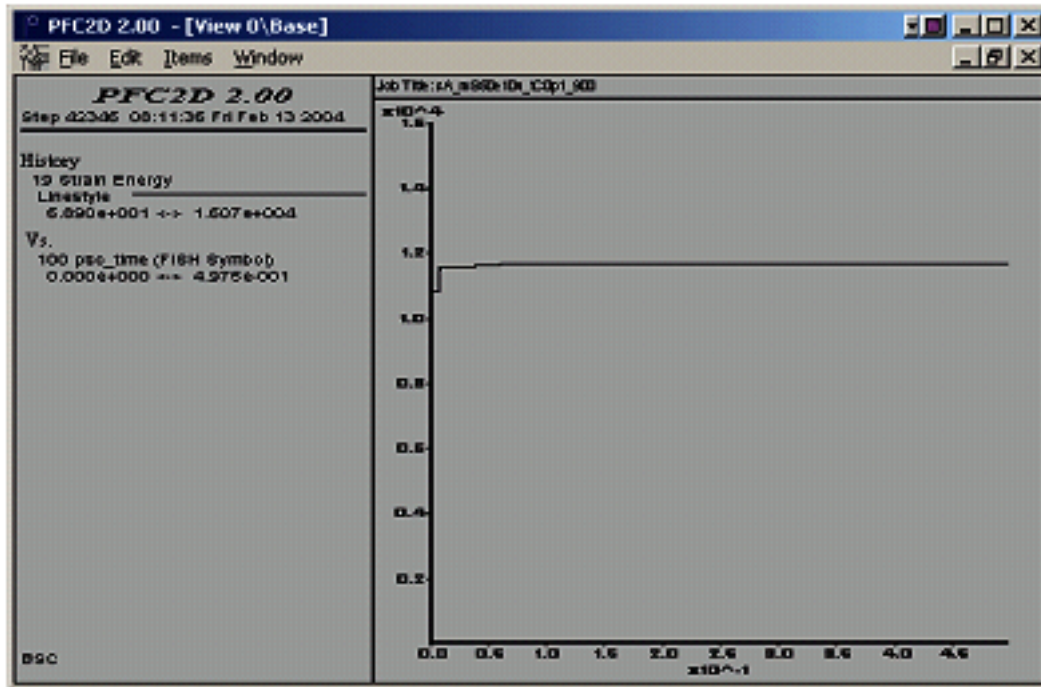
A typical static fatigue model, sA\_mS50eXu\_tC0p1-sf, was re-run for exploring impacts of PFC2D V.2.0 with FishTank 04lb. The model is a representative case of the static fatigue test simulation in Appendix S, which has 0.1 MPa of confining stress and 10 percent of void (lithophysal) porosity. Results of the re-run were identical with the previous run calculated from the previous version of PFC2D. Figure Q-5 presents the strain energy stored during the static fatigue simulations for both runs, which shows identical results for the runs. In addition to the results, their log files, sA\_mS50e10u\_tC0p1\_n-sf.log, that contained the information regarding numerical calculation were identical, with the exception of header, dates, and times (Figure Q-6).

A PFC3D biaxial model, sB1\_mKvbX\_tA, was re-run in order to investigate impacts of PFC3D V.2.0 with FishTank 04lb. Figure Q-7 shows the axial and confining stresses during the biaxial simulation, which have identical values. Also, Figure Q-8 shows that their log files, sB1\_mKvb2\_tAy.log, that contain the information regarding numerical calculation are identical except for header, dates, and times.

Based on the impact evaluation, it is concluded there is no impact to the re-qualification of PFC2D and PFC3D.



a)



b)

NOTE: a) previous run and b) impact run using re-qualified PFC2D.

Figure Q-5. Strain Energy Stored During the Static Fatigue Simulations

```

sA_m550e10u_tC0p1_n-sf.log - Notepad
File Edit Format Help
  ending cycle: 484959      av-unbal: 1.195e+003
  ending time: 03:25:50    max-unbal: 3.786e+005
Fish> SOLVE aver=1e-30 max=@psc_equil_ratio steps=500 ;p2D20
  starting cycle: 484959      av-unbal: 1.195e+003
  starting time: 03:25:50    max-unbal: 3.786e+005

  ending cycle: 485460      av-unbal: 1.126e+003
  ending time: 03:25:55    max-unbal: 2.932e+004
Fish> SOLVE aver=1e-30 max=@psc_equil_ratio steps=500 ;p2D20
  starting cycle: 485460      av-unbal: 1.126e+003
  starting time: 03:25:55    max-unbal: 2.932e+004

  ending cycle: 485961      av-unbal: 1.118e+003
  ending time: 03:26:00    max-unbal: 5.499e+004
[psc_solve]: user-defined limit reached
[sft_runtest]: axial-strain limit reached
Pfc2D> SET md_tag_name='-sf1'
Pfc2D> md_save_state
Fish> save @_fname
Pfc2D>; -----
Pfc2D>return
Pfc2D>; -----
Pfc2D>set log off
*****
* Log File Ended 03:26:01 Wed Aug 6 2003
*****

```

a)

```

sA_m550e10u_tC0p1_n-sf.log - Notepad
File Edit Format Help
  ending cycle: 484959      av-unbal: 1.195e+003
  ending time: 23:33:34    max-unbal: 3.786e+005
Fish> SOLVE aver=1e-30 max=@psc_equil_ratio steps=500 ;p2D20
  starting cycle: 484959      av-unbal: 1.195e+003
  starting time: 23:33:34    max-unbal: 3.786e+005

  ending cycle: 485460      av-unbal: 1.126e+003
  ending time: 23:33:47    max-unbal: 2.932e+004
Fish> SOLVE aver=1e-30 max=@psc_equil_ratio steps=500 ;p2D20
  starting cycle: 485460      av-unbal: 1.126e+003
  starting time: 23:33:47    max-unbal: 2.932e+004

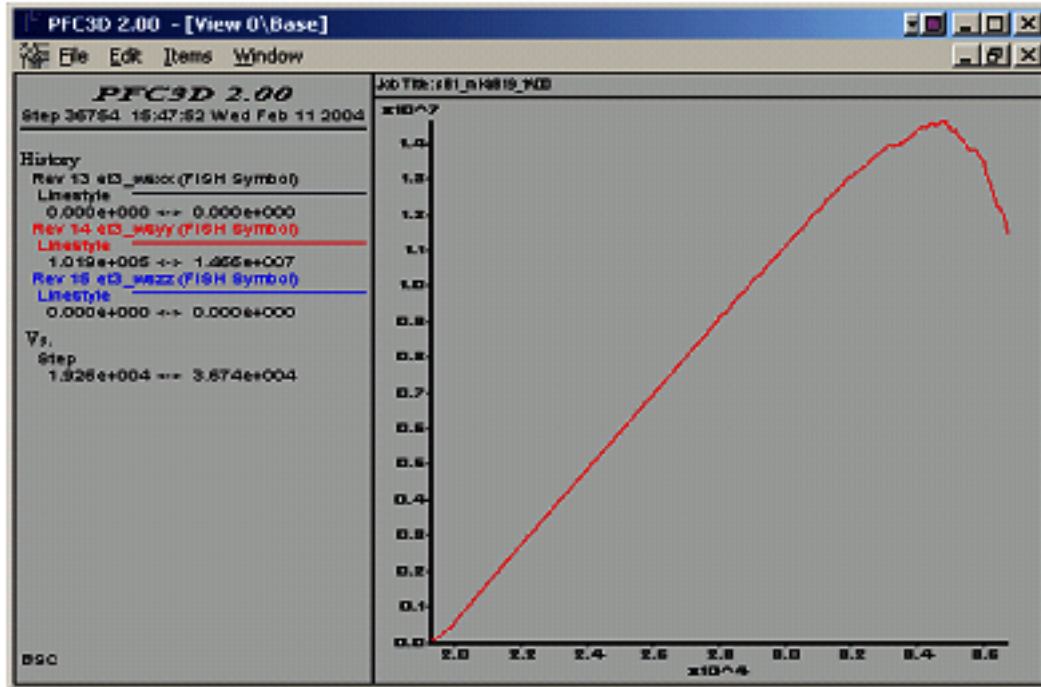
  ending cycle: 485961      av-unbal: 1.118e+003
  ending time: 23:33:59    max-unbal: 5.499e+004
[psc_solve]: user-defined limit reached
[sft_runtest]: axial-strain limit reached
Pfc2D> SET md_tag_name='-sf1'
Pfc2D> md_save_state
Fish> save @_fname
Pfc2D>; -----
Pfc2D>return
Pfc2D>; -----
Pfc2D>set log off
*****
* Log File Ended 23:34:02 Thu Feb 12 2004
*****

```

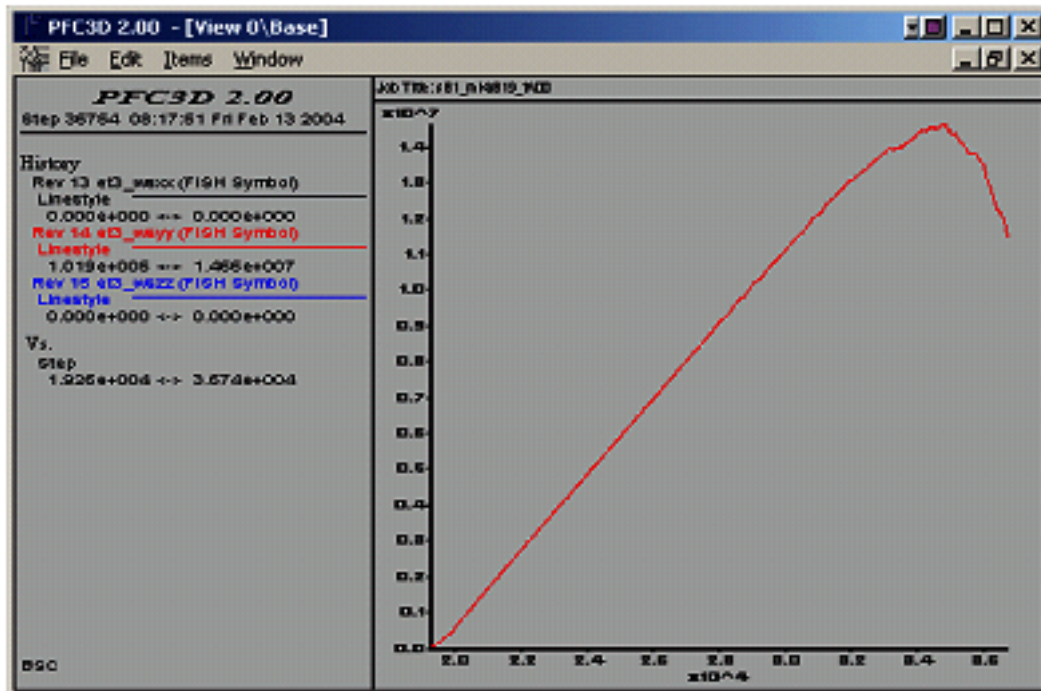
b)

NOTE: a) previous run; b) impact run using re-qualified PFC2D.

Figure Q-6. Log Files from PFC2D



a)



b)

NOTE: a) previous run; b) impact run using re-qualified PFC3D.

Figure Q-7. Axial (wsyy) and Confining Stresses (wsxx and wszz) During the Biaxial Simulations



```

sB1_mKvB2_tAy.log - Notepad
File Edit Format Help
starting time: 00:06:08      max-unbal: 3.601e+004
ending cycle: 39254        av-unbal: 3.419e+002
ending time: 00:06:33     max-unbal: 8.245e+004
Fish> cycle 100
starting cycle: 39254      av-unbal: 3.419e+002
starting time: 00:06:33   max-unbal: 8.245e+004
ending cycle: 39354      av-unbal: 3.523e+002
ending time: 00:06:57    max-unbal: 4.119e+004
Fish> cycle 100
starting cycle: 39354      av-unbal: 3.523e+002
starting time: 00:06:57   max-unbal: 4.119e+004
ending cycle: 39454      av-unbal: 3.561e+002
ending time: 00:07:22    max-unbal: 6.419e+004
Pfc3D> SET md_granular=0
Pfc3D>et3_gd3_triax
Pfc3D>;
Pfc3D> SET md_tag_name='-tw1'
Pfc3D>md_save_state
Fish> save @_fname
Pfc3D>; =====
Pfc3D>return
Pfc3D>; =====
Pfc3D>set log off
*****
* Log File Ended 00:07:24 Fri Feb 7 2003
*****

```

a)

```

sB1_mKvB2_tAy.log - Notepad
File Edit Format Help
starting time: 07:48:12      max-unbal: 3.601e+004
ending cycle: 39254        av-unbal: 3.419e+002
ending time: 07:48:25     max-unbal: 8.245e+004
Fish> cycle 100
starting cycle: 39254      av-unbal: 3.419e+002
starting time: 07:48:25   max-unbal: 8.245e+004
ending cycle: 39354      av-unbal: 3.523e+002
ending time: 07:48:38    max-unbal: 4.119e+004
Fish> cycle 100
starting cycle: 39354      av-unbal: 3.523e+002
starting time: 07:48:38   max-unbal: 4.119e+004
ending cycle: 39454      av-unbal: 3.561e+002
ending time: 07:48:50    max-unbal: 6.419e+004
Pfc3D> SET md_granular=0
Pfc3D>et3_gd3_triax
Pfc3D>;
Pfc3D> SET md_tag_name='-tw1'
Pfc3D>md_save_state
Fish> save @_fname
Pfc3D>; =====
Pfc3D>return
Pfc3D>; =====
Pfc3D>set log off
*****
* Log File Ended 07:48:52 Fri Feb 13 2004
*****

```

b)

NOTE: a) previous run; b) impact run using re-qualified PFC3D.

Figure Q-8. Log Files from PFC3D

INTENTIONALLY LEFT BLANK

**APPENDIX R**

**DRIFT PROFILE PREDICTION AND DEGRADED ROCK MASS  
CHARACTERISTICS IN LITHOPHYSAL UNITS**



## **DRIFT PROFILE PREDICTION AND DEGRADED ROCK MASS CHARACTERISTICS IN LITHOPHYSAL UNITS**

To a large extent, deformation of the rock mass occurs as a result of deformation of pre-existing joints or creation and deformation of new fractures, resulting in a change in rock mass permeability. It is observed that both normal (opening and closure) and shear (slip) deformation of joints affect joint permeability. However, because joint slip results in joint opening (due to dilatancy), joint permeability can be considered to be a function of joint opening only. If rockfall occurs, which is a consequence of rock mass deformation, the size and the shape of the emplacement drifts will change. Changes in permeability and drift geometry will affect percolation of groundwater around the drifts and potential for water seepage into the drifts.

The results for drift degradation and rock mass deformation from seismic loading (for preclosure and postclosure ground motions), thermal loading, and time-dependent drift degradation are generated as input data for seepage analysis. Results for a total of 30 scenarios of UDEC lithophysal modeling cases are provided. The blocks used in the UDEC Voronoi block model do not represent the actual internal structure of the lithophysal rock mass. The blocks are a tool in the numerical model used to simulate damage and fracturing of the rock mass (i.e., the potential fractures in this model do not correspond to actual features observed in the lithophysal units) as documented in Section 7.6.4. The joint data from the Voronoi block model presented in this appendix are provided to assess the overall degraded rock mass response. A description of each scenario is provided Table R-1. For each scenario, the following results are generated and included:

1. Plot of the geometry of the model (see Figures R-1 through R-30). The drift profile is generated deleting blocks that moved more than 0.15 m.
2. ASCII text with values of stress tensor components ( $\sigma_{xx}$ ,  $\sigma_{xy}$ ,  $\sigma_{yy}$ , and  $\sigma_{zz}$ ) at UDEC grid points (provided by coordinates  $x$  and  $y$ ).
3. ASCII text with Voronoi block model joint data (coordinates of center,  $x$  and  $y$ , normal displacement, length and orientation; i.e., a unit vector,  $n$ , normal to the joint) for the joints in the UDEC Voronoi block model.
4. ASCII text with averaged volumetric strain from fracture deformation as calculated in the UDEC Voronoi block model.

The UDEC model keeps track of all joints (i.e., contacts between the blocks) with joint aperture smaller than a predefined tolerance. In the simulations carried out for this report the contact tolerance is 0.0055 m. When the contact aperture becomes larger than the tolerance, the contact is deleted because the blocks involved in the contact are no longer interacting with each other. However, the joints with large openings (i.e., larger than 0.0055 m) are relevant for the seepage analysis and needs to be included in the list of joints created in the model due to deformation, and taken into account in calculation of the volumetric strain. An algorithm is developed which detects large-opening joints based on distance and co-linearity of block edges. The blocks in the vicinity of block edges (within a distance of 0.5 m and 0.7 m for block size of 0.2 m and 0.3 m, respectively) are checked for large apertures. Edges around the blocks are treated as co-linear if

the angle between them is smaller than  $10^\circ$ . The list of joints based on the UDEC contact list is supplemented with the list of joints with large apertures.

In the simulations carried out for this report, contact deformation in the UDEC model includes deformation due to the in situ stress state prior to excavation of the drift and any other subsequent loading. However, for the seepage analysis, it is of interest to have joint deformation and volumetric strain due to drift excavation and subsequent loading only. Therefore, in situ joint deformation is calculated analytically and subtracted from cumulative joint deformation.

The in situ stress is characterized by the horizontal ( $\sigma_{xx}^o = 3.5$  MPa) and the vertical principal stresses ( $\sigma_{yy}^o = 7.0$  MPa) acting in the plane of the model. The normal traction acting on a joint with a unit normal vector,  $n$ , is:

$$\sigma_n^o = \sigma_{xx}^o n_x^2 + \sigma_{yy}^o n_y^2 \quad (\text{Eq. R-1})$$

where  $n_x$  is the x-component of  $n$ , and  $n_y$  is the y-component of  $n$ . Consequently, the in situ joint deformation is (Itasca Consulting Group 2002 [DIRS 160331])

$$\Delta u_n^o = k_n \sigma_n^o \quad (\text{Eq. R-2})$$

where  $k_n$  is the joint normal stiffness.

The volumetric strain is calculated on a rectangular grid with horizontal and vertical spacing of 0.25 m based on joint deformation and area of the blocks. At each point of the grid, the joints within a predefined distance (i.e., a circle with a radius of 0.5 m and 0.75 m for block size of 0.2 m and 0.3 m, respectively) are detected. Areas of the joints within the circle,  $\sum_{j=1}^N A_j$ , and area of the blocks that form those joints,  $\sum_{b=1}^M A_b$ , are calculated. Thus, the volumetric strain is

$$\varepsilon_v = \frac{\sum_{j=1}^N A_j}{\sum_{b=1}^M A_b}. \quad (\text{Eq. R-3})$$

The information presented in this appendix, which is obtained as direct output from UDEC, is provided in DTN: MO0306MWDDPPDR.000.

Table R-1. Considered Scenarios for Drift Profile and Degraded Rock Mass Characteristics

Scenario	Brief Description of the Scenario
1	seismic with $5 \times 10^{-4}$ probability of exceedance ground motion, rock mass category 1, Voronoi block size 0.3 m
2	seismic with $1 \times 10^{-6}$ probability of exceedance ground motion, rock mass category 1, ground motion #12, Voronoi block size 0.3 m (Table 6-44, realization number 4)
3	seismic with $1 \times 10^{-6}$ probability of exceedance ground motion, rock mass category 1, ground motion #8, Voronoi block size 0.3 m (Table 6-44, realization number 6)
4	seismic with $1 \times 10^{-6}$ probability of exceedance ground motion, rock mass category 1, ground motion #9, Voronoi block size 0.3 m (Table 6-44, realization number 11)
5	seismic with $1 \times 10^{-6}$ probability of exceedance ground motion, rock mass category 1, ground motion #1, Voronoi block size 0.3 m (Table 6-44, realization number 12)
6	thermal at 10,000 years, rock mass category 1, Voronoi block size 0.3 m
7	degradation consideration, 0% cohesion reduction, Voronoi block size 0.3 m, and random block generation seed #1
8	degradation consideration, 20% cohesion reduction, Voronoi block size 0.3 m, and random block generation seed #1
9	degradation consideration, 40% cohesion reduction, Voronoi block size 0.3 m, and random block generation seed #1
10	degradation consideration, 60% cohesion reduction, Voronoi block size 0.3 m, and random block generation seed #1
11	degradation consideration, 80% cohesion reduction, Voronoi block size 0.3 m, and random block generation seed #1
12	degradation consideration, 100% cohesion reduction, Voronoi block size 0.3 m, and random block generation seed #1
13	degradation consideration, 0% cohesion reduction, Voronoi block size 0.3 m, and random block generation seed #2
14	degradation consideration, 20% cohesion reduction, Voronoi block size 0.3 m, and random block generation seed #2
15	degradation consideration, 40% cohesion reduction, Voronoi block size 0.3 m, and random block generation seed #2
16	degradation consideration, 60% cohesion reduction, Voronoi block size 0.3 m, and random block generation seed #2
17	degradation consideration, 80% cohesion reduction, Voronoi block size 0.3 m, and random block generation seed #2
18	degradation consideration, 100% cohesion reduction, Voronoi block size 0.3 m, and random block generation seed #2
19	degradation consideration, 0% cohesion reduction, Voronoi block size 0.2 m, and random block generation seed #1
20	degradation consideration, 20% cohesion reduction, Voronoi block size 0.2 m, and random block generation seed #1
21	degradation consideration, 40% cohesion reduction, Voronoi block size 0.2 m, and random block generation seed #1
22	degradation consideration, 60% cohesion reduction, Voronoi block size 0.2 m, and random block generation seed #1
23	degradation consideration, 80% cohesion reduction, Voronoi block size 0.2 m, and random block generation seed #1
24	degradation consideration, 100% cohesion reduction, Voronoi block size 0.2 m, and random block generation seed #1

Table R-1. Considered Scenarios for Drift Profile and Degraded Rock Mass Characteristics (Continued)

Scenario	Brief Description of the Scenario
25	degradation consideration, 0% cohesion reduction, Voronoi block size 0.2 m, and random block generation seed #2
26	degradation consideration, 20% cohesion reduction, Voronoi block size 0.2 m, and random block generation seed #2
27	degradation consideration, 40% cohesion reduction, Voronoi block size 0.2 m, and random block generation seed #2
28	degradation consideration, 60% cohesion reduction, Voronoi block size 0.2 m, and random block generation seed #2
29	degradation consideration, 80% cohesion reduction, Voronoi block size 0.2 m, and random block generation seed #2
30	degradation consideration, 100% cohesion reduction, Voronoi block size 0.2 m, and random block generation seed #2

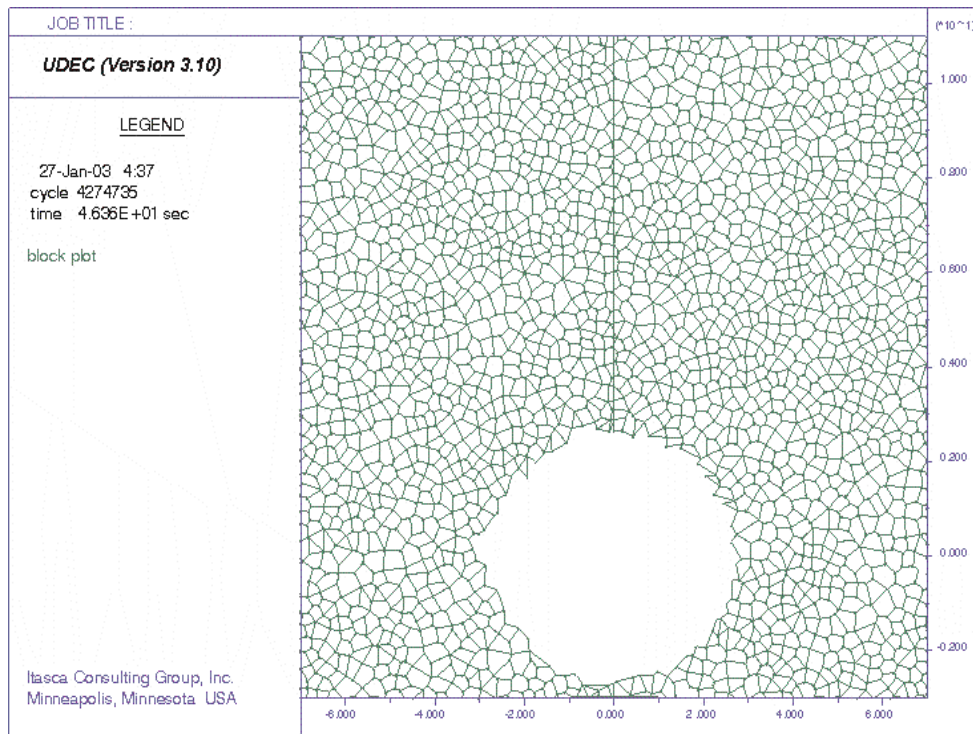


Figure R-1. Drift Profile for Scenario 1: Seismic with  $5 \times 10^{-4}$  Probability of Exceedance Ground Motion, Rock Mass Category 1, Voronoi Block Size 0.3 m



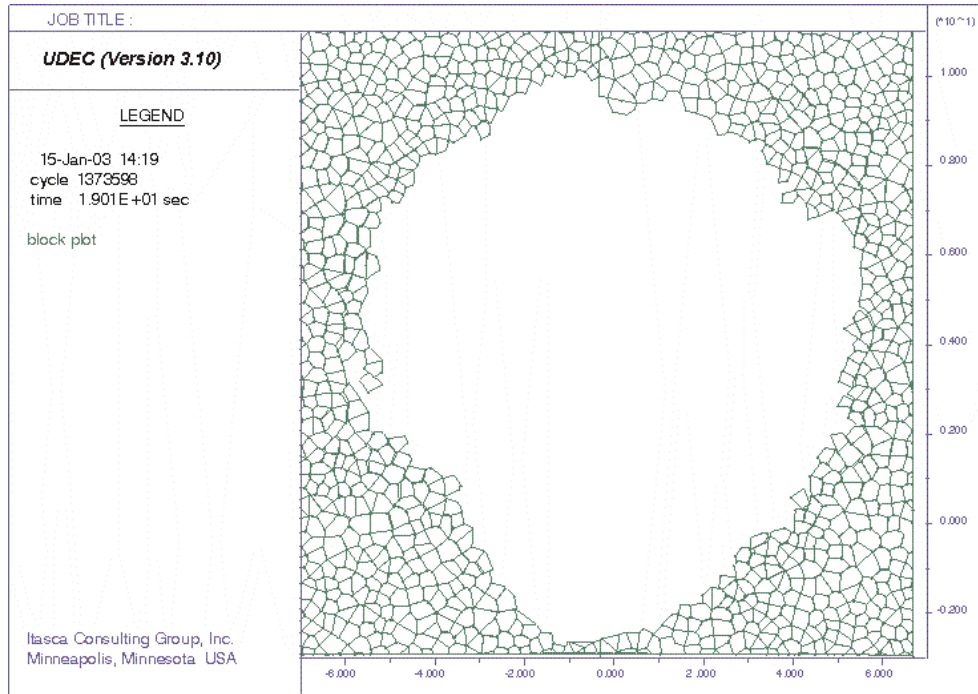


Figure R-2. Drift Profile for Scenario 2: Seismic with  $1 \times 10^{-6}$  Probability of Exceedance Ground Motion, Rock Mass Category 1, Ground Motion #12, Voronoi Block Size 0.3 m

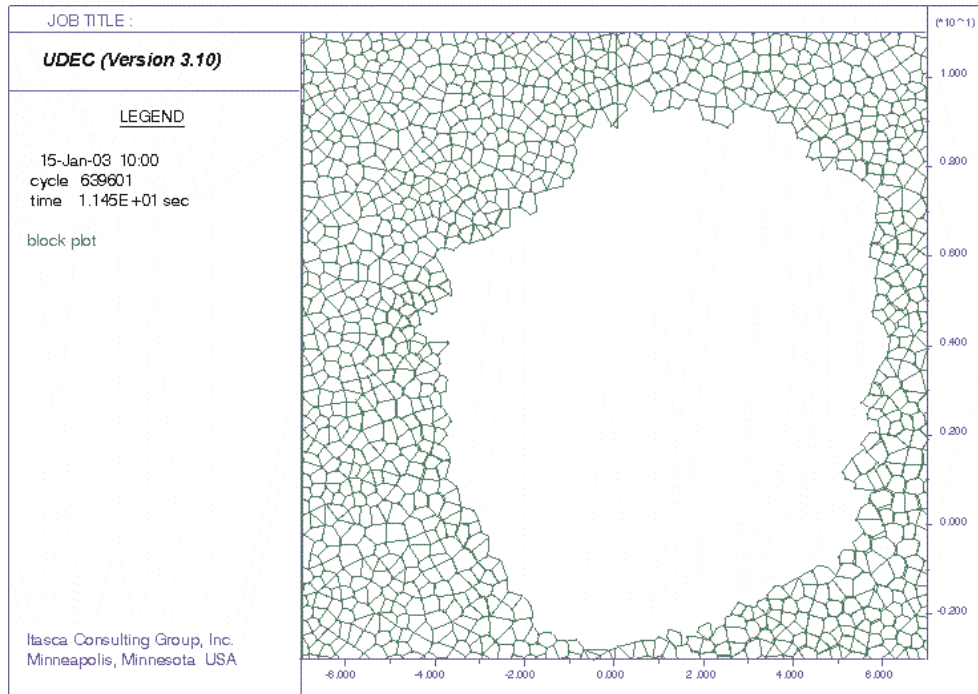


Figure R-3. Drift Profile for Scenario 3: Seismic with  $1 \times 10^{-6}$  Probability of Exceedance Ground Motion, Rock Mass Category 1, Ground Motion #8, Voronoi Block Size 0.3 m

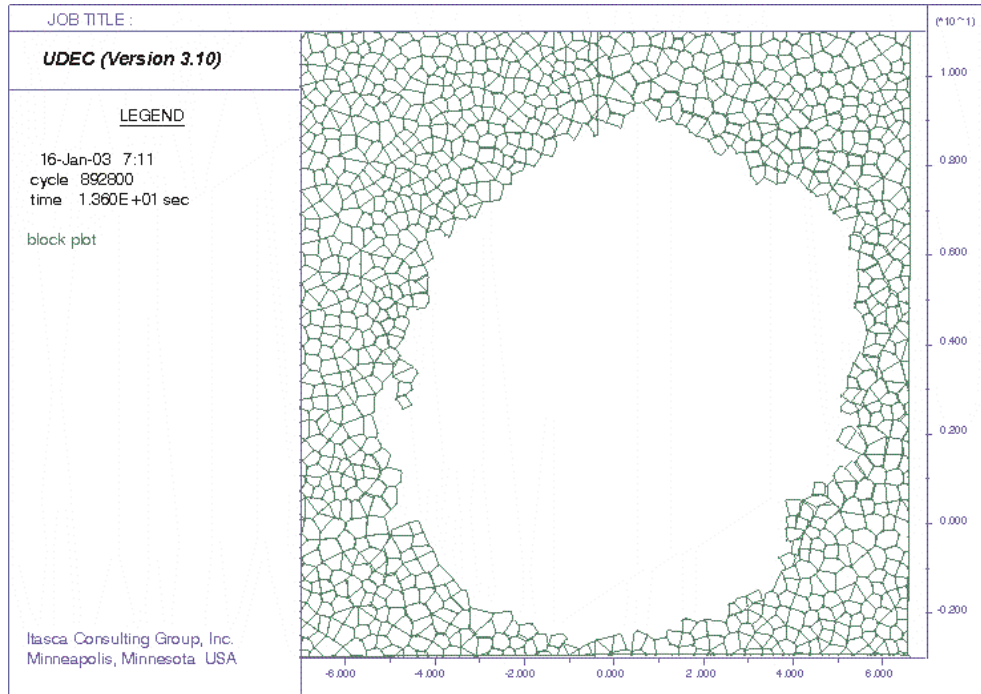


Figure R-4. Drift Profile for Scenario 4: Seismic with  $1 \times 10^{-6}$  Probability of Exceedance Ground Motion, Rock Mass Category 1, Ground Motion #9, Voronoi Block Size 0.3 m

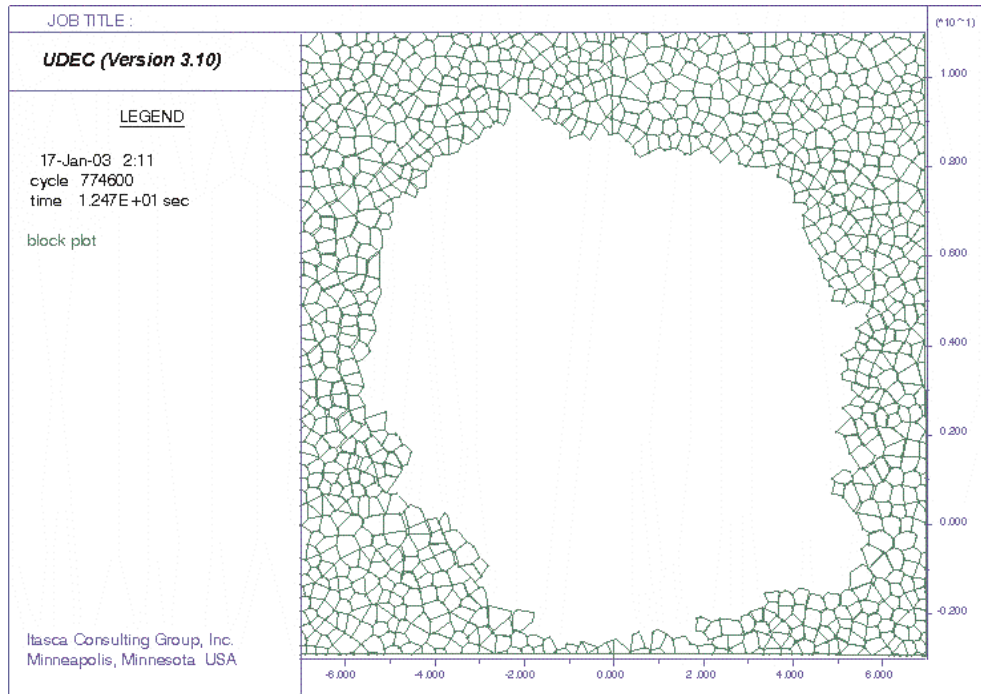


Figure R-5. Drift Profile for Scenario 5: Seismic with  $1 \times 10^{-6}$  Probability of Exceedance Ground Motion, Rock Mass Category 1, Ground Motion #1, Voronoi Block Size 0.3 m

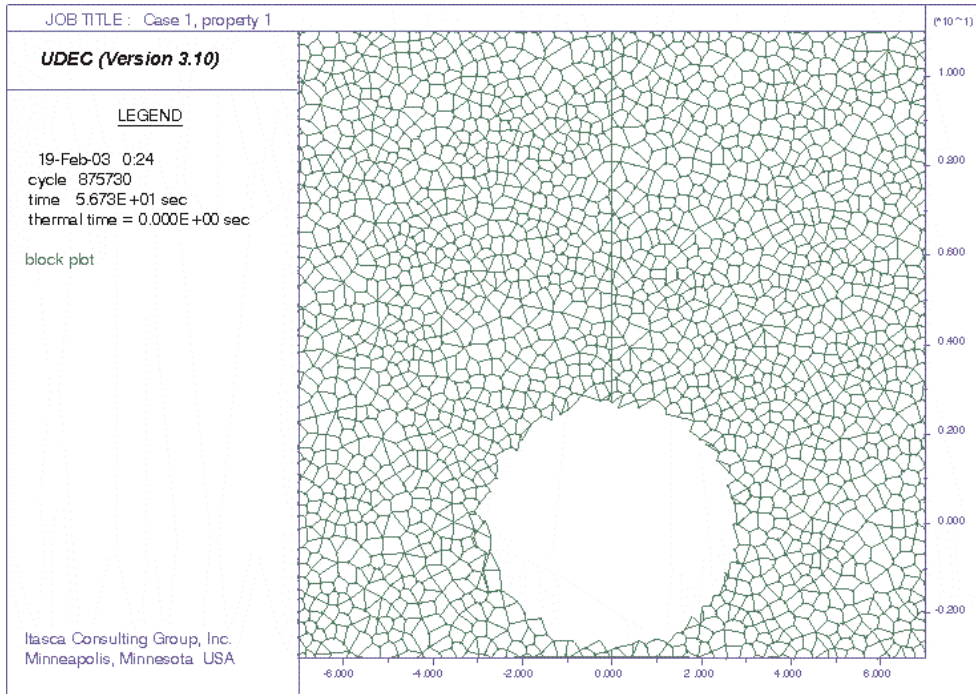


Figure R-6. Drift Profile for Scenario 6: Thermal at 10,000 Years, Rock Mass Category 1, Voronoi Block Size 0.3 m

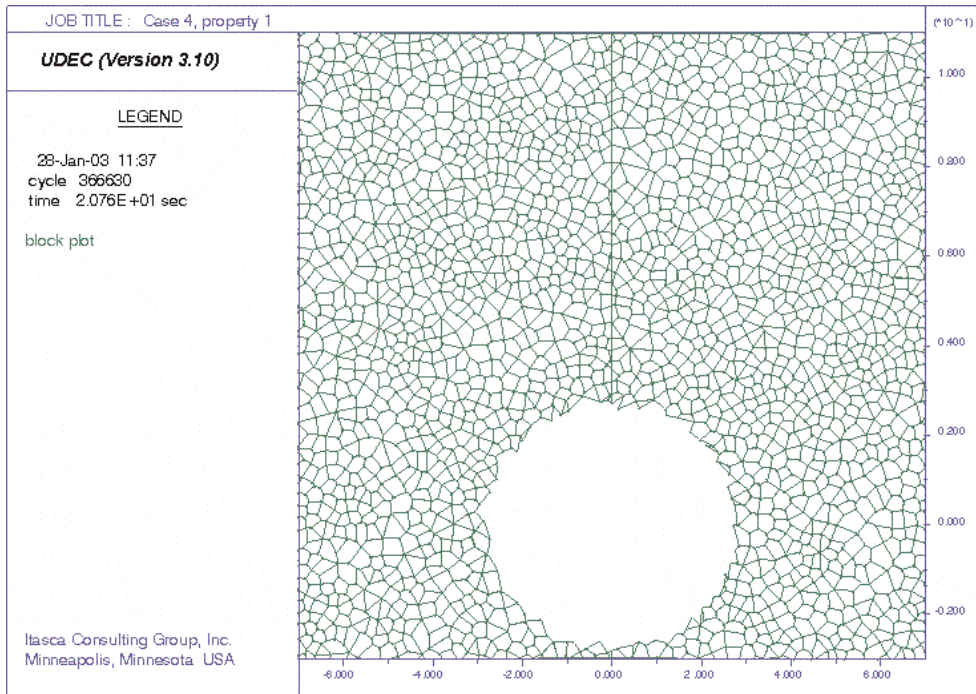


Figure R-7. Drift Profile for Scenario 7: Degradation Consideration, 0% Cohesion Reduction, Voronoi Block Size 0.3 m, and Random Block Generation Seed #1

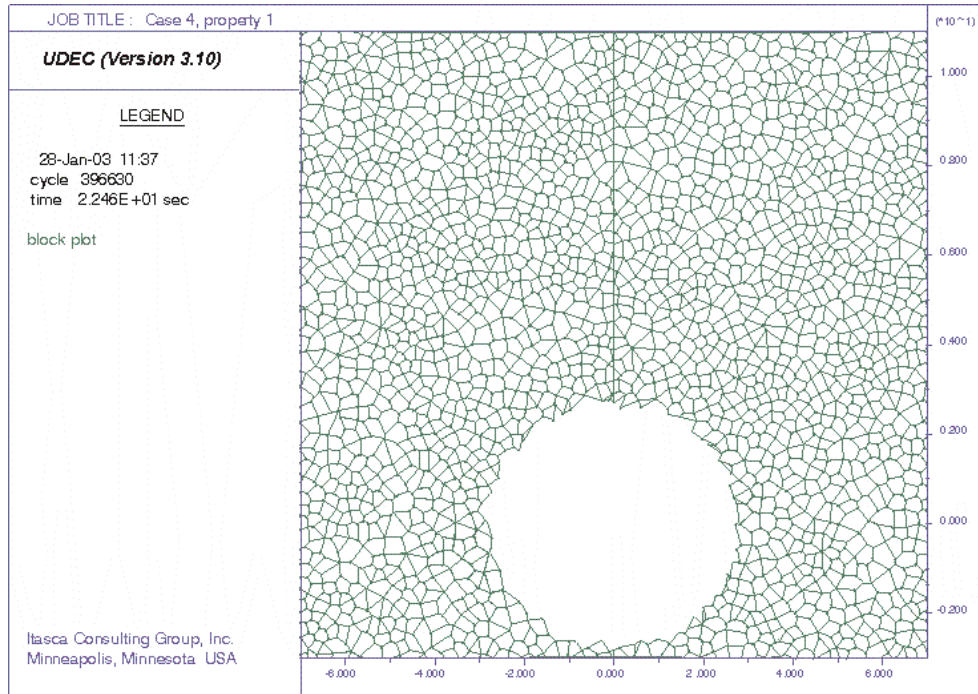


Figure R-8. Drift Profile for Scenario 8: Degradation Consideration, 20% Cohesion Reduction, Voronoi Block Size 0.3 m, and Random Block Generation Seed #1

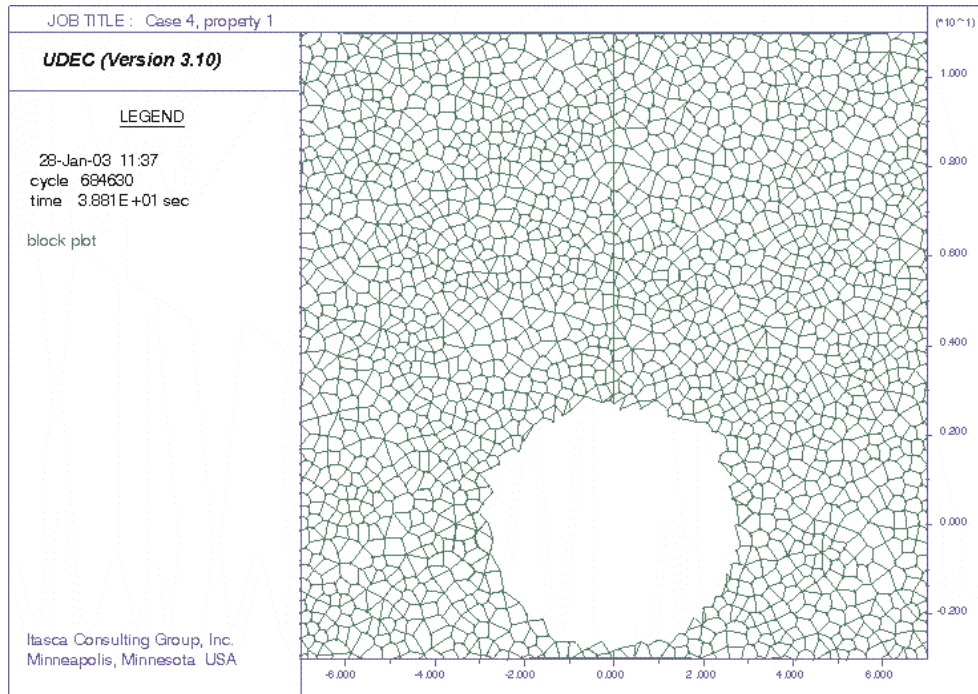


Figure R-9. Drift Profile for Scenario 9: Degradation Consideration, 40% Cohesion Reduction, Voronoi Block Size 0.3 m, and Random Block Generation Seed #1

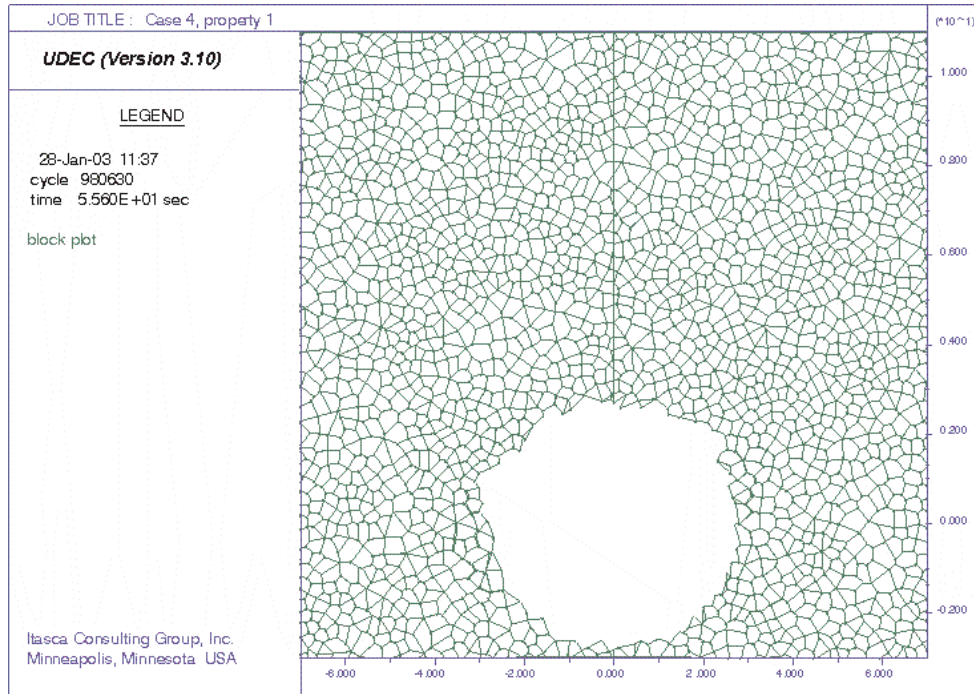


Figure R-10. Drift Profile for Scenario 10: Degradation Consideration, 60% Cohesion Reduction, Voronoi Block Size 0.3 m, and Random Block Generation Seed #1

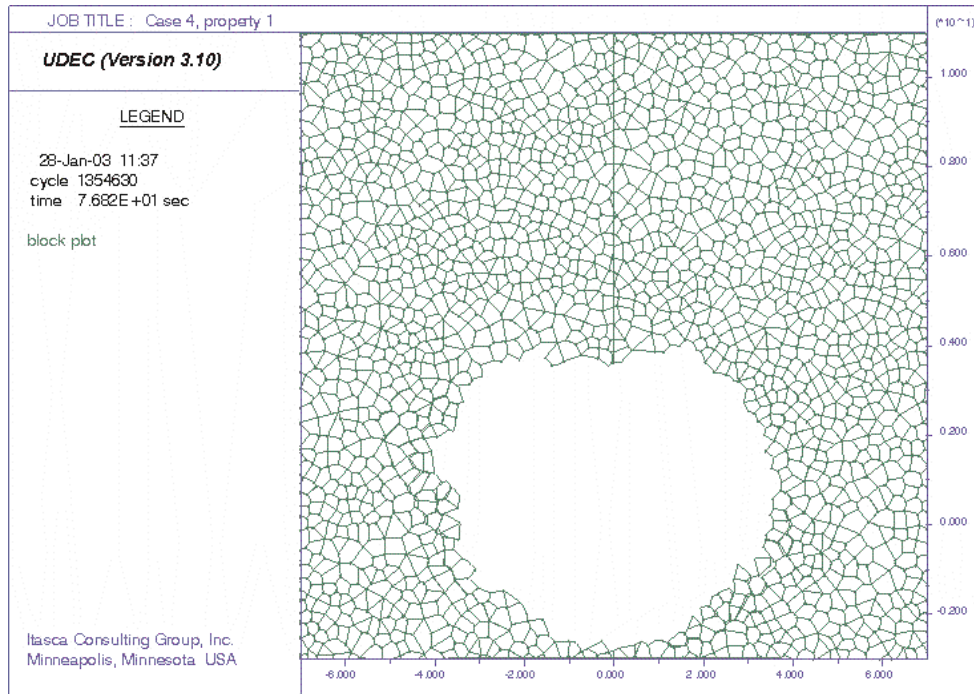


Figure R-11. Drift Profile for Scenario 11: Degradation Consideration, 80% Cohesion Reduction, Voronoi Block Size 0.3 m, and Random Block Generation Seed #1

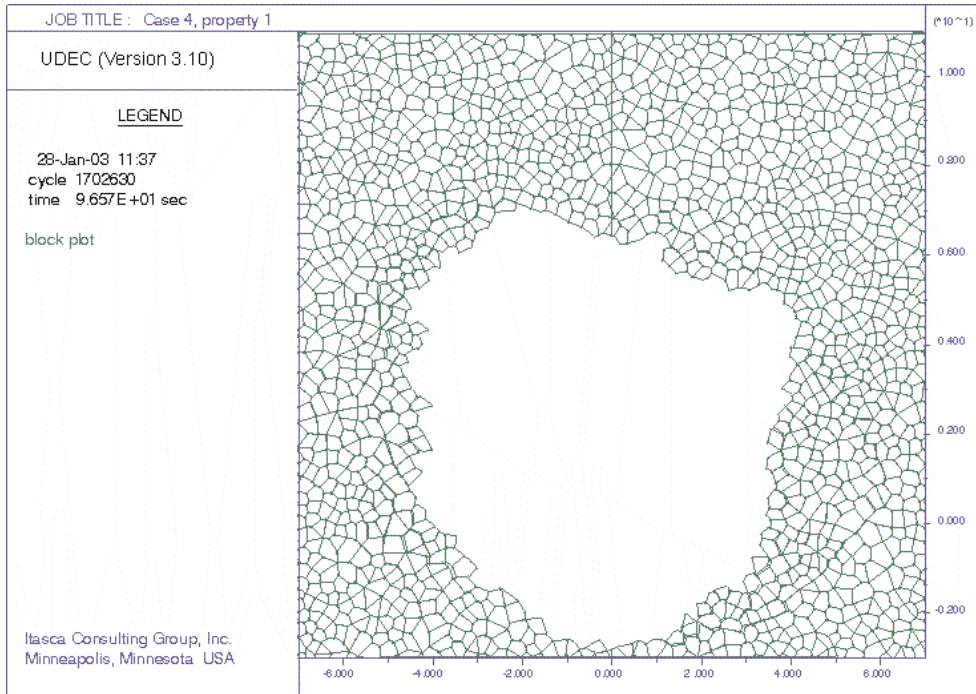


Figure R-12. Drift Profile for Scenario 12: Degradation Consideration, 100% Cohesion Reduction, Voronoi Block Size 0.3 m, and Random Block Generation Seed #1

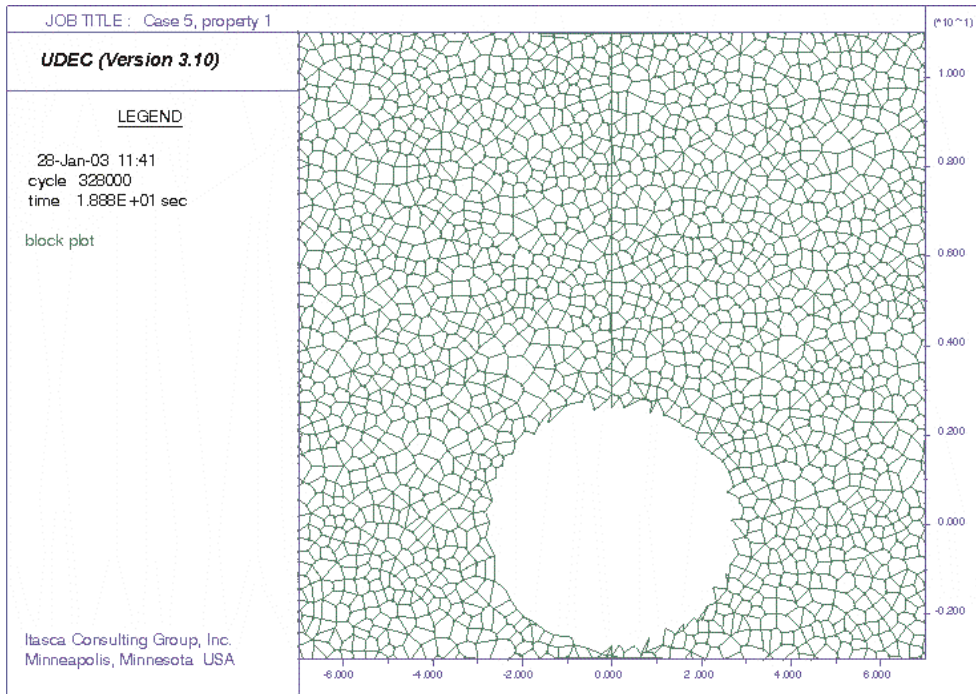


Figure R-13. Drift Profile for Scenario 13: Degradation Consideration, 0% Cohesion Reduction, Voronoi Block Size 0.3 m, and Random Block Generation Seed #2

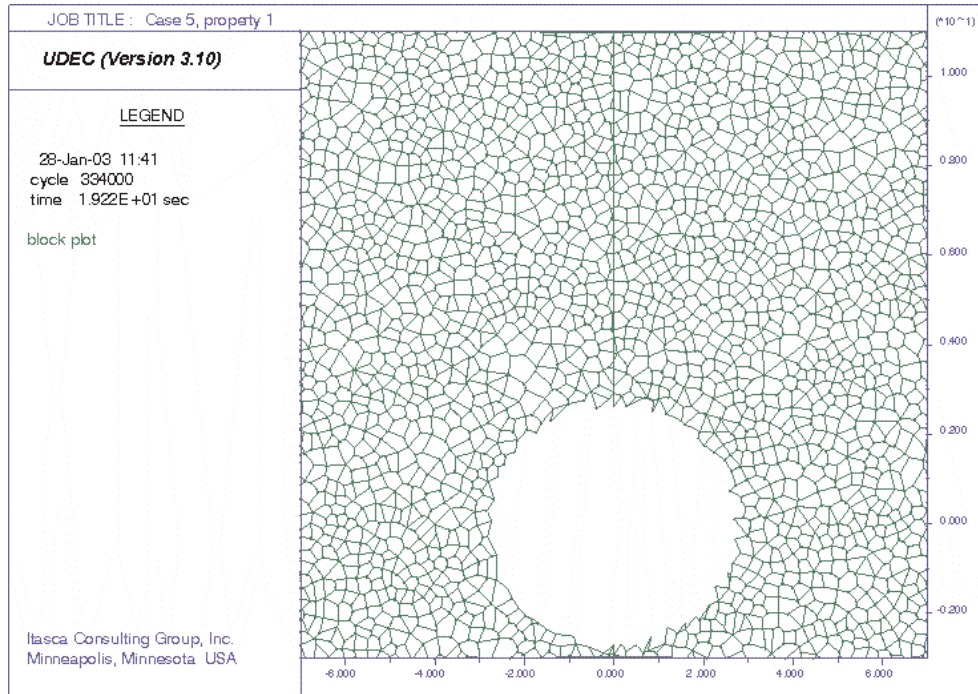


Figure R-14. Drift Profile for Scenario 14: Degradation Consideration, 20% Cohesion Reduction, Voronoi Block Size 0.3 m, and Random Block Generation Seed #2

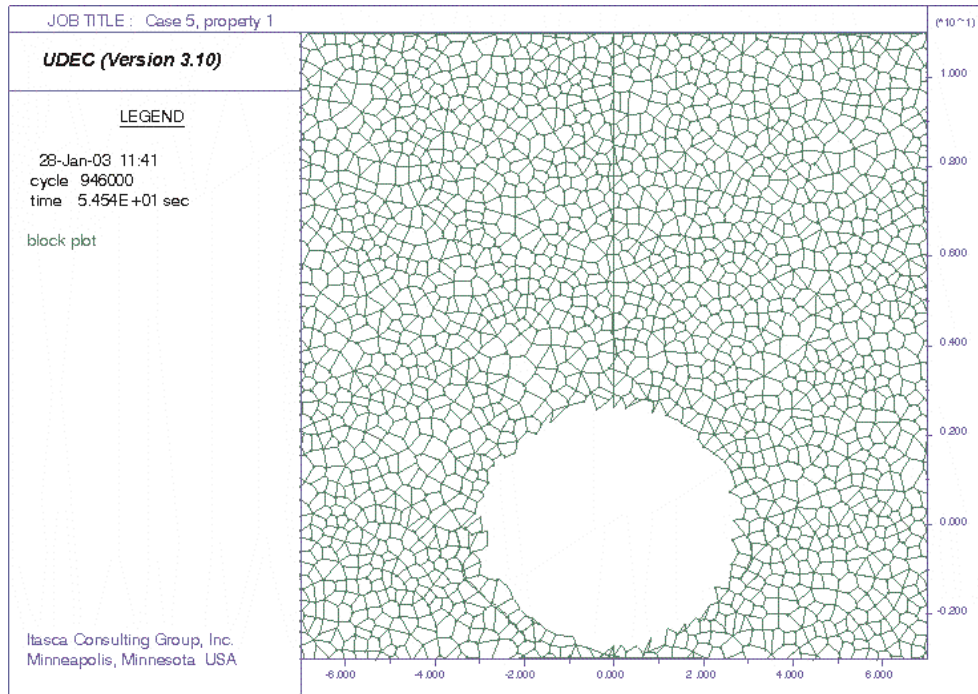


Figure R-15. Drift Profile for Scenario 15: Degradation Consideration, 40% Cohesion Reduction, Voronoi Block Size 0.3 m, and Random Block Generation Seed #2

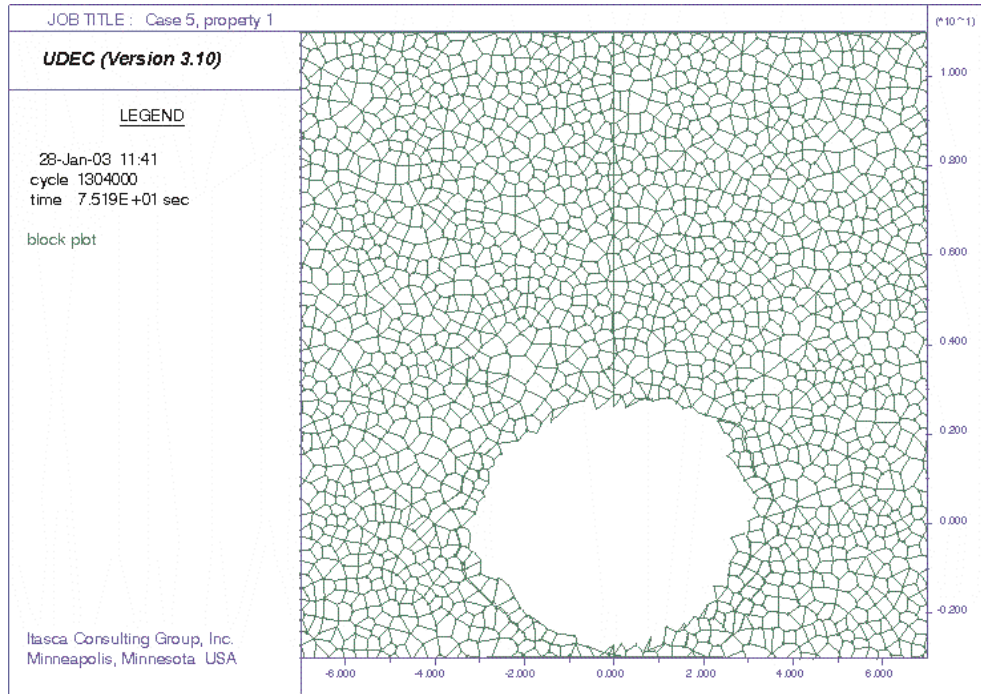


Figure R-16. Drift Profile for Scenario 16: Degradation Consideration, 60% Cohesion Reduction, Voronoi Block Size 0.3 m, and Random Block Generation Seed #2

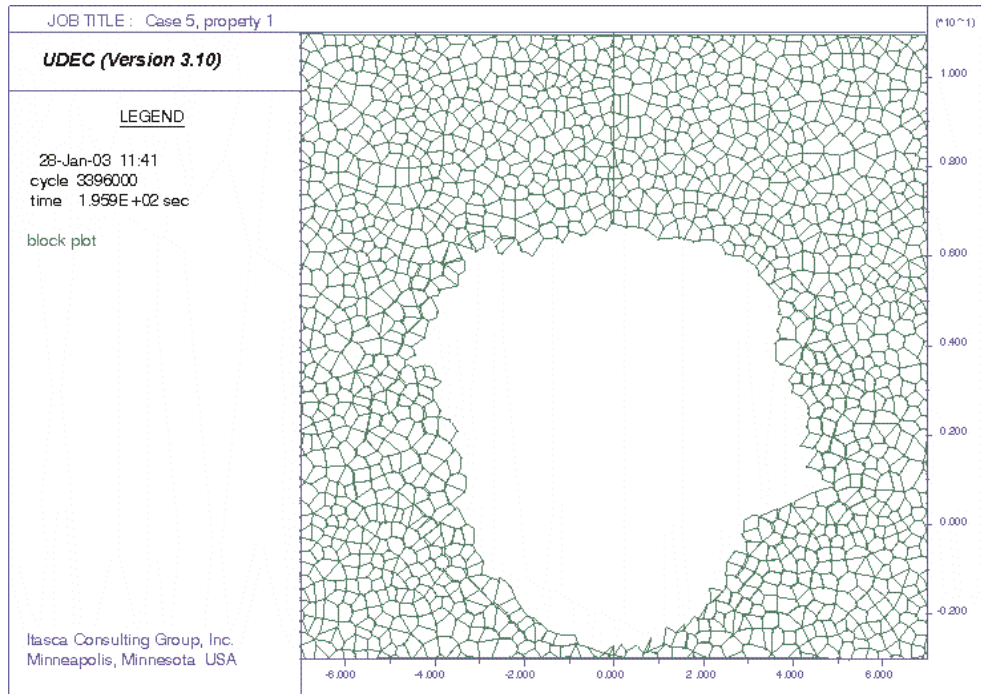


Figure R-17. Drift Profile for Scenario 17: Degradation Consideration, 80% Cohesion Reduction, Voronoi Block Size 0.3 m, and Random Block Generation Seed #2



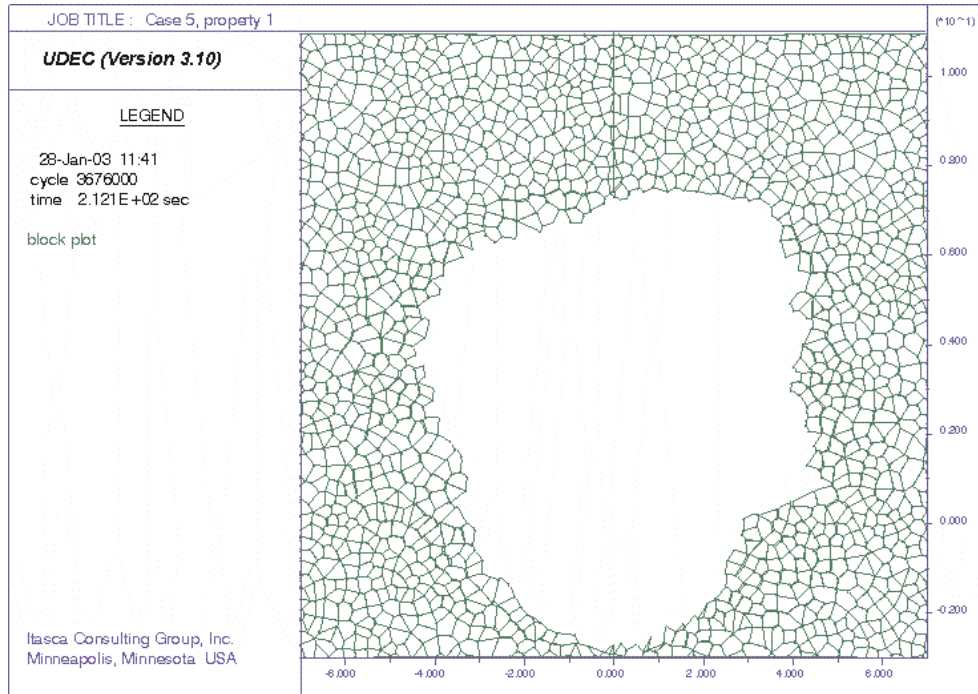


Figure R-18. Drift Profile for Scenario 18: Degradation Consideration, 100% Cohesion Reduction, Voronoi Block Size 0.3 m, and Random Block Generation Seed #2

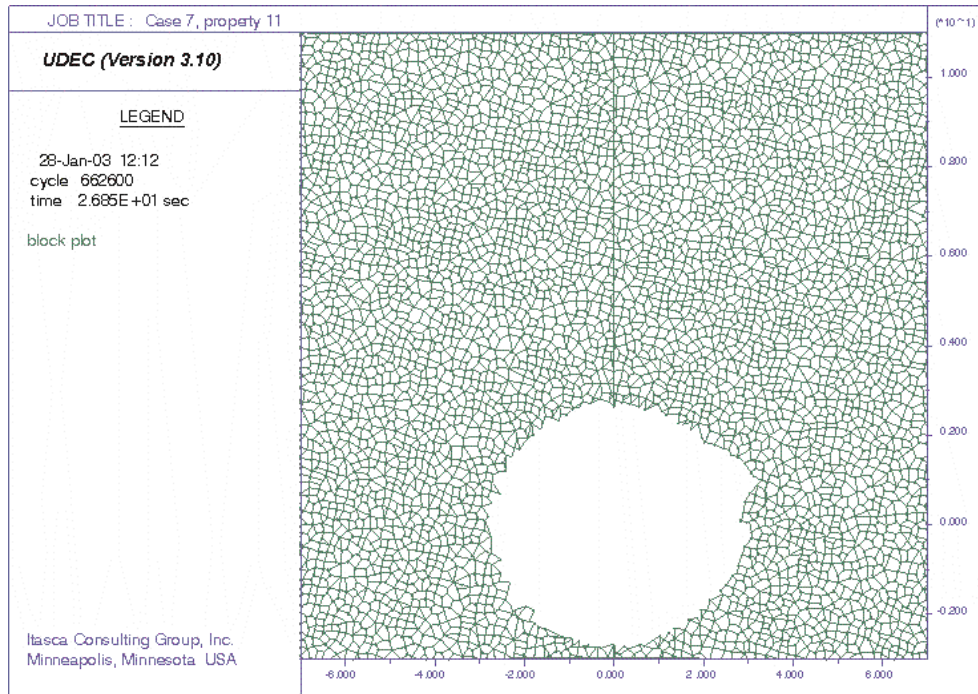


Figure R-19. Drift Profile for Scenario 19: Degradation Consideration, 0% Cohesion Reduction, Voronoi Block Size 0.2 m, and Random Block Generation Seed #1

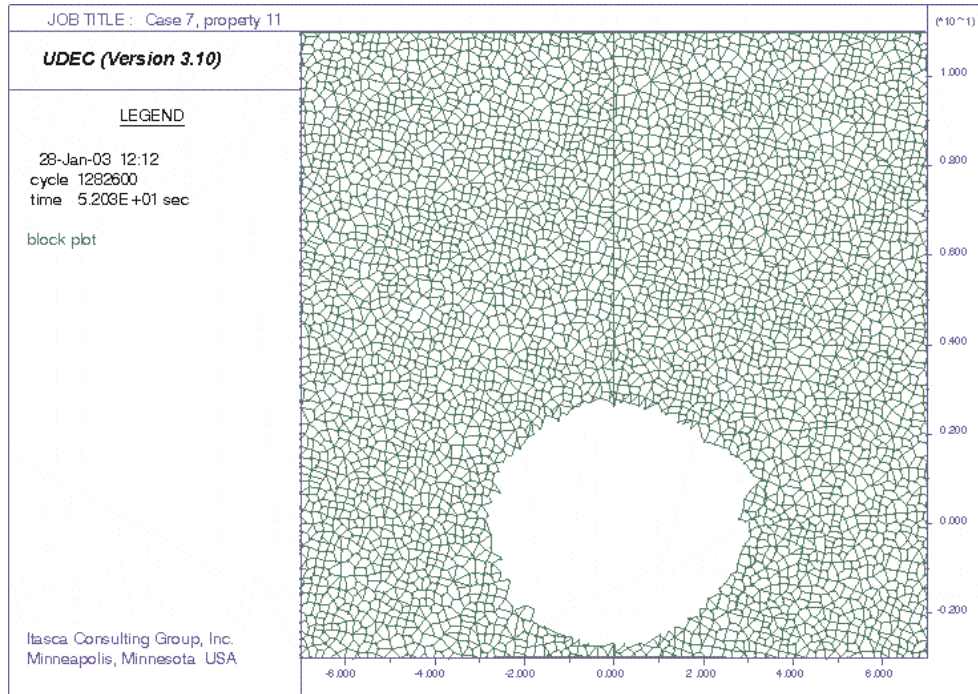


Figure R-20. Drift Profile for Scenario 20: Degradation Consideration, 20% Cohesion Reduction, Voronoi Block Size 0.2 m, and Random Block Generation Seed #1

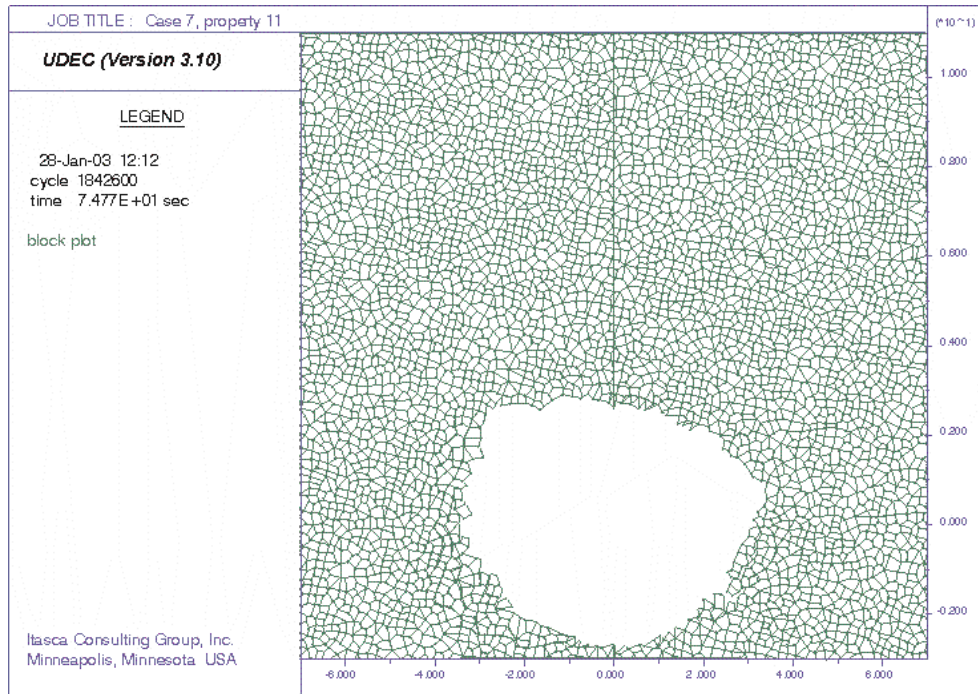


Figure R-21. Drift Profile for Scenario 21: Degradation Consideration, 40% Cohesion Reduction, Voronoi Block Size 0.2 m, and Random Block Generation Seed #1

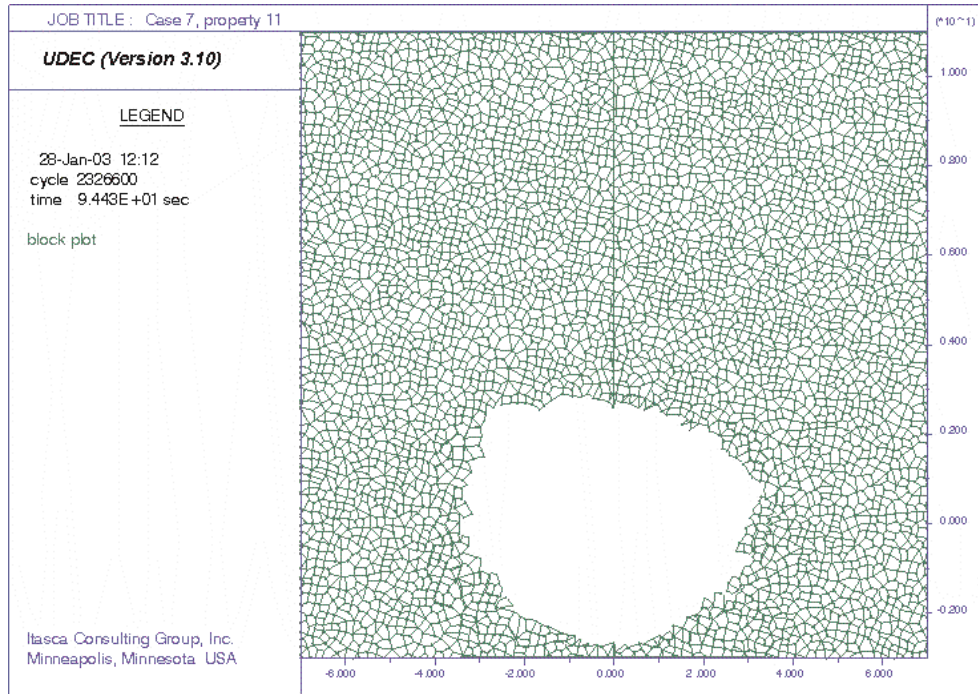


Figure R-22. Drift Profile for Scenario 22: Degradation Consideration, 60% Cohesion Reduction, Voronoi Block Size 0.2 m, and Random Block Generation Seed #1

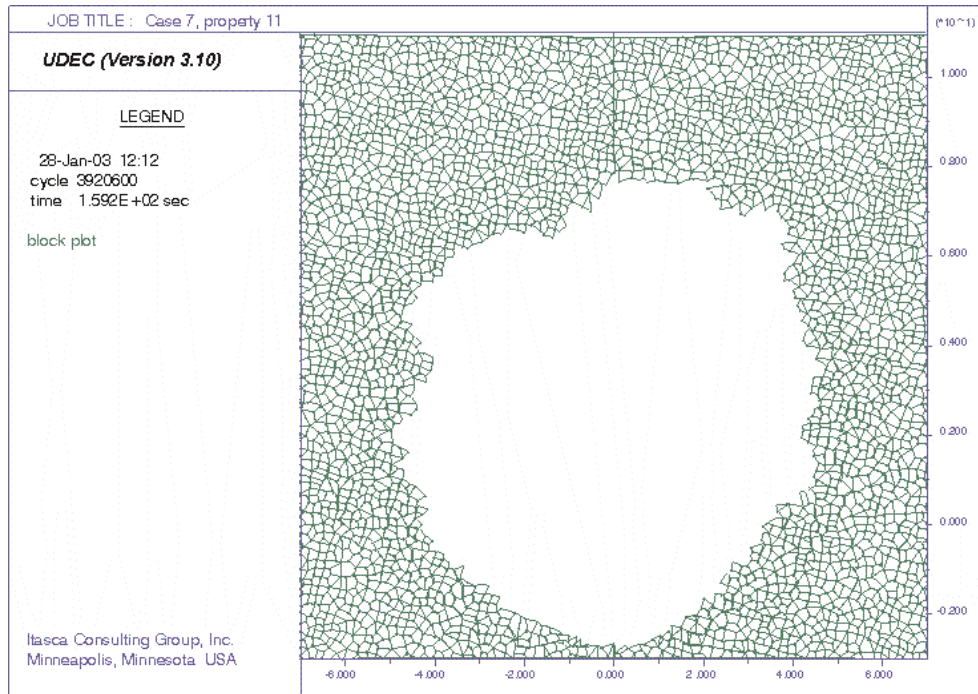


Figure R-23. Drift Profile for Scenario 23: Degradation Consideration, 80% Cohesion Reduction, Voronoi Block Size 0.2 m, and Random Block Generation Seed #1

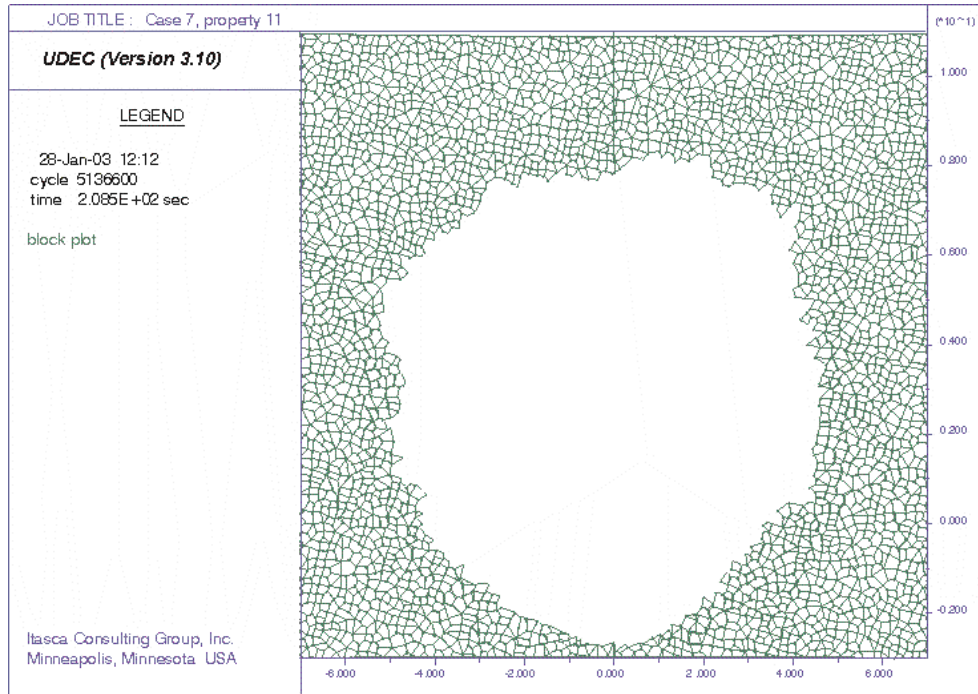


Figure R-24. Drift Profile for Scenario 24: Degradation Consideration, 100% Cohesion Reduction, Voronoi Block Size 0.2 m, and Random Block Generation Seed #1

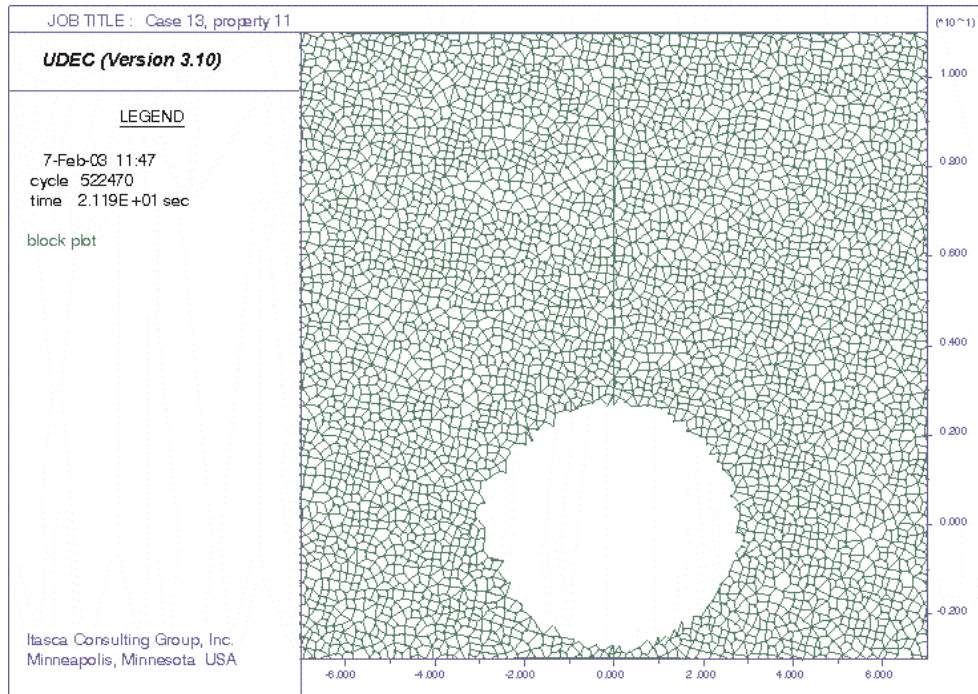


Figure R-25. Drift Profile for Scenario 25: Degradation Consideration, 0% Cohesion Reduction, Voronoi Block Size 0.2 m, and Random Block Generation Seed #2

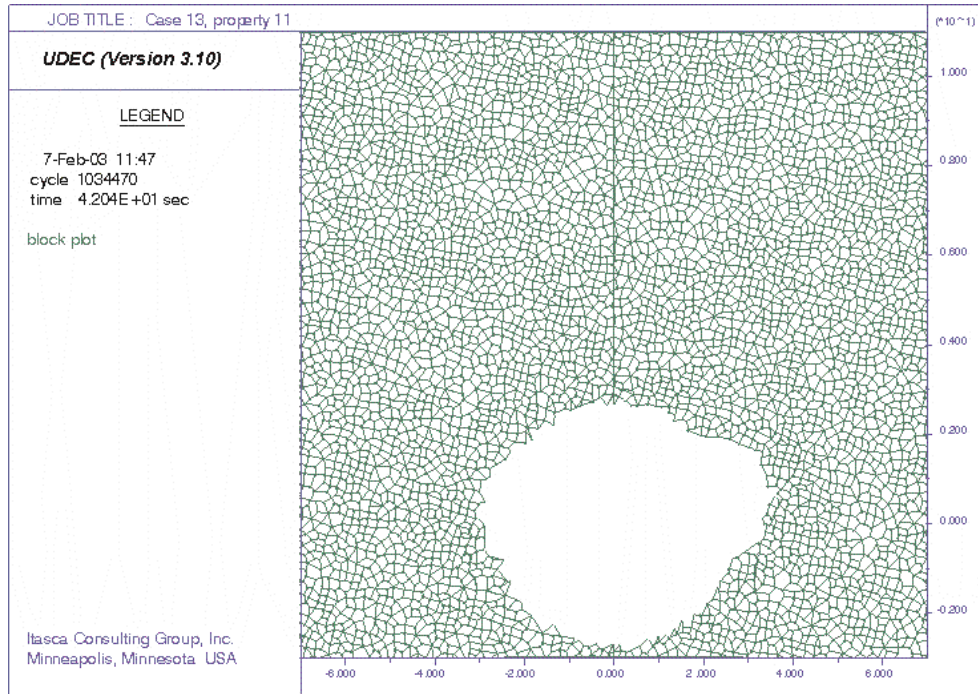


Figure R-26. Drift Profile for Scenario 26: Degradation Consideration, 20% Cohesion Reduction, Voronoi Block Size 0.2 m, and Random Block Generation Seed #2

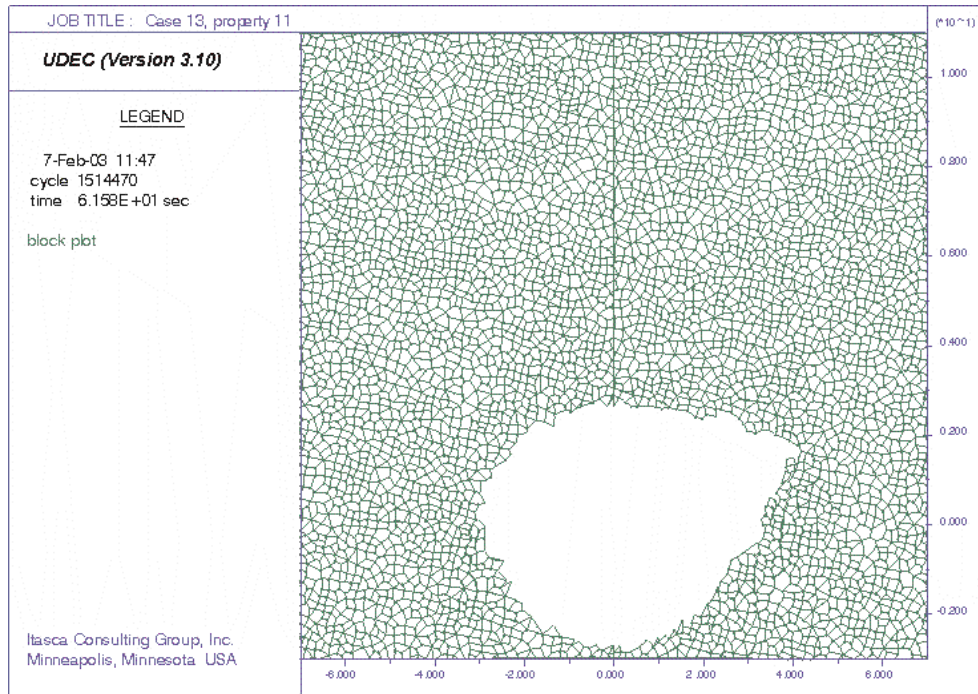


Figure R-27. Drift Profile for Scenario 27: Degradation Consideration, 40% Cohesion Reduction, Voronoi Block Size 0.2 m, and Random Block Generation Seed #2

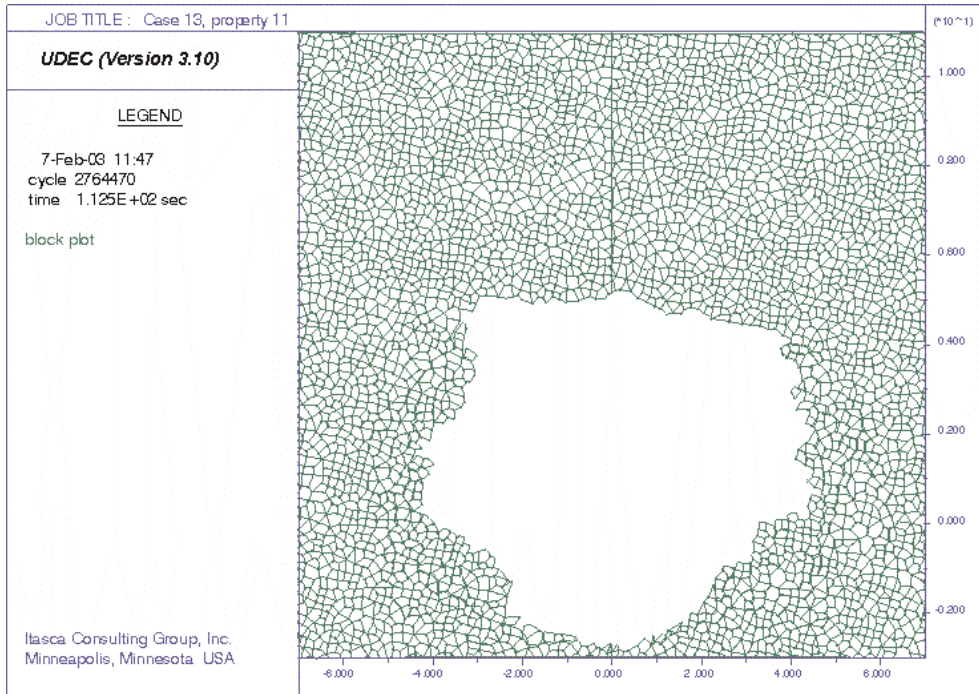


Figure R-28. Drift Profile for Scenario 28: Degradation Consideration, 60% Cohesion Reduction, Voronoi Block Size 0.2 m, and Random Block Generation Seed #2

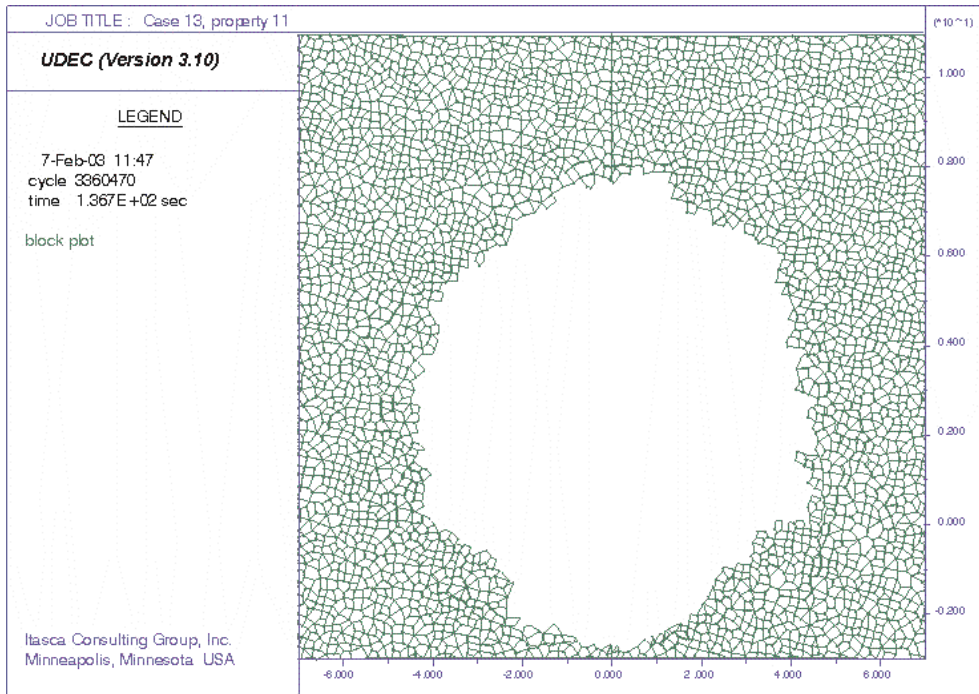


Figure R-29. Drift Profile for Scenario 29: Degradation Consideration, 80% Cohesion Reduction, Voronoi Block Size 0.2 m, and Random Block Generation Seed #2

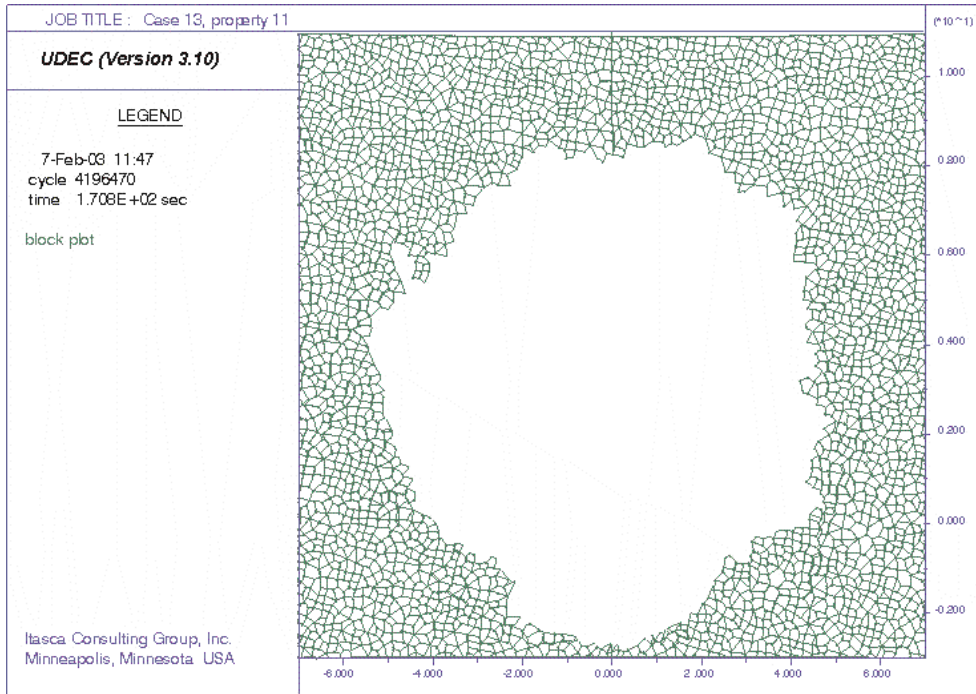


Figure R-30. Drift Profile for Scenario 30: Degradation Consideration, 100% Cohesion Reduction, Voronoi Block Size 0.2 m, and Random Block Generation Seed #2

INTENTIONALLY LEFT BLANK



**APPENDIX S**  
**ESTIMATING LONG-TERM DAMAGE FORMATION SURROUNDING**  
**EMPLACEMENT DRIFTS**



## ESTIMATING LONG-TERM DAMAGE FORMATION SURROUNDING EMPLACEMENT DRIFTS

### S1. INTRODUCTION

Predicting the time evolution of the drift profile and damage (fracturing) of the rock mass are necessary for assessing repository performance. The analysis of time-dependent drift degradation described in Section 6.4.2.4 is simplified and does not relate damage and deformation to time after drift excavation. Instead, rockfall and damage of the rock mass are calculated as functions of the level of cohesive strength reduction with no time scale being associated with this strength reduction. In the analysis presented in this appendix, the limited existing data (for Lac du Bonnet granite and nonlithophysal tuff) on time-dependent rock mass strength is used to predict the evolution of the drift profile as a function of time. The PFC stress corrosion model (Potyondy 2003 [DIRS 165550]) is used to assess the influence of confinement and lithophysal void porosity on the static-fatigue curves of lithophysal rock, and to generate curves of damage increase as a function of time for static-fatigue tests performed at different load levels. These curves are then used in the UDEC models of the drift for predictions of time-dependent damage and rockfall.

Additional time-dependent testing is currently underway. New data from this testing has been included in the analysis of time-dependent drift degradation (Section 6.4.2.4.2). The uncertainties and limitations associated with the static-fatigue test data and the modeling of time-dependent drift degradation are discussed in Section 6.5.

### S2. LONG-TERM BEHAVIOR OF ROCK AND PFC MATERIAL

#### S2.1 STATIC-FATIGUE BEHAVIOR OF GRANITE AND TUFF

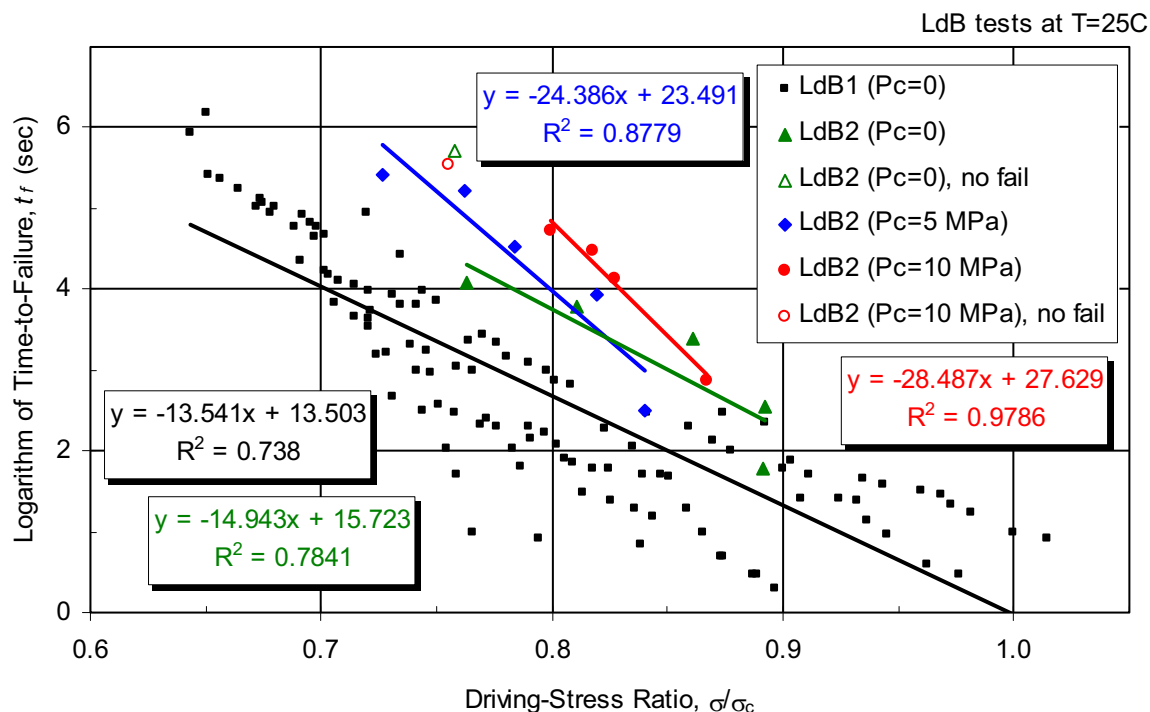
##### S2.1.1 Summary of Test Data

Static-fatigue data for Lac du Bonnet granite (LdB) is shown in Figure S-1. Potyondy and Cundall (2001 [DIRS 156895]) discuss the assumptions that went into the generation of these curves and provide additional data for Lac du Bonnet granite, Lac du Bonnet granodiorite and Barre granite. During the static-fatigue tests, environmental conditions of moisture and temperature were held constant and direct measurements were made of applied creep stress ( $\sigma_I$ ), applied confinement ( $P_c$ ) and time to failure ( $t_f$ ).<sup>2</sup> Figure S-1 shows four data sets produced by two different investigators; the data set of Schmidtke and Lajtai (1985 [DIRS 164774]) is labeled LdB1, and the data sets of Lau et al. (2000 [DIRS 164769]) are labeled LdB2. The Schmidtke and Lajtai (1985 [DIRS 164774]) specimens (2:1 aspect-ratio right circular cylinders of 31.7 mm diameter) were saturated before testing and kept submerged during testing at 25°C. Load

---

<sup>2</sup> The following notation is employed to describe the results of static-fatigue tests. The applied load in the axial direction and the confining pressure are denoted by  $\sigma_I$  and  $P_c$ , respectively. The axial load at failure during a short-term test is denoted by  $\sigma_f$ . The stress difference maintained during a static-fatigue test conducted at a confining pressure of  $P_c$  is  $\sigma = \sigma_I - P_c$ . The stress difference at failure during a short-term test is  $\sigma_c = \sigma_f - P_c$ . To facilitate comparison between different data sets, we generate a static-fatigue curve by plotting the logarithm of time-to-failure,  $t_f$ , versus the driving-stress ratio given by  $\sigma/\sigma_c = (\sigma_I - P_c) / (\sigma_f - P_c)$ . The peak strength,  $\sigma_f$ , is not known for a tested specimen. Different schemes to estimate this value have been employed by the different investigators (Potyondy and Cundall 2001 [DIRS 156895], pp. 114 to 115).

application was rapid, with full static-fatigue load being reached in about two seconds. The Lau et al. (2000 [DIRS 164769]) specimens (2.5:1 aspect-ratio right circular cylinders of 61 mm diameter) were saturated before testing and tested in a triaxial cell under drained conditions (i.e., water from a saturated sample is allowed to freely flow in or out of the sample during loading) at 25°C. Load application was slow, with full load being reached at a constant rate of 0.75 MPa/sec. For unconfined conditions, both data sets have a similar slope when fit with a straight line. While confined static-fatigue tests are limited, confinements of 5 MPa and 10 MPa increase the slope, and also increase the time-to-failure for  $\sigma/\sigma_c < 0.8$ .



Source: LdB1 data from Schmidtke and Lajtai (1985 [DIRS 164774]); LdB2 data from Lau et al. (2000 [DIRS 164769]).

Figure S-1. Static-Fatigue Data for Lac du Bonnet Granite (Confinements of 0, 5, and 10 MPa)

Martin et al. (1997 [DIRS 165960] and 1997 [DIRS 148875]) present static-fatigue results for a total of 16 specimens of welded (lithophysae poor) tuff from borehole NRG-7/7A at Yucca Mountain and from Busted Butte boulders taken from the same block of rock.<sup>3</sup> The specimens were 2:1 aspect-ratio right circular cylinders of 50.8 mm diameter. Load application was rapid, with full load being reached in less than 10 seconds. The 7 borehole specimens drained and vented to the atmosphere were tested at a temperature of 225°C and a confining pressure of 10 MPa at differential stresses ranging from 40 MPa to 130 MPa. None of these specimens had failed after loading for times ranging from  $2.5 \times 10^6$  to  $5.9 \times 10^6$  seconds. The nine (9) Busted Butte specimens were tested at a pore water pressure ( $P_p$ ) of 4.5 MPa, a temperature of 150°C and a confining pressure of 5 MPa at differential stresses ranging from 115 MPa to 150 MPa, and

<sup>3</sup> Martin et al. (1997 [DIRS 148875]) is the Sandia report describing the tests on the borehole specimens, and additional scoping studies are reported in Martin et al. (1995 [DIRS 100159]).

the test results are summarized in Table S-1. Six of these specimens failed at times less than  $2 \times 10^6$  seconds, while the remaining three specimens (BB-9392-H, -G, and -J) did not fail during the testing period. The times-to-failure for these six tests can be plotted versus applied load; however, the peak strength must be estimated in order to plot them versus driving-stress ratio for comparison with the Lac du Bonnet granite data in Figure S-2. For these purposes, the peak strength at a effective confinement of 0.5 MPa ( $P_c - P_p$ ) is estimated to be 151 MPa to give a failure time of one second for a driving-stress ratio of unity.<sup>4</sup>

Table S-1. Static-Fatigue Data for Busted Butte Specimens

Specimen	Confining Pressure, $P_c$ (MPa)	Stress Difference Maintained During Test, $\sigma$ (MPa)	Time-to-Failure, $t_f$ (sec)	Logarithm of Time-to-Failure, $\log(t_f)$ (sec)	Peak Strength, $\sigma_f$ (MPa)	Driving-Stress Ratio, $\sigma/\sigma_c$
BB-9392-K	5	149.0	1.2	0.08	151	0.99
BB-9392-N	5	141.0	4	0.60	151	0.94
BB-9392-E	5	134.6	250	2.40	151	0.89
BB-9392-C	5	134.2	636	2.80	151	0.89
BB-9392-F	5	132.8	5848	3.77	151	0.88
BB-9392-B	5	127.8	1960000	6.29	151	0.85
BB-9392-H	5	131.4	1180000	6.07	151	0.87
BB-9392-G	5	131.3	732000	5.86	151	0.87
BB-9392-J	5	115.0	2000000	6.30	151	0.76

NOTE: See footnote 1 in this Appendix for a discussion of the notation used in this table. Specimens were saturated and tested at a pore water pressure of 4.5 Pa and temperature of 150°C. Specimens were loaded directly to creep stress ( $\sigma_1$ ) in less than 10 seconds. Specimen diameter is 50.8 mm. Specimens BB-9392-H, BB-9392-G, and BB-9392-J did not fail during the test. Confining pressure is the effective value from the applied confining stress (5 MPa) and pore pressure (4.5 MPa). See Martin et al. 1997 [DIRS 165960].

It is noted that there is a difference in test temperature for the granite and tuff data (i.e., 25°C and 150°C, respectively). Based on a postulated physical mechanism for stress corrosion, which is a chemical reaction that increases its rate with increased temperature, it is determined that increasing temperature should decrease the time-to-failure for a fixed driving-stress ratio ( $\sigma/\sigma_c$ ).

### S2.1.2 Suitability of Static-Fatigue Data for Estimating the Long-Term Behavior of the Rock Mass Surrounding the Emplacement Drifts

The static-fatigue test data for granite (Schmidtke and Lajtai 1985 [DIRS 164774]; Lau et al. 2000 [DIRS 164769]) and tuff (Martin et al. 1997 [DIRS 165960]) were obtained from outside sources. In accordance with AP-SIII.10Q (Section 5.2), these data are considered qualified for use within this analysis and model report based on the reliability of the data sources, the qualifications of the organizations generating the data, and the availability of corroborating data, as documented in this section.

<sup>4</sup> The unconfined compressive strength values from Martin et al. (1993) for six saturated 50.8 mm diameter Busted Butte specimens tested at a strain rate of  $10^{-5} \text{ s}^{-1}$  ranged from approximately 105 MPa to 200 MPa, with a mean of approximately 128 MPa for the five weakest specimens.

**Extent to Which the Data Demonstrate Properties of Interest**—These data have been collected as part of thermal-mechanical stability studies in both the United States and Canada with the purpose of improving the fundamental understanding of long-term rock mass behavior around underground openings. This information represents the best available data for assessing long-term strength of tuff at Yucca Mountain. The granite data from the Canadian thermal-mechanical studies (i.e., Schmidtke and Lajtai 1985 [DIRS 164774] and Lau et al. 2000 [DIRS 164769]) provide a means of comparing the effects of rock type and demonstrating the similarity of the general nature of the time-to-failure data for different rock types. Additionally, corroborating data (described in this section) confirm the general consistency and similarity of the data sets for providing the long-term strength of rock.

**Lau et al. (2000 [DIRS 164769])**—Data from long-term loading tests on granite were developed by the CANMET Mining and Mineral Sciences Laboratories within Natural Resources Canada, which is a federal government department specializing in earth sciences. The mining group at CANMET has established a team of specialists in geomechanics, numerical modeling, and mechanical rock property testing. Their laboratories include state-of-the-art rock mechanics testing systems. Specimen preparation, test apparatus, test procedures, data collection, and analysis of data are well documented, providing a reliable source of data from long-term loading tests.

**Schmidtke and Lajtai (1985 [DIRS 164774])**—Data from long-term loading tests on granite were also developed by the Departments of Civil and Geological Engineering the University of Manitoba under the sponsorship of the Atomic Energy of Canada. This work was conducted by Dr. Emery Lajtai, Professor Emeritus of Civil Engineering at the University of Manitoba. Dr. Lajtai specializes in the fracture and deformation of rocks.

**Martin et al. (1997 [DIRS 165960])**—Creep and static-fatigue data for welded tuff from Yucca Mountain were developed by the combined efforts of New England Research, Inc. and Sandia National Laboratories. Sandia National Laboratories, with the support of New England Research, Inc., has been a primary developer of rock mechanics testing data within the Office of Civilian Radioactive Waste Management quality assurance program at Yucca Mountain. The collection of the creep and static-fatigue data for tuff, while completed independently from YMP sponsorship, was developed using YMP quality standards. The principal author of the creep and static-fatigue data for tuff, Dr. Randolph Martin, is the President of and Principal Scientist at New England Research, Inc. He has a Ph.D. from MIT, where his thesis research was entitled, “Time-Dependent Crack Growth in Quartz and Its Application to the Creep of Rocks.” Dr. Martin has a wide range of experience managing and performing both field and laboratory rock mechanics projects, including designing/building high-pressure equipment, testing rocks at elevated pressures and temperatures, and analyzing data with various (e.g. empirical, analytical, and numerical) techniques. The co-author of this data, Mr. Ronald Price, is a Senior Member of Technical Staff at Sandia National Laboratories. Mr. Price has had a central focus on the mechanical properties of tuffs, with special emphasis on Yucca Mountain tuffs, for over 22 years. His depth of knowledge of tuff rheological properties is particularly valuable for the present application.

**Corroborating Data**—New static-fatigue data for tuff (DTN: SN0406L0212303.002 [DIRS 170289], tuff 2004 data) have recently been collected and are used to corroborate the 1997 test data for tuff (Martin et al. 1997 [DIRS 165960]). The static-fatigue data are provided in Section 6.4.2.4 (Figure 6-155). Granite results are included as a means of comparing the effects of rock type and for demonstrating the similarity in the general nature of the time-to-failure data for different rock types. Scatter in the data is due to sample inhomogeneity, as well as the fact that the driving stress ratio (the horizontal axis) uses an estimated value for the unconfined compressive strength (adjusted for sample porosity) for normalizing the applied stress level.

Since there is significant variability in the unconfined compressive strength of each sample, there will be a scatter in the resulting plot of time-to-failure versus driving stress ratio. As seen in Figure 6-155, the welded tuff has a significantly slower time static fatigue failure than granite, as evidenced by the steeper slope of the linear fit to the data. This slower time-to-failure is presumably a result of the relatively homogeneous, fine-grained, high silica content nature of the tuff, as opposed to the heterogeneous nature of the grain structure of granite.

Linear fits to the unconfined compression data of Lac du Bonnet granite and to the tuff 1997 data only and to the welded tuff data (including both 1997 and 2004 data) are given (Figure 6-155). Although there is considerably more scatter in the 2004 test results, the linear fits to the data sets show the general consistency of the overall slope of the fits.

## **S2.2 STATIC-FATIGUE BEHAVIOR OF PFC2D MATERIAL FOR LITHOPHYSAL TUFF**

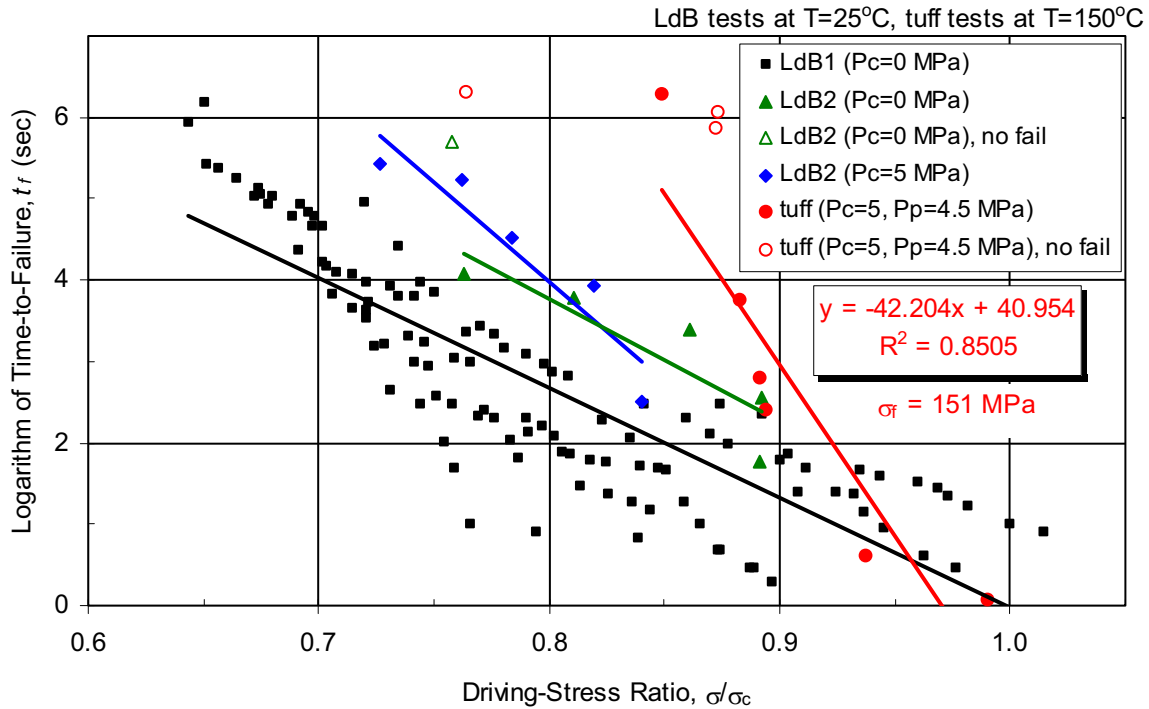
The PFC stress corrosion model is described in Potyondy (2003 [DIRS 165550]), and only the model behavior when applied to simulating lithophysal tuff is described here.<sup>5</sup>

### **S2.2.1 PFC2D Base Material and Specimen (Short-Term Behavior)**

The PFC model for lithophysal tuff is described in Section 7.5 and in *Subsurface Geotechnical Parameters Report* (BSC 2003 [DIRS 166660], Section 9.1). This PFC2D model (consisting of circular voids within a well-connected base material) has the microproperties and void geometry given in Table S-2, and provides the base material for which the stress-corrosion behavior is measured. Determination of the appropriate model conditions requires balancing many factors such as (1) behavior of previous models, (2) appropriate resolution of voids and bridges, and (3) ability to perform a simulation in a reasonable amount of time.

---

<sup>5</sup> Much of the development of the model has been funded by Atomic Energy of Canada Limited and Ontario Power Generation during the years 1995-2001 as part of its Thermal-Mechanical Stability Study, one aim of which has been to improve our fundamental understanding of short- and long-term rock-mass behavior around underground openings at ambient and elevated temperatures. The result of this work has been the development and verification of the Bonded-Particle Model for Rock - a mechanistically based numerical model for predicting excavation-induced rock-mass damage and long-term strength (by incorporating a damage process based on a stress-corrosion mechanism) in Lac du Bonnet granite (Potyondy and Cundall 2001 [DIRS 156895]).



Sources: LdB1 from Schmidtke and Lajtai (1985 [DIRS 164774]); LdB2 from Lau et al. (2000 [DIRS 164769]); tuff from Martin et al. (1997 [DIRS 165960]).

Figure S-2. Static-Fatigue Data for Welded Tuff and Lac du Bonnet Granite

The properties of the PFC2D material are obtained by testing 1:1 aspect-ratio specimens of one-meter diameter, with circular voids of 90 mm diameter and a 41.5 mm minimum bridge length. The use of 1:1 aspect-ratio specimens is justified due to frictionless boundary conditions. It is noted that the modulus and strength versus void porosity relations are similar for both 1:1 and 2:1 aspect-ratio specimens — the 2:1 aspect-ratio specimens are only slightly weaker than the 1:1 aspect-ratio specimens (see Figures S-3 and S-4).

The resolutions of previous PFC materials are shown in Table S-3. The materials in the first two columns are 2:1 aspect ratio specimens that were used to obtain the initial relations between modulus, strength and void porosity (see Figures 7-12 and 7-13). These 2D and 3D materials have average particle diameters of 17.1 mm and 52.3 mm, respectively, and the macroproperties of the 2D material are shown in Figures S-3 through S-5. The materials in the third and fourth columns are 1:1 aspect ratio specimens that differ only in the size of the circular voids. This 2D material has an average particle diameter of 9.9 mm, and the macroproperties of these 2D materials are shown in Figures S-3 through S-5. The material in the fourth column is used for the present work.



Table S-2. PFC2D Material for Lithophysal Tuff (Microproperties and Void Geometry)

Grains	Cement
$\rho = 2510 \text{ kg/m}^3$	N/A
$(D_{\max} / D_{\min}) = 1.5$ $D_{\text{avg}}$ varies	$\bar{\lambda} = 1$
$E_c = 14.8 \text{ GPa}$	$\bar{E}_c = 14.8 \text{ GPa}$
$(k_n / k_s) = 2.1$	$(\bar{k}^n / \bar{k}^s) = 2.1$
$\mu = 0.5$	$\bar{\sigma}_c = \bar{\tau}_c = \text{mean} \pm \text{standard deviation} = 48.11 \pm 11 \text{ MPa}$
<b>Void Geometry:</b> circular, $D_v$ varies, $B_{\min} = 41.5 \text{ mm}$	

NOTE: The PFC microproperties in this table were obtained by calibration of the PFC model to match the macro-behavior of tuff, as described in Section 7.6.3.  $\rho$  = grain density,  $D_{\max}$  = maximum particle diameter (mm),  $D_{\min}$  = minimum particle diameter (mm),  $D_{\text{avg}}$  = average particle diameter (mm),  $E_c$  = Young's modulus of the grains,  $\bar{E}_c$  = Young's modulus of the cement,  $k_n$  = particle normal stiffness,  $k_s$  = particle shear stiffness,  $\mu$  = grain friction coefficient,  $\bar{\lambda}$  = bond-radius multiplier of cemented contact,  $\bar{k}^n$  = normal stiffness of cemented contact,  $\bar{k}^s$  = shear stiffness of cemented contact,  $\bar{\sigma}_c$  = tensile strength of cemented contact,  $\bar{\tau}_c$  = shear strength of cemented contact,  $D_v$  = void diameter (mm),  $B_{\min}$  = minimum bridge length.

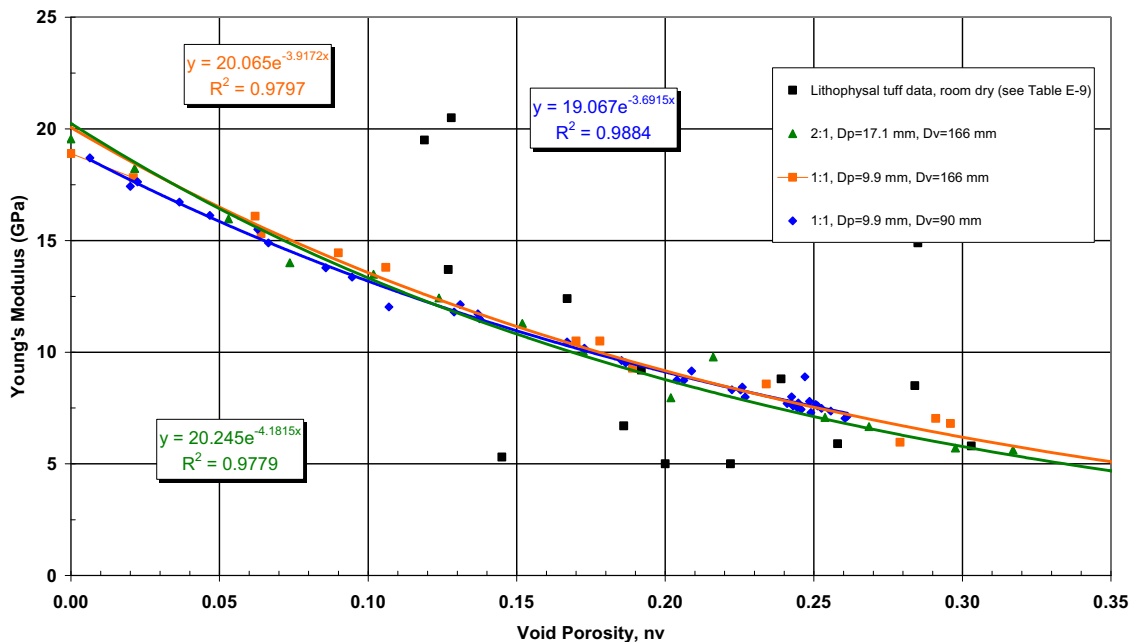


Figure S-3. Young's Modulus Versus Void Porosity for Lithophysal Tuff and PFC2D Models of Randomly Distributed Circular Voids

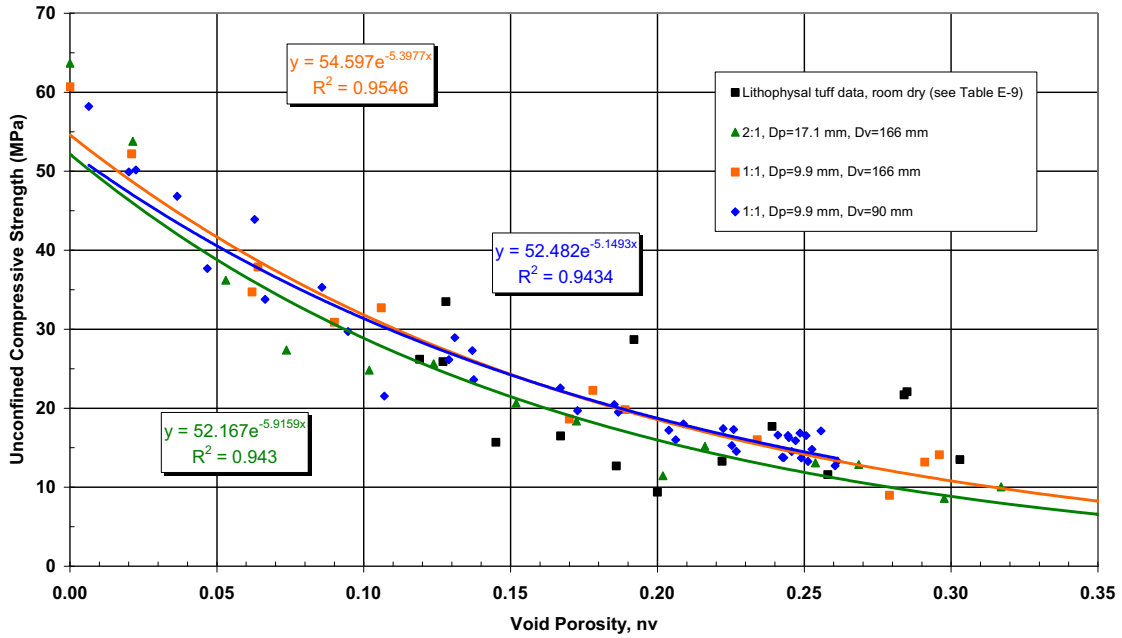


Figure S-4. Unconfined Compressive Strength Versus Void Porosity for Lithophysal Tuff and PFC2D Models of Randomly Distributed Circular Voids

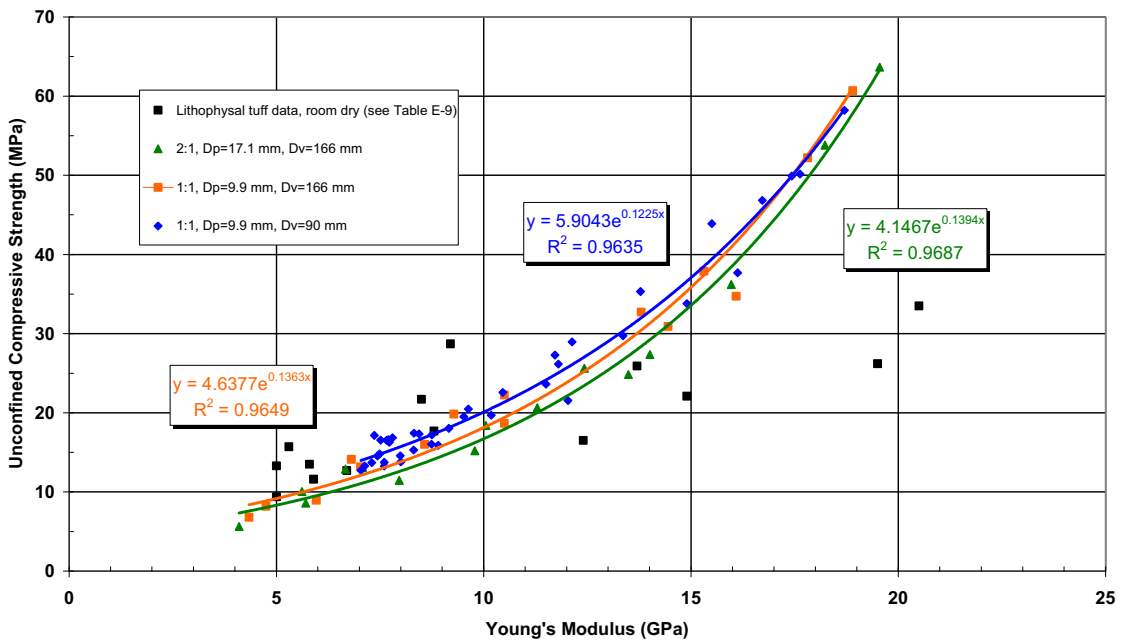


Figure S-5. Young's Modulus Versus Unconfined Compressive Strength for Lithophysal Tuff and PFC2D Models of Randomly Distributed Circular Voids

Table S-3. PFC Resolutions for Lithophysal Tuff Specimens

Resolution ( $D_s = 1000$ mm)	PFC3D 2:1 cyl.	PFC2D 2:1	PFC2D 1:1	PFC2D 1:1
$D_{avg}$ (mm)	52.3	17.1	9.9	9.9
$D_v$ (mm)	166	166	166	90
specimen, $\psi_s = D_s / D_{avg}$	19.1	58.5	101	101
void, $\psi_v = D_v / D_{avg}$	3.2	9.7	16.8	9.1
bridge, $\psi_B = B_{min} / D_{avg}$	0.8	2.4	4.2	4.2

NOTE:  $D_s$  = specimen diameter (mm),  $\psi_s$  = specimen resolution,  $\psi_v$  = void resolution,  $\psi_B$  = bridge resolution. All other parameters defined in Table S-2.  $B_{min} = 41.5$  mm.

### S2.2.2 PFC2D Base Material and Specimen (Long-Term Behavior)

The long-term behavior of the PFC2D material is characterized by performing a series of numerical static-fatigue tests on the PFC2D lithophysal-tuff model using the microproperties in Table S-4. The long-term behavior is controlled by the three PFC stress corrosion model parameters of  $\beta_1$ ,  $\beta_2$ , and  $\bar{\sigma}_a$ . These parameters do not affect the short-term behavior. The properties of the PFC2D material are obtained by testing 1:1 aspect-ratio specimens of one-meter diameter with void porosities of 0, 0.1, and 0.2 under static-fatigue conditions at confinements of 0.1 and 5 MPa. The PFC2D materials have average particle diameters ranging from 10 mm to 40 mm, giving the specimen, void, and bridge resolutions shown in Table S-5. The results presented here were produced for the mS50 specimens (average particle diameter of 20 mm), which provide a specimen resolution of 50 particles across a one-meter diameter specimen. The specimens with non-zero void porosities are shown in Figure S-6.

Table S-4. PFC2D Material for Lithophysal Tuff (Short- and Long-Term Microproperties and Void Geometry)

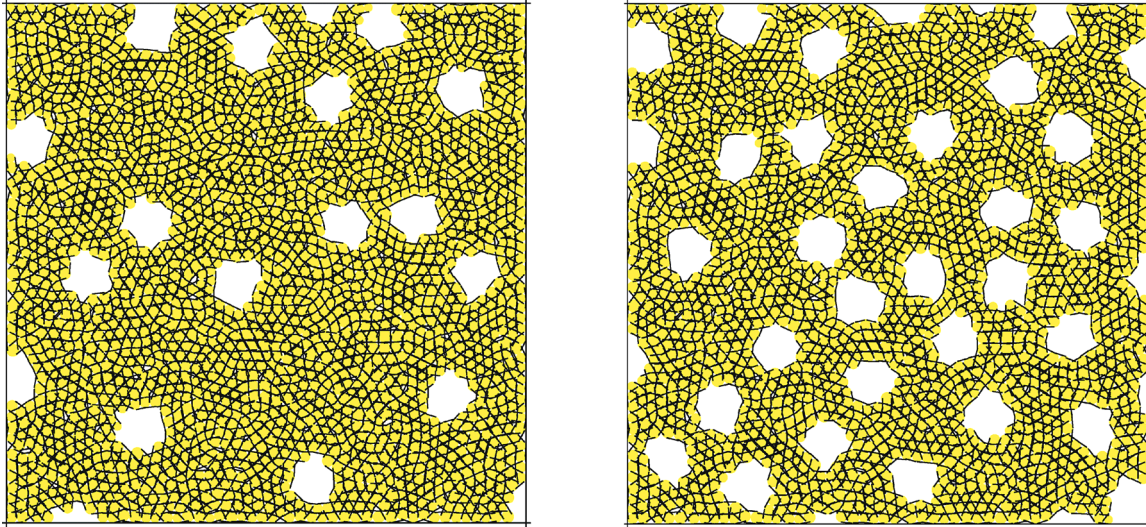
Grains	Cement
$\rho = 2510$ kg/m <sup>3</sup>	N/A
$(D_{max} / D_{min}) = 1.5$ $D_{avg}$ varies (10, 20, or 40 mm)	$\bar{\lambda} = 1$
$E_c = 14.8$ GPa	$\bar{E}_c = 14.8$ GPa
$(k_n / k_s) = 2.1$	$(\bar{k}^n / \bar{k}^s) = 2.1$
$\mu = 0.5$	$\bar{\sigma}_c = \bar{\tau}_c = \text{mean} \pm \text{standard deviation} = 48.11 \pm 11$ MPa
N/A	$\beta_1 = 5 \times 10^{-15}$ m/sec $\beta_2 = 30$ $\bar{\sigma}_a = 0$ MPa $f_r = 1 \times 10^{-4}$ , $n_s = 4$ , $f_s = 2$
<b>Void Geometry:</b> circular, $D_v = 90$ mm, $B_{min} = 41.5$ mm	

NOTE:  $\beta_1$  = rate constant (m/sec),  $\beta_2$  = rate constant (dimensionless),  $\bar{\sigma}_a$  = micro-activation stress,  $f_r$  = equilibrium ratio limit,  $n_s$  = number of steps until the first bond breaks,  $f_s$  = time step multiplier. All other parameters defined in Table S-2.

Table S-5. PFC2D Resolutions for Current Lithophysal Tuff Specimens

Resolution ( $D_s = 1000$ mm)	mS100 (fine)	mS50 (medium)	mS25 (coarse)
specimen, $\psi_s = D_s / D_{avg}$	100	50	25
void, $\psi_v = D_v / D_{avg}$	9.0	4.5	2.3
bridge, $\psi_B = B_{min} / D_{avg}$	4.2	2.1	1.0

NOTE: All parameters defined in Tables S-2 and S-3.



NOTE: Void porosities of 0.107 and 0.204.

Figure S-6. PFC2D Specimens of mS50 Material

### S2.2.3 Selection of Stress Corrosion Algorithm-Control Parameters

The equilibrium ratio limit,  $f_r$ , defines when the system has returned to static equilibrium after each stress-corrosion step. This study uses PFC2D version 2.0, for which the equilibrium ratio is taken as the ratio of maximum unbalanced force over maximum contact force. Numerical static-fatigue tests were performed on the mS50 material with no holes and with  $\bar{\sigma}_a = 19$  MPa at driving-stress ratios ranging from 0.25 to 0.90. The  $f_r$  was varied over three orders of magnitude from  $1 \times 10^{-3}$  to  $1 \times 10^{-6}$  while keeping the other algorithm-control parameters fixed at  $n_s = 2$  and  $f_s = 2.0$ . The failure times were  $4.91 \times 10^5$ ,  $3.66 \times 10^5$ ,  $3.85 \times 10^5$ , and  $3.66 \times 10^5$  seconds, respectively. A plot showing the total number of cracks<sup>6</sup> versus time for a driving-stress ratio of 0.75 is displayed in Figure S-7. These results suggest that the cracking during primary and secondary creep is not affected by the equilibrium ratio limit, but that cracking during the tertiary creep stage and the corresponding failure time is affected by the equilibrium ratio limit. Further study is required to determine what is the equilibrium ratio limit below which the failure time is constant. The results presented here demonstrate that values less than  $1 \times 10^{-3}$  produce similar primary and secondary creep. Therefore, to ensure similar primary and secondary creep, the results in this report were produced using an equilibrium ratio of  $1 \times 10^{-4}$ .

<sup>6</sup> The term “crack” is used throughout this appendix to refer to bond breakages in the PFC material.

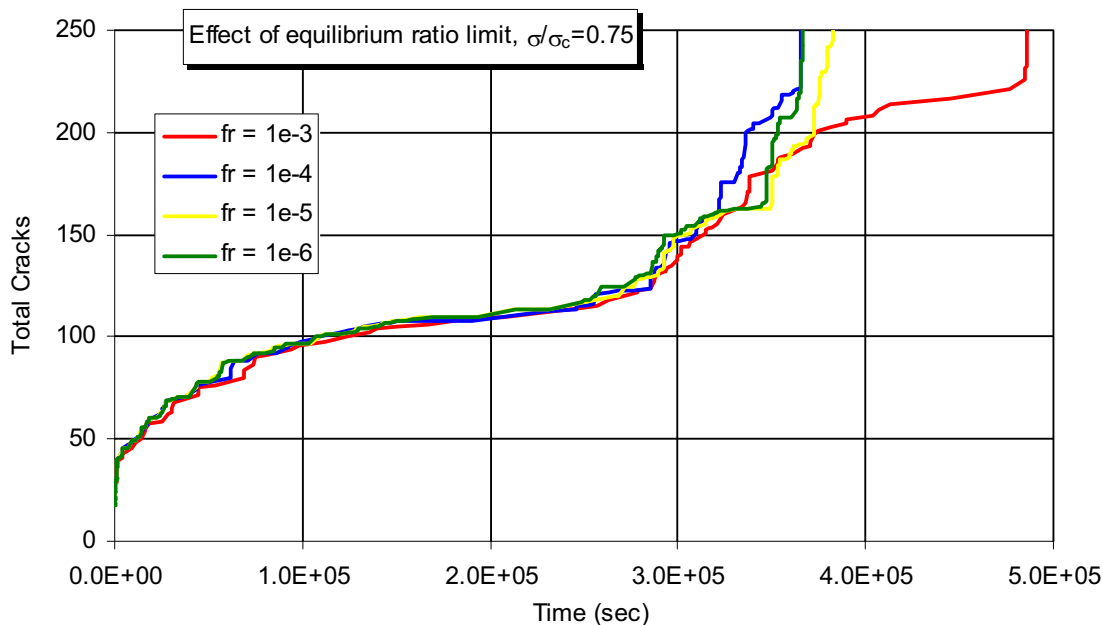
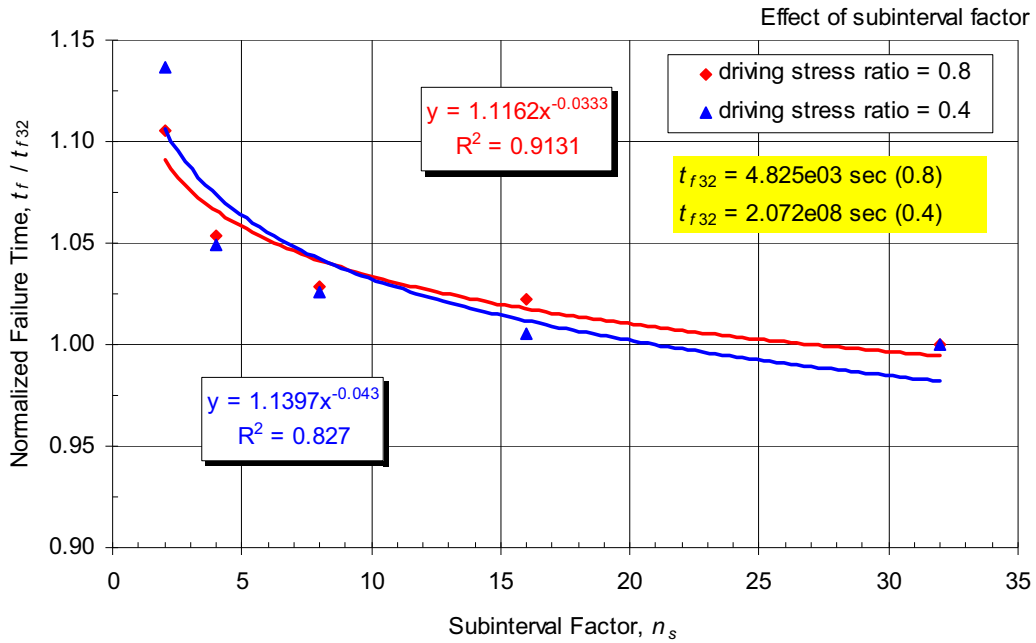


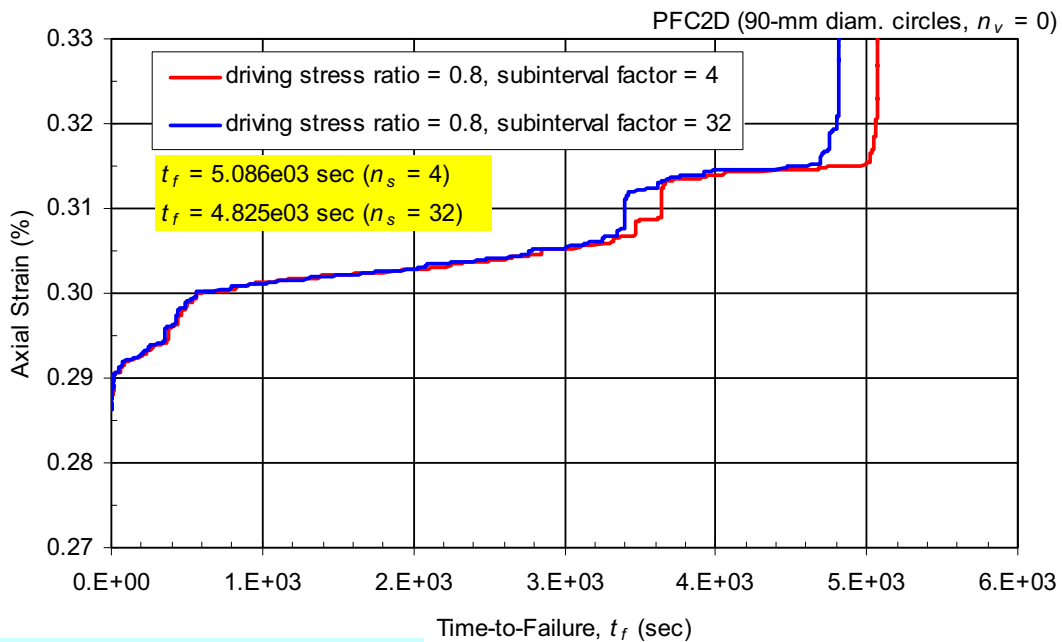
Figure S-7. Number of Cracks Versus Time for Different Equilibrium Ratio Limits

By default, the subinterval factor,  $n_s$ , is set to 2. The effect of increasing this value (and therefore decreasing the initial size of each stress-corrosion time step) is examined here. Numerical static-fatigue tests were performed on the mS50 material with no holes at driving-stress ratios of 0.4 and 0.8, and  $n_s$  was varied from 2 to 32 while keeping the other algorithm-control parameters fixed at  $f_r = 1 \times 10^{-4}$  and  $f_s = 2.0$ . The failure times are normalized by the corresponding failure time for  $n_s = 32$  and plotted versus the subinterval factor in Figure S-8. Increasing the subinterval factor reduces the size of each stress-corrosion time step, which reduces the error associated with considering that the forces remain constant during each step, and is in keeping with the conclusion that as  $\Delta t \rightarrow 0$ , the true macroscopic time-to-failure is approached from above. The creep response is similar for different subintervals as seen in Figure S-9. The results in this report were produced using a subinterval factor of 4. The subinterval factor of 4 results in an error of approximately 5 percent. This error is considered as acceptable with the level of uncertainty in this type of model.



NOTE: Driving-stress ratios of 0.8 and 0.4.

Figure S-8. Normalized Time-to-Failure Versus Subinterval Factor for mS50 Material for Numerical Static-Fatigue Tests (0.1 MPa Confinement)



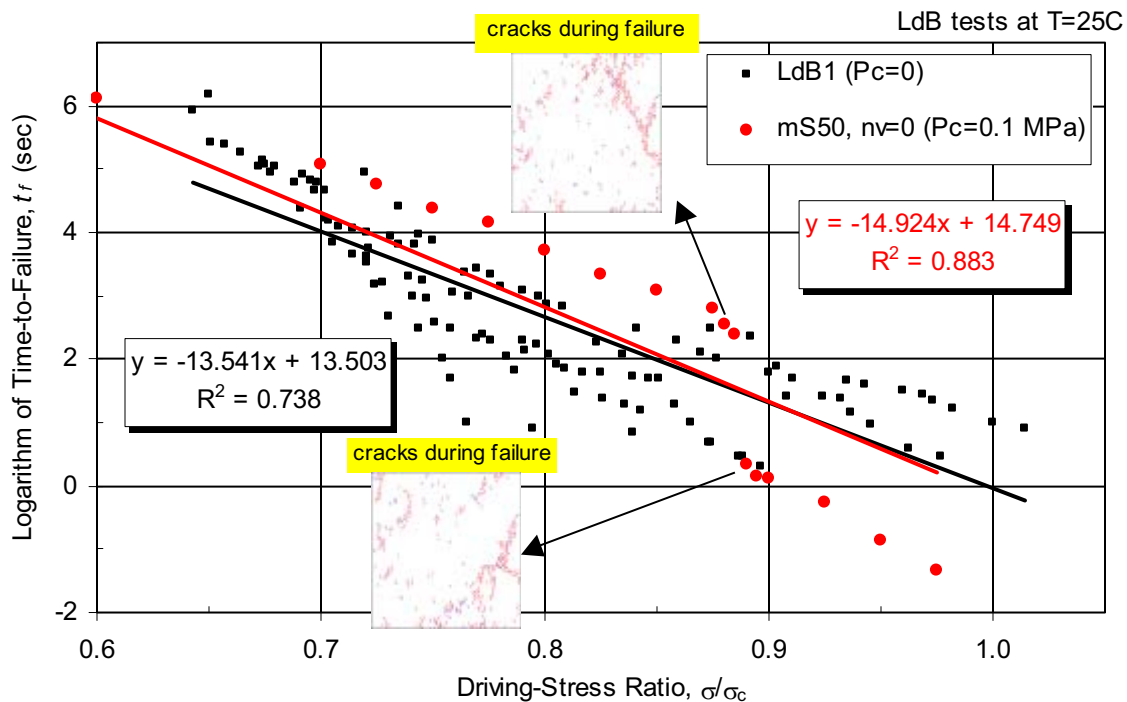
creep curve,  $P_c = 0.1$  MPa

NOTE: Driving-stress ratio of 0.8.

Figure S-9. Effect of Subinterval Factor on Creep Curves for mS50 Material for Numerical Static-Fatigue Tests (0.1 MPa Confinement)

### S2.2.4 Typical Model Behavior During a Static-Fatigue Test

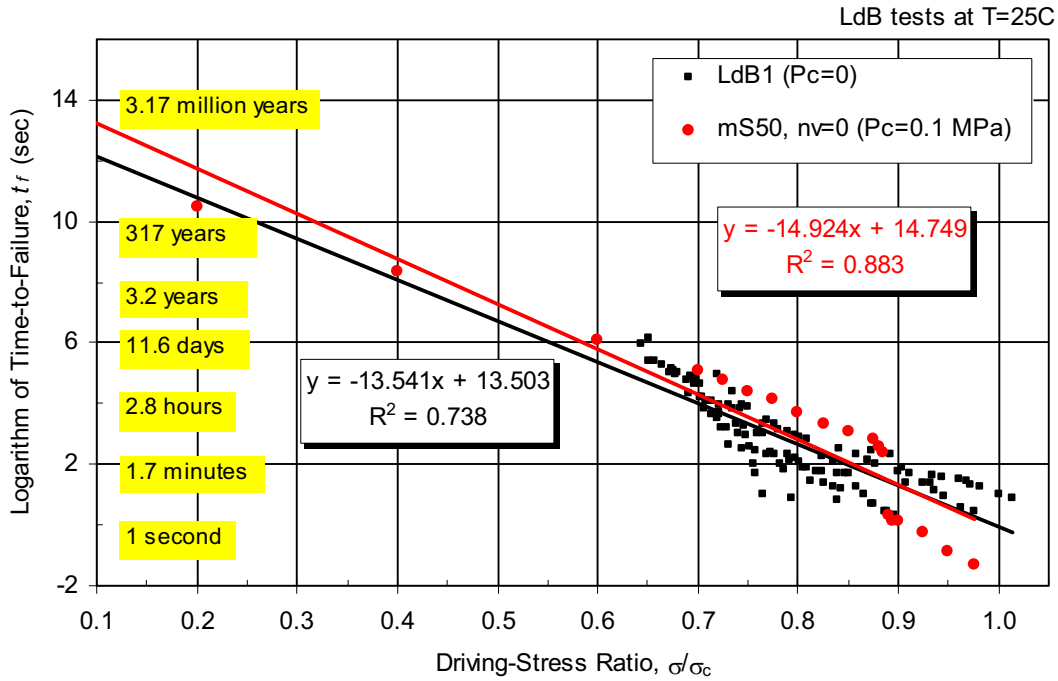
Numerical static-fatigue tests at a confinement of 0.1 MPa were performed upon the mS50 material with no voids to produce the static-fatigue curve shown in Figure S-10. The PFC stress corrosion model parameters of  $\beta_1$  and  $\beta_2$  were chosen to match the LdB1 data set in the range  $0.6 \leq \sigma/\sigma_c \leq 1.0$ . The bump in the curve for  $0.885 \leq \sigma/\sigma_c \leq 0.890$  is caused by a change in the failure mode of the specimen as shown in Figure S-10. The micro-activation stress,  $\bar{\sigma}_a$ , controls the minimum driving-stress ratio for which the time-to-failure becomes infinite. This lower limit for time-dependent failure is called the static-fatigue limit. There is, as yet, no scientific consensus on the value of the static-fatigue limit, although exponential extrapolation of the LdB1 data set by Schmidtke and Lajtai (1985 DIRS [164774]) gives a value of 0.45. Because the mS50 material is being used to generate damage curves to serve as input to the UDEC model, the conservative consideration that  $\bar{\sigma}_a = 0$  is used. A zero value of  $\bar{\sigma}_a$  means that stress corrosion will continue until the micro-tensile forces in the material have been removed. It is found that the time-to-failure is indeed finite for driving-stress ratios larger than 0.2, and that the static-fatigue curve is nearly linear for small driving-stress ratios (see Figure S-11).<sup>1</sup>



NOTE: Data set LdB1 from Figure S-1.

Figure S-10. Static-Fatigue Curve (0.1 MPa Confinement) for mS50 Material for Numerical Static-Fatigue Tests Compared with the Data and Curve for Lac du Bonnet Granite

<sup>1</sup>A better fit to the mS50 data would bend strongly downwards for driving-stress ratios that approach one (because the time-to-failure must approach zero), and would bend slightly downwards for driving-stress ratios that approach zero. Such a fit is used in Appendix S2.2.5.

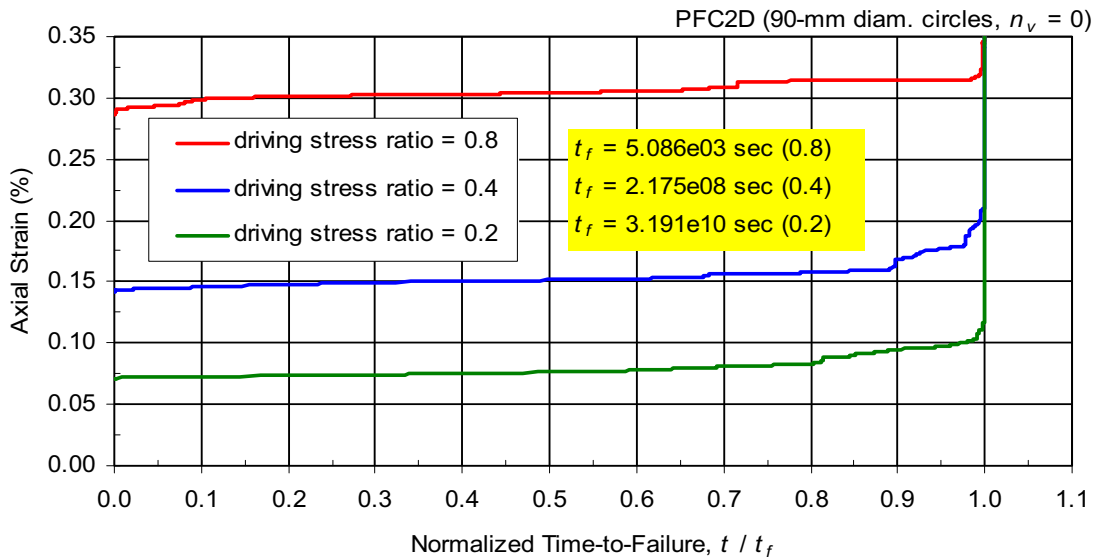


NOTE: Data set LdB1 from Figure S-1.

Figure S-11. Static-Fatigue Curve (0.1 MPa Confinement) for mS50 Material for Numerical Static-Fatigue Tests Compared with the Data and Curve for Lac du Bonnet Granite — Expanded Scales

Representative creep curves are shown in Figure S-12, where the axial strain is plotted versus normalized time-to-failure. The general behavior is one of primary, secondary and tertiary creep. The creep response is produced by the reduction of parallel-bond radii and by the formation of microcracks as can be seen in Figure S-13.

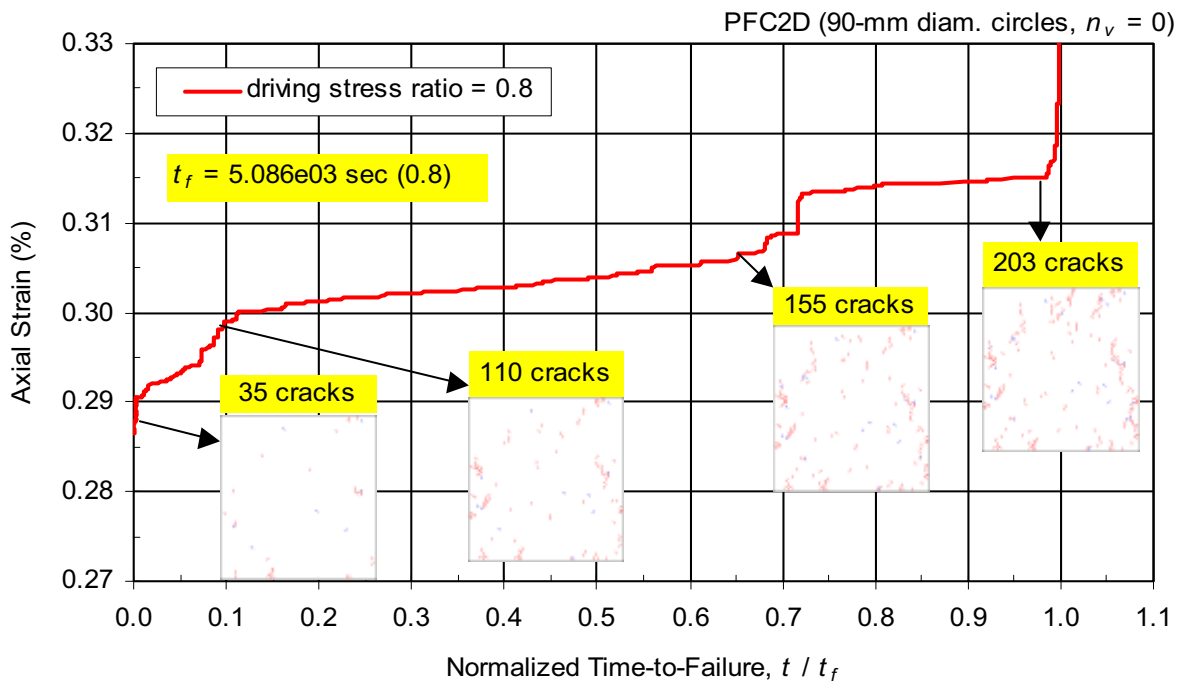




creep curves,  $P_c = 0.1$  MPa

NOTE: Driving-stress ratios of 0.2, 0.4 and 0.8.

Figure S-12. Creep Curves for mS50 Material for Numerical Static-Fatigue Tests (0.1 MPa Confinement)



creep curve,  $P_c = 0.1$  MPa

NOTE: Driving-stress ratios of 0.8.

Figure S-13. Creep Curve and Damage in mS50 Material for Static-Fatigue Test (0.1 MPa Confinement)

### S2.2.5 Effect of Void Porosity and Confinement on Static-Fatigue Curves

The effect of void porosity on the static-fatigue curves of the mS50 material is shown in Figures S-14 and S-15. While the slope of the curves varies slightly, it is generally observed that increasing the void porosity reduces the time-to-failure for the same driving-stress ratio, and the static-fatigue curves are similar. It seems that the curves for various void porosities may be converging for very small driving-stress ratios. Note that in these figures, the data is fit with a fourth-order polynomial instead of a straight line (see Figures S-16 and S-17). Based on the definition of a static-fatigue curve, the time to failure should be zero for a driving-stress ratio of one. The polynomial fit approximates this trend, whereas a linear fit does not. The polynomial fit is used for most figures in this section; however, a linear fit has been used in the remainder of the report. The exact form of the static-fatigue curve is not known, because of a lack of laboratory data for driving-stress ratios below 0.65; thus, for extrapolation purposes, a linear fit was deemed acceptable.

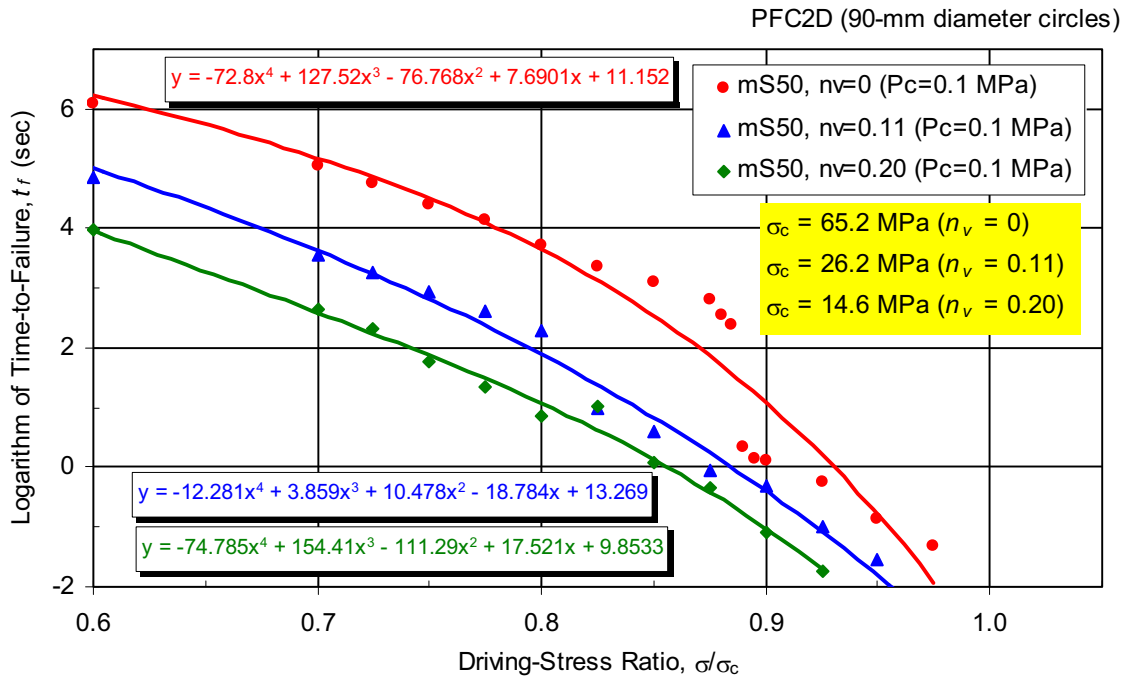


Figure S-14. Effect of Void Porosity on Static-Fatigue Curves (0.1 MPa Confinement) for mS50 Material

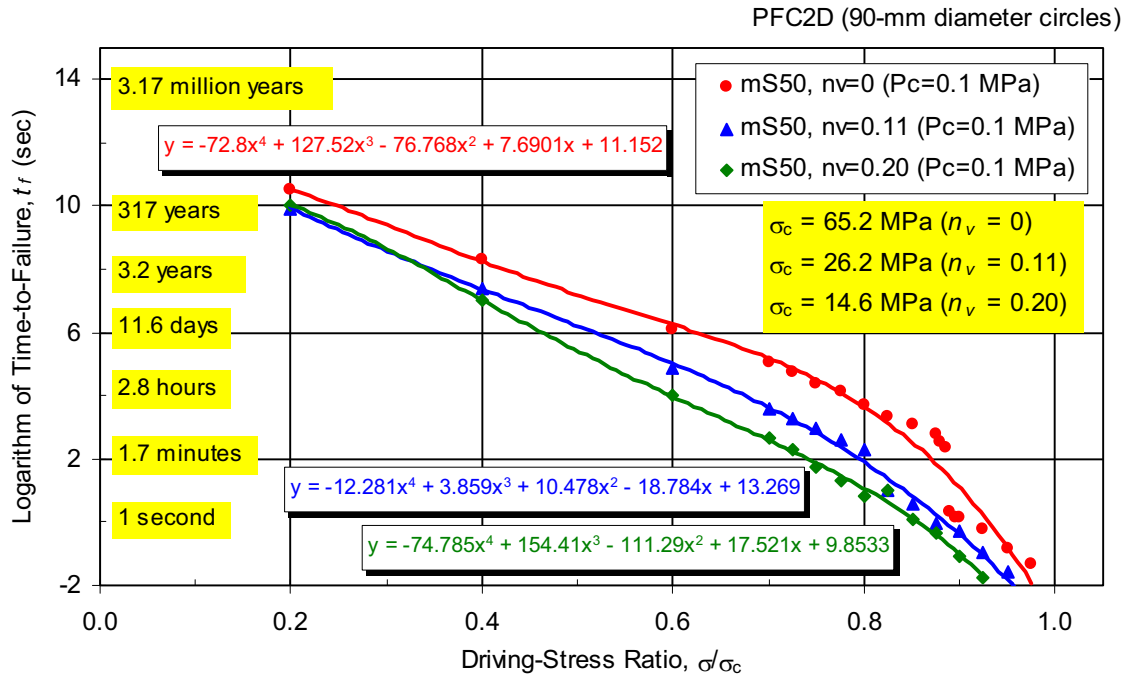


Figure S-15. Effect of Void Porosity on Static-Fatigue Curves (0.1 MPa Confinement) for mS50 Material — Expanded Scales

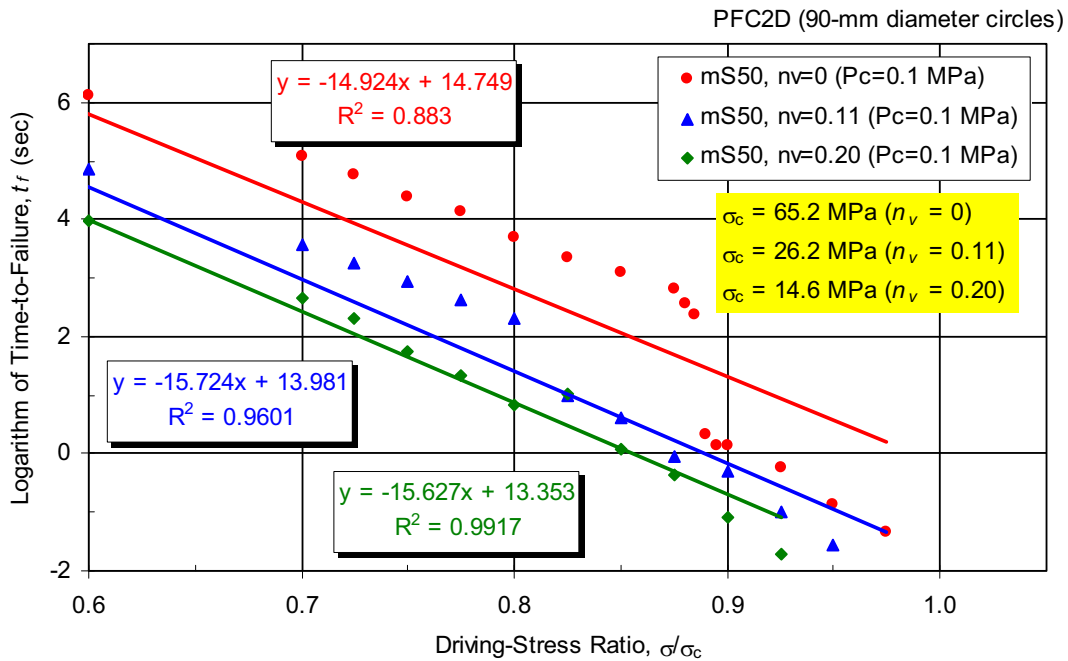


Figure S-16. Effect of Void Porosity on Static-Fatigue Curves (0.1-MPa Confinement) for mS50 Material (Straight-Line Fit)

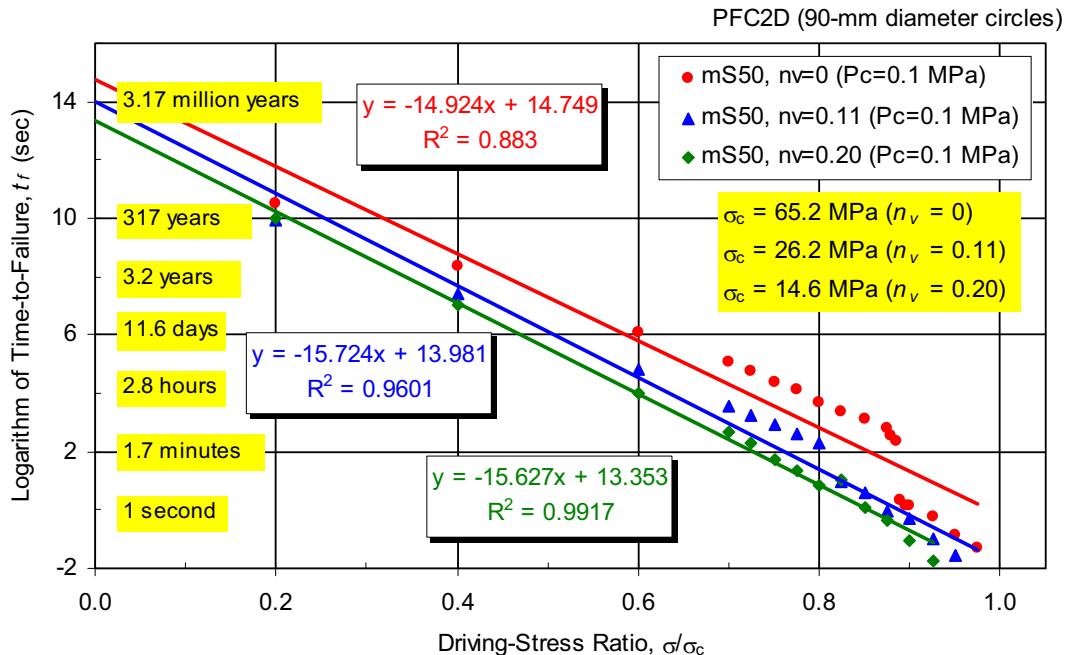


Figure S-17. Effect of Void Porosity on Static-Fatigue Curves (0.1 MPa Confinement) for mS50 Material (Straight-Line Fit) — Expanded Scales

If the linear fit is used for time-to-failure results obtained using PFC for different percentages of lithophysal porosity, the slope of the line is considered independent of the lithophysal porosity. The main effect of lithophysal porosity is translation of the time-to-failure line. Consequently, the line for 20 percent porosity intersects the horizontal line corresponding to 1 s time-to-failure for driving stress ratio of 0.85 (see Figure S-15). The strength after 1 s of loading time is considered to represent the short-term strength of a rock. This implies that if the lines in Figure S-15 are scaled with strength of the rock after 1 s loading time, the lines would coincide with each other. However, the consideration of time-dependent behavior contributes to an additional short-term strength reduction of approximately 15 percent (it is accounted for in the short-term strength reduction because it happens over a time period on the order of a second). In the calculation of time-dependent drift degradation, it is considered that time-to-failure curves are independent of lithophysal porosity. The effect of lithophysal porosity on short-term strength is accounted for because 5 different categories were analyzed. Variation of short-term strength between categories 1 and 5 is from 10 MPa to 30 MPa. The effect of time-dependency, within one or a few seconds, on short-term strength (of the order of 15 percent) is taken into account by the consideration of a wide range of strength variation. Although the time-to-failure curves for different lithophysal porosities are the same, the effect of lithophysal porosity on time-dependent drift degradation is significant. For example, uniaxial compressive elastic stress in the drift wall is estimated to be 17.5 MPa, which is derived considering that the vertical in situ stress ( $\sigma_v$ ) is 7 MPa and the horizontal-to-vertical stress ratio ( $k$ ) is 0.5 (see Section 6.3.1.1), using the relation  $\sigma_l = \sigma_v(3 - k)$  (Hoek and Brown 1982 [DIRS 120981], p. 105). Using the time-to-failure curve for tuff (Figure S-2), time to failure in category 2 corresponding to 28 percent porosity (such that UCS = 20 MPa resulting in a driving stress ratio of 0.875) is approximately 3 hours, while

time-to-failure in category 3 corresponding to 21 percent porosity (such that UCS = 25 MPa resulting in a driving stress ratio of 0.7) is approximately 8,200 years.

The effect of confinement on the static-fatigue curves of the mS50 material is shown in Figures S-18 and S-19. Increasing the confinement increases the time-to-failure for the same driving-stress ratio, and the static-fatigue curves are similar. The effect of void porosity on the static-fatigue curves of the mS50 material at 5 MPa confinement, is shown in Figures S-20 and S-21. Increasing the void porosity reduces the time-to-failure for the same driving-stress ratio; however, the effect is not seen for void porosities greater than 0.11. Based on this numerical assessment, it appears that the effect of void porosity on time-to-failure is reduced as confinement increases, and that there is a limiting void porosity above which no further reduction occurs.

The effect of voids on time-to-failure was investigated numerically (e.g., Figure S-20). The increase in porosity results in shorter time-to-failure. However, the slopes of the lines of time-to-failure versus driving stress ratio are practically the same. That implies that if the driving stress ratio is normalized with the strength for one minute of load duration, the lines would be the same. Thus, the time to failure is independent of the lithophysal porosity if plotted versus normalized driving stress ratio. The evolution of damage as a function of driving stress ratio and time normalized with time-to-failure is similar. Particularly for large driving stress ratios (greater than 0.5), which are of interest because they result in failure for time-scales of 10,000 years or less, there is very little damage increase until time-to-failure is reached when damage suddenly increases resulting in the collapse.

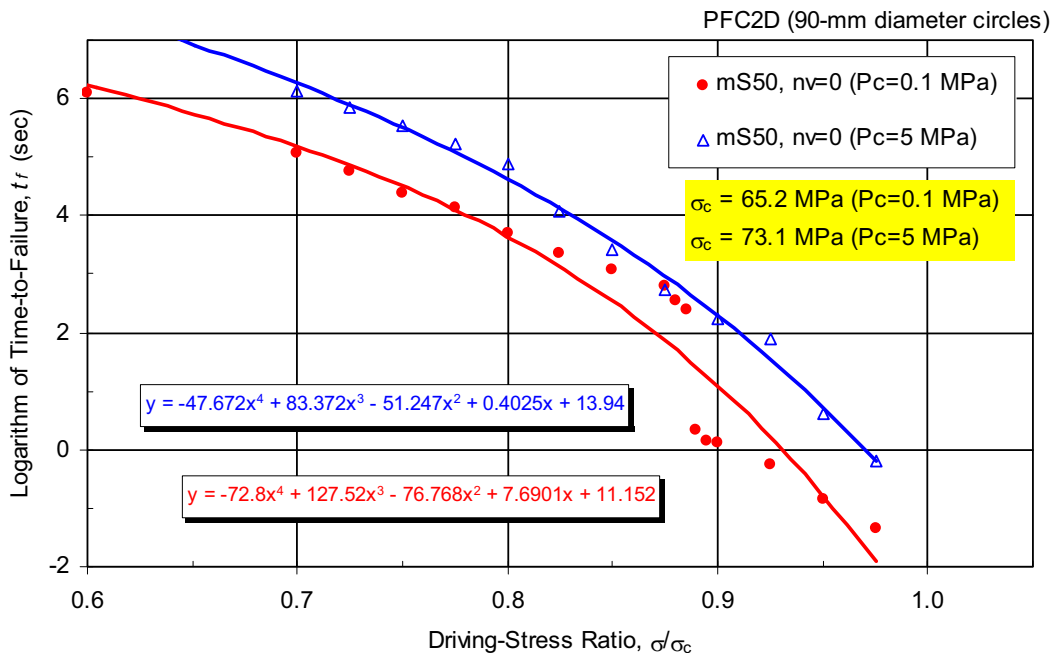


Figure S-18. Effect of Confinement on Static-Fatigue Curves for mS50 Material

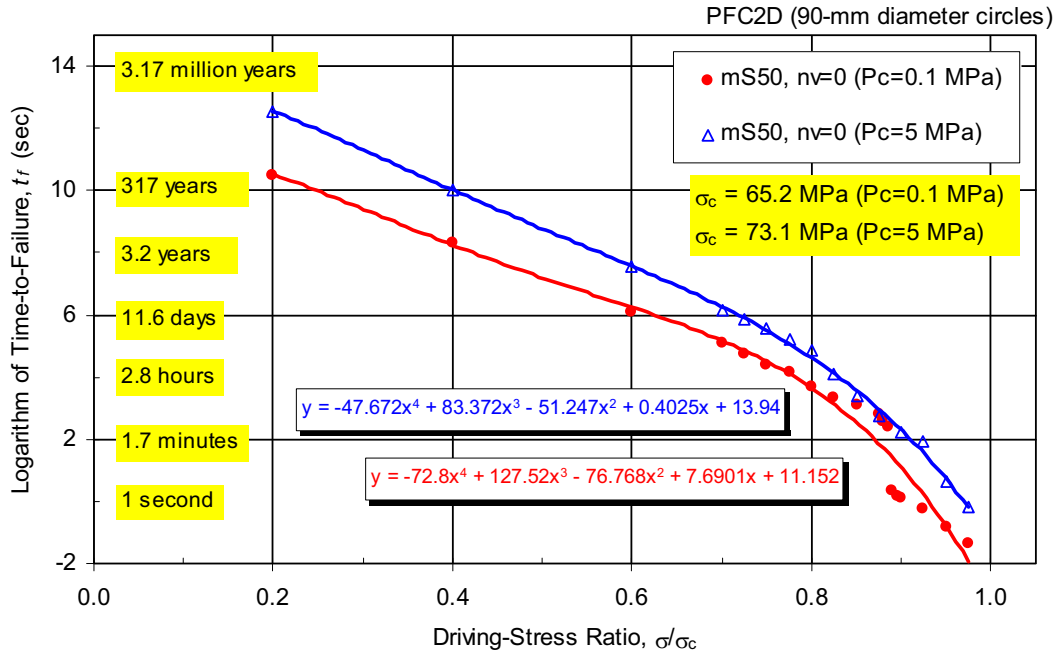


Figure S-19. Effect of Confinement on Static-Fatigue Curves for mS50 Material — Expanded Scales

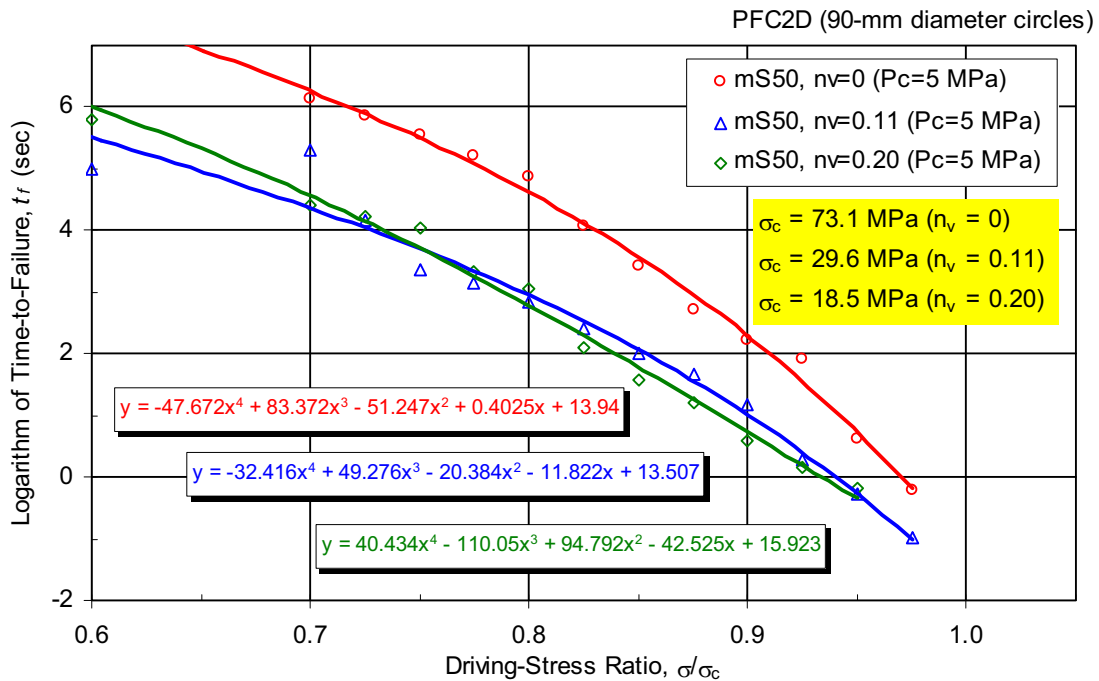


Figure S-20. Effect of Void Porosity on Static-Fatigue Curves (5 MPa Confinement) for mS50 Material

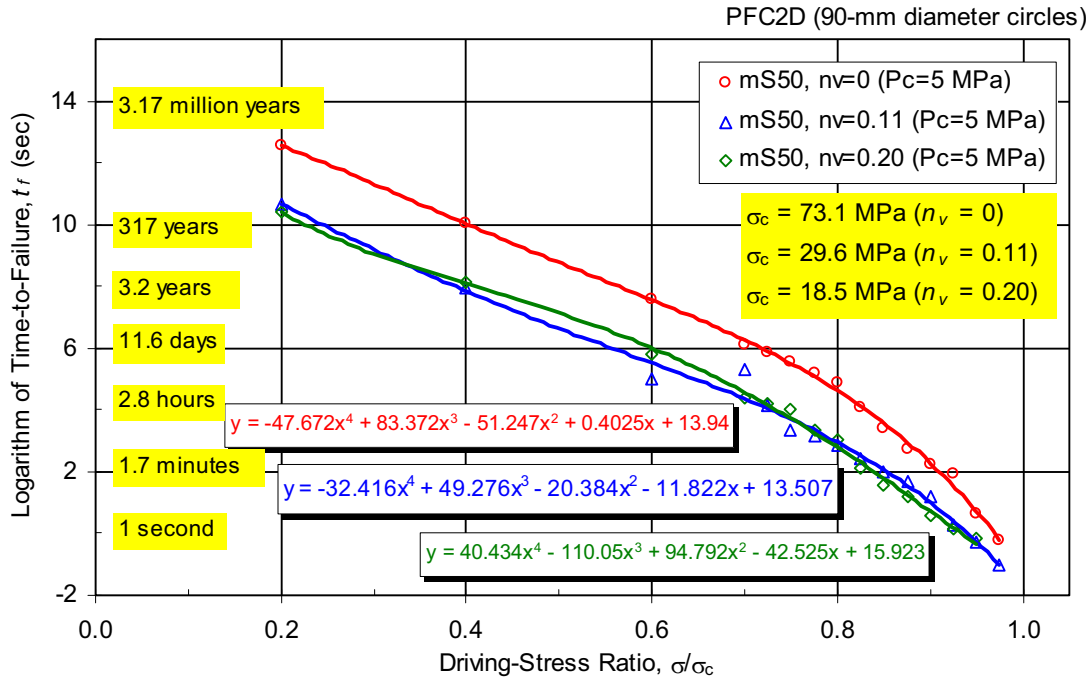


Figure S-21. Effect of Void Porosity on Static-Fatigue Curves (5-MPa Confinement) for mS50 Material — Expanded Scales

### S2.3 QUANTIFYING DAMAGE DURING A STATIC-FATIGUE TEST

The axial load at failure (peak strength) during a short-term test performed at an elapsed time,  $t$ , since the start of a static-fatigue test is denoted by  $\sigma_f^* = \sigma_f^*(t)$ . The values of  $\sigma_f^*$  are bounded by

$$\begin{aligned} \sigma_f^*(0) &= \sigma_f \\ \sigma_f^*(t_f) &= (\sigma/\sigma_c) (\sigma_f - P_c) + P_c \end{aligned} \quad (\text{Eq. S-1})$$

where the notation is defined in the first footnote of Section S2.1. The values of  $\sigma_f^*$  for times  $0 < t < t_f$  are found by stopping the static-fatigue test at the desired time and measuring the peak strength.

The strength degradation is quantified by means of a damage coefficient

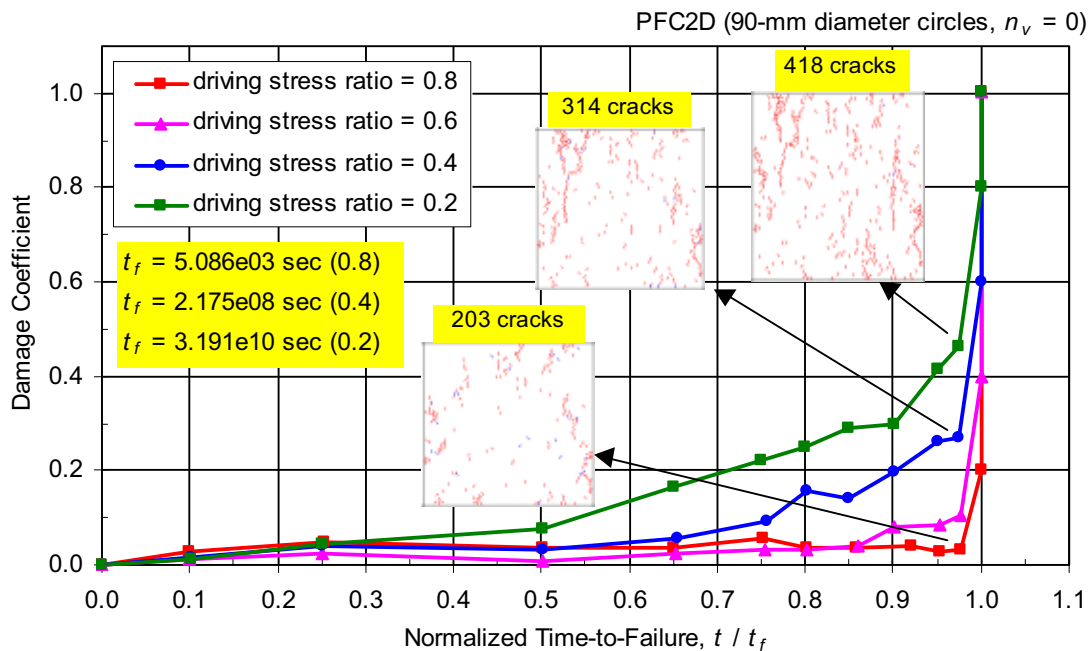
$$D = 1 - \sigma_c^* / \sigma_c \quad (\text{Eq. S-2})$$

where  $\sigma_c^* = \sigma_f^* - P_c$  is the stress difference at failure. Substituting values from Equation S-1 into this expression provides the following bounds for the damage coefficient:

$$\begin{aligned} D(0) &= 0 \\ D(t_f) &= 1 - (\sigma/\sigma_c) \end{aligned} \quad (\text{Eq. S-3})$$

The time evolution of the damage coefficient for the mS50 material tested at a confinement of 0.1 MPa is shown in Figure S-22, which was produced by performing 11 compression tests

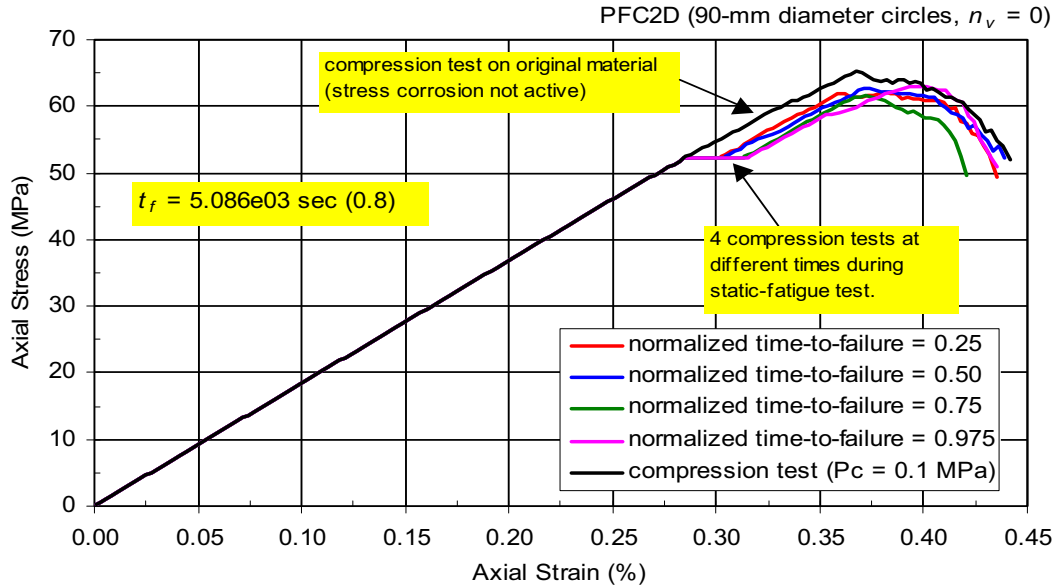
during the four numerical static-fatigue tests at driving-stress ratios of 0.8, 0.6, 0.4 and 0.2. Typical model responses during some of the compression tests are shown in Figures S-23 to S-25. It is noted that the curve for  $t/t_f = 0.975$  in Figure S-23 results in a higher axial stress compared to the other curves. This behavior is a result of complex interactions in the model (and in actual rock). The peak strength in an unconfined compressive strength test is a measure of a critical state forming, and if a very slightly different critical state forms, a slightly different strength will be measured. This means that there is no reason why it is not possible that the addition of a few additional cracks (and reduced parallel bond radii in the PFC the stress corrosion model) might not increase the strength. The critical state at peak is very complex, and a minor change in rearrangements of force chains (i.e., trajectories of magnified principal stresses) might lead to a small increase in strength. Most damage occurs during the final stages of a static-fatigue test, and tests performed at lower driving-stress ratios produce an earlier (in terms of normalized times-to-failure) onset of damage.



NOTE: Driving-stress ratios ranging from 0.2 to 0.8.

Figure S-22. Time Evolution of Damage Coefficient for mS50 Material During Numerical Static-Fatigue Tests (0.1 MPa Confinement)

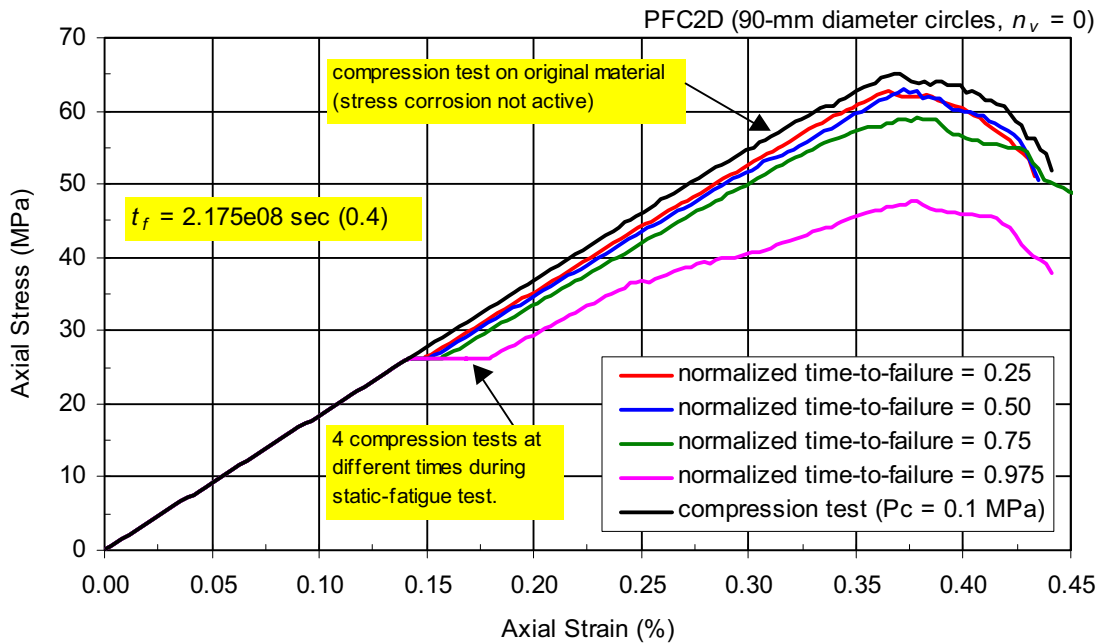




stress-strain curves,  $\sigma/\sigma_c = 0.8$

NOTE: Driving-stress ratio of 0.8.

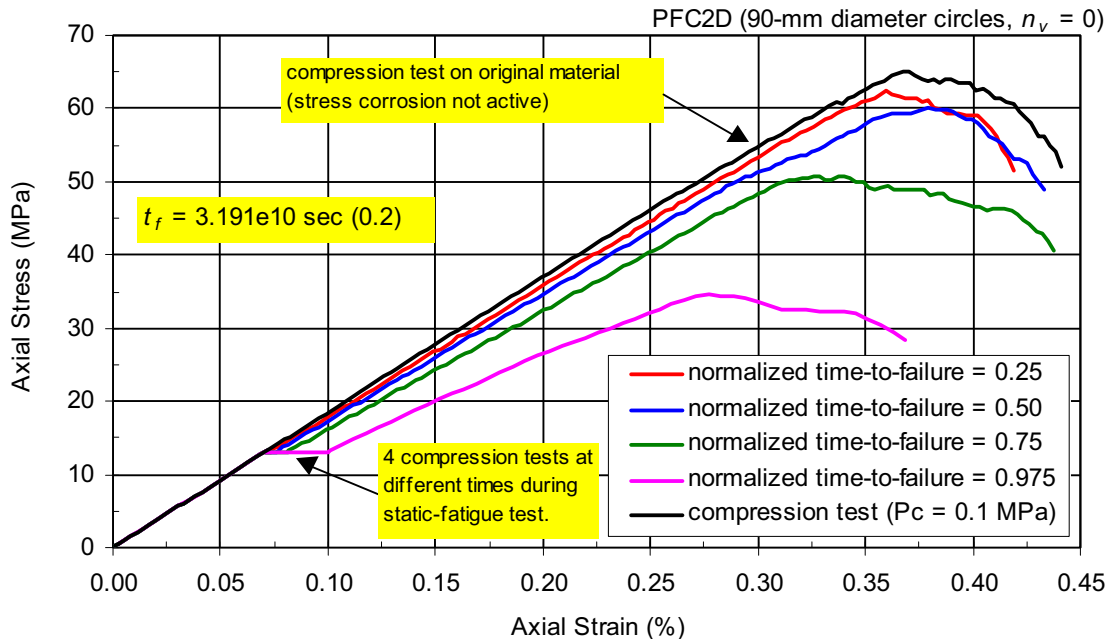
Figure S-23. Stress-Strain Curves for mS50 Material at Different Times During Static-Fatigue Test (0.1 MPa Confinement)



stress-strain curves,  $\sigma/\sigma_c = 0.4$

NOTE: Driving-stress ratio of 0.4.

Figure S-24. Stress-Strain Curves for mS50 Material at Different Times During Static-Fatigue Test (0.1 MPa Confinement)



stress-strain curves,  $\sigma/\sigma_c = 0.2$

NOTE: Driving-Stress Ratio of 0.2.

Figure S-25. Stress-Strain Curves for mS50 Material at Different Times During Static-Fatigue Test (0.1 MPa Confinement)

### S3. MODELING TUNNEL STABILITY WITH UDEC

The objective of the analysis presented in this section is to predict the amount of rockfall in the emplacement drifts due to long-term (approximately 10,000 years) strength degradation caused by stress corrosion of the lithophysal rock units combined with thermal and seismic loads.

The two-dimensional distinct element code UDEC (Version 3.1) was used to investigate drift degradation based upon the time evolution of damage due to strength degradation for different driving-stress ratios ( $\sigma/\sigma_c$ ).

#### S3.1 UDEC MODEL FOR DRIFT DEGRADATION

The same UDEC model validated and used to predict the amount of rockfall in the emplacement drifts (as documented in Sections 6.4 and 7.6) was used to investigate the long-term degradation caused by stress corrosion of the lithophysal rock units.

In the UDEC model, the rock mass is represented as an assembly of polygonal, elastic blocks. The entire domain is discretized into blocks using Voronoi tessellations (Itasca Consulting Group 2002 [DIRS 160331]). The joints between the blocks are considered to be linearly elastic-brittle. The elastic behavior of the joints is controlled by normal and shear stiffness. The joints can sustain finite tensile stress as prescribed by a tensile strength. The Coulomb slip condition governs the onset of slip as a function of joint cohesion and friction angle. If a joint fails either in tension or shear, tensile strength, friction and cohesion are reset to residual values. The model

allows for the formation of joints between blocks, separation and instability (under gravity) of portions of the rock mass around the drift. The average size of the Voronoi blocks is 0.3 m. No ground support was considered in the analysis.

The geometry of the UDEC model is shown in Figure 6-116. Only the region around the drift (where inelastic deformation is expected) is discretized into Voronoi blocks. The remainder of the model is composed of a few large elastic blocks.

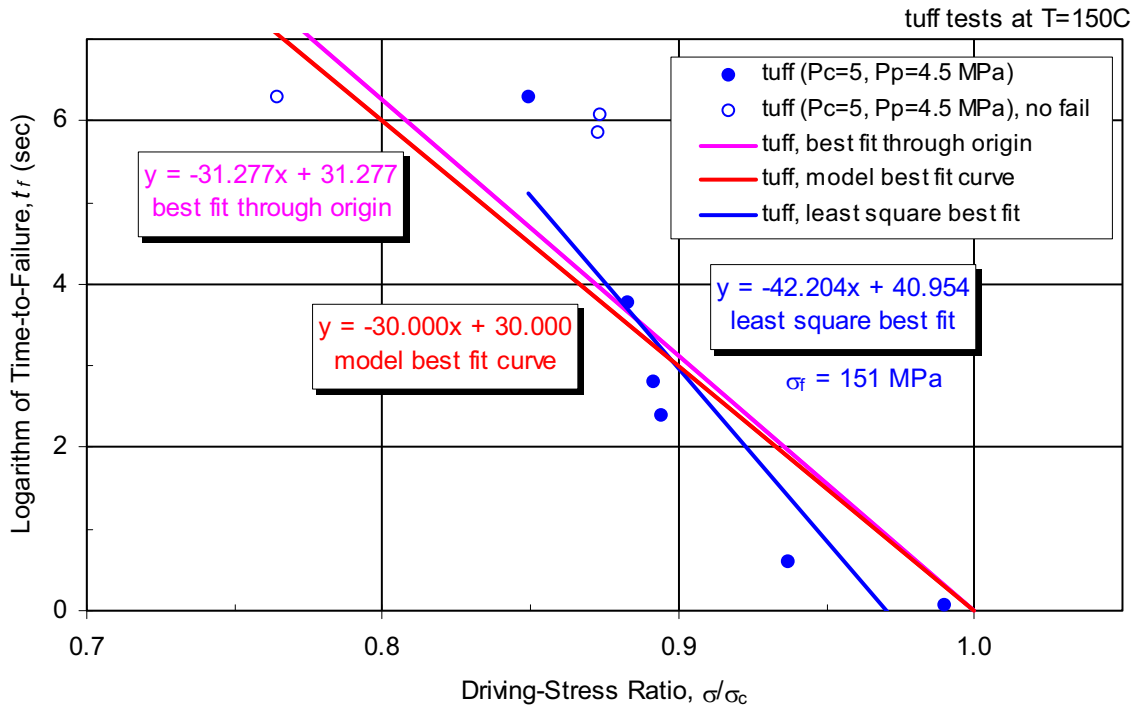
Four different categories of the lithophysal rock mass were used to investigate the long-term degradation caused by stress corrosion. The categories investigated were 1, 2, 3, and 5. The calibrated UDEC micro-properties for those categories are listed in Table 6-43.

### **S3.2 STATIC-FATIGUE CURVES AND THE EVOLUTION OF DAMAGE DUE TO STRENGTH DEGRADATION**

The static-fatigue behavior of Lac du Bonnet granite and welded lithophysal tuff forms the basis of the UDEC model for stress corrosion around a drift. The static-fatigue curves provide the time-to-failure ( $t_f$ ) of the material at a particular driving-stress ratio ( $\sigma/\sigma_c$ ).

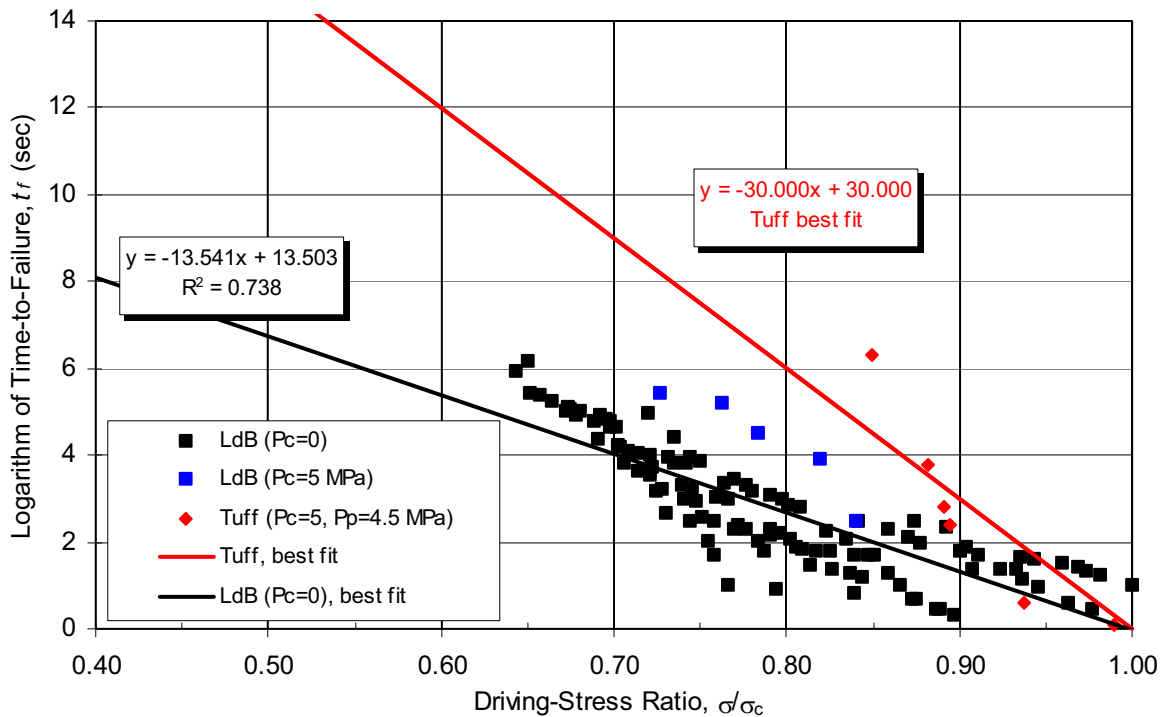
The static-fatigue data for Lac du Bonnet granite at 0 and 5 MPa confinement, tuff at 5 MPa confinement, and 4.5 MPa pore pressure, are shown in Figure S-2. Each data set was fit with a straight line, and the line was extrapolated to encompass driving-stress ratios ranging from zero to one. This is a conservative consideration, because the curves most likely approach infinity at a driving-stress ratio greater than zero (see the discussion in Appendix S2.2.4). Three lines for the tuff data are shown in Figure S-26. The blue line in the figure is the least-square linear fit through the tuff data, while the purple line (labeled “tuff, best fit through origin”) is the best fit for the tuff data with the origin (i.e., logarithm of time-to-failure = 0) set at a driving-stress ratio of one. Since the tuff data are limited and are for confined conditions (effective confining stress of 0.5 MPa) only, the UDEC model has used a simplified best fit (red line) for the tuff best-fit curve.

The two sets of extended curves that were used as input to the UDEC analyses are shown in Figure S-27: one set based on the Lac du Bonnet data and the other set based on tuff data.



Source: Tuff data from Martin et al. (1997 [DIRS 165960]).

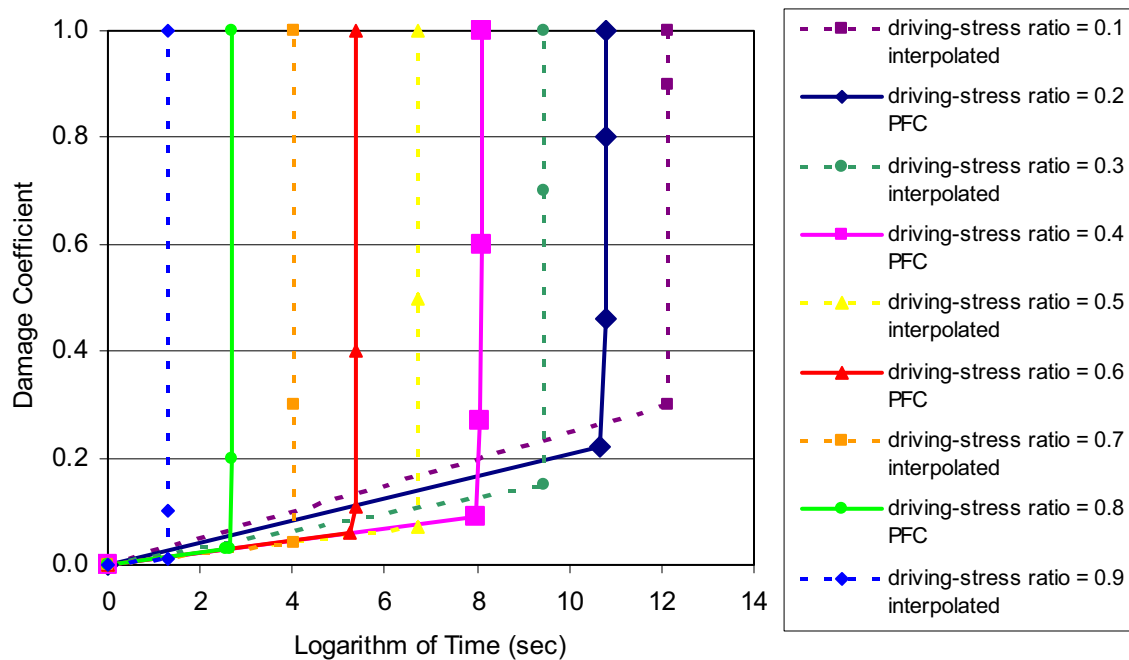
Figure S-26. Static-Fatigue Data for Welded Tuff and Best-Fit Lines



Source: LdB data from Schmidtke and Lajtai (1985 [DIRS 164774]) and Lau et al. (2000 [DIRS 164769]); tuff data from Martin et al. (1997 [DIRS 165960]).

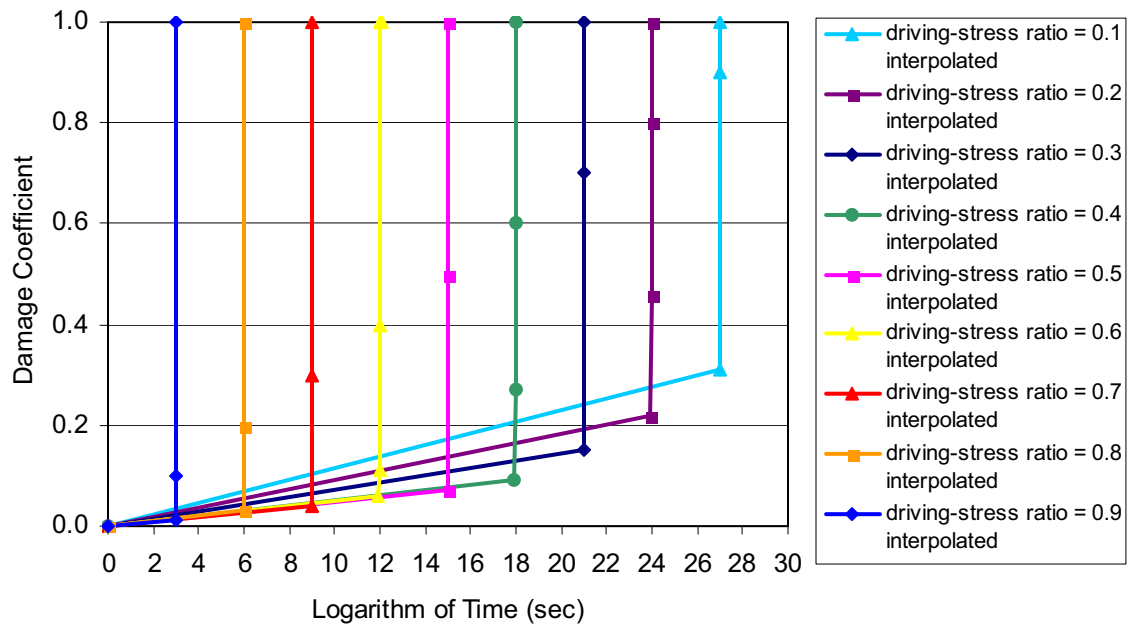
Figure S-27. Static-Fatigue Curves Used as Input to the UDEC Analyses

An understanding of the evolution of damage due to strength degradation during a static-fatigue test prior to the time-to-failure enables a modeling methodology to be developed whereby the strength of material is degraded with time based upon the local driving-stress ratio. The evolution of damage due to strength degradation for the static-fatigue curve (unconfined Lac du Bonnet granite) was developed using the PFC stress corrosion model and is shown in Figure S-22 for Lac du Bonnet granite. The evolution of damage for tuff (i.e., unconfined best-fit tuff) was not obtained by conducting a PFC simulation, but by changing the time scale of the relation between damage and time for the Lac du Bonnet granite. These damage curves were simplified (as shown in Figures S-28 and S-29), and then used along with the static-fatigue curves in Figure S-27 to provide the degradation input properties used in the UDEC analyses.



NOTE: Each curve has a vertical asymptote at a time-to-failure for a given driving-stress ratio, which is provided by the LdB ( $P_c = 0$ ) curve from Figure S-27. The evolution of damage up to the vertical asymptote (i.e., the failure time) is provided by the PFC stress corrosion model.  $P_c = 0$ .

Figure S-28. Damage Curves Used as Input to the UDEC LdB Analyses



NOTE: Each curve has a vertical asymptote at a time-to-failure for a given driving-stress ratio, which is provided by the tuff best fit ( $P_c = 0$ ) curve from Figure S-27. The evolution of damage up to the vertical asymptote (i.e., the failure time) was not provided by the PFC stress corrosion model, but was obtained by changing time scales for each curve proportional to the relation between damage and time for the Lac du Bonnet granite (Figure S-28).  $P_c = 0$ .

Figure S-29. Damage Curves Used as Input to the UDEC Tuff Best-Fit Analyses

Two parameters control the UDEC predictions of time-dependent strength degradation, and eventually the predictions of rockfall: a) time-to-failure, and b) damage rate before time-to-failure. The evolution of damage before failure can be approximated with a constant damage rate. Time-to-failure as a function of the stress state (i.e., the driving stress) is determined from the static-fatigue lines constructed by interpolation and extrapolation of testing results (obtained on tuff and Lac du Bonnet granite). Damage rates at different stress levels are generated using the PFC stress corrosion model. To address the concern about the level of uncertainty in PFC predictions, and how the damage rates affect the final result of the model (i.e., the rockfall induced by time-dependent strength degradation), the sensitivity of the model predictions to the damage rate was investigated. New damage curves are generated for tuff best-fit static-fatigue (shown in Figure S-30), where the damage rates for the driving stress levels are considered to be the same, equal to the maximum rate predicted by PFC.

The rockfall predictions due to time-dependent strength reduction, using damage curves from Figure S-30, are shown in Figure S-31. It is clear that the considered variation of damage rates has no practical effect on predicted rockfall. The time-to-failure is the main factor controlling evolution of the rockfall due to time-dependent strength reduction. Consequently, UDEC predictions are not very sensitive to the input from the PFC stress corrosion model.

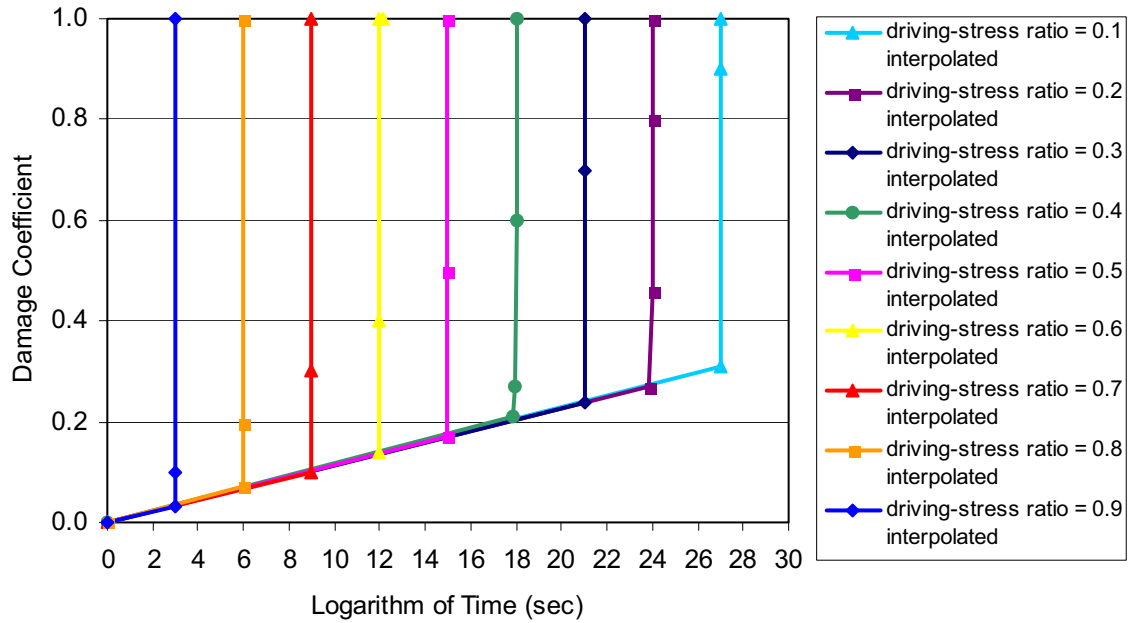


Figure S-30. Damage Curves for Sensitivity Analysis of Damage Rate

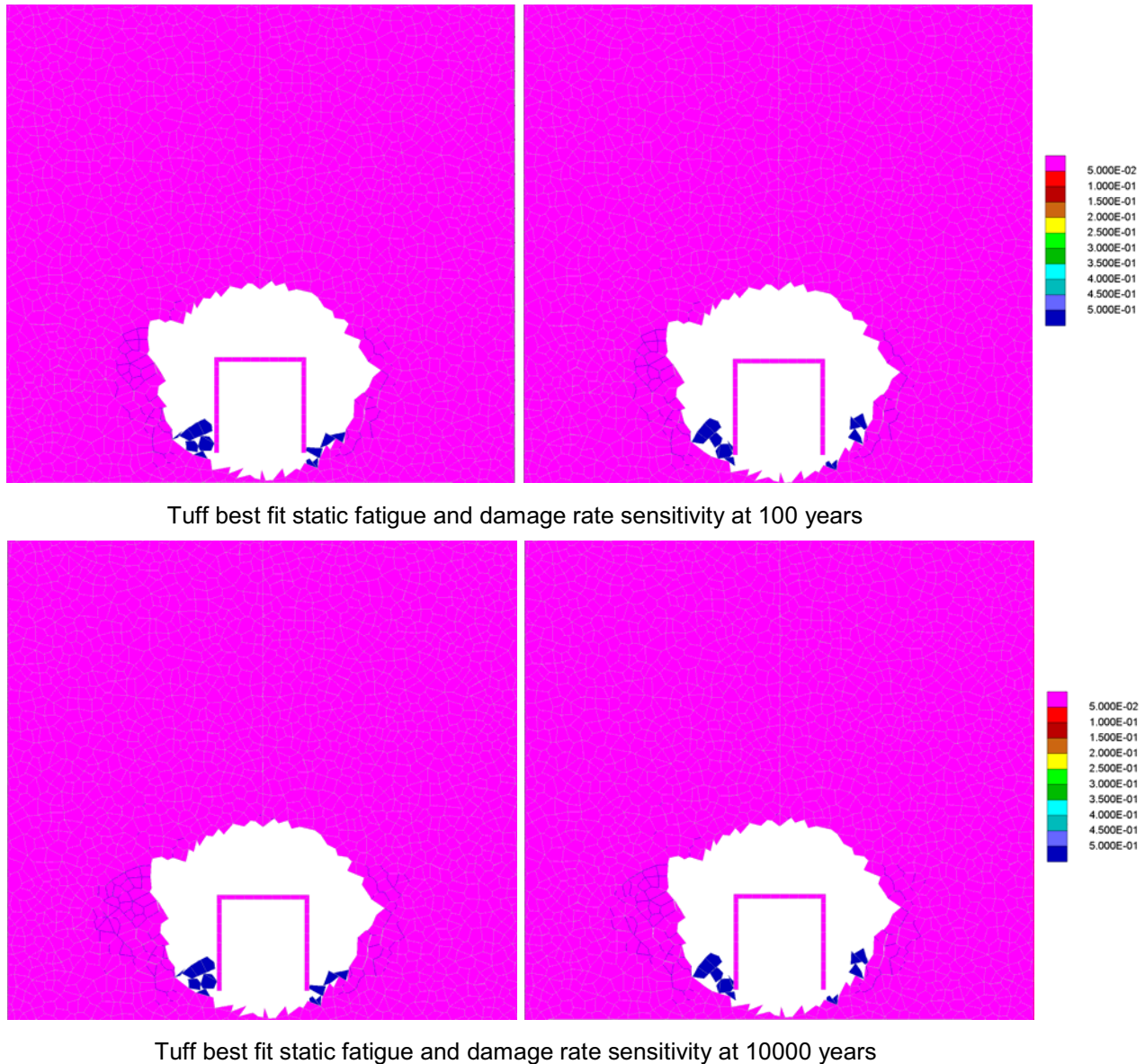


Figure S-31. The Effect of the Damage Rate on Rockfall Predictions Due to Time-Dependent Strength Degradation After 100 Years and 10,000 Years

### S3.3 UDEC STRESS CORROSION MODELING

The long-term strength degradation caused by stress corrosion of the lithophysal rock units was implemented in the UDEC model by incrementally referencing a series of evolution of damage due to strength degradation tables from the PFC stress corrosion model (shown in Figures S-28 and S-29). Based upon the local driving-stress ratio at the Voronoi block contacts within the UDEC model, the strength of the contact in the model is degraded as a function of time. The times considered were 1, 5, 10, 50, 100, 500, 1000, 5000 and 10,000 years.



Time-dependent strength degradation in the UDEC model is generalized by a damage coefficient,  $D$ , which is, in general, in the range between 0 and 1. The cohesion and tensile strength of the material are considered to be functions of time:

$$\begin{aligned} c(t) &= c_0 D(t) \\ T(t) &= T_0 D(t) \end{aligned} \quad (\text{Eq. S-4})$$

where  $c_0$  and  $T_0$  are the cohesion and tensile strength of joints in the UDEC model. The short-term strength of the UDEC synthetic model of the rock mass (large scale) is proportional to the cohesion and tensile strength of joints,  $c_0$  and  $T_0$ , respectively. Consequently, the time-dependent strength of the UDEC synthetic model of lithophysal rock mass will decay proportionally to  $D(t)$ .

It is considered that in the general case:

$$\frac{dD}{dt} = f(\mathbf{F}, D) \quad (\text{Eq. S-5})$$

where  $\mathbf{F}$ , a function of stress state and material strength, defines the load level (driving stress). For unconfined stress conditions (i.e.,  $P_c = 0$ ), the function  $\mathbf{F}$  must be identical to the ratio of the axial load and the unconfined short-term strength:  $\mathbf{F}(P_c = 0) \equiv \sigma_f / \sigma_f$ . The load at failure during a short-term test is calculated as follows (Jaeger and Cook 1979 [DIRS 106219], pp. 95 to 97):

$$\begin{aligned} \sigma_f &= P_c N_\phi + 2c\sqrt{N_\phi} \\ N_\phi &= \frac{1 + \sin \phi}{1 - \sin \phi} \end{aligned} \quad (\text{Eq. S-6})$$

where  $c$  and  $\phi$  are the rock mass cohesion and friction angle, respectively. It is considered that if time-to-failure for two different stress states is the same, then evolution of damage due to strength degradation for both states as a function of time is the same, irrespective of the confinement. Based on the existing data (Lau et al. 2000 [DIRS 146749]; Schmidtke and Lajtai 1985 [DIRS 164774]), it can be concluded that the confinement affects the slope,  $k(P_c) = \Delta(\sigma / \sigma_c) / \Delta \log(t_f)$ , of the static-fatigue line. For example, the slopes of the static-fatigue lines for LdB granite (Figure S-1) are:

$$\begin{aligned} k(0) &= 0.074 \quad 1/\log(\text{sec}) \\ k(5 \text{ MPa}) &= 0.041 \quad 1/\log(\text{sec}) \end{aligned} \quad (\text{Eq. S-7})$$

Because static-fatigue lines are available for only two values of confining stress (0 and 5 MPa) it was considered that the dependence of slope  $k$  on confinement  $P_c$  is linear. This consideration is not a consequence of limitation of the implementation, but due to limited data. The form of the function  $\mathbf{F}$  used in the UDEC model is as follows:

$$\mathbf{F} = 1 - \frac{k(0)}{k(P_c)} \left( 1 - \frac{\sigma}{\sigma_c} \right) \quad (\text{Eq. S-8})$$

The damage evolution  $D(F;t)$  was generated using PFC2D for values of function  $F$  in the range between 0 and 1 (see Figure S-22), and used as the UDEC input data in a tabular form (see Figure S-28.). Interpolation was carried out for stress states in the model during the simulation for which function  $F$  did not coincide with values for which the tables were provided.

It is realistic for implementation that the damage increment in Equation S-5 depends implicitly on stress history. The damage increment depends on accumulated damage, which is a function of the stress history. Although the stress state at a point can undergo complex history as a function of time (due to stress redistribution), it is sufficient in the simulation to keep track of accumulated damage only.

The calculation of the damage increment in the UDEC simulation was carried out in the following way. For a given time increment,  $\Delta t$ , it is considered that the stress state and the stress function,  $F$ , at a given point in the model are constant,  $F = F_i$ . The table of damage evolution  $D(F;t)$  is selected or interpolated based on tables provided. A point on the damage evolution curve corresponding to accumulated damage  $D_j$  is determined,  $D_j = D(F_i;t_j)$ . The damage increment is calculated as follows:

$$\Delta D = D(F_i;t_j + \Delta t) - D(F_i;t_j) \quad (\text{Eq. S-9})$$

Time increment(s) for the simulation must be selected. The criteria for selection are the accuracy of the simulation (stress state considered to be constant during the time increment) and calculation time. Preliminary investigations showed that initially selected time increments did not significantly affect model results. For example, the results in Figure S-36 are obtained for the same conditions as the results in Figure S-38, but using the following points in time: 1, 2, 3, 5, 10, 20, 30, 50, 100, 200, 300, 500, 1000, 2000, 3000, 5000 and 10,000 years. The results are not identical. However, the difference is insignificant considering other uncertainties in the model, and the use of the selected time increments is justified.

Damage is calculated and accumulated for joints. The stress state used for calculation of the damage is determined by averaging stresses in the blocks separated by a joint.

### **S3.4 MODELING RESULTS**

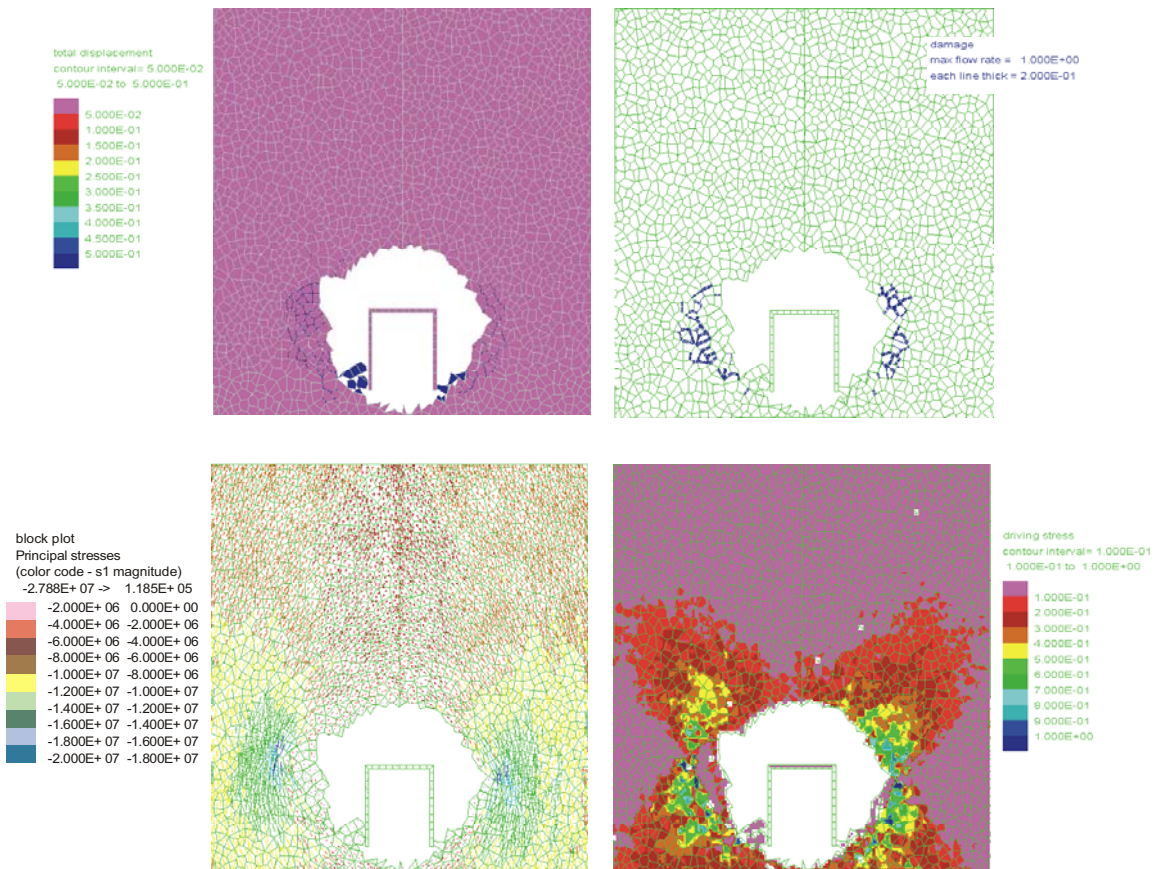
#### **S3.4.1 Time-Dependent Consideration in Lithophysal Units**

The drift degradation results are presented as damage and displacement plots at time increments of 1, 5, 100, 1000, 5000 and 10,000 years. A complete set of damage and displacement results for the tuff static-fatigue curves at lithophysal categories 1, 2, 3, and 5 are presented in this section. Lac du Bonnet granite static-fatigue curves are analyzed for lithophysal categories 1, 2, and 5, only, to show the range of results.

Two sets of static-fatigue curves (for Lac du Bonnet granite and tuff) were selected to bound expected time-dependent behavior of the lithophysal tuff, considering that limited data are available. The validity of the PFC stress corrosion modeling and the selected model parameters can be shown by a comparison with the observed behavior of the existing drifts at Yucca Mountain. The construction of the ESF main loop began in November 1992 and was completed

in April 1997, while the construction of the ECRB Cross-Drift began in December 1997, and was completed in October 1998. The ESF and ECRB Cross-Drift have been excavated and open for 5 to 12 years. While minor rockfall in the drifts was observed immediately after excavation, there is no indication of increased damage as a function of time, and no indication of rockfall as a consequence of time-dependent drift degradation. The ground support in the lithophysal rock in the ECRB Cross-Drift consists of rock bolts and wire mesh installed in the roof. The walls are not supported, and are comparable to the UDEC model results, which do not include ground support.

Figure S-32 shows the model state 500 years after excavation of the drift in category 2 tuff material considering the tuff best-fit static fatigue line. The damage occurs in the drift walls. Stresses are redistributed away from the drift sidewalls as the drift degrades. The stress redistribution causes the local driving-stress ratio to increase at greater distances from the excavation boundary.



NOTE: The top left figure shows the contours of displacement magnitudes (m) and fractures in the rock mass (blue lines); the top right figure shows accumulated damage, where the thickness of the blue lines are proportional to the accumulated damage (between 0 and 1); the bottom left figure shows the principal stress tensors (Pa) colored by the magnitude of the major principal stress; the bottom right figure shows the contours of the scaled driving stress (between 0 and 1).

Figure S-32. Model State for Tuff, Category 2 After 500 Years

Evolution of damage due to time-dependent strength degradation in the lithophysal rock mass (categories 1, 2, and 5) considering Lac du Bonnet granite static-fatigue, is shown in Figures S-33 through S-35. The stress states in the wall in category 2, and particularly in category 1, are close to the yield state under in situ stress conditions. There is a relatively large region of the rock mass, a couple of meters from the drift wall, loaded with driving stress,  $F$ , equal to, or larger than 0.7. The static-fatigue curve for the Lac du Bonnet granite implies that time-to-failure is 1 year for the driving stress approximately equal to 0.5. Consequently, there is a significant rockfall from the drift walls 1 year after drift excavation. Damage and rockfall increase with time (for categories 1 and 2), eventually resulting in total drift collapse for category 1. In the case of category 5, the driving stress around the opening is on the order of 0.3, resulting in relatively minor rockfall from the drift walls over a period of 10,000 years. Clearly, the model predictions after 5 and 10 years are in disagreement with observations in the ESF and ECRB. The tunnels, which have been open between 5 and 12 years, are stable. There are no observations of their degradation with time. It appears that static-fatigue curves for Lac du Bonnet granite result in too rapid deterioration of the drift, and do not provide a good representation of time-dependent behavior of the lithophysal tuff.

Evolution of damage due to time-dependent strength degradation in the lithophysal rock mass (categories 1, 2, 3 and 5) considering tuff static-fatigue, is shown in Figures S-37 through S-40 for tuff best-fit static-fatigue curves. Time-dependent strength degradation using the best-fit static-fatigue curves for lithophysal tuff has been extended to 20,000 years in Figure S-41 for categories 1, 2, 3, and 5.

It seems that category 1 underestimates the strength of the lithophysal rock mass. The tuff best-fit static-fatigue curve results in significant rockfall from the drift walls at 5 and 10 years after excavation (Figure S-37). The minor rockfall in Figure S-38 predicted by the model at 5 and 10 years after excavation, would have been prevented if the ground support was taken into account in the model (note that the rockfall comes from above the springline). Based on model validation with respect to the conditions in the ESF and ECRB, it seems that category 2 with a tuff best-fit static-fatigue curve is a conservative approximation of the mechanical behavior of the poorest quality lithophysal rock mass.

The best-fit tuff static fatigue line implies that a driving-stress ratio of approximately 0.60 results in approximately 20,000 years time-to-failure (see the tuff ( $P_c = 0$ ) best-fit curve in Figure S-27). The damage coefficient for this case is  $D_{20,000} \approx 1 - 0.60$  (Equation S-3), or 0.40, indicating there will be an approximate 40 percent cohesive strength reduction in 20,000 years. The drift profile for a 40 percent cohesive strength reduction case (i.e., 60 percent cohesive strength) was initially determined as shown in Figure 6-171c for category 1. Note that Figure 6-171c is similar to the category 1 profile in Figure S-41, indicating that at year 20,000, the rock mass is expected to have about 60 percent of its original cohesive strength due to time-dependent strength degradation.

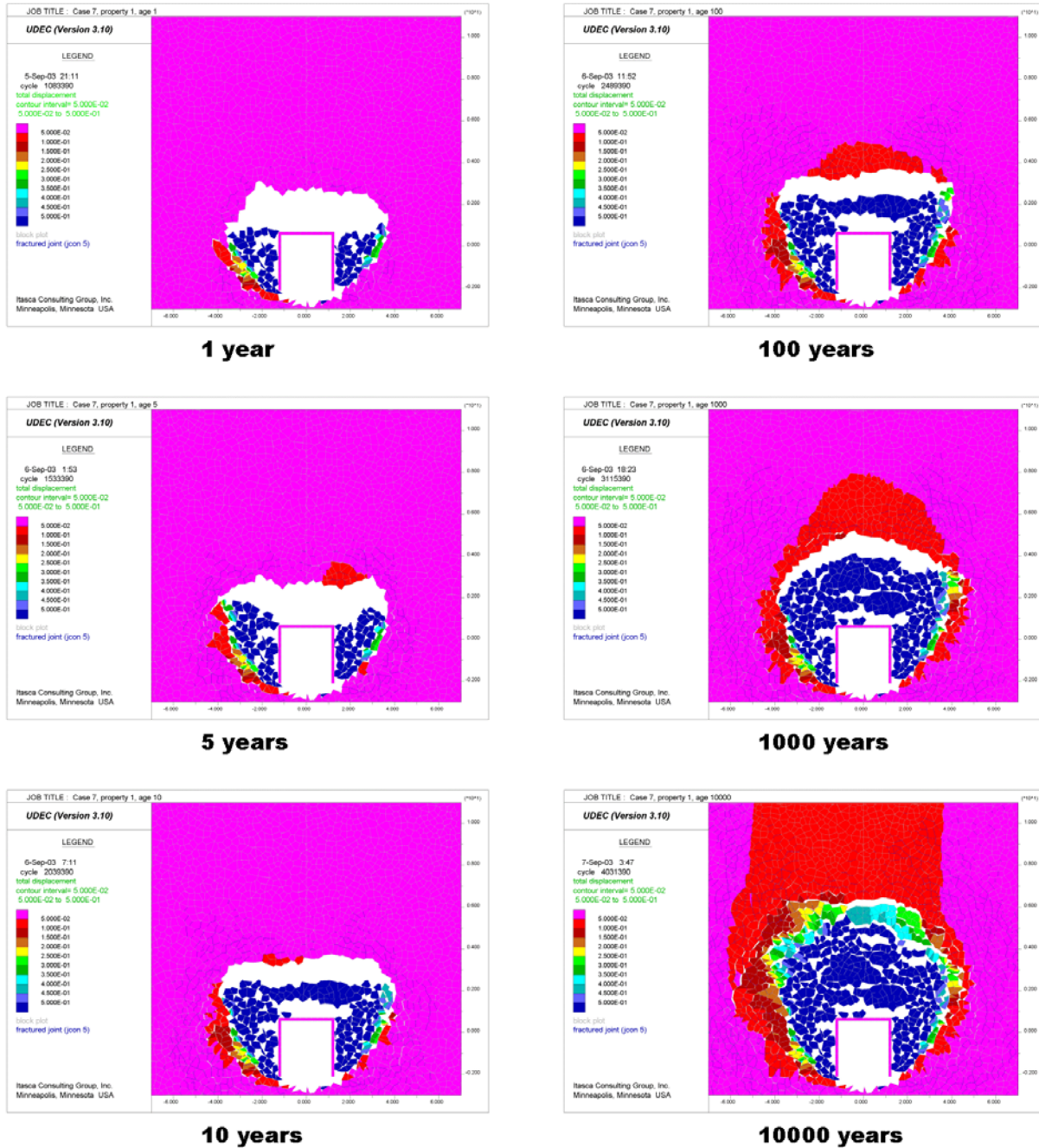


Figure S-33. Evolution of Damage Due to Strength Degradation for Category 1 – Lac du Bonnet Granite Static-Fatigue Curve

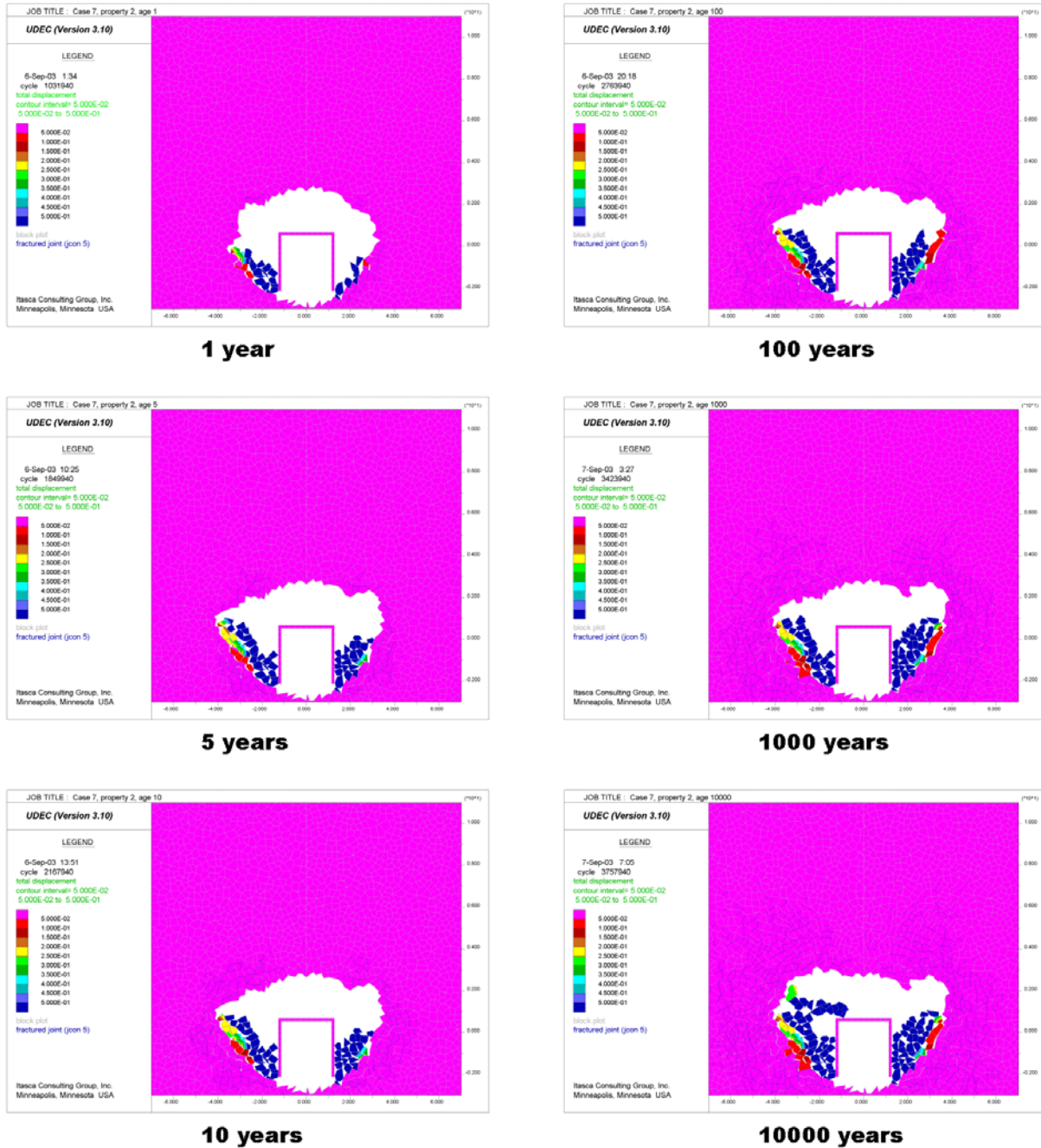


Figure S-34. Evolution of Damage Due to Strength Degradation for Category 2 – Lac du Bonnet Granite Static-Fatigue Curve

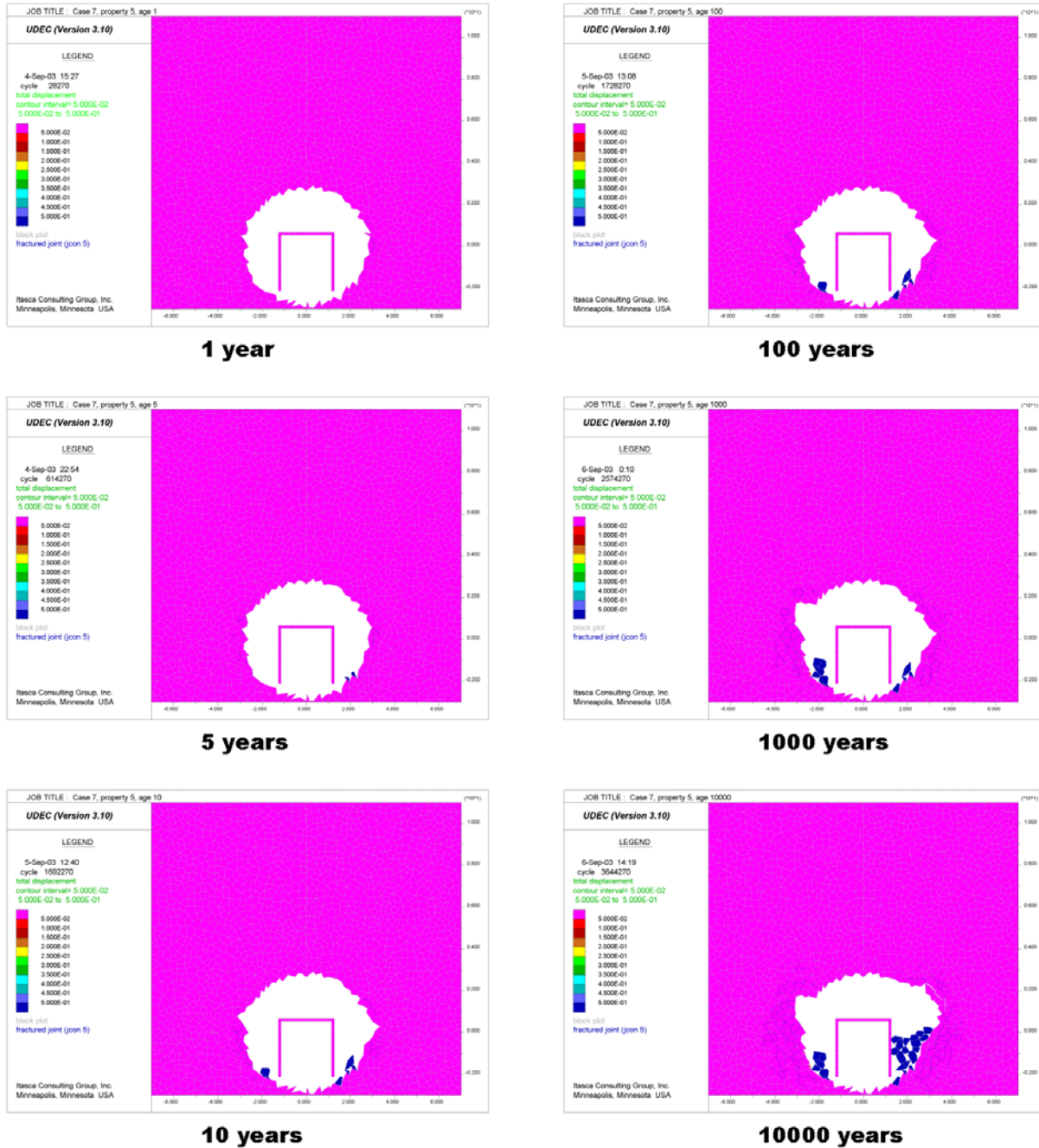


Figure S-35. Evolution of Damage Due to Strength Degradation for Category 5 – Lac du Bonnet Granite Static-Fatigue Curve

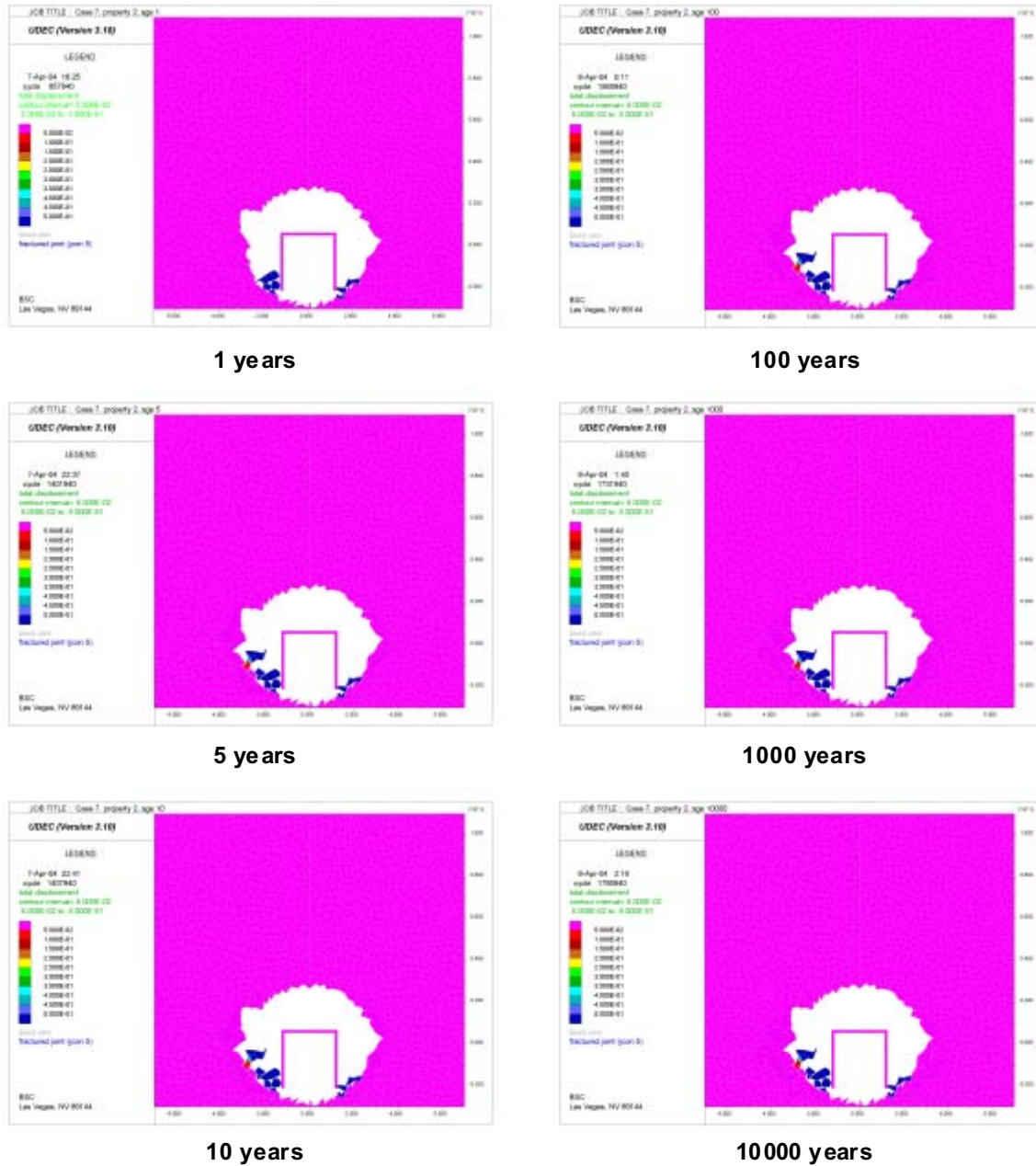


Figure S-36. Evolution of Damage Due to Strength Degradation for Category 2 – Tuff Best-Fit Static-Fatigue Curve (Reduced Time Increment)



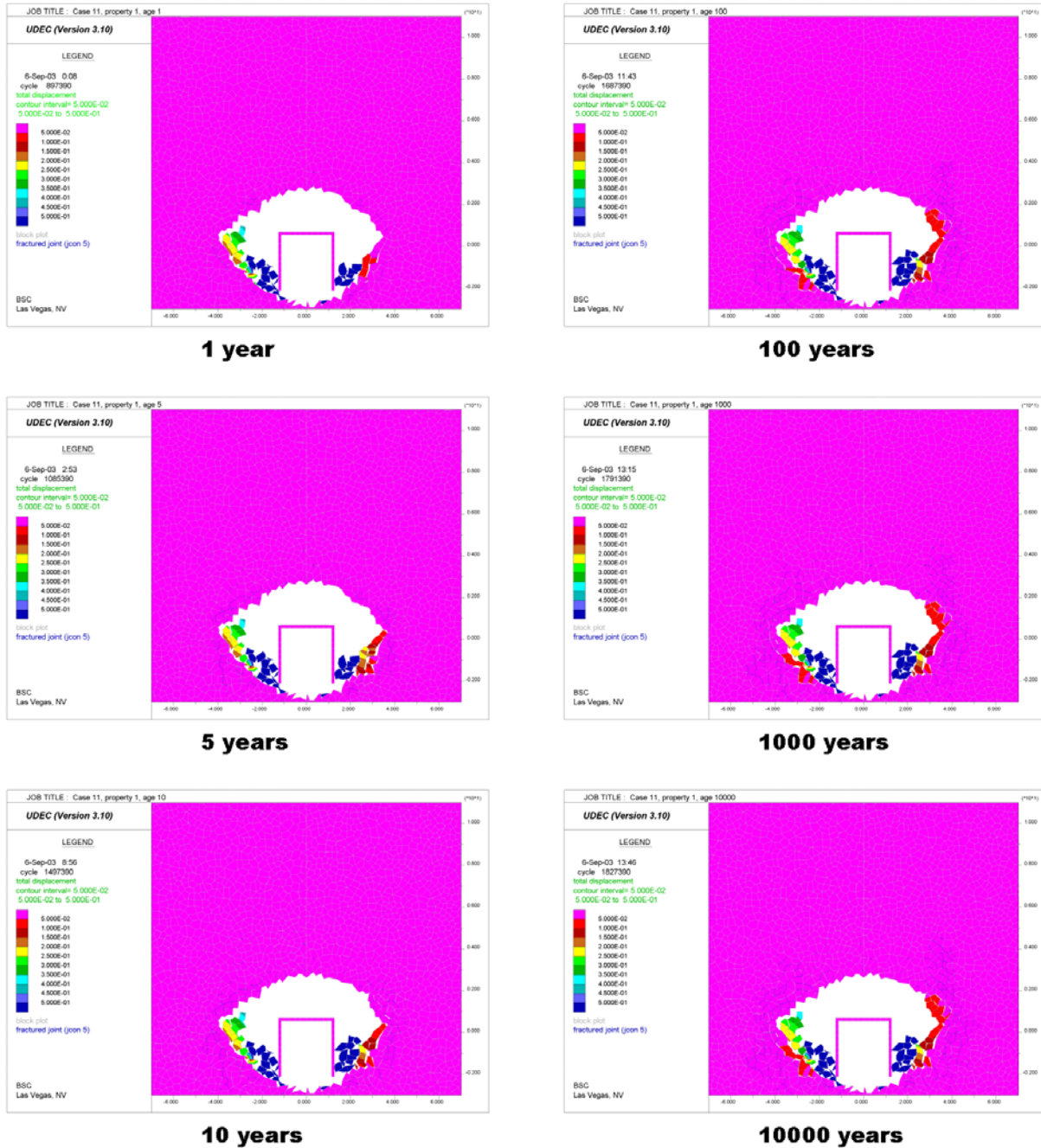


Figure S-37. Evolution of Damage Due to Strength Degradation for Category 1 – Tuff Best-Fit Static-Fatigue Curve

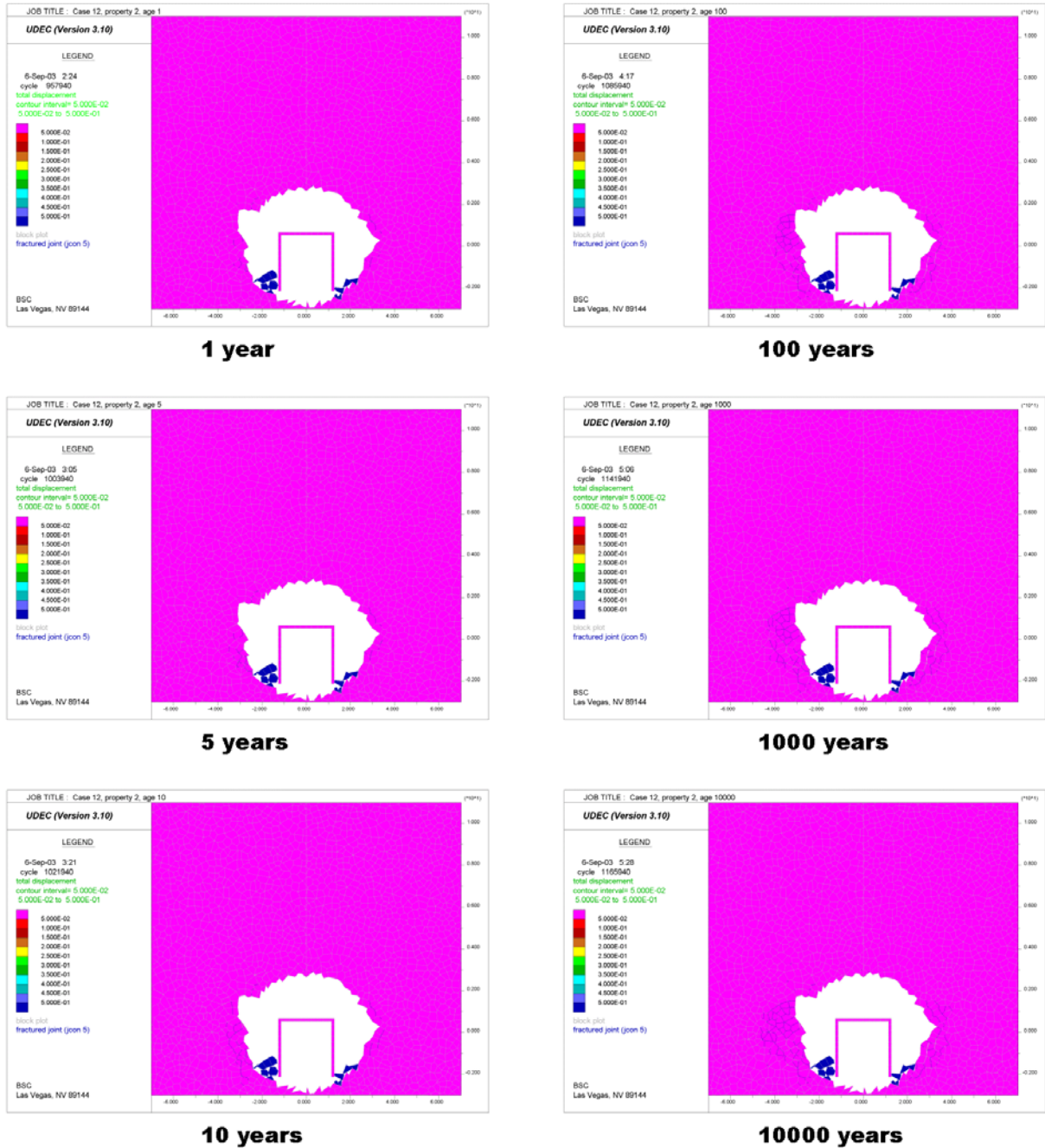


Figure S-38. Evolution of Damage Due to Strength Degradation for Category 2 – Tuff Best-Fit Static-Fatigue Curve

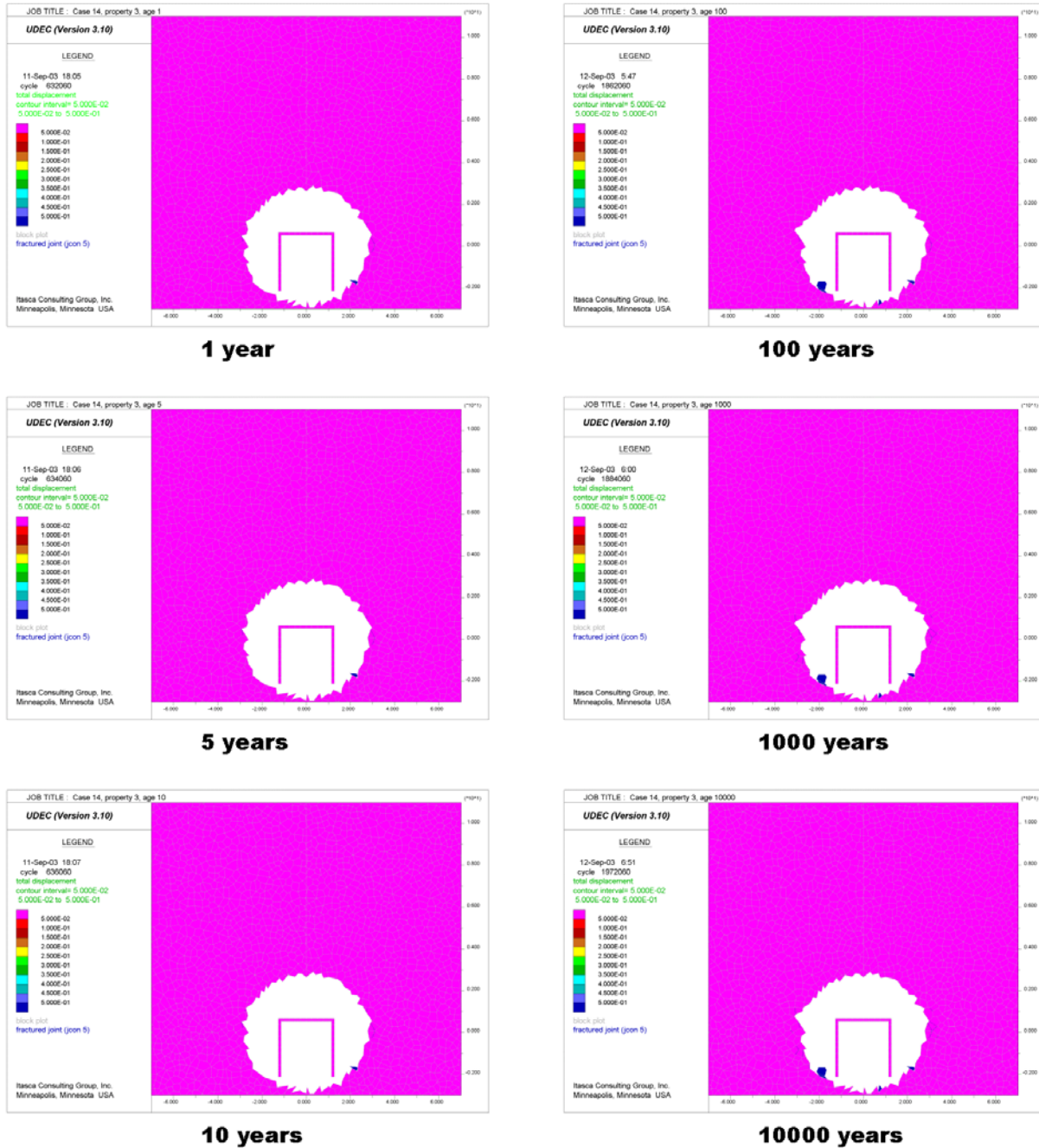


Figure S-39. Evolution of Damage Due to Strength Degradation for Category 3 – Tuff Best-Fit Static-Fatigue Curve

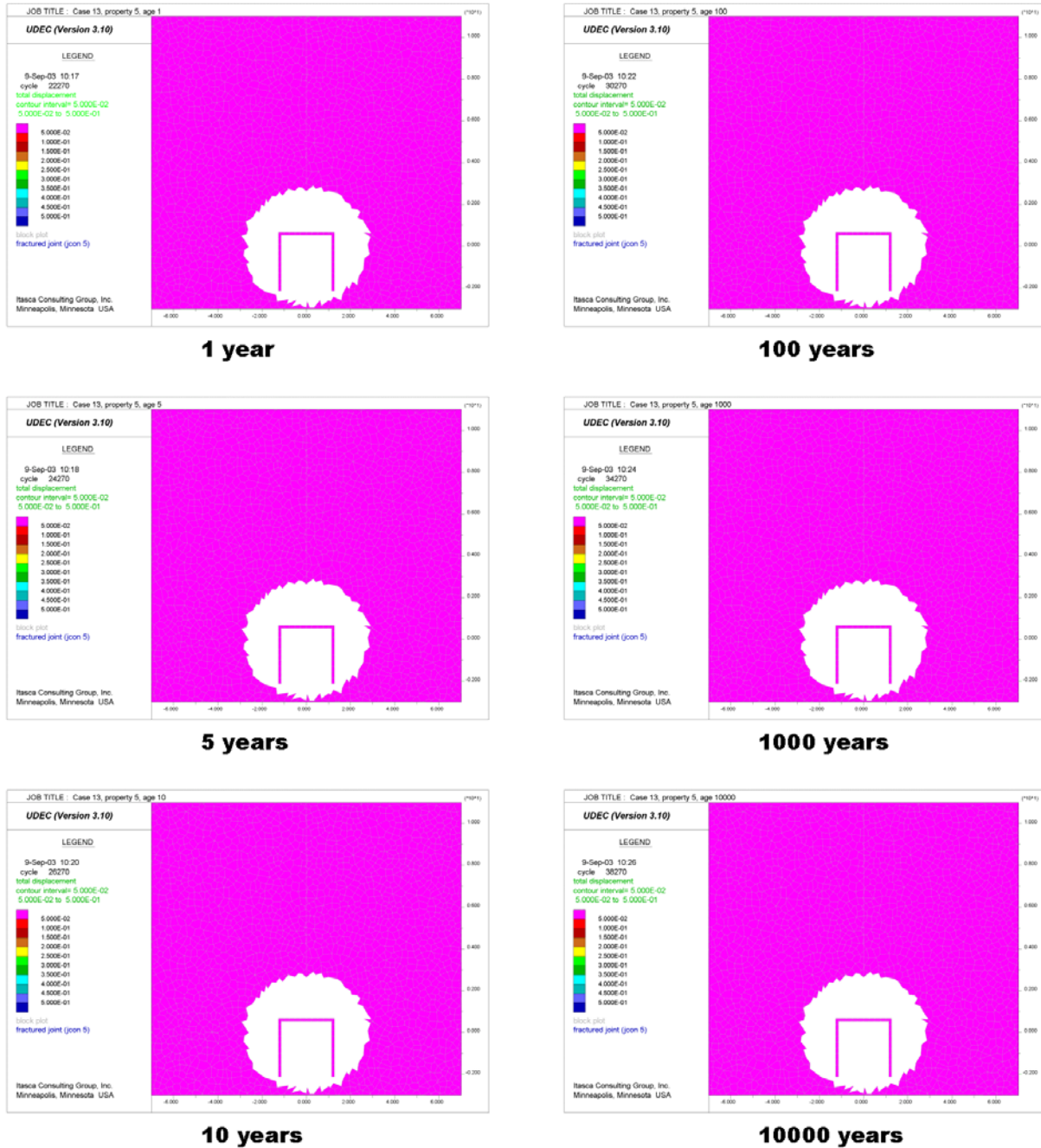
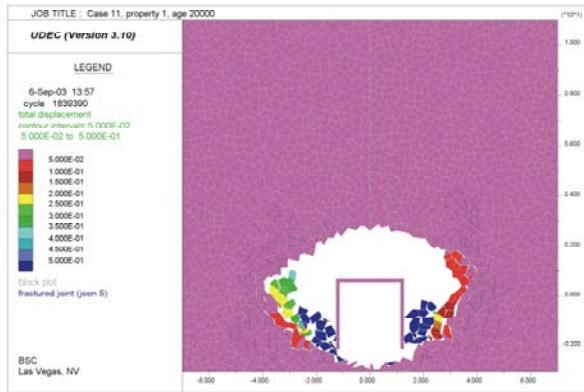
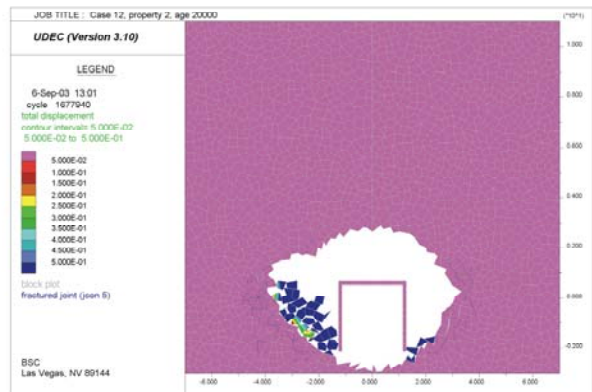


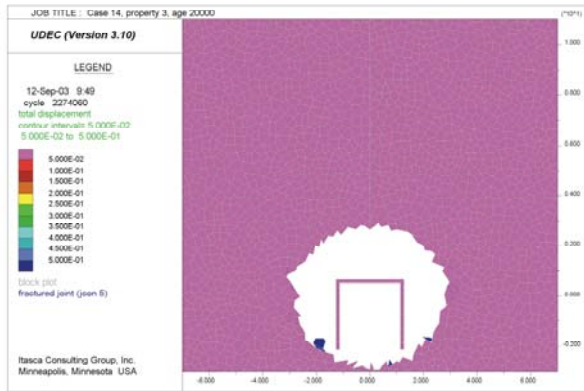
Figure S-40. Evolution of Damage Due to Strength Degradation for Category 5 – Tuff Best-Fit Static-Fatigue Curve



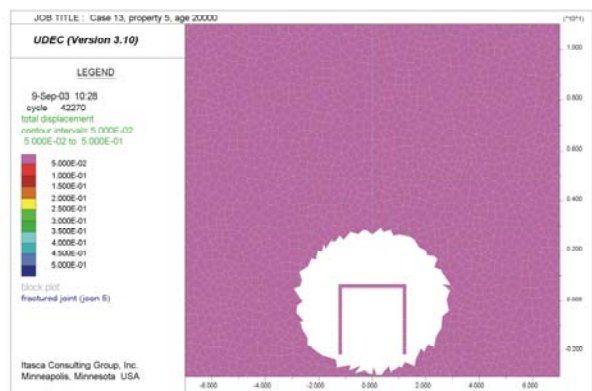
Category 1



Category 2



Category 3



Category 5

NOTE: The drift profiles show the effects of time-dependent strength degradation at 20,000 years. Thermal and seismic effects are not included with these drift profiles. Based on the comparison of model results to field data as described in this section, the category 2 rock mass is considered representative of the poorest quality lithophysal rock.

Figure S-41. Damage Due to Strength Degradation for Categories 1, 2, 3, and 5 – Tuff Best-Fit Static-Fatigue Curve at Year 20,000

### S3.4.2 Combined Thermal and Time-Dependent Effect in Lithophysal Units

Throughout the regulatory period of 10,000 years, the emplacement drifts and surrounding rock mass will be subject to a heating cycle. Time-dependent strength degradation will happen concurrently with transient, thermally induced stress changes. Increased stresses around the excavation will accelerate the process of strength degradation. The results of numerical simulation of drift degradation as a result of these two processes are shown in Figures S-42 through S-44. Time-dependent strength degradation is assessed using the tuff best-fit static-fatigue line. From the discussion in the previous section, it appears that the tuff best-fit static-fatigue line is consistent with the behavior of the excavated drifts at Yucca Mountain and the results of the testing on lithophysal rock mass completed so far. As expected, most rockfall occurs in category 2 rock mass, as shown in Figure S-42. Initially most of rockfall comes from

the walls, which are loaded almost to a yielding state for this rock mass category under in situ stress conditions. Strength degradation combined with a temperature increase, which at early times increases the hoop stress in the walls (not only in the roof), results in some rockfall from the wall at 5 and 10 years after emplacement of the waste. The large increase in the temperature, and consequently in the stresses, after the forced ventilation stops causes additional rockfall (at 80 years). At this stage, stress increase is predominantly in the roof. Therefore, some rockfall comes from the roof. It is counterintuitive that more rockfall is predicted in category 5 (Figure S-44) than in category 3 (Figure S-43). However, a large stiffness of category 5 lithophysal rock mass causes a large (larger than in category 3) increase in the hoop stress and yielding in the roof, even considering the short-term yield strength of the rock mass (Figure 6-144).

It should be noted that static-fatigue curves are temperature dependent. This dependence is not explicitly included in the analysis. However, the tuff data are obtained from tests conducted at 150° C (see Section S2.1), which is larger than the maximum temperature of the rock mass anticipated throughout the repository for the base case described in Section 6.2. Consequently, the results obtained in this analysis, although for “isothermal” static-fatigue curves are conservative.

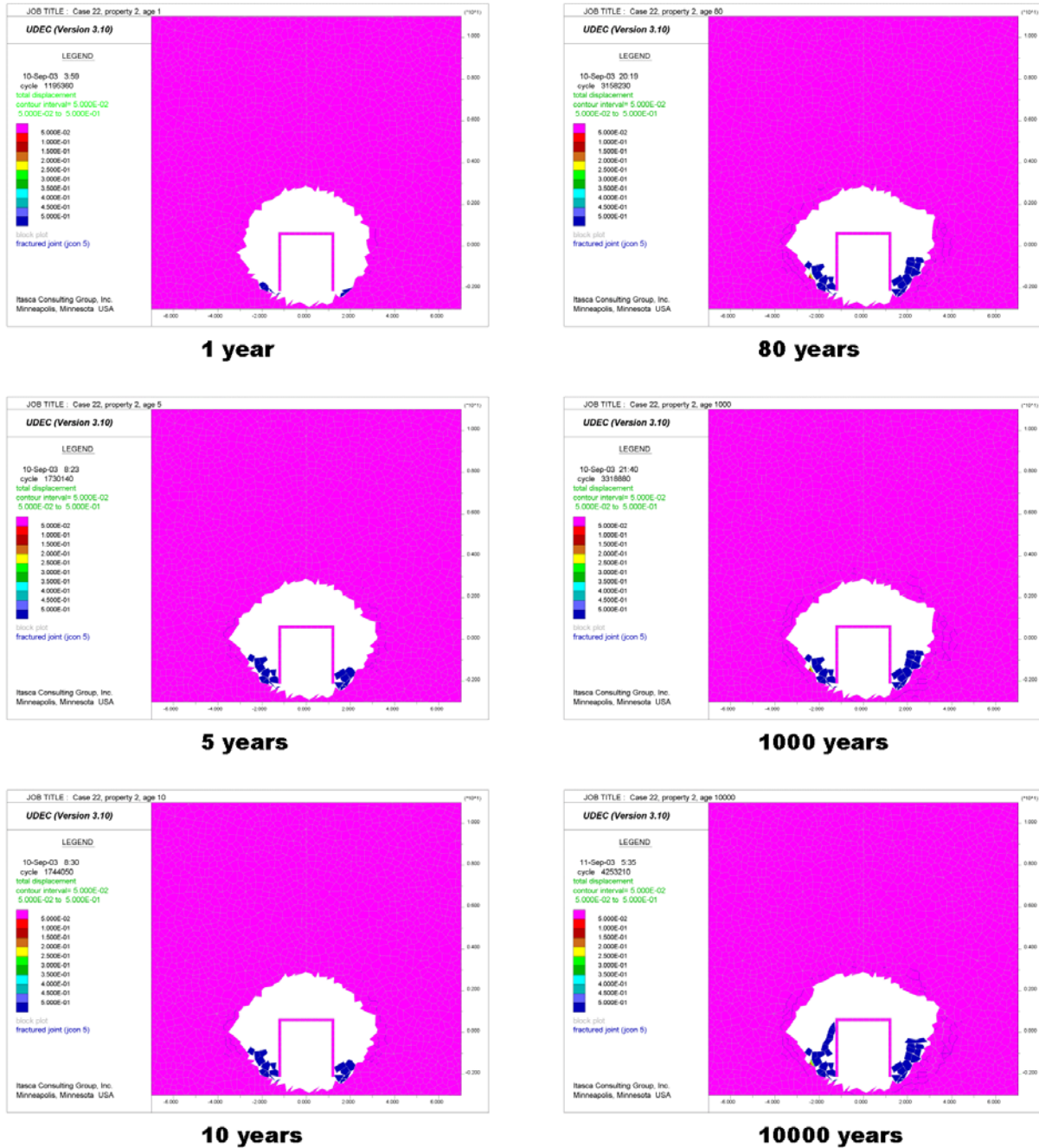


Figure S-42. Evolution of Damage Due to Strength Degradation and Thermal Load for Category 2 – Tuff Best-Fit Static-Fatigue Curve

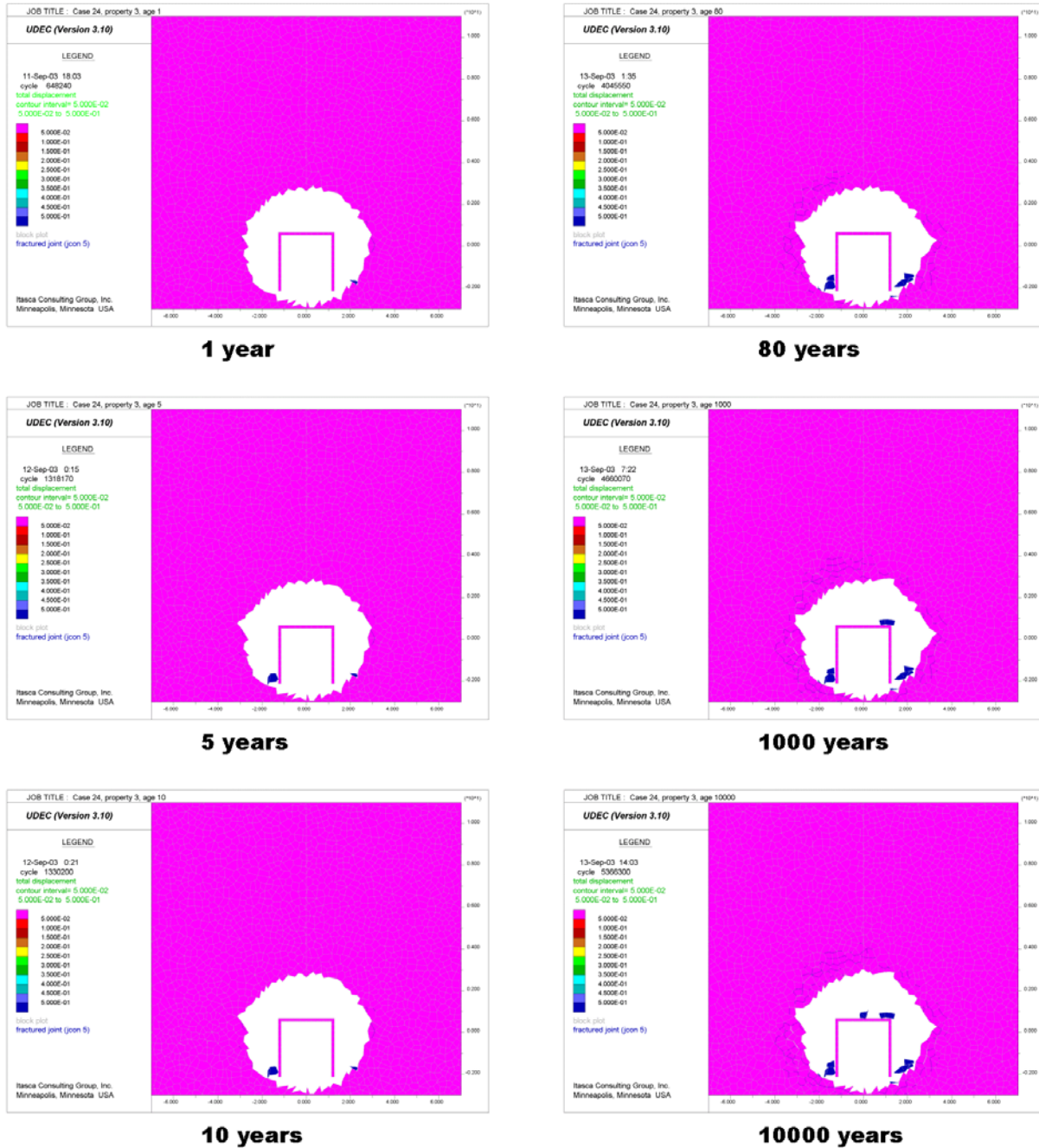


Figure S-43. Evolution of Damage Due to Strength Degradation and Thermal Load for Category 3 – Tuff Best-Fit Static-Fatigue Curve



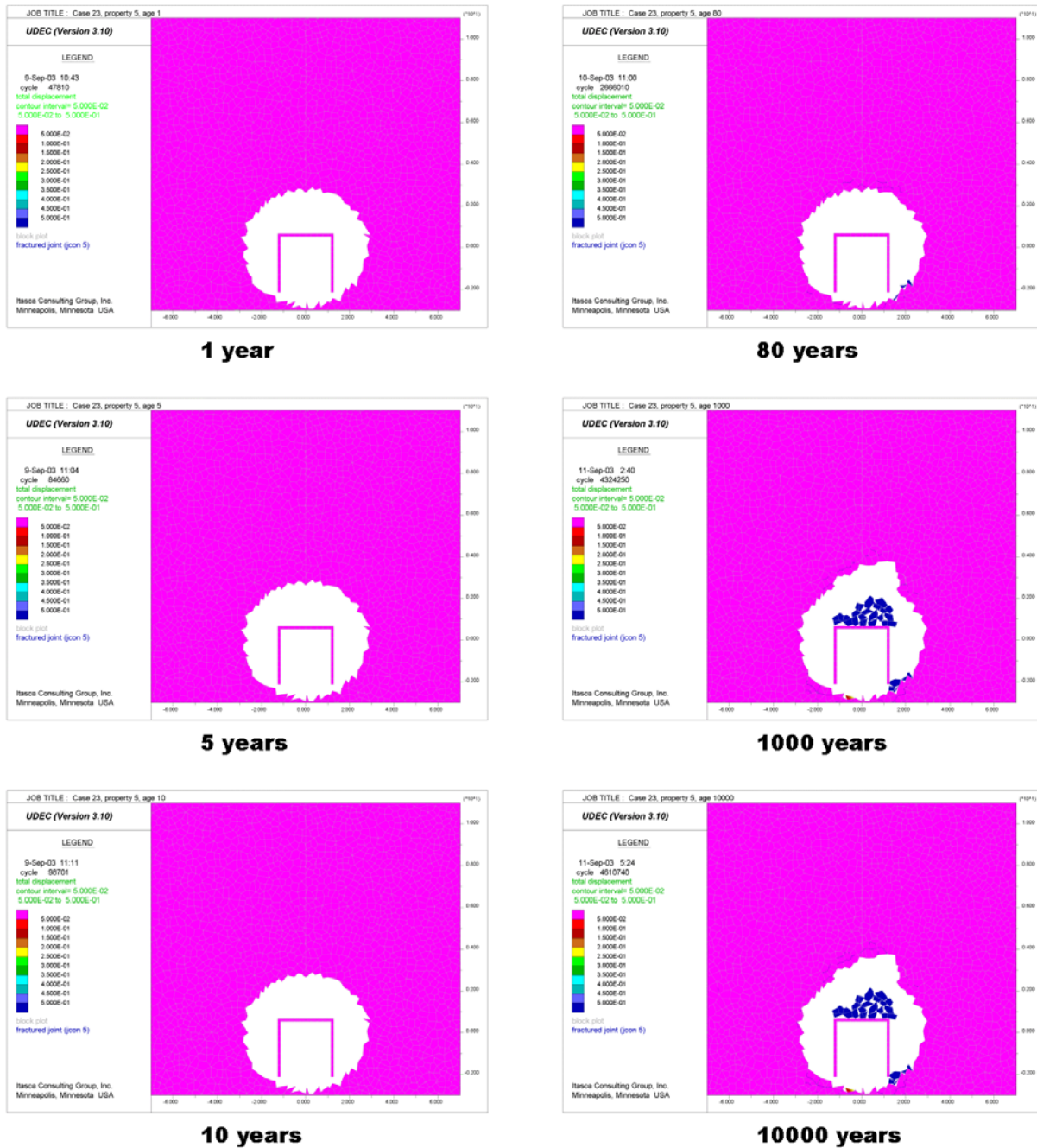


Figure S-44. Evolution of Damage Due to Strength Degradation and Thermal Load for Category 5 – Tuff Best-Fit Static-Fatigue Curve

### S3.4.3 Combined Seismic, Thermal, and Time-Dependent Effect in Lithophysal Units

The effect of the preclosure seismic loading ( $1 \times 10^{-4}$  probability of annual occurrence) was investigated for categories 2 and 5 of the tuff best-fit curve. An analysis of the combined effects of thermal and seismic loading is presented in Section 6.4.2.3. Note that because ground motion with  $1 \times 10^{-6}$  probability of annual occurrence results in complete drift collapse in lithophysal rock

(see Section 6.4.2.2), it was not of particular interest to investigate the effect of that level of ground motion combined with thermally induced initial stresses and time-dependent strength degradation. Instead, a ground motion with  $1 \times 10^{-4}$  probability of annual occurrence was considered. The state of the rock mass when the effect of seismic ground motion is most adverse for drift stability was selected based on an elastic stress path with respect to the short-term yield surface. Under such conditions, the critical state was reached 80 years after waste emplacement, when the temperatures and the thermal stresses around the drift reach the maximum. When the time-dependent strength degradation is considered, the state when the maximum stresses are generated around the drift is not necessarily the critical one. The largest stresses occur relatively early during the regulatory period. Subsequently, the stresses decay gradually, returning to the state that existed prior to heating. At the same time, the strength of the rock mass monotonically decreases as a function of time, such that the weakest rock strength occurs at the end of the regulatory period (i.e., at year 10,000). In order to investigate the worst-case effects of seismic ground motion on drift stability, dynamic analyses were carried out for the model states at 80 and 10,000 years after waste emplacement.

The model geometry before and after the dynamic simulation is shown in Figures S-45 and S-46 for seismic ground motion at 80 years after emplacement, and in Figures S-47 and S-48 for seismic ground motion at 10,000 years after emplacement. In each case, an additional rockfall is predicted due to the earthquake, which shakes down already damaged rock mass. This increase in the rockfall due to seismic loading is not significant in any of the cases, although it seems that there is more rockfall in the case of an earthquake at 10,000 years after waste emplacement.

The effect of multiple seismic events on stability of the emplacement drifts in category 2 lithophysal rock mass at different stages during the regulatory period was also investigated. Figure S-49 shows the model geometry after two identical  $1 \times 10^{-4}$  seismic events have shaken the emplacement drifts at 80 and 10,000 years of heating. These results should be compared with results shown in Figures S-45 and S-47 for a single seismic event in a rock mass of the same quality and age (80 and 10,000 respectively) after waste emplacement. The second event, although exactly the same ground motion, causes much less additional rockfall. In fact, after 10,000 years of heating, the second event does not produce any additional rockfall. Some relatively small additional rockfall can be observed on the left side of the drip shield for a repetitive seismic event taking place 80 years after waste emplacement. The second earthquake shakes down a small volume of the loose rock that remained in the drift roof after the first earthquake.

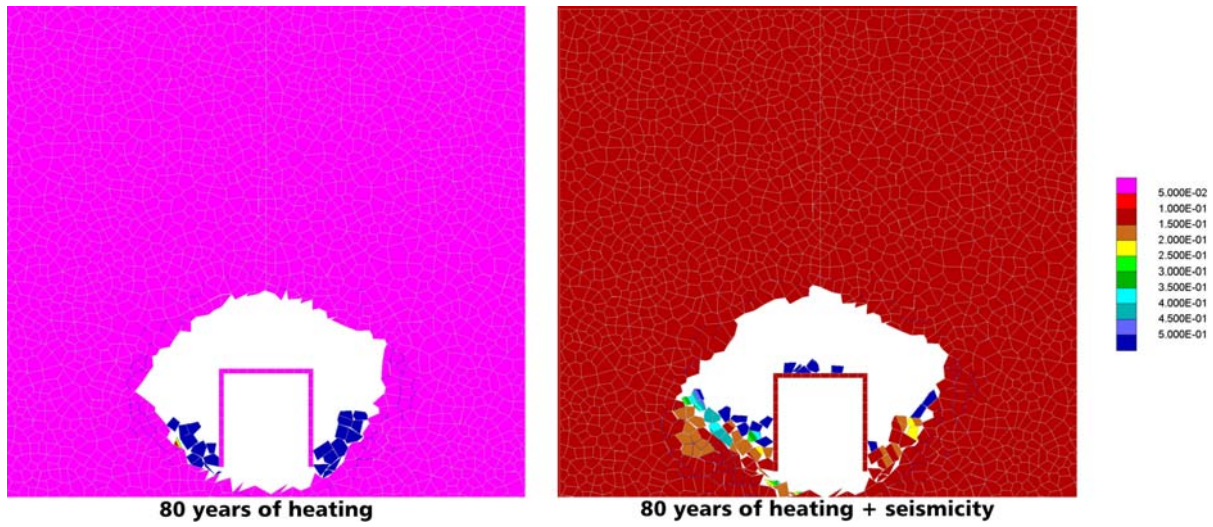
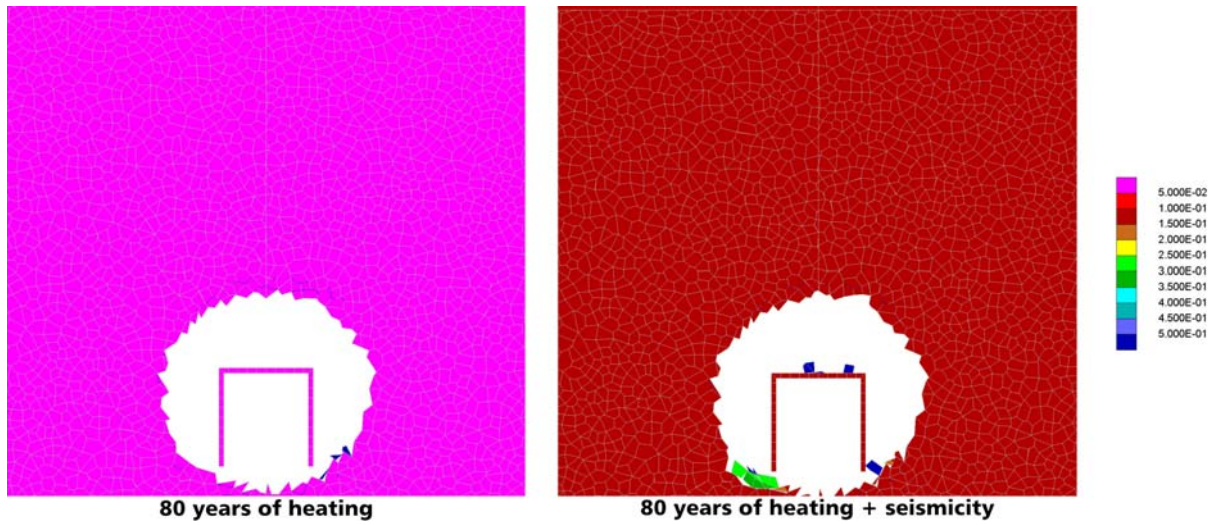
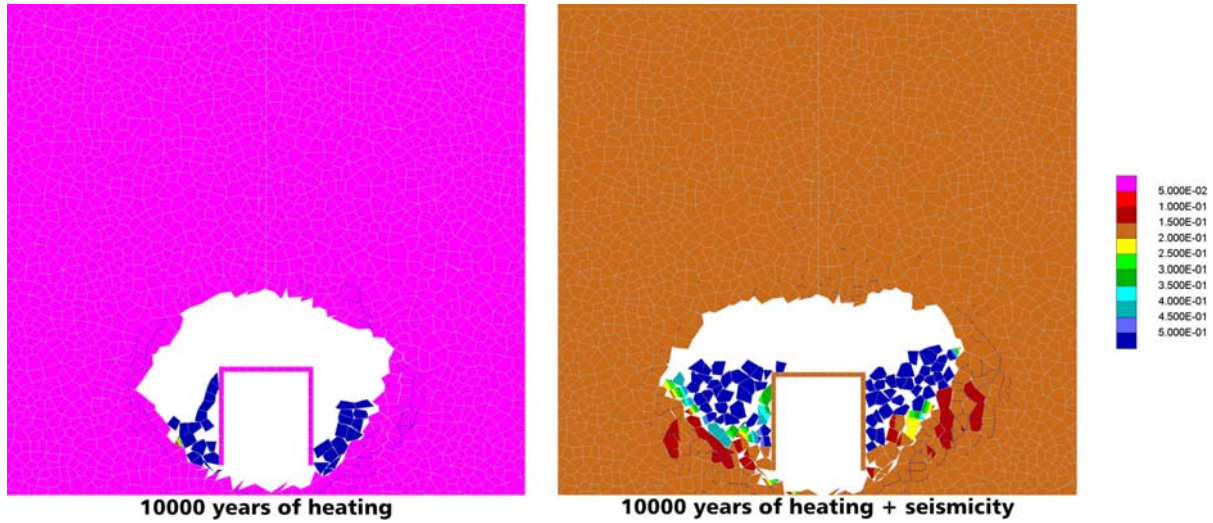


Figure S-45. Effect of  $1 \times 10^{-4}$  Ground Motion After 80 Years of Heating in Category 2: Contours of Displacement Magnitude (m)



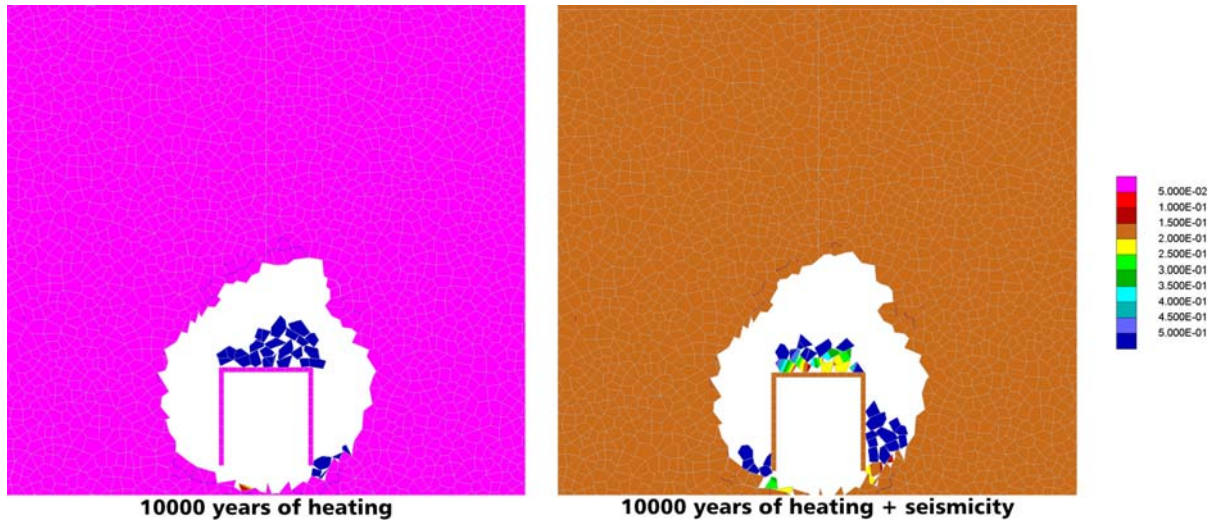
NOTE: There is a residual, rigid body translation of the model at the end of dynamic simulation because the entire seismogram was not simulated.

Figure S-46. Effect of  $1 \times 10^{-4}$  Ground Motion After 80 Years of Heating in Category 5: Contours of Displacement Magnitude (m)



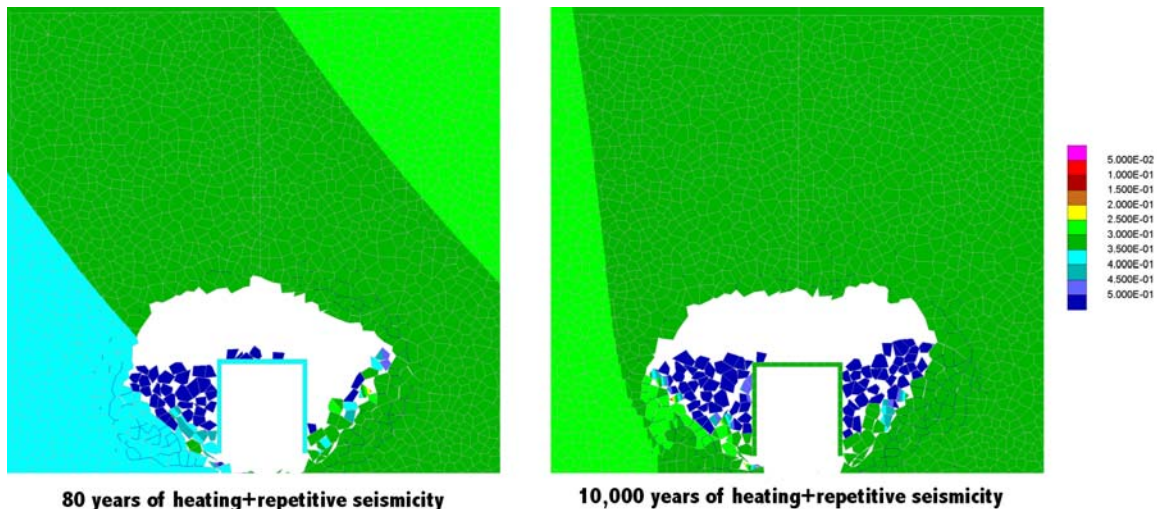
NOTE: There is a residual, rigid body translation of the model at the end of dynamic simulation because the entire seismogram was not simulated.

Figure S-47. Effect of  $1 \times 10^{-4}$  Ground Motion After 10,000 Years of Heating in Category 2: Contours of Displacement Magnitude (m)



NOTE: There is a residual, rigid body translation of the model at the end of dynamic simulation because the entire seismogram was not simulated.

Figure S-48. Effect of  $1 \times 10^{-4}$  Ground Motion After 10,000 Years of Heating in Category 5: Contours of Displacement Magnitude (m)



NOTE: There is a residual, rigid body translation of the model at the end of dynamic simulation since the entire seismogram was not simulated.

Figure S-49. Effect of Two Successive  $1 \times 10^{-4}$  Ground Motions in Category 2: Contours of Displacement Magnitude (m)

#### S4. CONSIDERATION OF SPATIAL VARIABILITY OF ROCK MASS STRENGTH

The lithophysal rockfall modeling presented in Section S3 considers a constant rock property category throughout the model. In reality, the lithophysal rock mass can contain multiple rock property categories within a 5 to 10 meter zone (see Section 7.3.2). The use of a constant rock property category throughout the rockfall model bounds the rockfall response since the poorest quality category (categories 1 and 2) will likely contain areas of higher quality rock, and therefore, the rockfall models for these categories will produce conservative (i.e., higher) predictions of drift damage and rockfall. Conversely, the highest quality category (category 5) will likely contain areas of poorer quality rock, and therefore, the rockfall model for this category may result in less damage and rockfall compared to actual conditions. A more realistic model of lithophysal rock mass conditions is described in this section, allowing for varied rock mass properties throughout the model. The results presented in this section supplement the analyses presented in Section S3 by providing a more realistic case for lithophysal drift degradation.

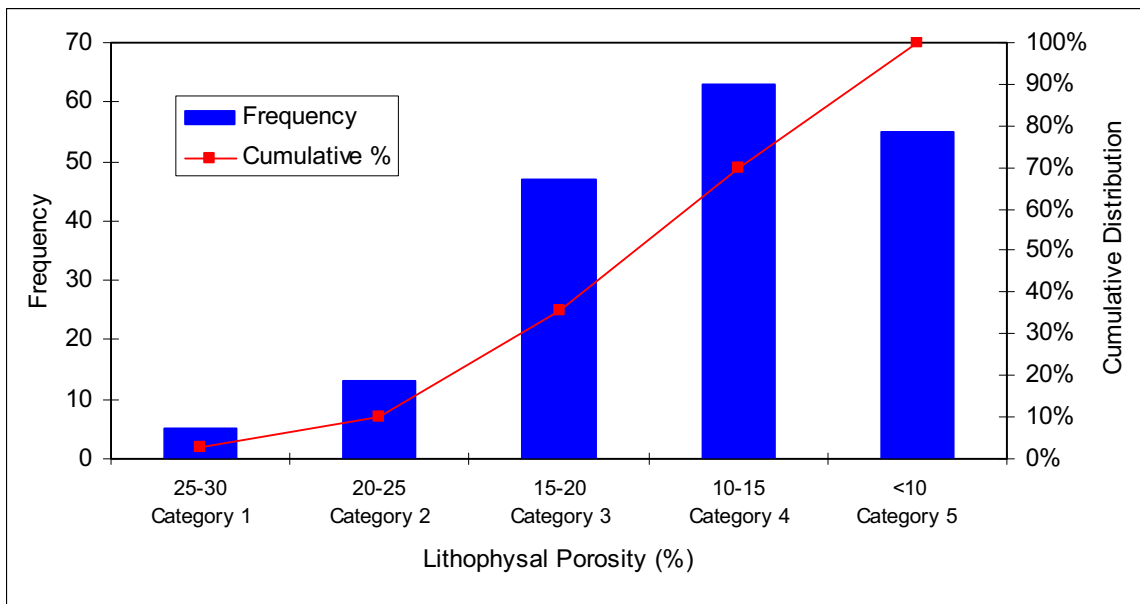
It is considered that the volume fraction of the lithophysae (referred to as porosity) is the only factor that controls mechanical properties of the lithophysal rock mass. The other factors certainly have an effect (e.g. jointing), but the volume fraction of the lithophysae is the most important. Therefore, the consideration is reasonable, while it considerably simplifies the task of establishing a correlation between the actual conditions of the rock mass and the mechanical properties used in the model. The correlation between the porosity and lithophysal rock mass categories from Table E-10 was used in the analysis.

The distribution of lithophysal porosity in the ECRB Cross-Drift is shown in Figure S-50. Spatial variation of porosity (developed in Appendix T) was simulated inside a  $50 \text{ m} \times 50 \text{ m} \times 40 \text{ m}$  volume. The simulated porosity, shown in Figure S-51, varies between 5 percent and 30 percent throughout the simulated region. The analysis was conducted using a

two-dimensional model for three different cross-sections and locations of the drift center within the simulated volume. Normal to the cross-section plane is always in the direction of the  $y$ -axis. The coordinates of the drift center (relative to the coordinate system shown in Figure S-51) are: a) Section 1,  $x = 25$  m,  $y = 5$  m,  $z = 37.5$  m; b) Section 2,  $x = 25$  m,  $y = 10$  m,  $z = 37.5$  m; and c) Section 3,  $x = 25$  m,  $y = 5$  m,  $z = 25$  m. Sections 1 and 2 are located in a region of the simulated volume with a large average porosity, while the third section is located in a region with a medium average porosity. The analysis has shown that there is no significant variability of the rockfall for different cross-sections throughout the simulated volume. Consequently, the use of a two-dimensional model is justified for the assessment of rockfall for a drift located in the lithophysal rock mass, accounting for actual variability of porosity and mechanical properties.

The porosity is interpolated in the centers of zones and joints of the UDEC model. Using the relations between porosity and rock mass categories (Table E-10) and between the rock mass categories and UDEC micro-properties (Table 6-43), variable properties of the blocks (bulk and shear moduli) and the joints (normal and shear stiffness, cohesion and tensile strength) are generated. Variability of block bulk modulus for Section 1 is shown in Figure S-52.

The results of the simulation for the thermal load combined with time-dependent strength degradation for Section 1 are shown in Figure S-53. The rockfall is very similar to the rockfall predicted for category 3, considering homogeneous rock mass properties, shown in Figure S-43. This is an expected result because the average properties for Section 1 are similar to category 3 rock mass properties.



NOTE: Lithophysal porosity data are from ECRB Cross-Drift station 14+44 to 23+26 (Appendix O and Section O6.6; see Microsoft Excel file, *Drift Deg AMR AF T-A-P Fit.xls*, worksheet "Volume Percent - Stats", which can be accessed through the TDMS using DTN: MO0408MWDDDMIO.002).

Figure S-50. Distribution of Lithophysal Porosity in the ECRB Cross-Drift

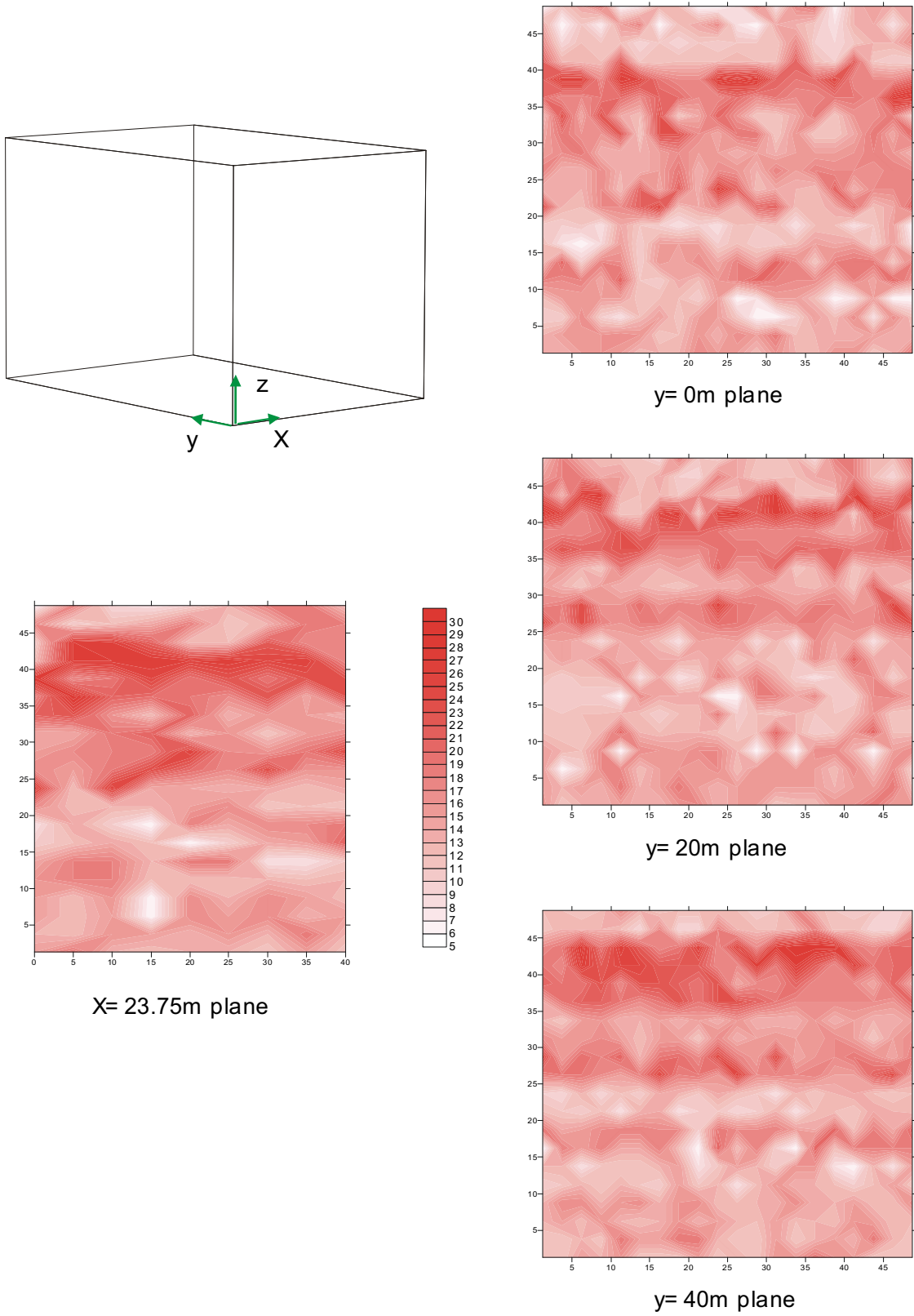


Figure S-51. Porosity Contours in Cross-Sections Through the 3D Simulated Porosity Field

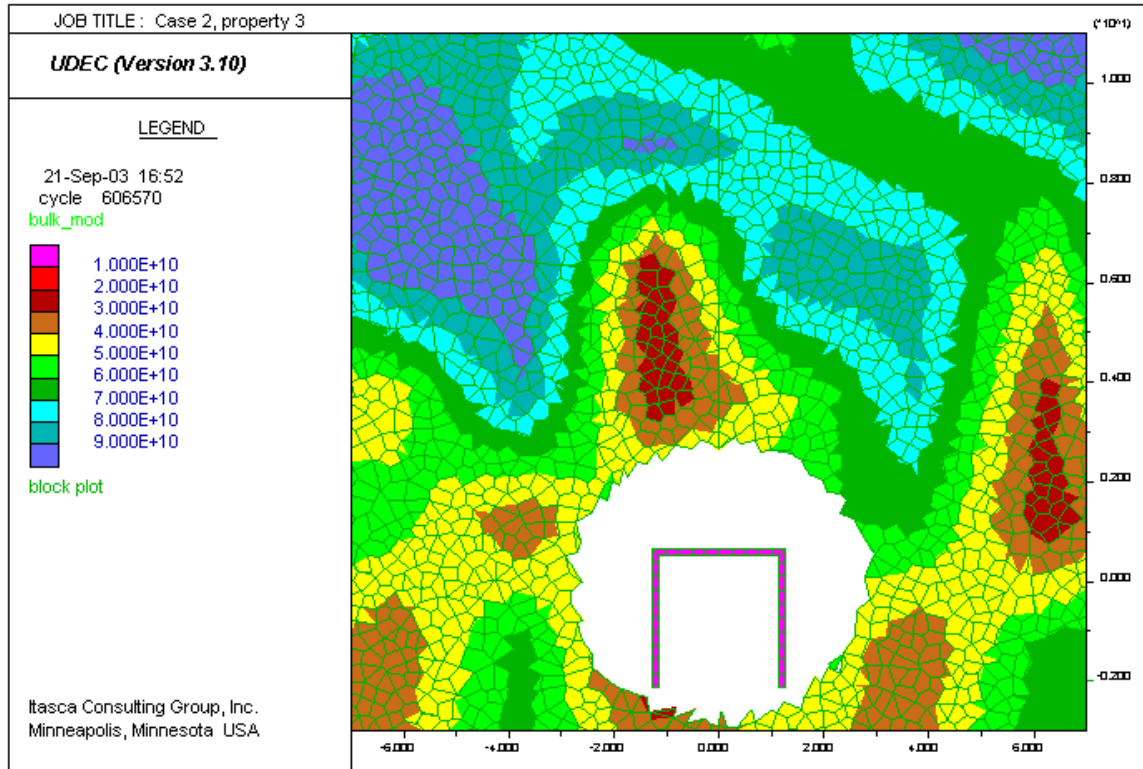


Figure S-52. Distribution of Block Bulk Modulus for Section 1



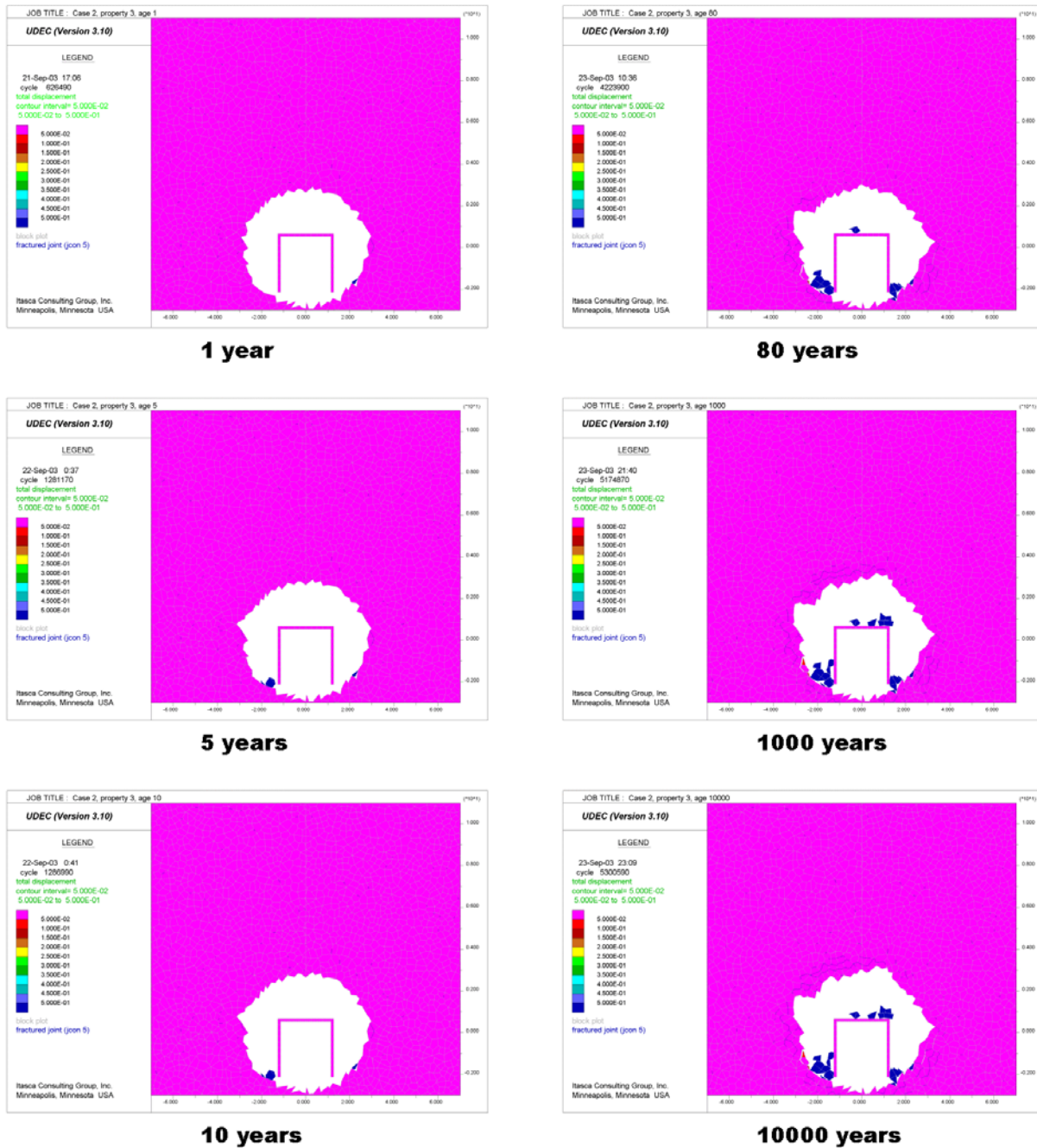


Figure S-53. Evolution of Damage Due to Strength Degradation and Thermal Load for Spatially Variable Properties, Section 1 – Tuff Best-Fit Static-Fatigue Curve

### S5. VALIDATION OF THE MODELING APPROACH

As one means of validating the PFC stress corrosion modeling approach for estimating long-term damage formation surrounding the ECRB Cross-Drift, two independent technical reviews were conducted using experts in the field of rock mechanics testing (see Section 7.5.2.3).

The first independent technical review is provided by Dr. Jaak Daemen, Professor of Mining Engineering and Department Chair at the University of Nevada, Reno. Dr. Daemen received his Ph.D. in Geological Engineering from the University of Minnesota where his research involved development of the analytical and numerical solutions for ground support – rock mass interaction. He worked for DuPont in development of ground support products prior to joining the University of Arizona, Department of Geological Engineering. Dr. Daemen's current research involves time-dependent testing of joints and intact tuff from the Yucca Mountain nuclear waste disposal site.

The second independent technical review is provided by Mr. Ronald Price and Dr. Randolph Martin. Mr. Price is a Senior Member of Technical Staff at Sandia National Laboratories. He has a M.S. in Geology from the Center for Tectonophysics at Texas A&M University, where his thesis research was entitled, “Effects of Anhydrite and Pressure on the Mechanical Behavior of Synthetic Rocksalt”. Since his arrival at Sandia in 1980, Mr. Price has planned, carried out and published results from laboratory studies on many different rock types and for many applications. He has, however, had a central focus on the mechanical properties of tuffs, with special emphasis on Yucca Mountain tuffs, for over 22 years. His depth of knowledge of tuff rheological properties is particularly valuable for the present application. Dr. Martin is the President of and Principal Scientist at New England Research, Inc. in White River Junction, Vermont. He has a Ph.D. from MIT, where his thesis research was entitled, “Time-Dependent Crack Growth in Quartz and Its Application to the Creep of Rocks.” Dr. Martin has a wide range of experience managing and performing both field and laboratory rock mechanics projects, including designing/building high-pressure equipment, testing rocks at elevated pressures and temperatures, and analyzing data with various (e.g. empirical, analytical, and numerical) techniques. His seminal work in the area of static fatigue makes him particularly valuable in the review of this material.

### **S5.1 OBJECTIVE AND SCOPE OF THE INDEPENDENT TECHNICAL REVIEW**

The technical review is limited to documentation on the validity of the PFC stress corrosion modeling approach applied to the rockfall models (i.e., draft documentation of this appendix). While the time of failure presented in the damage curves (Figures S-28 and S-29) is based on laboratory measurements, the shape of the curve as a function of time is determined from the PFC stress corrosion model, and has not been validated by test data. To assess the validity of the PFC stress corrosion model, the technical review addresses the following items:

- Provide an assessment of the bi-linear shapes of these damage curves to determine if they are reasonable and consistent with observations and measurements of static fatigue failure of rock specimens.
- Provide a discussion of the validity of the static-fatigue curves and the damage curves used as input to the UDEC analyses (Figures S-27 through S-29).
- Provide a discussion of the validity of the results (i.e., the predictions of drift degradation as a function of time-dependent strength degradation) produced by the UDEC rockfall model (Section S3.4.1).

## **S5.2 REVIEW CRITERIA**

The following criteria are used when reviewing the documentation on the validity of the PFC stress corrosion modeling approach:

- Is this information presented accurately using applicable methods, assumptions, and recognized techniques?
- Does existing model documentation provide adequate confidence required by the model's relative importance to the potential performance of the repository system to support model validation for its intended purpose and stated limitations?

## **S5.3 INDEPENDENT TECHNICAL REVIEW #1**

The review from Dr. Jaak Daemen is provided in this section.

This appendix presents a powerful analysis of potential time-dependent drift deterioration. The analysis is based on a convincing fundamental model of rock strength deterioration over time. The results provide considerable insight into what might be expected with regard to time-dependent drift deterioration.

While the strategy developed in this appendix is very convincing, the significance of specific results is less so, because of the lack of experimental input data, as recognized by the authors.

The shape of the bi-linear damage curves is eminently reasonable. However, the presentation of the sensitivity analysis (Section S3.2) and its implementation and results (Figure S-31) is exceedingly brief. It would help if this discussion could be expanded, could provide a bit more detail. The most convincing support for the damage curves is the "calibration" of the results based on the ESF and ECRB observations (Section S3.4.1).

The results are eminently reasonable, and provide significant insight into the likely drift degradation mechanisms and time frame. Although, as the report recognizes, there is considerable input data uncertainty, the sensitivity analyses performed give considerable confidence that the results are good predictors of likely drift degradation.

The information presented appears accurate, and the analysis uses applicable models, assumptions, and recognized techniques.

The model documentation provides adequate confidence about the potential repository system component performance, and will support model validation. Limitations associated with the model, in particular with regard to the paucity of experimental input data, are clearly identified.

## S5.4 INDEPENDENT TECHNICAL REVIEW #2

The review from Mr. Ronald Price and Dr. Randolph Martin is provided in this section.

This manuscript contains two sections. First, analysis of the time-dependent behavior of intact rocks on specimens using the PFC and second, a model incorporating the time-dependent strength of tuff into long-term strength of the roof and rock fall in the repository.

In general, the paper presents a good representation of the behavior of intact rock samples and how that might be used to predict long-term rock properties especially strength. The approach used in these models has been developed on other projects. Several modifications were made to the models to accommodate the strong porosity dependence of rock properties measured at the laboratory scale.

The PFC is used to model the time-dependent strain (creep) and the time-dependent strength (static fatigue) observed in laboratory measurements. The flexibility of the PFC model allows incorporation of (1) large-scale porosity in the sample and (2) time-dependent properties in the matrix bonds to adequately represent time-dependent processes in the bulk rock.

The approach used here has been successfully applied in Canada for granitic rocks. The model is calibrated with available rock properties measurements both in situ and in the laboratory. By tying the model to existing data, they were able to represent the behavior of the material and in particular its time-dependent properties reasonably well.

The PFC is a representation of the gross behavior of rock and does not provide insight into the physical processes leading to deformation or failure in the tuffs. However, in most codes this is the case and probably should not be considered as a serious defect in the model. What is needed to fully validate the model is additional in situ and laboratory data to check the predictive capability of the PFC.

The time-dependent deformation and failure results of the particle flow code are incorporated into the analysis of roof collapse. The approach that they used is clearly presented and is a reasonable for the long-term performance of the roof in the repository.

Again, as with the PFC, as additional measurements on time-dependent behavior and in situ strength become available, these data will be incorporated into the model to further refine the predictions.

Another suggestion is that they consider referring to some of the historical data on the long-term performance of existing tunnels. There is sufficient experience over the years on numerous mines in a variety of rocks that have been subjected to elevated temperatures (especially deep mines in South Africa). Sufficient

measurements have been made in some cases so that time-dependent changes can be used to bound the parameters in the model. No reference has been made as yet to such historical data in the report. It seems prudent that in order to demonstrate the models are valid and that the long-term predictions are defensible, these must be considered.

## S6. CONCLUSIONS

Time-dependent drift stability for unsupported emplacement drifts is predicted. Time-dependent strength degradation under an in-situ stress state was combined with thermal or seismic loading conditions expected during the regulatory period. Predictions are based on two sets of data: a) test results obtained for Lac du Bonnet granite, and b) test results obtained for nonlithophysal tuff.

The effect of lithophysae on time-to-failure is investigated using the PFC stress corrosion model. The time-dependent parameters of the model were selected to match a straight-line fit to the Lac du Bonnet granite static-fatigue curve. Voids (corresponding to lithophysal porosity) were then generated in the synthetic material, which was numerically tested again to generate static-fatigue curves for lithophysal rock with different percentages of lithophysal porosity. The analysis showed that lithophysal porosity does affect the static-fatigue curves. As a function of porosity, the straight-line fits are offset slightly relative to one another, but have the same slope. The variability is not significant and for the purposes of this application, considering uncertainties in the analysis, it was justified to consider that lithophysal porosity does not affect the static-fatigue curve when the driving stress is normalized with the short-term strength of the rock mass. Considering the stress in the absolute form, the lithophysal porosity has a significant effect on the time-to-failure.

The evolution of damage due to strength degradation for different levels of driving-stress ratio was studied using the PFC stress corrosion model. At different stages during the numerical simulation of static-fatigue tests, samples were loaded in compression (at 0.1 MPa confinement) to failure. These numerical tests indicate that damage increases gradually, at a very slow rate, until a relatively short time before time-to-failure for a given driving stress, when damage quickly increases, resulting in the sample failure.

Analysis of drift stability was carried out using the UDEC model in which the rock mass was represented as an assembly of Voronoi blocks. The cohesive strength of the synthetic material decays as a function of time according to the input static-fatigue lines and curves of damage evolution under the different levels of sustained load as a function of time. Predictions of the rockfall are not sensitive to variation of the damage rate (before the time-to-failure) within the range of rates predicted by the PFC stress corrosion model. The most important model parameter for rockfall predictions is time-to-failure as a function of the driving stress.

Model prediction for different categories (1 through 5) of rock mass quality, combined with different static-fatigue lines were compared with observations from the ESF and ECRB. The drifts have been open between 5 and 12 years and no indication of their time-dependent deterioration has been observed yet (note that the drifts are supported with bolts and wire mesh in the roof only). Comparison of the model predictions of drift behavior after 5 and 10 years

with underground observation led to the following conclusions: a) rock mass category 1 for tuff as a homogeneous medium around the drifts underestimates the strength of the poorest quality lithophysal rock mass, b) Lac du Bonnet static-fatigue lines are inconsistent with tunnel behavior, leading to some rockfall after 10 years for all rock mass categories, and c) the poorest quality rock mass can be represented as rock mass category 2 with the tuff best-fit static-fatigue curve. It appears that the tuff best-fit static-fatigue lines are in the best agreement with both observations of tunnel performance and the results from short-term tests on the lithophysal rock mass. Further analysis was carried out using the tuff best-fit static-fatigue line only.

The best-fit tuff static fatigue line implies that a driving-stress ratio of approximately 0.60 results in approximately 20,000 years time-to-failure (see the tuff [ $P_c = 0$ ] best-fit curve in Figure S-26), indicating there will be an approximate 40 percent cohesive strength reduction in 20,000 years. The drift profile for a 40 percent cohesive strength reduction case (i.e., 60 percent cohesive strength) was initially determined as shown in Figure 6-171c for category 1. Note that Figure 6-171c is similar to the category 1 profile in Figure S-41. Considering only time-dependent strength degradation, it is clear that the 60 percent through 100 percent strength reduction cases (Figures 6-171d, 6-171e, and 6-171f) do not occur within the first 20,000 years of the postclosure period.

A combination of the thermally induced stresses with time-dependent strength degradation results in more rockfall than predicted for each of the loading conditions independently. Most rockfall, which is a result of deterioration of the walls, occurs for category 2. However, this poor quality rock accounts for only a small percentage (i.e., approximately 10 percent as shown in Figure S-50) of the total lithophysal rock mass in the emplacement drifts. Also, the combination of thermally induced stresses with time-dependent strength degradation does not increase rockfall significantly over a period of 10,000 years, as shown by comparing Figures S-38 and S-42. Note that while thermal stresses were not analyzed for the period from 10,000 years to 20,000 years, it can be inferred that the thermal impacts will be minimal during this period, since the temperature during this period has returned to near ambient, as shown in Section 6.2. Therefore, for the nominal case (i.e., considering thermal and time-dependent effects, but excluding seismic effects), the expected drift profiles after 20,000 years are adequately represented by Figures S-41 through S-44. As rock mass quality increases, there is less rockfall from the walls and more rockfall from the drift roof (Figure S-44). Better quality rock mass is stiffer, resulting in larger thermal stresses in the roof.

Postclosure seismic ground motion with a  $1 \times 10^{-6}$  probability of annual occurrence results in complete drift collapse, with the geometry of the collapsed drift unchanged from the previous results (see Section 6.4.2.2). To analyze the coupled effects of seismic load, thermal load, and time-dependent strength degradation, seismic loading by a preclosure ground motion with a  $1 \times 10^{-4}$  probability of annual occurrence was considered at two stages during the regulatory period (accounting for damage and rockfall due to thermal load history and time-dependent strength degradation): 80 years after waste emplacement, when thermally-induced stresses are maximum and 10,000 years after waste emplacement, which is the worst-case condition (during the regulatory period) of time-dependent strength degradation. Preclosure seismic ground motion causes an additional, but not significant, rockfall, which comes as a result of shaking down already loose, broken ground.

Damage to the host rock is not significantly accumulating from multiple  $1 \times 10^{-4}$  probability of annual occurrence ground motions. That is, the  $1 \times 10^{-4}$  seismic event is shaking loose rock fragments that have already failed by strength degradation and thermal stress; no new fractures and failures are caused by this low amplitude ground motion, either at 80 years when thermal stress is at its peak or at 10,000 years, when long-term strength degradation has occurred. Lack of new damage is also anticipated for more probable seismic events, such as  $5 \times 10^{-4}$  or  $1 \times 10^{-3}$  probability of annual occurrence ground motions, because they have smaller amplitudes than the  $1 \times 10^{-4}$  probability of annual occurrence ground motion.

Most of the analyses were carried out for different rock mass categories, but considering homogeneous properties throughout the model. Mechanical properties of the lithophysal rock mass are variable as a function of the position within the lithophysal unit. There is concern that homogeneous models do not properly represent the mechanical behavior of a heterogeneous rock mass. A mechanical model (with variable properties) of drift stability was generated corresponding to porosity fields obtained from the cross-sections through a three-dimensional model of the lithophysal porosity, which is considered to be the factor controlling the quality of the rock mass. There is no significant variability in rockfall predictions from one cross-section to another. Also, the rockfall predictions are very similar to those obtained for rock mass category 3.

The presented analysis deals with time-dependent drift degradation explicitly relating the rockfall predictions to a specific time. The analysis uses the existing information about the time-dependent behavior of tuff (static-fatigue tests), and behavior of the existing drifts (ESF and ECRB) over time. However, there is still a significant level of uncertainty in the predictions, because they are obtained by extrapolation of the test results and observations on short time-scales (maximum 10 years) to very long time-scales (10,000 years).

INTENTIONALLY LEFT BLANK



**APPENDIX T**  
**SIMULATION OF LITHOPHYSAL POROSITY SPATIAL VARIATION**



## **SIMULATION OF LITHOPHYSAL POROSITY SPATIAL VARIATION**

### **T1. INTRODUCTION**

To assist in modeling the spatial variability of mechanical properties in two and three dimensions for areas and volumes surrounding tunnels, a simple method of projecting the two-dimensional distribution of lithophysal cavity porosity has been developed. The calculation described in this appendix is for rock in the lower lithophysal zone of the Topopah Spring Tuff (Tptpl), and it is based on the data from the ECRB Cross-Drift (see Appendix O). The ECRB Cross-Drift data represents one of the best and detailed distributions of lithophysal cavity porosity available, so these data are projected to a vertical simulated cross section that is perpendicular to the ECRB Cross-Drift. Once the spatial variation of the lithophysal cavity porosity has been determined for areas and volumes surrounding the tunnels, correlation equations for the porosity to unconfined compressive strength and Young's Modulus can be used distribute the elastic properties and material strength (see Appendix E, Table E-10).

Four steps are used for projecting and distributing lithophysal cavity porosity in a tunnel (such as the ECRB Cross-Drift) into a two-dimensional cross section that is perpendicular to the tunnel. A simplified summary of these four steps is described below and in Figure T-1, with a detailed explanation (with specific examples) provided in Section T6.

- Step 1. Lithophysal cavity porosity values are projected along the apparent dip of the lithostratigraphic unit to a vertical line that is perpendicular to the tunnel (Figure T-1a), and this vertical line forms the center of the cross section. For simplicity, only the values that project to the top and bottom of the vertical line are depicted (Figure T-1a), but each point along the tunnel can be projected along the same apparent dip.
- Step 2. The vertical line is divided into a series of sections or horizons, and these sections are projected along the apparent dip to form stratigraphically equivalent "windows" along the tunnel (Figure T-1b).
- Step 3. The distribution of values and descriptive statistics, for example mean and standard deviation, are determined for each "window", and these statistics are imparted to the correlative section on the vertical line (Figure T-1c).
- Step 4. Descriptive statistics for each section on the vertical line are propagated along a horizon across the cross section (Figure T-1d).

### **T2. INPUT DATA**

The data required for the projection of lithophysal cavity porosity in a vertical cross section include (1) the distribution of the lithophysal cavity porosity along the ECRB Cross-Drift (Appendix O) and (2) the strike and dip of the top of the Tptpl in the ECRB Cross-Drift (Mongano et al. 1999 [DIRS 149850], Table 1).

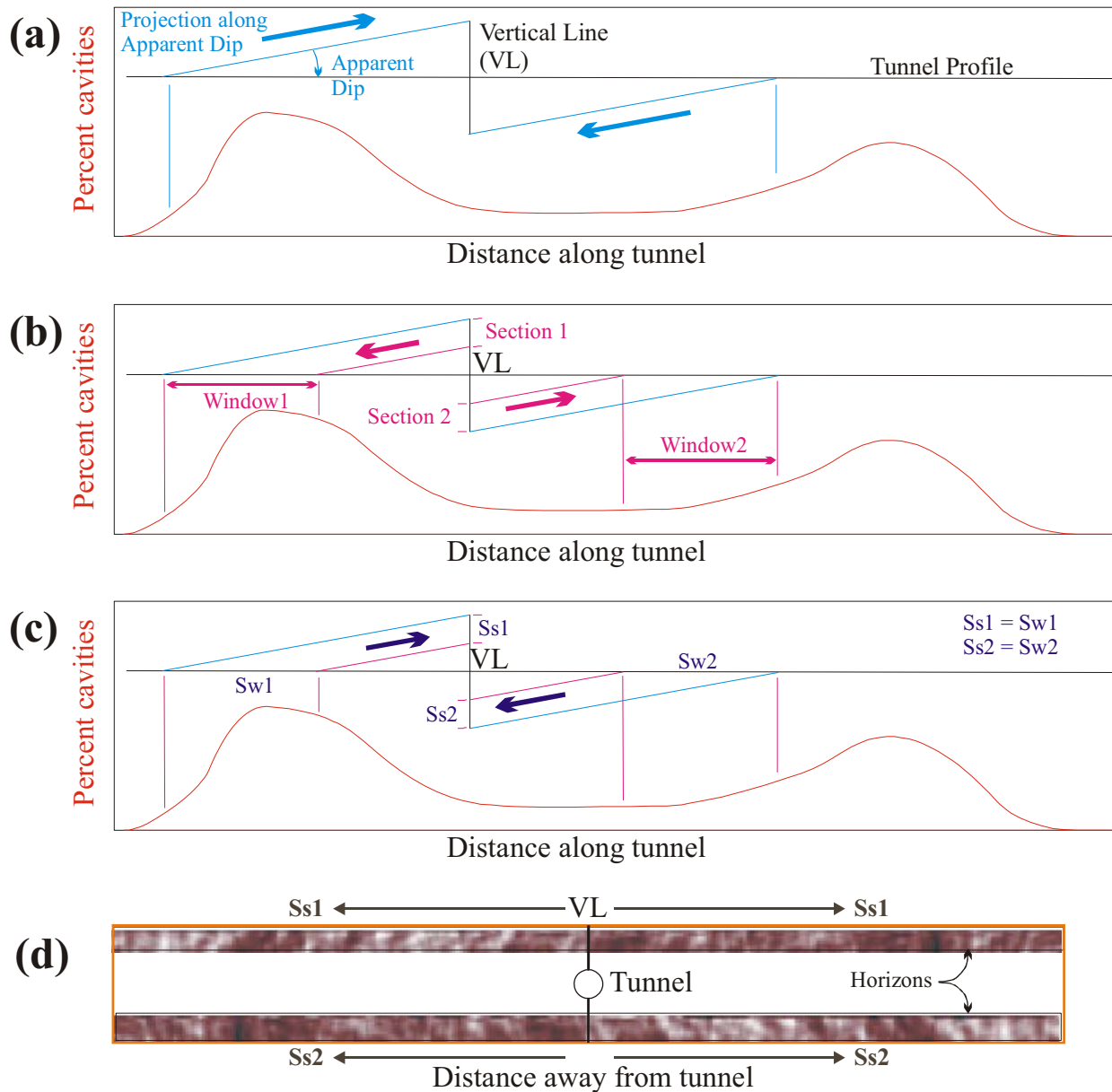


Figure T-1. Simplified Steps for Projecting and Distributing Lithophysal Cavity Porosity Values in a Tunnel Into a Two-Dimensional Cross Section

### T3. SOFTWARE USED IN THE CALCULATIONS

The input data, intermediate calculations, and results of the assessment of the distribution of lithophysal cavity porosity are stored and implemented in the Microsoft Excel file, *Lithophysal projection to vertical plane.xls* (DTN: MO0408MWDDDMIO.002). The transfers of values, calculations, logic functions, and descriptive statistics are done with standard functions in Excel. There are three small macros embedded in the Excel file, named “Prop\_Distribute,” “Contour\_Text,” and “Contour\_Fill.” These macros are exempt from the qualification

requirements of LP-SI.11Q-BSC, Software Management, since they are used solely for visual display of data:

- A. The “Prop\_Distribute” macro is an automated “copy and paste” function that takes the distributed values in a large (10×184 cell) “5 m window” table and makes a small (10×29 cell) “compacted” table of the values.
- B. The “Contour\_Text” and “Contour\_Fill” macros are basically the same and they simply change the format of the values or cells (but not the values themselves) in the 50×200 and 20×80 cell tables. The difference between these two macros is that one (“Contour\_Text”) colors the text (i.e., values), and the other (“Contour\_Fill”) changes the fill color of the cell and the color of the text (i.e., values).
- C. Confirmation that the macros are operating correctly can be made with simple visual comparisons of the large and small tables for the “Prop\_Distribute” macro, and the input data table with the 50×200 and 20×80 cell tables for the “Contour\_Text” and “Contour\_Fill” macros.

#### **T4. GEOMETRIC RELATIONS AND CONDITIONS IN THE CALCULATION**

Calculations of the distributed lithophysal cavity porosity in a vertical plane are based on six fundamental lithostratigraphic and geometric relations and conditions:

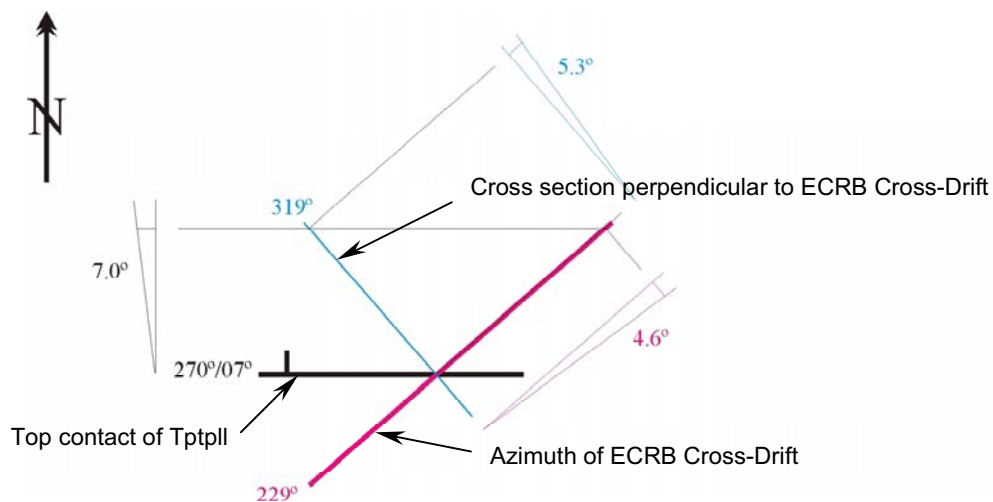
- A. Lithostratigraphic zones and subzones of the Topopah Spring Tuff are stratiform and are traceable across the repository area. However, some subzones might not occur across the entire repository area.
- B. The ECRB Cross-Drift transects the Tptpl as a shallowly inclined tunnel. Therefore, lithophysal cavity data represents vertical (and to some amount horizontal) variations in the lithostratigraphic features.
- C. Lateral continuity of variations in lithophysal cavity porosity in the tunnel is projected along the apparent dip of the Tptpl (and lithostratigraphic features) to a vertical line that is perpendicular to the tunnel.
- D. The vertical line is divided into 5 m tall horizons, and these horizons are projected along the apparent dip to the tunnel to form a series of “windows” along the tunnel.
- E. Each 5 m horizon along the vertical line contains the potential variability in porosity in their respective “window” along the tunnel.
- F. The statistical variation in porosity in each 5 m tall horizon is projected away from the tunnel along a vertical cross section that is perpendicular to the tunnel.

#### **T5. DETERMINATION OF THE APPARENT DIPS FOR INPUT**

The three-dimensional orientation of an inclined plane can be defined by a strike and dip, but an apparent dip is formed where the inclined plane intersects vertical planes along a section that is

not at a right angle to the strike of the vertical plane. The strike is the angle from north of a horizontal line in the inclined plane, and the dip is the angle from horizontal measured in a vertical plane that is  $90^\circ$  to the strike of the inclined plane. An apparent dip is the angle from the horizontal in a vertical plane of a line formed by the intersection of an inclined plane with the vertical plane.

An example of these geometric relations is illustrated in Figure T-2 with three planes. The inclined plane is the top contact of the Tptpl in the ECRB Cross-Drift and has a strike of  $270^\circ$  (Mongano et al. 1999 [DIRS 149850], Table 1). The true dip is measured in a plane perpendicular to the strike of the inclined plane, and is illustrated with the  $7^\circ$  dip. The ECRB Cross-Drift is contained in a vertical plane that has a strike of  $229^\circ$ . This strike is used because it is in the direction of the heading of the tunnel and in the area of the lithostratigraphic contact is in the direction of the inclination or plunge of the tunnel. A cross section perpendicular to the ECRB Cross-Drift forms a second vertical plane with a strike of  $319^\circ$ . The apparent dip of the lithophysal zone contact is  $4.6^\circ$  to the northeast (NE) in the plane of the cross drift and  $5.3^\circ$  to the northwest (NW) in the cross section perpendicular to the ECRB Cross-Drift. If another strike and dip were used, then the apparent dips will differ. For example, the top of the Tptpl in the ECRB Cross-Drift in the Geologic Framework Model (BSC 2004 [DIRS 170029]) has a strike and dip of  $345^\circ$  and  $5.8^\circ$ , respectively. The apparent dips are  $5.2^\circ$  NE in the plane of the ECRB Cross-Drift and  $2.5^\circ$  NW in the plane perpendicular to the ECRB Cross-Drift.



NOTE: The orientation of the Tptpl contact and the ECRB Cross-Drift is based on Mongano et al. (1999 [DIRS 149850]). The ECRB Cross-Drift is considered to be horizontal.

Figure T-2. Geometric Relations of Strike and Dip and the Apparent Dips in Cross Sections Parallel and Perpendicular to the ECRB Cross-Drift

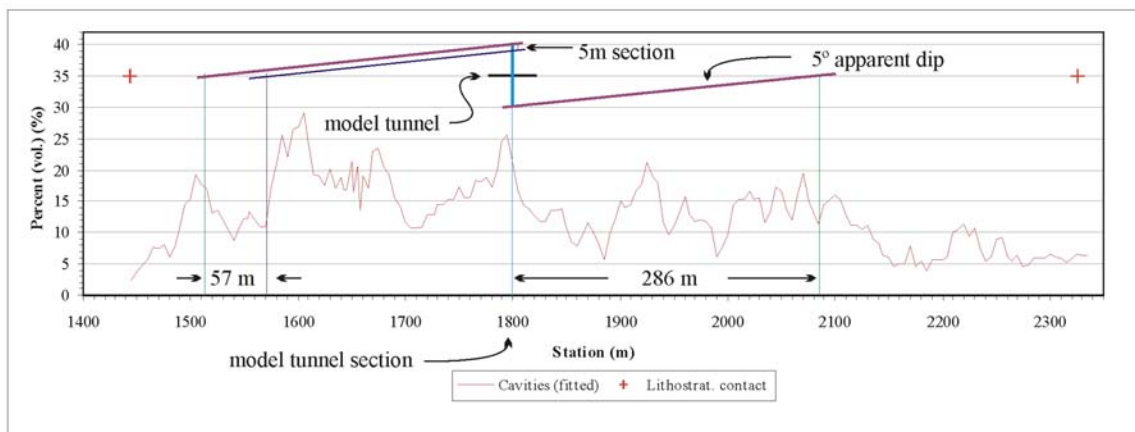
## T6. DISTRIBUTION OF LITHOPHYSAL CAVITY POROSITY IN THE ECRB CROSS-DRIFT AND SIMULATED VERTICAL CROSS SECTION

The stratiform geometry of the zones in the Topopah Spring Tuff occur throughout the repository area (Buesch et al. 1996 [DIRS 100106] and Buesch et al. 1996 [DIRS 101202], BSC 2004 [DIRS 170029]) as do many of the subzones such as the subzones of the Tptpmn (Buesch et al. 1996 [DIRS 100106], Buesch and Spengler 1998 [DIRS 101433]), although some subzones

might not occur across the entire repository area (Buesch and Spengler 1998 [DIRS 101433]). Variations in the orientation of lithostratigraphic contacts (Mongano et al. 1999 [DIRS 149850]) and the abundance (and percent) of lithostratigraphic features in the lower lithophysal zone, including lithophysal cavity porosity (Appendix O), are consistent with the ECRB Cross-Drift transecting a dipping lithostratigraphic section (Figure T-2). The lower lithophysal zone has not been divided into subzones, but the variations in features including the lithophysal cavity porosity are consistent with identification of 5 to 12 subzones (Figure T-3).

The lateral continuity of lithostratigraphic features, and the projection of these features along the apparent dip in the ECRB Cross-Drift, forms the principal component of creating a geologically informed calculation of the distribution of lithophysal cavity porosity in a vertical plane. Identification of a 50 m tall, vertical line (section) perpendicular to the tunnel is the first step in creation of the 50×200 m cross section (Figure T-3). Based on the apparent dip, the top and bottom of the vertical section can represent rocks from several hundred meters away from the centerline of the section. For example, with a 5° apparent dip, the equivalent rocks at the top and bottom of the vertical section are 286 m from the section (Figure T-3). With an apparent dip of 4.6° (Figure T-2), the projection for the top and bottom of vertical section is 311 m. This projection distance is consistent with the overall stratiform characteristics of the lithostratigraphic section.

The second step in creation of a cross section is to divide the vertical section into a series of 5 m tall sections or horizons. The projection along the apparent dip of the 5 m horizons result in a series of “windows” along the tunnel, and the position and length of each window results from the apparent dip. For example, with a 5° apparent dip, the equivalent window for the top 5 m horizon is 57 m long (Figure T-3). Each window contains unique variations in the number of measurements and the distribution of lithophysal cavity porosity values (Table T-1 and Figure T-4).



NOTE: The simulated cross section is at 1800 m with an apparent dip of 5° for the stratiform features.

Figure T-3. Variation in Lithophysal Cavity Porosity Along the ECRB Cross-Drift and the Geometric Relations of Calculation Components

Table T-1. Windows Containing Unique Variations of Lithophysal Cavity Porosity Values

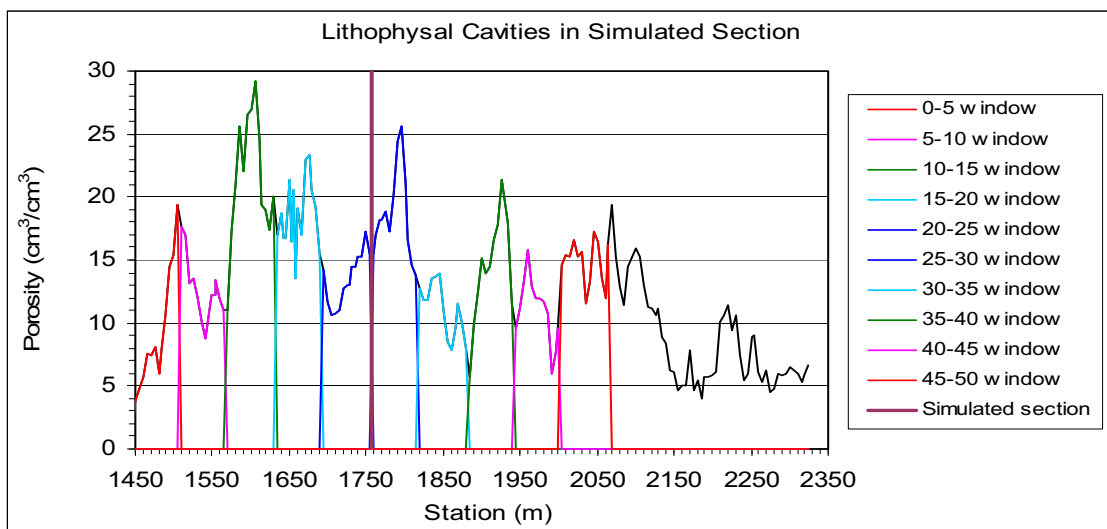
Station (m)	Cavity "fitted"	0-5 Window	5-10 Window	10-15 Window	15-20 Window
1445	2.5	null	null	null	null
1450	3.8	3.8	null	null	null
1455	4.7	4.7	null	null	null
1460	5.7	5.7	null	null	null
1465	7.6	7.6	null	null	null
1470	7.4	7.4	null	null	null
1475	8.2	8.2	null	null	null
1480	6.0	6.0	null	null	null
1485	7.9	7.9	null	null	null
1490	10.6	10.6	null	null	null
1495	14.4	14.4	null	null	null
1500	15.3	15.3	null	null	null
1505	19.4	19.4	null	null	null
1510	17.7	null	17.7	null	null
1515	17.0	null	17.0	null	null
1520	13.2	null	13.2	null	null
1525	13.6	null	13.6	null	null
1530	12.1	null	12.1	null	null
1535	10.2	null	10.2	null	null
1540	8.8	null	8.8	null	null
1545	11.0	null	11.0	null	null
1550	12.2	null	12.2	null	null
1552.8	12.2	null	12.2	null	null
1555	13.4	null	13.4	null	null
1560	12.0	null	12.0	null	null
1565	11.0	null	11.0	null	null
1570	11.0	null	null	11.0	null
1575	17.2	null	null	17.2	null
1580	21.0	null	null	21.0	null
1585	25.6	null	null	25.6	null
1590	22.1	null	null	22.1	null
1595	26.5	null	null	26.5	null
1600	26.9	null	null	26.9	null
1605	29.2	null	null	29.2	null
1610	24.6	null	null	24.6	null
1615	19.3	null	null	19.3	null
1620	19.0	null	null	19.0	null
1625	17.4	null	null	17.4	null



Table T-1. Windows Containing Unique Variations of Lithophysal Cavity Porosity Values (Continued)

Station (m)	Cavity "fitted"	0-5 Window	5-10 Window	10-15 Window	15-20 Window
1630	20.1	null	null	20.1	null
1635	17.0	null	null	null	17.0
1640	18.8	null	null	null	18.8

NOTE: This table shows a portion of the lithophysal cavity porosity input data that are divided into windows representing 5 m tall horizons in the simulated cross section. The "Cavity (fitted)" column provides adjusted mapped lithophysal porosity values as described in Appendix O (Section O5). Porosity values for each window are depicted in Figure T-4. Data in the "Station (m)" and "Cavity (fitted)" columns are from Appendix O (Section O6.6; see Microsoft Excel file, *Drift Deg AMR AF T-A-P Fit.xls*, worksheet "Volume Percent - Stats", which can be accessed through the TDMS using DTN: MO0408MWDDDMIO.002). These data are for a calculation with a centerline of the simulated cross section at 1756 m and an apparent dip of 4.6°.



NOTE: Apparent Dip of 4.6°, and 10 "Windows".

Figure T-4. Lithophysal Cavity Porosity in the Lower Lithophysal Zone of the ECRB Cross-Drift with the Centerline of the Simulated Cross Section at 1756 m

The third step in creation of a simulated cross section is to distribute the descriptive statistics of the lithophysal cavity porosity in each window in the associated 5 m tall horizon. The statistical variation in porosity in each horizon is represented by sampling the actual porosity values in the respective "window". Two methods using standard Excel functions have been used for this distribution; one function is "Choose" where the values in each window are randomly selected, and the other approach uses the random number generator in the analysis tool. For example, the first three 5 m horizons (0-5, 5-10, and 10-15 windows) in Table T-1 are depicted as Horizons "0", "5", and "10" and Y positions 1 to 15, respectively, in Table T-2 and T-3. Comparison of values in Table T-1 and parts of Table T-2 and T-3 indicate the same values occur in the tables.

Table T-2. Display of Part of the 50×200 Cell Table with Descriptive Statistics for Calculation of Lithophysal Cavity Porosity in a 50×200 m Simulated Cross Section with the Centerline Station 17+56

Table of porosity values (1x1 m grid)											
Horizon	Cell $\gamma^x$	1	2	3	4	5	6	7	8	9	10
0	1	7.6	4.7	19.4	7.6	8.2	8.2	10.6	7.6	7.9	3.8
0	2	6.0	7.4	8.2	19.4	7.9	10.6	14.4	7.9	15.3	7.9
0	3	6.0	15.3	15.3	7.9	7.4	6.0	4.7	3.8	15.3	7.6
0	4	10.6	10.6	10.6	7.9	3.8	3.8	19.4	7.9	7.6	7.6
0	5	8.2	15.3	7.9	10.6	5.7	8.2	7.4	6.0	7.9	7.6
5	6	13.2	11.0	17.7	11.0	17.7	10.2	12.2	12.1	12.2	12.2
5	7	11.0	12.1	12.2	10.2	12.2	8.8	12.2	11.0	12.2	12.0
5	8	12.2	13.6	12.0	12.2	11.0	8.8	12.1	12.2	11.0	12.0
5	9	17.7	13.6	10.2	17.0	10.2	17.0	8.8	11.0	12.2	10.2
5	10	12.2	12.2	12.1	11.0	12.2	10.2	13.4	12.2	13.2	17.7
10	11	26.5	26.9	22.1	25.6	19.0	21.0	17.2	26.9	17.2	26.9
10	12	11.0	26.5	24.6	26.9	19.0	29.2	19.0	21.0	17.2	19.0
10	13	24.6	17.4	26.9	19.0	19.0	19.0	19.3	29.2	25.6	17.4
10	14	17.4	26.5	17.2	17.2	24.6	21.0	26.9	26.5	20.1	26.9
10	15	22.1	17.2	19.0	17.4	26.9	26.9	21.0	11.0	17.2	21.0
15	16	18.8	16.5	13.6	20.5	20.5	22.9	21.4	20.6	16.5	20.6
15	17	16.8	15.5	22.9	20.5	16.5	17.0	13.6	19.1	13.6	17.0
15	18	20.6	19.3	15.5	17.0	17.0	19.3	20.6	19.1	16.8	17.0
15	19	20.5	13.6	23.4	16.8	23.4	16.8	20.6	22.9	15.5	20.5
15	20	23.4	21.4	19.3	15.5	16.8	21.4	20.5	17.0	21.4	17.0
20	21	10.7	15.5	13.0	15.5	11.0	15.3	15.3	15.3	12.8	15.3
20	22	13.0	14.5	17.3	11.0	11.7	13.0	17.3	14.5	10.6	10.6
20	23	15.5	15.3	11.7	15.3	14.2	14.5	10.6	14.5	10.6	11.0
20	24	15.3	14.5	15.5	13.0	15.5	15.3	11.7	14.5	13.0	10.7
20	25	10.7	10.6	11.0	15.5	11.0	14.5	15.3	11.0	15.3	14.5
25	26	16.9	24.5	17.3	20.1	18.1	15.5	20.1	18.1	13.8	13.8
25	27	18.1	25.6	14.5	17.3	18.1	20.1	21.1	17.3	14.5	14.5
25	28	17.3	15.5	18.8	18.1	17.3	21.1	17.3	18.8	17.3	18.1
25	29	20.1	20.1	18.1	24.5	18.8	21.1	18.1	13.8	18.1	21.1
25	30	18.1	18.1	15.5	18.1	13.8	18.1	14.5	24.5	18.1	21.1
30	31	12.7	13.5	8.5	12.7	13.5	8.5	8.5	12.7	11.6	10.0
30	32	8.1	11.8	10.8	13.9	13.9	13.5	13.9	7.8	8.1	8.5
30	33	9.7	12.7	9.7	9.7	10.8	10.0	11.8	13.9	9.7	11.6

Table T-2. Display of Part of the 50×200 Cell Table with Descriptive Statistics for Calculation of Lithophysal Cavity Porosity in a 50×200 m Simulated Cross Section with the Centerline Station 17+56 (Continued)







Table of porosity values (1x1 m grid)											
Horizon	Cell $\gamma^x$	1	2	3	4	5	6	7	8	9	10
30	34	13.5	10.0	11.8	13.6	13.6	7.8	13.6	13.9	11.6	11.8
30	35	7.8	10.0	10.8	13.6	10.0	8.5	13.6	7.8	10.8	8.5
35	36	12.3	19.1	21.3	12.3	17.8	12.3	13.9	15.2	5.7	21.3
35	37	15.2	5.7	12.3	16.6	13.9	12.3	14.4	5.7	16.6	17.8
35	38	19.1	5.7	5.7	19.1	11.6	15.2	14.4	18.0	18.0	18.0
35	39	21.3	13.9	12.3	19.1	12.3	13.9	17.8	16.6	18.0	15.2
35	40	15.2	13.9	9.8	19.1	15.2	17.8	16.6	9.8	16.6	16.6
40	41	10.7	10.7	12.9	11.1	13.3	7.7	15.8	9.6	7.7	11.7
40	42	7.7	13.3	10.7	13.3	10.7	10.7	11.9	15.8	6.0	11.1
40	43	7.7	11.9	11.7	9.6	6.0	12.9	15.8	11.7	13.3	12.9
40	44	11.9	6.0	7.7	10.7	11.1	11.9	12.9	12.9	12.9	11.1
40	45	15.8	9.6	12.9	9.6	6.0	12.9	11.1	11.9	7.7	7.7
45	46	12.0	16.5	17.3	17.3	16.3	16.3	13.2	15.3	16.3	11.6
45	47	13.5	12.0	11.6	13.2	16.6	11.6	15.6	15.3	15.3	13.5
45	48	15.6	12.0	15.3	15.6	16.6	15.2	16.6	13.5	15.3	15.6
45	49	12.0	15.3	17.3	15.3	16.3	16.3	13.2	17.3	11.6	14.5
45	50	16.3	16.3	13.5	13.2	17.3	13.2	16.6	15.2	16.6	13.5
Descriptive Statistics											
Simulated "X" position	1	2	3	4	5	6	7	8	9	10	
Mean	14.4	14.6	14.5	15.2	14.2	14.5	15.2	14.5	13.8	14.3	
Standard Error	0.7	0.7	0.7	0.6	0.7	0.8	0.6	0.8	0.6	0.7	
Median	13.5	13.9	13.2	15.4	13.9	14.2	14.5	14.2	13.7	13.6	
Mode	6.0	15.3	15.5	19.1	11.0	8.2	12.2	14.5	12.2	7.6	
Standard Deviation	5.0	5.3	4.8	4.5	4.9	5.3	4.2	5.5	4.1	5.0	
Sample Variance	24.6	28.1	22.6	20.0	23.8	28.6	17.2	30.7	17.1	25.2	
Kurtosis	-0.4	0.4	-0.1	0.1	0.2	0.2	0.5	0.4	0.2	0.1	
Skewness	0.4	0.6	0.6	0.5	0.2	0.5	0.2	0.6	0.1	0.5	
Range	20.5	22.2	21.2	19.3	23.1	25.4	22.2	25.4	19.9	23.1	
Minimum	6.0	4.7	5.7	7.6	3.8	3.8	4.7	3.8	5.7	3.8	
Maximum	26.5	26.9	26.9	26.9	26.9	29.2	26.9	29.2	25.6	26.9	
Sum	720.3	731.0	726.9	758.6	711.3	723.6	758.2	727.1	689.7	715.6	
Count	50	50	50	50	50	50	50	50	50	50	
Confidence Level (95.0%)	1.4	1.5	1.3	1.2	1.4	1.5	1.2	1.5	1.1	1.4	
Explanation of symbols (percent lithophysal cavity porosity)											
	<=5		<=10		<=15		<=20		<=25		>25

Table T-3. Display of Part of the 20x80 Cell Table with Descriptive Statistics for Calculation of Lithophysal Cavity Porosity in a 50x200 m Simulated Cross Section with the Centerline at Station 17+56

Table of porosity values (2.5x2.5 m grid)											
Horizon	Cell γ <sup>x</sup>	2.5	5.0	7.5	10.0	12.5	15.0	17.5	20.0	22.5	25.0
0	2.5	15.3	7.4	7.9	5.7	8.2	6.0	5.7	7.4	5.7	15.3
0	5.0	7.4	8.2	8.2	10.6	8.2	8.2	3.8	6.0	14.4	10.6
5	7.5	12.0	12.2	11.0	17.0	12.2	10.2	10.2	12.1	8.8	12.2
5	10.0	13.4	10.2	13.6	12.0	11.0	17.0	10.2	12.2	11.0	17.7
10	12.5	29.2	21.0	19.0	26.9	17.4	17.2	29.2	19.0	17.4	19.0
10	15.0	24.6	29.2	25.6	25.6	11.0	19.0	19.0	17.4	21.0	17.4
15	17.5	18.8	17.0	13.6	18.8	20.5	21.4	19.3	17.0	23.4	15.5
15	20.0	19.1	20.6	20.5	16.8	15.5	16.8	16.8	15.5	19.1	22.9
20	22.5	13.0	15.3	13.0	14.5	10.7	14.5	11.0	13.0	11.0	14.5
20	25.0	15.3	14.5	15.3	17.3	11.7	11.7	10.7	10.6	15.5	17.3
25	27.5	15.5	13.8	18.1	16.9	25.6	16.9	18.1	25.6	18.8	20.1
25	30.0	14.5	16.9	25.6	18.1	18.1	21.1	17.3	18.1	25.6	16.9
30	32.5	7.8	10.8	9.7	7.8	11.8	12.7	11.8	10.8	11.8	11.6
30	35.0	9.7	11.8	12.7	13.6	8.5	9.7	9.7	10.8	12.7	7.8
35	37.5	9.8	9.8	11.6	19.1	5.7	21.3	16.6	17.8	17.8	5.7
35	40.0	21.3	15.2	9.8	19.1	9.8	12.3	14.4	15.2	21.3	17.8
40	42.5	9.6	12.9	9.6	11.9	9.6	11.9	6.0	12.9	11.7	13.3
40	45.0	9.6	11.1	11.9	10.7	9.6	9.6	10.7	6.0	11.1	11.9
45	47.5	14.5	17.3	15.2	17.3	15.3	13.5	16.6	15.6	16.6	15.2
45	50.0	15.3	16.6	14.5	16.5	12.0	16.5	15.6	13.2	16.5	16.6
Descriptive Statistics											
Simulated "X" position	2.5	5.0	7.5	10.0	12.5	15.0	17.5	20.0	22.5	25.0	
Mean	14.8	14.6	14.3	15.8	12.6	14.4	13.6	13.8	15.6	15.0	
Standard Error	1.3	1.1	1.2	1.2	1.1	1.0	1.3	1.1	1.1	0.9	
Median	14.5	14.1	13.3	16.9	11.4	14.0	13.1	13.1	16.0	15.4	
Mode	14.5	#N/A	#N/A	19.1	8.2	#N/A	10.2	10.8	#N/A	#N/A	
Standard Deviation	5.6	5.1	5.2	5.2	4.8	4.5	5.9	4.8	5.1	4.2	
Sample Variance	31.8	25.9	26.6	27.3	23.3	20.5	34.3	22.7	26.4	17.3	
Kurtosis	1.0	2.3	0.5	0.4	1.5	-0.9	1.3	0.7	-0.5	0.3	
Skewness	1.0	1.2	1.0	0.2	1.2	0.0	0.6	0.4	0.1	-0.5	
Range	21.8	21.8	17.8	21.2	19.9	15.4	25.4	19.6	20.0	17.2	
Minimum	7.4	7.4	7.9	5.7	5.7	6.0	3.8	6.0	5.7	5.7	
Maximum	29.2	29.2	25.6	26.9	25.6	21.4	29.2	25.6	25.6	22.9	
Sum	295.8	291.7	286.4	316.3	252.4	287.7	272.6	276.5	311.4	299.5	
Count	20	20	20	20	20	20	20	20	20	20	
Confidence Level (95.0%)	2.5	2.2	2.3	2.3	2.1	2.0	2.6	2.1	2.3	1.8	
<b>Explanation of symbols</b> (percent lithophysal cavity porosity)											

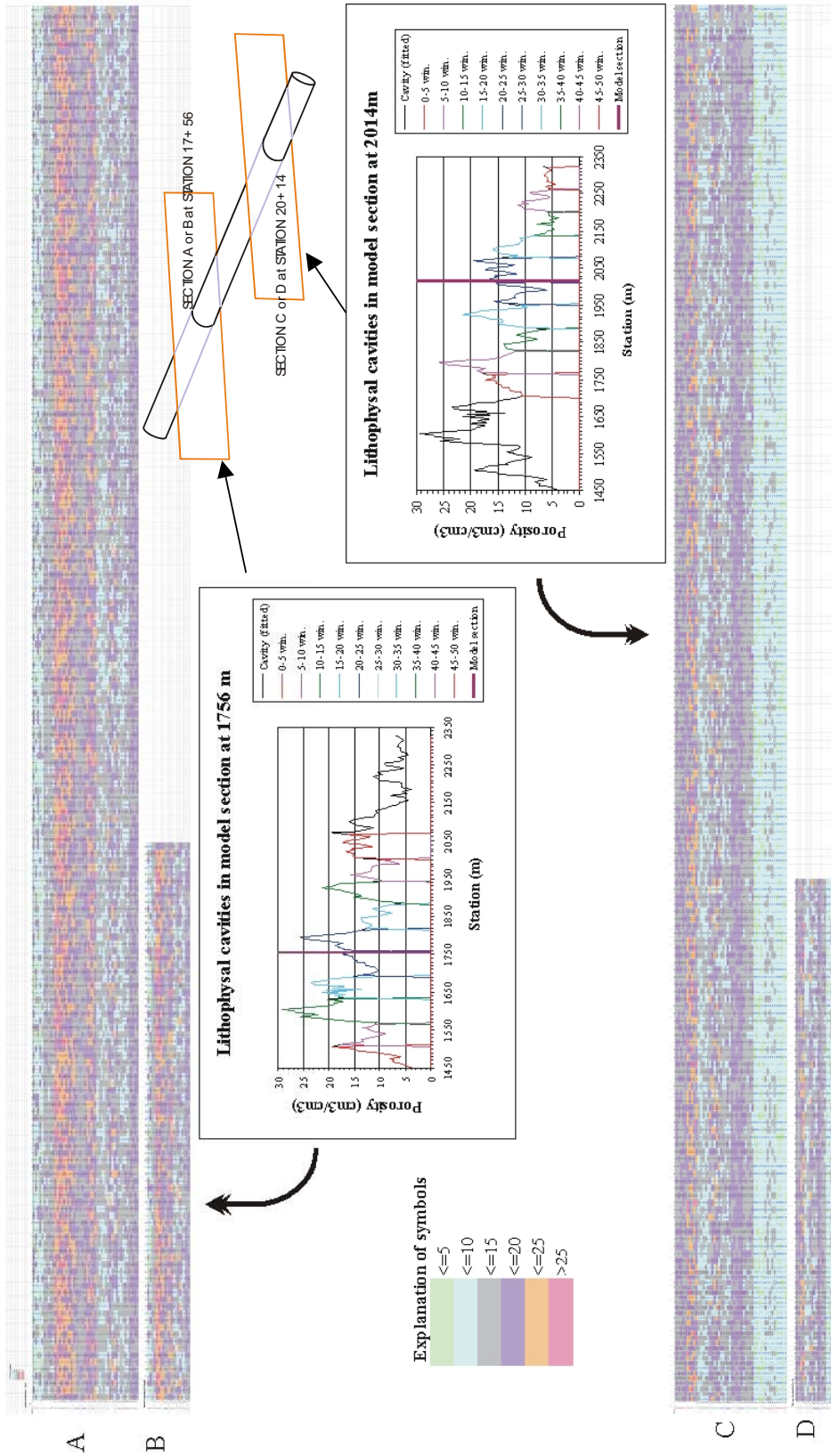
The fourth step in creation of a simulated vertical cross section is to project the 5 m horizons in the vertical section away from the vertical section to create the cross section. For a 200 m wide cross section, the projection away from the central vertical section is 100 m to either side. In this construct, the maximum “straight line” projection distance for an apparent dip of  $4.6^\circ$  and an along-the-tunnel projection of 311 m is only 327 m. This projection distance is consistent with the overall stratiform characteristics of the lithostratigraphic section. Figure T-5 displays two simulations of a  $50 \times 200$  m cross section using a  $4.6^\circ$  apparent dip, one for a center of the section at 1756 m and a second for a center at 2014 m. In these simulations, there is an overlap of 364 m along the tunnel and when projected to the vertical plane it represents an overlap of about 30 m of section (Figure T-5). Each simulation is depicted with a  $50 \times 200$  cell table representing a  $1 \times 1$  m grid (sections A and C) and a  $20 \times 80$  cell table representing a  $2.2 \times 2.5$  m grid (sections B and D). The four sections in Figure T-5 display similar stratiform relations.

Descriptive statistics (from standard Excel functions) for the input data in the various windows (Table T-4) with the selected statistics from 5 m tall horizons in the  $50 \times 200$  cell and  $20 \times 80$  cells indicate very good correlations. The descriptive statistics (from standard Excel functions) of the total Tptpl zone in the ECRB Cross-Drift is provided in Table T-4 (first column of values). Descriptive statistics for the total windows in the ECRB Cross-Drift (input) data and the total  $50 \times 200$  cell and  $20 \times 80$  cell tables indicate very high correlations (Table T-5). These correlations reinforce the technical soundness of this approach to project the distribution of lithophysal cavity porosity from the cross section data to a vertical plane.

## **T7. LIMITATIONS OF THE CALCULATION**

The calculations of the distribution of lithophysal cavity porosity from the ECRB Cross-Drift to a vertical plane that is perpendicular to the tunnel is based on sound geologic and geometric relations; however, there are a few limitations to the results:

- A. The calculations exemplified in this appendix are based on the consideration that the ECRB Cross-Drift is horizontal. The gradient of the tunnel is 1.5 percent ( $0.86^\circ$ ) from 07+73 to 16+02 and is 0.9 percent ( $0.52^\circ$ ) from 16+02 to 24+67 (Mongano et al. 1999 [DIRS 149850], pp. 3 to 6). So, although these inclinations are small, they can be factored into the apparent dip of the lithostratigraphic units and features to enhance the geologic and construction conditions.
- B. Using a constant apparent dip of  $4.6^\circ$  from the strike and dip of 270/07 for the top contact of the lower lithophysal zone in the ECRB Cross-Drift (Mongano et al. 1999 [DIRS 149850], Table 1) and the total intercept of the lower lithophysal zone in the ECRB Cross-Drift (from 14+44 to 23+26), the calculated thickness of the lower lithophysal zone is only 71 m. This calculated thickness is less than what is calculated and depicted by a variety of other methods, so the apparent dip of  $4.6^\circ$  is probably too shallow; therefore, the number and the distribution of values in each window along the tunnel might be over represented.
- C. The simulated cross section is constructed perpendicular to the tunnel; however, it does not include the apparent dip in the plane of the cross section. For example, using the features and data depicted in Figure T-2, the apparent dip in the cross section is  $5.3^\circ$  to the northwest.



NOTE: Cross section A is a 50x200 cell table representing a 1x1 m grid, and cross section B is a 20x80 cell table representing a 2.2x2.5 m grid for the simulated section at 17+56. Cross Section C is a 50x200 cell table representing a 1x1 m grid, and cross Section D is a 20x80 cell table representing a 2.2x2.5 m grid for the simulated section at 20+14.

Figure T-5. Two 50x200 m Simulated Cross Sections of Lithophysal Cavity Porosity at Stations 17+56 and 20+14

Because the values in each cell in the 50×200 and 20×80 cell tables are independently and randomly allocated, locally there are a few geologically inconsistent results. While this allocation technique results in very high correlations of the descriptive statistics between the input data and resulting cross-section horizons, it is possible that locally, the minimum and maximum values in a window or in adjacent windows can be in adjacent cells. This extreme change in lithophysal cavity porosity has not been observed in the ECRB Cross-Drift as shown by the gradual increase or decrease in values (although sharp changes can occur across distances of 5 to 10 m; Figure T-3). One result of this random allocation of values and the potential juxtaposition of large and small (or mostly values of one end of the distribution or another) is the variation in descriptive statistics in vertical sections (X positions; Table T-2 and T-3). The affect of this juxtaposition of minimum and maximum values is probably greater in the 20×80-cell table that represents a 2.5×2.5 m grid than in the 50×200 cell table that represents a 1×1 m grid. One way to minimize this affect is to filter the values in the tables and remove (or change) one or both of the juxtaposed values. Development of such a filter needs to focus on diminishing the anomalies, but maintaining the statistical integrity of the resultant calculated values.

Table T-4. Comparison of Descriptive Statistics for the Total Tptll Zone in the ECRB Cross-Drift, Individual Windows from the Input Data, and Selective Statistics for 5 m Tall Horizons in a 50×200 m Simulated Cross Section with 1×1 m and 2.5×2.5 m Grids

Descriptive Statistics (for Total Input and Windows)																
Statistic	Total ECRB Cross-Drift Data	0-5 Window	0-5 1x1 Grid	0-5 2.5x2.5 Grid	5-10 Window	5-10 1x1 Grid	5-10 2.5x2.5 Grid	10-15 Window	10-15 1x1 Grid	10-15 2.5x2.5 Grid	15-20 Window	15-20 1x1 Grid	15-20 2.5x2.5 Grid	20-25 Window	20-25 1x1 Grid	20-25 2.5x2.5 Grid
Mean	12.9	9.2	9.1	9.3	12.6	12.6	12.3	21.5	21.2	22.4	18.6	18.6	18.3	13.5	13.6	13.6
Standard Error	0.4	1.4	0.1	0.4	0.7	0.1	0.2	1.4	0.1	0.4	0.7	0.1	0.2	0.5	0.1	0.2
Median	12.7	7.7	—	—	12.2	—	—	21.0	—	—	18.8	—	—	13.6	—	—
Mode	17.0	#N/A	—	—	12.2	—	—	#N/A	—	—	17.0	—	—	13.0	—	—
Standard Deviation	5.4	4.8	4.6	4.7	2.5	2.3	2.4	5.0	4.7	4.6	2.8	2.7	2.6	2.0	2.0	2.0
Sample Variance	29.6	22.7	21.1	21.9	6.2	5.5	5.9	24.8	22.2	20.8	7.7	7.0	7.0	4.2	3.9	3.8
Kurtosis	-0.2	0.3			0.8			0.1			-0.6			-0.8		
Skewness	0.4	1.1	1.0	1.0	0.9	0.8	0.9	-0.4	-0.2	-0.5	0.2	0.2	0.1	0.0	0.0	0.0
Range	26.7	15.5	—	—	8.9	—	—	18.2	—	—	9.8	—	—	6.7	—	—
Minimum	2.5	3.8	—	—	8.8	—	—	11.0	—	—	13.6	—	—	10.6	—	—
Maximum	29.2	19.4	—	—	17.7	—	—	29.2	—	—	23.4	—	—	17.3	—	—
Sum	2352.1	110.9	—	—	164.4	—	—	279.9	—	—	279.2	—	—	189.5	—	—
Count	183	12	—	—	13	—	—	13	—	—	15	—	—	14	—	—
Confidence Level (95.0%)	0.8	2.7	—	—	1.3	—	—	2.7	—	—	1.4	—	—	1.1	—	—

Table T-4. Comparison of Descriptive Statistics for the Total Tptpl Zone in the ECRB Cross-Drift, Individual Windows from the Input Data, and Selective Statistics for 5 m Tall Horizons in a 50×200 m Simulated Cross Section with 1×1 m and 2.5×2.5 m Grids (Continued)

Descriptive Statistics (for Total Input and Windows)																
Statistic	Total ECRB Cross-Drift Data	25-30 Window	25-30 1x1 Grid	25-30 2.5x2.5 Grid	30-35 Window	30-35 1x1 Grid	30-35 2.5x2.5 Grid	35-40 Window	35-40 1x1 Grid	35-40 2.5x2.5 Grid	40-45 Window	40-45 1x1 Grid	40-45 2.5x2.5 Grid	45-50 Window	45-50 1x1 Grid	45-50 2.5x2.5 Grid
Mean	12.9	18.5	18.6	18.2	11.1	11.0	11.0	14.6	14.6	14.6	11.0	11.0	10.8	14.8	14.9	14.6
Standard Error	0.4	0.9	0.1	0.3	0.6	0.1	0.2	1.3	0.1	0.4	0.7	0.1	0.2	0.5	0.1	0.1
Median	12.7	18.1	—	—	11.6	—	—	14.8	—	—	11.4	—	—	15.3	—	—
Mode	17.0	18.1	—	—	11.8	—	—	#N/A	—	—	#N/A	—	—	#N/A	—	—
Standard Deviation	5.4	3.4	3.3	3.3	2.1	2.0	2.0	4.4	4.1	4.6	2.6	2.4	2.7	1.8	1.7	1.8
Sample Variance	29.6	11.6	10.8	10.6	4.4	4.1	4.1	19.0	17.2	20.8	6.7	5.9	7.5	3.2	2.9	3.3
Kurtosis	-0.2	0.5	—	—	-1.2	—	—	0.2	—	—	0.6	—	—	-0.6	—	—
Skewness	0.4	0.9	0.8	0.8	-0.2	-0.2	-0.1	-0.5	-0.5	-0.6	-0.2	-0.2	-0.3	-0.6	-0.6	-0.3
Range	26.7	11.9	—	—	6.1	—	—	15.6	—	—	9.8	—	—	5.7	—	—
Minimum	2.5	13.8	—	—	7.8	—	—	5.7	—	—	6.0	—	—	11.6	—	—
Maximum	29.2	25.6	—	—	13.9	—	—	21.3	—	—	15.8	—	—	17.3	—	—
Sum	2352.1	259.4	—	—	143.8	—	—	175.8	—	—	132.3	—	—	192.9	—	—
Count	183	14	—	—	13	—	—	12	—	—	12	—	—	13	—	—
Confidence Level (95.0%)	0.8	1.8	—	—	1.1	—	—	2.5	—	—	1.5	—	—	1.0	—	—

Table T-5. Comparison of Descriptive Statistics for the Total Windows from ECRB Cross-Drift (Input) Data and the Total 50×200 m Simulated Cross Section with 1×1 m and 2.5×2.5 m Grids

Descriptive Statistics for Total Windows							
Statistic	ECRB Cross-Drift Data	1x1 Grid	2.5x2.5 Grid	Statistic	ECRB Cross-Drift Data	1x1 Grid	2.5x2.5 Grid
Mean	14.7	14.5	14.5	Skewness	0.4	0.4	0.4
Standard Error	0.4	0.0	0.1	Range	25.4	25.4	25.4
Median	14.4	13.9	13.9	Minimum	3.8	3.8	3.8
Mode	17.0	11.6	11.6	Maximum	29.2	29.2	29.2
Standard Deviation	4.9	4.9	5.1	Sum	1928.1	145404.3	23193.6
Sample Variance	24.0	24.0	25.5	Count	131.0	10000	1600
Kurtosis	0.2	0.2	0.2	Confidence Level (95.0%)	0.8	0.10	0.25



**APPENDIX U**

**METHODOLOGY OF AND VERIFICATION OF THE INTERCHANGE AND  
APPLICATION OF ROCK MASS PRE- AND POSTCLOSURE TEMPERATURE  
PREDICTIONS FROM THE NUFT THERMAL CALCULATION TO THE UDEC AND  
FLAC MODELS**



**METHODOLOGY OF AND VERIFICATION OF THE INTERCHANGE AND  
APPLICATION OF ROCK MASS PRE- AND POSTCLOSURE TEMPERATURE  
PREDICTIONS FROM THE NUFT THERMAL CALCULATION TO THE UDEC AND  
FLAC MODELS**

Stability of the drift in the lithophysal and nonlithophysal rock mass due to thermal loading was analyzed using the UDEC and 3DEC discontinuum models as described in Sections 6.3 and 6.4. For consistency with other thermal calculations performed for performance assessment at Yucca Mountain, the UDEC and 3DEC programs were not used to determine the rock mass temperatures. Instead, the evolution of the temperature field after waste emplacement was obtained using the hydro-thermal code NUFT, which is one of the component submodels of the LDTH model, described in *Multiscale Thermohydrologic Model* (BSC 2004 [DIRS 169565]). The temperature fields were imported sequentially into UDEC (lithophysal rock) and FLAC (nonlithophysal rock) for a number of times after waste emplacement, making sure that the temperature change between two stages is relatively small (i.e., it does not result in a large stress change). The thermal stresses due to temperature changes were calculated, and the model was solved for equilibrium for the selected thermal times. The purpose of this appendix is to describe the process of application of the NUFT temperature fields to the UDEC and FLAC models, and to verify that this process results in proper NUFT rock mass temperature within the UDEC and FLAC models.

NUFT provides the temperature fields on a rectangular grid, which are stored in a spreadsheet (DTN: MO0408MWDDDMIO.002, file *LA1450\_NUFT\_Temp\_crss-sctn3.xls*; see example shown in Figure U-1). The temperature fields, corresponding to different thermal times, are extracted and stored in separate ASCII files (see example shown in Figure U-2.), which are read by UDEC. The UDEC model is composed of a large number of irregularly-shaped blocks which are, in turn, discretized into a number of triangular finite difference elements. The temperatures from the NUFT grid must be interpolated at the nearby UDEC grid points. To perform this interpolation, the NUFT elements that contain UDEC grid points must be identified. In order to speed up the search of the NUFT element that contains a UDEC grid point, the coordinates in the ASCII files are sorted by increasing  $x$ - and  $y$ -coordinates. The UDEC geometry is generated using the same coordinate system as the one used in NUFT. The origins of the coordinate systems in both models are at the center of the drift. The NUFT model uses the symmetry condition with respect to the vertical plane through the drift center. The symmetry was not used in the UDEC model for the mechanical simulations, but the temperature field is considered to be symmetrical, i.e.,  $T(x, y) = T(-x, y)$ .

NUFT 2D Multi-Scale TH (LDTH) model  
 TSPA-LA: 1.45 kW/m, 0 yrs emplacement duration (50 yrs Ventilation), closure at 50 yrs  
 90% integrated heat removal ratio

Location		Temperature (°C)					
		Pre-closure					
x	z	1	2	3	5	10	20
(m)	(m)	(°C)	(°C)	(°C)	(°C)	(°C)	(°C)
0.285	278.293	16.94	16.94	16.94	16.94	16.94	16.94
0.745	278.293	16.94	16.94	16.94	16.94	16.94	16.94
1.0855	278.293	16.94	16.94	16.94	16.94	16.94	16.94
1.43085	278.293	16.94	16.94	16.94	16.94	16.94	16.94
1.80055	278.293	16.94	16.94	16.94	16.94	16.94	16.94
2.2004	278.293	16.94	16.94	16.94	16.94	16.94	16.94
2.5801	278.293	16.94	16.94	16.94	16.94	16.94	16.94
2.9998	278.293	16.94	16.94	16.94	16.94	16.94	16.94
3.6998	278.293	16.94	16.94	16.94	16.94	16.94	16.94
4.8998	278.293	16.94	16.94	16.94	16.94	16.94	16.94
6.8998	278.293	16.94	16.94	16.94	16.94	16.94	16.94
10.1498	278.293	16.94	16.94	16.94	16.94	16.94	16.94
15.1498	278.293	16.94	16.94	16.94	16.94	16.94	16.94
22.6498	278.293	16.94	16.94	16.94	16.94	16.94	16.94
33.8249	278.293	16.94	16.94	16.94	16.94	16.94	16.94
0.285	277.385	16.96	16.96	16.96	16.96	16.96	16.96
0.745	277.385	16.96	16.96	16.96	16.96	16.96	16.96
1.0855	277.385	16.96	16.96	16.96	16.96	16.96	16.96
1.43085	277.385	16.96	16.96	16.96	16.96	16.96	16.96
1.80055	277.385	16.96	16.96	16.96	16.96	16.96	16.96
2.2004	277.385	16.96	16.96	16.96	16.96	16.96	16.96
2.5801	277.385	16.96	16.96	16.96	16.96	16.96	16.96
2.9998	277.385	16.96	16.96	16.96	16.96	16.96	16.96
3.6998	277.385	16.96	16.96	16.96	16.96	16.96	16.96
4.8998	277.385	16.96	16.96	16.96	16.96	16.96	16.96
6.8998	277.385	16.96	16.96	16.96	16.96	16.96	16.96
10.1498	277.385	16.96	16.96	16.96	16.96	16.96	16.96
15.1498	277.385	16.96	16.96	16.96	16.96	16.96	16.96
22.6498	277.385	16.96	16.96	16.96	16.96	16.96	16.96
33.8249	277.385	16.96	16.96	16.96	16.96	16.96	16.96
0.285	272.595	17.07	17.07	17.07	17.07	17.07	17.07
0.745	272.595	17.07	17.07	17.07	17.07	17.07	17.07
1.0855	272.595	17.07	17.07	17.07	17.07	17.07	17.07
1.43085	272.595	17.07	17.07	17.07	17.07	17.07	17.07
1.80055	272.595	17.07	17.07	17.07	17.07	17.07	17.07
2.2004	272.595	17.07	17.07	17.07	17.07	17.07	17.07
2.5801	272.595	17.07	17.07	17.07	17.07	17.07	17.07
2.9998	272.595	17.07	17.07	17.07	17.07	17.07	17.07
3.6998	272.595	17.07	17.07	17.07	17.07	17.07	17.07
4.8998	272.595	17.07	17.07	17.07	17.07	17.07	17.07
6.8998	272.595	17.07	17.07	17.07	17.07	17.07	17.07
10.1498	272.595	17.07	17.07	17.07	17.07	17.07	17.07

Source: DTN: MO0408MWDDDMIO.002, file LA1450\_NUFT\_Temp\_crss-sctn3.xls.

Figure U-1. Portion of the Excel Spreadsheet With the NUFT Output

```
0 -330.229 29.20
0 -317.2945 28.78
0 -296.7135 28.15
0 -282.534 27.67
0 -266.0695 27.10
0 -247.2465 26.57
0 -227.574 26.06
0 -205.997 25.52
0 -184.42 24.99
0 -162.843 24.49
0 -144.723 24.06
0 -133.9125 23.78
0 -121.6955 23.46
0 -105.9045 23.32
.
.
.
0 237.871 17.84
0 253.6255 17.47
0 261.6675 17.29
0 266.135 17.20
0 272.595 17.07
0 277.385 16.96
0 278.293 16.94
0.285 -330.229 29.20
0.285 -317.2945 28.78
0.285 -296.7135 28.15
0.285 -282.534 27.67
0.285 -266.0695 27.10
0.285 -247.2465 26.57
0.285 -227.574 26.06
0.285 -205.997 25.52
0.285 -184.42 24.99
0.285 -162.843 24.49
0.285 -144.723 24.06
0.285 -133.9125 23.78
0.285 -121.6955 23.46
0.285 -105.9045 23.32
0.285 -84.7085 23.42
0.285 -70.5585 23.91
0.285 -60.544 24.30
0.285 -43.044 25.77
0.285 -30.544 27.53
0.285 -22.544 29.18
0.285 -17.544 30.76
0.285 -14.044 32.74
0.285 -11.294 35.71
0.285 -9.044 40.22
.
.
.
```

Source: DTN: MO0408MWDDDMIO.002, file *temperature\_5080.dat*.

Figure U-2. Example of ASCII File With Temperature Field for 50.8 Years After Waste Emplacement

After the NUFT temperature field is read into UDEC, interpolation of temperatures was performed for the UDEC grid points. In UDEC, the temperature is a grid point variable. First, a UDEC grid point is located in one of the NUFT rectangular zones (Figure U-3). This operation can be done relatively quickly because the NUFT grid is rectangular. It is carried out by independent searches along  $x$ - and  $y$ -coordinate axes. After local coordinates  $\xi, \eta$  (of the UDEC grid point inside the NUFT zone) are determined (Equation U-1), the temperature is calculated using bi-linear interpolation based on temperatures at four NUFT grid points, as shown in Equation U-2.

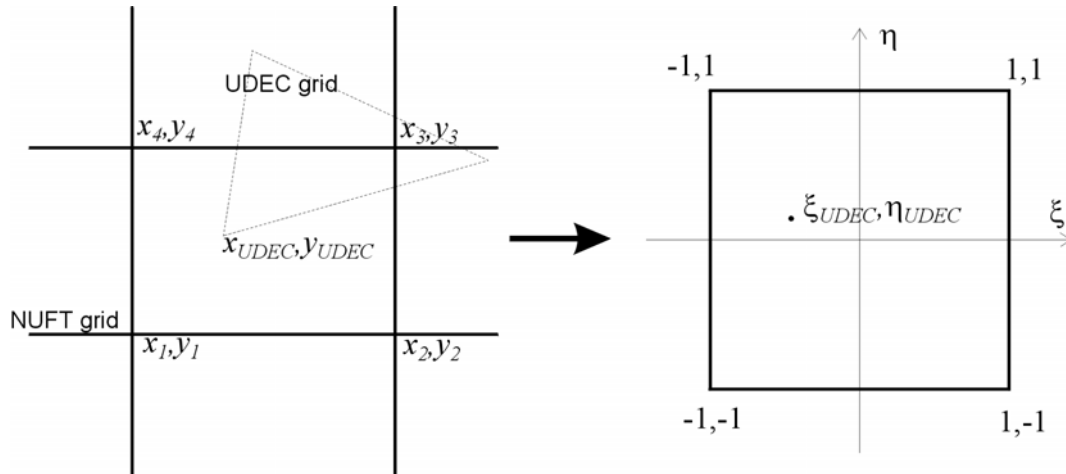


Figure U-3. Interpolation of UDEC Temperatures from the NUFT Grid

$$\xi_{UDEC} = 2 \frac{x_{UDEC} - x_1}{x_3 - x_1} - 1 \quad (\text{Eq. U-1})$$

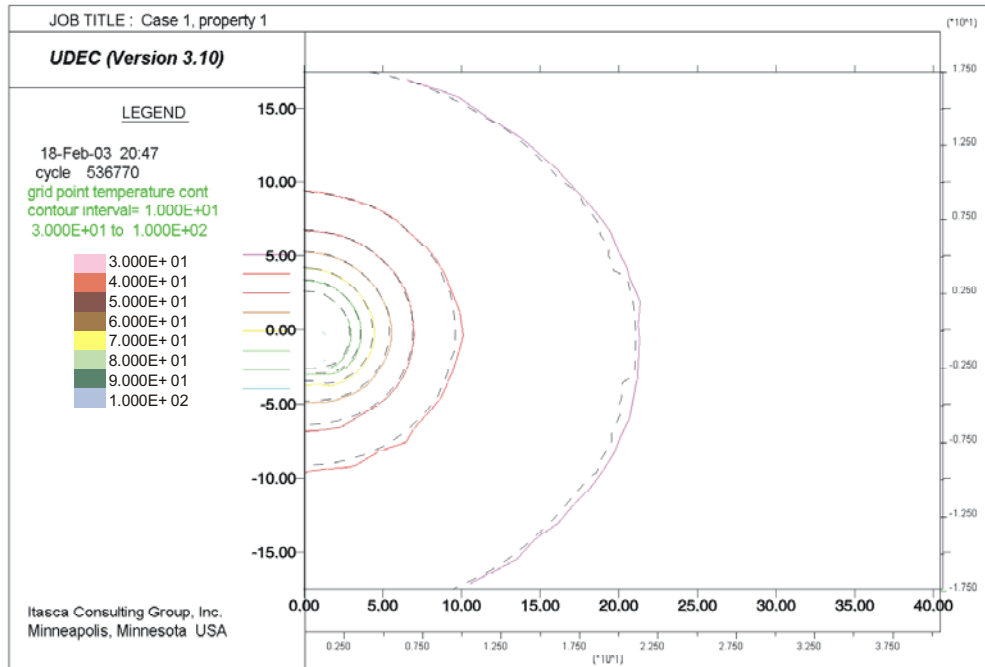
$$\eta_{UDEC} = 2 \frac{y_{UDEC} - y_1}{y_3 - y_1} - 1$$

$$\begin{aligned} f_1 &= \frac{1}{4}(1-\xi)(1-\eta) \\ f_2 &= \frac{1}{4}(1+\xi)(1-\eta) \\ f_3 &= \frac{1}{4}(1+\xi)(1+\eta) \\ f_4 &= \frac{1}{4}(1-\xi)(1+\eta) \end{aligned} \quad (\text{Eq. U-2})$$

$$T_{UDEC} = f_1 T_1 + f_2 T_2 + f_3 T_3 + f_4 T_4$$

The temperature field 50.8 years after emplacement of the waste, as provided by NUFT, is transferred into UDEC using the method described above. The contour lines of the temperature field imported in UDEC are compared with contour lines of the original temperature field in Figure U-4. The temperature profiles along the horizontal section through the drift center obtained from the NUFT data and after importing them into UDEC are compared in Figure U-5. The transfer of temperature field and interpolation are carried out correctly, as the contour lines and the profiles in the horizontal section are almost coincident.

The same algorithm was used for the FLAC model, the verification for UDEC model is therefore applicable to FLAC results.



NOTE: Temperature in degrees C; NUFT Results are dashed lines; Data transferred into UDEC solid colored lines.

Figure U-4. Comparison of Temperature Contours 50.8 Years after Waste Emplacement Obtained from the NUFT Results and the Data Transferred into UDEC

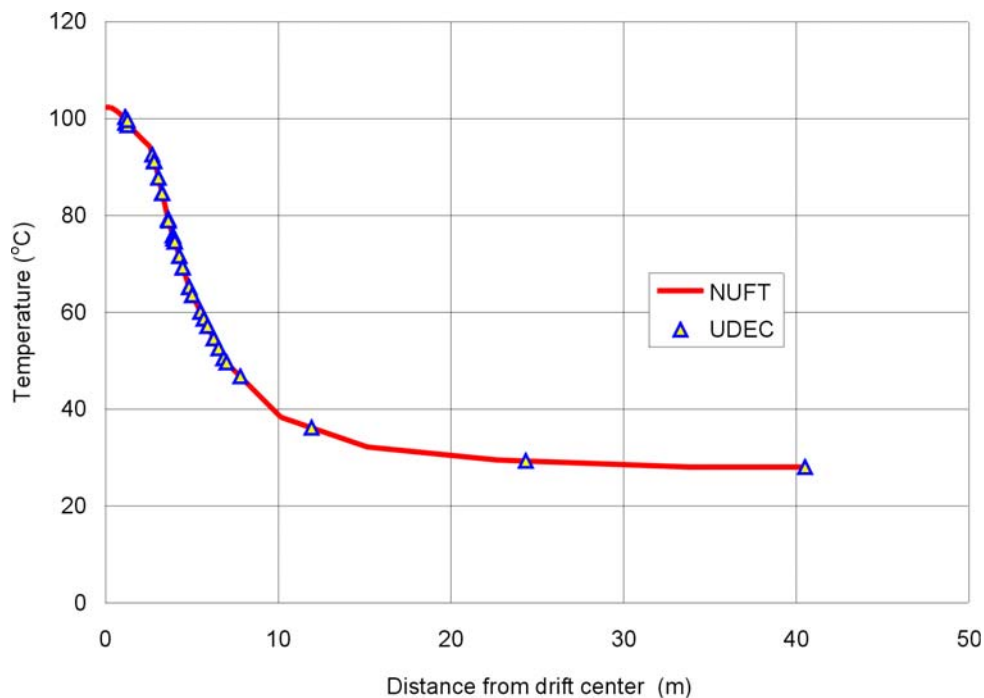


Figure U-5. Comparison of Temperature Profiles Along the Horizontal Section Through the Center of the Drift 50.8 Years after Waste Emplacement Obtained from the NUFT Results and the Data Transferred into UDEC

INTENTIONALLY LEFT BLANK



**APPENDIX V**

**CALCULATION OF BULKING AND IMPACT OF  
STRESS ARCHING FROM THE UDEC DISCONTINUUM MODEL**



## CALCULATION OF BULKING AND IMPACT OF STRESS ARCHING FROM THE UDEC DISCONTINUUM MODEL

### VI. INTRODUCTION

It is possible, using the UDEC Voronoi block model, to simulate the entire process of rockfall, including accumulation of the broken rock on the invert of the emplacement drift and on the top of the drip shield. The final configuration of the blocks and effective bulking are results of a simulation. Many approaches for calculating the extent of caving above excavations use bulking factor as an input to the analysis. In the UDEC Voronoi block model, the bulking is a model result, a function of many factors, including size distribution and shape of the blocks, friction angle between the blocks, and sequence of rockfall formation (i.e. if the rockfall first occurs from the crown or from the walls of the drift). However, it is useful to calculate the effective bulking factor of the caved rock resulting from UDEC simulations as a reference for comparison with other methods.

In order to calculate the bulking factor, the region of the rock mass that caved must be identified first. This region is determined based on the displacement magnitudes of the blocks. If the average block displacements are larger than a predefined length threshold, the block is classified to be a part of the rockfall. Considering that the caved rock completely fills the drift, the bulking factor is calculated as the ratio between the area inside the drift (area of the drift in the original configuration before the rockfall minus the area of the outline of the drip shield) and the area of the caved blocks. A larger value of the predefined threshold will result in a smaller region of caved rock and, consequently, a larger bulking factor. The displacement length threshold was selected based on inspection of the displacement contours. Figure V-1 illustrates the contours of the displacement field for Case 4 from Section 6.4.2.5. Although the legend of Figure V-1 indicates  $x$ -displacements, the figure actually represents contours of total displacement. The contour line corresponding to a displacement of 0.12 m appears to be a good choice for the outline of the caved rock around the emplacement drift, because there is a large displacement gradient inside that contour line. If the caved rock completely fills the drift, the available volume predefines the increase in volume of the caved rock. The volume of the rock mass (in its original configuration) that caved is calculated by simply adding the areas of the blocks classified to be a part of the rockfall. Note that UDEC's data structure has information about geometry, including area, of every block in a model. The total area,  $A_{co}$ , of the blocks in the model that displaced more than 0.12 m, calculated by summing their areas, is 88.71 m<sup>2</sup>. The calculated bulking factor is:

$$B = \frac{\pi R^2 - b_d h_d}{A_{co}} = \frac{23.76 - 7.31}{88.71} = 0.19 \quad (\text{Eq. V-1})$$

The area of the outline of the drip shield in the cross-section normal to the drift axis is 7.31 m<sup>2</sup> (the drip shield is 2.533 m wide and 2.886 m high).

Summation of block areas was also done manually. The blocks with average displacements larger than 0.12 m are printed out (Figure V-2). UDEC prints out, among the other information, the block masses, which are summed in Excel. The sum of masses of the caved blocks is

189,840 kg/m. The corresponding area for a density of 2,140 kg/m<sup>3</sup> is 88.71 m<sup>2</sup>—exactly the same number as obtained using the FISH function.

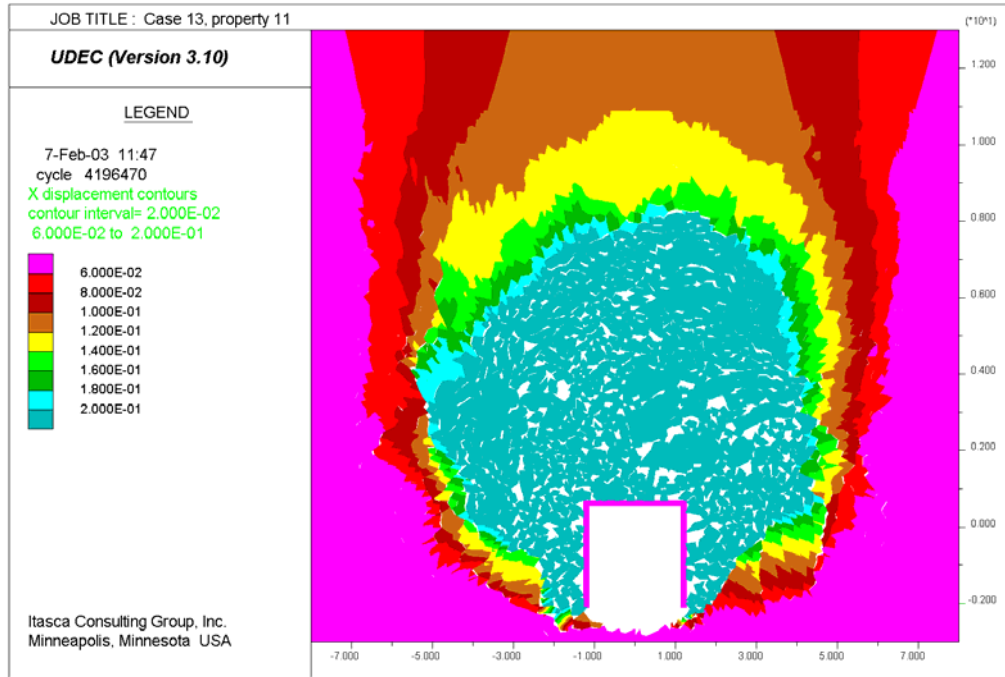


Figure V-1. Contours of Displacement Magnitudes (m): Case 4 of the Drift Degradation Analysis

The area of the rock mass that has caved and the bulking factor are also calculated manually in order to verify the procedure described in the previous paragraph. The outline of the caved rock mass is drawn and measured horizontally at every 1 meter increment of the cave height, which is approximately 14 m (see Figure V-3). The area of the cross-section of the cave,  $A_c$ , is 111.03 m<sup>2</sup>, equal to the sum of the widths indicated in Figure V-3 (multiplied by the 1 m increment height). The other approach is to approximate the cave with an ellipse (as indicated in red in Figure V-3). With a major axis of 14.0 m and a minor axis of 10.34 m, the area of the ellipse is 113.69 m<sup>2</sup>. The difference between these two estimates of cave area is very small, of the order of a couple of percent. The total area of the blocks that have caved is equal to the area of the cave minus the increase in volume (i.e. area filled with rubble):

$$A_{co} = A_c - \pi R^2 = 111.03 - 23.76 = 87.27 \text{ m}^2 \quad (\text{Eq. V-2})$$

The difference between the area of the caved rock mass calculated by adding areas of blocks in UDEC and manually integrating the area of the cave is less than 2 percent. The bulking factor, based on the manually estimated area of the caved rock mass, is:

$$B = \frac{\pi R^2 - b_d h_d}{A_c - \pi R^2} = \frac{23.76 - 7.31}{111.03 - 23.76} = 0.19 . \quad (\text{Eq. V-3})$$

Clearly, the bulking factor numerically calculated using UDEC is in agreement with the estimates obtained using simple methods.

```

block data

  block  mat const fixity   centroid coords.   mass   pol. mom.
address  no.  no.  cond.
2147913 10   3   0   1.378E+00 -1.850E+00 4.531E+01 1.898E-01
(fdef)
2147255 10   3   0   -2.461E+00 -1.149E+00 5.525E+01 3.490E-01
(fdef)
2146517 10   3   0   -7.434E-01  8.458E-01  7.498E+01 4.518E-01
(fdef)
2146336 10   3   0   -5.605E-01  7.503E-01  3.725E+01 1.647E-01
(fdef)
2146104 10   3   0   -1.600E+00 -1.276E+00 1.190E+02 1.193E+00
(fdef)
2145621 10   3   0   1.790E+00 -1.955E+00 3.791E+01 1.383E-01
(fdef)
2145226 10   3   0   1.436E+00 -1.870E+00 2.314E+01 1.041E-01
(fdef)
.
.
.
764634 10   3   0   -1.831E+00 -2.380E+00 1.380E+02 1.559E+00
(fdef)
757418 10   3   0   -1.992E+00 -2.182E+00 7.788E+01 5.579E-01
(fdef)
755122 10   3   0   1.533E-01  8.312E+00 9.266E+01 7.050E-01
(fdef)
753590 10   3   0   2.248E-01  8.476E+00 8.412E+01 5.655E-01
(fdef)
745568 10   3   0   -9.186E-02  1.025E+01 8.732E+01 6.199E-01
(fdef)
745169 10   3   0   -4.920E-01  1.018E+01 9.538E+01 7.205E-01
(fdef)
744531 10   3   0   -2.940E-01  1.028E+01 1.212E+02 1.138E+00
(fdef)
    
```

Source: File: loose\_blocks.log.

Figure V-2. Printout of Information for the Blocks with Average Displacement Larger than 0.12 m

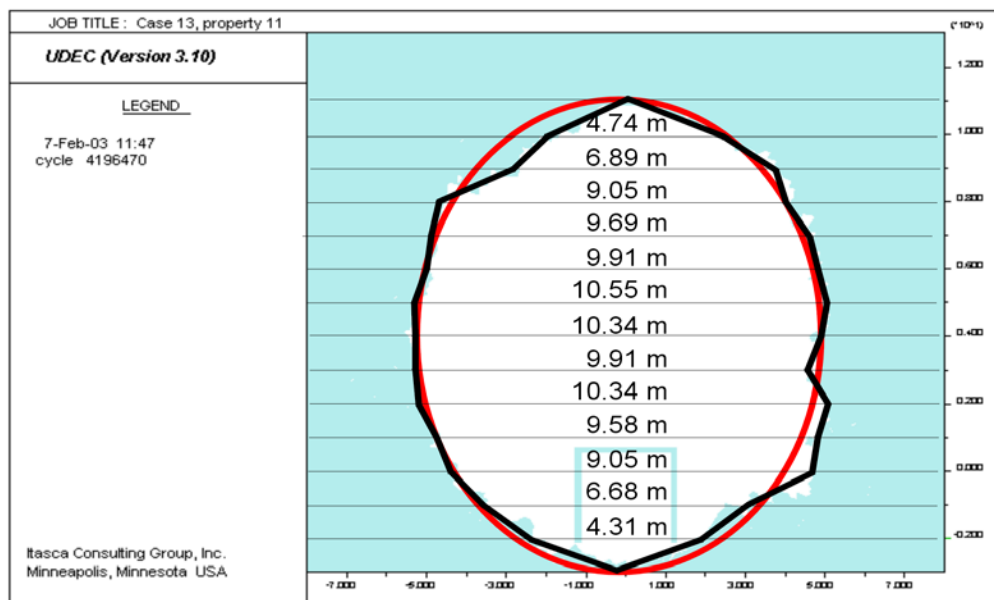


Figure V-3. Outline of the Caved Rock Mass and Its Dimensions Used for Manual Integration

## V2. STRESS ARCHING IN THE BROKEN ROCK ABOVE THE DRIP SHIELD ARCHING EFFECT FOR A RIGID, RECTANGULAR DRIP SHIELD

A calculation is presented here to demonstrate the impact of stress arching for the case illustrated in Figure V-1. Here, a rigid, rectangular drip shield is considered, which will result in less stress arching effect than would be expected for a deformable drip shield. For the approximate height (14.0 m) of the cave (measured from the invert of the drift), the dead weight of the broken rock on the drip shield is:

$$p = h \frac{\rho g}{1 + B} = (14.0\text{m} - 2.75\text{m} - 0.67\text{m}) \times \frac{2400\text{kg/m}^3 \times 10\text{m/s}^2}{(1 + 0.19)} = 213.4\text{kN/m}^2 \quad (\text{Eq. V-4})$$

where  $h$  is the height of broken rock above the drip shield, which is determined knowing the cave height (14.0 m), the drift radius (2.75 m), and the distance from the drift center to the top of the drip shield (0.67 m). The average vertical pressure on the drip shield as calculated by using UDEC, which integrates the forces acting between the drip shield and the blocks in the rubble, is 179.2 kN/m<sup>2</sup>. The arching inside the rubble accounts for only a 16 percent reduction in the load on the drip shield. LeFebvre et al. (1976 [DIRS 168919]) measured pressures of the fill on the corrugated steel arch, 15.5 m in span. The pressure was measured during backfilling of the arch. The fill consisted mainly of fine silty sand, compacted at 90 percent of the modified Proctor. The measured vertical stress, 2 ft above the top of the structure, shows that positive arching develops when the fill is approximately 3.5 m above the measurement point. At the end of construction, when the top of the embankment is approximately 12.5 m above the pressure cell, the measured pressure is only 25 percent of the overburden. Similar results are reported by Byrne et al. (1990 [DIRS 168921]) for an arch metal culvert, 13.4 m in span. The arch was 7.3 m high, covered by 9.6 m of natural sand and gravel compacted to between 95 and 100 percent of standard Proctor. The pressure cell was located 1.2 m above the crown of the arch. The stresses were measured as a function of the height of fill. Positive arching is observed when the fill was approximately 1.5 m above the pressure cell. At the end of construction, with 9.6 m of the cover, the measured vertical stress is 40 percent of the overburden. The pressure cells placed in the fill at the elevation of the springline show the vertical stress larger than the overburden, which is more evidence of the presence of a stress arch.

Stress arching is much more likely to develop in the caved rock, resulting from rockfall, than in sand or gravel, because: a) the average block size in the caved rock is larger than the grain size in sand or gravel, and b) the friction angle in the broken rock fill is larger than the friction angle in sand or gravel. Relatively large load (84 percent of overburden) of the broken rock for the rigid, rectangular drip shield predicted by the UDEC model, compared to measured loads on the steel arch culverts, is due to considerations that: a) the drip shield is infinitely stiff, and b) the drip shield is rectangular.

## V3. IMPACT OF DEFORMABILITY AND SHAPE OF THE DRIP SHIELD

The actual finite stiffness of the drip shield will result in deformation and increase load transfer through the broken rock (i.e., a positive arching effect). The top of the drip shield is designed to have an arched shape, which is more favorable for development of a stress arch in the cover (above the drip shield) than the rectangular shape considered in the previous example. The

arched shape of the top of the drip shield will promote lateral displacements of the blocks above, causing more load to be transferred through the broken rock than to the drip shield. In the following example, taken from Section 6.4, a random geometry of 20 cm blocks form the rock mass. The cohesion and tensile strength of the rock mass is reduced to force complete collapse and filling of the excavation until equilibrium is achieved. The approximate bulking factor for these simulations is 19 percent.

A comparison of loads to the drip shield is made for two cases: a) rigid drip shield with proper arched geometry, and b) a deformable drip shield with proper arched geometry. The drip shield in both cases is developed from finite difference elements within the UDEC model. The objective here is not to represent the exact geometry of the drip shield, which is a true three-dimensional frame structure, but to provide a two-dimensional model that reproduces the overall stiffness of the actual structure. To ensure that the model adequately represents this stiffness, it was calibrated against the LS-DYNA finite element model that is used for the detailed drip shield vibratory motion and damage assessment modeling (see, for example, *Drip Shield Structural Response to Rockfall*, BSC 2004 [DIRS 168993]). A sample problem was run with the LS-DYNA program in which the detailed drip shield model was subjected to a uniform vertical pressure over its crown. It was demonstrated that the simplified UDEC model correctly represents deformation of the drip shield (See Appendix Y).

The final collapsed state for the rigid and deformable cases are given in Figures V-4 to V-7. The deformable drip shield footings are allowed to slide on or separate from the invert. A friction coefficient of 0.5 is considered between the footing and the invert, although this value is not important in defining load in the drip shield. The invert, pallet and waste package are rigid and placed only to provide a boundary restraint to the drip shield legs. The displacement contours of the rubble and intact rock are given to help visualize the ultimate height of broken rock, as opposed to yielded or damage rock in the surrounding mass.

The deformation of the drip shield legs and sliding against the pallet due to side pressure of the broken rock on the sides of the drip shield are clearly visible in Figure V-6. The resulting average pressure on the top and sides of the drip shield are given in Table V-1 show that the average pressure on the top of the drip shield is approximately 25 percent lower, in this case, for the deformable drip shield, although the right hand side loading is increased significantly. Although a number of realizations are necessary for a complete comparison of the impact of rigid versus deformable considerations, this example provides an illustration of the methodology employed. The estimates of drip shield loading presented in the main body of the report (Section 6.4) consider a deformable drip shield.

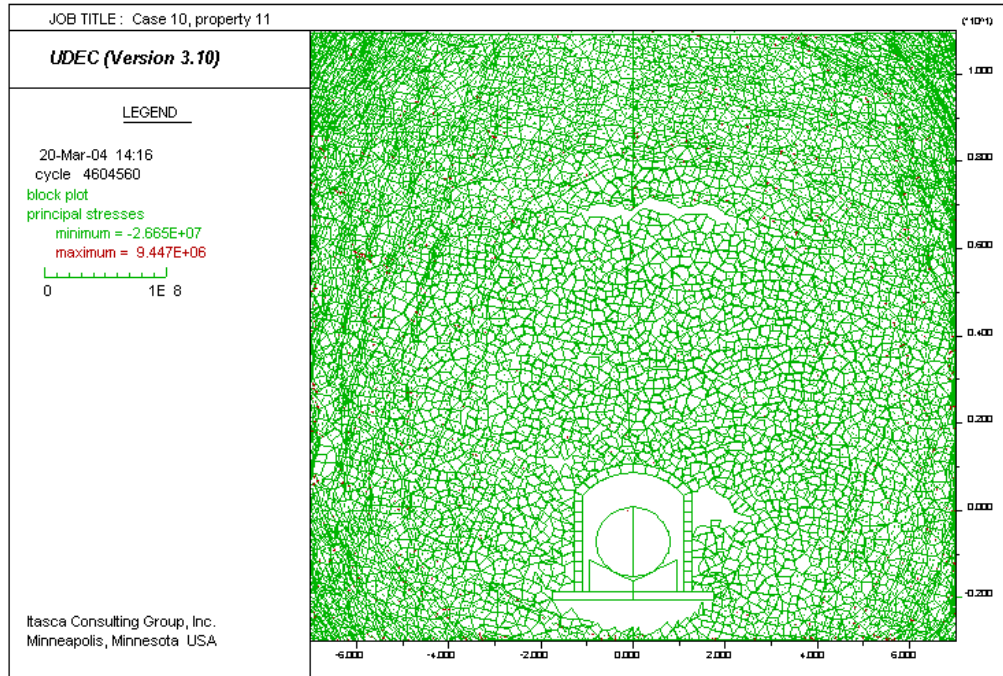


Figure V-4. Quasi-static Drift Degradation, 0.2-m Block Size: Equilibrium State for Rigid Drip Shield with Arched Top, Bottom Fixed to the Invert

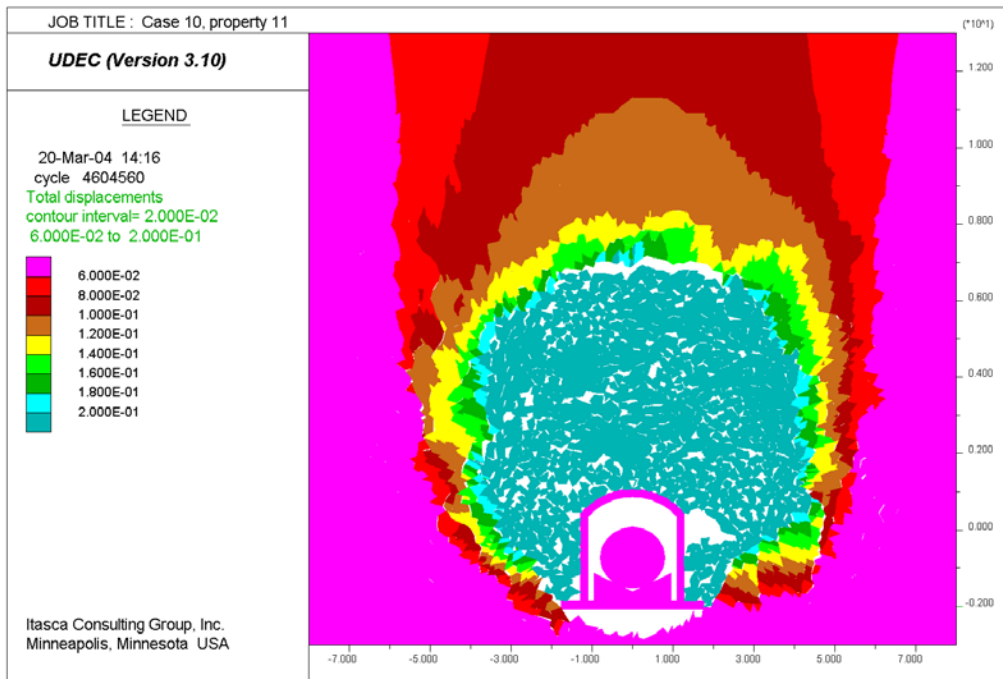


Figure V-5. Quasi-static Drift Degradation, 0.2-m Block Size: Contours of Displacement (m) Magnitude for Rigid Drip Shield with Arched Top, Bottom Fixed to the Invert



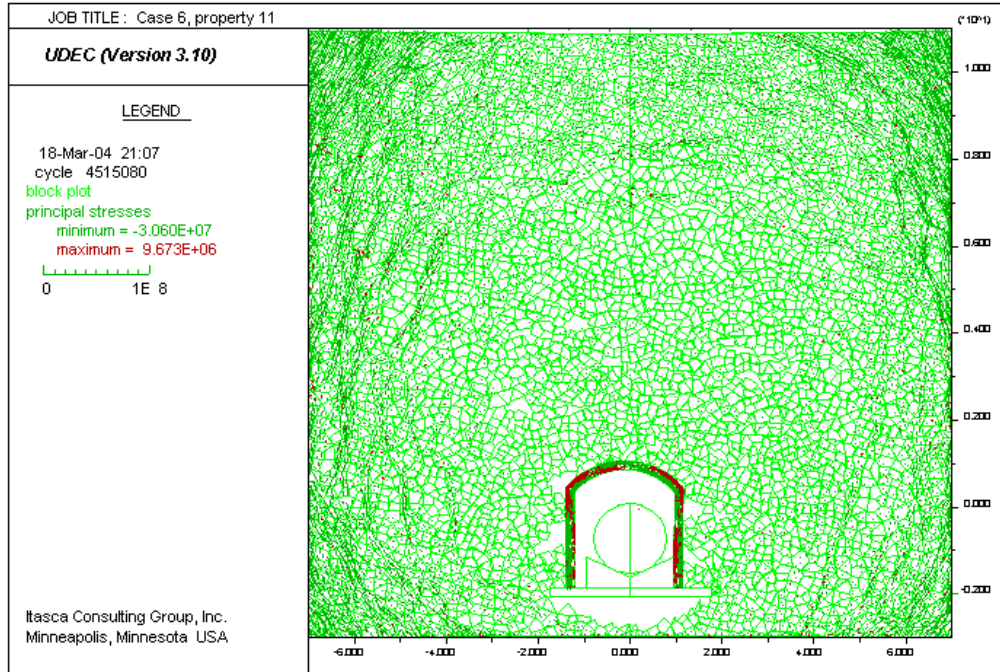


Figure V-6. Quasi-static Drift Degradation, 0.2 m Block Size: Equilibrium State for Deformable Drip Shield with Arched Top, Bottom Rests on the Invert

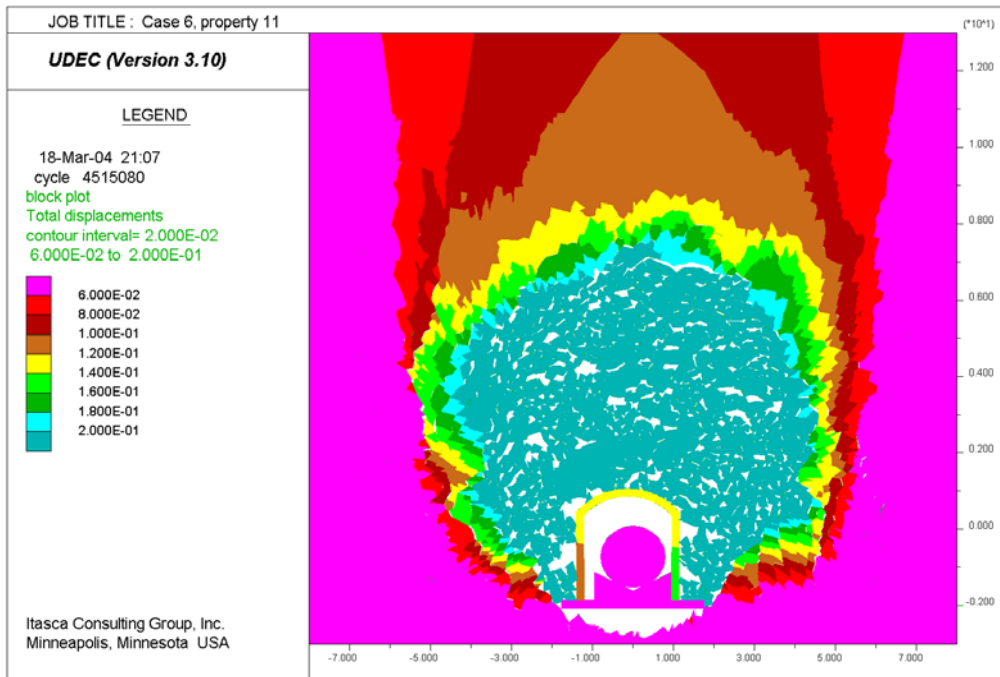


Figure V-7. Quasi-static Drift Degradation, 0.2 m Block Size: Contours of Displacement (m) Magnitude for Deformable Drip Shield with Arched Top, Bottom Rests on the Invert

Table V-1. Quasi-static Drift Degradation, 0.2 m Block Size: Average Loads on the Drip Shield for Cases with Invert

<b>Drip Shield</b>	<b>Left kN/m<sup>2</sup></b>	<b>Top kN/m<sup>2</sup></b>	<b>Right kN/m<sup>2</sup></b>
Rigid, arched top, bottom fixed to invert	66.45	144.15	11.28
Deformable, arched top, bottom rests on invert	41.54	108.92	58.76

**APPENDIX W**  
**BOUNDARY CONDITIONS IN THE THERMAL-MECHANICAL MODEL**



## BOUNDARY CONDITIONS IN THE THERMAL-MECHANICAL MODEL

The thermal-mechanical analysis of drift stability in the lithophysal rock was carried out using a two-dimensional model. The vertical model boundaries are placed in the plane half-distance between two drifts. The symmetry conditions of stresses and deformation considered on that plane (i.e., the “roller” boundary condition) are applied on the vertical model boundaries. There are no natural boundaries below the repository. The ground surface is the natural mechanical boundary above the repository. The model size in the vertical direction is considered finite. The horizontal model boundaries are artificial, truncation boundaries, created to limit the model size and calculation time. In the UDEC thermal-mechanical calculations, it was considered that the horizontal model boundaries are 17.5 m below and above the drift axis. The vertical model size is 35 m. The bottom model boundary was considered to be fixed. The uniform normal stress equal to the weight of the truncated overburden was applied on the top model boundary as a stress boundary condition. It is necessary to demonstrate that the model size and the selected boundary conditions do not affect significantly model results. The stresses around the drift (in the roof and the wall) are predicted (with continuum elastic model in FLAC) using three different model geometries: 30 m (Figure W-1), 60 m (Figure W-2) and 120 m (Figure W-3) vertical model dimensions. The horizontal model size is the same in the three cases. The simulations were carried out for two extreme cases of material properties in the lithophysal rock mass, Categories 1 and 5.

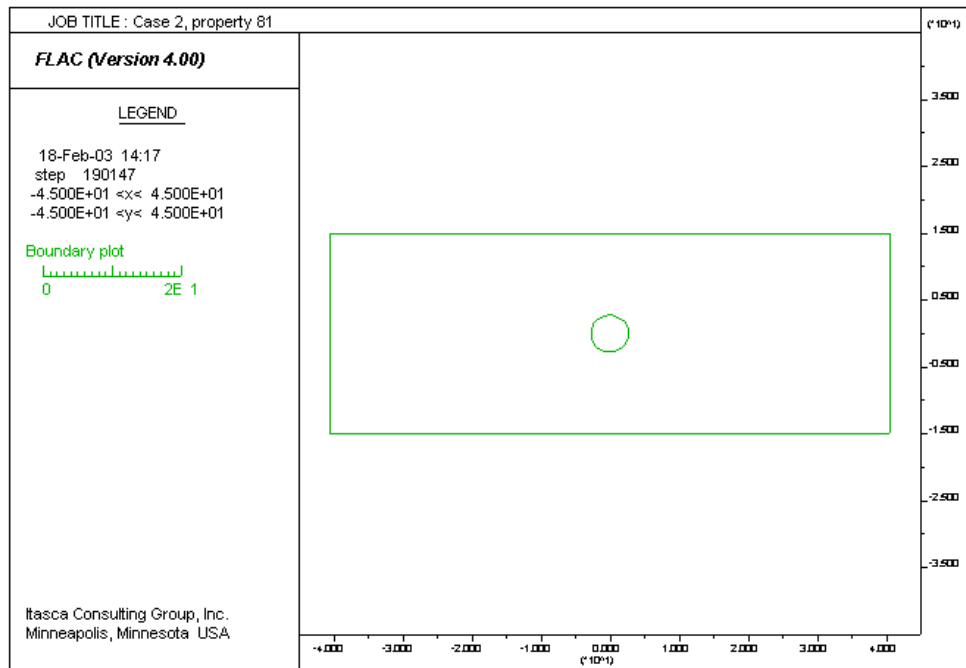


Figure W-1. Geometry of the Model: Vertical Model Dimension 30 m

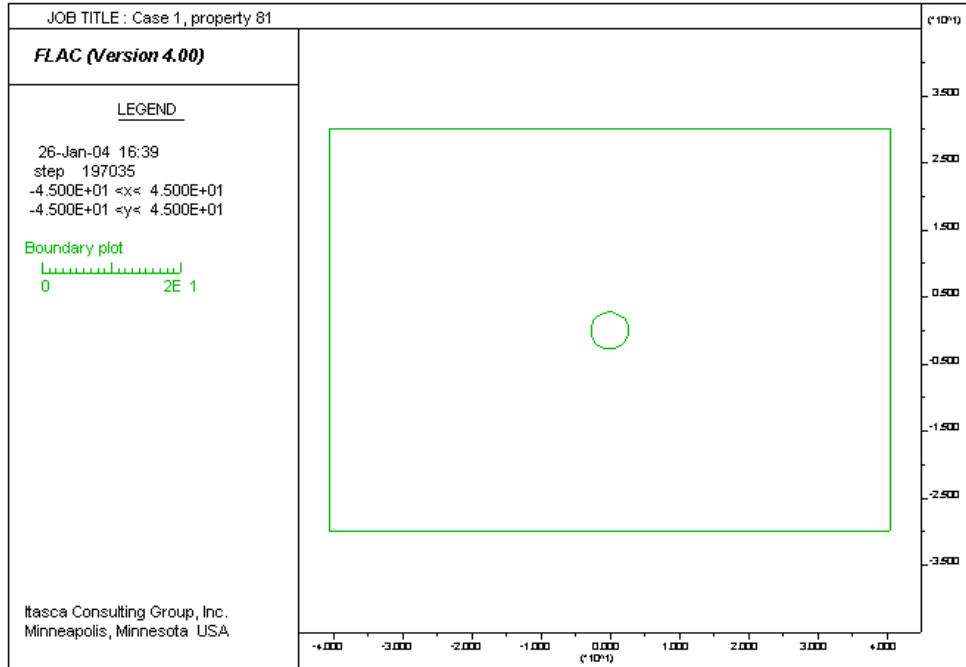


Figure W-2. Geometry of the Model: Vertical Model Dimension 60 m

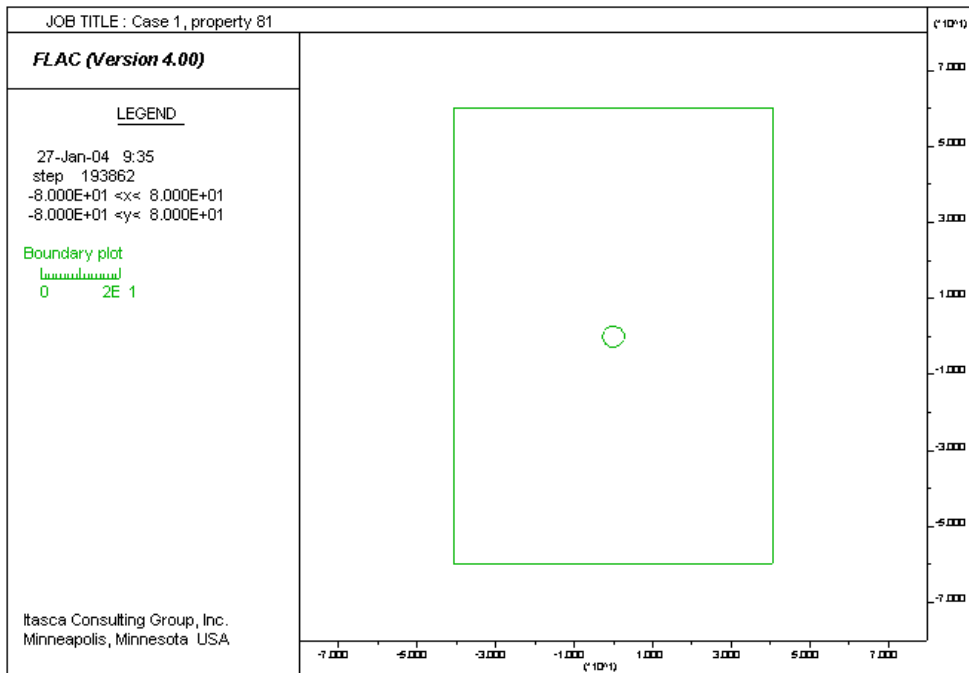
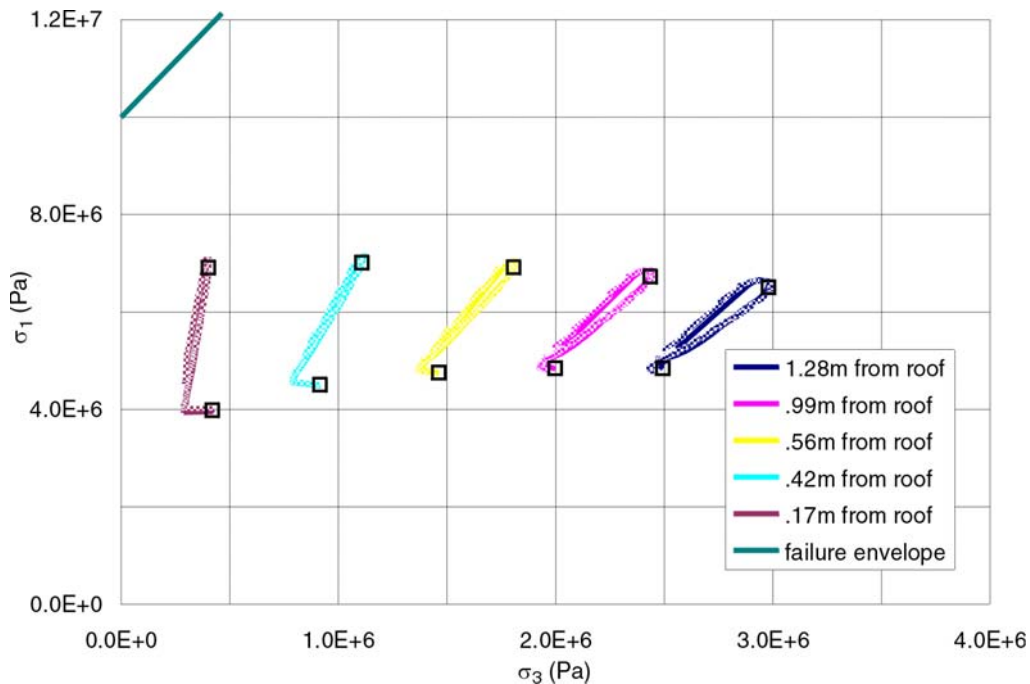


Figure W-3. Geometry of the Model: Vertical Model Dimension 120 m

The stress paths in the principal stress space at five points in the roof and in the wall are generated for the simulated cases. The results for Category 1 are shown in Figures W-4 and W-5. The model size (in the range between 30 m and 120 m) has no effect on predicted stress paths. If the model were extended to the ground surface, the results would not be different. The results for Category 5 are shown in Figures W-6 and W-7. Stresses in the crown are practically

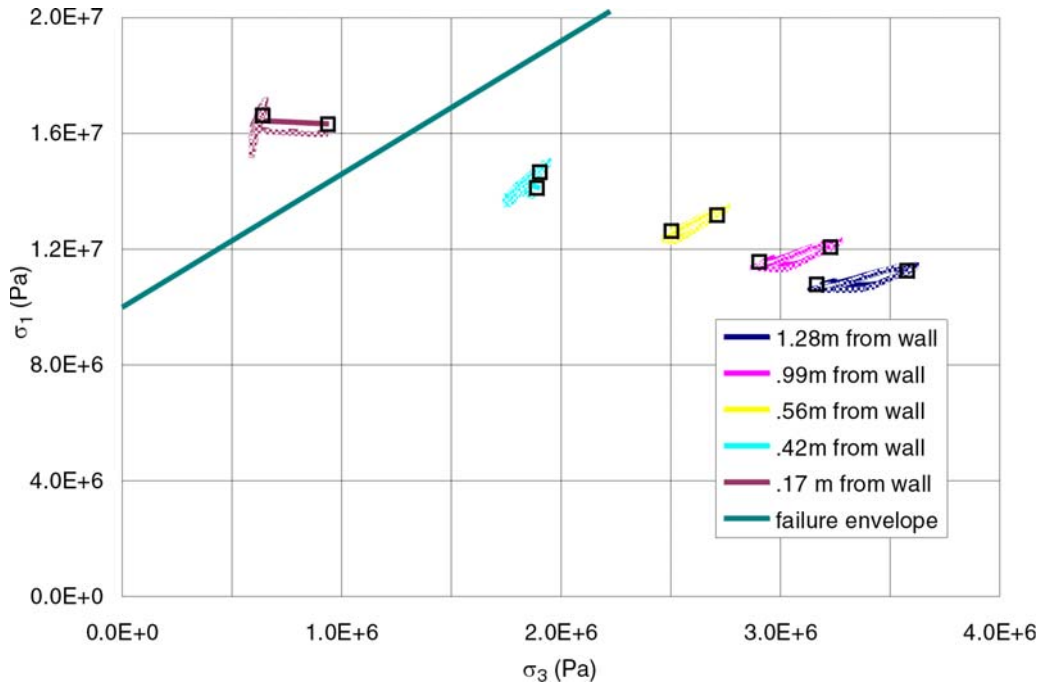
independent of the model size. The effect of the model size can be observed on stress paths recorded at the points in the wall. The maximum value of the major principal stress during the thermal cycle at the point 0.14 m from the wall is approximately 20 percent larger in the 60 m model than in the 30 m model. The stress difference between the 60 m and 120 m models is insignificant. That stress change does not cause yield in the drift wall since it is below the yield surface and consequently does not effect model predictions of rockfall. Also, at the points that are at 0.5 m from the drift wall or further, the increase in the vertical model size results in increase in the both principal stresses resulting in the stress state moving away from the yield surface, and more favorable stability conditions. With an exception of the point very close to the wall surface, the smaller size model results in more conservative conditions from the perspective of rockfall predictions. The different stress path as a function of model size take place over a relatively short period of time (compared to the duration of the regulatory period), between 50 years and 100 years after waste emplacement, just after ventilation shut down.

The selected vertical model size (35 m) and the boundary conditions on the bottom and the top model boundaries are satisfactory for the analysis of drift degradation.



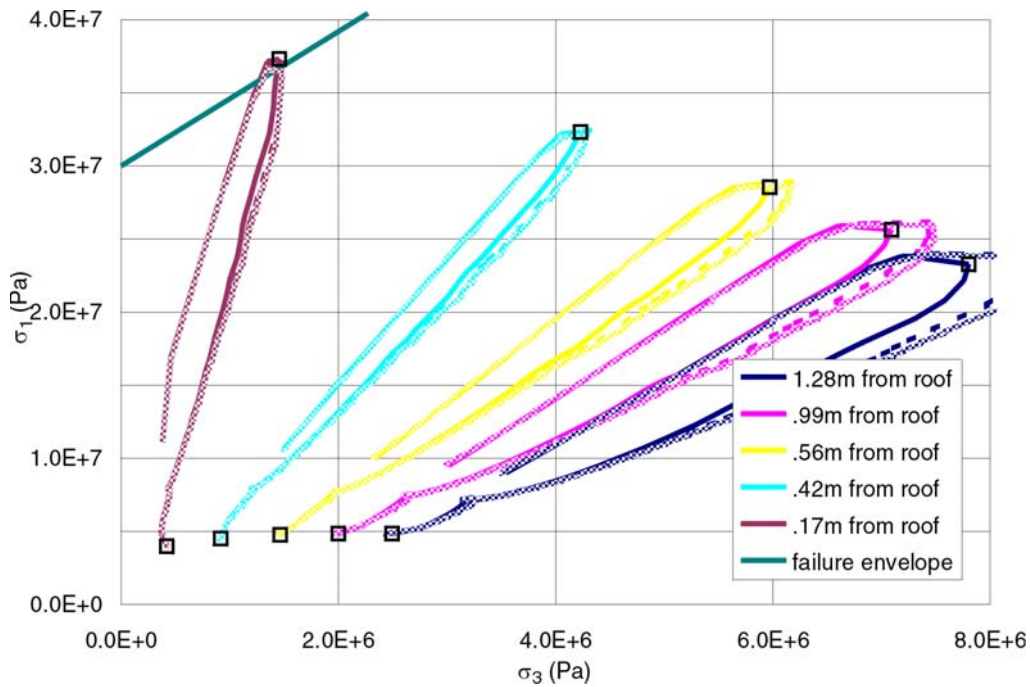
NOTE: 30 m model size – solid line; 60 m model size – dashed line; 120 m model size – pale line.

Figure W-4. Stress Paths in the Drift Crown for Category 1



NOTE: 30 m model size – solid line; 60 m model size – dashed line; 120 m model size – pale line.

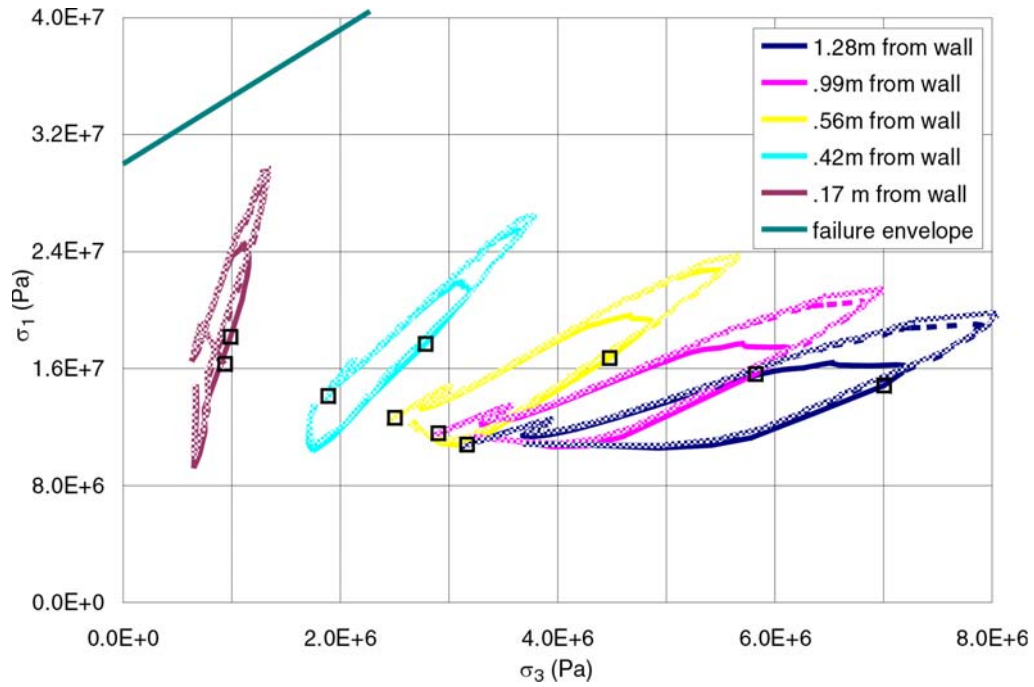
Figure W-5. Stress Paths in the Drift Wall for Category 1



NOTE: 30 m model size – solid line; 60 m model size – dashed line; 120 m model size – pale line.

Figure W-6. Stress Paths in the Drift Crown for Category 5





NOTE: 30 m model size – solid line; 60 m model size – dashed line; 120 m model size – pale line.

Figure W-7. Stress Paths in the Drift Wall for Category 5

INTENTIONALLY LEFT BLANK

**APPENDIX X**  
**LISTING OF SITE-SPECIFIC GROUND MOTION PARAMETERS**



## LISTING OF SITE-SPECIFIC GROUND MOTION PARAMETERS

Site-specific ground motions for five levels of annual probability of exceedance,  $5 \times 10^{-4}$ ,  $1 \times 10^{-4}$ ,  $1 \times 10^{-5}$ ,  $1 \times 10^{-6}$ , and  $1 \times 10^{-7}$ , are included in this study. The  $5 \times 10^{-4}$  and  $1 \times 10^{-4}$  ground motions are for preclosure consideration, while the  $1 \times 10^{-5}$ ,  $1 \times 10^{-6}$  and  $1 \times 10^{-7}$  ground motions are for postclosure. The preclosure level motions are provided for comparison to the postclosure levels. A total of 15 sets of Point B ground motions (i.e., ground motions developed at repository horizon) were selected for each annual postclosure hazard level. The multiple sets ensure a reasonable distribution of spectral shapes and time history durations. For each set of ground motions, two horizontal components (H1 and H2) and one vertical component (V) of acceleration, velocity, and displacement are supplied.

Two sets of  $1 \times 10^{-6}$  ground motions were used. The difference in these sets is described in DTN: MO0403AVDSC106.001, file *10-6 TH memo.doc*. The original set (i.e., DTN: MO0301TMHIS106.001) is used in Section 6.4.2.2. Since this ground motion results in complete drift collapse for lithophysal rock, it was not necessary to repeat the analyses using the revised set (i.e., DTN: MO0403AVDSC106.001).

Only one ground motion was provided for the preclosure hazard levels because of the deterministic-based design approach for preclosure consideration. This appendix provides a complete listing of the peak ground velocity (Tables X-1 to X-5), Arias Intensity (Tables X-6 to X-10), and Power Spectral Density (Tables X-11 to X-15).

Ground velocity time histories are provided for fixed time intervals in the ASCII files contained in the DTNs listed below each table. Files for ground velocity are the ones with extension of *vts* or *vth*. Peak ground velocity is obtained by opening the *vts* or *vth* files in the Excel program and using the spreadsheet function *abs()* (absolute value) and *max()* (maximum value). The values for Arias Intensity can be directly extracted from the ASCII files with file extension *dur* contained in the DTNs. Power Spectral Density is obtained by transforming the velocity time history to the frequency domain using the fast Fourier transform function in Mathcad. Next, the square of the velocities is integrated along the frequency domain. The Mathcad files used to obtain the Power Spectral Density are described in Appendix A (Table A-1, files *\*.powe cal.mcd*).

Table X-1. Peak Ground Velocity (cm/sec) for Preclosure Ground Motions

Ground Motion Set	H1	H2	V
$5 \times 10^{-4}$	19.00	17.72	17.73
$1 \times 10^{-4}$	38.38	43.78	47.51

Source: DTNs: MO0407TMHIS104.003 [DIRS 170599] and MO0306SDSAVDTH.000 [DIRS 164033].

Table X-2. Peak Ground Velocity (cm/sec) for  $1 \times 10^{-5}$  Ground Motions

Ground Motion Set	H1	H2	V
1	104.58	83.31	70.88
2	104.58	125.02	145.25
3	104.58	262.05	398.11
4	104.59	100.41	152.27
5	104.58	166.71	106.52
6	104.54	45.61	173.88
7	104.51	89.33	333.16
8	104.56	152.20	98.16
9	104.59	357.76	281.76
10	104.60	31.81	50.16
11	104.60	126.04	120.31
12	104.54	70.34	100.60
13	104.58	103.75	318.01
14	104.62	40.87	92.78
16	104.56	67.43	137.53

Source: DTN: MO0402AVDTM105.001 [DIRS 168890], file vts.zip.

Table X-3. Peak Ground Velocity (cm/sec) for  $1 \times 10^{-6}$  Ground Motions (Revised Set)

Ground Motion Set	H1	H2	V
1	244.14	195.41	111.29
2	244.12	268.58	233.12
3	244.14	642.80	609.45
4	244.10	259.50	297.45
5	244.07	257.01	113.84
6	244.13	132.27	270.94
7	244.66	242.17	637.11
8	244.14	401.84	153.58
9	244.16	817.00	457.09
10	244.02	78.24	84.58
11	244.12	255.98	127.82
12	244.14	271.53	194.53
13	244.13	303.50	337.21
14	244.15	125.60	245.79
16	244.12	158.41	211.80

Source: DTN: MO0403AVDSC106.001 [DIRS 168891], file Vts.zip.

Table X-4. Peak Ground Velocity (cm/sec) for  $1 \times 10^{-6}$  Ground Motions (Original Set)

Ground Motion Set	H1	H2	V
1	244.00	243.35	229.79
2	243.79	243.90	229.34
3	254.63	242.69	228.36
4	243.61	243.28	228.37
5	243.35	243.39	229.27
6	244.11	243.05	229.59
7	243.86	244.08	229.92
8	244.21	243.93	229.78
9	244.01	243.98	229.62
10	241.90	238.07	230.00
11	243.76	243.82	229.73
12	243.27	242.83	229.76
13	243.95	243.95	229.77
14	244.13	244.27	230.13
16	243.99	244.07	229.80

Source: DTN: MO0301TMHIS106.001 [DIRS 161868], file 10-6THb.zip.

Table X-5. Peak Ground Velocity (cm/sec) for  $1 \times 10^{-7}$  Ground Motions

Ground Motion Set	H1	H2	V
1	535.26	428.42	298.44
2	535.32	588.89	625.10
3	535.27	1409.30	1634.20
4	535.27	569.05	797.61
5	535.27	563.65	305.27
6	535.27	290.00	726.52
7	536.24	530.78	1708.30
8	535.14	880.81	411.80
9	535.22	1791.10	1225.70
10	535.24	171.62	226.79
11	535.23	561.25	342.73
12	535.39	595.47	521.62
13	535.27	665.45	904.21
14	535.28	275.36	659.11
16	535.27	347.33	567.89

Source: DTN: MO0403AVTMH107.003 [DIRS 168892], file Vts.zip.

Table X-6. Arias Intensity (m/sec) for Preclosure Ground Motions

Ground Motion Set	H1	H2	V	Sum
$5 \times 10^{-4}$	0.59	0.67	0.46	1.72
$1 \times 10^{-4}$	4.21	4.51	8.97	17.69

Source: DTNs: MO0407TMHIS104.003 [DIRS 170599] and MO0306SDSAVDTH.000 [DIRS 164033].

Table X-7. Arias Intensity (m/sec) for  $1 \times 10^{-5}$  Ground Motions

Ground Motion Set	H1	H2	V	Sum
1	32.90	34.36	36.06	103.32
2	30.76	38.43	123.30	192.49
3	16.02	22.53	47.60	86.15
4	12.09	15.47	19.97	47.53
5	16.20	11.15	13.48	40.83
6	6.99	5.30	18.21	30.50
7	3.99	3.75	49.48	57.22
8	8.45	12.70	15.53	36.68
9	21.64	52.24	138.70	212.58
10	8.60	3.51	14.05	26.16
11	8.27	6.67	14.64	29.58
12	3.93	4.05	6.69	14.67
13	9.41	16.03	25.95	51.39
14	2.57	2.46	7.28	12.31
16	2.71	1.57	6.85	11.13

Source: DTN: MO0402AVDTM105.001 [DIRS 168890], file dur.zip.

Table X-8. Arias Intensity (m/sec) for  $1 \times 10^{-6}$  Ground Motions (Revised Set)

Ground Motion Set	H1	H2	V	Sum
1	234.70	252.80	114.00	601.50
2	205.60	250.00	413.30	868.90
3	120.10	152.80	135.00	407.90
4	177.90	218.70	140.90	537.50
5	77.53	52.45	28.52	158.50
6	68.81	56.33	78.73	203.87
7	62.98	60.60	466.90	590.48
8	71.44	109.00	60.79	241.23
9	169.20	351.80	464.50	985.50
10	58.58	26.02	56.83	141.43
11	56.60	44.59	44.66	145.85
12	57.63	59.04	46.19	162.86
13	97.55	169.50	122.60	389.65



Table X-8. Arias Intensity (m/sec) for  $1 \times 10^{-6}$  Ground Motions (Revised Set) (Continued)

Ground Motion Set	H1	H2	V	Sum
14	62.75	73.01	118.80	254.56
16	23.29	14.90	33.94	72.13

Source: DTN: MO0403AVDSC106.001 [DIRS 168891], file *Dur.zip*.

Table X-9. Arias Intensity (m/sec) for  $1 \times 10^{-6}$  Ground Motions (Original Set)

Ground Motion Set	H1	H2	V	Sum
1	246.40	303.80	481.70	1031.90
2	228.60	188.10	471.20	887.90
3	139.00	22.53	33.45	194.98
4	179.10	176.30	282.30	637.70
5	57.90	80.54	149.50	287.94
6	41.90	159.70	70.89	272.49
7	64.79	58.10	216.60	339.49
8	64.55	35.10	212.60	312.25
9	174.00	38.51	90.62	303.13
10	93.55	185.50	614.60	893.65
11	63.25	73.79	146.10	283.14
12	96.98	40.30	117.10	254.38
13	81.51	131.00	56.29	268.80
14	43.49	386.10	206.20	635.79
16	24.26	41.52	85.64	151.42

Source: DTN: MO0301TMHIS106.001 [DIRS 161868], file *dur.zip*.

Table X-10. Arias Intensity (m/sec) for  $1 \times 10^{-7}$  Ground Motions

Ground Motion Set	H1	H2	V	Sum
1	1128.00	1215.00	819.60	3162.60
2	988.70	1202.00	2972.00	5162.70
3	577.30	734.70	970.60	2282.60
4	855.60	1052.00	1013.00	2920.60
5	372.90	252.20	205.10	830.20
6	330.80	270.80	566.10	1167.70
7	302.60	291.10	3357.00	3950.70
8	343.30	523.60	437.00	1303.90
9	812.90	1691.00	3340.00	5843.90
10	281.80	125.20	408.60	815.60
11	272.10	214.40	321.10	807.60
12	277.20	283.90	332.10	893.20
13	469.00	815.00	881.40	2165.40
14	301.60	350.90	854.40	1506.90
16	112.00	71.63	244.00	427.63

Source: DTN: MO0403AVTMH107.003 [DIRS 168892], file *Dur.zip*.

Table X-11. Power Spectral Density (m<sup>2</sup>/sec) for Preclosure Ground Motions

Ground Motion Set	H1	H2	V	Sum
5×10 <sup>-4</sup>	1287	1427	901	3615
1×10 <sup>-4</sup>	8251	7359	9672	25282

Source: DTNs: MO0407TMHIS104.003 [DIRS 170599] and MO0306SDSAVDTH.000 [DIRS 164033].

Table X-12. Power Spectral Density (m<sup>2</sup>/sec) for 1×10<sup>-5</sup> Ground Motions

Ground Motion Set	H1	H2	V	Sum
1	5594	3024	5896	14514
2	8826	15622	20070	44518
3	5708	34876	175806	216390
4	38760	31748	47600	118108
5	18787	17025	25098	60910
6	35838	2702	68988	107528
7	21865	15657	140657	178179
8	9688	11694	9819	31201
9	16553	91014	88415	195982
10	7799	929	2315	11043
11	10747	14344	29290	54381
12	21548	10193	18214	49955
13	39915	37122	288495	365532
14	50317	2198	27392	79907
16	15940	5339	22348	43627

Source: DTN: MO0402AVDTM105.001 [DIRS 168890].

Table X-13. Power Spectral Density (m<sup>2</sup>/sec) for 1×10<sup>-6</sup> Ground Motions (Revised Set)

Ground Motion Set	H1	H2	V	Sum
1	25137	15521	13552	54210
2	38218	56878	44828	139924
3	21097	127952	271411	420460
4	143472	142743	162474	448689
5	34247	32007	24550	90804
6	92128	19052	94674	205854
7	94514	74336	309918	478768
8	37159	69337	23214	129710
9	62740	389694	168328	620762
10	36474	4801	6386	47661
11	37799	46690	31106	115595
12	108978	78619	75170	262767
13	149590	155633	324138	629361

Table X-13. Power Spectral Density (m<sup>2</sup>/sec) for 1×10<sup>-6</sup> Ground Motions (Revised Set) (Continued)

Ground Motion Set	H1	H2	V	Sum
14	180951	13466	67867	262284
16	75416	26879	46547	148842

Source: DTN: MO0403AVDSC106.001 [DIRS 168891].

Table X-14. Power Spectral Density (m<sup>2</sup>/sec) for 1×10<sup>-6</sup> Ground Motions (Original Set)

Ground Motion Set	H1	H2	V	Sum
1	29936	21251	39224	90411
2	46225	42946	33651	122822
3	26398	15208	30807	72413
4	109976	90561	30803	231340
5	23474	38142	75680	137296
6	42567	53873	37483	133923
7	71944	48153	18740	138837
8	29360	22606	43412	95378
9	56045	34205	22540	112790
10	50542	34874	47166	132582
11	33239	61177	56971	151387
12	122679	40647	85307	248633
13	88844	89105	68762	246711
14	103244	73012	42195	218451
16	56962	52193	58160	167315

Source: DTN: MO0301TMHIS106.001 [DIRS 161868].

Table X-15. Power Spectral Density (m<sup>2</sup>/sec) for 1×10<sup>-7</sup> Ground Motions

Ground Motion Set	H1	H2	V	Sum
1	120827	74606	97450	292883
2	183772	273453	322334	779559
3	101411	615062	1951533	2668006
4	689917	686412	1168272	2544601
5	164712	153940	176528	495180
6	442885	91587	680740	1215212
7	454046	357113	2228184	3039343
8	178537	333143	166899	678579
9	301482	1872982	1210336	3384800
10	175483	23099	45916	244498
11	181710	224448	223650	629808
12	524097	378094	540483	1442674
13	719146	748201	2330664	3798011
14	869763	64725	488013	1422501
16	362583	129224	334650	826457

Source: DTN: MO0403AVTMH107.003 [DIRS 168892].

INTENTIONALLY LEFT BLANK

**APPENDIX Y**  
**VALIDATION OF THE UDEC DRIP SHIELD MODEL**



## VALIDATION OF THE UDEC DRIP SHIELD MODEL

### Y1. INTRODUCTION

The analysis of the rockfall inside the emplacements drifts at Yucca Mountain under different loading conditions (e.g. in situ stress, thermally induced load and seismic load) has been carried out using the two-dimensional, distinct element code UDEC. The rock mass is represented as an assembly of polygonal (Voronoi) blocks of relatively small size (e.g., 0.2 m or 0.3 m) compared to the drift size. It was considered in the initial calculations that the drip shield was rectangular (with dimensions approximately corresponding to the actual drip shield geometry), infinitely stiff, and slaved to free-field movement of the rock mass (i.e., movement unaffected by interaction of the seismic wave with the drift). One of the objectives of the rockfall analysis is to estimate the drip shield loads, either due to dynamic impact during the rockfall or quasi-static load of the caved rock when it reaches equilibrium. If the drip shield is considered to be infinitely rigid, the predicted loads are conservative and sometimes can be excessively large. In order to assess the level of conservatism in predicting loads, the drip shield also is modeled as deformable.

Representation of the deformable drip shield in the two-dimensional model, calculation of the model geometrical and mechanical properties, and model validation are discussed in this appendix.

### Y2. CALCULATION OF GEOMETRICAL AND MECHANICAL PROPERTIES

The complex geometry of the drip shield, as illustrated in Figures Y-1 to Y-4 in different views and sections, is three-dimensional and, as such, was considered in the analysis of its performance under different loads. However, in the UDEC model for rockfall predictions, the drip shield was approximated in two dimensions. A typical longitudinal segment in the middle of the drip shield equal to the spacing of 1071.6 mm between the stiffeners (Figure Y-2) was considered to be representative of the drip shield geometry. The geometry of the cross-sections in the top and the side-wall of the drip shield, as used to calculate the geometrical characteristics, are shown in Figures Y-4 and Y-5, respectively. The drip shield dimensions used for the calculation are listed in Table Y-1. The height of the sidewall stiffener varies between 86.27 mm at the top to 27.69 mm at the base. In the UDEC approximation of the drip shield, it is considered that the height of the stiffener is constant, equal to 86 mm (Figure Y-5). This consideration is conservative, as it results in a stiffer drip shield and, consequently, larger predicted loads. The calculated geometrical characteristics of the two cross-sections are listed in Table Y-2.

The drip shield was represented using a regular grid and triangular, two-dimensional zones. Consequently, each cross-section is rectangular with a given height,  $h$ , and unit width,  $b$ . The heights of the cross-sections were calculated from the moment of inertia, using the following formula:

$$I = \frac{1}{12}bh^3 \quad (\text{Eq. Y-1})$$

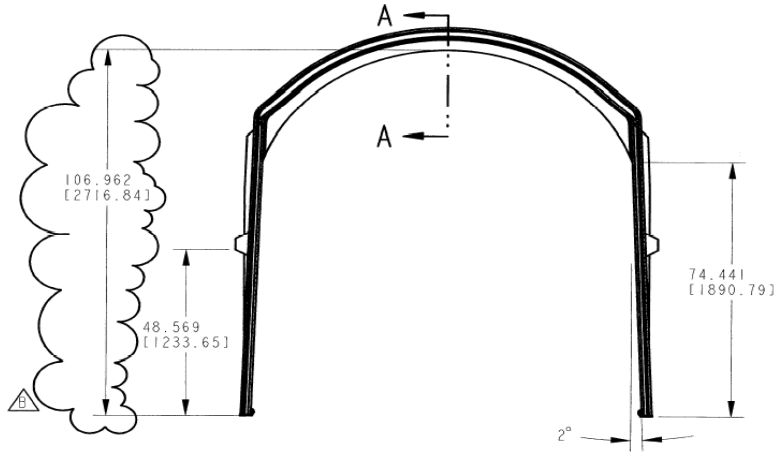
where  $b = 1$ . The calculated heights of the rectangular cross-sections are 6.2 cm and 5.7 cm in the top and the sidewall of the drip shield, respectively. With these dimensions, the UDEC model of the drip shield matches moments of inertia of different cross-sections of the drip shield, but the areas of the cross-sections in the UDEC model are larger. This discrepancy has negligible effect on predicted displacements, because axial deformation of beams can be neglected in bending dominated deformation (as is the case for the drip shield).

In order to correctly model bending of the beams, represented by the two-dimensional, constant-strain, continuum zones, it is necessary to have at least four or five zones per beam thickness. For beam 6.2 cm or 5.7 cm thick, the zone size would be of the order of 1 cm. Such a small zone size in the drift stability model would result in a number of numerical problems and very long calculation times (particularly for dynamic simulations). The product  $EI$  is the measure of beam stiffness, where  $E$  is the Young's modulus. To overcome the problem of small zone size, the heights of the cross-sections and Young's modulus were rescaled, maintaining the product  $EI$  constant, according to the following formula:

$$\bar{E} = E \left( \frac{h}{\bar{h}} \right)^3 \quad (\text{Eq. Y-2})$$

where  $\bar{E}$  and  $\bar{h}$  are rescaled values of Young's modulus and height of the cross-section, respectively. Different parts of the drip shield are designed to be constructed from titanium grades 7 (Ti-7) and 24. Young's moduli at 150°C for Ti-7 and Ti-24 are  $E = 101$  GPa and  $E = 108$  GPa, respectively (BSC 2004 [DIRS 168993]). The Poisson's ratio is 0.32. It was considered conservatively (with small overall error) that the entire drip shield was built from Ti-24 (i.e., a Young's modulus of 108 GPa). After rescaling according to Equation Y-2, a Young's modulus of 3.22 GPa and cross-section heights of 20 cm and 18.3 cm in the top and the sidewall, respectively, were used for the drip shield in the UDEC simulations of the emplacement drift stability. Geometry of the drip shield, as idealized in the UDEC model, is shown in Figure Y-6. Because of the relatively large thickness of the drip shield in the UDEC model, compared to its height and span, the neutral axis of the UDEC representation was selected to coincide with the outline of the actual drip shield geometry. (The geometry of the drip shield is such that neutral axis is very close to the outline.)

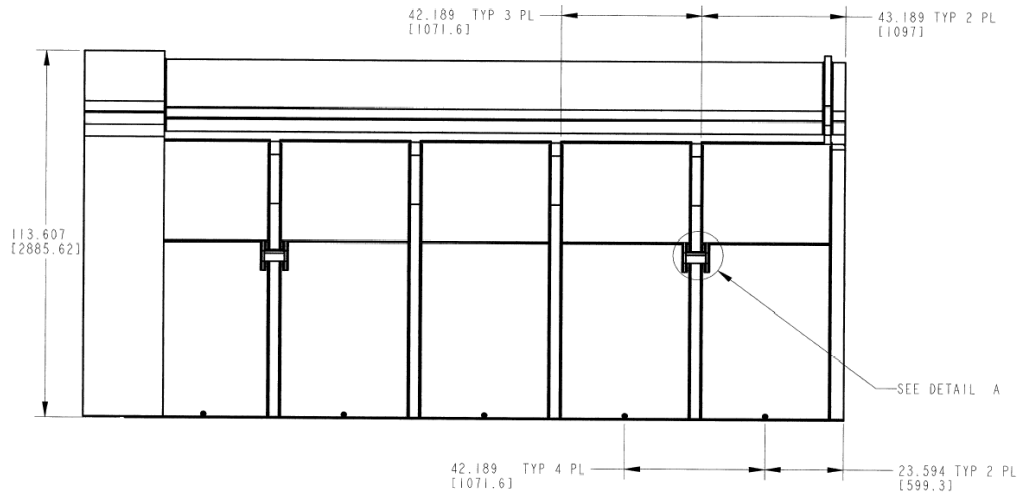




Source: BSC 2004 [DIRS 168993], Attachment I, p. I-2.

NOTE: Dimensions are in inches [millimeters].

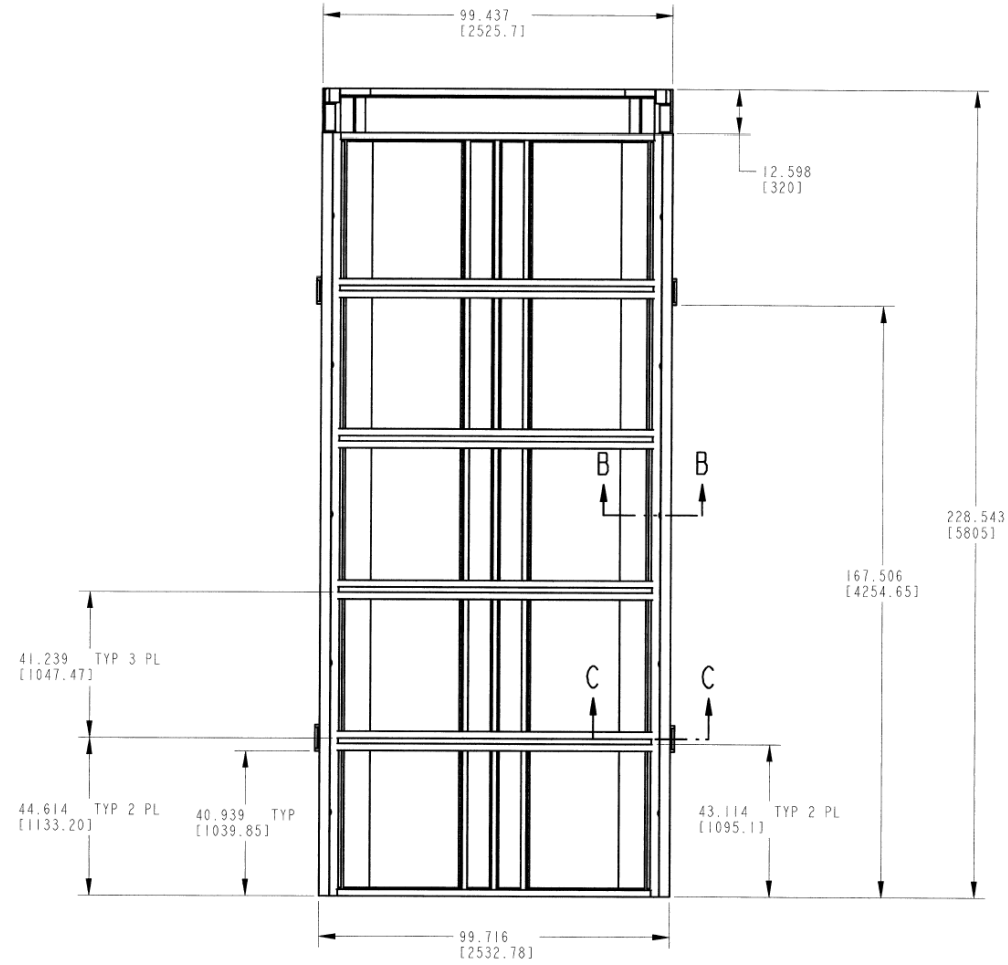
Figure Y-1. Geometry of the Drip Shield: Cross-Section



Source: BSC 2004 [DIRS 168993], Attachment I, p. I-2.

NOTE: Dimensions are in inches [millimeters].

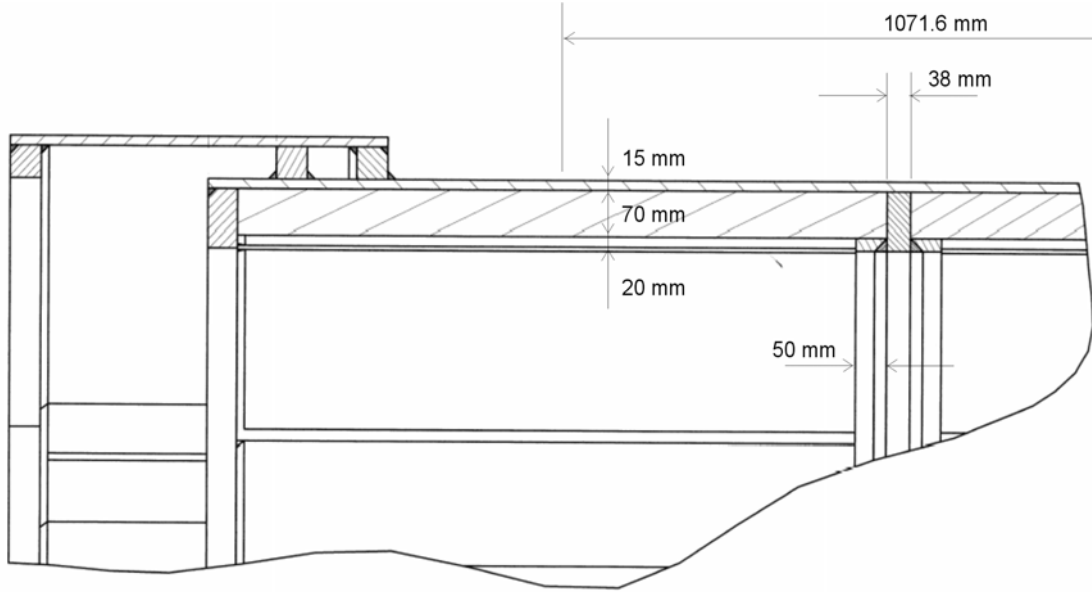
Figure Y-2. Geometry of the Drip Shield: Side View



Source: BSC 2004 [DIRS 168993], Attachment I, p. I-2.

NOTE: Dimensions are in inches [millimeters].

Figure Y-3. Geometry of the Drip Shield: Plane View



Source: BSC 2004 [DIRS 168993], Attachment I, p. I-2.

Figure Y-4. Section A-A through the Roof of the Drip Shield Indicated in Figure Y-1

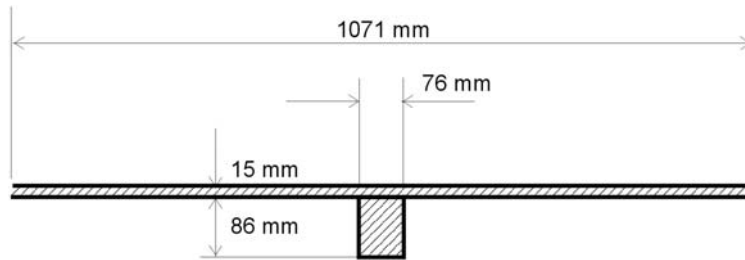


Figure Y-5. Horizontal Section Through the Wall of the Drip Shield

Table Y-1. Drip Shield Dimensions

Nominal Length	Nominal width	Nominal Height
5805 mm	2532.78 mm	2885.62 mm
228.543 in	99.716 in	113.607 in

Source: BSC 2004 [DIRS 169220], Table 1.

Table Y-2. Geometrical Characteristic of Cross-Sections

	Top	Side-wall
I [cm <sup>4</sup> ]	2156.4	1617.8
A [cm <sup>2</sup> ]	214.8	226.0

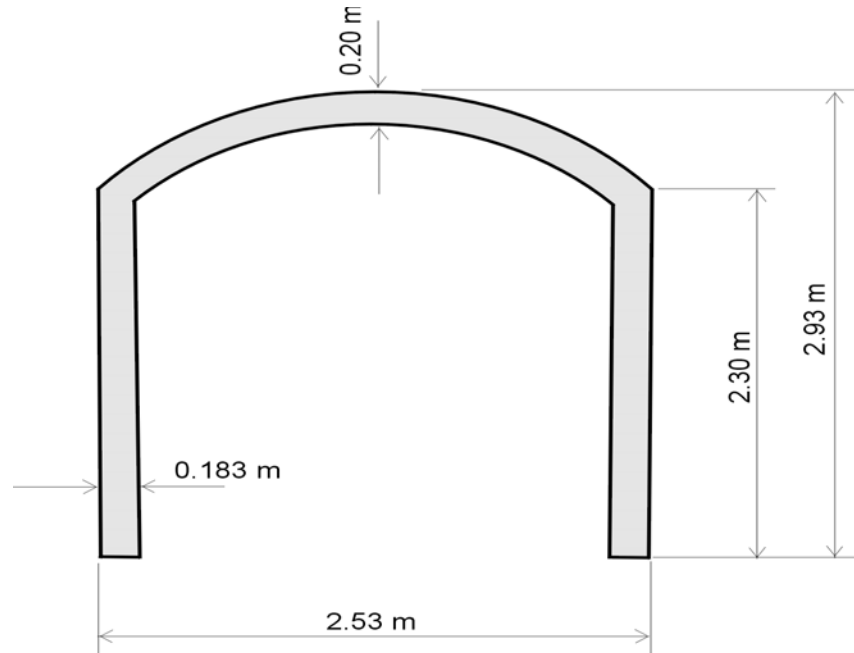


Figure Y-6. Geometry of the Drip Shield as Idealized in the UDEC Model

### Y3. VALIDATION OF THE DRIP SHIELD MODEL

In order to demonstrate that the UDEC model of the drip shield correctly represents its deformation, two tests were carried out. In the first test, the UDEC results were compared with FLAC results obtained using FLAC structural element logic. The actual geometrical properties (shown in Table Y-1) and Young's modulus were used in the FLAC simulations. Because of the plane-strain deformation of the drip shield and the plane-stress formulation of the structural element logic in FLAC, the Young's modulus in the FLAC model was modified according to the following formula:

$$E' = \frac{E}{1-\nu^2} \quad (\text{Eq. Y-3})$$

Two loading cases were considered. The results for loading case 1 (illustrated in Figure Y-7), the vertical concentrated force acting in the middle of the drip shield, are shown in Figures Y-8 to Y-12. The maximum vertical displacement calculated in UDEC is 6.31 mm (Figure Y-10), compared to 6.05 mm calculated in FLAC (Figure Y-12). The error is 4 percent. The results for loading case 2 (illustrated in Figure Y-13), the horizontal concentrated force acting at the top of the drip shield sidewall, are shown in Figures Y-14 to Y-18. The horizontal vertical displacement calculated in UDEC is 1.60 cm (Figure Y-16), compared to 1.67 cm calculated in FLAC (Figure Y-18). The error is 4 percent in this case as well. In the second test, the UDEC results were compared with results obtained using the code LS-DYNA, in which the drip shield was modeled as a three-dimensional body. For loading case 3 (illustrated in Figure Y-19), the uniformly distributed load on top of the drip shield, LS-DYNA predicts vertical displacement in the middle of the top of the drip shield of 2.4 cm. The UDEC results are shown in Figures Y-20

to Y-22. The maximum vertical displacement in the middle of the drip shield is 2.4 cm (Figure Y-22).

#### Y4. CONCLUSIONS

The deformable drip shield is represented in the two-dimensional UDEC model using continuum, constant-strain zones that form beams of constant thickness. To optimize UDEC simulations, the thickness and Young's modulus of beams were rescaled to maintain their stiffness.

It is demonstrated that the simplified UDEC model correctly represents deformation of the drip shield.

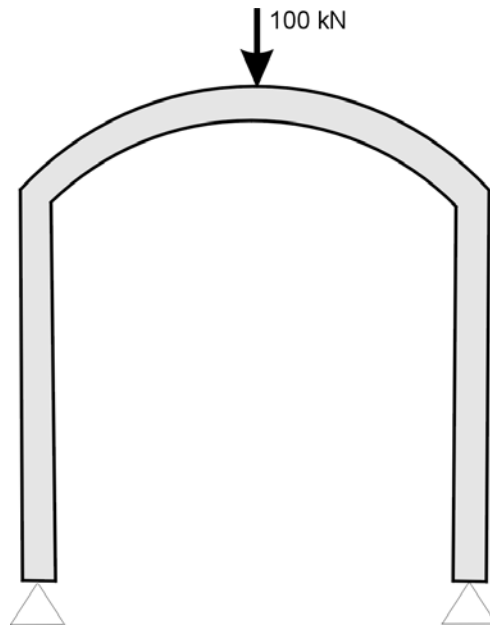


Figure Y-7. Loading Case 1

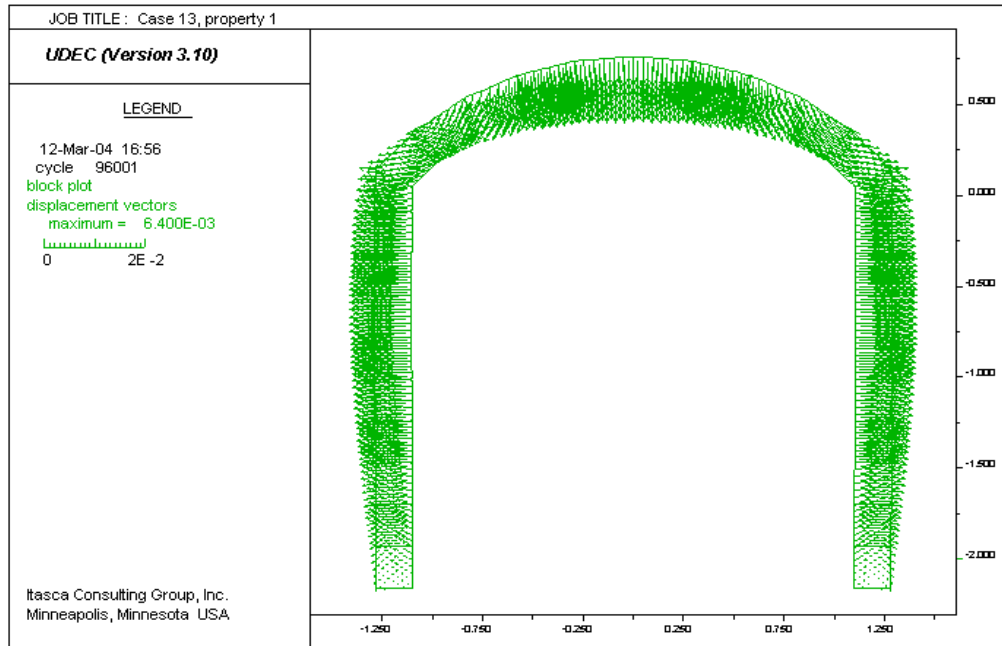
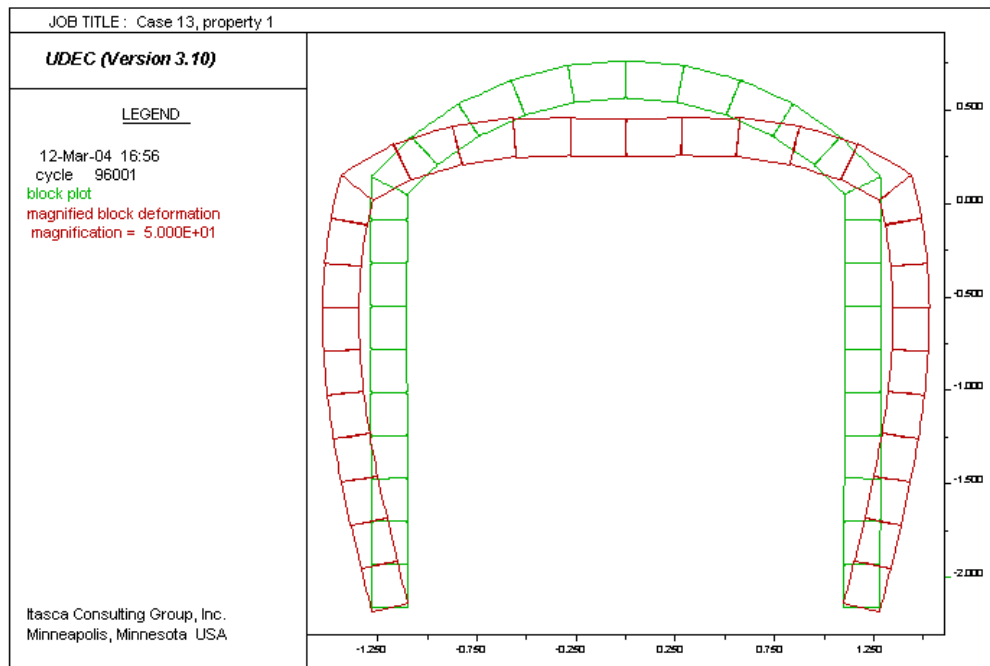


Figure Y-8. Deformation (m) of the Drip Shield for Loading Case 1



NOTE: Deformation magnified 50 times.

Figure Y-9. Original and Deformed Configuration of the Drip Shield for Loading Case 1

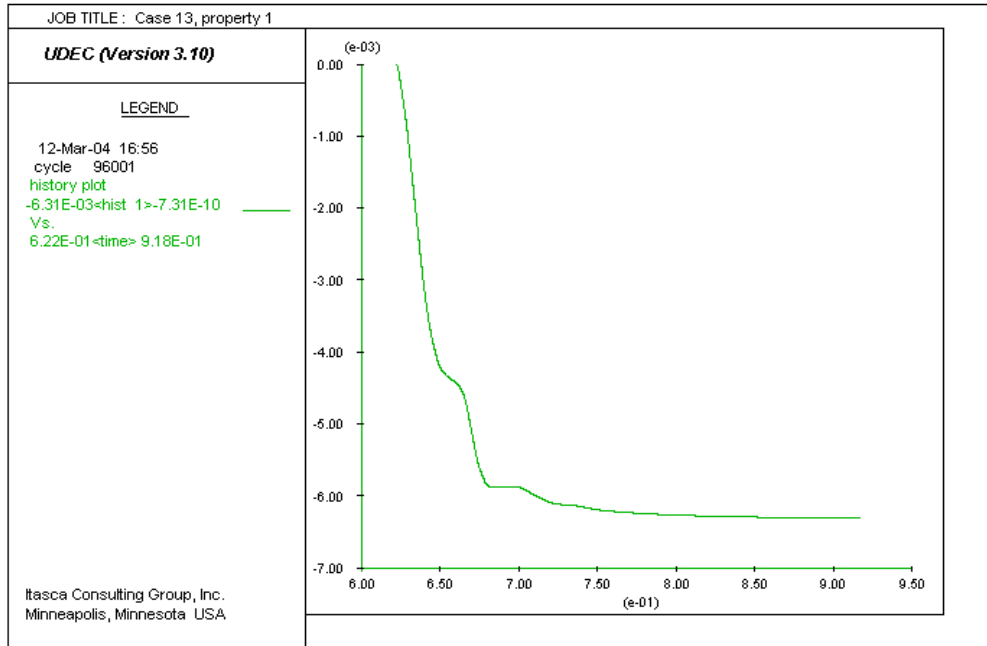


Figure Y-10. History of Vertical Displacement (m) of a Point on the Drip Shield Where Vertical Concentrated Force is Applied for Loading Case 1

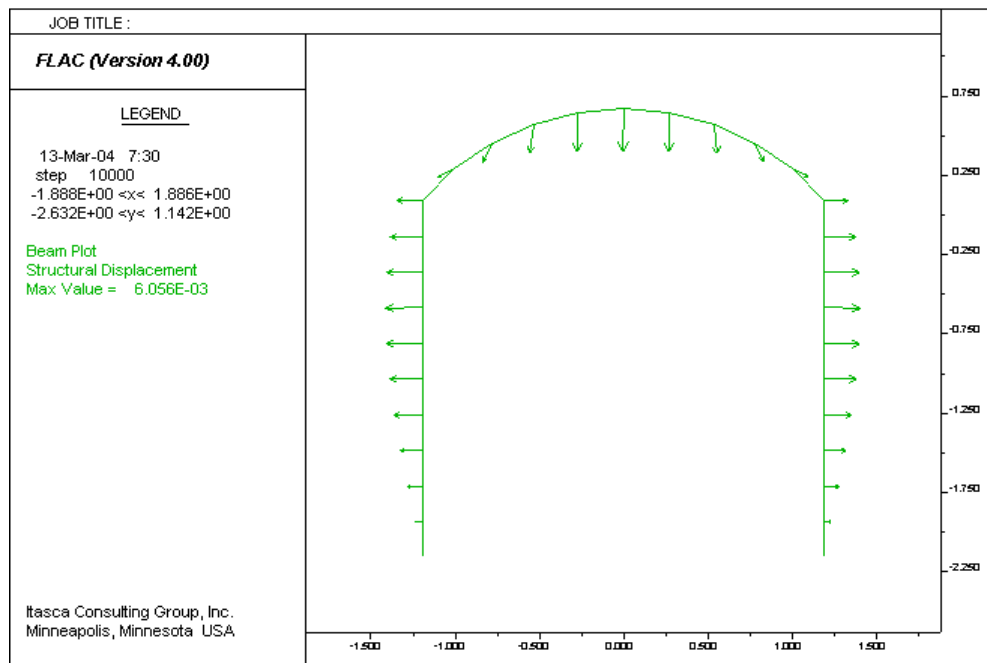


Figure Y-11. Deformation of FLAC Structure Elements for Loading Case 1

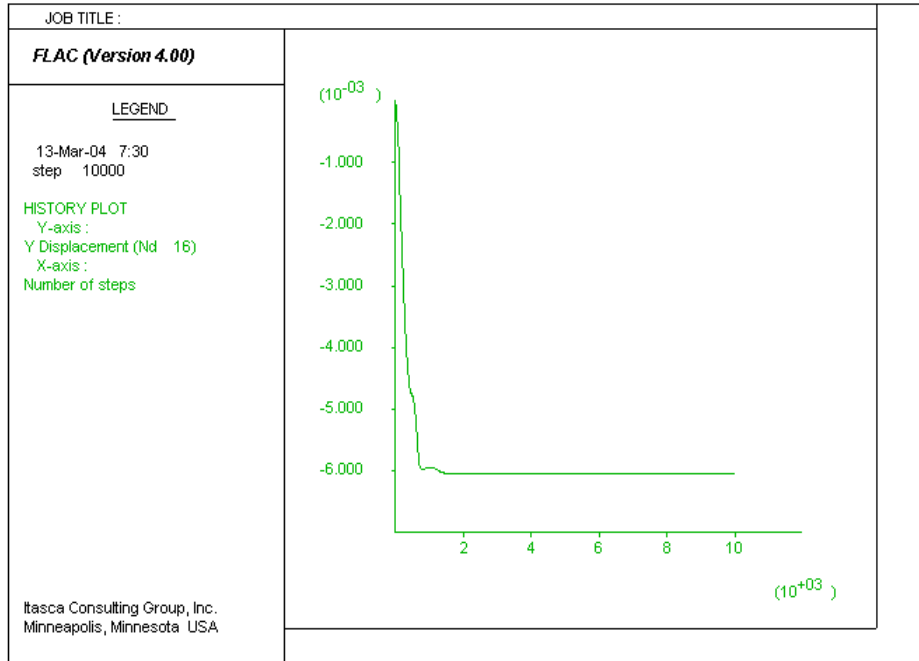


Figure Y-12. History of Vertical Displacement (m) of a Point on the Drip Shield Where Vertical Concentrated Force is Applied for Loading Case 1 Calculated Using FLAC Structural Elements

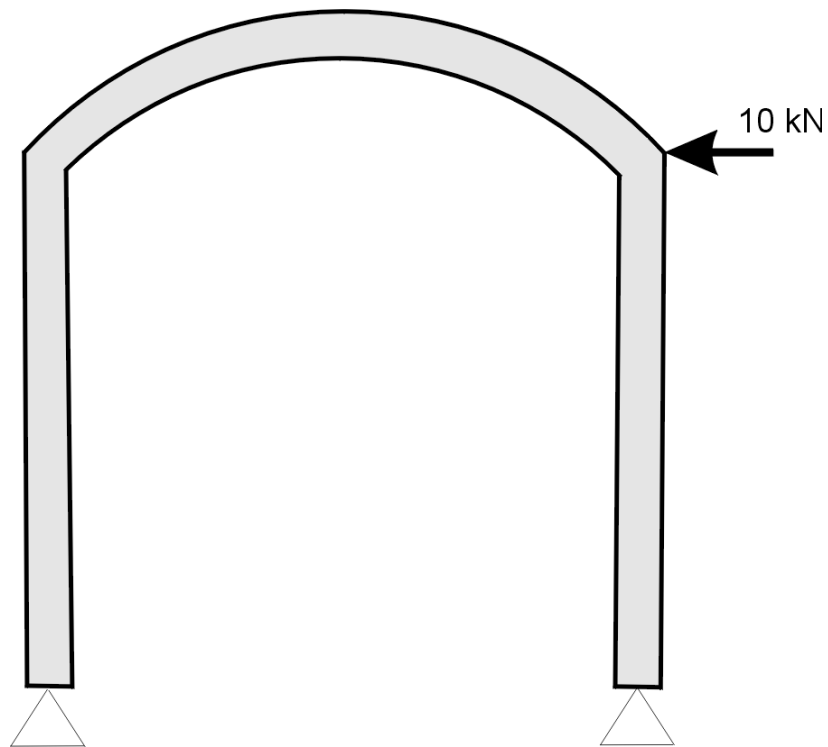


Figure Y-13. Loading Case 2



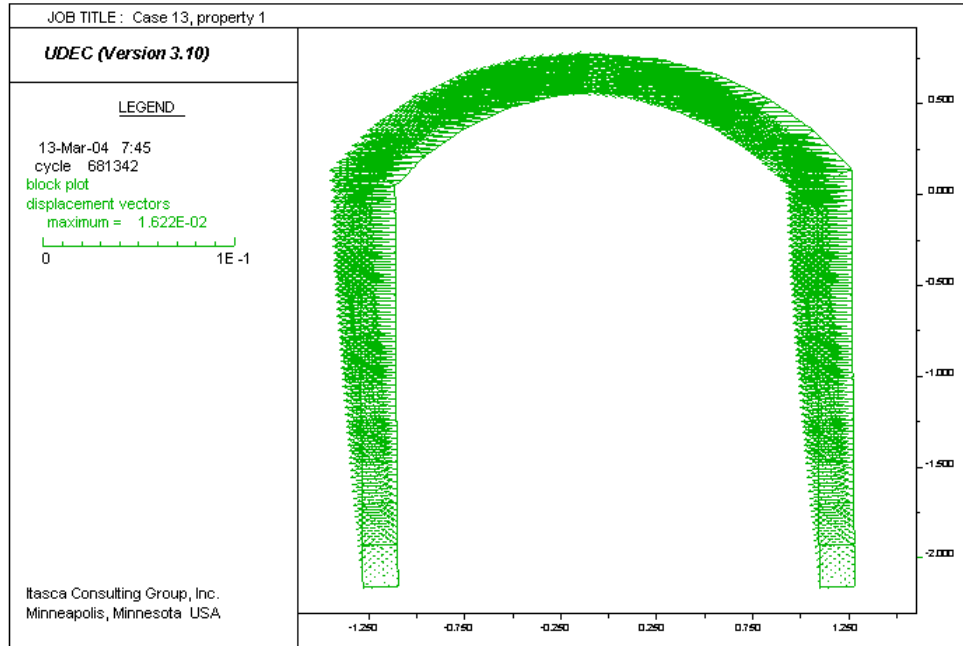
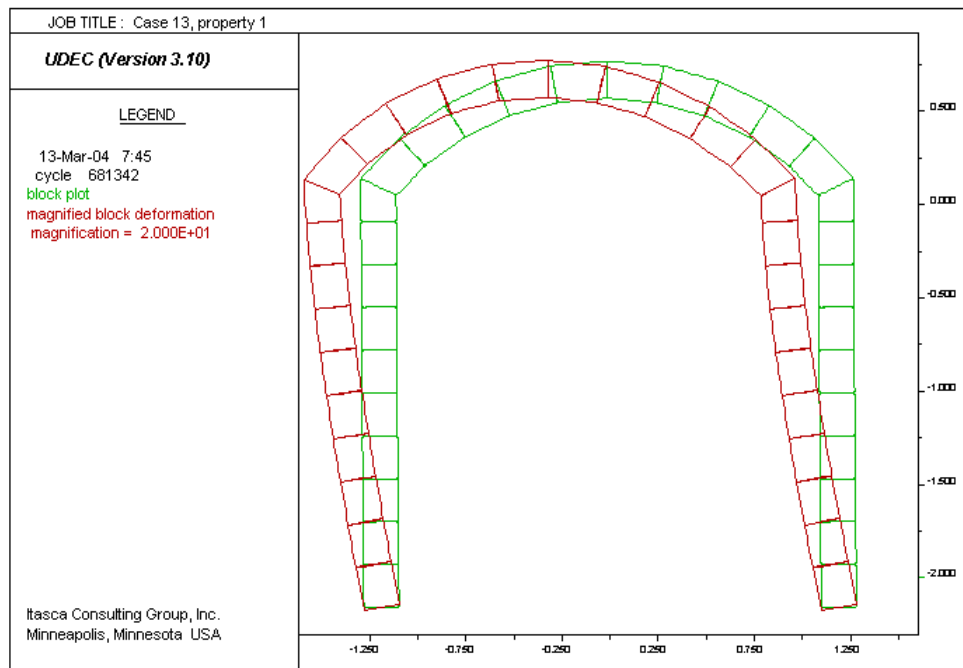


Figure Y-14. Deformation (m) of the Drip Shield for Loading Case 2



NOTE: Deformation magnified 20 times.

Figure Y-15. Original and Deformed Configuration of the Drip Shield for Loading Case 2

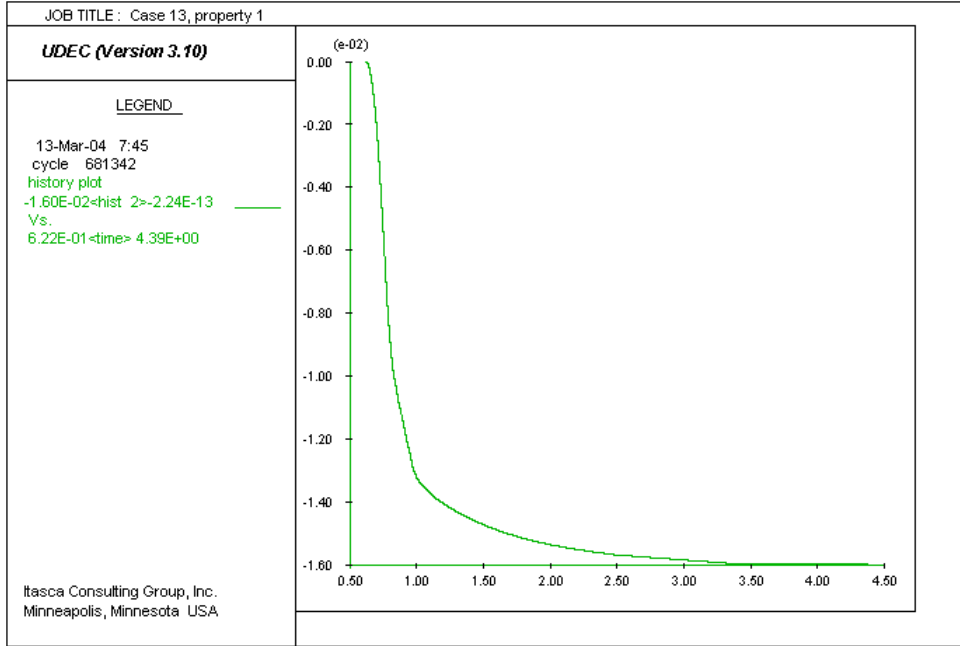


Figure Y-16. History of Vertical Displacement (m) of a Point on the Drip Shield Where Vertical Concentrated Force is Applied for Loading Case 2

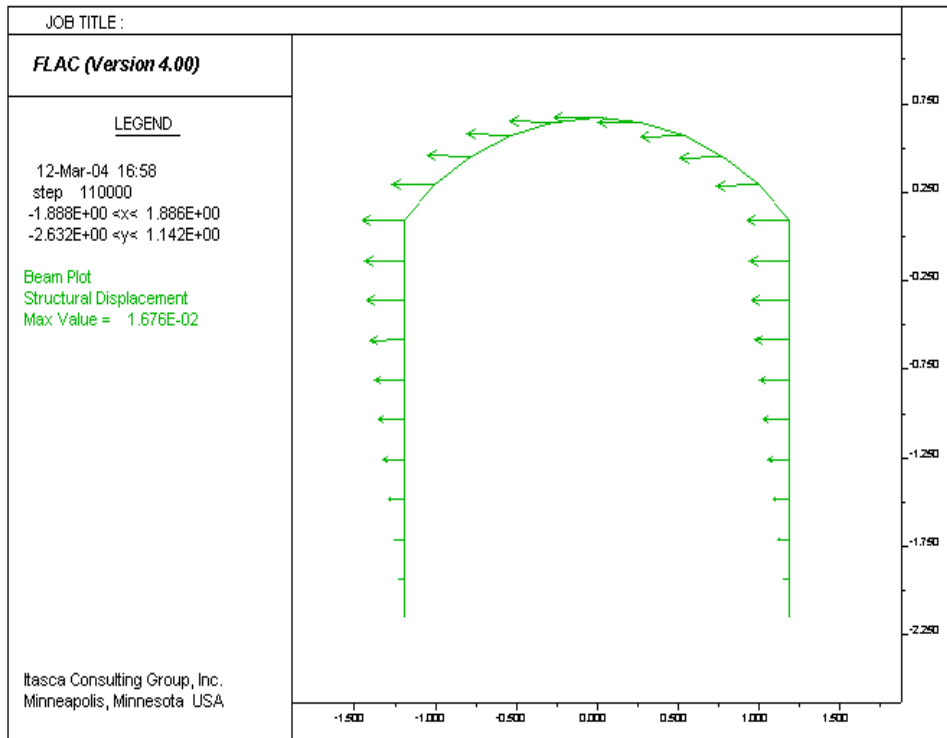


Figure Y-17. Deformation of FLAC Structure Elements for Loading Case 2

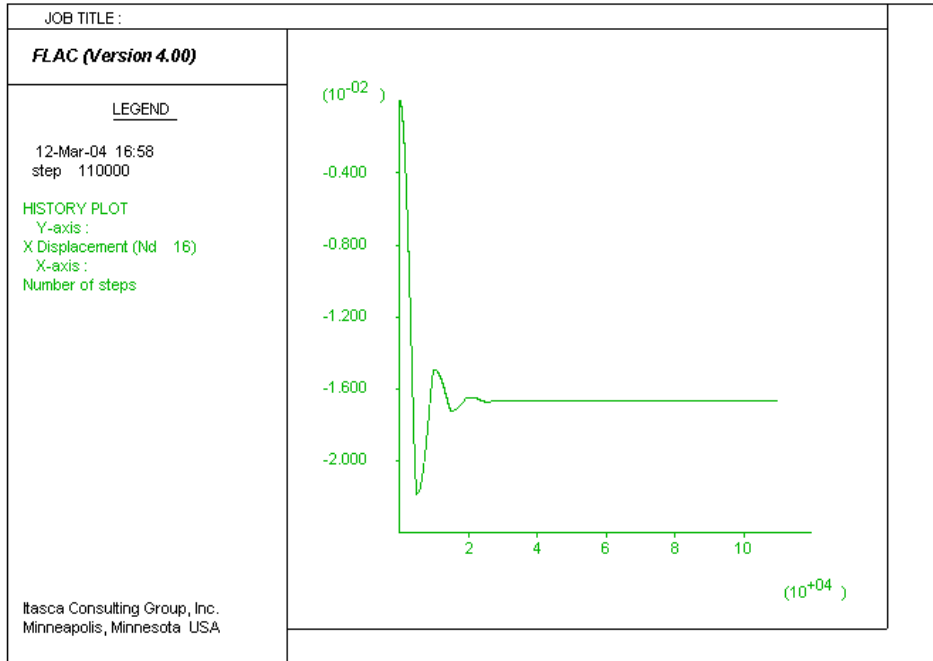


Figure Y-18. History of Vertical Displacement (m) of a Point on the Drip Shield Where Vertical Concentrated Force is Applied for Loading Case 2 Calculated Using FLAC Structural Elements

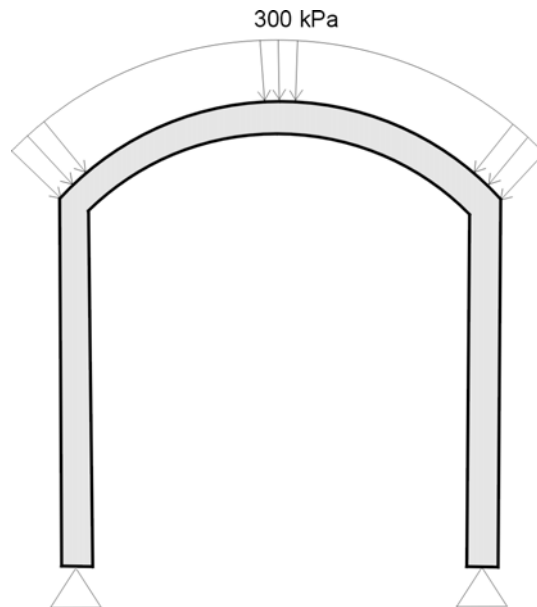


Figure Y-19. Loading Case 3

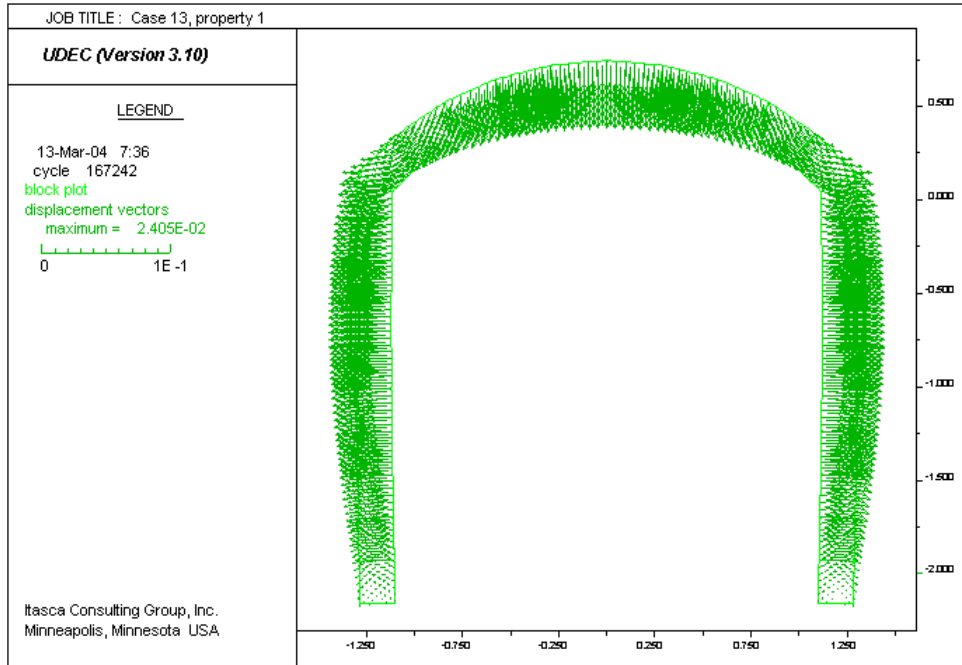
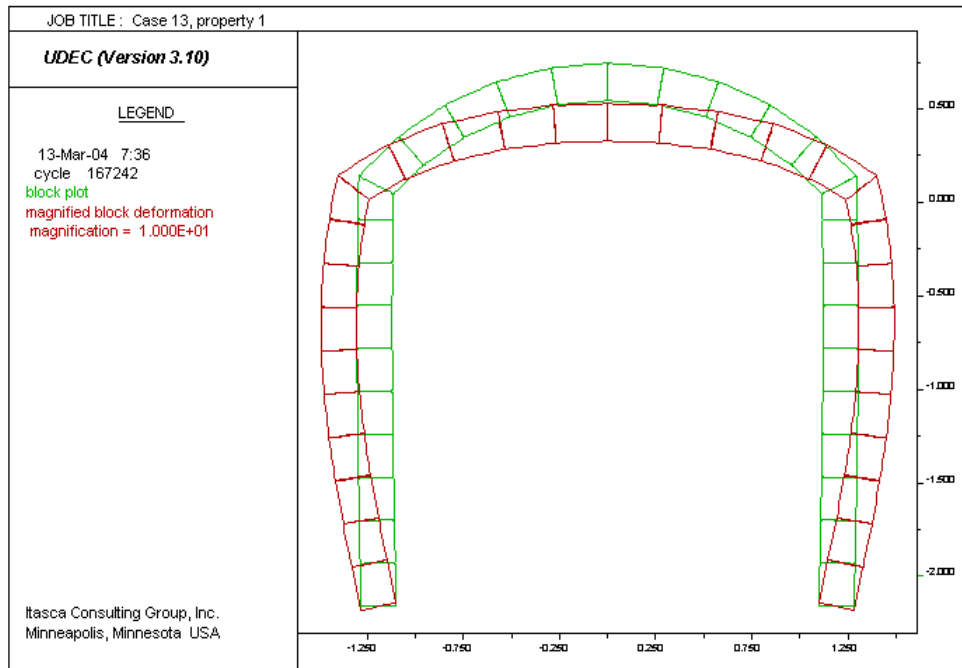


Figure Y-20. Deformation (m) of the Drip Shield for Loading Case 3



NOTE: Deformation magnified 10 times.

Figure Y-21. Original and Deformed Configuration of the Drip Shield for Loading Case 3

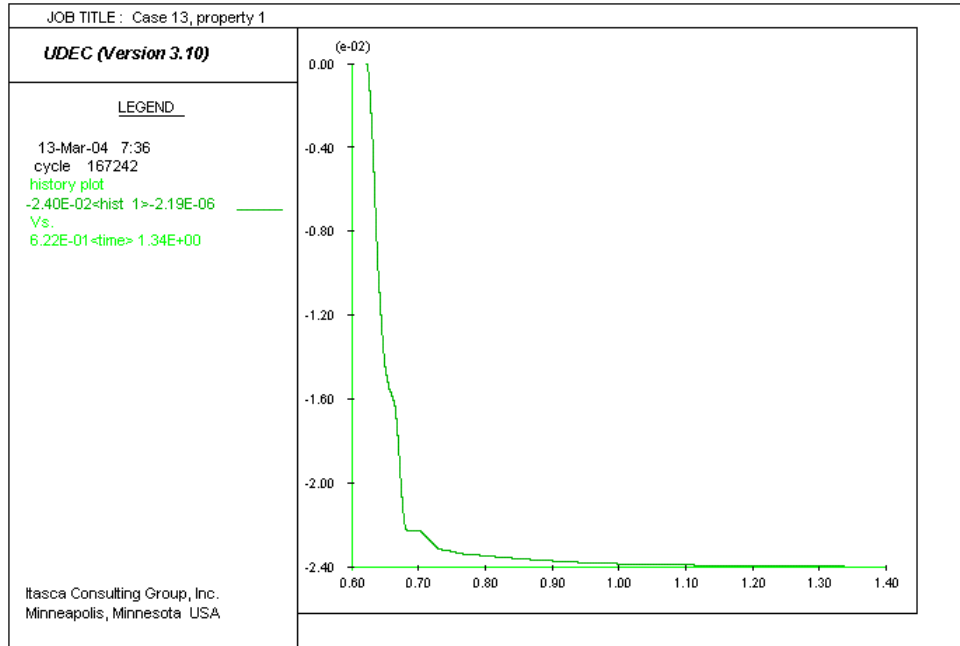


Figure Y-22. History of Vertical Displacement (m) of a Point on the Drip Shield Where Vertical Concentrated Force is Applied for Loading Case 3

INTENTIONALLY LEFT BLANK